Università degli Studi di Pavia

Dipartimento di Scienze della Terra e dell'Ambiente

SCUOLA DI ALTA FORMAZIONE DOTTORALE

MACRO-AREA SCIENZE E TECNOLOGIE

DOTTORATO DI RICERCA IN SCIENZE DELLA TERRA E DELL'AMBIENTE

Pierre Müller

Physical stratigraphy, heterogeneity development and provenance evolution of the sand-rich pre-collisional Bordighera turbidite system

Anno Accademico 2017-2018
Ciclo XXX

Coordinatore
Prof. Roberto Sacchi

Tutor
Prof. Andrea Di Giulio

Co-tutor
Dott. Marco Pattaci

Abstract

The Upper Cretaceous San Remo Unit of the Western Ligurian subduction flysch complex represents a trench fill that comprises a basal complex (San Bartolomeo Fm.) and two thick turbiditic sequences, a low-efficiency siliciclastic turbidite system (Bordighera Sandstones) that interfingers with a calcareous turbiditic sequence (San Remo Helminthoid Flysch) which becomes increasingly abundant towards the lateral and distal domains. In order to evaluate the outcrop analog potential of the coarse-grained, sand-rich axial fan, the Bordighera Sandstones have been investigated by detailed facies analysis. Main emphasis was placed on the quantification of inter-sandbody heterogeneity due to hybrid event bed (HEB) development. In the context of complex tectonic deformation and partly limited lateral outcrop exposure, the utilization of sedimentological metrics (e.g. amalgamation ratios, sandstone-mudstone-ratios, grain size distribution trends and facies proportions) provided an effective tool for the determination of depositional environments. Basin-scale statistical analyses of horizontal and vertical trends in facies distributions furthermore facilitated the quantitative assessment and spatial allocation of facies heterogeneity distribution along the sand fairway.

Along a downstream transect, three main depositional domains - marked by strikingly contrasting dominant lithofacies proportions – have been differentiated. The proximal domain, interpreted as representing low-sinuosity channel fills, resembles homogeneous successions of massive clean sands. A medial domain of short basin-ward extent exhibits composite lenticular and tabular bed geometries. This medial realm is interpreted to represent the transition in between channelized and unchannelized facies associations and is defined by the presence of scour features. It comprises minor portions of bed types that account for facies heterogeneity. By contrast, the distal domain, dominated by laterally extensive, clustered sheet-like sandstone bodies, is interpreted as representing terminal lobes. These sheet sands are dominated by the presence of transitional flow deposits such as mudclast-rich beds and hybrid event beds. A close environmental relationship between meso-scale scouring and rapid flow transformation could be documented that apparently controlled the observed shift in facies proportions. Remarkably, the widespread occurrence of HEBs within axial zones of the preserved elongated sand fairway contrasts models that predict HEB distribution to be characteristic of outer fan environments. Moreover, the atypical nature of a low-efficiency turbidite system (i.e. defined by low initial mud concentrations) being highly prone to HEB-related heterogeneity is interpreted as the result of enhanced availability of cohesive mud due to the heterotopic intercalations of the calcareous Helminthoid Flysch.

As the geodynamic evolution of the Western Tethyan realm during the incipient stages of Alpine convergence remains a matter of controversial debate, the multi-proxy sediment provenance analysis of the two terrigenous members, the basal complex and the coarse-clastic Bordighera Sandstones, provides insights towards a better understanding of the complex pre-collisional evolution of the Piemont-Ligurian domain and the bounding continental margins. Petrographic analysis characterizes the basal complex succession as texturally mature quartz-rich sandstones. By contrast, the conformably superimposing coarse-grained Bordighera Sandstones represent texturally and compositionally immature first-cycle arkoses. This observation suggests a gradual provenance evolution from a stable craton or transitional continental provenance setting towards a scenario defined by rapidly uplifted bedrock (granitoid plutons and low-grade metamorphic geobodies).

New geochronological data (U-Pb detrital zircon ages) reveal peaks in the detrital spectra which are practically compatible with well-documented magmatic and metamorphic pulses that affected the Southern Variscides. Potential provenance terranes comprise microcontinental fragments that represented the hyperextended Western Tethys margins. Quantitative confrontation of detrital age clusters with available literature crystallization age datasets of candidate source areas suggests the strong affinity of the clastic detritus towards the Paleo-European margin, documenting that the lower plate (i.e. the passive margin) provided the major sand supply into the subduction trench at the onset of Alpine convergence.

Riassunto

L'unità di San Remo del Cretaceo superiore appartenente al complesso di flysch subduttivi delle Liguridi occidentali, rappresenta il riempimento di una fossa che comprende un compleso basale (Fm. di San Bartolomeo) e due spesse sequenze torbiditiche, rappersentate da un sistema a bassa efficienza silicoclastico (Arenarie di Bordighera) che si interdigita con una sequenza torbiditica calcarea (Flysch ad Elmintoidi di San Remo) che, attraverso il dominio laterale e distale, diventa progressivamente più abbondante. Per poter valutare le potenziali analogie degli affioramenti della conoide altamente sabbiosa e di granulometria grossolana delle Arenarie di Bordighera, queste ultime sono state studiate con dettagliate analisi di facies. Molta enfasi è stata posta alla quantificazione delle eterogeneità "inter-sandbody" dovute allo sviluppo di hybrid event beds (HEBs). In una situazione di complesse deformazioni tettoniche e con una parziale esposizione laterale degli affioramenti, l'utilizzo di parametri sedimentologiche (tasso di amalgamazione, rapporto arenaria-argillite, trend di distribuzione delle granulometrie e proporzioni delle facies) forniscono uno strumento efficiente per determinare l'ambiente di deposizione. Inoltre, analisi statistiche dei trends di distribuzione orizzontali e verticali su scala di bacino hanno facilitato la valutazione quantitativa e posizionale nella distribuzione delle eterogeneità attraverso i corpi sabbiosi.

Lungo il transetto lungo corrente, tre domini deposizionali evidenziati in maniera sorprendente dalle proporzioni delle litofacies sono stati differenziati. Il dominio prossimale, interpretato come rappresentativo di un riempimento di canali a bassa sinuosità, è composto da successioni omogenee e massicce di sabbia pulita. Un dominio mediale carratterizzato da geometrie lenticolari e tabulari di breve estensione e minori proporzioni di sabbie argillose. Questo dominio è interpretato come la rappresentazione della transizione tra associazioni di facies canalizzate e non canalizzate. Contrariamente al precedente, il dominio distale è dominato da gruppi di corpi di arenaria laminati è intrpretato come una rappresentazione dei lobi terminali. Questi orizzonti sabbiosi tabulari ("sheet sands") sono dominati da depositi di flussi transizionale quali livelli ricchi in clasti di argilla e HEB. Una relazione stretta tra incisioni a media scala e trasformazione di flussi rapidi può essere documentato dal cambiamento delle proporzioni delle facies osservato. La larga diffusione delle HEB nelle zone preservate di depositi allungati dell'asse centrale contrasta i modelli che definiscono gli HEB come peculiari dell'ambiente della conoide esterna. Inoltre, la atipicità di un sistema torbiditico a bassa efficienza (i.e. porzione di argille inizialmente ridotta) che diventa molto incline alle etereogeneità correlate agli HEB è interpretata come il risultato di una crescente disponibilità di fango coesivo dovuto alle intercalazioni eterotopiche con il Flysch ad Elmintoidi.

Visto il dibattito ancora aperto riguardo all'evoluzione geodinamica del bacino della Tetide Occidentale durante le prime fasi della convergenza Alpina, l'analisi multi-proxy della provenienza dei sedimenti dei due membri terrigeni - il complesso basale e le Arenarie di Bordighera - fornisce spunti per una miglior comprensione della complessa evoluzione pre-collisionale del dominio Ligure-Piemontese e i circostanti margini continentali. Analisi petrografiche identificano il complesso basale come un'arenaria tessituralmete matura e ricca in quarzo. La componente grossolana delle Arenarie di Bordighera, sovraimposte in continuità a quest'ultime rappresentano, invece, a livello tessiturale e composizionale delle arcose tessituralmente e composizionalmente immature. Queste osservazioni suggeriscono la graduale evoluzione della provenienza da un cratone stabile o transizionale verso un basamento in rapida esumazione (plutoni granitici e unità metamorfiche di basso grado).

Nuovi dati geocronologici (datazioni U-Pb nei zirconi detritici) rivelano picchi di distribuzione nei detriti che sono compatibili con le ben documentate pulsazioni magmatiche e metamorfiche che hanno colpito il Sud-Varisico. I potenziali territori di provenienza comprendono frammenti microcontinentali che rappresentano il margine iperesteso della Tetide Occidentale. Raffronti quantitativi tra i cluster di età dei detriti e i datatasets disponibili in letteratura delle età delle aree sorgenti suggeriscono una forte affinità con il marine Paleo-Europeo, mostrando che la placca inferiore (i.e. il margine passivo) debba funzionare come sorgente principale di detrito nella fossa subduzione durante le fasi iniziali della convergenza Alpina.

Ich hatte die Lehre gehört; sie gegen Ungläubige verteidigt
und unter argwöhnischen Prüfungen an strenge Richter zurückgegeben.
Und nun mußte ich in einem unbewachten Augenblick gewahr werden,
daß ich nichts gelernt hatte, rein gar nichts;
daß mir dies Fundament aller irdischen Weltanschauung
nicht zum eigenen inneren Besitz geworden war.
Niemals bis zu diesem einmaligen, unvergeßlichen Augenblick,
da ich es zum ersten Mal mit eigenen Augen sah
und also zum ersten und endgültigen Male zum Geologen wurde:
Die Erde lebt!

HANS CLOOS

Gespräch mit der Erde

These teachings I had heard and believed. I had defended them against the incredulous and recited them before stern judges in searching examinations.

But now, in an unguarded moment, I had to realize that I had learned nothing at all. Because that concept of the physical world had not become a true possession of my own - not until this unique and unforgettable moment when, by seeing it with my own eyes, for the first time and forever I became a geologist:

The earth is alive!

HANS CLOOS

Conversations with the Earth

Acknowledgements

I would not be writing these lines without significant contributions of people who borrowed their time, offered parts of their experience and provided the inspiration needed at the very moment. Above all, I would like to thank my main supervisors, Prof. Andrea Di Giulio and Dr. Marco Patacci, which made this project a very interesting and broadening experience. Andrea Di Giulio provided an admirable style of professional guidance that is difficult to describe: He *da capo* personified the perfect balance between a pointing in the right direction at the right moment and at the same time giving me the liberty to introduce and implement my own ideas in a truly stimulating research environment. Not only did he give me the unique opportunity of working on a such beautiful turbidite system that has drawn so little sedimentological interest so far, but he also enabled me to go on fantastic field trips (which he always justified with explanations like "if it helps you to become a better geologist"). Equally important, he supported me as a foreign student in a strange country whenever help was needed, and this form of support is highly appreciated. Marco Patacci provided indispensable assistance by immediately being available at any given time (to be more precise, within the shortest delay imaginable) for any demand that suddenly came up, from data plotting to proof reading and from to organizing things in proper ways. Moreover, he showed me the ropes of getting data robust and meaningful after acquiring enormous amounts of data in the field, and, importantly, he advised me on how to bring things in shape afterwards. Probably the most important form of help Marco provided was the patience he brought up in correcting all the mistakes I made along the way, and I am thankful for that. I know that I learned a lot from the both of you and I want to express my sincere gratitude for that.

Prof. Ausonio Ronchi is thanked for final proofreading and sedimentological discussions all along the way. Dr. Antonio Langone (CNR Pavia) introduced me into the world of geochronology, and my thanks goes out for stimulating discussions, his endless help with isotopic age tables and of course for letting me operate on machines (Made in Germany, eh?) that are not available at your local *Brico*. Dr. Matteo Maino´s assistance is highly acknowledged. Besides from his ever-steady availability for stimulating discussions, he importantly contributed to this work with more than just a crash course into Alpine geology, as he gave me a thorough introduction into the geology of pre-Alpine basement rocks of the Western Alps. Dr. Alessio Sanfilippo helped with numerous discussions and answers about geochemistry. In addition, I could draw great inspiration from the beautiful excursions he took me out to where I learned a lot (and boy did we eat good). All the people mentioned in this paragraph to this day encourage me to become a better geologist, and I am happy about this.

Many thanks are due to Gaia Militello and Laura Gaggero from University of Genova as well as to Michela Idiomi and Andrea Ortenzi from ENI S.p.A. San Donato Milanese, for assisting with zircon cathodoluminescence imaging. Prof. Massimiliano Zattin (Uni Padova) gently aided with zircon separations. Financial support for the PhD project was provided by the University of Pavia research grand. Generous contributions from the TRG sponsors consortium made the extensive field work and my participation in meetings and conferences possible. Gianna, Gianni and

Alberto Orengo are warmly acknowledged for providing their place at Badalucco as a refuge during fieldwork in the Valle Argentina. The staff of the Rifugio Ca' da Cardella in Mendatica is acknowledged for their hospitality as well. The suggestions of external researchers that reviewed my work helped to improve this thesis a lot. These people include Dr. Thomas Hadlari, Prof. Salvatore Milli, Dr. Viktor Terlaky and Prof. Massimiliano Zattin and I want to sincerely thank all of them.

Arriving in an unknown place at the beginning was certainly not an easy task. People I became friends with helped me a lot, and when Pavia was just Pavia, you guys allowed me to escape to some of the most beautiful and strangest places I have ever been to. From the Monte Rosa screes in Macugnaga (Simone Boxler and family, and all the other nice people I met) down to Pieve Vergonte in the Valle del Toce (Luca "Dudee" Blardone, his family and the crazy Ossolani folks), your nice hospitality could never be forgotten! I had the chance of assisting Riccardo Teloni during the field work around Marradi, and apart from seeing a such classic turbidite succession, I truly enjoyed the culture, the food and of course the friendship, so thank you for that! I shared nice moments with numerous fellow students from the DSTA Pavia, this is a shout out, so you better know who you are.

I want to thank my family from the bottom of my heart. Their continuous support and encouragement constitute the cornerstone for all the things I have achieved so far. This thesis is dedicated to you! Essentially the inner circle, my parents and everyone close, jumped in every time when whatever form of help was needed, no matter what distance separated us, and I am truly happy to have a such bond around me. To Tricia: Once again you showed me how much I can rely on you. I know the sacrifices you made just to be there for us, and my words cannot express what this means to me. This here is another step towards our future, and you know that I am truly excited for what is coming.

Finally, many thanks to the thesis committee, Prof. Fabrizio Berra and Prof. Fabrizio Berra, for finding the time to read this thesis.

Table of contents

List of tables

List of figures

Chapter 1: Introduction and purposes of this study

Deep-water sandstones constitute prolific hydrocarbon reservoirs, and the exploration of deep–water reservoirs along continental margins has steadily increased since the 1970´s. Significant economic interests address passive margin deep-marine petroleum plays (e.g. Shanmugam & Moiola, 1995; Sprague et al., 2003). The bulk of industrial research on submarine fans concerns geological features that are crucial for the development of predictive reservoir models (e.g. Weimer, 2000; Posamentier & Kolla, 2003; Posamentier & Walker, 2006). These key features of interest include the geometries and dimensions of sandstone bodies, the internal hierarchy that governs individual architectural elements and the stratigraphic evolution of turbidite systems. Initial data acquisition for hydrocarbon exploration is principally performed by seismic imagery. However, the remote locations of deep-water successions complicate their detailed scientific investigation from both academic and industrial point of views. Essentially the immense dimensions of deep-water fans symbolize the problem of addressing turbidite systems at the appropriate scale, as submarine fans represent the largest sediment accumulations on earth (Talling, 2012). Although recent advances in seismic imagery resolution and increased information resultant from drill core datasets provided further understanding on the deep-water depositional record, the internal characteristics of architectural elements and their characteristic stacking patterns merely remain partially understood. This drawback may be explained by the limited vertical resolution of seismic imagery and the typically wide spacing of cost-exhaustive wells. From an explorational perspective, internal lateral and vertical reservoir connectivity of individual elements of turbidite systems represent the crucial parameters of consideration. Nevertheless, facies heterogeneity resulting in reduced hydrocarbon production efficiency typically emerges at the bed-scale, hence below the resolution of standard seismic surveys.

Outcrop analogue studies have proven to represent a valuable method to bridge the gap in resolution in between seismic imagery and core-derived one-dimensional insights into deep-water stratigraphy (e.g. Slatt, 2000; see also Vinnels et al., 2010 and references therein). Outcrop-analogue research provided fundamental insights into vertical and horizontal facies characteristics and proved the complexity of facies distributions in turbidite systems. Nonetheless, the majority of understanding of the internal architecture of turbidite systems is derived from outcrop studies of well-preserved, hugely undeformed to weakly deformed foreland basin fills. The most studied analogue systems are the Brushy Canyon Formation, the Grès d´ Annot, the Hecho Group, the Jackford Group and the Marnoso Arenacea, Ross and Skoorstenberg Formations, among many others (e.g. Mutti & Ricci Lucchi, 1972; Chapin et al., 1994; Shanmugam & Moiola, 1995; Elliot, 2000; Sullivan et al., 2004; Johnson et al., 2001; Gardner et al., 2003; Hodgson et al., 2009; Tinterri & Muzzi Magalhaes, 2011). Nonetheless, regarding the fact that the main targets of deep-water hydrocarbon exploration are situated in passive margin settings, studies of pre-collisional turbidite systems which should represent suitable analogues for passive margin petroleum plays, tend to be underrepresented in outcrop-analogue research. This might likely be resultant form the typically strongly deformed and tectonically overprinted nature that characterizes syn-orogenic turbidite systems (Slatt, 2000). Accordingly, this thesis aims to integrate various quantitative sedimentological aspects of bed-scale heterogeneity development in order to advance the comparatively understudied models for turbidite systems deposited during the earliest stages of plate convergence.

The Bordighera Sandstones represent a such pre-collisional sand-rich turbidite system that was deposited in a subduction trench scenario in the Piedmont- Ligurian oceanic basin (Sagri, 1980; Vanossi et al., 1986; Di Giulio, 1992). They form part of the San Remo-Monte Saccarello Unit of the Cretaceous-Paleocene Helminthoid Flysch Complex of the Penninic Nappe stack of the Western Ligurian Alps (Di Giulio, 1992; Maino et al., 2012, 2015). The San Remo-Monte Saccarello Unit is composed of three formations. The lowermost formation is epitomized by the San Bartolomeo Formation, a thin-bedded and very fine-grained turbiditic unit, interpreted to represent a basin plain environment (Cobianchi et al., 1991; Galbiati & Cobianchi, 1997). This basal complex is conformably superimposed by the coarse-clastic Bordighera Sandstone and the calcareous San Remo Helminthoid Flysch that represents the latest depositional phase of the trench fill. Essentially in its distal and lateral domains, the sand-rich Bordighera turbidite system exhibits a partially heterotopic sedimentation pattern with the calcareous Helminthoid Flysch (Sagri, 1980), giving rise to abundant hybrid event bed emergence. As the Bordighera turbidite system has been poorly studied from a sedimentological perspective, it offers the opportunity of investigating syn-orogenic, interfingering siliciclastic and calcareous deep marine successions deposited during the onset of Alpine subduction.

The sediment gravity flow spectrum is traditionally regarded as comprising two end-members, namely cohesive flows (debris flows) and frictional flows (turbidity currents) (e.g. Lowe, 1982; Mulder and Alexander, 2001; Talling et al., 2012). Yield strength and grain interactions account for the dominant particle support mechanisms in debris flows, whereas the primary supporting mechanism of turbidity currents is represented by fluid turbulence (Sumner et al., 2009). In recent years, research efforts have been directed at better understanding flow states intermediate between the two end-members and that share both laminar and turbulent flow properties (e.g. Baas et al., 2009; Southern et al., 2015). Flume experiments (e.g. Baas et al., 2009, 2011) reveal that the concentration of clay within the flow plays a crucial role on emerging rheological flow heterogeneity as it dampens turbulence. Deposits that record both or intermediate flow characteristics commonly comprise a roughly two-part arrangement of a lower mud-poor sandstone portion and an upper mud-rich sandstone. Such deposits have increasingly been documented in studies from various settings (e.g. "slurry flows" of Lowe and Guy, 2000 and Sylvester and Lowe, 2004; "linked debrites" of Haughton et al., 2003; "hybrid event beds” of Haughton et al., 2009; “transitional flow deposits” of Kane and Pontèn, 2012; “matrix-rich sandstones” of Terlaky and Arnott, 2014). The presence of the abovementioned mud-rich intervals within hybrid event beds accounts for their negative impact on both lateral and vertical sandstone permeability, and the occurrence of such deposits can result in sudden and unexpected reduced hydrocarbon production efficiency (e.g. Sylvester and Lowe, 2004; Amy et al., 2009; Fonnesu et al., 2015; Porten et al., 2016). Consequently, since the last decade studies on turbidite systems prone to this type of heterogeneity that arises at the bed-scale increasingly became the center of attention of both academic and applied research.

Sediment petrography and sediment provenance analyses investigate the compositional and textural characteristics of terrigenous sediments. Detrital modal compositions of sand-sized clastic detritus reflect the evolution and the nature of the exposed parent rocks that provided the provenance of clastic detritus that was supplied into sedimentary basins (e.g. Pettijohn et al., 1972; Dickinson & Valloni, 1980; Dickinson et al., 1983). Accordingly, the relationship between hinterland tectonics and associated sediment dispersal pathways towards the final environments of deposition of the detritus can be reconstructed. Moreover, the textural and compositional maturity of sandstones allows to infer their history in terms of modifications by chemical weathering and processes physical processes such as erosion, transport and deposition as well as diagenetic alterations (e.g. Dickinson & Suczek, 1979; Suttner & Dutta, 1986; Weltje & von Eynatten, 2004). Notwithstanding, the solitary quantification of detrital components does not provide estimations on the age of the parent rocks and the thermal history they underwent (Fedo et al., 2003; Andersen, 2005). Recent advances in provenance studies highlight the advantage of the combination of petrographic investigations with geochronological and thermochronological methods and hence elaborate a “multi-proxy” source discrimination (e.g. Dickinson & Gehrels, 2009; Di Giulio et al., 2012, 2017; Beltrán-Triviño et al., 2016). Chronological methods encompass a full spectrum of geochronometers that can be utilized to reconstruct the exhumation and cooling history of provenance areas by means of thermochronology, estimate erosion and sedimentation rates and define the maximum depositional age of sedimentary successions (See Carrapa, 2010 for review on closure temperatures of individual mineral phases and their fields of application). Due to the high preservation potential of zircon grains and their ability to endure multiple recycling events, U-Pb detrital zircon chronology represents one of the most frequently applied techniques in provenance research as this approach allows the precise comparison of detrital zircon age populations to chronological datasets of first-order geological processes (i.e. ages of magmatic and metamorphic crystallization) that affected potential source terrains (e.g. Fedo et al., 2003; Satkoski et al., 2013, among many others). A straightforward, intuitive standard tool in provenance analysis is the simple incorporation of paleocurrent data, that unravels the direction from where the clastic detritus was derived and therewith probably provides one of the most relevant tools in paleogeographic

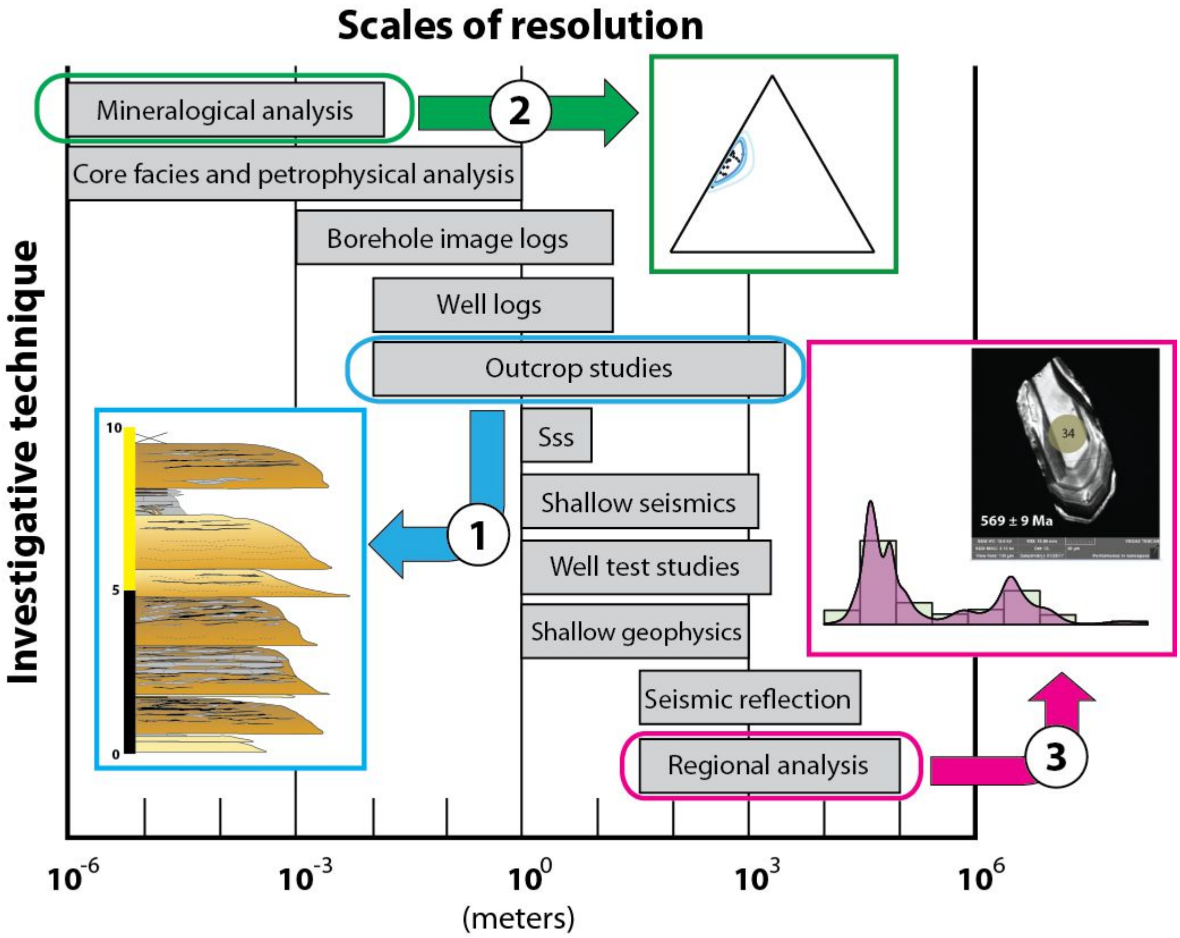

Fig. 1. Scales of resolution that can be assessed by different methodologies in turbidite research and scales addressed in this study. Inspired by Mutti & Normark (1987) and Posamentier & Walker (2006).

reconstructions as it furthermore reveals important aspects of the general configurations of sedimentary basins (see Fildes et al., 2010 and comment by Thomas et al., 2010).

The purpose of this work is hence to provide new insights into comparably understudied pre-collisional sedimentary systems, and essentially to appraise heterogeneity distributions in mixed siliciclastic-calcareous deep-marine environments. Moreover, the yet controversially debated role of oblique convergence on subduction margins and the enquiry about which margin provided the principal source of clastic detritus (e.g. Beltrán-Triviño et al., 2013; Ragusa et al., 2017) during the geodynamic evolution of the Western Tethys are addressed by means of a multi-proxy sediment provenance study. With the goal of covering a broad range of scales of resolutions (Fig. 1), this study integrates a field-based sedimentological dataset with petrographic and geochronological analyses. The main aim of this combined approach is to link the (1) detailed sedimentological characteristics of the Bordighera Sandstones that can be revealed by detailed outcrop studies with (2) a petrographic study that emphasizes on the determination of the provenance terrane that provided the coarse-clastic detritus and its tectonic evolution. Moreover, the application of (3) single grain dating techniques (i.e. detrital zircon chronology) is conducted in order to place the observed stratigraphic trends into the regional-scale geodynamic framework of incipient subduction, as this case study might serve as an exemplary model for pre-collisional deep-water systems deposited during the onset of oceanic subduction.

The organization of the main purposes of this thesis is two-fold. On the one hand the sedimentological chapter of the thesis (Chapter 5) examines and discusses the outcrop-derived dataset and emphasizes on the sedimentological characterization of the Bordighera Sandstones. The primary objectives of this chapter are to unravel the overall geometries and dimensions of the sand-rich system and, moreover, to re-evaluate the previous work on the Bordighera Sandstones in the light of sediment gravity flow transformations that promoted bed-scale heterogeneity due to the presence of hybrid event beds. Bed-scale heterogeneity will be quantitatively evaluated in relation to the occurrence of hybrid event beds in architectural elements that develop due to divergent degrees of confinement. The key questions that will be addressed in the sedimentological chapter include:

- Which architectural elements does the Bordighera turbidite system comprise and what are the main sedimentary facies types that define these?
- What is the overall internal built-up and the stratigraphic evolution of the turbidite system?
- What are the quantitative and qualitative expressions of hybrid event beds in the sand-rich turbidite system and what is their relation to a loss of flow confinement?
- How do observed down-current and cross current tendencies in facies distribution, grain size distribution and sand-to-mud ratios suit into classification models of low-efficiency turbidite systems? What are the implications of observed spatial trends in heterogeneity development for predictive models for the spatial distribution of hybrid event bed-prone sand-rich turbidite system?
- What bed stacking patterns can be predicted in composite siliciclastic-calcareous deep-water systems, and what is the impact of interbedded different lithologies on subsurface reservoir properties?
- Does the Bordighera turbidite system serve as a potential analogue for sand-rich turbidite systems that are prone to hybrid event bed emergence?

On the other hand, the second main part (Chapter 6) investigates the Bordighera turbidite system from a regional-scale perspective. For the purpose of providing a detailed provenance determination, a comprehensive multidisciplinary approach is being conducted. The main aim of integrating the results from sediment provenance analysis into the sedimentological results from Chapter 5 is to offer constraints on the pre-accretionary tectonic evolution of the oldest member of the Western Ligurian Flysch units in Upper Cretaceous times by investigating the stratigraphic evolution. The main research questions accounted for in this chapter are the following:

- What are the regional-scale implications that can be deduced from a marked environmental shift that marks the onset of coarse-clastic sedimentation and how is the facies shift reflected in the detrital signal? To what degree do the observed trends in compositional and textural maturity of pre-collisional siliciclastic correspond to generalized provenance models for sedimentary systems deposited at the initial stages of oceanic collision?
- To what extent can a direct relationship between source rock lithologies and resulting gravity flow facies and turbidite system dimensions be drawn? Do the lithological characteristics of parent rocks impact on depositional architecture?
- How do the constrains derived from detrital zircon chronology contribute to the understanding of Upper Cretaceous geodynamics of the Western Tethys during the incipient stages of convergence? Was the sediment – as proposed by numerous models – primarily derived from the rising axial belt of the active margin or could the clastic detritus have been sourced from the "passive" margin counterpart?

Organization of this thesis

Chapter 2 "Introduction to Deep-marine sedimentation" offers a thorough literature review of the state of the art of knowledge on sediment gravity flows, the transformations that such flows might undergo and the current knowledge on submarine fan models. Particular emphasis is put on reviewing the current advances in the understanding of different mechanisms that result in flow transformations and the discussion of predictive models for the development and distribution of transitional flow deposits resultant from substrate entrainment.

Chapter 3 "Introduction to Sediment Petrography and Provenance analysis" presents the current methodologies applied in sediment provenance studies. The practices of sandstone petrography and the implications of textural and compositional characteristics of clastic detritus for source area configurations are being reviewed. Moreover, an outline of the concept of geochronological methods, and in particular the integration of detrital zircon U/Pb geochronology into provenance studies, is introduced.

Chapter 4 "Introduction to the Study area" provides a comprehensive overview of the structural and stratigraphic setting of the study area. Regarding the structural and stratigraphic inheritance of the Piemont-Ligurian ocean and the consequences of a such structural prequisite on the syn-orogenic paleogeographic and geodynamic evolution, the geological framework of the Western Tethys since the commencement of the Alpine cycle is highlighted. Moreover, the regional stratigraphic setting of the study area and a summary of the results from previous sedimentological work on the Bordighera Sandstones are introduced.

Chapter 5 "Sedimentological characterization of the Bordighera Sandstones - Physical stratigraphy, Stacking pattern analysis and Quantitative assessment of bed-scale heterogeneity distribution in a pre-collisional sand-rich turbidite system" addresses the sedimentological characterization of the Bordighera turbidite system. Emphasis is put on the high-resolution process sedimentological investigation of sediment gravity flow deposits. Moreover, the evaluation of the distribution of individual lithofacies types in different depositional domains is addressed by means of quantitative analysis of facies proportions. Emphasis in put on those lithofacies that impact on reservoir properties. Chapter 5 in major parts reproduces a research paper: "Mueller, P., Patacci, M., Di Giulio, A. (2017). Hybrid event beds in the proximal to distal extensive lobe domain of the coarse-grained and sand-rich Bordighera turbidite system (NW Italy). Journal of Marine and Petroleum Geology, 86, 908-931". For that reason, chapter 5 implies an element of repetition.

Chapter 6 "Provenance analysis of the sand-rich Bordighera Sandstones and the basal complex – Implications for source area evolution during stages of early convergence" puts emphasis on the determination of the nature and tectonic evolution of the source terrain that resulted in the development of a low-efficiency turbidite system. Detrital zircon ages provide new constraints on the exhumation history of pre-Alpine basement rocks and allow for the incorporation of the basin-scale sedimentological observations into the broader context of the complex geodynamic history of the Southern Penninic realm. Chapter 6 is currently in preparation for submission to Sedimentary Geology.

Chapter 7 "Conclusions and recommendations for further work" provides a summary of the findings of this work and discusses the consequences that can be drawn from the results of this study. A novel model for coarse-grained, mixed siliciclastic-calcareous turbidite systems is introduced. Suggestions for further work are being proposed that could bridge the gap of knowledge on pre-Alpine subduction flysch successions from both a Western Alpine and from a Northern Apenninic geological point of view.

Chapter 2: Introduction to Deep-marine sedimentation

2.1 Introduction

Sedimentation in the deep-marine realm occurs through a range of transport processes in which subaqueous mixtures of unconsolidated detritus and liquid components are deposited. These processes include down-slope sediment distribution by gravitational forces, along-slope sediment motion by bottom-water circulation (i.e. contour currents) or vertical sedimentation by pelagic settling from suspension (e.g. Stow et al., 1996; Stow & Mayall, 2000; Shanmugam, 2006; see Fig. 2.1). The sediment-transport mechanisms that account for the volumetrically most significant emplacement of sediment into the final depositional environment in the deep-marine realm are gravity-induced (Talling et al., 2012). These down-slope displacements of sediment-fluid mixtures are a consequence of the combination of instabilities of sediment mixtures through density differences and the incidence of a gravitational component resultant from a gradient in slope. Compositional effects, along with internal texture of the transported grains and the availability of pore liquids, control the degree of sediment instability (e.g. Stow et al., 1996). Sediment remobilization is instantiated by excess density contrasts between the sediment mixture and its surrounding seawater. Accordingly, those sediment movements are termed sediment gravity flows or sediment density flows (e.g. Middleton & Hampton, 1973; Mulder & Alexander, 2001). The commencement of a sediment density flow is achieved when a critical stability threshold is surpassed, and the shear strength of the sediment-fluid mixture is exceeded.

The inception of sediment transport into the deep-marine realm is typically assigned to a destabilization of the shelf-edge that regularly represents the staging area of where the unconsolidated sediment has previously been accommodated. Shelf-edge instabilities that result in flow origination are controlled by a variety of triggering mechanisms. Mechanisms that can prompt sediment density flows include ocean swells, storm waves and tidal effects, seismic triggering, glacial loading and sea bed liquification embodied by water escape and biogenic or thermogenic methane gas (Mulder et al., 2011). Moreover, eustatic seal-level changes, salt diapirism in intra-slope basins and excessive sedimentation rates of deltaic feeder systems as well as direct river discharge and the erosional effect of hyperpycnal flows are regarded as promoting shelf-edge failure (Mulder et al., 2003; Shanmugam, 2012 and references therein). Naturally, a combination of the above listed factors may arise and trigger gravity-induced sediment transport. Gravity-driven resedimentation processes can be differentiated into two broad classes (Mulder, 2011). The distinction is drawn in between mass-transport processes of coherent sediments that are transported in the form of an entire unit and fluid-flow sediment displacements of incoherent sediments mixtures that encompass a disaggregation of the particles and their mixing with the ambient fluid.

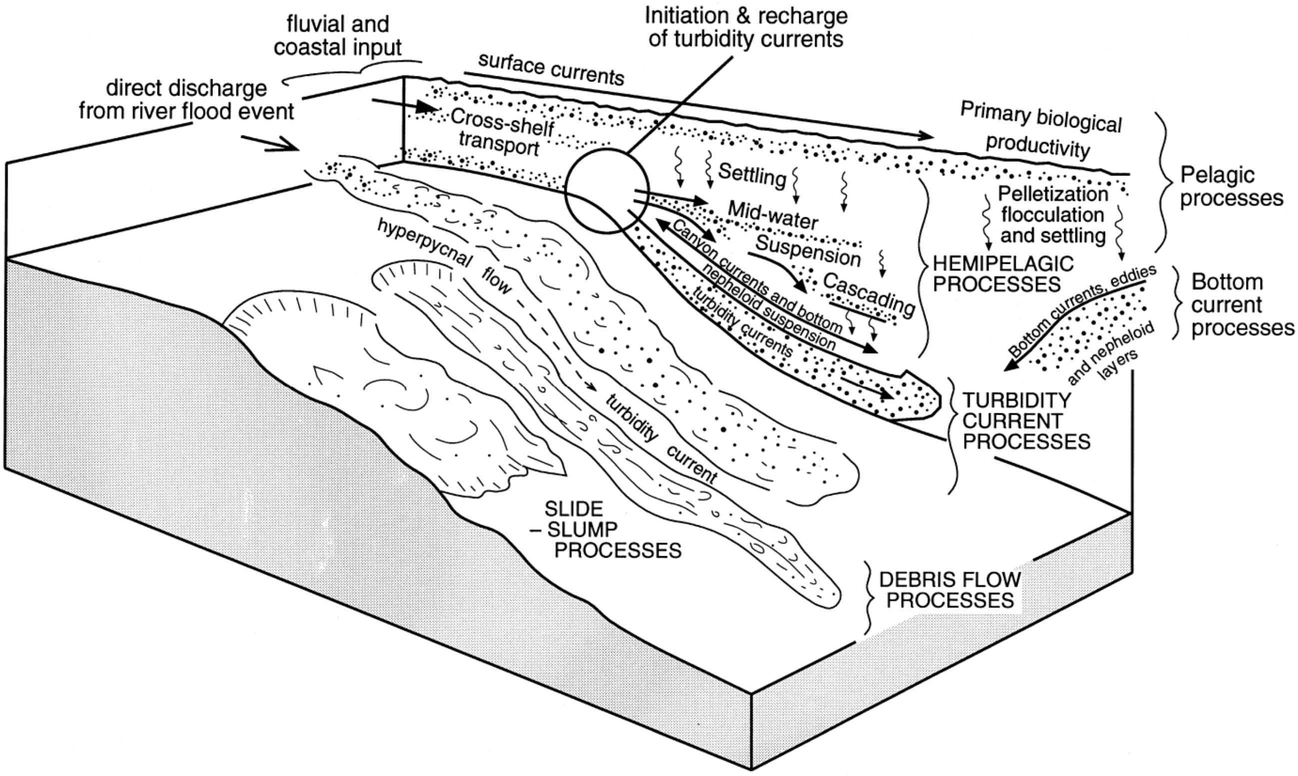

Fig. 2.1. Schematic illustration of the variety of marine sedimentation processes below shelf-break bathymetries highlighting down-slope (gravity-induced), along-slope (bottom-current) and vertical fallout (pelagic) sedimentation processes. Adapted from Stow & Mayall (2000).

2.2 Coherent mass-transport processes

Large volumes of internally coherent accommodations of unconsolidated material are typically distributed in the staging parts of deep-water system and are moved into deeper bathymetries by mass-transport processes. Studies of mass-transport deposits (e.g. Moscardelli et al., 2006; see also Stow et al., 1996 and Shanmugam, 2012) suggest that the down-slope transport of sediment masses into the deep-marine realm might be subject to transformations from sediment displacement of coherent blocks into incoherent flows (Fi. 2.2 A-D). With further travel distance, a disaggregation of the coherent mass through fluid entrainment might occur and promote sediment density flow development (Shanmugam, 2012). Mass-transport processes require a gradient in slope to commence and remain in motion and can be subdivided into slides and slumps (e.g. Stow et al., 1996; Moscardelli et al., 2006; Fig. 2.2). Slides exemplify translational movements of sediment masses that move along planar gliding surfaces ("decollement") where the bulk of shear forces take effect. Owing to this the deposits show merely minimal degrees of internal deformation (Shanmugam, 2012; see Fig. 2.2 B). On the contrary, slumps, which equally represent whole units of coherent sediment mass, are characterized by internal ductile deformation of the fabric of the unconsolidated mass due to a rotational shear component (Fig. 2.2 C). Comparable to slides, the sediment motion during the slumping process primarily occurs along a basal glide plain that represents a zone of high shear rates. The additional deformational component is the result of the diverse lithological composition that generates zones of dissimilar pore fluid pressure which act as secondary shear planes that produce internal folding and contorted bedding (Collinson et al., 1996). Style and extent of internal deformation are dependent on the rigidity and internal lithological composition of the moved mass (Van Loon, 2009). The spatial manifestation of slumps is not limited to the staging areas of deep-marine sedimentation such as the continental slope or canyons and gullies as they frequently occur in association with flanks and eroded walls of submarine channels (e.g. Pickering & Corregidor, 2005; Moscardelli et al., 2006; Covault et al., 2016).

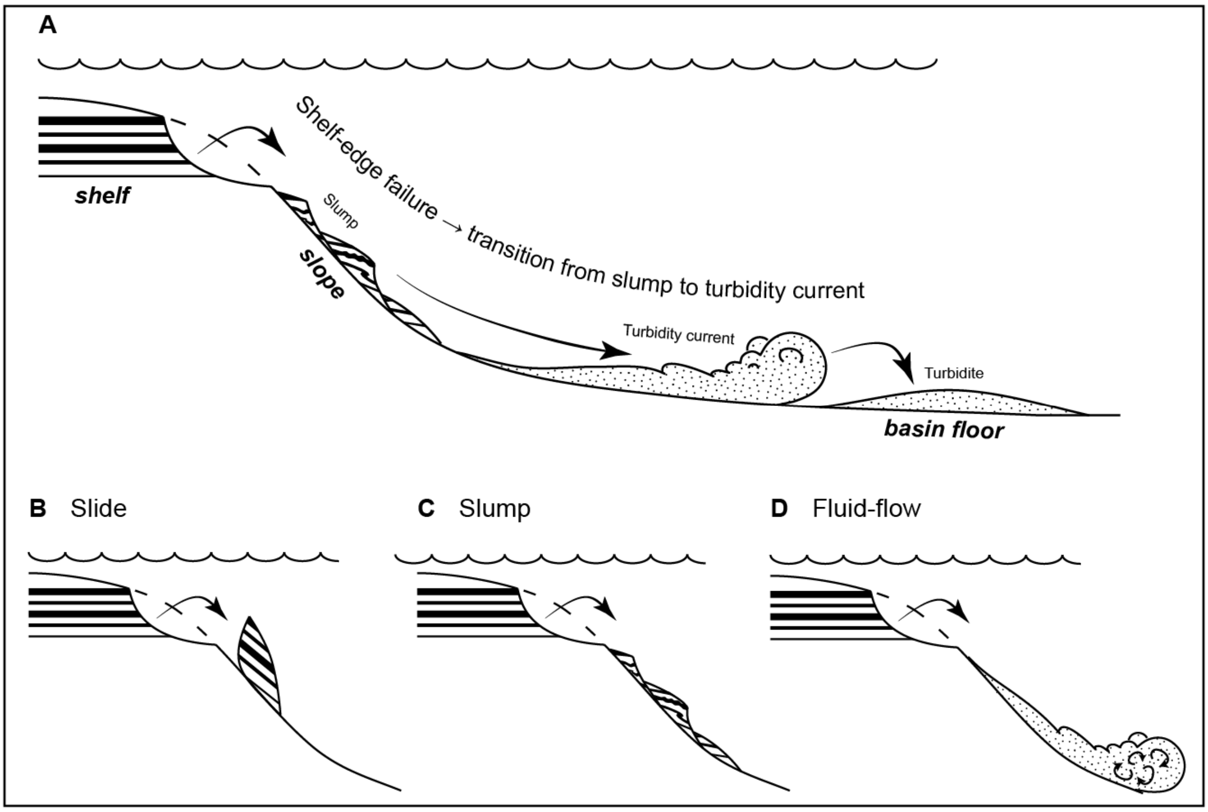

Fig. 2.2. (A) Staging areas of gravity-driven transport processes along the shelf-edge and the continental slope. Note the capability of flows to transform from coherent to incoherent movements during down-slope displacement; (B) Transport by a slide characterized by the preserved internal fabric of the coherent mass, (C) Transport by a slumping process that incorporates internal ductile deformation of coherent sediment block and (D) Down-dip flow evolution towards displacement of incoherent sediment as a consequence of particle disaggregation. Modified from Covault (2011).

2.3 Incoherent mass-transport processes: Sediment density flows

By reason of their unpredictable occurrence in remote deep-water environments and their commonly catastrophic character, direct observations of natural sediment gravity flows are principally restricted (Talling et al., 2012). In situ measurements are limited to relatively fine grain sizes and can be conducted through particle traps, current meters and turbidity meters (Mulder et al., 2011). Attempts in classifying sedimentary processes induced by gravitational effects are therefore mainly based on examinations of the resulting deposits (e.g. Lowe, 1982; Mulder & Alexander, 2001; Talling et al., 2012). Notwithstanding, experimental observations in flume analogues (e.g. Baas & Best, 2002; Baas et al., 2009, 2011; Postma et al., 2008; Tilston et al., 2015; de Leuw et al., 2016) along with steadily increasing theoretical modeling concepts (e.g. Felix, 2002; Necker et al., 2002; Espath et al., 2014) provide essential insights into sediment density flow dynamics. Difficulty arises in providing an unambiguous classification of the complex varieties of sediment density flows. The mechanism that supports the sediment particles (e.g. Middleton & Hampton, 1976; Lowe, 1979, Stow et al., 1996), the mechanical behavior of the processes responsible for sediment motion (rheology) (Shanmugam, 2012) as well as the combination of sediment concentration and flow properties (Mulder & Alexander, 2001) can be utilized in order to provide a classification scheme. The sediment gravity flow spectrum is traditionally regarded as comprising two end-members, namely cohesive flows (debris flows) and frictional flows (turbidity currents) (e.g. Lowe, 1982; Mulder and Alexander, 2001; Talling et al., 2012). Yield strength and grain interactions account for the dominant particle support mechanisms in debris flows, whereas the primary supporting mechanism of turbidity currents is represented by fluid turbulence (Sumner et al., 2009). As the simplified classification proposed by Mulder and Alexander (2001) comprises the integration of physical parameters such as flow duration, cohesion of the particles, sediment concentration and particle-support mechanisms (Fig. 2.3), their approach will be widely employed in the following process-sedimentological interpretations of Chapter 5.

Cohesive (laminar) flows

Cohesive flows (debris flows) are motions of fluid-particle mixtures characterized by pseudo-plastic mechanical behavior. Plastic rheology of the high-concentration sediment mixture emerges from high interstitial proportions of suspended clay. Cohesive forces are essentially generated in the clay fractions and provide matrix strength as the dominant particle-support mechanism (e.g. Middleton & Hampton, 1976; Lowe, 1979; Mulder & Alexander, 2001; Talling et al., 2012). Such matrix strength develops due to cohesive forces that arise by the fact that clay mineral surfaces are attracted towards each other by inter-particle (Van der Waal´s) forces (e.g. Castellanos, 2005; Baas et al., 2011). These electrostatic bonds overcome repulsive forces between negatively-charged clay particles and therewith prevent flow turbulence. Different clay minerals have divergent physical and chemical properties and therewith provide different extents of cohesive strength between the clayey particles (Baas et al., 2011). In addition, the pressure of the pore fluids, buoyancy, and grain-to-grain interactions can maintain large clasts in suspension (Mulder & Alexander, 2001; Talling et al., 2012).

Cohesive debris flows are characterized by quasi-laminar flow behavior that can be described as the movement of a gliding rigid block of sediment above a thin, weakly turbulent lubricating layer of fluid or slurry mud (Shanmugam, 2006; Baas et al., 2011; see also velocity profiles in Fig. 2.3). Because of the low permeability of the dense clayey matrix of the rigid plug, the rigid plug exhibits low permeability. Resulting from this, entrainment of fluid into the plug and flow depletion are substantially reduced so that the front of the cohesive debris flow can hydroplane on the basal shear layer (Mohrig et al., 1998). This defines minor erosional capacity of such flows and can moreover result in enhanced run-out distances (Mulder & Alexander, 2001). Deposition of debris flows occurs abruptly ("*en masse*") by means of cohesive freezing that is achieved when the forces that define flow hindrance overcome the driving shear force (Middleton & Hampton, 1973). On account of the quasi-laminar flow behavior and the related lack of differential settling, the deposits of cohesive debris flow are typified by poor grading, poorly-developed fabric and poor sorting (e.g. Talling et al., 2012). Nonetheless, resulting from the said shearing along a basal glide plain, inverse grading and crude imbrication can be developed at the basal part (Fig. 2.3) by reason of kinematic sieving and dispersive pressure (Mulder, 2011). Cohesive debris flows can transform towards frictional flows by means of dilution of the frontal part of the flow and fluid entrainment into the lower part of the flow (Mulder & Alexander, 2001) or as the result of experiencing a hydraulic jump (Fisher, 1983).

Hyperconcentrated density flows

Hyperconcentrated density flows typically represent the basal boundary layer of cohesive debris flows and turbidity currents. In comparison to cohesive flows, hyperconcentrated density flows are typified by similarly high ratios between sediment and fluid. The distinction from cohesive debris flows is drawn out by the significantly lower share of cohesive components (Mulder & Alexander, 2001). Estimations of the sediment-volume concentration in hyperconcentrated flows span a wide range from ca. 20 % up to 60 % (e.g. Pierson & Costa, 1987; Shanmugam, 2012). The precise threshold value between cohesive and frictional flow behavior based on the shares of cohesive and non-cohesive particles is however hard to define as flow characteristics additionally rely on flow velocity and fluid content (Mulder & Alexander, 2001). According to the absence of cohesive particles, hyperconcentrated density flows are frictional flows that encompass separated particles which provide the basis for grain-

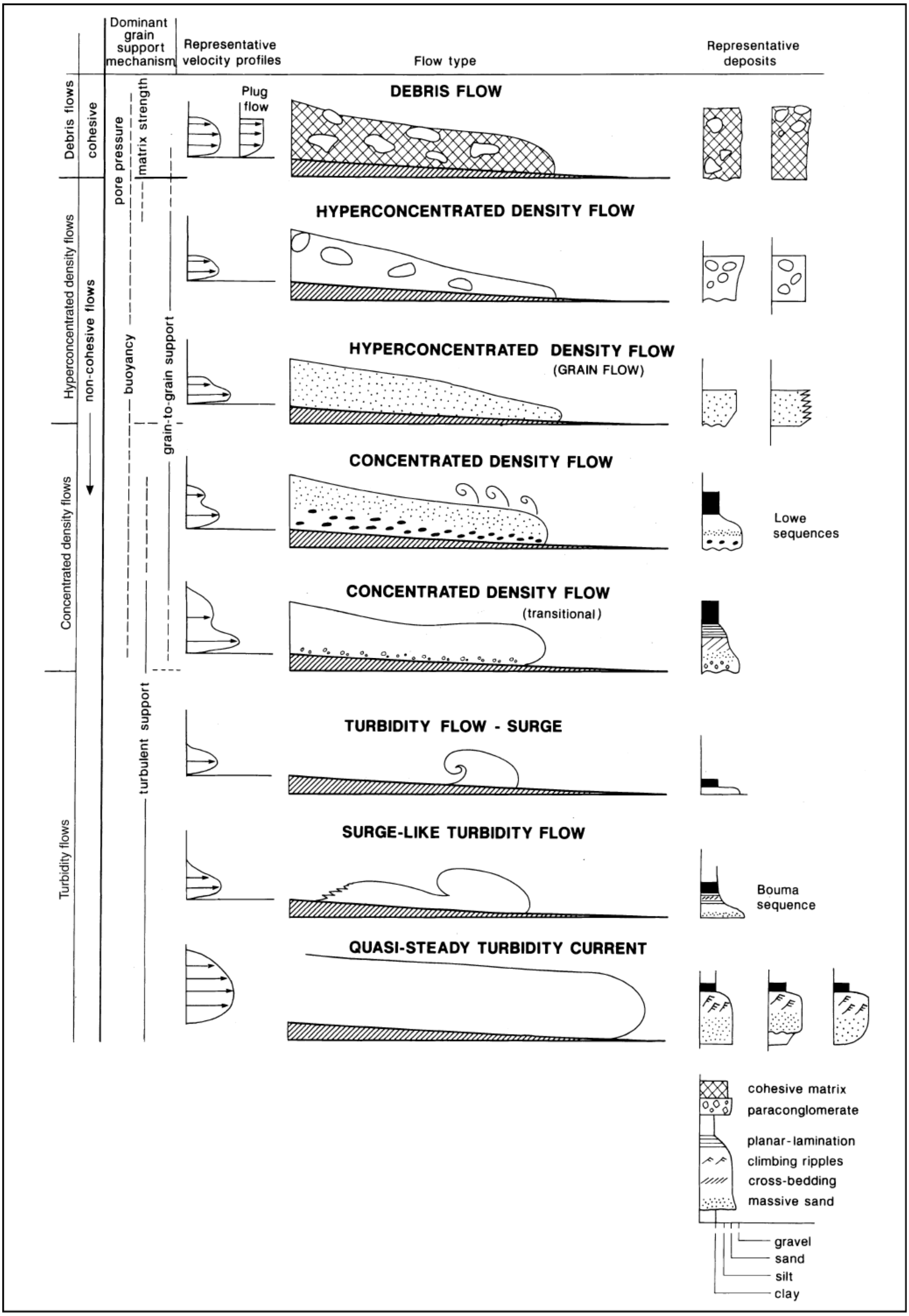

Fig. 2.3. The depositional spectrum of sediment density flows based on the combination of particle-support mechanisms, sediment concentration, flow character and nature of the resultant deposits. Adapted from Mulder & Alexander (2001).

to-grain collisions. The authors furthermore state that sediment-volume concentrations above 40 % prevent fluid turbulence. Although grain-to-grain collisions represent the dominant particle-supporting mechanism, cohesive forces assist to develop buoyancy by means of upward-directed fluid pressure which can provide a principal factor in maintaining sediment in suspension. Moreover, grain-to-bed collisions (i.e. bedload transport) account for the oftentimes erosive nature of hyperconcentrated density flows and the incorporation of eroded substratum (cf. Hsü, 1959; 2004; Mulder & Alexander, 2001; Terlaky & Arnott, 2014).

Hyperconcentrated density flows are competent to transport huge rafts (Fig. 2.3). Deposition occurs by frictional freezing consequential to the loss of excess pore pressure from grain-by-grain interactions. Small-scale surges result in successive layer-by-layer accretion of the sediment. Owing to this, grading is generally poorly developed, even if local inverse grading can be established that is associated with vertical velocity gradients and laminar flow development. (Mulder & Alexander, 2001). Notwithstanding, the above-mentioned presence of discrete particles and the related high degree of inter-granular connectivity promote progressive flow dilution. By means of enhanced entrainment of ambient fluid and successive decrease in sediment concentration, hyperconcentrated density flows can evolve into concentrated density flows (Mulder, 2011). The transition into concentrated density flows goes along with a change in the particle support mechanism as sediment suspension in concentrated density is additionally characterized by turbulence.

Concentrated density flows

Because of progressed dilution through fluid entrainment and related reduced sediment concentration, concentrated density flows behave as Newtonian fluids (Lowe, 1982). The distinction from hyperconcentrated density flows solely based on sediment concentration is yet complicated since physical parameters such as grain size, flow thickness and the degree of sorting need to be considered (Mulder & Alexander, 2001). Concentrated density flows are characterized by diverse particle-support mechanisms. During transport, the importance of individual mechanisms can vary significantly, notwithstanding that dispersive pressure represents the dominant particle-supporting mechanism (e.g. Lowe, 1982; Stow et al., 1996), even if the influence of this mechanism is not yet as intense as in hyperconcentrated flows (Mulder & Alexander, 2001).

The basal parts of flows are generally dominated by grain-to-grain interactions and buoyancy. The coarsest particles are transported as bed load which may provoke a strong erosional capability of flows and the emergence of traction structures. Concentrated density flows are strongly erosional and entrained material might play a crucial role on sustaining the density gradient towards the ambient fluid (Mulder & Alexander, 2001). Eroded substrate may represent a large fraction of the bulk of sediment volume deposited. Continuous entrainment of water is principal to keeping flows maintained and prevent freezing. The dominant support-mechanism of dispersive pressure resultant from grain-to-grain interactions is gradually substituted by fluid turbulence. This results in vertical flow stratification defined by a lower inertia region denotive of high sediment concentration which is overridden by a viscous turbulent flow typified by lower sediment concentrations (Postma et al., 1988). The turbulent upper flow provides additional shear stress to the basal part. It should be noted that per definition the turbulent constituent, which affects the upper part of the flow in maintaining sediment in suspension, must only partially contribute in concentrated density flows (Mulder & Alexander, 2001; Tilston et al., 2015). According to Mulder & Alexander (2001), the boundary towards hyperconcentrated density flows is not well-defined and can only be drawn out with respect to divergent flow characteristics as concentrated density flows are sufficiently diluted enough to allow fully turbulent flow in the upper parts of flows and the fact that differential settling can take place. Remarkably, the authors point out that concentrated density flows might represent transitional states in between hyperconcentrated density flows and fully turbulent flows. Deposition of concentrated density flows occurs through frictional freezing. Concentrated density flow deposits are characteristically depicted by coarse-tail grading, that is superimposed by a massive, poorly graded sandy or gravelly interval (Mulder & Alexander, 2001). Nevertheless, inversely graded varieties that display traction-derived structures are typical as well, additionally depicting the transitional character between concentrated density flows and high-density turbidity current (cf. Lowe, 1982).

A broad potential continuum from cohesive debris flows into hyperconcentrated flows and concentrated density and finally to turbulent flows (and vice versa) has been proposed (e.g. Fisher, 1983; Stow et al., 1996; Mulder & Alexander, 2001; Mulder, 2011; Shanmugam, 2012). Consequently, the complex nature of the sediment density flow spectrum is manifested in pronounced trends of down-slope flow transformations in between their well-understood end members. Fig. 2.4 provides a synopsis of the sediment density flow types presented in this chapter and the relationships with their governing physical parameters. Density flow characteristics are essentially reliant on sediment-volume concentrations (Fig. 2.4 A), the amount of entrained fluids and the proportions of cohesive particles that affect the sediment-support mechanisms. Furthermore, downslope flow velocity variations result in a complex interplay in between these aspects. The substantial decrease in gradient that typifies the continental slope break marks the location where hydraulic jumps arise (e.g. Mutti, 1992; Postma & Cartigny, 2014). On account of flow expansion, related enhanced turbulence and rapid flow deceleration, this zone is fundamentally prone to flow transformations (See Fig. 2.4 B, C and D).

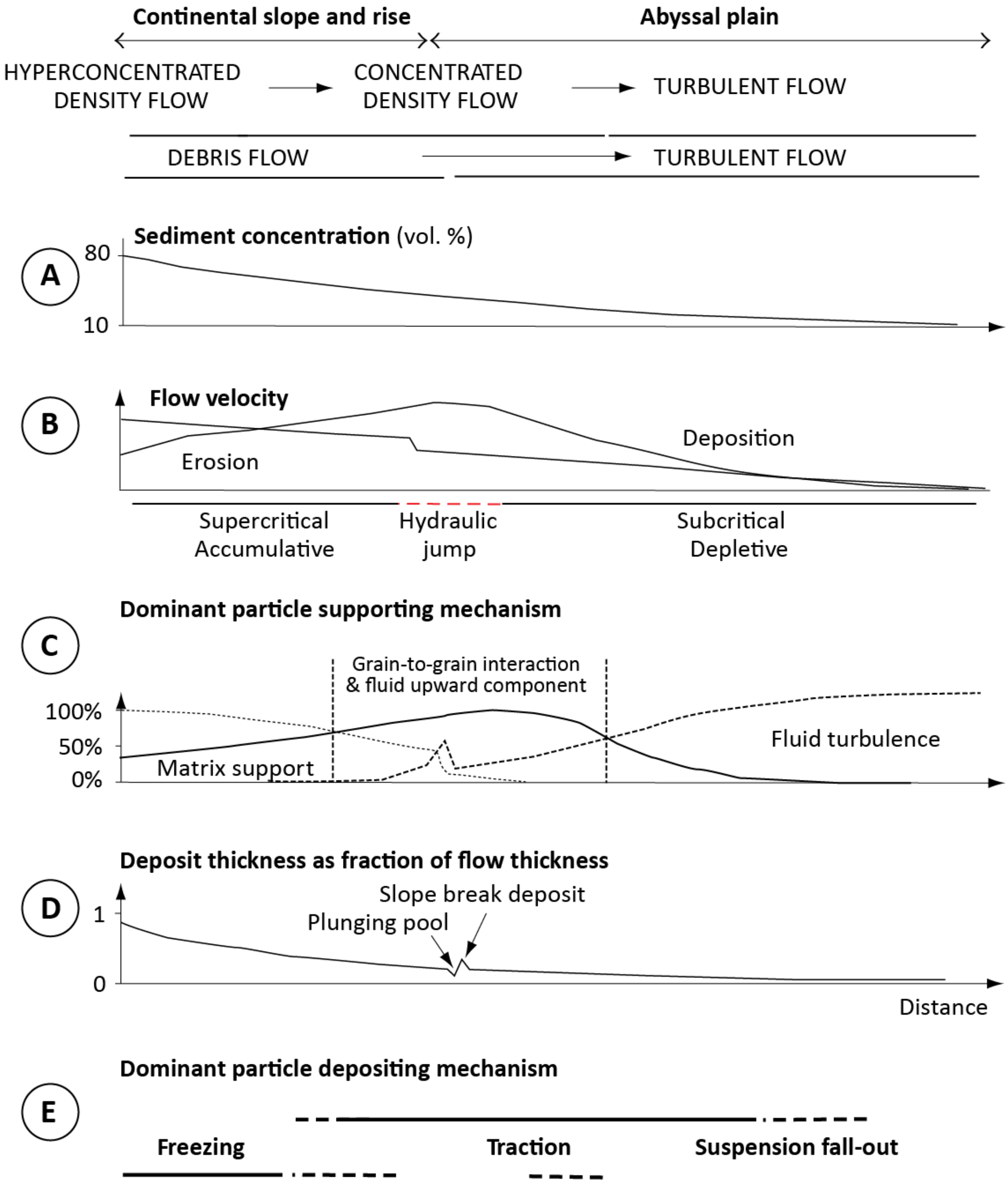

Fig. 2.4. Diagram illustrating conceivable flow transformations during transport from the continental slope to the abyssal plain. (A) The down-ward reduction of sediment concentration goes along with a transformation from hyperconcentrated density flows into concentrated density flows which might evolve into turbulent flows. (B) Idealized flow-velocity profiles. Note the impact of the hydraulic jump (indicated in red color), located at the base of the continental slope, on both flow velocity and on (C) the dominant particle-support mechanism. Moreover, related to rapid flow expansion, the hydraulic jump affects flow thickness (D). Spatial allocations of transitions of dominant depositing mechanisms are illustrated in (E). Modified after Mulder & Alexander (2001) and Mulder (2011).

Turbulent flows

The groundwork for the “turbidite” concept was initiated by Kuenen & Migliorini (1950), who, based on combined laboratory and field investigations, related normal graded bedding in sandstones to waning turbidity currents. Bagnold (1956) recognized the bi-partite vertical organization of gravity flows of that encompass a lower inertia region and an upper part characterized by turbulent flow. Moreover, Bagnold (1962) determined that a sediment-volume concentration of 9 % or less defines the threshold value for turbulent flows *sensu stricto* since the particles in these flows are fully supported by the turbulent, randomly oriented motion of the fluid. For a detailed review on the historical development in turbidite research the reader is referred to the comprehensive review of Mutti et al. (2009). The widely followed definition of turbulent flows or turbidity currents *sensu lato* (cf. Middleton & Hampton, 1973) is that they represent flows of Newtonian behavior in which the particle-supporting mechanism is mainly represented by the upward-directed force of fluid turbulence. Additional sediment-supporting mechanisms are restricted to the less dilute basal region where sediment concentration is higher than the Bangold threshold (e.g. Middleton & Hampton, 1973; Lowe, 1979, 1982; Mulder & Alexander, 2001). These mechanisms comprise grain-to-grain interactions, buoyant lift through displacement of dense fluid by particle settling and hindered settling. Accordingly, turbidity currents *sensu lato* are defined by a vertical stratification resulting from divergent flow dynamics (e.g. Mulder et al., 2011).

From a horizontal perspective, the morphology of an idealized turbidity current is characterized by separation into partitions along the flow path. Theses partitions are denotive of divergent flow dynamics and embrace a distinctive head, body and tail (Pickering et al., 1989; Middleton, 1993). The frontal part of the flow, the head, is the zone where the highest sediment concentration and the coarsest grain size fractions are present. It is the thickest and most turbulent part of the flow, which results in the mainly erosional character of the head. From a three-dimensional perspective, the morphology of the bulged-shaped head of the flow comprises a complex array of lobes and clefts near the bed that result from density instabilities at the front of the flow (Kneller & Buckee, 2000). Essentially the clefts that separate the lobes are locations of ambient fluid entrainment. The zone of the most extensive entrainment of ambient fluid is located at a transitional zone that separates the head from the body. This zone, referred to as the neck, is marked by the presence of turbulent mixing billows generated by Kevin-Helmholtz instabilities that promote mixing with the ambient fluid and supplies eroded sediment into the flow body (Tilston et al., 2015). The body of the flow is the fastest moving region of the flow that typified by virtually steady flow velocities and thickness (Kneller & Buckee, 2000). Due to continuous ambient fluid entrainment, the flow body comprises two distinct parts: A basal dense region that is mainly depositional and an upper less dense region. The rapidly

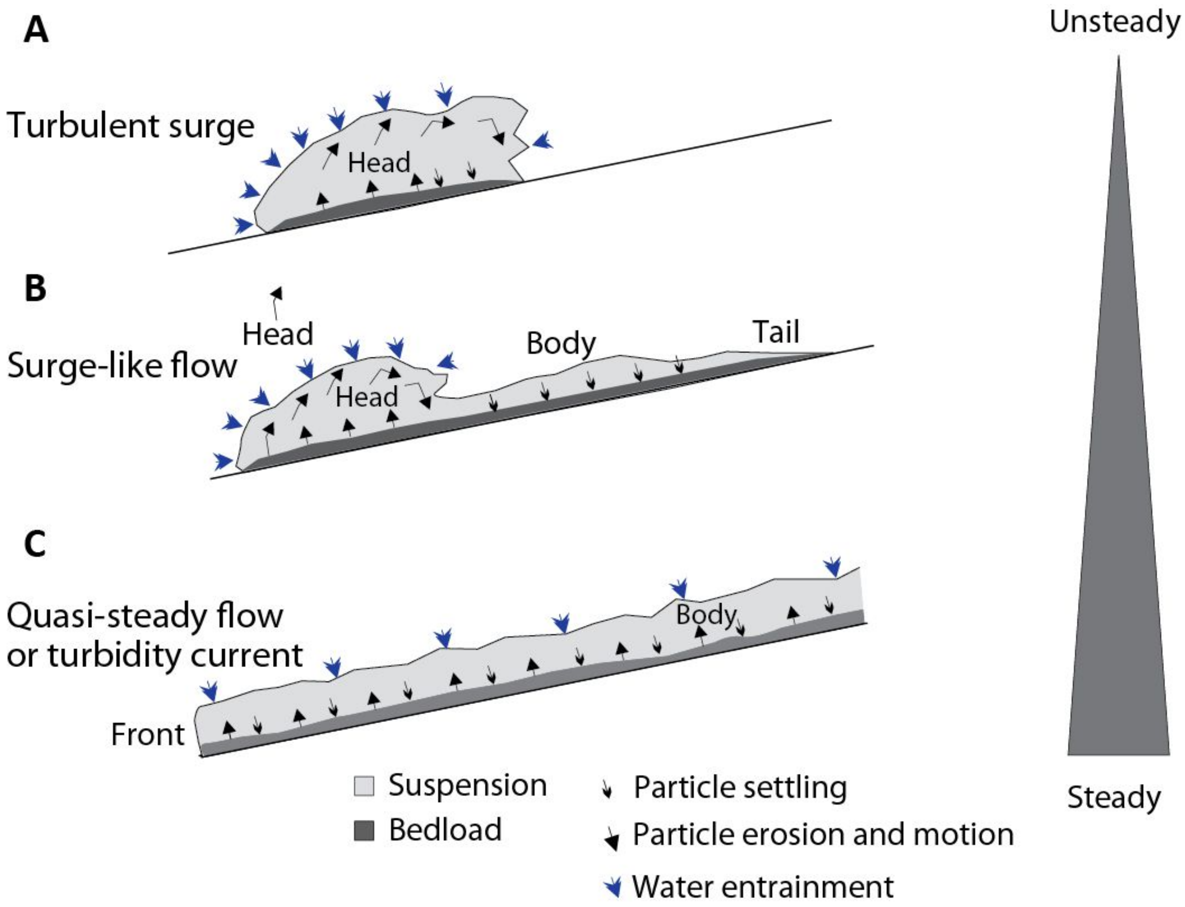

Fig. 2.5. Turbulent flow morphology related to flow steadiness and sediment load as defined by Mulder & Alexander (2001). Adapted and modified from Mulder et al. (2011).

thinning tail of the flow is the most dilute part of the flow and commonly dominated by the fine-grained fraction that gradually settles (Mulder et al., 2011).

Notwithstanding, divergent flow behaviors and flow morphologies arise from different durations of the waxing phase of turbidity currents and in relation to flow magnitude (Kneller, 1995). Accordingly, Mulder & Alexander (2001) proposed the differentiation of turbidity currents into surge flows, surge-like turbidity currents and quasi-steady turbidity currents (Fig. 2.5). In the case of surge flows, steady flow conditions are immediate and very short-lived (up to a few hours). Due to discontinuous sediment supply, the body of the flow instantly migrates into the head which results in a flow morphology that solely comprises the head of the flow (Fig. 2.5 A). Surge-like flows are similarly short-lived (even if they can last for days), but are also defined by greater flow magnitude. Their morphology is defined by the presence of a head, a body and a tail (Fig. 2.5 B). Unsteadiness of surge-like flows is expressed as the velocity of the body of the flow might fluctuate over time and distance. The head of the flow is commonly erosive (Fig. 2.5 B). Contrastingly, quasi-steady turbidity currents are defined by their high flow magnitude and steady flow conditions and can be sustained for weeks or even months. Their morphological expression is limited to the presence of the flow body (Fig. 2.5 C). According to Mulder

& Alexander (2001), the divergent morphological characteristics of the three turbidity current classes have implications on the inference of the origins of flows. The unsteady flow behavior and the relatively small sediment load that typify turbulent surges suggest that such short-lived flows were generated by the collapse of suspension clouds. As a reason of their well-developed morphology that implies more sustained sediment supply, Mulder & Alexander (2001) suggest that surge-like flows regularly originate through transformation of flow types with higher sediment concentration which were subjected to acceleration and fluid entrainment, although an origin caused by failures of sediment accumulation at river mouths is alternatively considered (Mulder, 2011). On the contrary, the long duration and the comparably monotonous morphological expression reflect a divergent flow origin of quasi-steady turbidity currents. The authors associate these characteristics to nearly constant sediment supply that endures for extended periods. Therefore, quasi-steady turbidity currents are interpreted to be directly fed by river discharge and represent suspended-load dominated hyperpycnal currents. In general, such continuous hyperpycnal turbidity currents are characterized by lower sediment concentration and lower flow velocities than surge-like turbidity current varieties (e.g. Mulder & Alexander, 2001; Zavala et al., 2011).

Depositional mechanisms and facies spectrum of turbidity currents *sensu lato*

Based on sediment concentration, numerous workers differentiated turbidity currents into high-density and low-density types turbidity currents (Kuenen, 1950, 1966; Middleton, 1967, 1970, 1993; Lowe, 1982; Pickering et al., 1989; Mulder & Cochonat, 1996; see Fig. 2.6 A-C). Discrete vertical trends within a single flow event deposit provide the basis for understanding the physical conditions during deposition (e.g. Middleton & Hampton, 1976; Lowe, 1982; Pickering et al., 1986; Stow et al., 1996). Bouma (1962) identified a recurring vertical textural trend of sedimentary structures in fine-grained, thin-bedded turbiditic sandstones of the Annot Sandstones. Based on proximal to distal field relationships (i.e. presence or absence of the full sequence of intervals and down-dip fining), Bouma postulated that these sandstones were deposited from waning, progressively depleting low-density turbidity currents that accumulated in a depositional cone. Consequently, Bouma (1962) proposed the archetypal vertical “turbidite” facies motif, the Bouma sequence (Fig. 2.6B). The Bouma sequence comprises five distinct intervals. The depositional features of the lowermost structureless (Ta) interval indicate rapid deposition from suspension. The planar-laminated Tb interval reflects traction sedimentation that requires sustained upper flow regime conditions. Traction sedimentation under lower flow regime conditions accounts for the ripple-laminated Tc interval. than planar-lamination that characterizes the Tb interval reveals traction sedimentation under lower flow regime conditions. The fine-grained, parallel-laminated silty interval (Td) denotes lower flow regime traction sedimentation, whereas the muddy fraction indicates suspension sedimentation of the turbulent cloud (e.g. Middleton & Hampton, 1976; Lowe, 1982).

Lowe (1982) expanded the Bouma sequence for low-density turbidites to coarser, more proximal deep-marine sandstones (Fig. 2.6A). Albeit infrequently observable in a single event sedimentation unit, the idealized vertical sequence that characterizes the deposits from high-density turbidity current includes: A basal, occasionally cross-stratified gravelly interval requires traction sedimentation (R1). This interval is superimposed by a gravelly interval (R2) devoid of sedimentary structures that results from suspension sedimentation. The S2 division is inferred to reflect traction sedimentation by high-density turbidity currents. Inversely-graded traction carpets that characterize the S2 interval result from deposition from dispersive pressure. Massive sandstone intervals (S3) reflect direct suspension sedimentation from a waning, unsteady high-density turbidity current typified by high sediment fallout rates (Lowe, 1982). Nevertheless, according to Kneller & Branney (1995), the structureless texture of the subdivision points towards deposition during quasi-steady flow conditions. Noteworthy, the structureless S3 division of the Lowe sequence can be regarded as roughly corresponding to the lowermost structureless lowermost division (Ta division) of the Bouma sequence (see Fig. 2.6 C).

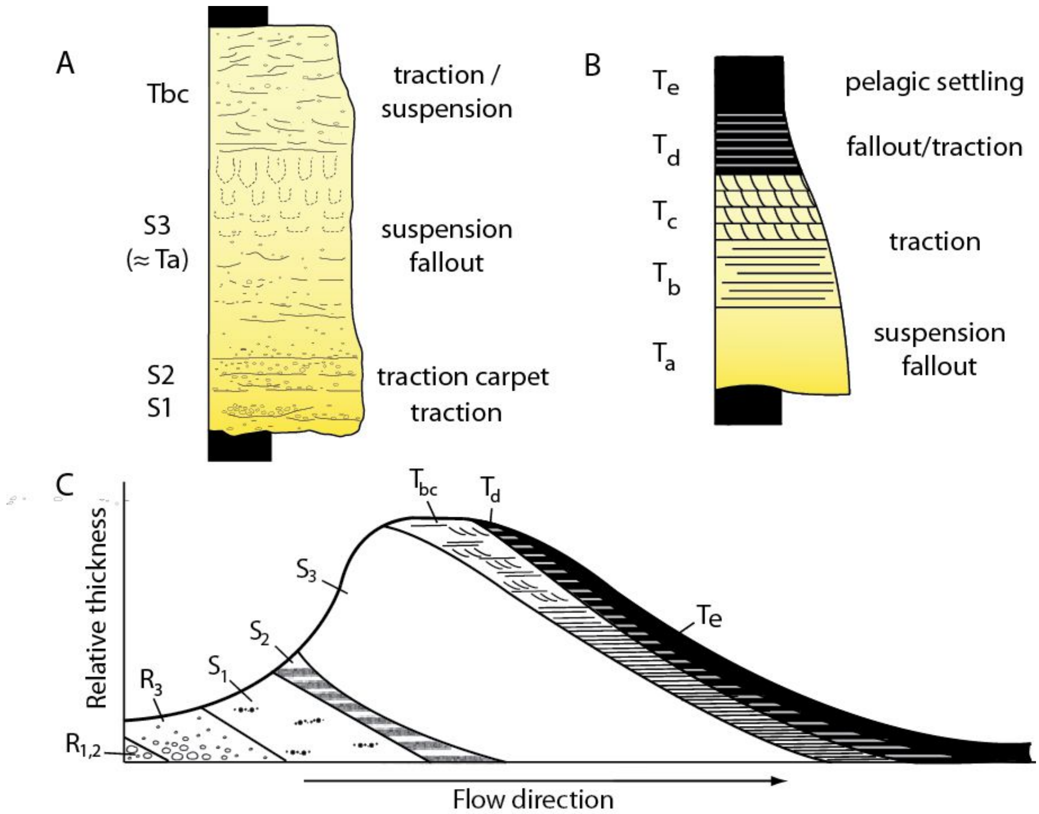

Fig. 2.6. Idealized turbidite (sensu lato) deposits of A) high-concentration flows (Lowe (1982) sequence) and B) low-concentration flows (Bouma (1962) sequence); C) Idealized single flow down-dip turbidite architecture with respect to flow distance and turbidite interval thickness. Modified from Talling et al., 2013.

2.4 Flow transformations from laminar to turbulent flow regime resulting from flow unsteadiness

Apart from flow transitions due to the entrainment of ambient fluid or the loss of interstitial fluid, sediment density flows can be subject to changes in between laminar and turbulent flow regime during the down-current runout of the transported sediment fluid mixture resulting from flow unsteadiness (e.g. Fisher, 1983; Mutti, 1992; Kneller & Branney, 1995; Mohrig & Marr, 2003; Mulder et al., 2011). Steady flow conditions are expected to exclusively depict the two end-members of sediment gravity flows, fully laminar and fully turbulent flows, whereas a variety of controlling factors that promote temporal and spatial transitional states in between the two end-members have been proposed (Fisher, 1983; Mutti, 1992). These include down-dip variations in slope gradient, hydraulic jumps as well as complex sea-floor topography characterized by alternating degrees of flow confinement. According to Mulder et al. (2011), motives for hydrodynamic flow transformations comprise five scenarios (Fig. 2.7):

(A) A *body transformation* denotes a transformation from a laminar to a turbulent flow regime without a substantial change in sediment-fluid concentration and flow volume. Flow body transformation is generally related to a rapid positive shift in slope gradient (e.g. Mutti, 1992; Mulder, 2011; Fig. 2.7 A). As the advancement of enhanced turbulent flow regime is commonly associated with an increase on erosional capability, a significant modification of both flow volume and flow concentration would be expected. On that premise, body transformations are hence rarely observed under natural conditions (Mulder, 2011).

(B) A comparable transition from laminar to turbulent can be related to an abrupt negative change in slope gradient at the break of slope. The negative change in slope gradient results to flow expansion that forces the transition from a thin, supercritical flow towards a subcritical flow typified by higher flow volume (Postma et al., 2009; Fig. 2.7 B). The spatial transition in flow dynamics (or inversely) is characterized by a *hydraulic jump*. Sediment density flow transformation because of a hydraulic jump promotes a substantial increase in erosive capability and therewith results in the entrainment that facilitates the significant increase in flow volume (Parker et al., 1987; Garcia & Parker, 1989; Russel & Arnott, 2003).

(C) *Gravitational transformation* of a flow is defined by the development of a basal laminar part due to enhanced flow concentration in a flow that was initially defined by a fully turbulent regime (Fig. 2.7 C). Due to the higher sediment concentration, turbulence is suppressed within the basal part. The basal part defined by laminar flow regime becomes segregated from the overriding upper turbulent part that remains diluted (e.g. Fisher, 1983; Mutti, 1992). This process is involved in the formation of the typical motif of the Lowe (1982) sequence (cf. Mulder, 2013).

(D) *Surface transformation* occurs through entrainment of ambient fluid in high concentration flows (Fig. 2.7 D). Consequently, the flow becomes more and more dilute and, because of the decrease in concentration, turbulent flow conditions advance at the upper part of the flow that can outrun the initially higher concentration laminar flow (Mohrig & Marr, 2003).

(E) *Elutriation transformation* encompasses progressed flow dilution and enhanced fluidization (Mulder, 2011; see Fig. 2.7 E) The fine particles in the sediment mixture become detached from the flow by the upward-directed force of vertically escaping fluids and suspension fallout (e.g. Middleton & Hampton, 1976; Mutti, 1992). Thus, fine particles detach from the dense basal part of the flow and advance into the dilute cloud of the flow that is characterized by a turbulent flow regime.

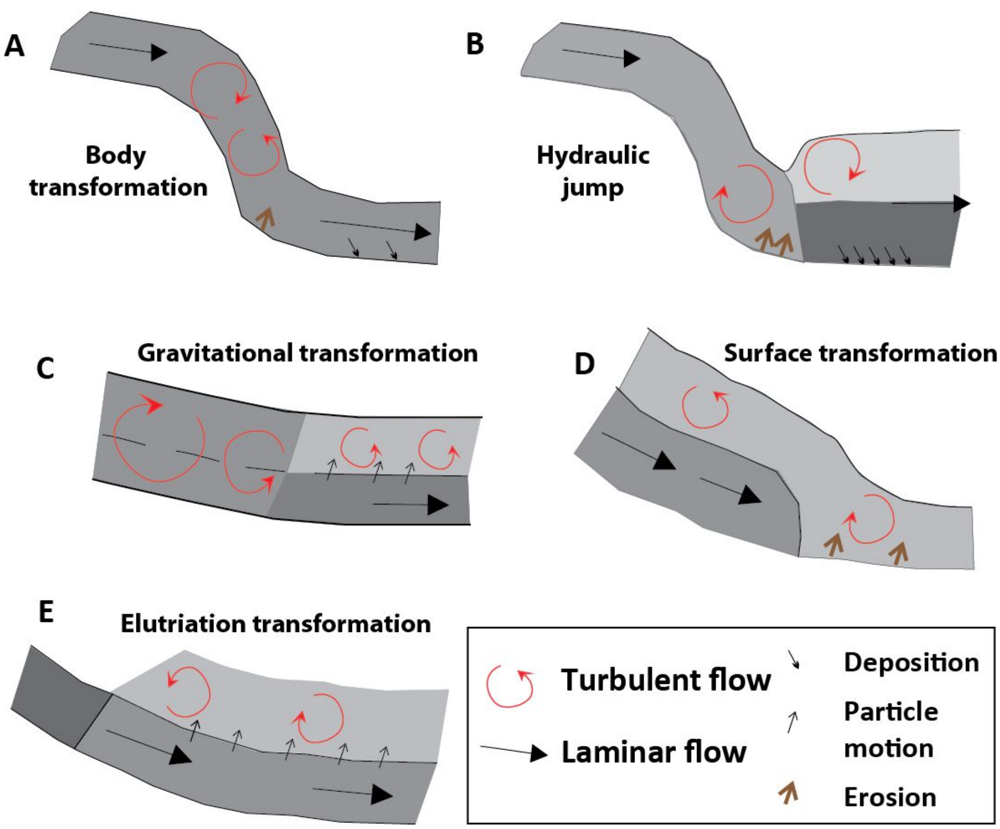

Fig. 2.7. Basin-ward flow transformations due to flow unsteadiness. (A) Body transformation from laminar to turbulent flow regime defined by constant volume of interstitial flow. (B) Hydraulic jump flow transformation laminar to turbulent regime typified by increasing volume of the interstitial flow. (C) Gravitational transformation defined by flow segregation into a high-concentration basal laminar flow resulting from gravity-induced particle settling and an overriding more dilute turbulent part. (D) Surface transformation defined by the progressive formation of an upper turbulent part through dilution and flow entrainment. (E) Elutriation transformation denoted by flow segregation into a lower high-concentration laminar flow and an overriding turbulent dilute upper part by means of upward motion of interstitial fluid and fine particles. Modified from Fisher (1983) and Mulder (2011).

2.5 Sediment density flow transformations due to cohesive particle entrainment

Sediment density flows exhibiting textural characteristics that reveal evidence of flow transformation due to the entrainment of cohesive particles represent a substantial deviation from the models of gravity flow transformations presented above. The resulting deposits of sediment density flows in which turbulence has been dampened due to enhanced proportions of cohesive substrate display distinct vertical changes in bed fabrics. The common facies motif corresponds to a basal, mud-poor ("clean") sandstone division that is overlain by at least one subdivision typified by intense mud content within the sandy matrix. Vertically alternating repetitions of this motif might occur. Flume experiments reveal that even relatively small concentrations of cohesive mud can effectually suppress turbulent fluid motion in density flows (e.g. Baas & Best, 2002; Baas et al., 2011; Sumner et al., 2009; cf. Talling, 2013; Fig. 2.8). Essentially at lower flow velocities, initially turbulent flows can abruptly transform into quasi-laminar plug flows (Baas et al., 2009).

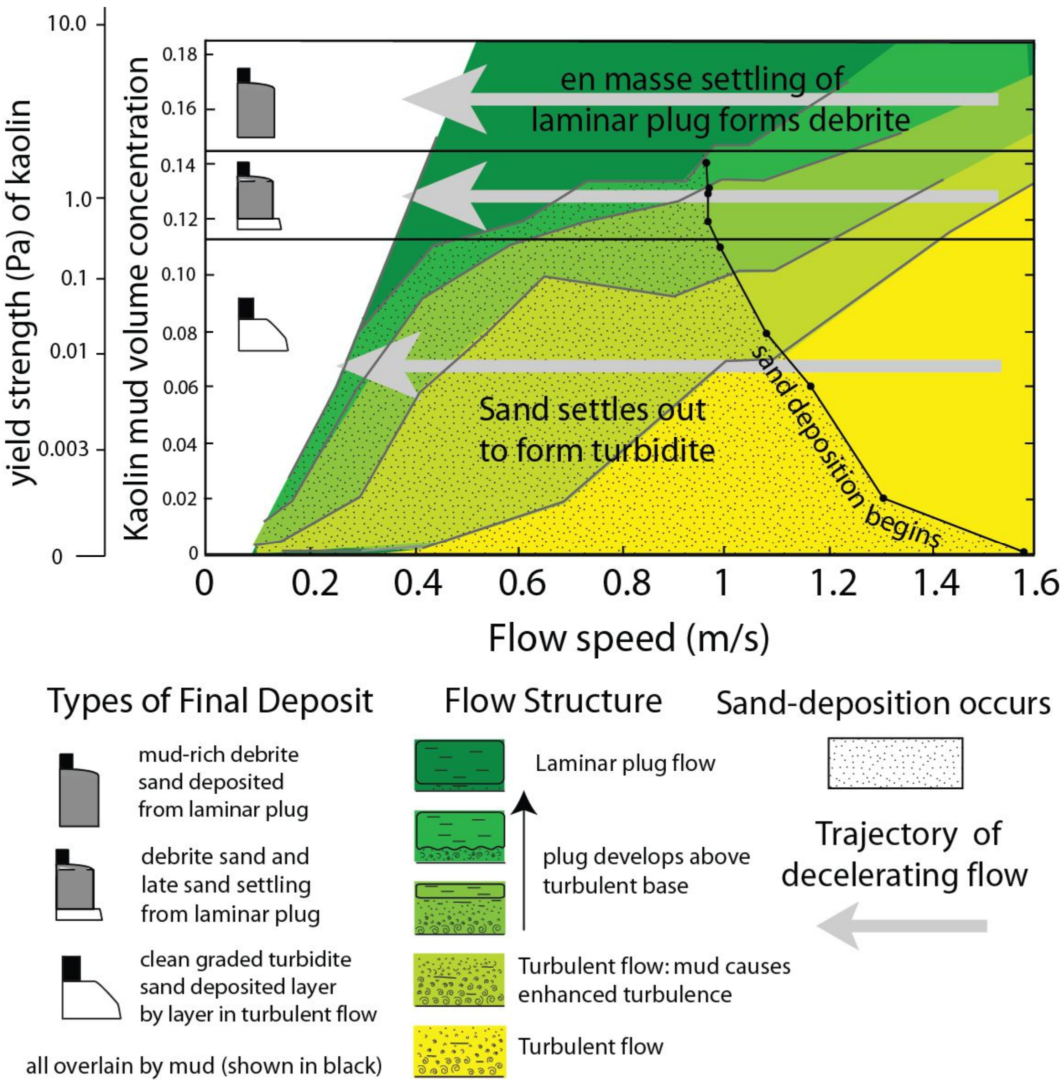

Fig. 2.8. Relationships between flow velocity, flow structure, clay concentration and resulting depositional characteristics in density flows enriched in cohesive mud. Adapted from Talling (2013).

Notwithstanding, attributable to difficulties in the formation of comparable deposits in flume experiments due to flow velocity and flow run-out limitations, major portions of the knowledge have been achieved by means of outcrop studies. Emphsis has been put on the investigation of deep-water deposits that record evidence of intermediate flow behavior. Albeit a co-genetic origin of equivalent deep-marine deposits has already been recognized in earlier studies (e.g. "sandwiched debrites" of Ricci Lucchi & Valmori, 1980; "sand-mud mixture containing floating mud chips" of Zeng et al., 1990), a renewed awareness of the importance of such transitional flow deposits can be assigned to the frequent recognition of such strata in North Sea fields and their negative impact on hydrocarbon production efficiency. Ever since, co-genetic deposits are increasingly reported from the deep marine sedimentary record (e.g. Sylvester & Lowe, 2004; Patacci et al., 2014; Terlaky et al., 2014; Southern et al., 2016; Fonnesu et al., 2016, 2017; see review in Talling, 2013). Disregarding, discrepancy prevails in providing both an all-encompassing classification schemes and a consistent nomenclature of deposits of sediment flows intermediate to entirely turbulent or quasi-laminar rheologies. These deposits have been termed slurry beds (e.g. Lowe & Guy, 2000; Lowe et al., 2003; Sylvester & Lowe, 2004; Muzzi Maghalaes & Tinterri, 2010), co-genetic debrite-turbidites (Talling et al., 2004), linked debrites and hybrid event beds (Haughton et al., 2003, 2009), matrix-rich sandstones (Terlaky et al., 2014), submarine transitional flow deposits (Kane & Pontèn, 2012; Southern et al., 2017) and hybrid submarine flows (Talling, 2013).

Deposits of hybrid event beds

According to the model of Haughton et al. (2009), the idealized deposit of hybrid event beds displays five divisions that might account for variable individual thicknesses (See Fig. 2.9). The basal subdivision of the idealized deposit is embodied by a graded or ungraded structureless sandstone interval denotive of dewatering structures that typically contains isolated mudclasts (H1). The lack of primary structures in the basal deposits might suggest that deposition occurred by rapid suspension fallout from a rapidly collapsing high-density turbidity current defined by a 'short' runout distance. Alternatively, the structureless appearance might be explained by the overriding debris flow that prevented primary sedimentary structures to form. The basal interval gradually passes into a banded sandstone (H2) that displays vertically alternating cleaner paler sands and darker argillaceous sandstone bands. The H2 division is interpreted to reflect intermediate flow rheology defined by intermittent turbulence suppression. The chaotic, debritic argillaceous sandstone subdivision (H3) is marked by a sheared fabric and encompasses variable concentrations of mud clasts and sand patches. The sheared, chaotic fabric is interpreted to mirror quasi-laminar flow behavior. The sand-patches likely result from upward injection of sand due to loading. The overlying fine grained, laminated mud-poor sandstone (H4) points to traction processes of a dilute turbulent flow. The clayey mudstone cap (H5) reflects deposition through suspension fallout. Nonetheless, a single event bed does not necessarily comprise all the above-mentioned divisions (e.g. Talling et al., 2012, 2013; Fonnesu et al., 2017).

Outcrop observations led to the proposal of several mechanisms that could trigger co-genetic flows (e.g. Haughton et al., 2003; 2009; Talling, 2013). Haughton et al. (2003) highlighted that the frequently observed facies motif of a clean basal sandstone being superimposed by a cohesive debrite is the result of a single sedimentation event and thus mirrors the down-dip flow transformation of a debris flow into a turbidity current (the "linked debrite" model). According to this explanation, the structureless sandstone moved independently ahead of the debris flow. This mechanism interpreted to have promoted co-genetic flow behavior is directly related to the heterolithic composition of material that accumulated at the shelf edge. The initial failure of the staging area promoted sandy material to flow in the form of a turbulent flow that was superimposed by the bypassing debris flow. The structureless texture of the basal sandstone is interpreted to result from a combination of rapid fallout from suspension and the effect of the overriding debris flow that prevented the development of traction structures. Talling (2013) relates the capability of the debris flow to bypass the sandy deposit to hydroplaning.

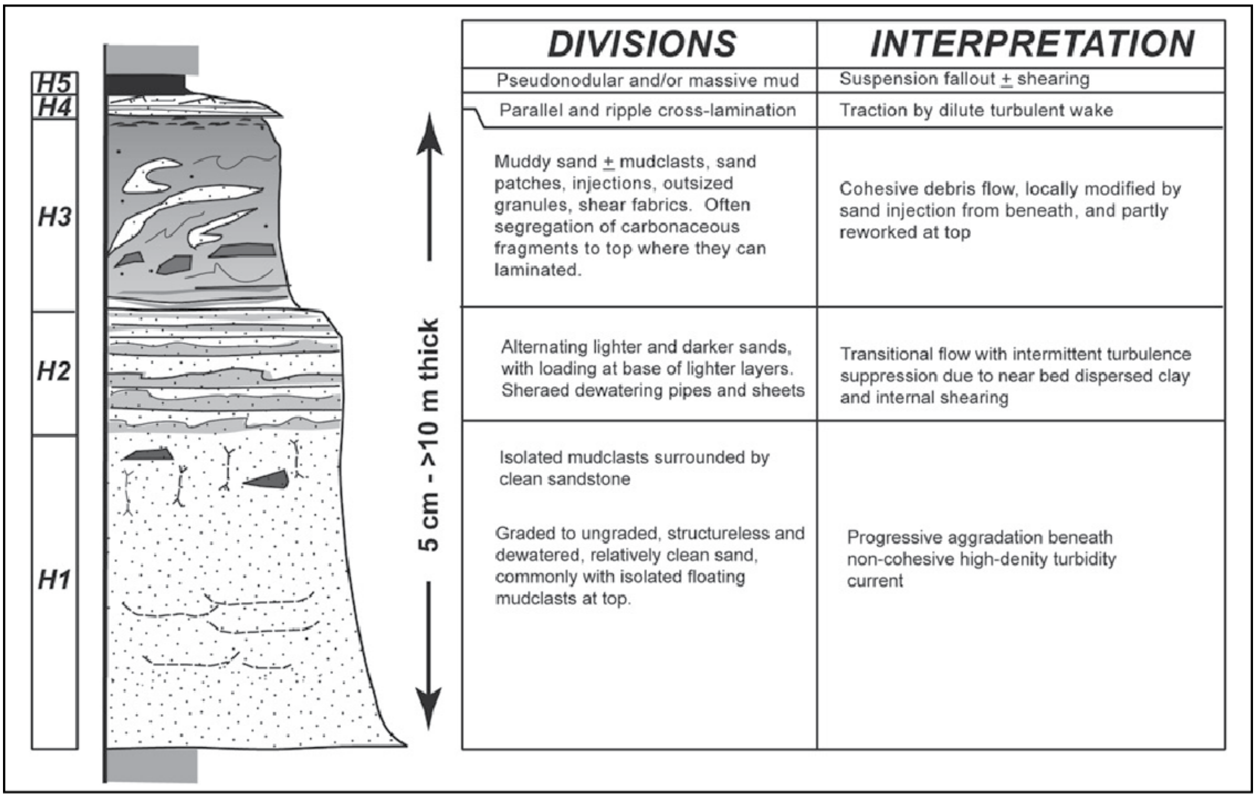

Fig. 2.9. Idealized stratigraphic expression of a hybrid event bed deposit *sensu* Haughton et al. (2009).

A departure from a such flow evolution that implies a heterogeneous composition of the parent flow is that of the effect of entrained cohesive mud resulting in turbulence dampening (e.g. Haughton et al., 2009; Baas et al., 2009, 2011; see also Fonnesu et al., 2016 for review on controlling factors on HEB development). This model suggest that turbulent flows erode muddy substrate along their flow path and that entrained clasts and rafts progressively become disaggregated by the turbulent nature of the flow during basin-ward travel. The disaggregated clay particles effectively dampen turbulence and induce intermediate flow states. Flume experiments (e.g. Baas et al., 2009; Sumner et al., 2009; Baas and Best, 2011) demonstrated that hybrid flow behavior is subject to five rheological stages (See flow structure in Fig. 2.8). Notwithstanding, owing to the fact that experimental insights into flow transformations are characterized by limited run-out distances, the erosion of cohesive material could not be imitated, and the experiments were conducted with sand-clay mixtures of deviating initial clay concentrations. The results of these experiments demonstrated that increased clay concentrations suppress turbulence and promote the development of a plug-like flow region that propagates from the upper part of the flow downward. Importantly, the experiments reveal that a turbulence-enhanced flow develops at low clay concentrations, in which high flow velocities prevent clay from developing cohesive properties. With high clay concentrations, a quasi-laminar plug-flow region develops that occupies most of the flow structure and is moving along a basal shear zone. A different explanation for co-genetic flow development is the longitudinal segregation of cohesive material into the rear of the flow that resulted in divergent flow behavior (Haughton et al., 2009). This model however implies an initial composition of the resedimented sand that comprised significant portions of mud and silt and excludes acquisition of clayey substrate by erosion.

Spatial and stratigraphic occurrence of hybrid event beds and transitional flow deposits

Hybrid event beds and comparable deposits characterized by an argillaceous sandstone division have largely been reported from distal environments of tectonically active lobe-dominated sand-rich and mud-rich submarine fans (e.g. Haughton et al., 2009; Hodgson, 2009; Muzzi Magalhaes and Tinterri, 2010; Fonnesu et al., 2017; Spychala et al., 2017a). Moreover, hybrid event beds have been documented in proximity to basin margins, where flows are interpreted to decelerate rapidly through interaction with the laterally confining slopes (e.g. Barker et al., 2008; Patacci et al., 2014). Notwithstanding, the occurrence of such beds has also been reported from more proximal environments of largely unconfined turbidite systems, specifically in channelized realms located at the toe of slope of deep-sea fans (Henstra et al., 2016) or in the immediate downstream vicinity of the channel-lobe transition zone (Terlaky and Arnott, 2014). Reasoning from this fact, the environmental distribution of hybrid event beds might expose further perceptions about their evolution.

Several environmental controls were proposed to explain the widespread occurrence of hybrid event beds. Talling et al. (2007) and Talling (2013) suggest that hybrid event bed development can be related to subtle changes in slope gradient. A positive alteration in gradient would hence result in deceleration of the flows and lead to laminar flow development, whereas a negative gradient change would result in flow acceleration and subsequent restoration of turbulent flow conditions. The scenario that a positive gradient change impacts on flow transition appears to be comparable to hybrid event bed development interpreted to be associated with rapid deceleration of flows that contained significant mud concentrations in onlapping relationships to confining slopes (Barker et al., 2008; Patacci et al., 2014). A recent investigation by Southern et al. (2015) stressed the influence of complex sea-floor topography on transitional flow development. The case study encompasses a succession developed in a ponded mini-basin in which flows were prone to multiple reflections and highlights the irregular, comparatively patchy pattern of argillaceous sandstone distribution. Nevertheless, ongoing research on hybrid event beds includes the distinct allocation of mud entrainment. Keeping in mind that transitional flow deposits are typically documented from distal sub-environments (cf. Talling, 2013), numerous studies attribute the location of mud entrainment to proximal environments and relate them to an up-dip source directly linked to the initial failure of the staging areas (e.g. Haughton et al., 2003; Amy & Talling, 2006; Hodgson et al., 2009), which would suggest that long down-dip distances are required for hybrid flow development. However, merely a limited number of studies documented deposits of transitional flows along wide down-current distances (e.g. Amy & Talling, 2006; Kane & Pontèn, 2012; Fonnesu et al., 2017), and recent studies (e.g. Terlaky et al., 2014; Fonnesu et al., 2016; Henstra et al., 2016) reveal that a more local position of mud entrainment in basin floor environments needs to be considered as representing a zone where flows were characterized by enhanced erosional capacity. These studies highlight the importance of flow expansion and resulting enhanced turbulence which typically occurs in immediate vicinity to positions typified by a substantial loss in the degree of confinement and suggest that a such setting might appropriate for the typical occurrence of transitional flow deposits in distal lobe environments and lobe fringes.

Haughton et al. (2009), Talling (2013) and Spychala et al. (2017b) infer from the stratigraphic occurrence of hybrid event beds that the style of stratigraphic clustering is autogenically controlled and ultimately related to trends in lobe progradation and retrogradation. Accordingly, the presence of hybrid event beds throughout the full stratigraphic interval is interpreted to point towards a constant tectonic effect that affects the staging area. Stratigraphic presence of hybrid event beds limited to the basal parts of stratigraphic sections mirrors the progradational phase of fan initiation, whereas their exclusive occurrence at the tops of sections might point towards outsized flows that reached the distal parts of the basin. Reasoning from this fact, a scenario in which hybrid beds arise sporadically present throughout the stratigraphic development would suggest a comparatively stable depositional setting.

2.6 Turbidite facies tracts models

A disparate assessment of sediment density flow classification is being represented by a longitudinal description of the transitional tendencies of distinct facies or facies association distributions from the deltaic to deep-marine depositional environments (Mutti, 1992; Gardner et al., 2003; Mutti et al., 2003, 2009; Remacha et al., 2005; Zavala et al., 2011). This conceptional basis, the facies tract concept as defined by Mutti (1992), outlines the basin-ward evolutionary relationships of the synchronous deposits derived from the longitudinal transformations of a single sedimentary density flow deposit or a bed-set. This genetically derived facies classification approach distinguishes density flow deposits according to the main transporting and depositing sedimentary processes operating along a time-equivalent depositional profile (Mutti, 1992; Mutti et al., 2009). The main goal of the development of a conceptual facies tract is that of providing a predictive framework for expected flow transitions and their depositional facies located up-dip or down-dip of an investigated section (e.g. Mutti, 1992; Zavala et al., 2011). A such facies tract determination not only requires a comprehensive understanding of the depositional environment, it moreover necessitates feasible long-distance stratigraphic tracing of beds. Examples of proposed facies tracts for high- and low-efficiency flows (Gardner et al., 2003) and an updated model emphasizing on hydraulic jump transformation (after Mutti, 1992 and Gerard, 2001) are illustrated in Figs. 2.10 and 2.11:

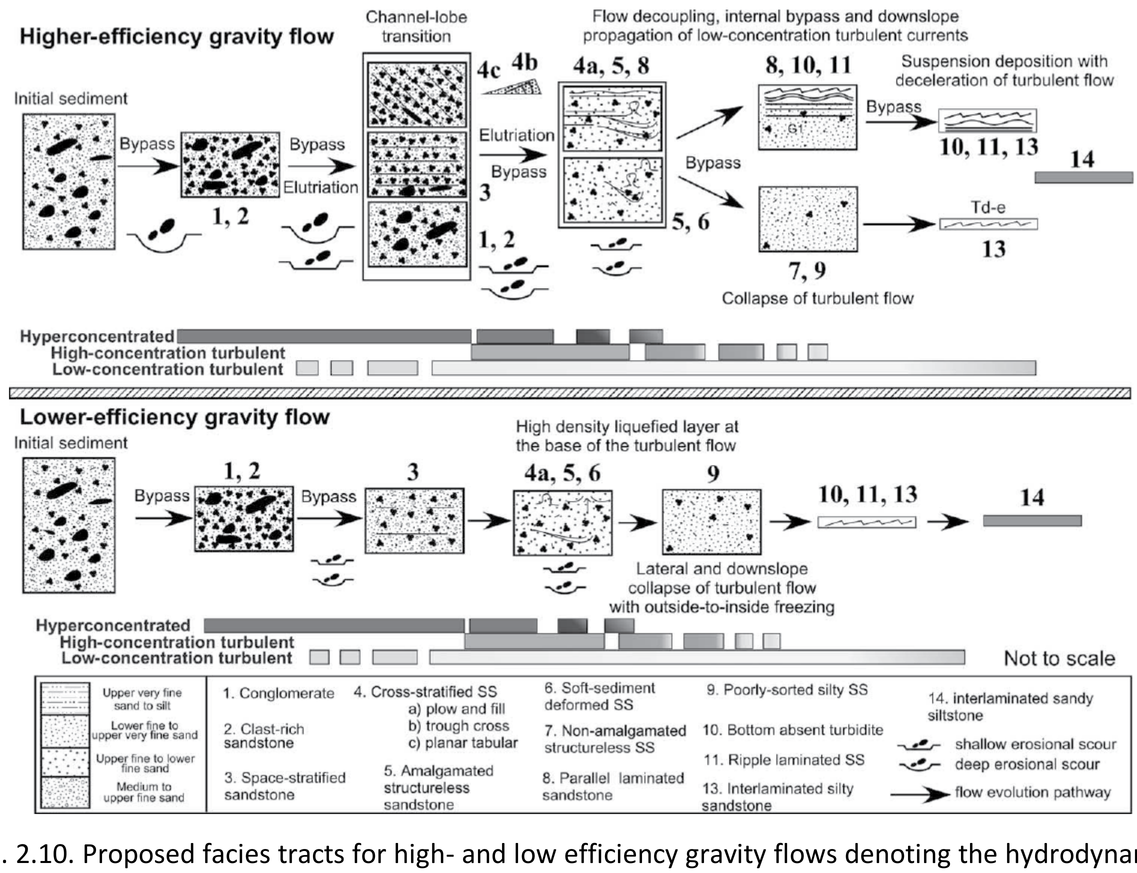

Fig. 2.10. Proposed facies tracts for high- and low efficiency gravity flows denoting the hydrodynamic characteristics of individual flows and their probable transformations. Adapted from Gardner et al. (2003).

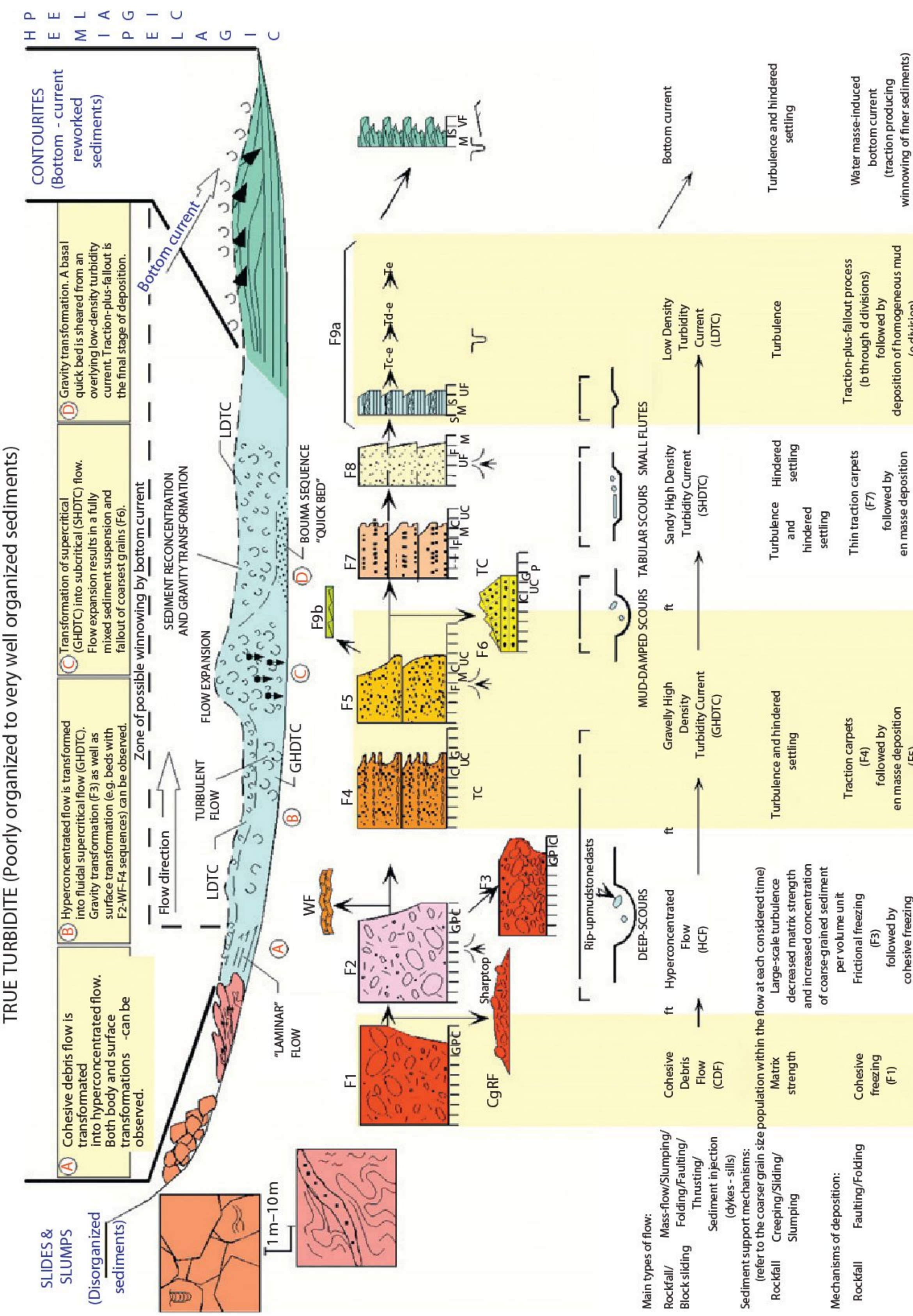

Fig. 2.11. Proposed idealized basin-ward facies tract scheme depicting flow volume and the location of the hydraulic jump according to Mutti (1992) and Gerard (2000). Adapted from Mulder (2011).

2.7 Submarine Fan models

The repetitive emplacement of siliciclastic sediment density flows in the deep-marine realm forms significantly thick sandstone successions that potentially provide excellent reservoir characteristics (See also Chapter 1). Accordingly, the construction of system-scale depositional models started to become the focus of both academia and industry research from the 1970´s onwards (e.g. Normark, 1970; Mutti & Ricci Lucchi, 1972; Mutti & Gibhaudo, 1972; Brown & Fisher, 1977; Walker, 1979; Bouma, 1985; Shanmugam & Moiola, 1988, 1991; Pickering et al., 1989; Reading & Richards, 1994). Owing to the virtually uncountable and steadily growing numbers of publications concerning the complexity of submarine fan models, this brief outline is by no means a complete listing, the reader is instead referred to the comprehensive reviews of Posamentier & Walker (2006), Mutti et al. (2009) and Mulder (2011). At the initiation of submarine-fan model descriptions, two independent approaches in providing fan-scale architectural models were derived. In general, early submarine fan models interpreted turbidite systems as displaying a radial pattern. Based on the seismic analysis of modern systems, Normark (1970) established the first model that subdivided submarine fans into three provinces, the upper fan, the middle fan and the lower fan. Normark (1970) described the upper fan as an environment situated at the termination of incisive submarine canyons and that is dominated by levee-flanked sinuous feeder channel systems. The middle fan was distinct as representing a transit zone that comprises distributary channels that longitudinally pass into "depositional lobe" sand bodies and termed this environment "suprafan depositional lobes". The lower fan province is typified by the exclusive presence of homogeneous sheet-like sandstone lobes that superimpose fine-grained basin plain successions. Exclusively based on field observations of turbiditic deposits of the Northern Apennines and the Hecho Group, a model for ancient submarine fans was proposed by Mutti & Ricci Lucchi (1972). The ancient fan model comprises an inner fan built up of channels that bifurcate into multiple channels on the mid-fan. In contrast to the recent fan model of Normark (1970), the mid-fan of ancient turbidite systems does not comprise depositional lobes. The outer fan of ancient systems is dominated by the presence of depositional lobes. However, Mutti & Ghibaudo (1972) demonstrated the presence of feeder channels and distributary channels that fed lobes at their terminations. Brown & Fisher (1977) highlighted the importance of shifting locations of active and inactive of feeder channels and the resulting complex three-dimensional architecture of turbidite systems (Fig. 2.12A). Subsequent to the advent of the concept of sequence stratigraphy, the effects of eustatic fluctuations and geodynamic settings on progradational and retrogradational trends of facies associations were incorporated into updated models (e.g. Vail, 1977; Mitchum, 1984; Mutti, 1985). Based on a synthesis of the improved understanding of ancient and modern turbidite systems, Walker (1978) included the process-based facies concepts of Mutti and Ricci Lucchi (1975) into a reorganized model that combined system-scale progradation trends with spatial and temporal facies distributions and therewith

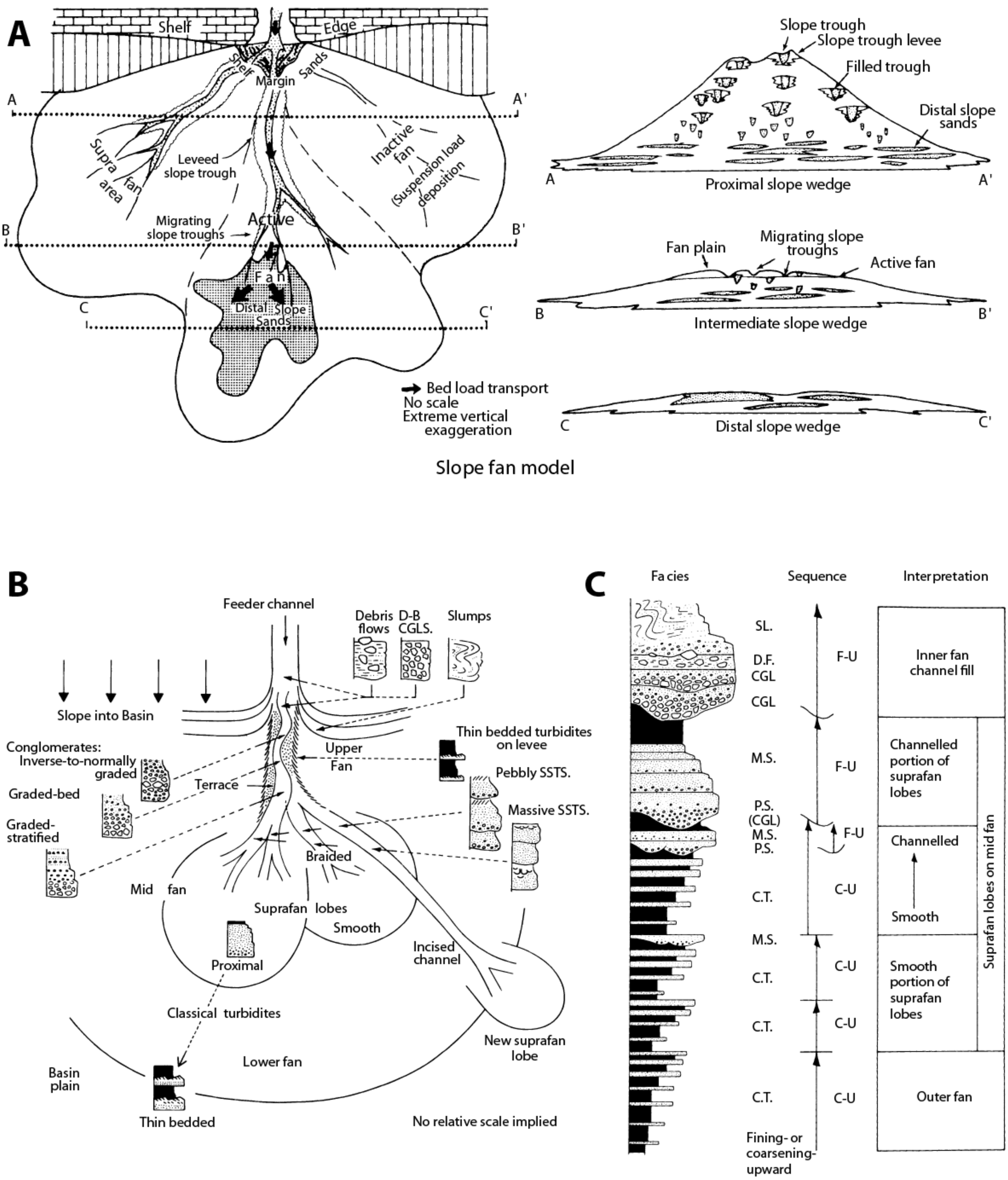

Fig. 2.12. (A) Base of slope submarine fan model outlined by the presence of channels that typically display a dendritic pattern and locally expand to distal fan domains where channels feed attached lobes. Note the shifting and abandonment of channels and associated lobes. Adapted from Brown & Fisher (1977). (B) Submarine fan model illustrating characteristic facies distributions in fan sub-environments and the progradation and shifting of lobes. Adapted from Walker (1978). (C) Proposed idealized vertical sequence for turbidite fan provinces that represent a prograding submarine fan. Adapted from Walker (1978).

provided the first predictive facies model for turbidite fans (Fig. 2.12B). Moreover, the idealized vertical succession, previously introduced by Mutti & Ricci Lucchi (1972) – could be related to pro- and retrogradational patterns (Fig. 2.12C) and hence integrated the concept of sequence stratigraphy. Shanmugam & Moiola (1988) proposed a submarine classification primarily based on geodynamic csettings. The model comprises two end-members: passive margin fans and active margin fans. Passive margin fans comprise immature passive margin fans (North Sea-type) that embody small-scale sandy systems denotive of well-developed lobate sand bodies. Contrastingly, mature (Atlantic-type) passive margin fans represent large muddy systems defined by the negligible presence of sand lobes. Active margin fans typically represent small sandy systems defined by well-defined channel systems and large lobe complexes. Reading & Richards (1994) considered a variety of controlling factors (size of source area, sediment volume and caliber, point-source VS ramp VS transversal fed systems, slope gradient) and provided a classification for submarine fan models as illustrated in Fig. 2.13.

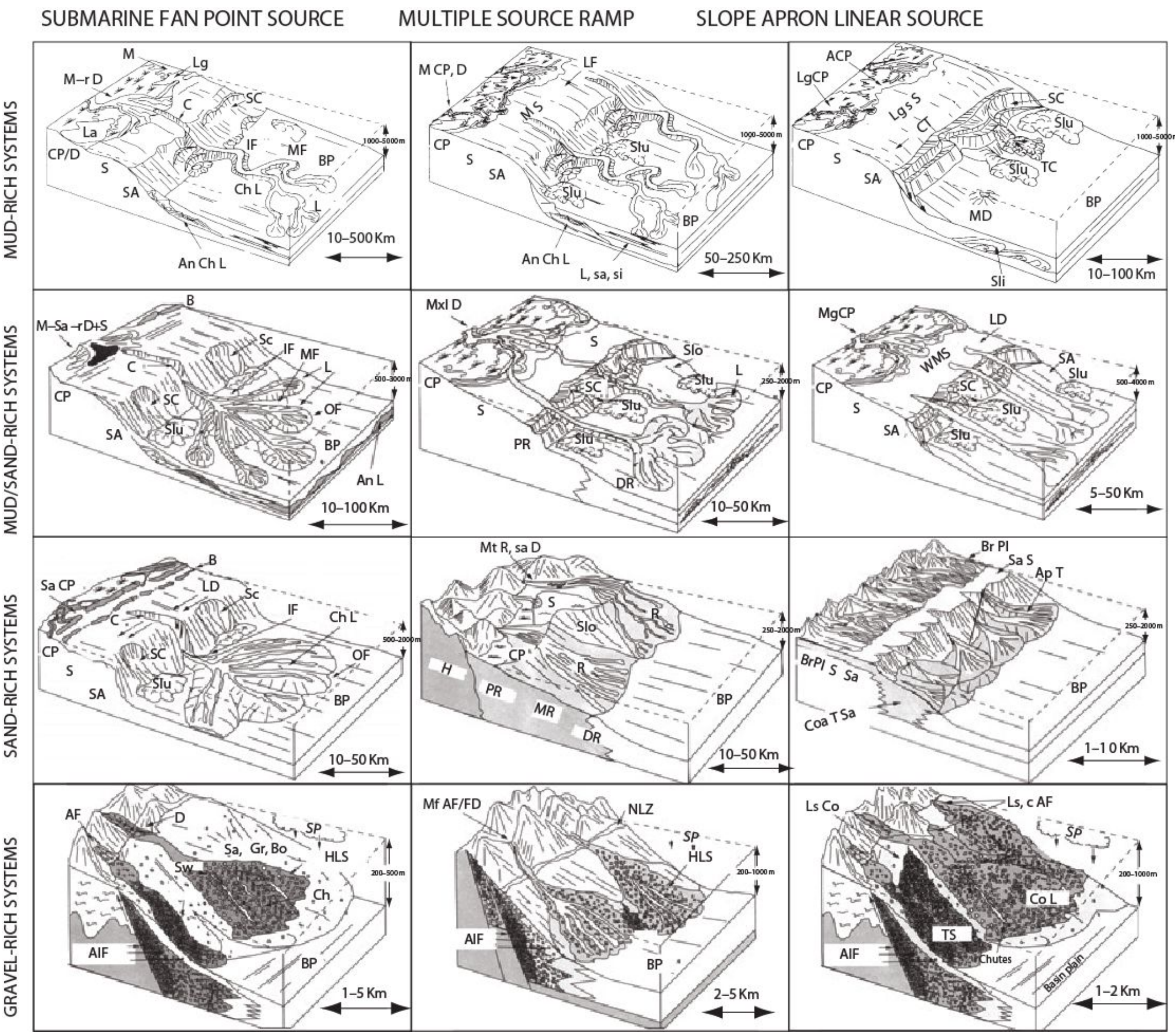

Fig. 2.13. Submarine fans classification owing to sediment staging area morphology, sediment volume and caliber, style of feeding, gradient of slope. Adapted from Mulder (2011); after Reading & Richards (1994).

Improvements in seismic reflection data acquisition and side-scan sonar imagery provided further insights into the diversity of fan sub-environments that describe the complex submarine fan morphology. As previous, rather generalized submarine systems models missed to incorporate the determined fan complexity, research emphasis switched to translating the architectural element approach developed for fluvial systems (Miall, 1985) into the examination of the deep-marine realm, as Mutti & Normark (1991) defined architectural elements as the "basic mappable components of submarine fans". These primary architectural elements include channels, lobes, variably-sized erosional scours, the channel-lobe transition zone located between the channelized and non-channelized environments and overbank deposits that represent lateral constituents of channels. Because of complications in comparing ancient and modern turbidite systems, Mutti & Normark (1987, 1991) satisfied the requirements for comparative schemes at spatially and temporally equal scales. Comparable to the concept of bounding surfaces within fluvial architecture (Miall, 1988), the authors introduced a five-fold spatial and temporal hierarchy classification of siliciclastic deep-sea systems (Fig. 2.14). Each ordered scale is bounded by a surface that mirrors a shift in conditions. Whereas the first hierarchical order corresponds to the entire turbidite complex, the second order resembles the turbidite system, the third and fourth orders exemplifies the turbidite stage or sub-stage, respectively, while the fifth order encompasses the single turbidite event bed. Among many other works that enhanced the understanding of the wide range of diversity in deep-water architectural elements (e.g. Pickering et al., 1995; Clark and Pickering, 1996), Stow & Mayall (2000) provided a comprehensive summary of the principal architectural elements of turbidite systems that is illustrated in Fig. 2.15:

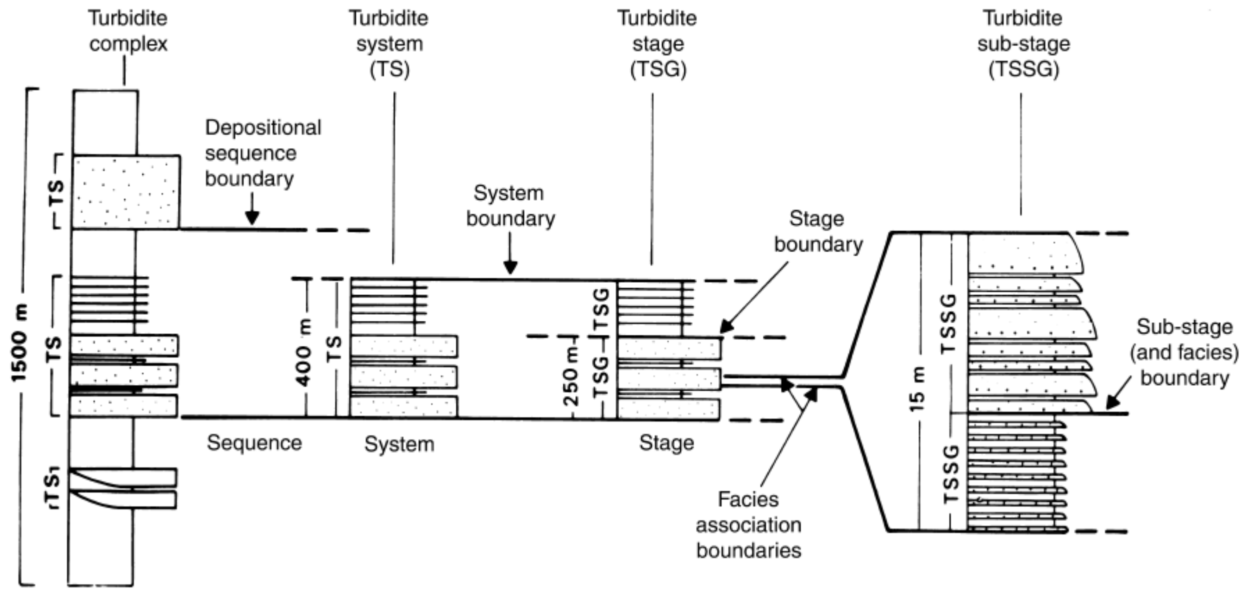

Fig. 2.14. Hierarchical classification scheme for depositional units of turbidite systems. Adapted from Mutti & Normark (1987).

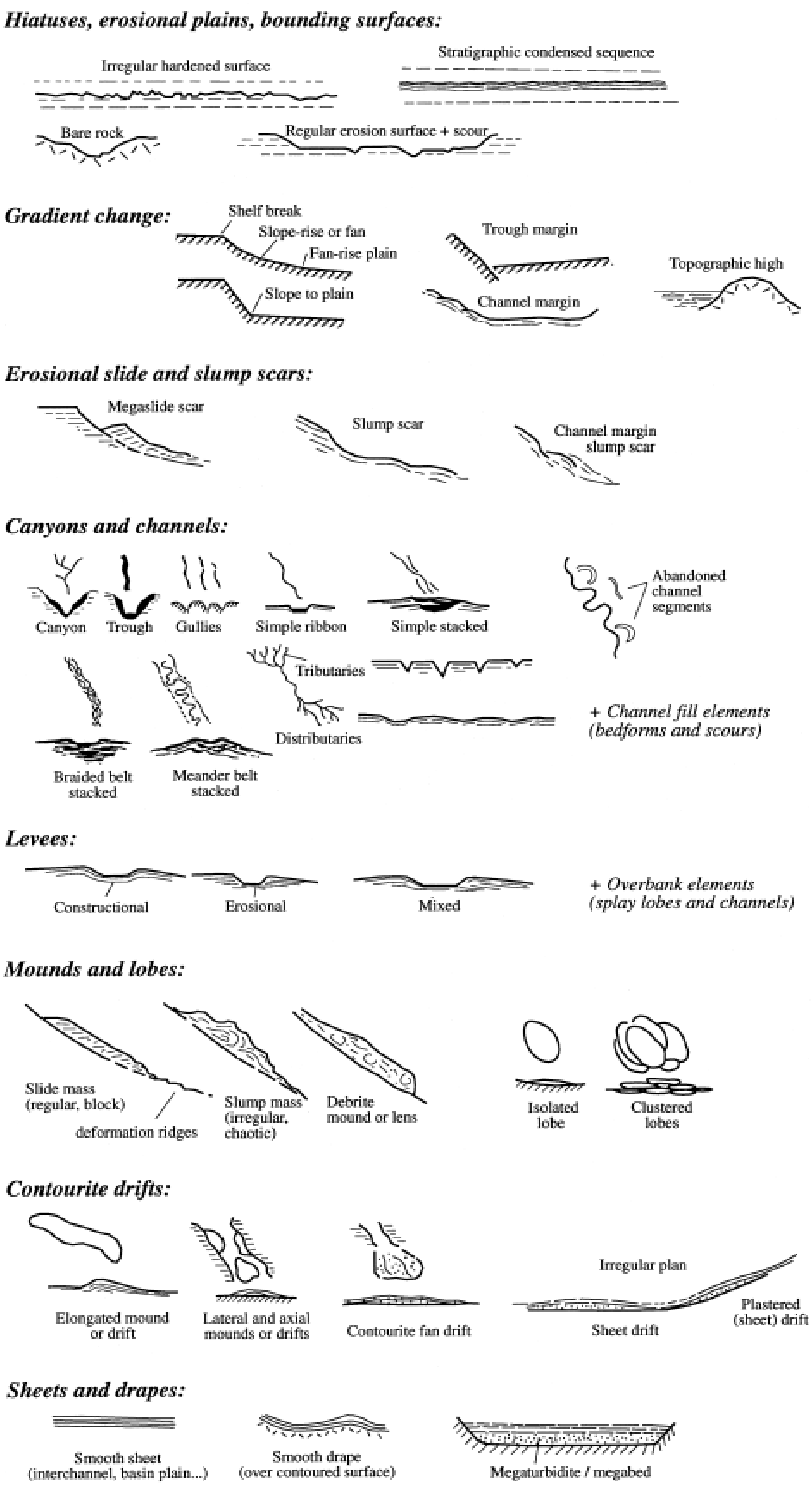

Fig. 2.15. Graphical summary of the primary architectural elements and their cross-sectional expressions in deep-marine depositional settings. Adapted from Stow & Mayall (2000).

2.8 Submarine fan classification based on the flow efficiency concept and implications for grain size distribution

A divergent categorization of submarine fans has been introduced by Mutti (1979; 1985). According to the system´s capability in transporting sand particles for long basin-ward distances, Mutti (1979) proposed two end-members that are portrayed by high-efficiency and low-efficiency turbidite systems (Fig. 2.16A). Flow capacity encompasses the volume of sediment that can be transported by a single flow, whereas the flow efficiency concept represents the ability of a flow to transport sediment basin-ward depending on the clay content (Mutti, 1979). Mutti et al. (1999) expanded the flow efficiency concept into the system´s ability "to effectively segregate its (the sediment´s) grain size populations into distinct facies types with distance". High-efficiency transporting systems are typically mud-rich, as they are dominantly built up of mud-rich sediment density flows that are capable to transport sand fractions over long distances, demonstrating the requirement of plentiful proportions of fine-grained particles in keeping sand in suspension. Sand-rich systems are not capable of providing long down-dip transport of sand. The textural composition of the coarse-grained sediment load that dominates low-efficiency systems is typically immature (Mattern, 2005), suggesting that the development of sand-rich systems is strongly related to tectonic activity. Low-efficiency systems are commonly distributed along active margins (Shanmugam & Moiola, 1988). They may either be fed by a point source or they might be derived from a transversal provenance morphology, resulting in frequently coalescing sand-rich fans (see also Fig. 2.13).

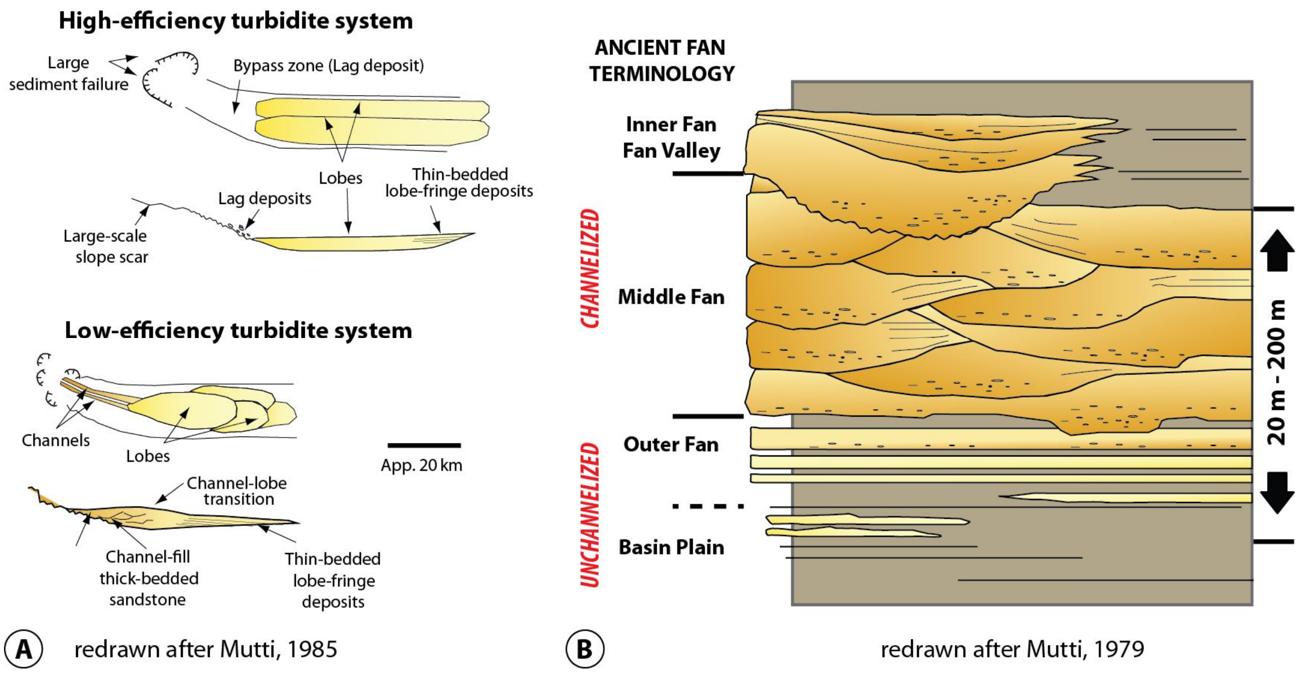

Fig. 2.1.16. (A) Depositional characteristics of high-efficiency and low-efficiency systems. Note the detached emplacement of lobes in high-efficiency systems and lobes attached to feeder channels in low-efficiency systems. Redrawn after Mutti (1985). (B) Stratigraphic expression of sand-rich fans. Redrawn after Mutti (1979).

Due to high degrees of amalgamations, sand-rich fans exhibit a complex stratigraphic architecture and bedding patterns that tend to complicate local correlations (Mattern, 2005; Fig. 2.16B). The flow efficiency concept not only governs the overall dimensions and system-scale architecture, since the type of sediment caliber explicitly affects the individual turbidite event bed architecture (Mulder, 2011). Compositionally immature sediments derived from coarse-grained source environments tend to be dominantly constituted by coarse to very coarse-grained deposits resulting from the deceleration of hyperconcentrated to concentrated density flows. Consequently, massive sandstones represent the bulk of low-efficiency systems´ architecture and can form a basin-ward continuum characterized by the pronounced scarcity of mud (Fig. 2.17A). By contrast, compositionally mature sediments define high-efficiency systems. As the presence of coarse fractions is inheritably limited, coarse-grained deposits are restricted to the very proximal realm as they are related to the transformation of mass-failures. Elutriation generates clay- and silt-rich turbidity currents that account for the bulk volumes of individual event beds (Fig. 2.17B). The very fine-grained fractions generally tend to be bypassed for long down-dip distances (Mulder, 2011) and can basin-ward extend for up to 1500 km (e.g. Talling et al., 2007).

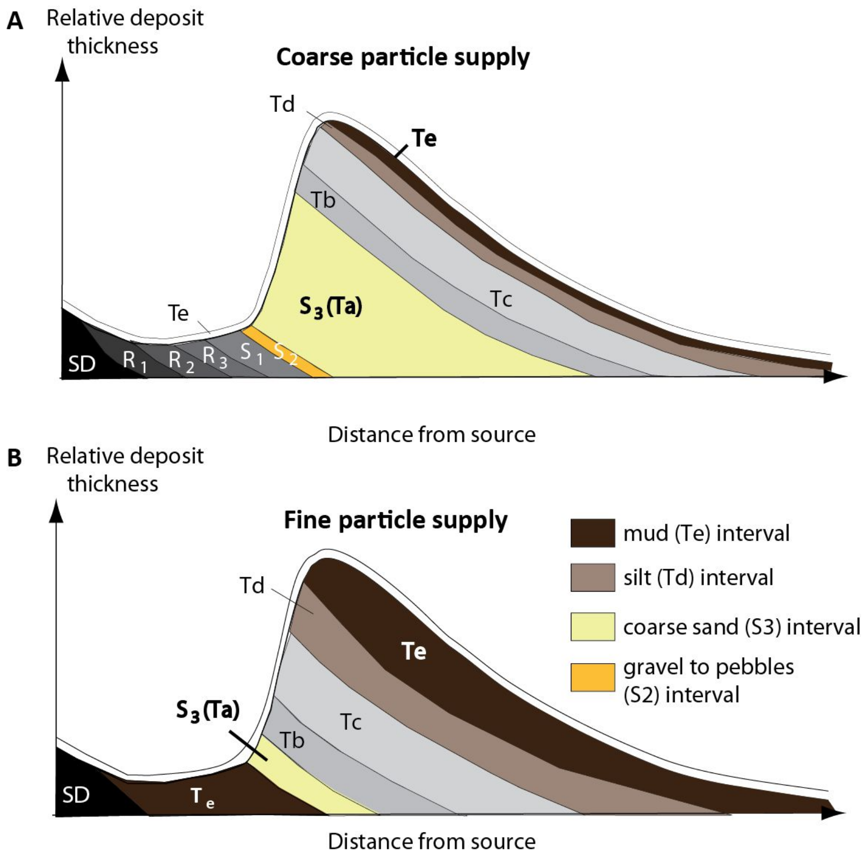

Fig. 2.1.17. Updated "idealized" single event bed architecture proposed by Mulder (2011). Source-dependent dominant grain size distributions are taken into consideration. (A) Coarse-grain provenance derived turbidite architecture typified by the dominance of the sand fraction. (B) Fine-grained provenance derived turbidite. Note the contrasting thickness distributions of the muddy to silty particle fractions over coarse fractions. Modified after Mulder (2011).

3 Introduction to Sedimentary Petrography and Provenance analysis

3.1 Modal detrital framework analysis

The interplay of an array of variables, for instance provenance, physical transport, weathering and diagenesis, defines the composition of terrigenous sedimentary rocks (e.g. Basu, 1985; Critelli et al., 1997). Compositional variations between terrigenous sandstones are typically illustrated in ternary diagrams, with the end-member poles (quartz, feldspar and lithic fragments) illustrating recalculated proportions of the main parameters of detrital grain types. Based on the relative abundance of these three key framework parameters, a descriptive classification of terrigenous sandstones can be established (e.g. McBride, 1963; Folk, 1965; Dickinson, 1970, 1985; Pettijohn, 1975; Garzanti, 2016). The classic descriptive classification scheme introduced by Pettijohn (1975) is illustrated in Fig. 3.1.

Relative proportions of distinct types of terrigenous sand grains furthermore reveal the nature and the origin of the parent rocks of the clastic detritus. The constituents of clastic detritus mirror the tectonic setting of sedimentary basins (e.g. Dickinson et al., 1983; Weltje, 2004; Garzanti et al., 2007) as the plate tectonic setting of the provenance area delineates the principal control on sandstone composition (Dickinson, 1985). A summary of the classification of grain classes utilized in the Gazzi-Dickinson model (applied in this study) is provided in table 2.1. Despite for the classification of lithic fragments, the Gazzi-Dickinson model can be regarded as being practically identical to the Folk (1965) sandstone classification scheme.

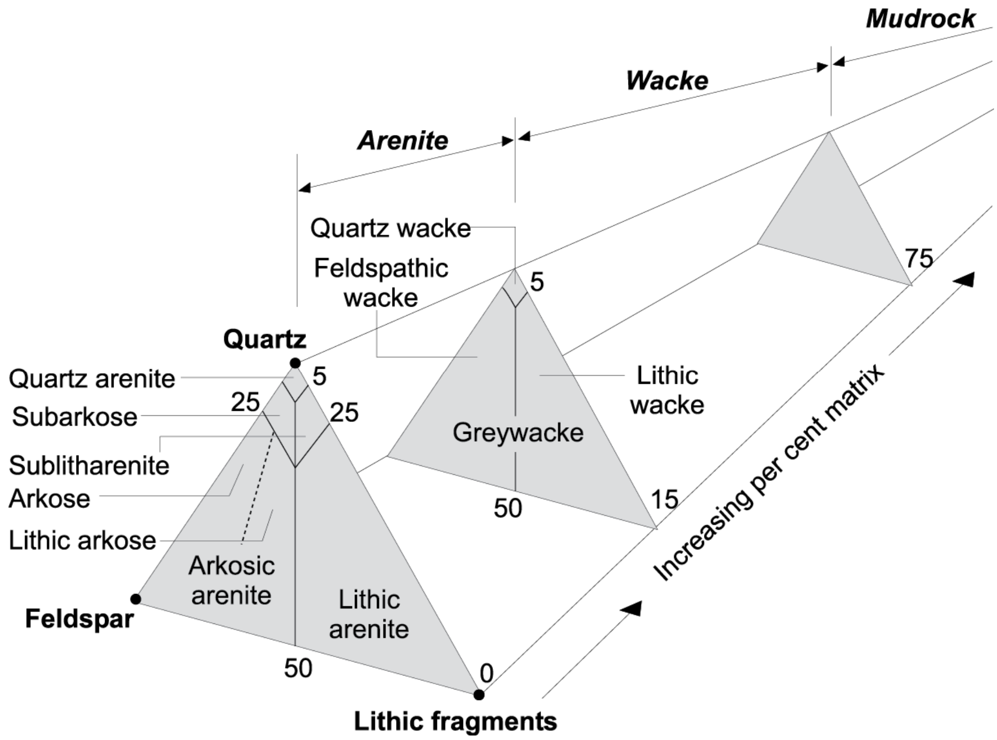

Fig. 3.1. Descriptive classification scheme for siliciclastic rocks after Pettijohn (1975).

Quartzose Grains	**(Qt = Qm + Qp)**				
	Qt	=	total	quartzose	grains
	Qm	=	monocrystalline	quartz	(> 0. 0625 mm)
	Qp	=	polycrystalline	quartz	(or chalcedony)
Feldspar Grains	**(F = P + K)**				
	F	=	total	feldspar	grains
	P	=	plagioclase	grains	
	K	=	Kfeldspar	grains	
Unstable lithic fragments	**(L = Lv + Ls)**				
	L	=	total	unstable	lithic fragments
	Lv	=	volcanic/metavolcanic	lithic	fragments
	Ls	=	sedimentary/metasedimentary	lithic	fragments
Total lithic fragments	**(Lt = L + Qp)**				
	Lc	=	extrabasinal detrital limeclasts (not included in L or Lt)		

Table 2.1. Classification and abbreviations of principal grain classes. Modified from Dickinson (1985).

The principal technique conducted for identifying the modal detrital composition is that of point-counting. This quantitative technique involves the determination of a statistically robust number of grains on a thin-section (e.g. Dickinson et al., 1983; Di Giulio & Valloni, 1992). Warranting that the same point is not described more than once, detrital grain and matrix as well as cement proportions are being recorded. In the interest of establishing a statistically robust representation, typically 300 to 500 points of the thin-section are being counted moving the center of a grid defined by sample grain size.

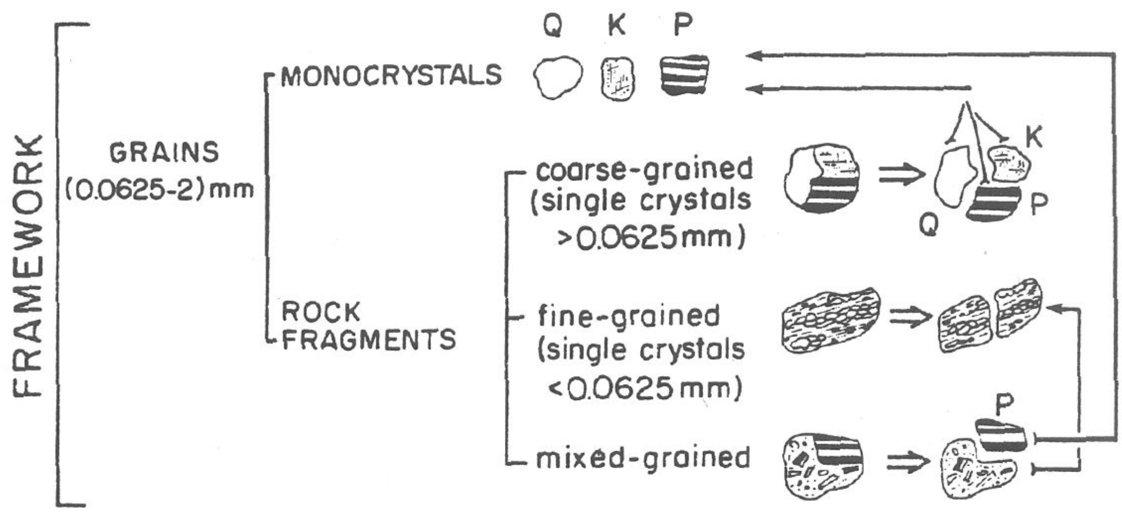

Fig. 3.2. Summarized scheme for the counting method of the Gazzi-Dickinson method. Adopted from Zuffa (1980).

Two principally different approaches regarding the methodology of point-counting can be differentiated (e.g. Basu, 1985; Ingersoll et al., 1985; Di Giulio & Valloni, 1992). The traditional approach (commonly referred to as the "Indiana School"; cf. Basu, 1985) regards any polymineralic grain - independently from the grain size of the single constituents - of dimensions greater than 0.0625 mm as a rock fragment. By contrast, the Gazzi-Dickinson approach ("Stanford School"; cf. Ingersoll et al., 1984) considers a grain (in the following example a quartz grain) of dimensions greater than 0.0625 mm within a polymineralic grain as a single quartz grain. Following the Gazzi-Dickinson method, lithic fragments would only be regarded as a lithic fragment if its dimensions are smaller than 0.0062mm, even if it represents the constituent of a polymineralic grain. In this way, the Gazzi-Dickinson method shows the advantage that it is not dependent on grain-size and is therewith independent from mechanical break-down processes. Sandstone samples derived from the same parent rock reveal the same composition even if they underwent dissimilar mechanical in comparison to the Folk method ("Indiana school"). However, applying the method of the "Indiana School", a such grain would, according to grain-size dependent dissimilarities (polycrystalline fragmentations) hence result in different compositional proportions. Modal framework analysis following the Gazzi-Dickinson method is typically performed with the intention of establishing tectonic field interpretations (Dickinson & Suczek; 1979; Dickinson et al., 1983). In summary, the main difference between the presented approaches is the method used for classifying coarse polymineralic grains. A detailed discussion and comparison of the advantages and disadvantages of both approaches has been provided in several works (e.g. Ingersoll et al., 1984; Suttner & Basu, 1985; Zuffa, 1985).

As the physical appearance of detrital grains is most probably subject to modifications or even might be destroyed by post-depositional changes such as diagenesis and metamorphism, the relationship between tectonic setting and sandstone composition, solely based on framework modes might not in all circumstances reflect the accurate tectonic setting (e.g. Bhatia, 1983; Weltje, 2002; Garzanti & Aldo, 2007). Physical mixing of clastic detritus derived from two or multiple provenance terrains in hinterland areas furthermore embodies a key mechanism that might generate compositional variability and thus may result in conceivable modifications of modal framework composition (e.g. von Eynatten et al., 2003; Weltje, 2004).

3.2 Implications of sandstone modal composition for sediment provenance

Detrital modal compositions reflect the evolution and the composition of the sediment source. Dickinson & Suczek (1979) and Dickinson et al. (1983) proposed three primary provenance settings which comprise (1) continental blocks (cratons) and uplifted basement, (2) magmatic arcs and (3) recycled orogens (see Figs. 3.3). Continental blocks represent provenance terrains made up of stable continental cratons and platforms such as passive continental margins that promote enhanced maturity of the siliciclastic sediments as illustrated by quartzose compositions and high K-feldspar to plagioclase ratios. Uplifted basement represents a provenance terrain marked by plate boundaries that experience tendencies of intraplate deformation of continental block mass. Rapid uplift is therewith reflected by the classical arkosic modal framework (quartzo-feldspathic) typified by almost absent lithic fragments. Active magmatic arc provenances are mainly located along volcanic arcs that cover the igneous belt and within granitoid plutons of the arc roots. The characteristic modal framework signature is that of feldspatholithic sands dominated by volcanic fragments that pass towards quartzo-feldspathic compositions. Recycled orogens sediment sources are dominantly composed of sedimentary successions and subordinate volcanic rocks. These may partially be metamorphosed and subject to erosion through orogenic uplift and tend to generate quartzolithic compositions.

As the relative proportion of a certain detrital grain is both dependent on the abundance of the given crystal in the source rock and its resistance to mechanical and chemical erosion, both the paleo-geology of the provenance area and the maturity of the clastic detritus can therewith be inferred from ternary diagrams (e.g. Graham et al., 1976; Zuffa, 1985; Cibin et al., 2003; Di Giulio et al., 2012). Moreover, paleoclimatic conditions of the parent rocks that represent the provenance domain of the siliciclastic sediment can be derived from the position within the ternary plot (e.g. Suttner & Dutta, 1986; Johnsson et al., 1988; Weltje, 2006). In this study, the Gazzi-Dickinson approach has been followed, with the aim of obtaining source area constrains from optical thin-section analysis (point-counting). Incorporating the proportions of quartz, feldspar and lithic fragments into ternary diagrams permits the classification of sandstones based on their framework composition. Subsidiary diagrams focus on subsets of these three principal components according to Folk (1965). A brief review of the objectives of plotting distinct end-member parameters and interpretation guidelines regarding their potential provenance implications will be discussed in the following:

The QtFL diagram (Fig. 3.3 A) is indicative of sediment maturity as transport mechanisms of the siliciclastic sediment is revealed through the relative grain stability. Accordingly, emphasis is put on maturity of the detritus that experiences variable degrees of weathering. The QmFLt plot (Fig. 3.3 B) embraces polycrystalline quartz and chert fragments (Qp) into the total lithic fragment (Lt) end member and thus takes grain size variations of the source rock into consideration (Dickinson, 1985). Plots of QpLvLs proportions (Fig. 3.4A) differentiates the principal lithic fragments by discriminating between sedimentary and metasedimentary lithic fragment (Ls), volcanic lithic fragment (Lv) and combined polycrystalline quartz and chert fragments (Qp) and consequently discriminates between subduction-related source rocks, collision suture and fold-and-thrust-belt sources, and arc orogen sources (Dickinson & Suczek, 1979). The QmPK plot (Graham et al., 1976; see Fig. 3.4 B) dismisses lithic fragments and emphasizes on the proportions of the two main feldspar varieties plagioclase (P) and potassium feldspar (F). This plot allows the discrimination between plagioclase-rich sources of a magmatic arc origin and continent-derived parent rocks that tend to be enriched in alkali feldspar.

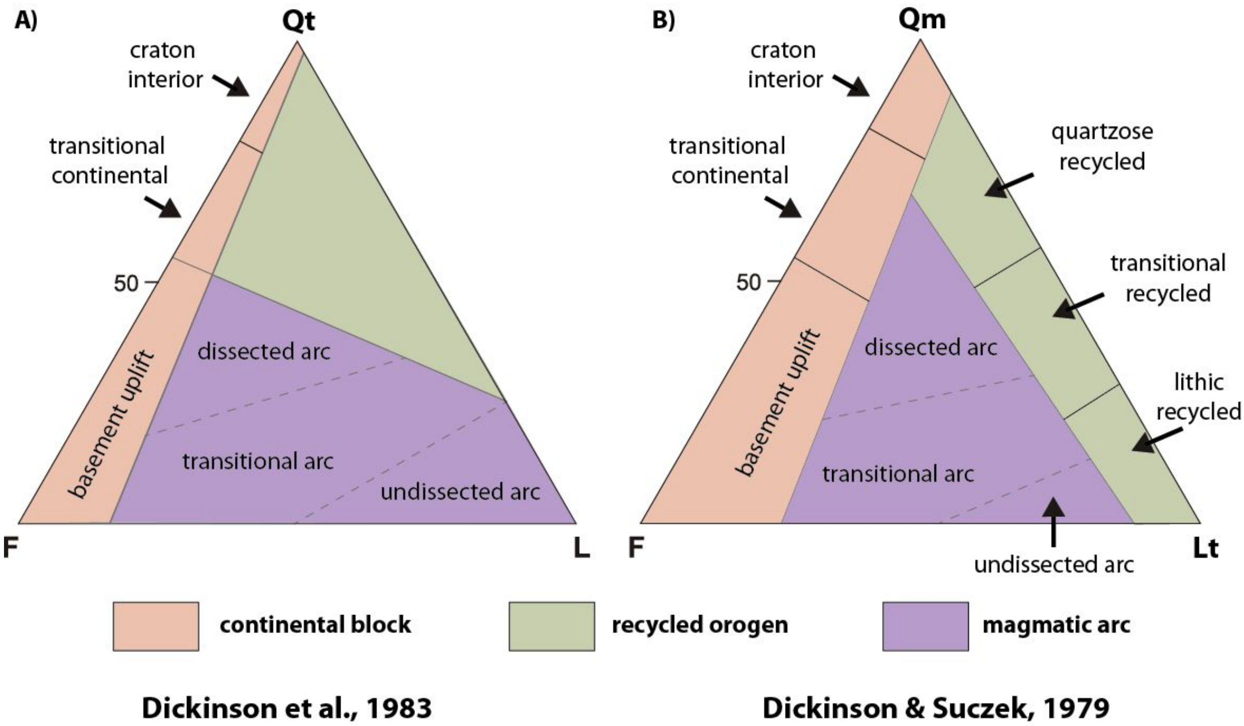

Fig. 3.3. Interpreted relationships between modal composition and tectonic setting tectonic denotive for provenance discrimination fields after (A) Dickinson et al., 1983 and (B) Dickinson & Suczek (1979).

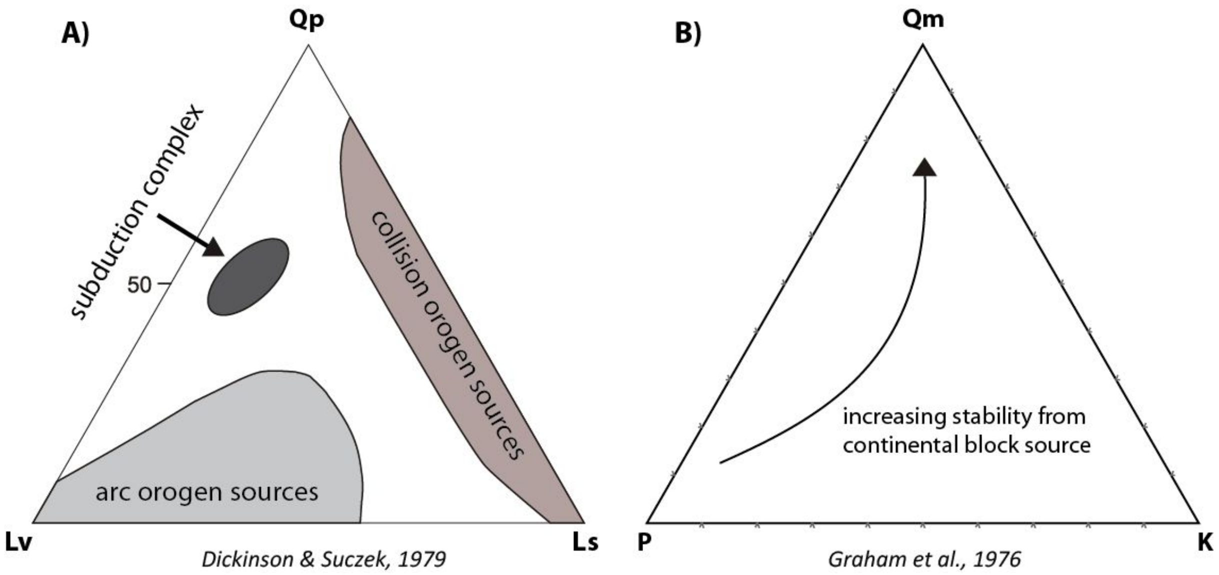

Fig. 3.4. Examples of interpretations of provenance discrimination diagrams. (A) QpLvLs plot underlining the division between arc-orogen sources, subduction-related parent rocks and collisional regime sources (after Dickinson & Suczek, 1979). (B) QmPK plot putting emphasis on the proportions of feldspar varieties that allows the distinction between magmatic arc and continent source rocks (after Graham et al., 1976).

3.3 Recent developments in provenance discrimination through modal framework composition analysis

Garzanti et al. (2007) emphasize on the importance of the complexity observed within orogenic settings (axial belt source rocks) in providing source areas and propose an updated classification scheme for the interpretation of modal framework compositions. Furthermore, ensuing recycling due to physical weathering within composite mountain belts is integrated into the interpretative scheme of modal framework ternary diagrams. An overview of the suggested primary provenance settings is concisely presented and illustrated in Fig. 3.5.

- **Magmatic arc:**

Equal to the provenance domain defined by Dickinson et al. (1983), the modal composition of sediments derived from the undissected magmatic arc provenance is dominated by volcanic detritus delivered from the cover of the magmatic arc. Subordinate portions of plutonic detritus are characteristic for the plutonic roots of the arc massif that become exposed in the dissected magmaticarc provenance. The progressive increase of quartz, K-feldspar, and blue-green hornblende at the expense of volcanic lithic grains and pyroxenes ideal defines the idealized compositional trend recorded by terrigenous sequences accumulated in forearc and other arc-related basins during unroofing of the arc massif.

- **Ophiolite provenance:**

A new provenance domain for ophiolites that escaped subduction and orogenic metamorphism is proposed. These tectonically accreted or obducted segments of oceanic lithosphere have the tendency to produce mafic to ultramafic detritus with peculiar petrographic and mineralogical features (Nichols et al. 1991). Discrete petrographic signatures reflected in heavy mineral assemblages denotative of distinct sections of the oceanic crust characterize evolutionary trends of the modal framework composition. In particular, stages of prolonged exposure of deep oceanic crust is mirrored by the presence of minerals indicative of primitive oceanic rocks such as olivine and chrome spinel.

- **Axial belt provenance:**

This additional new provenance domain defined as being the most distinctive provenance setting for orogenic belts represents an updated interpretation of the “transitional recycled” provenance field of Dickinson et al. (1983). Mountain belts formed through continent-continent collision are built up of axial belts that consisting of piles of neo-metamorphic nappes. Consequently, the detrital modal framework is a function of various metamorphic grades of nappes that constitute the axial zone and the relative abundance of continental versus oceanic protoliths as well as the sedimentary cover. The

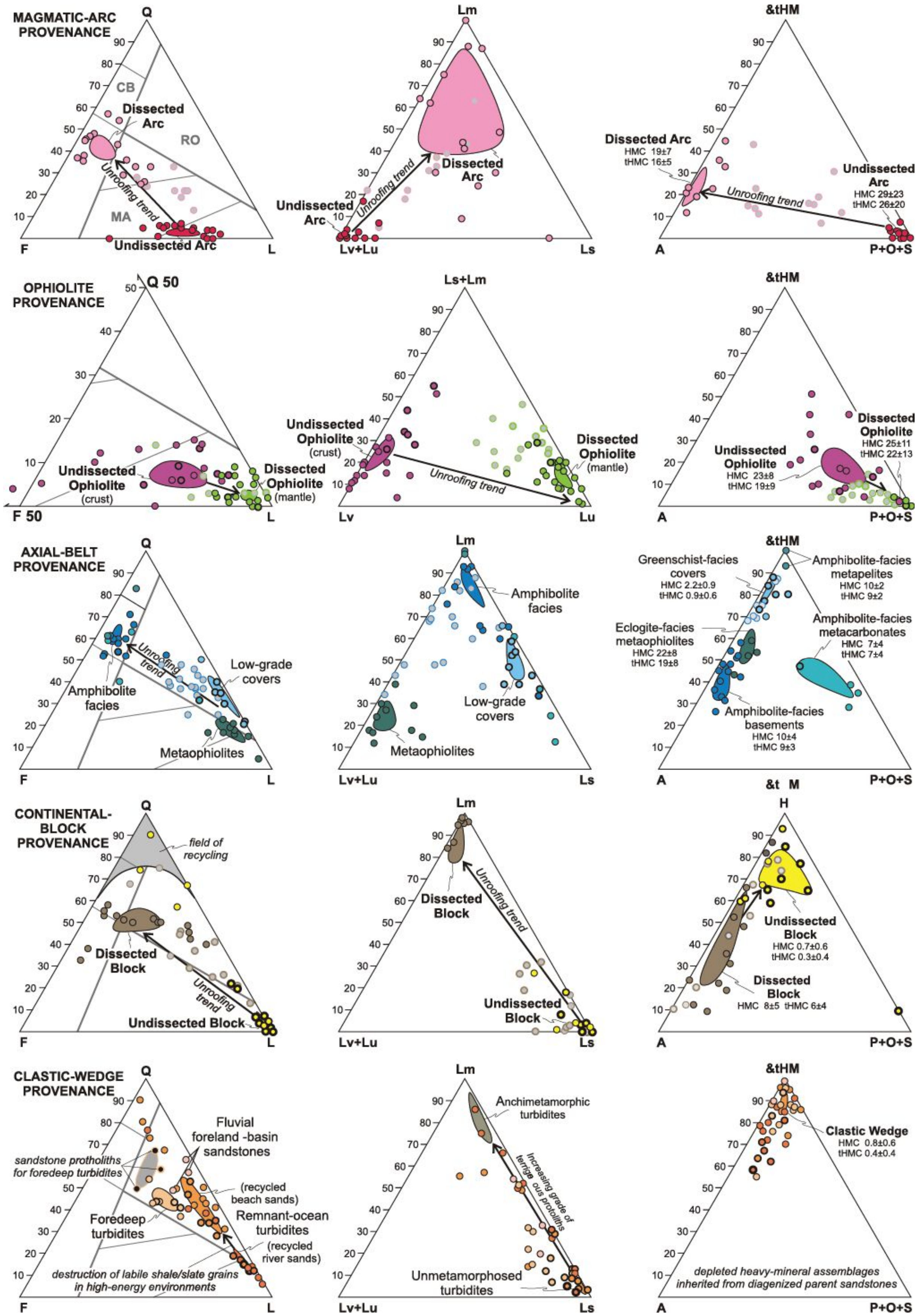

Fig. 3.5. Updated provenance field discrimination scheme after Garzanti et al. (2007).

unroofing of the orogen is accompanied by the exposure of nappes that display progressively increasing metamorphic grades. This might favor the enrichment of feldspars and heavy minerals proportions in the clastic detritus. The socket of the orogen is generally marked by the abundance of quartzo-feldspathic lithic fragments rich in hornblende. At the final stage of exhumation, high-pressure metasedimentary minerals such as chloritoid, staurolite, kyanite and sillimanite become increasingly copious.

- **Continental block provenance:**

The continental block provenance field largely in accordance with that of Dickinson et al. (1983). The modal composition of the clastic detritus reflects plutonic, sedimentary and metasedimentary source rocks that generally comprise quartz, feldspar and metamorphic and volcanic rock fragments. Progressive exhumation of deeper crustal rocks is reflected by evolutionary trends in modal compositions. Shifts from a dominance of sedimentary-volcaniclastic lithic fragments typical for cover sequences denotative of quartz-rich composition providing evidence for polycyclicity to quartzo-feldspathic and feldspathic metamorphoclastic signatures are typical. At the expense of metamorphic rock fragments, heavy minerals proportions are expected to increase with subsequent erosion of the continental block socket.

- **Clastic wedge provenance:**

Recycled parent sandstones derived from allochthonous and autochthonous cover sequences tend to produce a similar compositional framework to that of the typically quartzolithic mountain belt-derived detritus of the axial belt provenance domain. Notwithstanding, a significant increase in unstable mudrock-clasts in this detritus characteristic for poly-cyclic reworking is to be observed. Very low proportions of parent recycled stable to ultra-stable heavy minerals mirror the dissolution of less stable heavy minerals during the stages of diagenesis of the parent rocks.

- **Mixed provenance in anorogenic settings**

Likewise, anorogenic tectonic environments tend to produce distinct detrital framework compositions (Garzanti, 2015): Potential source rocks at divergent plate margins include continental blocks as well as rift-related volcanic rocks shedding feldspatho-lithic volcaniclastic sand-rich in clinopyroxene. Where pull-apart basins are tectonically inverted during late rifting stages, recycling of syn-rift clastic successions may produce quartz-rich sands with poor heavy-mineral suites.

- **Mixed provenance in orogenic settings**

Recycling and mixing of detritus derived from the proposed five primary provenances can result in highly complex mixed provenance detrital compositions signatures (Garzanti, 2015). Orogens can be regarded as resulting from the colligation and the piling of combinations of tectonic domains that are organized in subparallel elongated belts which provide the provenance for mixed detritus. A limited number of orogen archetypes are identified that represent different geological objects generated by subduction processes involving the lithospheric-scale products of different geodynamic scenarios in both footwall or hanging wall. Probable detrital modes, heavy mineral assemblages and unroofing trends are to be expected.

3.4 Single grain techniques for sediment provenance inference: Detrital zircon chronology

Radiogenic geochronological and thermochronological investigations provide crucial constraints on the absolute timing and the duration of geological processes (e.g. Allègre, 2008; Carrapa, 2010; see Fig. 3.6). Low-temperature thermochronology studies (e.g. cosmogenic dating, U/Th (He) dating and apatite fission track thermochronology) offer the opportunity of investigating both exhumation and erosion rates of orogenic chains as well as the thermal history of basinal systems. The assessment of thermochronometers defined by higher closure temperatures (e.g. single crystal rutile, monazite, titanite and zircon U/Pb chronology) allows the precise age determination of the original crystallization time of magmatic rocks and the overprinting history of metamorphic rocks (Carrapa, 2010). Consequently, in view of the enhancement of provenance discriminations established by petrographic analyses, the integration of detrital single crystal geochronology developed as an increasingly applied complementary tool in sediment provenance analysis in the past decades (e.g. Gehrels, 2000; Fedo, 2003; Fonneland et al., 2004; Vermeesch, 2004; Andersen, 2005; Dickinson & Gehrels, 2009; Carrapa, 2010). The benefit of detrital geochronology is that it allows the determination of the crystallization age of single detrital crystals and thus provides significant supplementary information about the provenance of their hosting sedimentary rocks (e.g. Gehrels, 2014; Schoene, 2014).

This absolute age component can be revealed by the utilization of isotope radioisotope dating, a technique that grounds on the process of constant radiometric decay (Allègre, 2008). Atoms comprise a nucleus which is surrounded by an electron cloud. The nucleus itself consists of nucleons constituted by protons and neutrons, with the sum of protons and neutrons being termed the mass number (A). The number of protons is described by the atomic number (Z). The number of neutrons is termed (N), and is calculated by the number of minus the sum of neutrons and protons (N = A-Z).

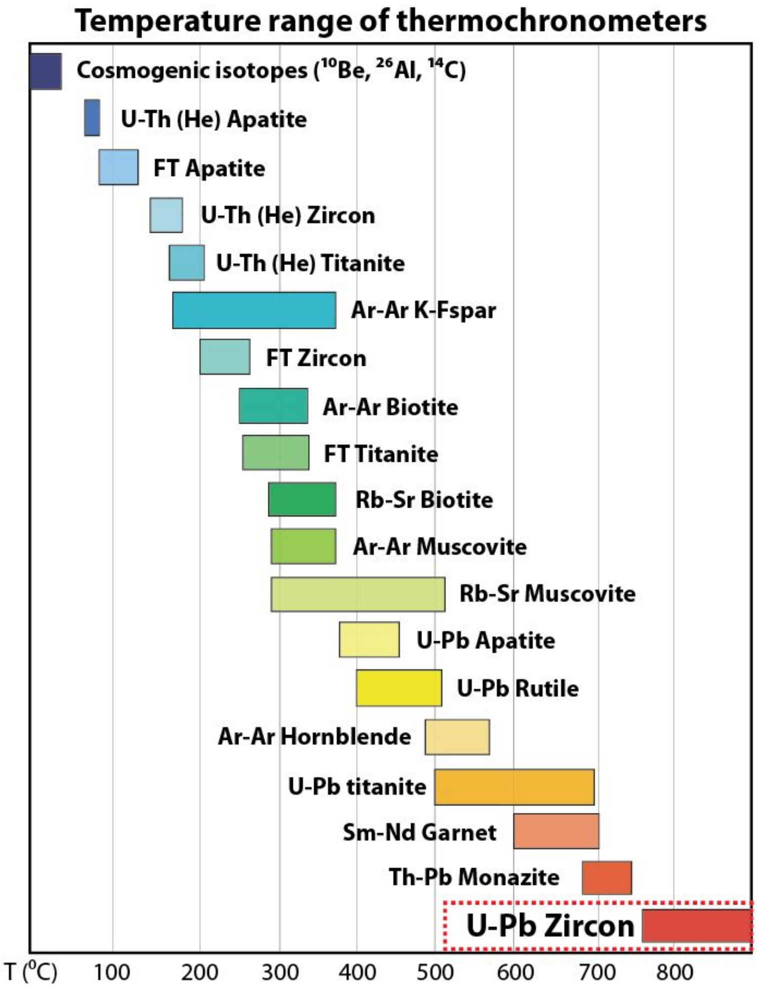

Fig. 3.6. Compilation of thermochronometers and respective closure temperatures used in Earth Sciences. Modified from Ganguly & Tirone (2009; available at www.geo.arizona.edu).

Owing to the fact that differences in the number of neutrons occur, numerous elements consist of several atomic species with equal nuclear charge but different atomic masses which are termed isotopes or unstable nuclides (Allègre, 2008). If the ratio between the number of neutrons and protons reaches a critical value, the unstable nucleon starts to alternate (over intermediate unstable daughter isotopes) towards a stable daughter isotope to satisfy Einstein´s laws of conservation of energy and mass by release of particles or radiation (see Fig. 3.7 for the example of the U-(Th-)Pb isotopic decay series). Given the fact that the decay occurs constantly over time, the rate at which a radioactive parent isotope decays to a radiogenic daughter isotope per unit time only depends on the number of parent isotopes present. According to the Curie-Rutherford-Suddy law, the decay of each isotope is described by its distinctive decay constant and its radioactive half-life time which defines the concept of geochronology:

$$\frac{dN}{dt} = -\lambda N$$

where N is the number of neutrons, and λ is the proportionality constant that represents the probability constant that expresses the probability that the radioactive decay takes place at a given time. The measurement of the ratio between the proportions of parent isotopes and daughter isotopes therewith permits the calculation of the decay constant, the value that describes the temporal relationship between the ratio of the parent isotope and the respective daughter isotope. Radioactive decay is manifested by a variety of processes (Allègre, 2008):

- α-decay occurs when the parent isotope emits a particle comprising two protons and two neutrons. It forms part of the U-Th-He and ^{147}Sm-^{143}Nd series.

- β-decay takes place when the parent isotope emits a particle of either negative (β^- decay) or positive charge (β^+ decay). β^- decay represents the mechanism that controls the ^{40}K-^{40}Ca and 87Rb-87Sr systematics, whereas β^+ decay takes place in the U-Th-Pb and ^{40}K-^{40}Ar systematics.

- γ-decay develops if the nucleus transforms from a higher to a lower energy state without a change in the number of nucleons coming about. The parent and daughter isotopes consequently represent the identical chemical element. A such transformation is realized by the emission of a high-energy photon.

- spontaneous nuclear fission may develop in very heavy nuclei when sufficient energy of the neutrons results in a reaction that disintegrates the nucleus into two parts of dissimilar size. The uneven size results in the generation of free neutrons that result in β^- decay.

3.5 The U-(Th-)Pb systematics

Uranium isotopes are generally unstable and together with thorium decay to form stable, non-radiogenic lead (Pb) isotopes (e.g. Fedo et al., 2004; Allègre, 2008; Fig. 3.7). The basic principle of U-Pb dating is that the Pb^{2+} cation is commonly excepted during the crystallization process and that the quantity of natural Pb in zircon is principally constant (Carter & Bristow, 2000). Radiometric dating of uranium isotopes is commonly derived from the two main decay series: ^{238}U decays into ^{206}Pb and ^{235}U decays into ^{207}Pb and ^{232}Th decays to ^{208}Pb. The decay mechanisms, half-lifes and decay constants of the three commonly used isotopic systems can be summarized as the following:

$$^{238}U \rightarrow {}^{206}Pb + 8\,\alpha + 6\,\beta^- + Q;\ \text{(Half-life = 4468 Ma)};\ \lambda_{238} = 1.55125 \text{x} 10^{-10} a^{-1}$$
$$^{235}U \rightarrow {}^{207}Pb + 7\,\alpha + 4\,\beta^- + Q;\ \text{(Half-life = 704 Ma)};\ \lambda_{235} = 9.8485 \text{x} 10^{-10} a^{-1}$$
$$^{232}Th \rightarrow {}^{208}Pb + 6\,\alpha + 4\,\beta^- + Q;\ \text{(Half-life = 1405 Ma)};\ \lambda_{232} = 0.4933 \text{x} 10^{-10} a^{-1}$$

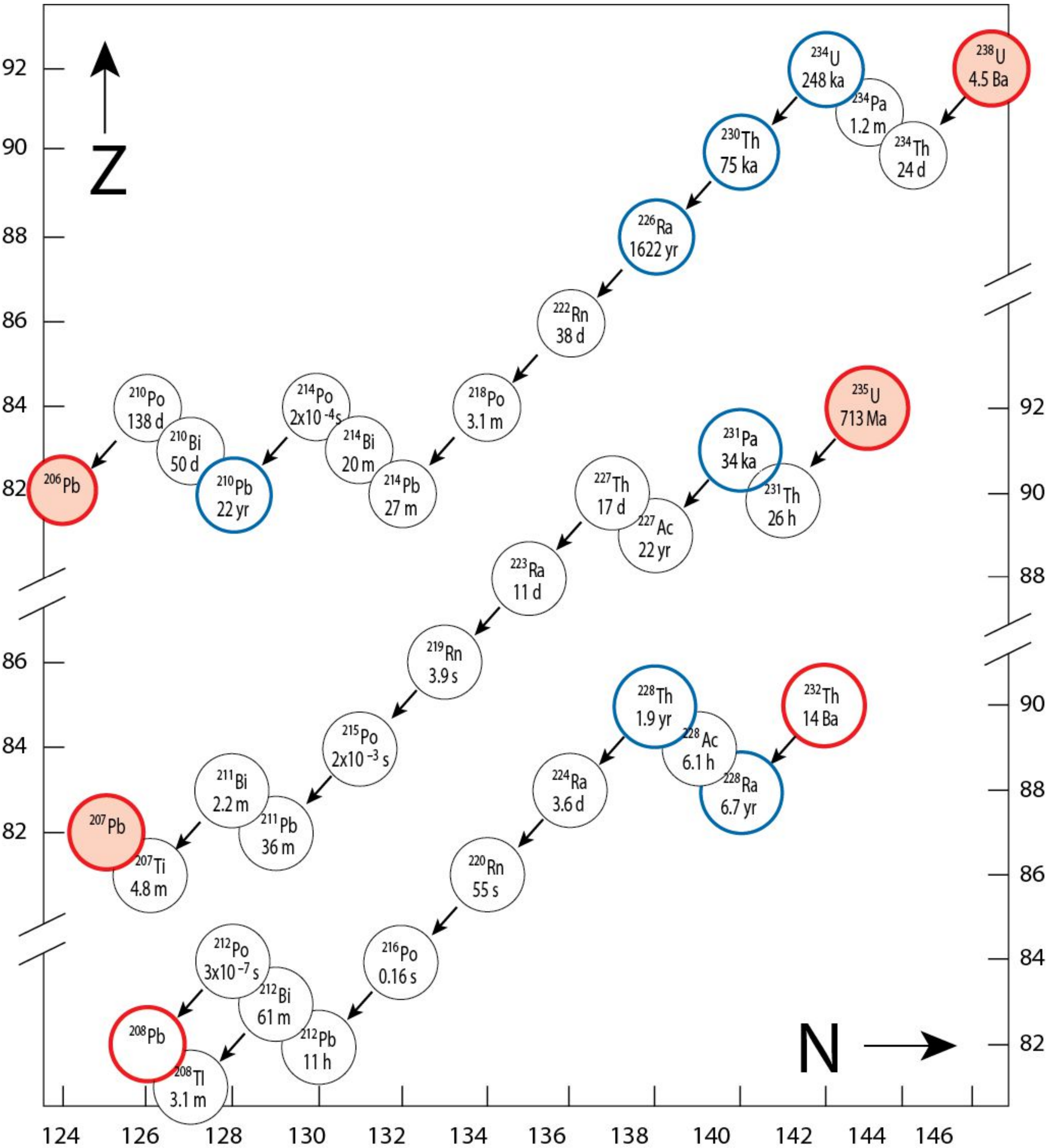

Fig. 3.7. The ^{238}U-^{206}Pb, the ^{235}U-^{207}Pb and the ^{232}Th-^{208}Pb isotopic decay series that form the basis of U-(Th)-Pb radiometric dating. Modified from Allègre (2008).

The availability of two independent decay systems among the same parent-daughter pair (i.e. the ^{238}U-^{206}Pb and ^{235}U-^{207}Pb alpha decay chains) along with well-established decay constants allows an internal evaluation of the obtained results (Bowring et al., 2006). Given the fact that the ages of the two-aforementioned isotopic systems match, the analysis is regarded as being concordant (e.g. Allègre, 2008; Schoene, 2014). The common way of presenting results from U-Pb chronology is the practice of concordia diagrams (Wetherill 1956; Fig. 3.8). Within the Concordia diagram, the concordia line describes the temporal relationship between the ratios of $^{206}Pb/^{238}U$ and $^{207}Pb/^{235}U$ according to their decay constants (Wetherill, 1956). The In case the values of both calculated ratios match (i.e. the $^{206}Pb/^{238}U$ and $^{207}Pb/^{235}U$ ratios are equal), these plot along a curve that is termed "concordia", and the determined age can be interpreted as reliable (Fig. 3.8). Because of the difference in decay constants in between the two isotopic chains, the concordia line has a curved shape. If the two considered ages are not in agreement the analysis is treated as being discordant and regarded as unreliable. Discordance might result from a variety of disruptions in the geological history of the mineral grain such as additional gain of uranium or thorium or episodic loss of lead from the crystal structure (see Bowring et al., 2006 and Schoene, 2014 for reviews and discussions). A typical source for Pb loss are the partial opening of the system through metamorphic overprint (metamictization), the loss of lead along defects in the crystal latrice or the mixing of zircon components with different ages during analysis (e.g. cores and rims). Moreover, fluid infiltration through hydrothermal circulations might result in Pb loss (e.g. Hoskin & Schaltegger, 2003). Discordant analyses yet might contain valuable age information that are however difficult to interpret in detrital data. In contrast to the dating of homogeneous rock bodies where the ages of different events that affected the minerals are recorded in the U–Pb data, a complex interpretation needs to be assumed for discordant detrital age spectra (Reimink et al., 2016).

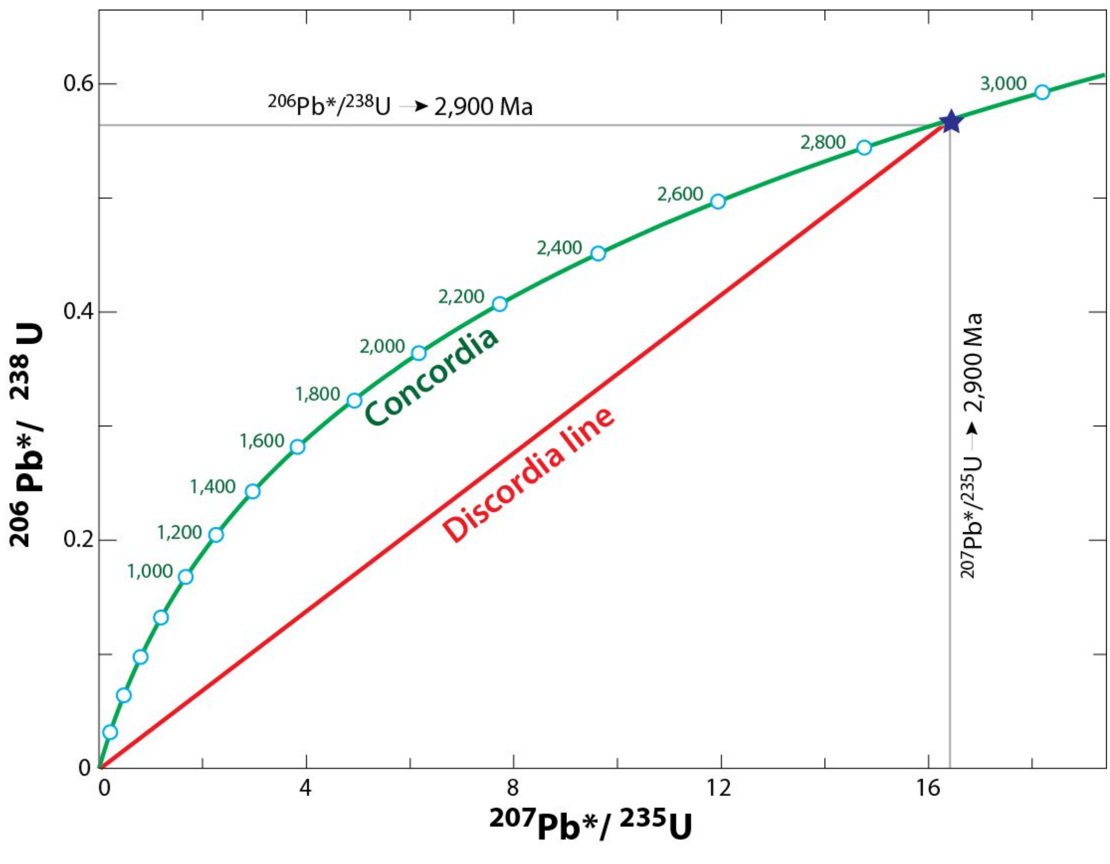

Fig. 3.8. The concordia diagram of Wetherill (1956) illustrating the concordia line (green color) and the discordia line (red color). Slightly modified from Gehrels (2014).

3.6 Zircon imaging

To avoid the risk of analyzing crystals typified my lattice damages or analyzing crystal zones of complex inheritance that might yield mixed radiometric ages, the crystals are commonly visually investigated prior to dating. Data imaging is typically performed by means of scanning electron microscopy (SEM) or cathodoluminescence (CL) detectors. The aim of zircon imaging is to reveal the internal structures of the grains in order to provide proper targets for the laser ablation procedure (e.g. Corfu et al., 2003; Gehrels, 2014; Schoene, 2014)

3.7 Analytical techniques: Mass spectrometry

The precise measurement of isotopic compositions and ratios is established by mass spectrometry, a technique that sorts and measures accelerated ions and isotopes according to their masses as they passage through a magnetic field (Allègre, 2008). The mass spectrometer consists of three major components: a source, a magnet and a collector that operate under vacuum conditions to prevent the ions of losing their charges due to collisions. The ion source is typically represented by a filament or a plasma torch. The function of the source is to bring about and to accelerate ions from atoms. The mass analyzer, an electromagnet, sorts the ions based on their masses. Finally, the ion detector (a Faraday-bucket) collects and measures the ion charges by carrying them along an electrical resistor. Measured potential differences permit the calculation of the ionic current and conclusions on the isotopic composition can be drawn.

Three main types of mass spectrometers, each of which has its own advantages and disadvantages, are typically utilized (e.g. Gehrels et al., 2009; Schoene, 2014): (1) ID-TIMS (isotope dilution thermal ionization mass spectrometry), (2) SIMS (secondary ionization mass spectrometry and (3) LA-ICPMS (laser ablation inductively coupled plasma mass spectrometry). The ID-TIMS method involves the dissolution of the analyzed grains, whereas in SIMS and LA-ICPMS dating analyses a microbeam is used. Consequently, both the latter procedures allow individual zones of the crystals to be dated, but do not detect with a similarly high precision than ID-TIMS. The SIMS or SHRIMP (Sensitive High-resolution Ion MicroProbe) method provides in-situ dating at high spatial resolution and thus allows dating crystals that show complex inheritance. However, the method however requires complex instrumentation and is time-consuming and expensive. The advantages of the LA-ICPMS (in comparison to SIMS) are that the dating of the mineral can be performed in-situ and its cost-effective and fast handling. The disadvantages of the method are the bigger spot size and the lower precision (Schoene, 2014).

3.8 Detrital zircon chronology

Among many other geochronometers (commonly defined by lower closure temperatures), zircon ($ZrSiO_4$) represents one of the most frequently minerals in geochronology, as it integrates small concentrations of uranium (U) and to a lesser extent thorium (Th) but exludes lead (Pb). Due to their cost-efficient and high precision formation age determinations, constrains from of detrital zircon crystal analyses gained steadily increasing significance as an important geochronometer and at the present day represents the most commonly used detrital geochronometer (e.g. Bowring et al., 2006; Gehrels, 2014; Schoene, 2014). Zircons are ubiquitous in crystalline and metamorphic rocks, and moreover are highly resistant to mechanical and chemical weathering. For that reason, zircons are omnipresent in sandstones (e.g. Fedo et al., 2004; Thomas et al., 2011). With respect to the high closure temperature of greater than 800°C (cf. Thomas et al., 2011), zircon grain ages record the time of zircon formation in igneous or high grade metamorphic environments. On the one hand, this high closure temperature also results in a high resistance to thermal overprinting ("resetting") of the U-Pb dating system (Carter & Bristow, 2000; Carter & Moss, 2009). Metamorphic overprint can however be reflected in rim overgrowth of inherited zircon cores (Schoene, 2014). On the other hand, the enhanced durability classifies zircons as likely serving as a closed system for geochronologic investigations, which allows zircon grains to be reworked through multiple sedimentary cycles (Carrapa, 2010; Thomas, 2011). The use of detrital zircon ages finds an array of applications in sedimentological and stratigraphic analyses, out of which at the present day the integration into provenance analysis is the most applied (e.g. Cawood et al., 2003, Dickinson & Gehrels, 2009). The basic principal of detrital zircon chronology is to link age datasets obtained from detrital zircon investigated in a sandstone sample with crystallization ages or the timing of high-grade metamorphic events of potential source terrains (e.g. Fornelli et al., 2014; Carrapa, 2010). This approach comprises the detailed comparison of detrital zircon ages with bedrock crystallization age distributions of candidate source regions (cf. Thomas, 2011 and references therein). With that said, a fundamental understanding of the crystalline geology of source terrain candidates is required to link the ages represented in the detrital spectra to source terrane crystallization ages (e.g. Gehrels, 2014).

Detrital zircon chronology can moreover practically be incorporated into stratigraphic investigations (Bowring et al., 2006). One important stratigraphic application of detrital zircon geochronology is the concept of the maximum depositional age. The concept is that a sedimentary unit can technically not be older than the youngest detrital zircon grain found and can essentially be applied to sedimentary successions that lack biostratigraphic information (e.g. Dickinson & Gehrels, 2009; Gehrels, 2014). Notwithstanding, the precise determination of the depositional age of sedimentary successions by means of detrital zircon chronology is limited to the availability of syn-depositionally crystallized zircons that would in most cases require a geographic adjacency of the sedimentary basin to a contemporaneously active volcanic (likely arc-type) source (cf. Cawood et al., 2012; Malkowski et al., 2016). The lag-time concept is defined as the perception of the temporal difference between the age of crystallization of the zircon grain and the age of deposition and mainly represents the time needed to exhume the rock to the surface (e.g. Garver et al., 1999, Bernet et al., 2011). Therewith, on the one hand the maximum depositional age is defined as the crystallization age. On the other hand, exhumation rates can be derived. Moreover, orogenic phases can be reconstructed in the sense that a constructional phase of mountain building can be deduced if lag times stratigraphically decrease up-section. A steady-state orogenic phase can be assumed if continuous lag times are observed stratigraphically upwards. A decaying state of mountain building can be reconstructed when individual lag times increase up-section (e.g. Carrapa, 2010; Payton & Carrapa, 2013). An ongoing debate concerns the number of detrital zircon grains that are statistically significant for geological reconstructions (e.g. Sircombe; 2000; Andersen, 2005; Vermeesch, 2004; 2012). While Andersen (2005) suggests a minimum of 52 detrital zircon grain ages in providing statistically robust datasets, Vermeesch (2012) delineates the number of analyzed grain as no smaller than 113 grains in order to gain information on ages that might be missed below the 5 % confidence.

The visualization of obtained zircon ages is commonly achieved by plotting age frequency distributions and probability density plots (e.g. Ludwig, 2003) or kernel density estimates (e.g. Sircombe & Hazelton, 2004; Vermeesch, 2004, 2012). The vast majority of provenance studies by way of detrital zircon chronology were performed through visual comparisons of vertically arranged normalized probably density plots or kernel density estimates of the samples concerned (e.g. Nelson, 2001; Dickinson & Gehrels, 2009; Di Giulio et al., 2012 among many others). However, as this approach is evidently subjective and therewith potentially subject to bias, more recent studies address the quantitative comparison of zircon age distributions by incorporating statistical evaluations (see Saylor & Sundell, 2016 for comprehensive review).

3.9 Statistical evaluation of detrital zircon age data

Four methodologies that allow quantitative comparisons of age spectra are integrated into this work and are briefly introduced. The Kolmogorov-Smirnov test (KS-test) represents a statistical approach that reveals whether two distributions originated from the same parent population (cf. Satksoski et al., 2013; Saylor & Sundell, 2016). In terms of detrital zircon age spectra analysis, the probability calculated by the K-S test represents the "likelihood" that two randomly selected populations would have been derived from the same parent population. This likelihood of compared age distributions is expressed in the p-value. If the KS-test p-value is greater than 0.05, a 95% confidence that the two samples originated from the same source can be inferred (Satksoski et al., 2013, Saylor & Sundell, 2016).

An alternative statistical approach for the quantification of variations in age distributions between two or more samples is represented by the "likeness" metric as introduced by Satkoski et al. (2013). The likeness value signifies the percent of likelihood between two probability density distributions which is calculated as one minus the summation of absolute differences between all PDP. Consequently, likeliness values close to 100% relate to a high degree of likeness between two age distributions. The similarity coefficient as introduced by Gehrels (2000) quantifies the extent of overlapping in between combined probability density functions and kernel density estimate distribution of compared samples. A similarity coefficient of 1 corresponds to identical samples, whereas a coefficient of 0 would indicate a total absence of matches between the compared populations. Moreover, statistical evaluations of large age datasets can be performed by means of the "cross-correlation" method (Saylor et al., 2013; cf. Saylor & Sundell, 2016). Illustrated by cross-plots that evaluate the presence or absence of age peaks as well as the relative magnitude and the shape of peaks, samples with identical age peaks will result in R^2 values of 1.

Chapter 4: Introduction to the Study area

4.1 Introduction and geographical indication

The study involves the investigation of outcrops of the Bordighera Sandstones. The Bordighera Sandstones form part of the San Remo-Monte Saccarello Unit (SR-MS) which crops out in the Ligurian province of Imperia. The SR-MS encompasses a mountainous area is located at the boundary between the internal and the external Western Alps (Fig. 4.1 A). It forms part of the Ligurian Alps, a roughly E-W- trending structure that represents the junction between the Western Alps to the Northwest and the Liguro-Provencal basin (the Ligurian Sea) to the south. The Eastern border of the Ligurian Alps is depicted by the Apennines, whereas in the northern part it borders the Po plain and the Tertiary Piedmont Basin. (Fig. 4.1 B) The SR-MS represents the basal component of the Cretaceous-Paleocene Western Ligurian Helminthoid Flysch Nappe that depicts the uppermost part of the Penninic Nappe pile (e.g. Vanossi et al., 1986; Di Giulio, 1992; Seno et al., 2005; Maino et al., 2015). Following the major Alpine contraction stages, the Ligurian Alps were involved in the rifting and subsequent ocean spreading between the alpine mainland and the Corso-Sardinia block (Foeken et al., 2003).

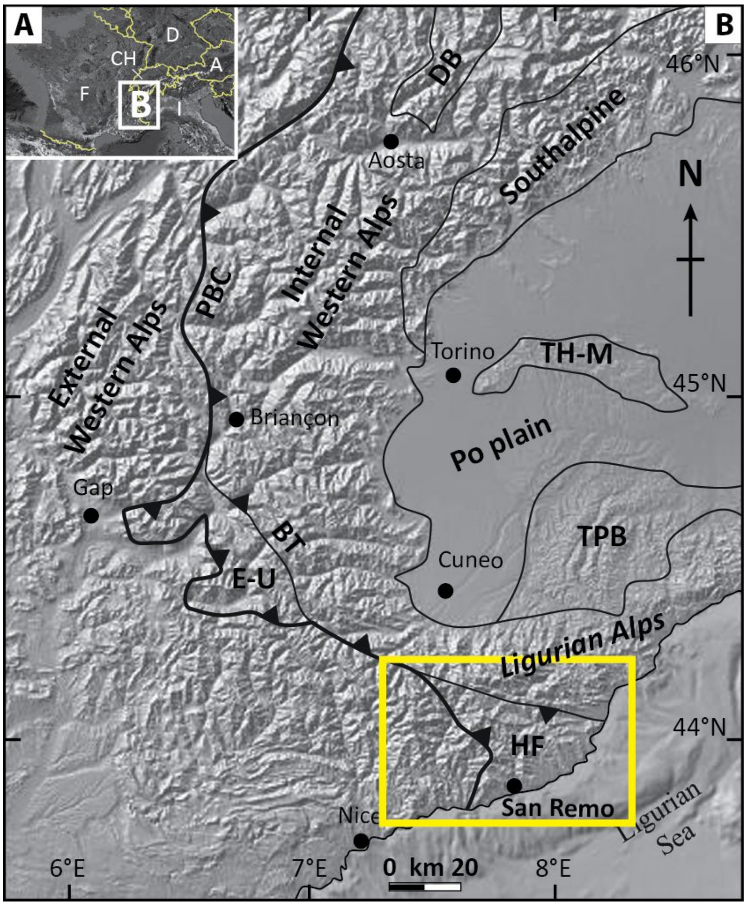

Fig. 4.1. (A) Geographic location of the study area within the framework of the Western Alps. (B) The location of the study area is highlighted in the yellow box. Modified from Maino et al. (2015).

4.2 Regional overview: Geological outline of the Alps

The Alps form an arc-shaped orogenic belt of northwest-ward vergence (Fig. 4.2) characterized by tectonic units that experience an almost 180° variation of tectonic strike (e.g. Dal Piaz et al., 2003; Schmid et al., 2004; Froitzheim et al., 2008; Handy et al., 2015). Located at the boundary between the European and the Apulian plate, the collisional belt covers dimensions of ca. 1000 km in length and roughly 100-250 km in width. The European Alps are the result of the collision of several continental and oceanic units that formerly constituted parts of the margins that bounded the Tethyan oceans (Schmid et al., 2004). From a geographical perspective, the orogen comprises four main domains: The Southern Alps, the Eastern Alps, the Central Alps and the Western Alps. These domains, mirroring dissimilar Mesozoic to Paleogene paleogeographic elements, were affected by different tectonic episodes of the Alpine orogeny (Froitzheim et al., 1996). The orogeny represents a strikingly asymmetric structure owing to the widely accepted hypothesis that they are built up of a composite of two orogenies resulting from an array of subduction and collisional events. These events are related to the opening and subsequent closure of three oceanic embayments and their associated continental margins (e.g. Froitzheim et al., 1996; Dal Piaz et al., 2003; Schmid et al., 2004; Mohn et al., 2010). The arcuate shape of the mountain belt is on the one hand interpreted as simply reflecting the geometry of the WNW-directed oblique collisional movement of the Apulian plate indenter. On the other hand, strike-slip deformation of the southern verge of the chain because of crustal-scale counterclockwise rotation of the Apulian plate since Eocene times promoted the development of the arcuate geometry (e.g. Schmid & Kissling, 2000; Collombet et al., 2002; Handy et al., 2014; Malusà et al., 2015).

The onset of the Alpine cycle started in the Early to Middle Jurassic and encompassed two independent orogenies that originated from rifting, sea-floor spreading, subduction and collisional processes (e.g. Froitzheim & Manatschal, 1996; Stampfli et al., 2002). The Eo-Alpine event is associated with the subduction of the Meliata ocean, whereas the Alpine event results from the subduction of the Piemont-Ligurian and Valais oceanic domains and successive continental collision of Europe and the Apulian plate (Froitzheim et al., 1996). From SE to NW, the ages of these oceanic basins display a progressive younging trend (Froitzheim et al., 1996). The Meliata ocean opened in the Early Triassic and closed in Late Jurassic times, the Piemont-Liguria ocean opened in Middle Jurassic times and closed in the Paleocene to Early Eocene, whereas the Valais basin opening is dated to the Late Jurassic to Early Cretaceous and closure to Eocene times. These oceanic basins furthermore included a range of continental fragments. A subdivision of the Alpine realm into four plate tectonic units that mirror the Mesozoic to Paleogene paleogeography is widely accepted (e.g. Froitzheim et al., 1996, 2008; Schmid et al., 2004; Handy et al., 2010). According to the synopsis of Froitzheim et al. (2008), these paleogeographic / tectonic superunits (illustrated in Fig. 4.2) are depicted by:

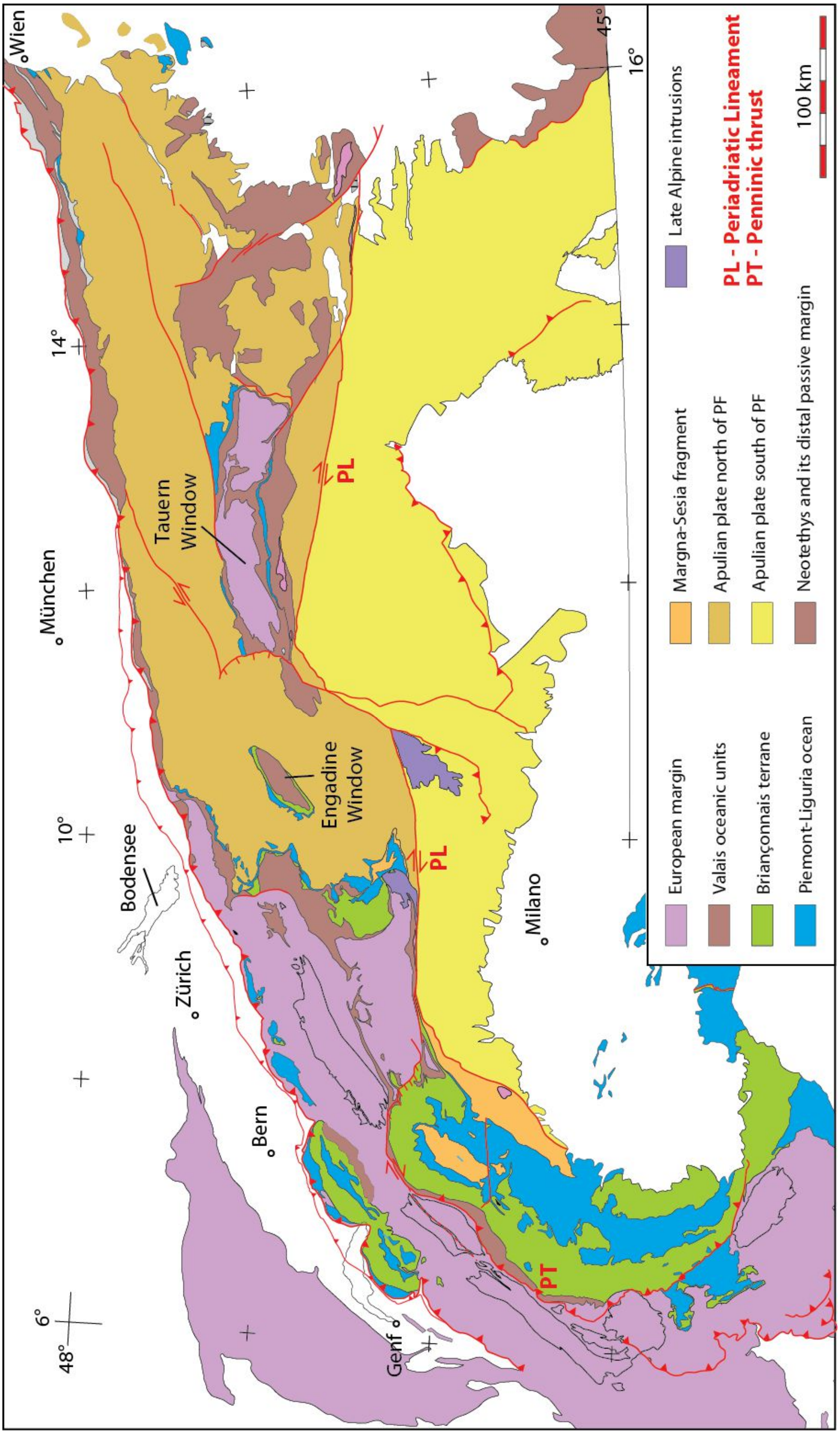

Fig. 4.2. Simplified tectonic map illustrating the major paleogeographic units of the Alps. Modified after Froitzheim et al. (1996) and Schmid et al. (2004).

(1) the Dauphinois-Helvetic realm, the most external and lowermost of the main tectonic units. This domain embodies to the Mesozoic to Paleogene proximal Paleo-European margin (i.e. mainly sedimentary cover units partly detached from their crystalline basement). It comprises portions of the Variscan basement complex that crops out in the External Massifs (e.g. Argentera, Pelvoux, Belledonne, Montblanc, Aiguilles Rouges, Aar and Gotthard massifs) and autochthonous, generally non-metamorphized cover units composed of sedimentary succession ranging from the Mesozoic to the Paleogene in age.

(2) the Penninic realm, a tectonic super-unit that comprises a series of oceanic and continental nappe piles which delineate the Alpine suture zone. In a broader sense, it represents the Alpine Tethys and its bordering continental margins. It can be subdivided into four units that comprise (a) the Subpenninic nappes built up of crystalline massifs derived from the distal European margin, (b) the Lower Penninic nappes that embody the oceanic North-Penninic Valais basin, (c) the Middle Penninic nappes that represent a continental fragment referred to as the Briançonnais, and the Upper Penninic nappe which comprises the Piemont-Liguria oceanic unit and continental microfragments such as the Sesia and Dent Blanche nappes.

(3) the Austroalpine nappes which typify the uppermost tectonic unit. It unites nappe piles derived from the distal margin of the Adriatic plate. The superunit is subdivided into the Lower and Upper Austroalpine Nappes. Altogether, the Austroalpine domain embraces a series of thrust sheets that are primarily built up of slivers of upper continental crust and individual sedimentary covers. The Lower Nappes includes the external units of the Sesia-Lanzo domain. The Upper Austroalpine nappe stacks form two complexes: The Northern Calcareous Alps that mainly represent Permo-Mesozoic sediments and the Central Austroalpine that dominantly embrace Variscan basement rocks and minor Permo-Mesozoic cover successions. The nappe stack already underwent major thrusting in Cretaceous times.

(4) the Southern Alps that constitute the continental realm of the Adriatic plate. It is principally composed of middle and lower continental Adriatic crust and Carboniferous to Tertiary cover sediments. The Southern Alpine edifice represents a more southerly part of Adria, whereas the Austroalpine depicts a part of Adria located further North. In contrast to Austroalpine edifice from which the Southern Alps are separated by the Tertiary-age Periadriatic lineament. It should be noted that the Southern Alps were not involved into Alpine metamorphism.

2.3.3 Paleogeographic evolution of the Tethyan realm

The formation of the Alpine belt is the result of a southeast-northwest propagation of a series of tectonic events. A synthesis of the timing of oceanic crust formation and high-pressure metamorphism of different Alpine paleogeographic is provided in Fig. 4.3. Prior to the Alpine cycle – in the Upper Paleozoic, Europe and Adria formed part of the same macro-continent (Pangea), which resulted from multi-stage collisions between Gondwana, Laurussia and Avalonia during the Variscan orogeny (von Raumer et al., 2003). The pre-rift history of the Alpine Tethys can be dated to Upper Carboniferous to Lower Permian times and is attributed to the final convergence and successive extensional collapse of the Variscan orogeny. This collapse was accompanied by regional uplift and lithospheric thinning (Stampfli & Kozur, 2006). Following astenospheric upwelling, the development of extensional basins associated with bounding transcurrent and transtensive faults denote a general change in tectonic regime (Froitzheim & Manatschal, 1996; Dal Piaz, 2001; Rosenbaum & Lister, 2005). A fundamental difference in terms of timing and dynamics of the Alpine orogenic cycle is documented between the Austroalpine domain and the Western Alps (Stampfli & Kozur, 2006):

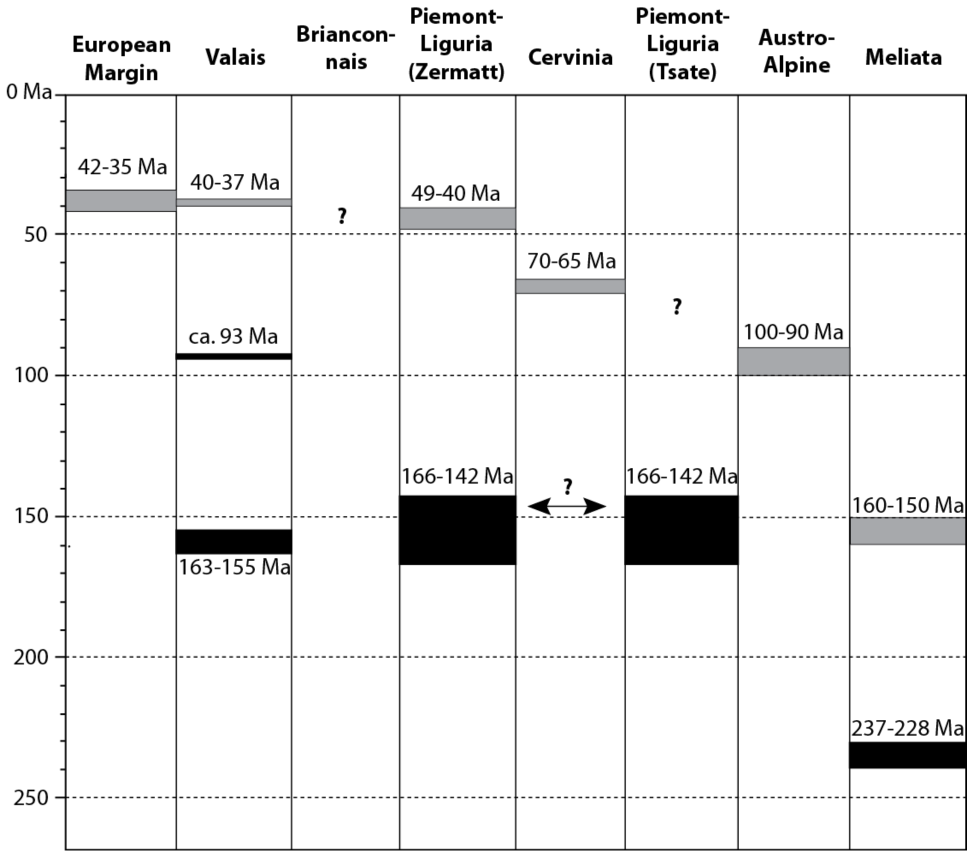

Fig. 4.3. Compilation of available age data for ocean spreading (black boxes) and high-pressure metamorphism during subduction stages (grey boxes) of the main Alpine geographic units. Despite for the Meliata ocean spreading ages that are based on biostratigraphic observations, ages are radiometric data from U-Pb, Sm-Nd and Lu-Hf ages. Modified compilation after Froitzheim et al. (2008).

Eastern Tethyan domain

In the Eastern Tethys, the opening of the Meliata Ocean in the form of a back-arc ocean of the Eastern Tethys in Early Middle Triassic times can be regarded as marking the onset of the Alpine cycle (Froitzheim et al., 2008). The Meliata Ocean represented a marginal basin located between the Austroalpine domain in the NW and the Southalpine domain in the SW (Fig. 4.4 A). At the end of the Triassic, east-directed closure of the Meliata ocean commenced. This oceanic closure presumably occurred in the form of intra-oceanic subduction beneath the Vadar ocean, a back-arc basin located above the subduction zone placed further east-ward (e.g. Stampfli et al., 1998; Froitzheim et al., 2008; see Fig. 4.4 B). By the Early Cretaceous, subduction advanced to the western Austroalpine domain. Collision of the Adriatic margin with the island arc above the subduction zone promoted the northwestward propagation of the Austro-Alpine nappes (Stampfli et al., 1998). As a consequence of the closure of the Meliata oceanic embayment, the Southern Alps and the Adriatic plate from that time on formed a coherent block. Notwithstanding, the consequence of the geodynamic evolution of the Eastern Tethyan realm for the Western Tethys remains poorly understood (cf. Handy et al., 2010).

Western Tethyan domain

From Jurassic times, rifting in the Western Tethyan realm occurred in two main stages, culminating in the break-ups of the Piemont-Ligurian ocean and the Valais embayment (Froitzheim & Manatschal, 1996; Froitzheim et al., 2008; Handy et al., 2010). Following a stage of crustal extension from Liassic to Lower Middle Jurassic times, the Piedmont-Ligurian ocean started to open in Late Jurassic times (see Fig. 4.4 B; for a more detailed illustration of the large-scale paleogeographic evolution of the Western Tethyan realm since the Triassic see also Fig. 4.5). Ocean spreading is contemporaneous with the development of the central Atlantic Ocean (Rosenbaum & Lister, 2005; Marroni & Pandolfi, 2007). Initial sea-floor formation was related to the upwelling of the subcontinental mantle of the Adriatic plate. According to Froitzheim & Manatschal (1996), the first stage - assigned to Hettangian to Sinemurian times - is typified by the development of east-dipping normal faults. Rifting resulted in a passive margin geometry that conforms to the symmetric pure-shear detachment model of Wernicke (1985). Contrastingly, from Toarcian times to the Middle Jurassic, an arrangement of west-dipping detachment faults became established that promoted asymmetric extension. Radiometric determinations of zircon ages of accreted ophiolite yield ages of ca. 165 Ma to 160 Ma (Schaltegger et al., 2002; Tribuzio et al., 2016). The phase of ocean spreading lasted for about 40 Ma, suggesting spreading rates of ca. 2cm/a (Handy et al., 2010). The subduction of the Piemont-Ligurian ocean below the Adriatic plate is inferred to have commenced in the Lower Cretaceous around 100 Ma (Froitzheim et al., 2008).

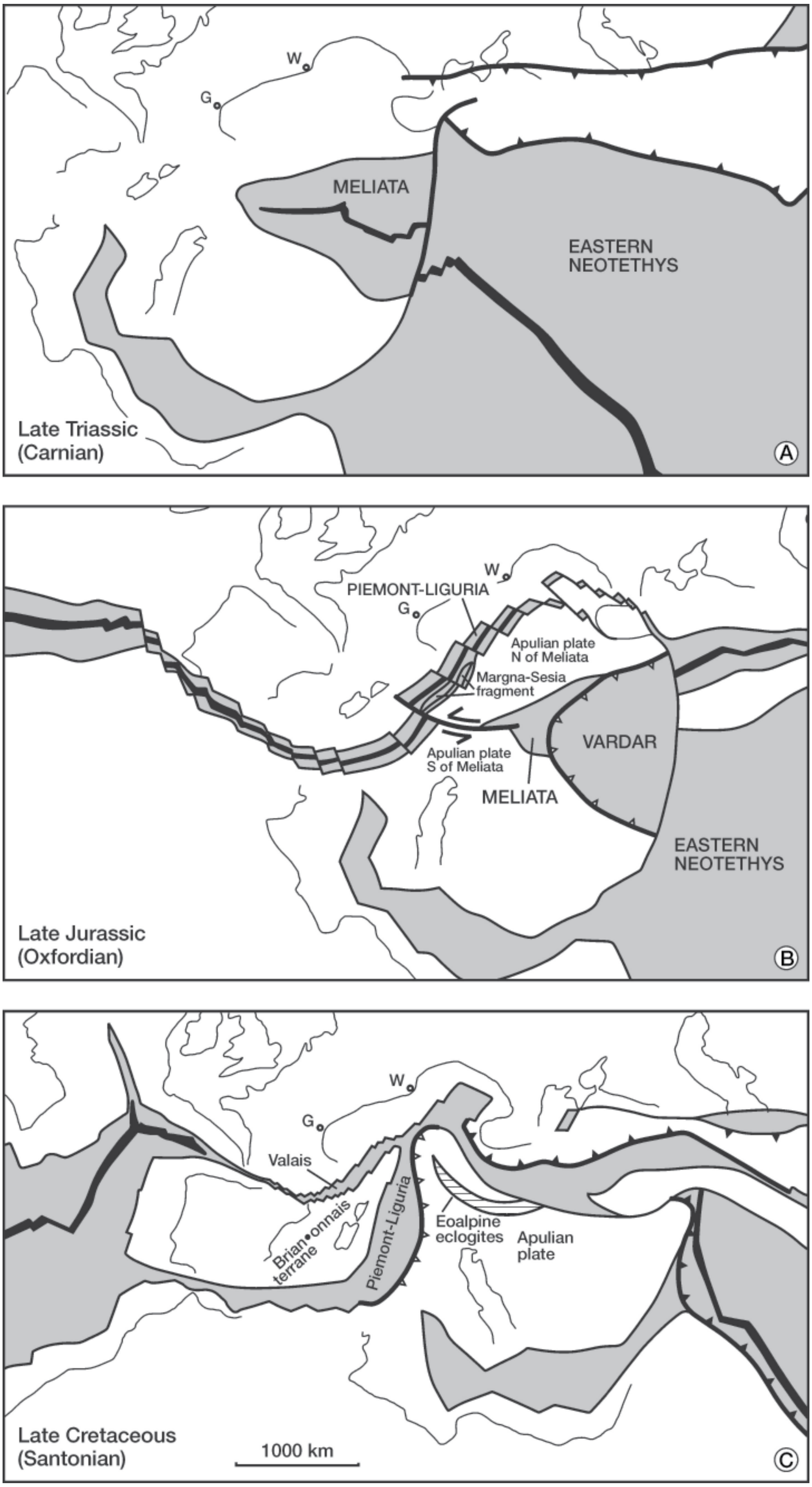

Fig. 4.4. Large-scale paleogeographical reconstruction of the Tethyan realm in A) Late Triassic, B) Late Jurassic and B) Late Cretaceous times. G: Genève; W: Wien (Vienna). After Frank, 1987, Stampfli, 1993, Schmid et al. 1997 and Stampfli et al. 2001. Adapted from Schmid et al. (2004).

In the context of the Atlantic Ocean opening a major transform fault developed from the boundary between the Late Jurassic and Early Cretaceous onward. It propagated both northward and southwestward towards the Bay of Biscay, connected the North Atlantic with the Alpine Tethys and separated Iberia from the European Plate (Stampfli et al., 2002; Froitzheim et al., 2008). This tectonic event marks the inset of the opening of the Bay of Biscay and the Valais embayment in the Western Alpine domain (Fig. 4.4 C). Based on radiometric age determinations of ophiolites that crop out in the northern part of the Valais embayment and in the Northern Apennines, spreading can be dated to have started around 166 Ma (Liati et al., 2005; Tribuzio et al., 2016). Breakaway and spreading of the Valais Ocean furthermore gave rise to the rifting of the Briançonnais ribbon continent off Iberia. In a roughly similar temporal context with respect to the Piemont-Ligurian ocean, the onset of subduction the Valais embayment commenced in the Late Cretaceous (Froitzheim et al., 2008).

The closure of both Western Tethyan oceanic environments occurred in south- to southeast-dipping subduction zones. Age determinations of eclogite facies metamorphism of the Valais embayment and the Piemont-Ligurian ocean reveal that metamorphism occured slightly earlier in southeastern zones and prograded towards the Northwest (Sesia-Lanzo Zone ca. 65 Ma, Zermatt-Saas-Fee ophiolites ca. 44 Ma and the European continental margin ca. 35 Ma; cf. Rubatto et al., 1998). This would indicate that the remnant parts of the Piemont-Ligurian ocean were closed by ca. 40 Ma (Schettino & Turco, 2011). Accordingly, most probably two separate subduction zones existed during the Paleocene and Early Eocene. One subduction zone was presumably located at the southern margin of the Valais Ocean and continued through the Pyrenees to the southern margin of the Bay of Biscay (Liati et al., 2005), whereas the southernmost prolongation of the subduction zone located at the southeastern margin of the Piemont-Ligurian Ocean continued to Corsica (e.g. Froitzheim et al., 2008; Molli & Malavieille, 2011). The Paleocene was characterized by a significant decrease in convergence rates between Iberia and Africa that presumably caused gravitational collapse of the Eo-Alpine orogen. Following this paucity, in the Early to Middle Eocene convergence rates gently increased again and continued subduction of the Western Tethys below the Adriatic plate (Schettino & Turco, 2011). Subsequently the succession of the Piemont-Ligurian ocean (ophiolite sequences and their sedimentary cover) together with the Paleozoic to Cenozoic sedimentary cover of the Briançonnais domain accreted into the Alpine accretionary prism. During the Late Eocence to Early Oligocene continental collision was established when westward thrusting of the front of the wedge advanced onto the European continental margin that was represented by the Dauphinoise domain (e.g. Froitzheim et al., 1996; Seno et al., 2005; Decarlis et al., 2013).

Structural pre-requisite of the Piemont-Ligurian oceanic domain

The lithospheric-scale structural inheritance defines a key controlling factor on the evolution of sedimentary systems as it essentially affects basin geometries and orientations of sediment fairways in siliciclastic systems (e.g. Butler et al., 2006; Pinter et al., 2017). Thus, the structural pre-requisite of the Western Tethys and specifically that of the Piemont-Ligurian ocean is regarded as playing a crucial role on the relation between the provenance area and the stratigraphic architecture of the Western Ligurian Flysch units. Decarlis et al. (2014) infer an inherited structural setting of the extended Northern Tethyan continental margin realm that was dominated by NE-SW-trending normal faults which were connected by orthogonally oriented transverse faults. The paleogeographic evolution and the structural make-up of this key area is illustrated in greater detail in Fig. 4.5.

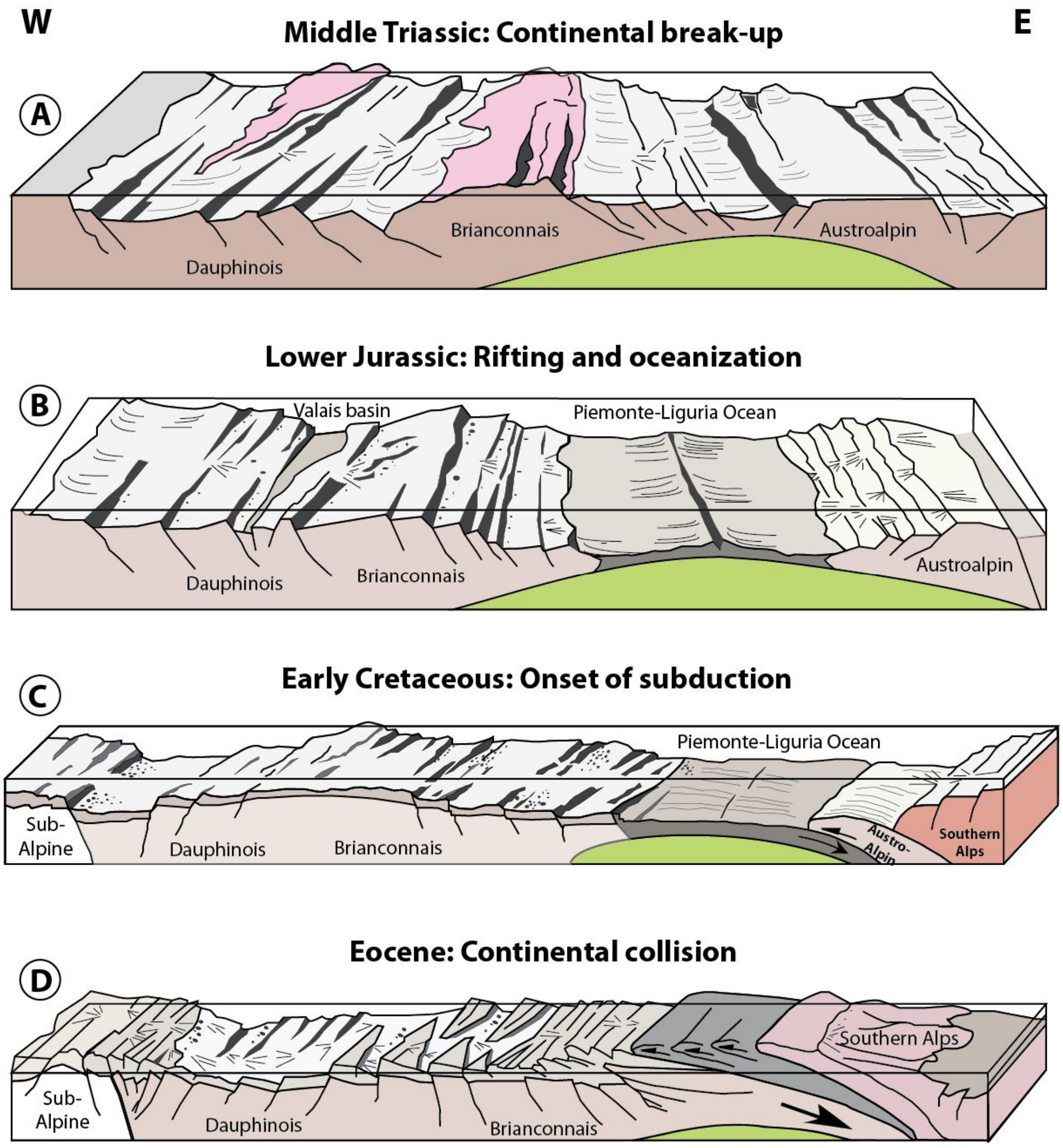

Fig. 4.5. Self-explaining cartoon that illustrates the schematic geodynamic evolution of the Piemont-Ligurian ocean. Stages of continental break-up, rifting and ocean opening (A & B) and subduction followed by continental collision (C & D) are exemplified. Modified after Debelmas et al. (1983).

4.4 Geological setting of the Ligurian Alps within the Western Alpine belt

The study area is part of the southwestern Ligurian Alps that represent the southernmost segment of the Alpine collisional belt (Vannosi et al., 1986; Seno et al., 2005; Maino et al., 2012; Decarlis et al., 2013;). The Ligurian form a SW-NE trending structure that were subject to a complex history of deformational events of the Western Alpine belt (e.g. Di Giulio, 1992; Seno et al., 2005). Prior to collision the Western Alps comprised five main paleogeographic domains (Fig. 4.6) that are either of continental European affinity or of oceanic origin (e.g. Beltrando et al., 2010; 2014; Decarlis et al., 2013; 2014). These domains are outlined by:

(a) The proximal European margin that comprises an array of nappe piles. The Helvetic domain, (in the French-speaking areas referred to as "Dauphinoise") depicts the hyper-extended European continental margin and its Mesozoic to Tertiary cover sequences. The outer (eastward) boundary, by some authors incorporated in the Lower Penninic nappes (e.g. Mohn et al., 2010; Beltrando et al., 2014) marks the transition towards the oceanic Valais sub-basin (e.g. Froitzheim & Manatschal, 1996; Decarlis et al., 2013). Dominantly rift-related calcareous cover sequences superimpose both the external (Aiguilles Rouges and Mont Blanc) and the internal crystalline massifs (Monte Rosa, Gran Paradiso and Dora Maira).

(b) The Lower Penninic Nappe unit that originated from the Valais oceanic sub-basin. This oceanic trough represents an eastern sub-basin of the Alpine Tethys located between Europe to the West and the Briançonnais continental rise to the East (Froitzheim et al., 2008). The timing of the opening of the Valais sub-basin is can be assigned to Upper Jurassic times; the opening is hence slightly time-delayed in comparison to the opening of the Piemont-Ligurian ocean (Liati et al., 2005). Sedimentation is interpreted to have occurred in deep abyssal plains. The basin-fill is partly deposited on its oceanic substratum. Cretaceous ophiolites are primarily superimposed by deep-marine shales of Cretaceous age that grade into Tertiary flysch successions (Caron et al, 1989).

(c) The Middle Penninic Nappes that are constituted by the Briançonnais ribbon continent (e.g. Boring & Stampfli, 1999; Decarlis et al., 2013; Weber et al., 2015). The Briançonnais domain represents the eastern continuation of the Iberian plate that separated the Piemont-Liguria ocean from the Valais sub-basin. In relation to Middle Jurassic age opening of the Atlantic Ocean, a major transform fault developed that connected the North Atlantic with the Alpine Tethys and fractured the European Plate. The Iberian Plate got divided from Europe and gave rise to the Valais Ocean opening (Froitzheim et al., 2008). It embodies the northward passive continental margin that bounds the Jurassic Piemont-Liguria ocean and is built up of undifferentiated Pre-Mesozoic and Variscan bedrocks that are overlain by rifting-related Upper Jurassic sedimentary covers and volcanic successions (Stampfli et al., 1998; Schmid et al., 2004; Decarlis et al., 2013). The Briançonnais domain comprises three paleogeographic realms that are defined as the inner Briançonnais, bounded by the Subbriançonnais area that embodies the lateral, northernmost transition of the Briançonnais to the Valais trough, and the Ultrabriançonnais or Prepiemontais domain (Mohn et al., 2010; Decarlis et al., 2013) representing its southern distal passive margin towards the Piemont-Ligurian ocean.

(d) Units of the Upper Penninic Nappe formed from the Piemont-Ligurian ocean and the adjacent sections of the distal Adriatc margin (Froitzheim & Manatschal, 1996). The Piemont-Ligurian ocean evolved in a relatively short time span in Middle Jurassic times. Following the continental rifting stage exhumation of the subcontinental mantle of the Apulian microplate-promoted sea-floor spreading (e.g. Mohn et al., 2010; Beltrando et al., 2014). Ophiolite emplacement was followed by radiolarite deposition and hemipelagic sedimentation. Since the Lower Cretaceous, flysch sediments were accumulated in trench environments.

(e) An additional unit that, according to its geographic location in the Western Alps, is the Margna-Sesia nappe (Froitzheim et al., 2008). It comprises a series of microcontinental fragments that constitute a continental fragment of the Apulian margin. It comprises the Sesia zone, the Dent Blanche Nappe, the Mount Mary Nappe and the Pillonet Klippen (Dal Piaz et al., 2003; Bousquet et al., 2004; Schmidt et al., 2004). The continental fragment rifted apart from the Apulian margin during the opening of the Piemont-Liguria ocean and later became amalgamated into the accretionary wedge of the active Southern Alpine margin.

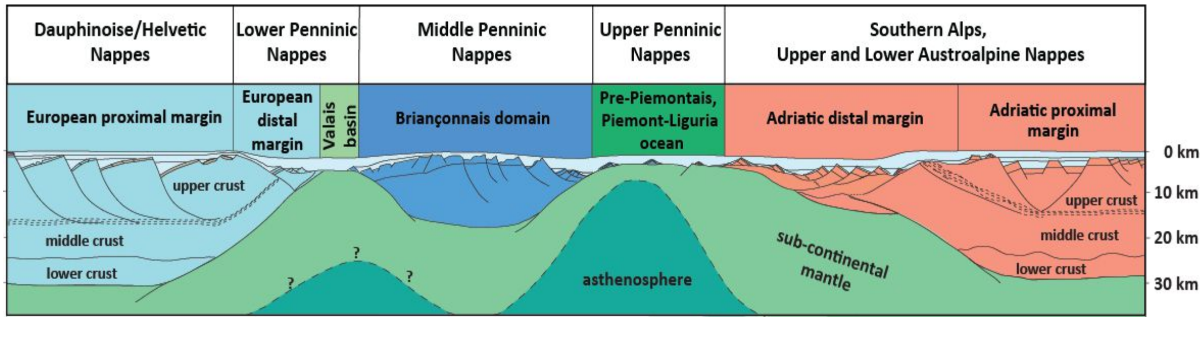

Fig. 4.6. Paleogeography of the Western Alps and the Adriatic margin in Middle to Upper Jurassic times (based on seismic survey data and stratigraphic relationships). Modified from Beltrando et al. (2010; 2014).

4.5 The Helminthoid Flysch Nappes

4.5.1 Paleogeographic and sedimentological characteristics of the Helminthoid Flysch

The Cretaceous to Paleogene Helminthoid Flysch Nappes represents the detached cover of the Valais embayment and the Piemont-Ligurian ocean (Lanteaume, 1962; Vanossi et al., 1984; Wildi, 1987; Di Giulio, 1992; Froitzheim et al., 2008). Present-day positions of Helminthoid Flysch Nappes are widely scattered along the Alpine belt and the Northern Apennines (Fig. 4.7). Besides the Western Ligurian succession, Helminthoid Flysch nappes comprise the Dranses, Gurnigel, Schlieren and Wägital Nappes in the Swiss Alps, the Autapie and Parpaillon Nappes in the external Western Alps (Kerckhove, 1969; Caron et al., 1989) and the Northern Apennine Helminthoid Flysch Nappes that are placed on top of the External Ligurian Units (Scholle, 1971; Marroni et al., 2001). As a consequence of ongoing convergent tectonics in Late Cretaceous times and subduction of the Piemont-Ligurian ocean beneath the Southern Alpine margin, vast volumes of unconsolidated muddy calcareous material were re-sedimented into trench environments. Turbiditic flows deposited the calcareous mud into various abyssal domains of the Western Tethys that were situated below the carbonate compensation depth (e.g. Kerckhove, 1969; Scholle, 1971; Sagri, 1980; Argnani et al., 2004; Trümpy et al., 2006). A southward younging trend of the initiation of calcareous flysch sedimentation from Early Cretaceous calcareous successions in the Swiss Alps towards a Late Cretaceous onset of sedimentation in the Western Alps and Northern Apennine sectors can be perceived (Wildy, 1987; Caron et al., 1989).

The etymology of the Helminthoid Flysch is derived from the characteristic pre-turbiditic substrate feeding trace fossils ("*Helminthoides irregluaris*") that mark the soles of the calciturbidites (Uchman, 2007). The typical facies motif of Helminthoid Flysch sediments is that of thin-to very thick-bedded fine-grained, typically light-colored ("Alberese") appearance of the calcareous turbiditic sediments. The huge volume of individual beds, together with the generally fine-grained nature of the often thick-bedded turbidites together with the lack of shell fragments suggests that the calcareous ooze was previously stored on continental shelves (Scholle, 1971; Hesse, 1975). Ongoing debate prevails concerning the paleogeography and the provenance of the large volume of the turbiditic deposits (e.g. Wildi, 1987; Cartanzariti et al., 2007). In particular, owing to difficulties in defining paleocurrent patterns, uncertainties exist whether the calcareous turbidites were previously stored along the Adriatic margin or along the European margin. The thick-bedded Helminthoid Flysch successions characteristically superimpose laterally extensive thin-bedded, very fine-grained deep-marine sediments. These in many cases blackish or vary-colored shaly turbiditic deposits are interpreted as representing distal basin plain successions and are therefore termed basal complexes ("complessi di base"; e.g. Vanossi et al., 1984).

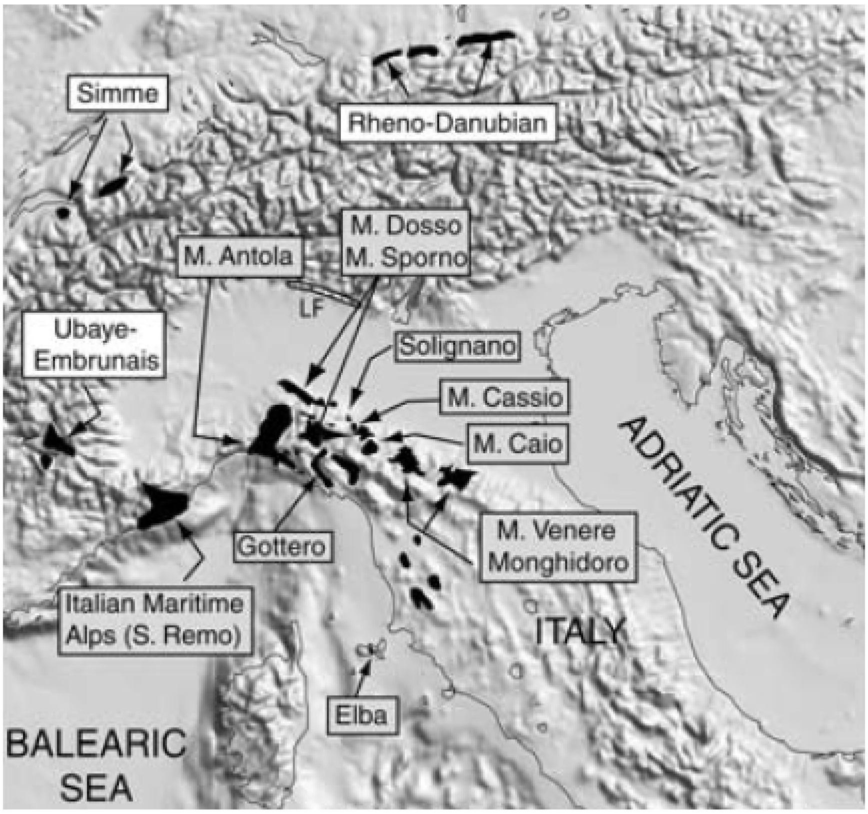

Fig. 4.7. Distribution of main Helminthoid Flysch outcrops within the Alps and the Northern Apennines. Adapted from Argnani et al. (2008).

A general consensus exists that deep-marine sedimentation designating the Helminthoid Flysch successions were deposited both in the Valais embayment and in the Piedmont-Ligurian oceanic basin (e.g. Kerckhove, 1969; Wildi, 1985, 1987; Caron et al., 1989; Bernoulli & Winkler, 1990). Mohn et al. (2010) and Decarlis et al. (2014) report an inherited structural setting of the Western Alpine Thetyan realm which is dominated by NE-SW-trending normal faults that were connected by orthogonally oriented transverse faults. In consequence of the structural transformation towards a convergent tectonic regime between Europe and Adria and the related development of a subduction zone beginning in Cretaceous times, the Western Ligurian Flysch succession got incorporated into an accreting Upper Cretaceous-Paleogene prism (Sestini, 1970; Di Giulio, 1992; Marroni & Pandolfi, 2007).

4.5.2 The Western Ligurian Helminthoid Flysch Units

Four main units constitute the Western Ligurian Helminthoid Flysch: The San Remo-Monte Saccarello Unit, the Moglio-Testico Unit, the Borghetto Unit and the Colla-Domenica-Leverone Unit, (Fig. 4.8). The chronostratigraphic organization of the units, divided by southward dipping thrusts with the oldest unit resting on top of the nappe pile, documents the tectonic inversion pattern characteristic for ordered accretionary prisms (Marini & Terranova, 1983; Di Giulio, 1992). While the three strati-

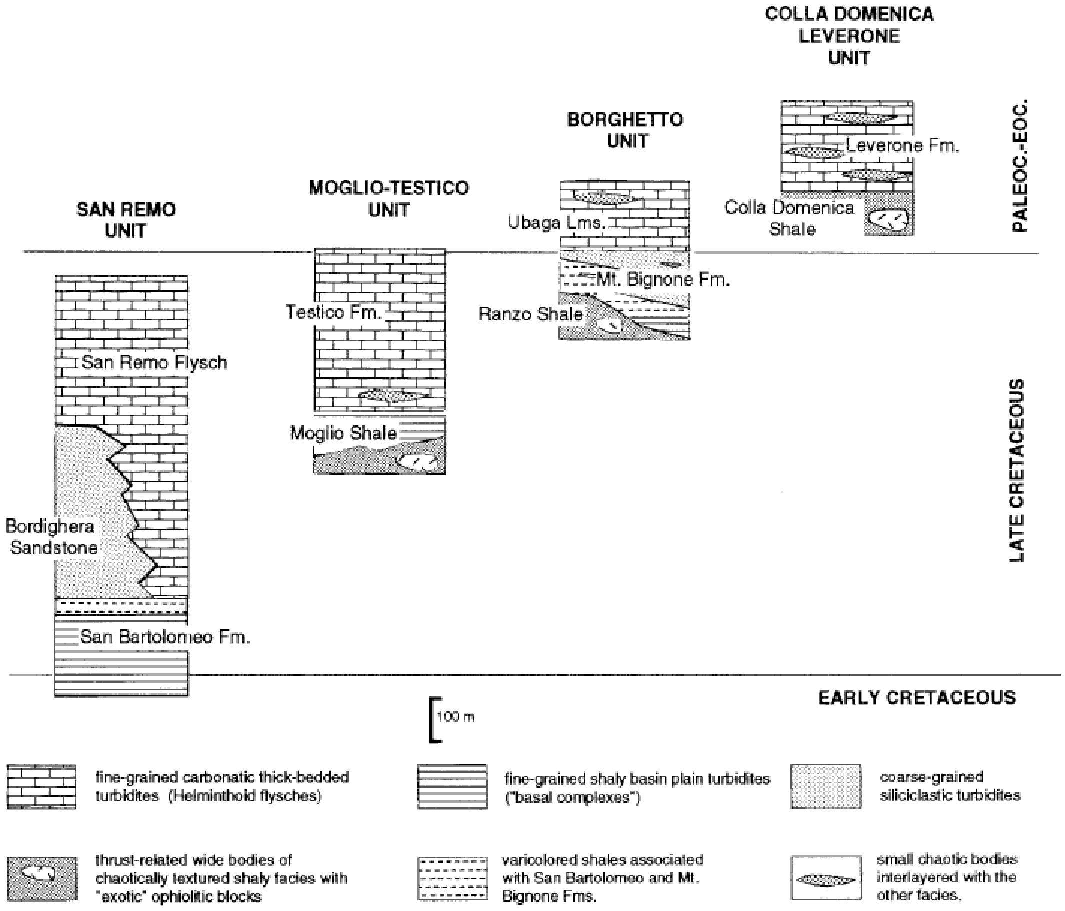

Fig. 4.8. Chronostratigraphic correlation scheme of the Western Ligurian Helminthoid Flysch nappe. Adapted from Di Giulio (1992).

graphically younger units underwent multi-phase ductile-brittle deformation, the San Remo-Monte Saccarello Unit is characterized by a rather simple structural overprint that is denoted by relatively large-scale, open SW-verging kink folds (Di Giulio, 1992; Seno et al., 2005; Maino & Seno, 2016). Within the Western Ligurian Helminthoid Flysch, intercalations of siliciclastic, microconglomeratic successions become prominent in two cases: The Quarziti di Montebignone and the Bordighera Sandstones (Vanossi et al., 1986; Di Giulio, 1992).

4.5.3 The San Remo-Monte Saccarello Unit

The study area addresses the of the San Remo-Monte Saccarello Unit (SR-MS). The succession crops out in a roughly triangular are close to the French-Italian border (Fig. 4.9). It represents the basal component of the Cretaceous-Paleocene Helminthoid Flysch Nappe that forms the uppermost part of the Penninic Nappe (e.g., Seno etal., 2005; Perotti et al., 2011, Maino et al., 2015). The unit is composed of three lithostratigraphic members that are - from base to top - represented by the San Bartolomeo Formation, the Bordighera Sandstones and the San Remo Helminthoid Flysch (Fig. 4.10). Few systematic sedimentological studies (e.g. Sagri, 1980, Vanossi, 1982) involved the stratigraphic evolution that reveals some abrupt facies shifts in between the two siliciclastic members, the San Bartolomeo Formation and the Bordighera Sandstones. In particular, the detailed sedimentological characterization of the Bordighera Sandstones is encompassed. On the one hand a such investigation offers an excellent outcrop case study for analyzing trends in facies distributions in a poor-efficiency system that is subject to hybrid event bed emergence. Moreover, the comprehensive determination of the source area of the Bordighera turbidite systems is performed with the aim of providing further understanding on the complex development recorded in numerous flysch successions of the Piemont-Ligurian ocean prior to Alpine collision.

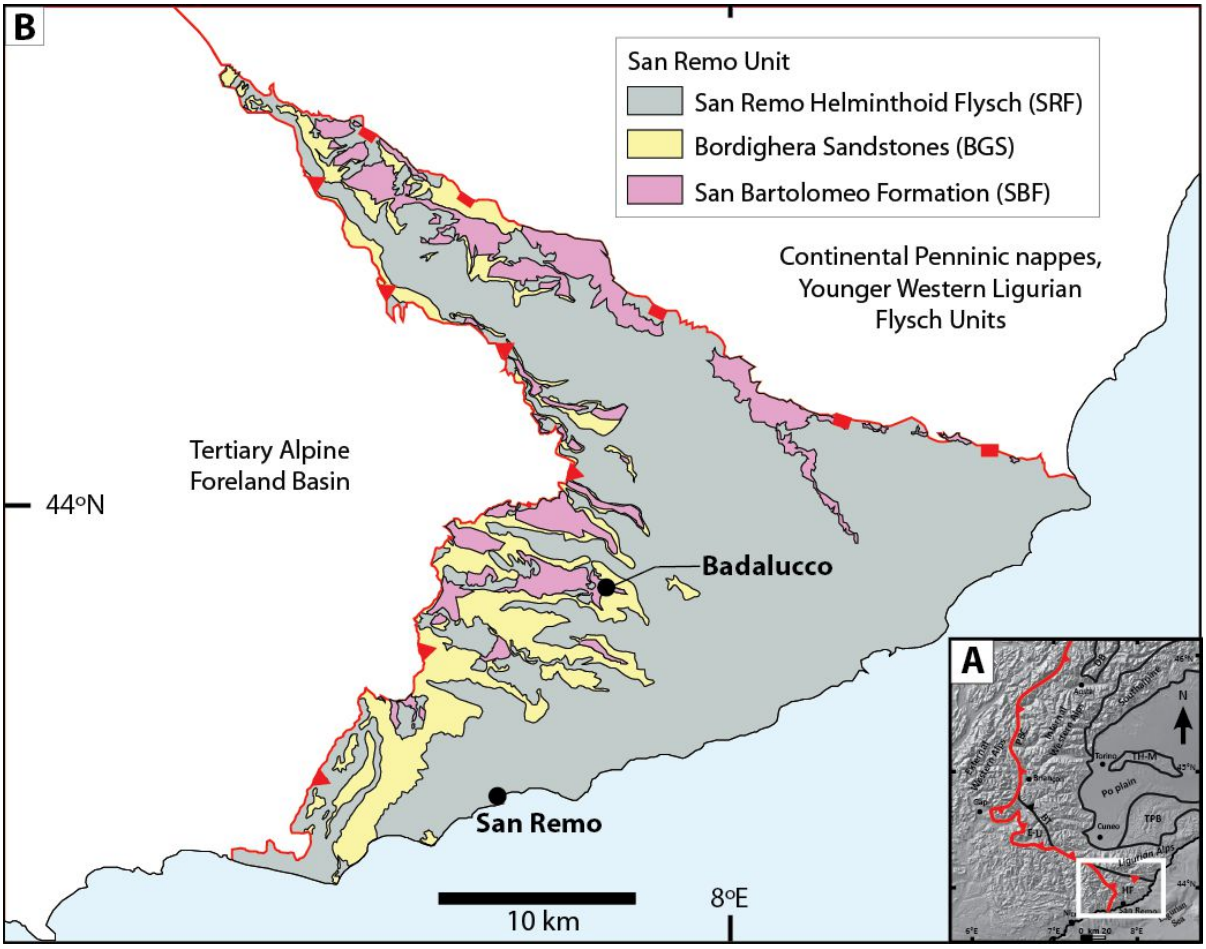

Fig. 4.9. Geological map of the study area. Modified from Lanteaume et al. (1968).

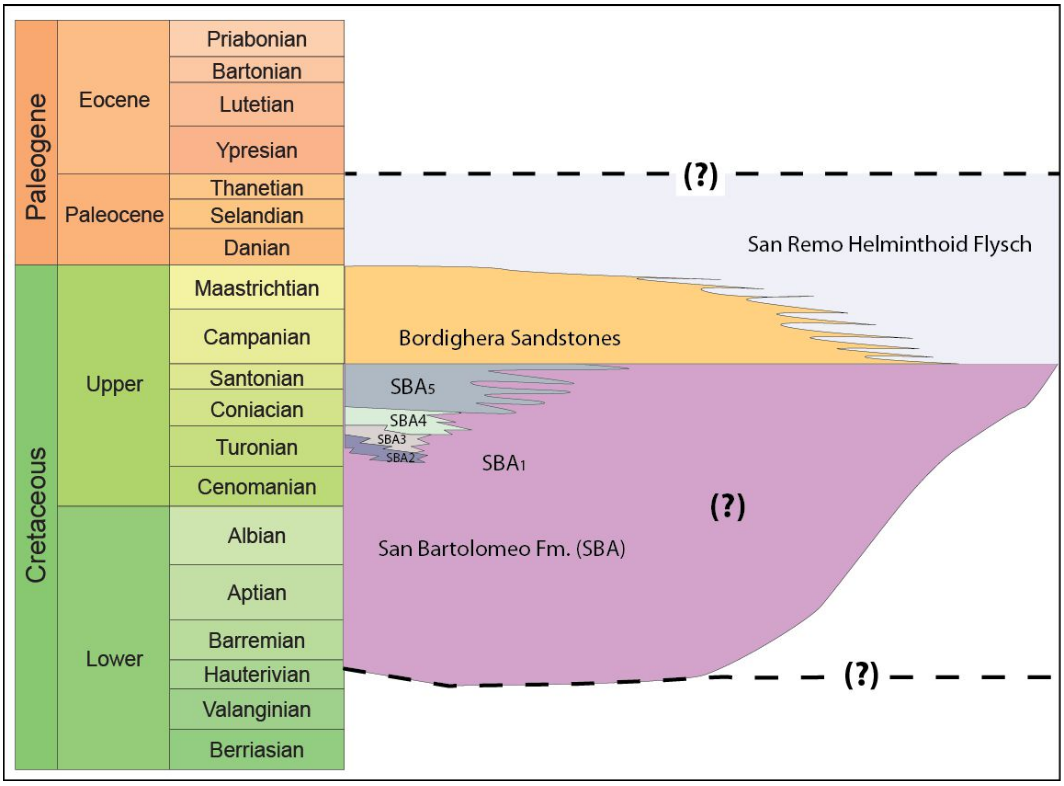

Fig. 4.10. Chronostratigraphic framework of the San Remo-Monte Saccarello unit. Modified after Cobianchi et al. (1991), Di Giulio (1992) and Giammarino et al. (2010).

The base of the unit is made up of the San Bartolomeo Formation that comprises a succession of laterally extensive, thin-bedded and very fine-grained calcarenitic turbidites. On that basis, this lowermost member has been interpreted as representing the "basal complex" deposited in a basin plain environment (Sagri, 1980). The San Bartolomeo Formation is subdivided into five litho-zones (Di Giulio & Galbiati, 1985; Cobianchi et al., 1991). A general trend from varicolored shales rich in manganese located at the base towards sandier pelitic shales at the top of the formation can be recognized. The lowermost litho-zone, termed SBA_a, comprises rhythmically alternating calcareous shales and minor intercalations of siltstones and fine- to very fine-grained sandstones. The SBA_b litho-zone is made up of alternations of siliciclastic mudstones, quartz-rich siltstones and sporadically occurring fine- to very fine-grained sandstones. Similarly, the SBA_c litho-zone is depicted by vary-colored shales. The SBA_d litho-zone comprises fine- to medium quartzarenites that exhibit normal grading and reach thicknesses of up to 30 cm. Finally, the SBA_e litho-zone is made up of thin-bedded calcareous mudstones and - towards the top - show intercalations of arkosic sandstones. Based on biostratigraphic observations from foraminiferal faunas, the depositional age of the San Bartolomeo Fm. can be limited to Upper Hauterivian to Upper Campanian age (Cobianchi, et al., 1991; Galbati & Cobianchi 1998). The basal complex reaches a thickness of ca. 200 – 300 m (Giammarino et al., 2010) and is apparently conformably superimposed by both the Bordighera sandstone and the San Remo Helminthoid Flysch (Di Giulio & Gabliati, 1985; Di Giulio, 1992).

The Bordighera Sandstones (“Bordighera Sandsteine” of Richter, 1961) consist of dominantly medium- to thick-bedded coarse-grained to microconglomeratic sandstones (Lanteaume, 1962; Sagri, 1980; Giammarino et al., 2010). The siliciclastic succession reaches a maximum thickness of 250 m and crops out in a roughly arcuate transect that covers an area of ca. 25 x 45 km (See Fig. 4.9). Sagri (1980) provided a comprehensive sedimentological depiction and proposed the Bordighera Sandstones as representing a cone-shaped submarine fan that displays an overall South to North, proximal to distal facies pattern. Moreover, he delineated the Bordighera sandstones as consisting of three main depositional environments. Based on lithofacies observations, bed geometries and fining-upward cyclicity, the proximal part has been interpreted to represent a channelized environment. According to the author, the channelized domain passes into progradational lobe associations that are defined by packages of massive sandstones displaying internal thickening-upward sequences that occur in association with minor portions of thin-bedded turbidites. The lateral areas of the progradational lobe associations are marked by the presence of fine-grained turbidites and hemipelagites. These sediments exhibit both symmetric and thickening-upward cyclicity and have hence been associated with fan-fringe environments. According to these facies relationships, Sagri (1980) interpreted the Bordighera Sandstones as a “poorly efficient turbidite system” sensu Mutti (1979). Remarkably, Sagri (1980) already noted that “on account of sedimentological and compositional features, deposition along an active margin is suggested for the Bordighera Sandstones” and pointed towards the difficulty to “ubicate the deposition area of the Bordighera Sandstones in the complex paleogeography of Western Liguria”.

The San Remo Flysch is primarily made up of medium- to thick- bedded, fine-grained calcareous turbiditic sediments and ranges in thickness between 100 m and 650 m (Giammarino et al., 2010). In accordance with observations of Cretaceous Helminthoid Flysch successions in the Northern Apennines (i.e. Antola Flysch; cf. Scholle, 1971) and the Eastern Alps Flysch zone (Gault, Zementmergel and Hällritzer Formations; cf. Hesse, 1975), these formations have formerly been interpreted to having been deposited at the talus of the continental slope below the carbonate compensation depth (e.g. Sagri et al., 1980; Powichrowski, 1989; Fontana et al., 1994). Resultant from a scarcity of microfaunas, the depositional ages of the San Remo Flysch and Bordighera Sandstone remain imprecisely defined, and the onset of sedimentation can merely be attributed to Campanian to Maastrichtian times (e.g. Di Giulio, 1992; Giammarino et al., 2010). Essentially in their vertical and lateral extents, the latter formations are characterized by a heterotopic interfingering sedimentation pattern.

4.6 Deformational history of the Ligurian Alps

In the context of the convergence between Europe and the Adriatic intender, two main deformational phases affected the Ligurian Alps (e.g. Vanossi, 1991; Seno et al., 2005). As a detailed review of the complex restoration of the controversially debated geodynamics of the Ligurian Alps (e.g. Dallagiovanna et al., 1997; Seno et al., 2005; Maino et al., 2012) is beyond the scope of this sedimentological work, the models for tectonic development of the area proposed for the orogenic (Seno et al., 2005) and the post-orogenic exhumation (Foeken et al., 2003) are presented hereafter.

The collision between Europe and Adria induced the progradation of the Alpine nappes. According to Seno et al. (2005), the first event that affected the Ligurian Alps can be related to the SW-directed subduction of the Piemont-Ligurian ocean in Maastrichtian times. The detached Helminthoid Flysch succession was incorporated into an intra-oceanic subduction prism, whereas its substratum entered the subduction zone. In the Early Eocene, the Helminthoid Flysch succession were thrusted southeast-ward onto the European continental margin. Furthermore, the development of a duplex of the internal Briançonnais domain can be dated to that age. From the Middle to the Late Eocene, in the context of ongoing subduction, exhumation progressed along the subduction channel. Inward displacement of the Briançonnais duplex promoted thickening of the duplex, and forced the arrival of the Briançonnais in the subduction zone. This resulted in the break-up of the duplex into an array of units. In the Late Eocene continental collision was established that led to the displacement of the Pre-piemontais domain and its subsequent overthrusting by the already exhumed duplex of the internal Briançonnais. Continental collision was accompanied by a counter-clockwise rotation of the Adriatic plate in the Oligocene (Maffione et al., 2008). Stacking and imbrication of the nappe pile comprising was practically complete. According to their relative position regarding the subduction channel, the incorporated units were affected by different grades of metamorphic overprint.

The second main phase defined a significant geodynamical change characterized by the termination of contractional dynamics since the Late Eocene. The termination of subduction and exhumation is interpreted to be caused by the insertion of an Adriatic wedge. This insertion resulted in hinterland backfolding and the opening of the Ligurian-Provençal back-arc basin. In the outer parts of the Briançonnais domain backfolding gave rise to the development of new thrusts. Late Oligocene kinematics were characterized by the persistence of backfolding that controlled the first emplacement of the Penninic front onto the Dauphinoise realm. The final emplacement, marked by a second deformation of the Dauphinoise realm, occurred in the Lower Miocene. Following to the main stages of Alpine contraction, the Ligurian Alps were subject to rifting related to the opening of the Ligurian-Provençal basin. Foeken et al. (2003) identified significant vertical movements from the Neogene until present times by apatite low-temperature thermochronology. Furthermore, evidence of local deformation events in the Miocene and in the Plio-Quaternaty suggests asymmetric exhumation. Based on stratigraphic observations, a significant decrease in minimal exhumation rates from the Pliocene to recent times are reported. Determination of exhumation rates suggest the erosion of topography larger than 2.2 km to the present day.

Chapter 5: Sedimentological characterization of the Bordighera Sandstones -

Physical stratigraphy, Stacking pattern analysis and Quantitative assessment of bed-scale heterogeneity distribution in a pre-collisional sand-rich turbidite system

Abstract

The Upper Cretaceous Bordighera Sandstone of NW Italy is a coarse-grained, sand-rich elongated turbidite system (ca. 15 x 45 km in outcrop) up to 250 meters thick, interpreted to have been deposited in a trench setting. The siliciclastic succession interfingers with muddy calcareous turbidites, which become more abundant toward the lateral and distal domains. Bed type associations allow the distinction of a proximal channelized domain which transitions to a more distal lobe domain, characterized by abundant mudclast-rich sandstones and by bipartite and tripartite beds with a mud-rich middle or upper division (hybrid event beds). The transition between the proximal and distal domains occurs over a relatively limited spatial extent (ca. 5 km). The presence of lenticular bed-sets made up of coarse grained and mud-poor sandstones throughout the distal domain suggests that distributary channels were present, indicating sediment bypass further down-dip toward the most distal and not preserved parts of the system. Hybrid event beds - commonly associated with distal and marginal fan environments such as fan fringes - are present throughout the lobe domain and extend for up to ca. 30 km in down-dip distance. They are more abundant in the proximal and axial depositional lobe domain and their appearance occurs within a short basin-ward distance from the inferred channel-lobe transition zone. Flow expansion at the termination of the channelized domain and the enhanced availability of cohesive substrate due to the presence of intra-basinal muddy calcareous beds are interpreted as the key controls on the emergence of the abundant mudclast-rich sandstones and hybrid event beds. The abrupt appearance and the persistent occurrence of such beds across an extensive domain have implications for characterizing bed-scale (sub-seismic) heterogeneity of deep-water clastic hydrocarbon reservoirs.

5.1. Introduction

Siliciclastic deep-water reservoirs gained steadily growing global importance as targets for hydrocarbon exploration, as deep-water sandstones conventionally constitute prolific hydrocarbon reservoirs. Major economic interests focus on deep-marine petroleum plays situated in sedimentary basins along passive margins (e.g. Weimer et al., 2007). Various studies of turbidite systems have proven the complexity of facies distributions within such systems (e.g. Vinnels et al., 2010 and references therein). The petrophysical properties that determine the reservoir quality of siliciclastic reservoirs result from depositional processes (i.e. depositional porosity) as well as from post-depositional alterations during compaction and diagenesis (Mansurberg et al., 2008). The primary porosity of sandstones depends – among other controls such as modality of sand grain size distribution and related intergranular pore space – on the amount of detrital clay dispersed within the matrix at the time of deposition (Sylvester & Lowe, 2004; Lien et al., 2006; Porten et al., 2016). This clay matrix content is depending on to both the initial amount of mud in the flow and/or the proportions of clayey particles acquired by local entrainment through erosion of substrate or by disaggregation of rip-up clasts (Dillinger et al., 2013).

The sediment gravity flow spectrum is traditionally regarded as comprising two end-members, namely laminar flows (cohesive debris flows) and non-cohesive turbulent flows (e.g. Lowe, 1982; Mulder & Alexander, 2001; Talling et al., 2012). In recent years, research efforts have been directed at better understanding flow states intermediate between the two end-members and that share both laminar and turbulent flow properties (e.g. Baas et al., 2009; Southern et al., 2015). Flume experiments (e.g. Baas et al., 2009; 2011) reveal that the concentration of clay within the flow plays a crucial role on emerging rheological flow heterogeneity as it dampens turbulence. Deposits that record both or intermediate flow characteristics commonly comprise a roughly two-part arrangement of a lower mud-poor sandstone portion and an upper mud-rich sandstone and have been documented in numerous studies from various settings (e.g. “slurry flows” of Lowe & Guy, 2000 and Sylvester & Lowe, 2004; “linked debrites” of Haughton et al., 2003; “hybrid event beds” of Haughton et al., 2009; “transitional flow deposits” of Kane & Pontén, 2012; “matrix-rich sandstones” of Terlaky & Arnott, 2014). As bed-scale heterogeneity has a negative impact on both lateral and vertical sandstone permeability, the occurrence of such deposits can result in sudden and unexpected reduced hydrocarbon production efficiency (e.g. Sylvester & Lowe, 2004; Amy et al., 2009; Fonnesu et al., 2015; Porten et al., 2016). Consequently, in the last decade studies on turbidite systems prone to this type of bed-scale heterogeneity increasingly came to the center of attention of both academic and applied research. Hybrid event beds (HEBs) are a type of deposits characterized by the presence of a mud-rich division sandwiched between clean sandstone divisions (Haughton et al., 2009), resulting in a reduced primary porosity and permeability in comparison to classic turbidite sandstones. This enhanced mud content is interpreted to result from progressive clay entrainment during flow evolution (see also Haughton et al., 2003; Amy & Talling, 2007; Davis et al., 2009; Fonnesu et al., 2016). According to Haughton et al. (2009), the idealized deposit of such beds displays five divisions that tend to show variable individual thicknesses. A basal, structureless graded or ungraded sandstone (H1) that gradually passes into a banded sandstone (H2) which exhibits alternating cleaner paler sands and darker argillaceous sandstone bands, a chaotic, debritic argillaceous sandstone subdivision (H3) with variable concentrations of mud clasts and sheared sand patches, a fine grained, laminated mud-poor sandstone (H4) and a clayey mudstone cap (H5). Nevertheless, a single event bed does not necessarily comprise all of the abovementioned divisions (e.g. Talling et al., 2012; Fonnesu et al., 2016; 2017).

Hybrid event beds and other deposits characterized by the presence of an argillaceous sandstone division have largely been reported from distal environments of tectonically active lobe-dominated sand-rich and mud-rich submarine fans (e.g. Haughton et al., 2009; Hodgson et al., 2009; Muzzi Magalhaes & Tinterri, 2010; see review in Fonnesu et al., 2015). Moreover, hybrid event beds have been documented in proximity to basin margins, where flows are interpreted to decelerate rapidly through interaction with the laterally confining slopes (e.g., Barker et al., 2008; Patacci et al., 2014). Nonetheless, the occurrence of such beds has also been recognized in more proximal environments of largely unconfined turbidite systems, specifically in channelized realms located at the toe of slope of deep-sea fans (Henstra et al., 2016) or in the immediate downstream vicinity of the channel-lobe transition zone (Terlaky & Arnott, 2014).

The bulk of studies infer that the development of hybrid event beds can be related to acquisition of cohesive muds occurred in up-slope locations (Haughton et al., 2009; Hodgson et al., 2009). Recent studies however revealed that more local mud entrainment and subsequent rapid deposition of transitional flow and hybrid event bed deposits (Terlaky & Arnott, 2014; Fonnesu et al., 2016). Owing to the fact that the purely siliciclastic Bordighera turbidite system is outlined by an interfingering sedimentation pattern with the calcareous Helminthoid Flysch turbidites, this instance offers the unique opportunity to study both the locations of mud entrainment and the down-dip behavior of flows that were subject to flow transformations.

This chapter presents the outcrop study-derived sedimentological characterization of the Upper Cretaceous Bordighera Sandstones (BGS), with the main emphasis on improving the understanding on spatial trends in facies heterogeneity and grain size distributions in high net-to-gross turbidite systems. In particular, the present study aims to provide insights into hybrid event bed development in a sand-rich turbidite systems deposited in a subduction trench scenario prior to continental collision. The bed-scale reservoir heterogeneity linked to the presence of hybrid event beds is expected to occur below typical seismic resolution. Comprehensive outcrop studies are therefore of vital importance in order to advance models regarding the vertical and lateral spatial distribution of facies heterogeneity in hydrocarbon reservoirs which cannot be captured by analysis of seismic datasets.

2. Background geology

The Upper Cretaceous Bordighera Sandstone (BGS) crops out in northwest Italy (Fig. 5.1) and is part of the San Remo-Monte Saccarello Unit of the Cretaceous-Paleocene Helminthoid Flysch Complex of the Penninic Nappe stack of the Western Ligurian Alps (Maino et al., 2012; 2014; Decarlis et al., 2013). Deep-marine sediments of the Helminthoid Flysch accumulated in the Piedmont-Ligurian oceanic basin (Vanossi et al., 1986). The Helminthoid Flysch succession became progressively incorporated into an Upper Cretaceous-Paleogene accretionary prism (Di Giulio, 1992) that finally became involved in the Ligurian Alps collisional system. Four main units constitute the Western Ligurian Flysch complex with the San Remo-Monte Saccarello Unit representing the topmost. The chronostratigraphic organization of these units, divided by southward dipping thrusts with the oldest unit resting on top of the nappe pile, documents the typical tectonic inversion shown by accretionary wedges (Di Giulio, 1992). While the three lowermost and younger units underwent multi-phase ductile-brittle deformation, the oldest topmost San Remo-Monte Saccarello Unit is characterized by a rather simple structural overprint denoted by relatively large-scale, open SW-verging kink folds causing a tectonic shortening of roughly 30 per cent, according to available maps and structural data (Giammarino et al., 2010; Maino et al., 2012).

The San Remo-Monte Saccarello Unit is composed of three formations (Fig. 5.2). The lowermost is the Upper Hauterivian to Upper Campanian San Bartolomeo Formation (SBF), a thin-bedded and very fine-grained turbidite unit (Cobianchi, et al., 1991; Galbiati & Cobianchi, 1998). This is overlain by the Bordighera Sandstone (BGS), mainly consisting of medium- to thick-bedded, coarse- to medium-grained siliciclastic turbidites (Sagri, 1980) and which constitutes the focus of this paper. Finally, the succession is capped by the San Remo Flysch (SRF), partially heterotopic with the Bordighera Sandstone and primarily made up of medium- to thick- bedded, fine-grained calcareous turbidites featuring the characteristic Helminthoid-type ichnofossils. According to Sagri & Marri (1980), the San Remo Flysch was deposited within an abyssal environment below the carbonate compensation depth.

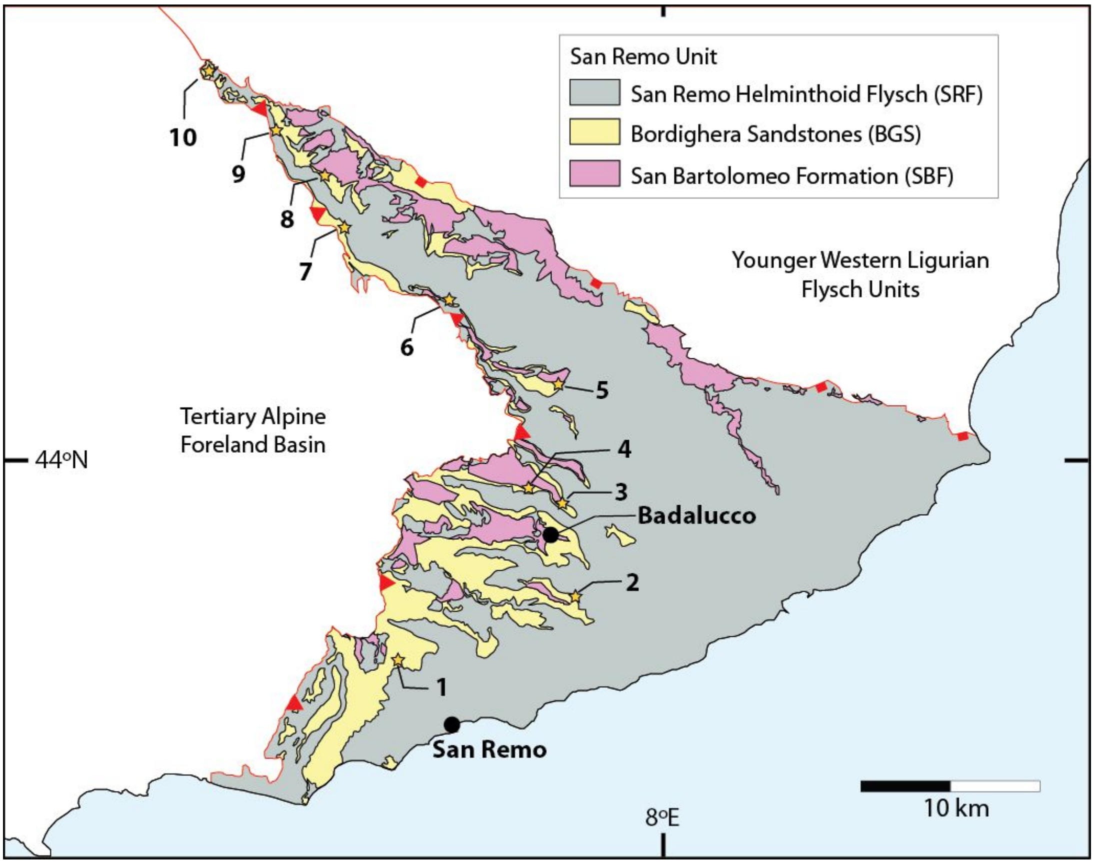

Fig. 5.1: Geological map of the study area (modified after Lanteaume, 1962) and locations of measured stratigraphic sections 1-10.

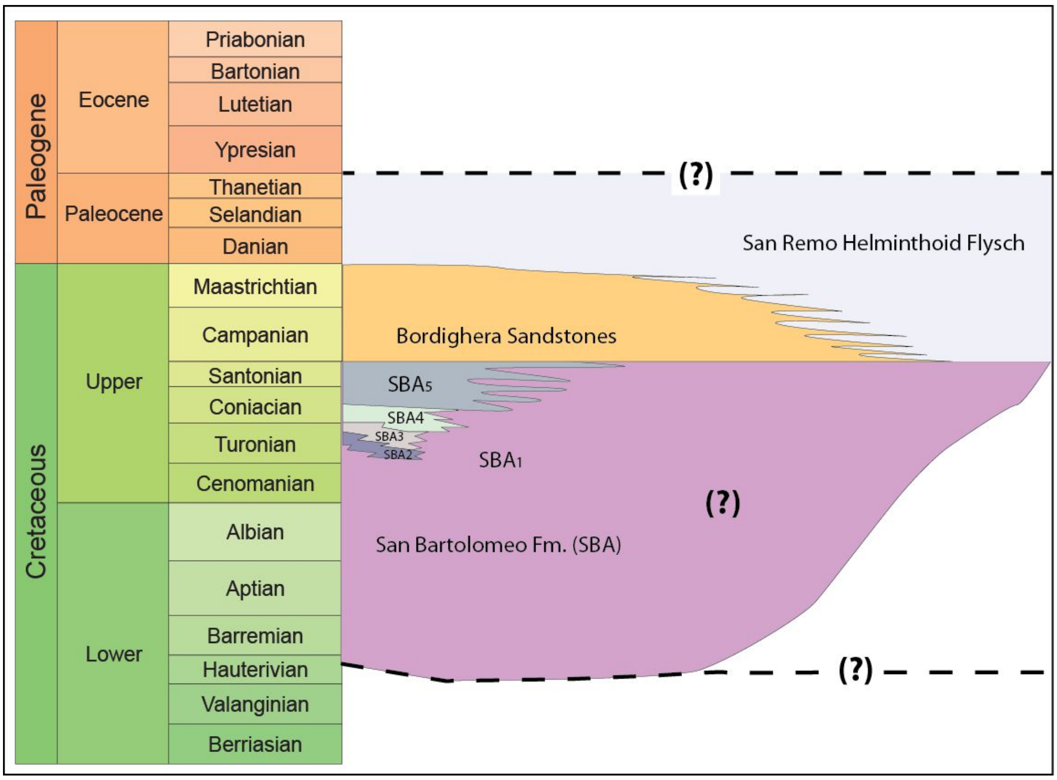

Fig. 5.2. Chronostratigraphic framework of the San Remo-Monte Saccarello Unit. Modified after Cobianchi et al. (1991), Di Giulio (1992) and Giammarino et al. (2010).

5.3 Methodology

The study is based on sedimentological investigation of 10 sections along an arcuate SW-NW transect (see Fig. 5.1), along the inferred main sediment transport direction. Sedimentological features were examined by detailed stratigraphic logs (measured with 1 cm resolution and drawn at 1:50 scale) with roughly 1600 beds measured and described (ca. 1400 m in total thickness). A high-precision Jacob's staff (Patacci, 2016) was used to improve accuracy of measurements of some covered intervals. Maximum and mean grain sizes were determined in the field with a standard grain size chart and a hand lens. Measurements of paleocurrent indicators were also undertaken (groove marks, flute casts and ripples; n = 127). An ad-hoc bed type classification was developed, with special emphasis on mudclast-rich and argillaceous sandstone beds. Field estimations on the amount of mud dispersed within sandstones were performed on the basis of rock color and weathered surface texture. As the present-day distance between measured sections is less than the distance at the time of deposition due to SSW'-NNE' directed tectonic shortening of about 30 % (Maino & Seno, 2016), restored distances were computed. Outcropping dimensions of the preserved part of the system are 15 km cross-current by ca. 45 km along-current, striking roughly parallel to the orientation of tectonic shortening. For the purpose of restoring different sections to their relative depositional position, the distances between sections along the SSW'-NNE' part of the transect were increased by 30%, resulting in an estimated extension of the exposed part of the system to ca. 15 km x 60 km.

The dataset acquired stratigraphic logging was subsequently compiled for statistical analyses. Detailed graphic sedimentological logs are attached in Appendix 1.1. The parameters accounted for statistical analyses include the following parameters: bed number (beginning from stratigraphic base to top), stratigraphic position of bed base and bed top, the identified bed type and both the full event bed thickness and the individual thickness of the mudcap, the maximum basal grain size, and the fact whether beds are amalgamated or not. Moreover, the differentiation between siliciclastic and calcareous mud was performed. The detailed dataset of the aforementioned variables and bed type proportions are attached in Appendix 1.2. Bed type proportions were calculated and plotted using MS Excel and Matlab. Amalgamated interval proportions (amalgamation ratio) were also computed. Amalgamated intervals were defined as sandstone intervals characterized internally by multiple (at least one) sand-on-sand contacts outlined by abrupt grain size breaks and bounded at their lower and upper boundaries by a thin clay or fine silt interval. They can be compared to the bed-sets defined by an absence of mudcaps of Stanbrook et al. (2015). The amalgamation ratio for a stratigraphic section was calculated as the ratio of the thickness of all the amalgamated sandstone intervals to the entire stratigraphic thickness. This parameter helped refine the inferred position of individual sections with respect to the axis of the sand fairway (e.g. Romans et al., 2009; Pringle et al., 2010) and to discriminate in between channelized and unchannelized depositional environments (Mattern, 2002).

5.4 Bed types

Six main bed types comprising thirteen sub-categories have been distinguished. Their main features are summarized in Table 5.1. Descriptive and interpretive schemes of bed types conform to the criteria proposed by Lowe (1982), Mulder & Alexander (2001), Baas et al. (2009), Haughton et al. (2009) and Southern et al. (2017), facilitating the deduction of properties of sediment density flows (i.e. sediment concentration, particle support mechanism, types of particles and flow duration) from the characteristics of the deposit. Bed types 1 and 2 are interpreted as representing the coarse-grained depositional spectrum of sandy siliciclastic sediment density flows. Bed types 3 and 4 are interpreted to represent deposits of flows transporting finer grain sizes of mixed siliciclastic and calcareous or exclusively of calcareous composition. Bed types 5 and 6 are characterized by a siliciclastic matrix with various amounts of siliciclastic and calcareous mud-clasts. They are interpreted as part of a continuous spectrum of beds formed as a consequence of progressive clay enrichment due to entrainment of muddy substrate and that can be classified as transitional flow deposits (*sensu* Baas et al., 2009; 2011; Southern et al., 2017) or hybrid event beds (*sensu* Haughton et al., 2009). Description and interpretation of hybrid event beds was conducted in accordance with the proposed model of Haughton et al. (2009).

Bed Type 1.1: Microconglomerates

Description:

Bed type 1.1 comprises brownish-orange to light greyish, thick- to very thick-bedded, polymictic microconglomeratic sandstones ranging from 0.45 m to 5.87 m in thickness. The mean thickness is roughly 1.35 m. Maximum grain-sizes range from coarse pebbles (max. 2.1 cm x 4.5 cm) to fine sand. Bed type 1.1 deposits are generally characterized by remarkably poor sorting. Average grains roundness is sub-angular to sub-rounded, even if locally angular pebbles are to be found at the bases of beds. Clasts within the basal part of beds typically exhibit roughly bedding-plane parallel to sub-horizontal imbrication (Fig. 5.3 A). The most distinct textural feature of bed type 1.1 strata is the presence of coarse-tail grading. This coarse-tail grading is expressed by a very abrupt fining of the uppermost part of the lowermost microconglomeratic basal division (mean interval thickness ca. 3 – 12 cm), defined by basal granules to medium pebbles that are distributed in a coarse to very coarse sandy matrix. The lowermost parts of beds rapidly grade into medial parts that display poorly developed normal grading. In terms of grain size, the medial part is comprised of coarse to very coarse

BT	Bed type description & interpretation	Geometry (10s of m)	clay silt vfss fss mss css vcss gran pebb cobb
1.1	**Medium- to very thick-bedded, coarse-tail graded microconglomerates.** Absence of stratifications. **Common dewatering dishes** and sheets. Sporadic loading structures. **Frequent amalgamations**. Maximum basal grain size: angular pebbles. **Minor portions of mud-clasts**. **Thickness: 0.45-5.87 m; mean: 1.35 m.** **Interpretation: Hyperconcentrated density flows (Mulder & Alexander, 2001)**	lenticular / tabular	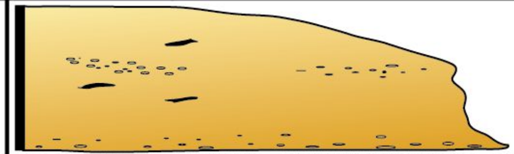
1.2	**Thin-bedded structureless clast-supported microconglomerates.** Granule- to small pebbles in coarse to very coarse sandy matrix. Matrix typified by **general absence of clay**. Abrupt normal grading towards tops of beds. Very rare basal inverse grading. **Thickness: 0.12-0.45 m; mean: 0.30 m.** **Interpretation: Non-cohesive debris flows (Mulder & Alexander, 2001)**	tabular	
1.3	**Medium- to thick-bedded inversely graded microconglomerates. Inverse basal grading** followed by well-developed, continuous normal grading. Either structureless appearance or beds displaying a range of primary physical structures (clast imbrications, cross-stratifications, planar-parallel, wavy and current-ripple laminations). Rapid grain size jumps. **Thickness: 0.35-2.45 m; mean: 0.85 m.** **Interpretation: High density turbidity currents (S1 & S3 of Lowe, 1982)**	lenticular / tabular	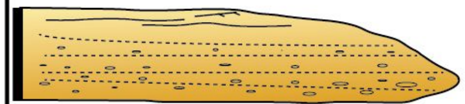
2.1	**Thin- to thick-bedded, graded structureless sandstones**. Common fluid escape structures (dewatering dishes and deformed dewatering sheets). **Absence of sedimentary structures resulting from traction processes**. Minor proportions of intraformational siliciclastic and calcareous rip-up clasts. **Thickness: 0.07-2.20 m; mean: 0.50 m.** **Interpretation: High- to low-density turbidity currents (S3 of Lowe, 1982)**	lenticular / tabular	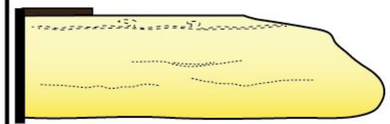
2.2	**Thin- to thick-bedded, graded structured sandstones.** Sedimentary structures (low angle planar-parallel- & ripple laminations, climbing ripples) restricted to medial and upper parts of beds. Intense convolute laminations. Very rare rip-up clasts. **Thickness: 0.10-1.55 m; mean: 0.50 m.** **Interpretation: Low density turbidity currents (Mulder & Alexander, 2001)**	lenticular / tabular	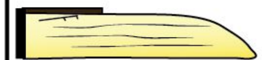
3	**Heterolithic intervals** (clastic & calcareous fine beds): mudstones, calcareous micrites, siltstones, vfsst to fsst & micrites. Wavy- to ripple laminations, rare planar laminations. Abundant trace fossils. Sst soles: *Gordia, Ophiomorpha, Planolites*. Calcareous beds: *Nereites, Chondrites, Thalassinoides, Urohelminthoides.* **Thickness 0.12-3.10 m; mean: 0.40 m.** **Interpretation: Low density turbidity currents (Mulder & Alexander, 2001)**	tabular	
4	**Thin- to thick-bedded calcilutites & calcarenites.** Either ripple-laminated or structureless appearance. Locally meter-scale injections of coarse sst (clastic sills and dikes; max. ca. 35 cm x 6.5 m). Abundant *"Helminthoid"* traces at soles: *Nereites irregularis, Chondrites, Urohelminthoides; Ophiomorpha & Planolites*.**Thickness 0.03-2.25 m; mean: 0.25 m.** **Interpretation: Low density turbidity currents (Mulder & Alexander, 2001)**	tabular	

Table 5.1. Summary of bed type descriptions and interpretations.

BT	Description	Geometry (10s of m)	clay silt vfsst fsst msst csst vcsst gran pebb cobb
5.1	**Normal-graded sandstones enriched (< 10%) in siliciclastic & calcareous mud-clasts**. Mud-clasts and mud-blocks scattered in clusters throughout entire beds. Clasts aligned broadly parallel to bedding. Locally minor degree of clast deformation. Tendency of rip-up clasts to be found within lowermost halfs of beds. Laterally extensive thin (< 5 mm) "mud-strings" locally displaying symmetrical, sinuous in phase pattern. Erosive basal contacts. **Thickness: 0.17-2.09 m; mean: 0.75 m**. **Interpretation: Incipient hybrid event beds (Fonnesu et al., 2015; 2017)**	lenticular / tabular	
5.2	**Coarse-tail graded sandstones enriched (>10%) in dominantly calcareous mudclasts**. Entrained fine-grained material illustrates **variable degree of distortion**; clasts locally "sheared" along horizontal planes. Incorporated material commonly distributed throughout upper half of beds. Calcareous rafts often surrounded by siliclastic "mud-rims". Erosive basal contacts. **Thickness: 0.38-2.55 m; mean: 1.30 m.** **Interpretation: Incipient hybrid event beds (Fonnesu et al., 2015; 2017)**	tabular	
6.1	**Medium to thick bedded, coarse-tail graded tri-partite hybrid event beds**. **Tri-partite vertical arrangement**: Basal division: "clean" structureless sandstone. Overlying **matrix-supported debritic division** characterized by high concentrations of **strongly deformed calcareous clasts** in csst matrix. Minor proportions of siliciclastic clasts. Max. clast size: 1.20 m x 2.40 m. Uppermost parts of debritic interval display signs of increased amount of dark siliclastic mud. Beds capped by relatively thin "clean" ripple-laminated msst to fsst. Sharp boundary between lower divisions marked by continuous, undulating horizon of dark siliciclastic mud. Sharp, erosive basal contacts. **Thickness: 0.27-3.83 m; mean: 1.30 m.** **Interpretation: Hybrid event beds (*sensu* Haughton et al. 2009)**	tabular	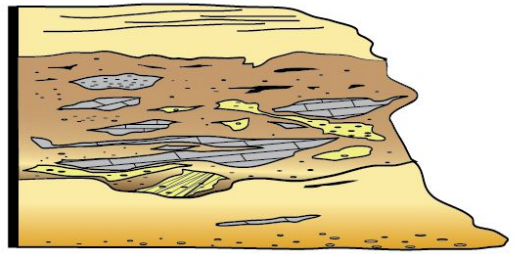
6.2	**Medium to thick bedded, coarse-tail graded bi-partite hybrid event beds**. **Bi-partite internal arrangement**: **"Clean" basal subdivision** locally exhibiting dewatering dishes; **dark, chaotic matrix-supported debritic upper subdivision**. **Partly disrupted blocks** of mud in csst matrix. Locally blocks of heterolithic stratigraphy. Non-linear boundaries displaying "rugged" course. Gerneral lack of primary sedimentary structures. Sharp, erosive basal contacts. **Thickness: 0.40-3.25 m; mean: 1.40 m.** **Interpretation: Hybrid event beds (*sensu* Haughton et al. 2009)**	tabular	
6.3	**Medium- to thick-bedded, argillaceous, matrix-supported, coarse-tail graded clast-to block dominated beds with poorly distinguishable contacts between divisions. Thin basal mud-poor sandstone. Matrix-supported debritic interval** characterized by dominance of elongated calcareous blocks. Horizontal alignement of rafts. **Minor degrees of deformation of rafts**. Delayed normal grading towards tops. Erosive basal contacts. **Thickness: 0.85-2.65 m; mean: 1.55 m.** **Interpretation: Hybrid event beds (*sensu* Haughton et al. 2009)**	tabular	

Table 5.1 (continued). Summary of bed type descriptions and interpretations.

sand comparable to that of the matrix of the bed bases. With respect to entire bed thicknesses, the medial part accounts for the major part of strata. Towards the uppermost 5 – 10 cm´s of individual beds, the medial interval rapidly fines to medium- to fine sandstone (delayed grading). Locally, essentially in the very proximal domain of the studied system, lateral grading can be observed as well. Despite for faint laminations towards the very tops of beds, beds commonly do not display primary sedimentary structures. Notwithstanding, bed type 1.1 strata are typified by the omnipresence of commonly sub-horizontally oriented soft-sediment deformational structures (Fig. 5.3 B). These dewatering features are generally distributed within the coarse sand-grained, medial interval of beds and comprise concave-upward water-escape dishes and dewatering sheets. These dewatering structures can readily be recognized by their slightly finer grain-size when compared to that of their "hosting" coarser sandstones. Lateral extents of water-escape dishes are limited to up to 12 cm, whereas dewatering sheets laterally extents for up to meters. Vertical interspacing in between dewatering dishes is in the range of ca. 3 to 10 cm.

Microconglomerates generally appropriate to a massive appearance, even if beds sporadically exhibit traction carpets and crude planar stratifications. Moreover, local faint ripple-scale cross laminations can be found. Sporadically, multiple laterally discontinuous traction carpets overlying each other are present. These are outlined by clast-supported gravelly intervals (thickness 2.5-8 cm) that gently fine upward into medium to coarse sand. The traction carpets are commonly oriented parallel to bedding or moderately inclined. In rare cases, the traction carpets can be partly deformed and show curvilinear to "whirly" pathways. (Fig. 5.3 E).

Bed soles are sporadically marked by the very rare abundance and low diversity of mostly simple and branching trace fossils represented by the ichnogenera *Ophiomorphia*, *Planolites* and *Thalassinoides*. The occurrence of these bioturbations is limited to beds that either represent the bases of fining-upward cycles or beds that mark the onset of siliciclastic sedimentation of the Bordighera sandstone, superimposing and merely locally incising into thin- to very thin-bedded San Bartolomeo Formation strata. Basal bed contacts are typically sharp and typically of erosive character. Essentially in the most proximal domain, bed bases locally display loading into underlying finer grained strata and frequently exhibit flame structures (Fig. 5.3 D). At the outcrop scale, beds show good lateral continuity and allow bed geometries to be defined as of both tabular and lenticular expression. Accordingly, noticeable lateral thickness variabilities are to be observed. Sole structures are typically restricted to groove casts and indicate a bimodal SSW´-NNE´ paleocurrent orientation. The very sparse presence of flute casts reveals a dispersal pattern from SSW´. Maximum incisional depths of these erosional features commonly do not exceed ca. 3-5 cm, while the width of these marks reaches up to ca. 25 cm. Tops of beds are mostly sharp displaying both flat and undulating shapes. Microconglomerates merely contain minor concentrations of intraformational rip-up clasts that do not display clear trends in spatial distribution within beds. These rip-up clasts, consisting of both siliciclastic and calcareous matter, are typically of tabular, angular shape with a wide range of dimensions from ca. 0.2 cm x 1 cm up to 4 cm x 30 cm. Frequent amalgamation features, underlined by notable grain-size breaks (Fig. 5.3 C), denote bed sets of bed type 1.1 strata. The maximum thickness of amalgamated stacks extends up to 23.62 m. Locally, shallow scourings beneath amalgamation contacts have been observed, with incisive erosional reliefs of up to roughly 20 cm in depth.

Interpretation:

Based on the poor sorting, and the internal largely massive texture, these beds were presumably deposited through rapid fallout from high-density turbidity currents (sensu Lowe, 1982) of bi-partite character, defined by a basal quasi-laminar flow and an upper turbulent layer. The deposit characteristics show a strong similarity to the Lowe (1982) S1 and S3 divisions. Common dewatering dishes and sheets point towards an origin related to oversaturated, fluid-rich flows (Lowe & LoPiccolo, 1974). The sub-horizontal orientation of the concave-upward dewatering dishes indicate the vertical expulsion of interstitial fluids as a result of rapid deposition and a subsequent absence of preservation of primary depositional structures (e.g. Van Loon, 2009). Nonetheless, the combination of coarse-tail grading with abundant dewatering structures cannot rule out an alternative interpretation, namely that of a transport by hyperconcentrated to concentrated flows (*sensu* Mulder & Alexander, 2001). The local occurrence of thin, faint ripple-laminated uppermost intervals of beds would suggest that these hyperconcentrated to concentrated density flows were overridden by more dilute turbulent flows. The characteristic coarse-tail grading illustrates excessive near-bed sediment concentration (Malgesini et al., 2015) and hence supports the interpretation of a hyperconcentrated-to concentrated density flow origin of the basal interval. The dominance of groove marks over flute structures additionally supports the assumption of a hyperconcentrated to concentrated density flow origin of bed type 1.1 strata (Hsü, 1959). The highly concentrated coarse-tail graded lowermost part would suggest traction carpet deposition, whereas the poor to absent grading within the medial parts of beds indicates that deposition most likely occurred by rapid fallout from suspension ("en masse deposition" of Lowe, 1982) from rapidly decelerating turbulent flows. Rapid deceleration points to flow expansion (e.g. Jobe et al., 2010; Talling et al., 2012). Coarse-tail graded lowermost parts of beds and locally observed laterally discontinuous traction carpets within the medial parts of beds reflect the complexity of flow characteristics outlined by internal stratification (Sohn, 1997; Janbu et al., 2007). In this case, deposition is related to rapid frictional freezing of a traction carpet following hindered settling.

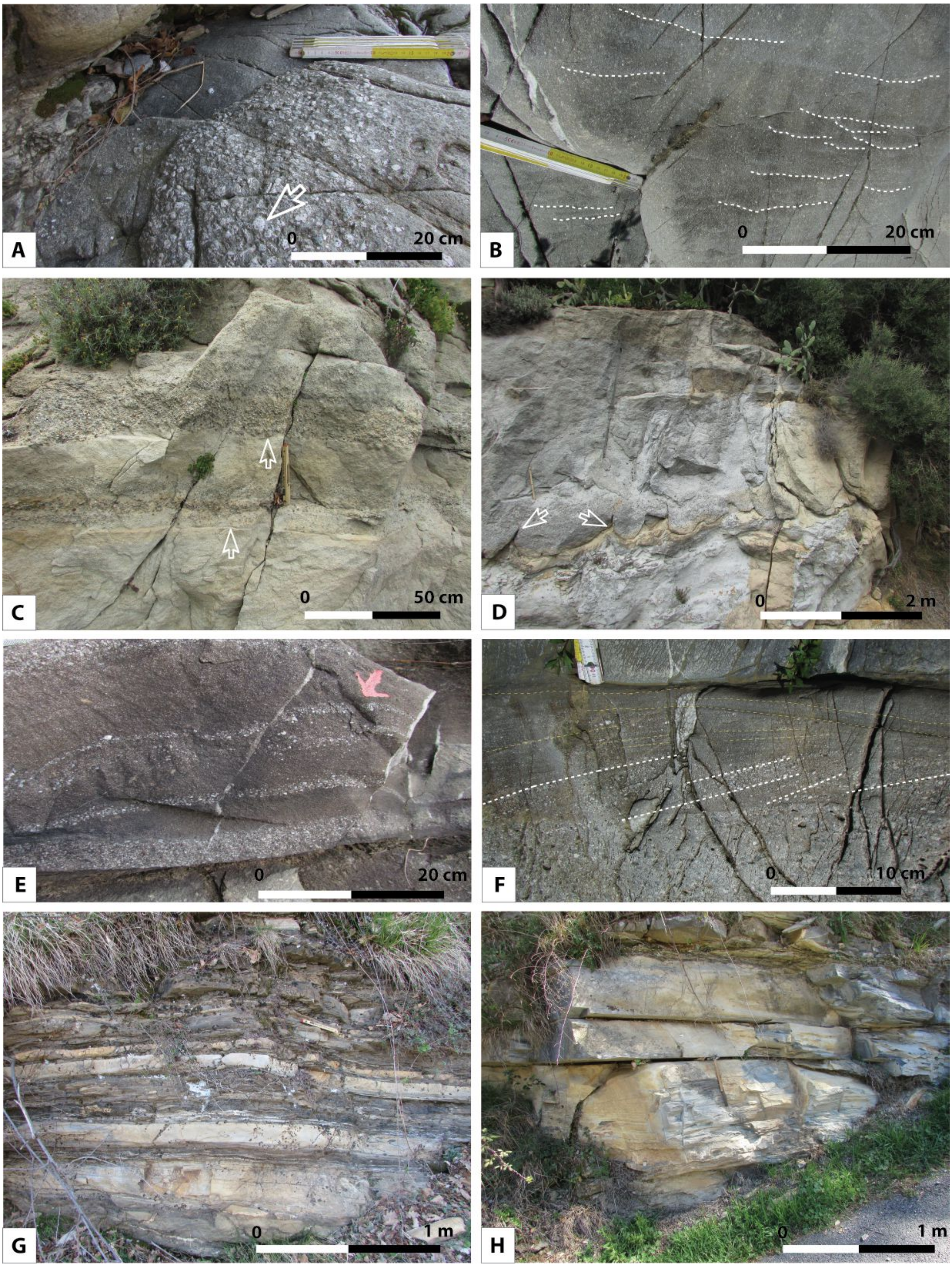

Fig. 5.3. Outcrop examples of selected bed types (1-4). (A) Coarse-tail graded pebbly base of bed type 1.1; the bed is overturned, and the field of view shows the basal surface of the bed. Note the angular shape of basal pebbles (arrow); section 2, "Badalucco-Quarry". (B) Dewatering dishes in bed type 2.1 strata; section 4, "Montalto River". (C) Amalgamations (arrows) between bed type 1.1 microconglomerates in the axial proximal realm; outcrop close to "Ospedaletti". (D) Basal loading of bed type 1.1 into underlying finer-grained strata. Note deformed base with flame structures (arrows).

Outcrop close to “Ospedaletti”. (E) Slightly deformed traction carpets superimposing coarse-tail graded base of bed type 1.1; section 2, Badalucco-Quarry. (F) Bed type 1.3 displaying typical vertical arrangement of a pebbly structureless base overlain by a coarse sandy medial part with cross-stratifications, followed by weakly inclined cross-lamination and wavy-to ripple-laminated toward the top of the bed. Note the abrupt grain size jump between the basal and middle divisions. Section 4, “Montalto River”. (G) Heterolithic interval characterized by alternating calcareous and siliciclastic fine-grained thin beds; section 5, “Carmo dei Brocchi”. (H) Alternating medium-to thick-bedded calcareous beds; section 6, “Monte Frontè”.

Dispersive pressure created by grain-by-grain collisions underneath shearing high-density turbulent flows (Lowe, 1982; Kneller & Branney, 1995) would explain this textural make-up. The irregular and deformed nature of some traction carpets might indicate such shearing and reworking by internal sediment waves (“pulsing” sensu Cartigny et al., 2014) and points towards highly unsteady flow behavior typified by multiple coarse-grained pulses (c.f. “fluxoturbidites” of Slaczka & Thompson, 1981; see also Leszczynski et al., 2015). Delayed normal grading and the presence of traction related sediment structures toward the top of beds suggests progressive grain settling during the waning stages of the overriding turbulent flows (Kneller & Branney, 1995) and supports the interpretation of turbulent flows typified by internal stratification. Interpretations of outcrop datasets and flume experiments prove that the characteristic presence of coarse-tail grading and multiple traction carpets is suggestive of internal hydraulic jumps within a single event (Postma, 1988; Postma et al., 2009) and suggests that these flows apparently underwent multiple stages of flow transformation. Moreover, the combination with coarse-tail grading and abundant occurrence of traction carpets are supposed to hint towards a depositional environment in immediate adjacency to the channel-lobe transitional zone (cf. Postma et al., 2009). Furthermore, Postma et al. (2009) suggest that the spatial expression of coarse-tail grading within the channel-lobe zone is exclusively ascribed to sheet-like beds. Nevertheless, coarse-tail graded bed type 1.1 strata have been noted in beds exhibiting both tabular and lenticular geometries, thus challenging this observation. Angular clasts of granule- to pebble grain size at the bases of beds, in combination with the poor sorting, indicate a comparatively proximal vicinity to the sediment source (Kilhams et al., 2014), while the angular, low-sphericity shape of rip-up clasts is revealing a minor degree of reworking (cf. Johansson & Stow, 1995), which would hence point towards a relatively short transport distance after entrainment.

Both outcrop-scale lenticular and tabular bed geometries indicate that bed type 1.1 sediments represent either channel-fill sediments (e.g. Campion et al., 2000; 2005; Hubbard et al., 2008; Etienne et al., 2013) or sediments deposited in close relationship to a rather less confined depositional setting (cf. Rontzien et al., 2014). With respect to the rather unidirectional paleocurrent orientations, the association of bed type 1.1 strata to low-sinuosity submarine channels can be pointed out (e.g. Hesse et al., 2001; Crevello et al., 2007). The abundant amalgamations underline the interpretation of deposition within a such high-energy environment. The high ratios of amalgamation reflect limited time intervals in between individual subsequent sedimentation events and the enormous erosive nature (Lien et al., 2006).

Bed type 1.2: Microconglomeratic lag

Bed type 1.2 comprises thin-bedded, orange-brownish to greyish structureless layers with thicknesses ranging from 0.12 m to 0.45 m. The average thickness is approximately 0.25 m. The texture of sediments is that of a structureless, clast-supported microconglomerate in microconglomeratic grains are organized in a brownish to light greyish, coarse to very coarse sandy matrix that is defined by the general lack of mud. The roundness of grains can be restricted to sub-angular to angular. An important feature of bed type 1.2 sediments is the moderate to good sorting of the sediments which is strongly dominated by medium sized granules to small pebbles. Beds are characterized by a generally poor grading, even if subordinately basal inverse grading was observed. Furthermore, towards the tops of beds locally relatively abrupt normal grading has been noted. Primary sedimentary structures as a result of traction processes or dewatering structures are generally absent. Clasts show a disorganized dispersal pattern, as preferred clast imbrications of clasts are absent as well. The mainly spherical clasts cover a broad spectrum of components. The larger pebbly clasts are typically of plutonic and gneissic fragments, whereas the coarse sandy grain fraction is typically represented by quartz and feldspathic grains, although to a minor amount sedimentary fragments have been observed. Beds exclusively display sheet like geometries and are characterized by flat, sharp basal contacts and sharp tops of typically flat and only subordinately irregular to wavy expression. Signs of erosional nature like scour marks, tool marks or entrained mud clasts have not been documented.

Interpretation:

The clast-supported texture of these beds suggests that a frictional flow was the dominant transport mechanism (Lowe, 1982; Amy and Talling, 2008). In particular, the practical absence of clay within the coarse matrix points towards a non-cohesive debris flow. The good sorting and the scarcity of normal grading implies a hyperconcentrated density flow (cf. grain flow of Mulder & Alexander, 2001) as being the dominant transport mechanism. Accordingly, bed type 1.2 is interpreted to represent basal parts or remnant lags of by-passing high-energy flows (Stevenson et al., 2015). The deposition from sustained, frictional hyperconcentrated density flows is interpreted to have occurred through frictional freezing (Mulder & Alexander, 2001). Local abrupt normal grading towards the tops of beds is interpreted to illustrate “dumping” or winnowing by overriding, bypassing flows. In addition, the open-framework suggests an effective sorting mechanism that caused extraction of the finer grained fractions. A such inferred removal of certain grain size fractions would additionally support the significant bypassing nature that typified the coarse-clastic turbiditic system (Stevenson et al., 2015).

Bed Type 1.3: Inversely graded microconglomerates

Description:

Bed type 1.3 is made up of orange-greyish to light brownish, medium- to thick-bedded, polymictic microconglomeratic sandstones that range from 0.35 m to 2.46 m in thickness (mean thickness: ca. 0.85 m). Clast compositions include mostly sub-angular to sub-rounded quartz grains, feldspar varieties and minor portions of granitic fragments Grain-sizes range from coarse pebbles (max. 2.1 cm x 4.5 cm) to fine sand. Beds are characterized by a remarkably poor degree of sorting. Grains are arranged in an exclusively matrix-supported texture. The matrix is typically coarse to medium sand that exposes normal grading and contains essentially low mud proportions. The most distinctive feature of bed type 1.3 strata is the inverse grading at the basal parts of beds. The inversely graded interval reaches individual thicknesses of up to roughly 5 to 10 cm's, and is followed by well-expressed, continuous normal grading all the way up to the tops of beds. The lower parts of beds commonly appropriate to a structureless texture and only sporadically exhibit crude stratifications and clast imbrications. By contrast, the uppermost parts typically show a range of primary physical structures such as planar-parallel, wavy- and ripple-laminations. A frequently observed vertical sequence is that of crudely stratified basal intervals that develop into upper intervals defined by low-angle planar parallel laminations which are followed by wavy laminations to current-ripple laminations. Notwithstanding, incomplete sequences marked by the absence of individual types of laminations and stratifications have been observed as well, even if there appears to be a general trend of tops typically displaying ripple-lamination. Moreover, several bed type 1.3 strata are defined by distinct grain size jumps, typified by structureless pebbly lowermost parts and coarse sandy medial parts that display cross-stratifications (Fig. 5.3 F). Notably, very sporadic presence of fluid escape structures attest that these represent almost negligible features. Moreover, beds are defined by the absence of trace fossils.

Bed type 1.3 sediments are generally sharp-based and only in exceptional cases exhibit evidence of erosive nature. The majority of beds demonstrate outcrop-scale (lateral exposure ca. 10- 20 m) tabular geometries, although subordinate lenticular varieties have been noted as well. The tops of beds are generally sharp and typically of flat, and only in rare exceptions of wavy shapes. Loading structures at the bases or sole markings are infrequently to be found. Nevertheless, it should be noted that exclusively flute casts have been documented that reveal a general north-ward paleocurrent dispersal. Minor amounts of intraformational rip-up clasts characterize bed type 1.3 strata.

Interpretation:

Based on the inversely graded bases followed by normal grading and the presence of primary sedimentary structures, bed type 1.3 is interpreted to have been deposited through traction fallout from suspension by high-to low-density turbidity currents. Inverse basal grading is interpreted to reflect traction carpet deposition, comparable to the S1 subdivision of Lowe (1982). Abrupt grain-size breaks from pebbles to coarse sand are interpreted to reflect bypass of the granule and very coarse sand fraction down-dip (Stevenson et al., 2015). The typical sequence of crudely stratified lowermost intervals superimposed by laminated topmost intervals is interpreted as being partly analogous to the idealized deposits of high-density turbidity of Lowe (1982). The structureless to crudely stratified lower part of beds shares marked similarities with the S3 division of Lowe (1982), whereas the wavy-to current ripple-laminations are interpreted to mirror intervals of the Bouma Tbc sequence. Beds are hence interpreted to have been deposited by gradually decelerating turbulent flows (Bouma, 1962; Lowe, 1962; Mulder and Alexander, 2001). Notably, the presence of crude stratifications and primary sedimentary structures reveals the significance of traction processes during deposition (Bouma, 1962; Lowe, 1982) and could therewith hint towards prolonged flow duration that has frequently been interpreted to be associated with channelized flows or flows that expanded at the terminus of channel confinement (e.g. Stow & Johansson, 2000; Milli et al., 2007; Jobe et al., 2010). Disregarding a precipitate environmental attribution, bed type 1.3 is interpreted to represent the typical deposits of high- to low-density turbidity currents (Bouma, 1962; Lowe, 1982).

Bed type 2.1: Structureless "clean" Sandstones

Description:

This bed type comprises very thin- to thick-bedded "clean" sandstones of brownish greyish to light greyish color. Bed thicknesses vary between 0.07 m and 2.25 m. Mean thickness in the range of approximately 0.5 m. The maximum grain size is coarse to very coarse sand, whereas the minimum grain size observed is fine sand. The mean grain size can be accounted to medium sand, beds are hence defined by a moderate degree of sorting. Bed type 2.1 is made up of sub-rounded to rounded, spherical grains that are organized in a well-sorted matrix made up of medium- to fine sand. Moreover, the bright color of the sandstones that essentially becomes apparent in a river-polished outcrop, indicates insignificant concentrations of cohesive fine-grained material. The majority of strata show normal, typically delayed “content” grading with only minor proportions of beds exhibiting basal inverse grading. The typifying feature of these sediments is their commonly structureless, massive appearance delineated by a general absence of primary sedimentary structures. In some places, dewatering dishes with lateral extensions of up to ca. 8 cm have been observed (Fig. 5.3 B). Simple, non-branching, cylindrical biogenic structures of the ichnogenera (?) *Paleophycus* and *Planolites* of horizontal, bedding plane-parallel courses have infrequently been observed at the sole of structureless sandstones.

Bases of beds are exclusively sharp. Locally, erosive manner is manifested by cm-scale groove marks at the soles of individual beds. Flute casts have not been observed. Sporadically, bed type 2.1 exhibits the presence of small quantities of sub-angular, cm-scale (max. 2.5 cm x 6 cm) rip-up clasts. It should however be noted here that these intraformational clasts, composed of either siliciclastic or calcareous matter, only represent very minor concentrations of the total bed volume. Bed tops are sharp and exhibit planar as well as undulating pathways. The tops locally display gradual fining into overlying silty sediments. Bed bases are commonly of flat, even shape. At the outcrop scale (10´s of meters), the majority of beds display tabular geometries. Rare beds that display wedge-shaped to lenticular geometries have been noted. Nevertheless, no evidence of scouring was observed, as beds rather appear to compensate pre-existing morphology. Infrequently, amalgamations of bed type 2.1 strata have been documented.

Interpretation:

With regards to the characteristic, typically delayed normal grading and the absence of primary sedimentary structures, type 2.1 beds are interpreted to have been deposited by rapid fallout from suspension under concentrated density flows or turbulent flows (Mulder and Alexander, 2001). The lack of sedimentary structures reflects rapid deposition, with sediment fallout being too fast to be reworked by traction processes (Lowe, 1982). Dewatering features additionally suggest rapid deposition. Moreover, the fact that most beds show tabular geometries points towards rapid sedimentation occurred by grain-by-grain deposition due to rapid flow expansion, presumably due to a marked loss in the degree of confinement (Postma et al., 2009; Stow and Johansson, 2000). The exclusive presence of groove marks supports this interpretation (e.g. Hsü, 1959; Mutti, 1992).

Bed type 2.2: Thin- to thick-bedded, graded, structured sandstones

Description:

Bed type 2.2 comprises moderately sorted, normally graded thin- to thick-bedded (0.10-1.15 m; mean 0.50 m) fine- to medium "clean" sandstones. In a vertical sequence from their bases toward their tops, beds typically display low-angle planar parallel laminations overlain by wavy and current-ripple laminations. In rare cases, the upper parts of beds show climbing ripples. Locally, beds exhibit dewatering dishes typically associated with small-scale convolute laminations. Bases and tops of beds are sharp and commonly flat. On very rare occasions, small clusters of rip-up clasts can be observed. At the outcrop scale (ca. 15-20 m), beds display both lenticular and tabular bed geometries.

Interpretation:

Normal grading, the abundance of primary sedimentary structures and the moderate degree of sorting suggest deposition by fully turbulent flows (Mulder & Alexander, 2001; Crane & Lowe, 2008). With respect to the successive occurrence of laminations, flows can be ascribed to low-density turbidity currents that exhibit partial Bouma sequences. Low-angle planar laminations are interpreted to reflect traction processes beneath a turbulent flow characterized by upper flow regime conditions (Froude-Nr. > 1), corresponding to the Bouma Tb interval. Wavy and current-ripple laminations towards the top of beds indicate late-stage tractional reworking beneath a depleted low-density turbidity current, characterized by deposition under a lower flow regime (Froude-Nr. < 1) in unidirectional flows (Bouma Tc interval, see Bouma, 1962; Mulder & Alexander, 2001).

Bed type 3: Heterolithic intervals (clastic and calcareous fine and thin beds)

Description:

Heterolithic packages range from 5 cm up to meters thick. Individual beds consist of thin (<30 cm), graded fine sandstones and calcareous beds intercalated with mudstones and siltstones (Fig. 5.3 G). The proportions of individual components can vary considerably. Sandstone beds frequently exhibit wavy- to ripple- laminations. Soles of both sandy and calcareous beds display abundant trace fossils and a clear distinction between ichnofossils assemblages of siliciclastic and calcareous beds can be drawn. Sandstone soles typically feature a trace fossil suite comprising simple, straight and curvilinear non-branching structures such as *Gordia*, *Ophiomorpha* and *Planolites*. On the contrary, branching, meandering and helical trace fossils represented by abundant specimen of *Nereites irregularis* (cf. "*Helminthoides*"; Uchman, 2007), *Thalassinoides*, *Urohelminthoida* and various taxa of the ichnogenus *Chondrites* are developed at the bases of calcareous strata. Bases and tops of the thin sandstone and calcareous beds are sharp, while mudstones and siltstones intervals can have either sharp or gradational contacts. At the outcrop scale (10´s of meters), beds show tabular geometries.

Interpretation:

Heterolithic packages are interpreted as resulting from alternating low-energy depositional processes. As denoted by the characteristic normal grading, the fine-grained silty to sandy clastic and calcareous thin beds are interpreted as resulting from suspension fallout of fine-grained tails of diluted turbidity currents. Wavy- and current ripple-laminated fine-grained beds are analogous to Bouma Tc to Td intervals and illustrate traction processes during final waning-flow stages (Mulder & Alexander, 2001). Interbedded muddy intervals are interpreted to represent hemipelagic to pelagic settling and indicate periods of turbidite quiescence (Lien et al., 2006).

Bed type 4: Thin- to thick-bedded calcilutites and calcarenites

Description:

Medium- to thick-bedded, graded greyish calcareous sediments (Fig. 5.3 H). Grain size ranges from very fine sand (only at the very base of beds) to mud. Beds either have a structureless appearance or, predominantly in the case of the thinner ones, display wavy- to current-ripple laminations towards the beds top. Soles of beds portray a moderate diversity and high abundance of trace fossils. Comparable to the trace fossils found at the bases of calcareous beds of bed type 3, the observed trace fossil suite corresponds to the typical Helminthoid Flysch trace fossil assemblage. The trace fossil community is dominated by various specimens of the ichnogenera *Helminthoides* (= *Nereites irregularis*; cf. Powichrowski, 1989; Uchman, 2007), *Urohelminthoida* and *Chondrites*. Minor *Orphiomorpha* and *Planolites* traces are also found. Among the peculiarities of bed type 4 is the local presence of sub-horizontal injections of coarse sand within the thick beds (Fig. 5.4 A). They are generally lenticular and elongated, with maximum dimensions of up to 0.35 m x 6.50 m. Very rare examples of sub-vertical to vertical injections can also be observed, and in some cases they can be traced downwards to their parent sand layer. At the outcrop scale (exposure of up to 100 m), beds appear to be of tabular geometry. Bed bases are generally sharp and flat. Tops are sharp as well, tending to show a wavy shape. Amalgamation of bed type 4 is rare.

Interpretation:

Based on the combination of the normal grading and the presence of primary sedimentary structures, bed type 4 is interpreted to record deposition from low-density calcareous turbidity currents. Wavy laminations and ripple-laminations record the effect of traction processes during waning stages of dilute turbulent flows (e.g. Mulder & Alexander, 2001; Felletti, 2016). Localized upward injections of siliciclastic sand from underlying beds are interpreted to reflect the remobilization of the clastic substrate as a result of fluid overpressure due to gravitational loading (e.g. Andresen & Clausen, 2014; Cobain et al., 2015). Triggering mechanisms for remobilization could include seismic activity, rapid burial or instability of superimposing strata (see Hurst et al., 2011 for review). In the Bordighera Sandstone, with respect to the subduction geodynamic setting (e.g. Di Giulio, 1992), seismicity appears to be the most probable emplacement trigger.

Bed types 5: Mud-clast enriched sandstone beds

Description:

Bed type 5 comprises thin- to thick-bedded microconglomeratic sandstones containing varying proportions of dispersed mud-clasts. Bed thicknesses vary between 17 cm and 2.55 m, with a mean thickness of 1.10 m. Beds are characterized by a general absence of primary sedimentary structures. Locally, dewatering dishes and sheets are present. Based on the amount and the dominant composition of mud-clasts, two different sub-types (type 5.1 and 5.2) can be distinguished. Bed type 5.1 is defined by roughly equal shares of siliciclastic and calcareous mud-clasts that generally make up less than 10 % of individual beds (Fig 5.4 B). In contrast, bed type 5.2 contains ca. 10-20 % of mud-clasts. In addition, bed type 5.2 mud-clasts are predominantly made up of calcareous substrate, although in some places clusters of scattered siliciclastic mud-flakes are present (Fig. 5.4 C). The two sub-types are also defined by textural differences, in particular by the vertical position of mud-clasts within the beds. Bed type 5.1 mud-clasts are usually distributed in the lower part of the beds or immediately above the bed bases. They are commonly aligned parallel to bedding and show minor degrees of deformation. Conversely, mud-clasts of bed type 5.2 are preferably located in the uppermost parts of beds. They are commonly larger than those in bed type 5.1 and locally appear to be disrupted or deformed. Another characteristic feature of bed type 5.2 clasts is the presence of "rims" of dark siliciclastic mud around some of the large calcareous clasts. Additionally, differences in basal grading profiles can be observed. Bed type 5.1 commonly shows normal grading, with the occasional exception of basal inverse grading followed by normal grading. In contrast, bed type 5.2 exclusively exhibits coarse-tail grading. Both bed types can display thin (< 0.5 cm) horizons of dark siliciclastic mud that can be traced laterally for up to ca. 2.5 m and are characterized by an irregular, wriggling pathway. Bed bases are sharp. Small-scale erosional relief (cm- to dm-scale incisions) occurs locally. Tops are generally sharp as well and they are typically flat, although locally they can be wavy. At the outcrop scale (lateral exposure up to ca. 30 m), bed type 5.1 displays both lenticular and tabular bed geometries, whereas bed type 5.2 strata exclusively exhibit tabular geometries. Observation of lateral passages of bed type 5.1 into bed type 5.2 is rare. Amalgamations of bed type 5 frequently occur, with a maximum number of three amalgamation surfaces being observed within one package. No trends in the vertical arrangement of superimposing bed type 5 varieties is observed.

Interpretation:

The common normal grading of bed type 5.1, along with the absence of primary sedimentary structures, point towards high density turbidity currents as being their transport mechanism (Lowe, 1982). The combination of the structureless appearance and normal grading would suggest deposition by fallout from a suspension that prevented tractional processes (S3 division of Lowe, 1982). Mud-clast concentrations illustrate the erosive nature of flows. The occurrence of mud-clasts in clusters prevalently distributed in the lower parts of beds can be interpreted as demonstrating that these clasts were transported along a discrete interface between portions of the flow marked by different densities (cf. Postma et al., 1988). Bed type 5.1 is therewith interpreted as resulting from sediment gravity flows that comprised a turbulent upper part and a lower part showing signs of commencing turbulence dampening (e.g. Sylvester & Lowe, 2004, Southern et al., 2015). Bedding-parallel alignment of mud-clasts suggests that the lower parts of the flows were characterized by incipient turbulence modulation through cohesive mud entrainment ("transitional flow deposits" of Kane & Pontèn, 2012).

Bed type 5.2, showing a combination of a general lack of primary sedimentary structures, coarse grain size and local presence of dewatering structures also appears to have been deposited by high-energy turbulent flows, presumably analogous to the S2 and S3 subdivisions of high-density turbidity currents of Lowe (1982). However, the characteristic presence of coarse-tail grading hints towards a hyperconcentrated flow origin of the basal part (Mulder & Alexander, 2001). The common bedding-parallel orientation of clasts points towards a weakly turbulent flow mechanism that comprises a zone outlined by laminar flow conditions in which these clasts were dispersed (Stow & Johansson, 2000). High proportions of the muddy components point towards a transition towards cohesive flow behavior ("plug flow" *sensu* Baas et al., 2009; see Talling et al., 2013). Based on this two-part internal organization, flows are interpreted to be of co-genetic origin, comprising a basal hyperconcentrated density flow overlain by a weakly turbulent flow of high sediment concentration in which enhanced mud entrainment suppressed turbulence (Postma et al., 2009; 2014; Terlaky & Arnott, 2014). High sediment concentration provided the particle-support mechanism for floating mud-clasts (cf. Talling et al., 2013). Bed type 5 might therefore be considered as representing an incipient stage in the development of hybrid event beds *sensu* Haughton et al. (2009).

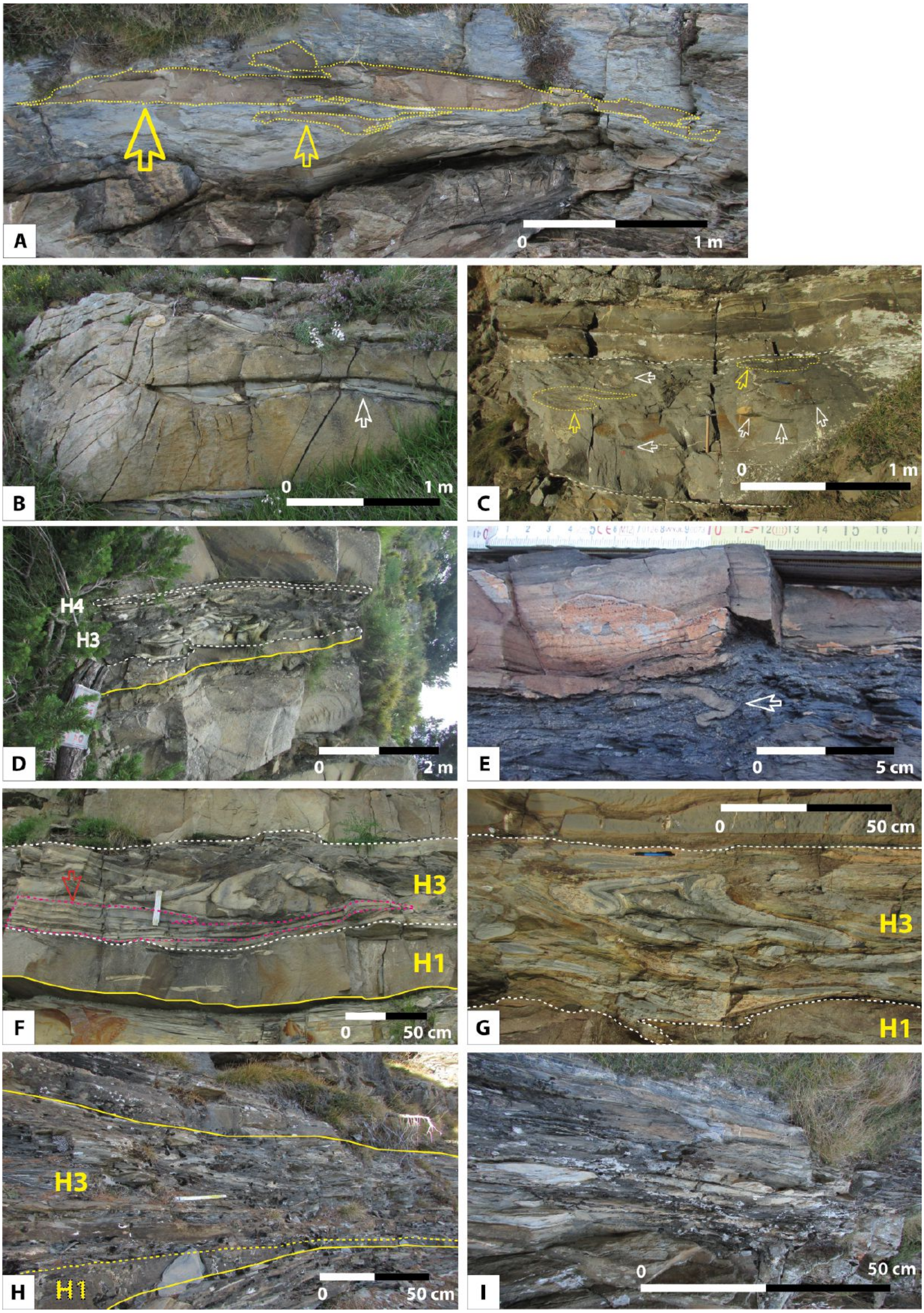

Fig. 5.4. Outcrop examples of selected bed types (4-6). (A) Sill-like clastic sand injection into thick-bedded calcareous mud (Bed type 4); section 8 "Margheri Binda". (B) Bedding-parallel "floating" calcareous clast (arrow) incorporated into bed type 5.1 strata; section 5, "Carmo dei Brocchi". (C)

Cluster of calcareous and siliciclastic mud clasts (yellow arrows) within bed type 5.2. Note the broadly bedding-parallel alignment of the smaller clasts (white arrows). Section 6 "Monte Frontѐ". (D) Tri-partite hybrid event bed characterized by strongly disrupted and folded calcareous clasts. Yellow line indicates the base of the bed. Note the thin capping H4 division; section 6 "Monte Frontѐ". (E) Detail of upper part of bed shown in (D): laminated H4 division superimposing the debritic H3 division. Note the dark color of the matrix of the H3 division indicating clay dispersed into the uppermost part of the coarse sandstone matrix and the down-ward injection of H4 clean sand into the H3 interval (arrow). (F) Bi-partite hybrid event bed (bed type 6.1) containing a block of preserved heterolithic stratigraphy incorporated in the H3 division (red arrow). Note strongly deformed large calcareous mud-clasts above the block. Section 6 "Monte Frontѐ". (G) Detail of mud-clast deformation of bed shown in (F). Note the sheath-folded deformation of the calcareous clsts. (H) Example of bed type 6.3, characterized by gradational HEB divisions. Note the roughly bed-parallel calcareous clasts and blocks making most of the H3 division and the thin H1 interval. Section 10 "Cima di Velega". (I) Detail of bed type 6.3, showing roughly bed-parallel clasts and very dark sandy matrix.

Bed types 6: Hybrid event beds (HEBs)

Description: Medium- to thick-bedded microconglomeratic sandstones that contain a mud-clast-dominated debritic division. Thicknesses of beds vary between 0.27 m and 3.62 m (average thickness 1.40 m.) Beds are characterized by internal divisions that show very different texture and that are organized in a distinct vertical sequential order. A poorly sorted, mud-poor basal sandstone interval marked by the absence of traction structures is generally present. Occasionally, small concentrations of mud-clasts and dewatering dishes occur. Basal grain size of the structureless sandstone is up to small pebbles of sub-angular to angular shape. Basal intervals are characterized by the presence of coarse-tail grading followed by poorly developed normal grading.

The basal interval is overlain by a disorganized, argillaceous interval enriched in intraformational mud-clasts. Mud-clasts make up at least 20% of the interval, but often they represent a much larger proportion. From a textural perspective, the debritic interval can be described as a matrix-supported mud-clast conglomerate in which clasts are distributed chaotically. The host matrix of the mud-clasts is coarse to very coarse sand and displays delayed normal grading towards the top of the interval. In comparison to the mud-poor sandstone below, it does not exhibit a substantial decrease in grain-size. Mud-clasts are typically angular and have elongated shapes. They primarily consist of calcareous mud. Minor amounts of dark siliciclastic mud-clasts and very rare sandstone intra-clasts are also present. Mud-clasts sizes range from cm-scale up to large blocks (average mud-clast size ca. 5 x 15 cm; maximum documented size: ca. 1.75 m x 2.5 m). The sharp contact between the clean sandstone and the debritic division above is usually marked by a thin (cm-scale), laterally continuous wavy horizon of dark siliciclastic mud (except in Bed type 6.3; see below).

Due to their great variability, Bed types 6 strata can be differentiated into three sub-categories (6.1 to 6.3). The main classification criterium is the number of divisions recognized. Bed type 6.1 displays a tri-partite internal makeup that in addition to the two divisions described above comprises a thin (max. ca. 10 cm) mud-poor graded sandstone interval with current ripple-laminations that "caps" the debrite division (Fig. 5.4 D). On the contrary, bed types 6.2 and 6.3 are defined by their bi-partite internal organization (Fig. 5.4 F and 5.4 H), with the difference being in the sharp (6.2) or gradational (6.3) character of the divisions boundary. The character of the chaotic division provides a further substantial criterion for distinction. The color of the muddy coarse sandy matrix of the debritic interval is used as a proxy for mud-content (with a darker matrix being muddier). In bed type 6.1 only the upper part of the debritic division matrix is characterized by a dark color (Fig. 5.4 E), while in bed type 6.2 a dark color typically characterizes the entire upper half of the interval and in bed type 6.3 the entire debritic intervals is dark (Fig. 5.4 H and 5.4 I). The dimensions of mud-clasts in bed types 6.1 and 6.2 are generally greater than in bed type 6.3. In some occurrences, bed type 6.2 comprises up to m-scale blocks of preserved and locally undeformed heterolithic stratigraphy (Fig. 5.4 F). In bed types 6.1 and 6.2 mud-clasts are distributed chaotically (Figs. 5.4 D and 5.4 F), whereas bed type 6.3 mud-clasts are more organized, showing a bedding-parallel or quasi-parallel alignment (Fig. 5.4 I). The chaotic fabric of bed types 6.1 and 6.2 debritic divisions is often accompanied by a strongly disrupted, folded or sheared nature of the calcareous clasts. Essentially in the debritic intervals of bed type 6.2, the typical deformational style is that of complex sheath folding (See Fig. 5.4 G). By contrast, bed type 6.3 typically comprises isolated clasts that have elongated shapes and do not reveal compelling evidence of deformation.

Basal bed contacts are generally sharp, frequently featuring scouring into underlying sediments. Scours are of m-scale lateral dimensions, with maximum incisional depths of ca. 25 cm. Surfaces of bed tops are commonly flat, occasionally slightly undulating. At the outcrop scale (several 10´s of meters), bed type 6 usually displays tabular geometries. Amalgamation contacts between bed types 6 and bed types 5 are common. In rare cases bed type 6.1 features depositional lateral pinch-outs of the debritic interval (within a few meters), with a transition into bed type 5.

Interpretation:

The characteristic vertical sequential arrangement and varying textural characteristics of bed type 6 divisions demand individual interpretations. Based on the structureless appearance and the poorly graded texture, the mud-poor coarse-tail graded basal divisions are interpreted as deposited by highly concentrated turbidity flows, analogous to hyperconcentrated density flows of Mulder & Alexander (2001). Sporadic dewatering structures and retarded normal grading entail that these flows were presumably transitional to high-density turbidity currents (sharing strong similarities with the S1-S2 turbidite divisions) *sensu* Lowe (1982). The presence of mud-clasts highlights the erosive nature of these flows, underlining the presence of bedload processes. Deposition is interpreted to have occurred through rapid fallout of the suspended load (Lowe, 1982), with the scarcity of mud throughout the coarse-tail graded interval hinting towards deposition by frictional freezing and successive vertical accretion (Mulder & Alexander, 2001).

The matrix-supported texture of the chaotic division that is dominated by disorganized clasts and elongated blocks of calcareous mud suggests transport by laminar flows (cohesive debris flows) defined by the portion of cohesive mud that provides matrix strength as the sediment supporting flow mechanism (Mulder & Alexander, 2001). This interpretation is supported by the presence of either disorganized or broadly bedding-parallel oriented floating clasts and blocks (e.g. Sohn et al., 2002). Angular shapes of mud-clasts indicate limited abrasion (e.g. Hanáček et al., 2013; Cobain et al., 2015) and therewith suggest a relatively short transport distance after entrainment and subsequent rapid collapse of flows (Fonnesu et al., 2016). In particular, the block-dominated nature of bed type 6.2 - in which components of preserved underlying stratigraphy are incorporated into the chaotic subdivision - suggests local mud acquisition and the early stage of hybrid flow development (cf. Terlaky & Arnott, 2014; Fonnesu et al., 2016). This interpretation is in accordance with the model proposed by Terlaky & Arnott (2014) that observe clean sandstones containing large rafts made up of preserved internal stratigraphy in a proximal lobe environment and essentially in close vicinity to the axis of flows. Nevertheless, the common sheath-folded nature clasts in bed type 6.2 is interpreted as reflecting progressed laminar flow state conditions (Mulder et al., 2011) and might thus suggest comparatively local substrate entrainment followed by rapid collapse of the flows (cf. Fonnesu et al., 2016).

Differences in the amount of mud dispersed within the debritic matrix appear to be associated to a decrease in mud-clast size and a higher degree of roundness of mud-clasts and are hence interpreted as related to different stages of the disaggregation of mud-clasts (cf. "starry night" texture of Haughton et al., 2003; Terlaky & Arnott, 2014). Deposition of the debritic interval is interpreted to have occurred *en masse*, resulting from cohesive freezing as the shear resistance of these flows became balanced with the gravitational force (Mulder & Alexander, 2001). The normal graded mud-poor sandstones displaying current ripple-laminations that "cap" the debritic interval of bed type 6.2 are interpreted as representing the deposit of low-density turbidity currents (Mulder & Alexander, 2001), illustrating deposition and tractional reworking under a dilute tail of the flow that maintained turbulent flow behavior (H4 of Haughton et al., 2009).

Bed type 6 strata are interpreted to record a flow transformation from turbulent to cohesive within one single sedimentation event and therefore can be considered hybrid event beds *sensu* Haughton et al. (2009). With respect to the inferred flow mechanisms of bed type 5 deposits, bed type 6 is interpreted as resulting from more advanced stages of co-genetic flow development during a single sediment gravity flow event (cf. Haughton et al., 2003). The distinction between bed type 5 and bed type 6 is therewith drawn out by the greater proportion of mud-clasts that became incorporated in the coarse sandy matrix. Bed type 6 deposits are interpreted to develop laminar flow development as a result of further increase in clay proportions within the flow compared to bed type 5.

3.5. Bed type assemblages and their environmental significance

Seven different bed type associations, grouped into three main environmental associations, have been identified in the studied sections of the Bordighera Sandstone. Representative outcrop photographs are shown in Fig. 5.5 and their main features are summarized in Tables 5.2.1 to 5.2.3. Their description and interpretation in terms of depositional environment are discussed in the following section.

Bed type association 1: Channelized associations

Bed type association 1.1: Basin-floor axial feeder channel association

Description:

Bed type association 1.1 predominantly consists of "clean" beds types. Mud-poor massive, structureless microconglomerates and medium- to very coarse-grained sandstones represent more than 90 % of bed type proportions. At location 2 (Fig. 5.1) this facies association forms a considerably homogenous sandstone body that reaches a thickness of roughly 150 m. Even if lateral dimensions are difficult to constrain due to limited lateral outcrop exposure (Fig. 5.5 A), the exposed large-scale architecture suggests that the width of the sandbody was certainly in the range of at least 1 km or even more. Outcrops accessible for sedimentological ionvestigations (ca. 30 m of lateral exposure) reveal both tabular and lenticular geometries at the bed scale. Lenticular bed geometries are observed either in association with incisional contacts of microconglomeratic beds into microconglomerates and sandstones or they occur as scours into heterolithic intervals. Observed incisional depths are generally small (dm-scale; minimum ca. 10-15 cm). However, local truncations of more than 1 m have been documented (Fig. 5.5 B). Presence of slumped intervals has not been observed. Bed-sets typically encompass clean microconglomerates and sandstones. They are commonly organized in fining-up sequences that internally show high degrees of amalgamation (overall amalgamation ratio: ca. 75%). Thicknesses of amalgamated intervals vary between ca. 0.8 m and 14.5 m. Within these intervals, a notable feature is the predominance of structureless beds (ca. 65%) over beds displaying tractional structures. Amalgamated intervals are separated by fine-grained intervals made up of both siliciclastic and calcareous muddy beds, alternating with thin siltstones and fine-grained sandstones beds (0.03-0.25 m thick). The low proportion of muddy intervals results in a considerably high sand-to-mud ratio greater than 10:1. Paleocurrent measurements of basal sole structures (groove marks and minor flute casts) reveal unidirectional flows directed toward the North (vector mean = 2ºN; n = 14; see Table 5.2.1).

Interpretation:

The coarse sediment grain size, incisional basal contacts and high amalgamation ratio denote high-energy flow regimes. Dominant proportions of microconglomerates and minor medium- to very coarse-grained "clean" sandstones in association with lenticular bed geometries and internal bed-set organization characterized by fining-upward cycles suggest deposition within a channelized environment (e.g. Campion et al., 2005; Brunt et al., 2013; McHargue et al., 2011, Marchand et al., 2015). A number of observations point towards an axial position within a channel-belt, namely: high portions (75% of stratigraphic thickness) of amalgamated intervals (e.g. Elliott, 2000; Romans et al., 2009), dominance of structureless sandstones over beds displaying primary sedimentary structures (see Grecula et al., 2003) and the scarce presence of beds containing rip-up clasts (Hubbard et al., 2008; 2014; Macauley & Hubbard, 2013).

Fig. 5.5 (next page). Bed type associations. (A) Sandbody geometry of the interpreted channel axis typified by high sand proportions (bed type association 1). Lateral onlap of bed-sets is interpreted to demonstrate erosional character of the channel. View towards N-NW. Exposure cropping out on the opposite side of the valley of "Badalucco-Quarry" (Section 2). (B) Incisional bases truncating into finer-grained strata characteristic of the axial channelized association. Section 2 "Quarry Badalucco". (C) Heterolithic intervals typifying bed type association 1.2. Section 1 "Monte Bignone". (D) Composite tabular and lenticular bed geometries characterizing bed type association 2. Note the predominance of tabular bed geometries and the high sand-to-mud ratio. Section 4 "Montalto River". (E) Detail of tabular scour surface at the base of overturned thick mudclast-rich bed (bed type association 2). Yellow arrows indicate the orientations of groove casts ornamenting the scour surface. Mean paleocurrent direction is towards the NNW. Section 4 "Montalto River". (F) Example of bed type association 3.1 cropping out in an anticlinal structure. Note the sheet-like geometry and high sand-to-mud ratio. Section 6 "Monte Frontè". (G) Bed type association 3.2 characterized by sheet-like geometry and by a reduced sand content in comparison to bed type association 3.1. Section 9 "Monte Bertrand".

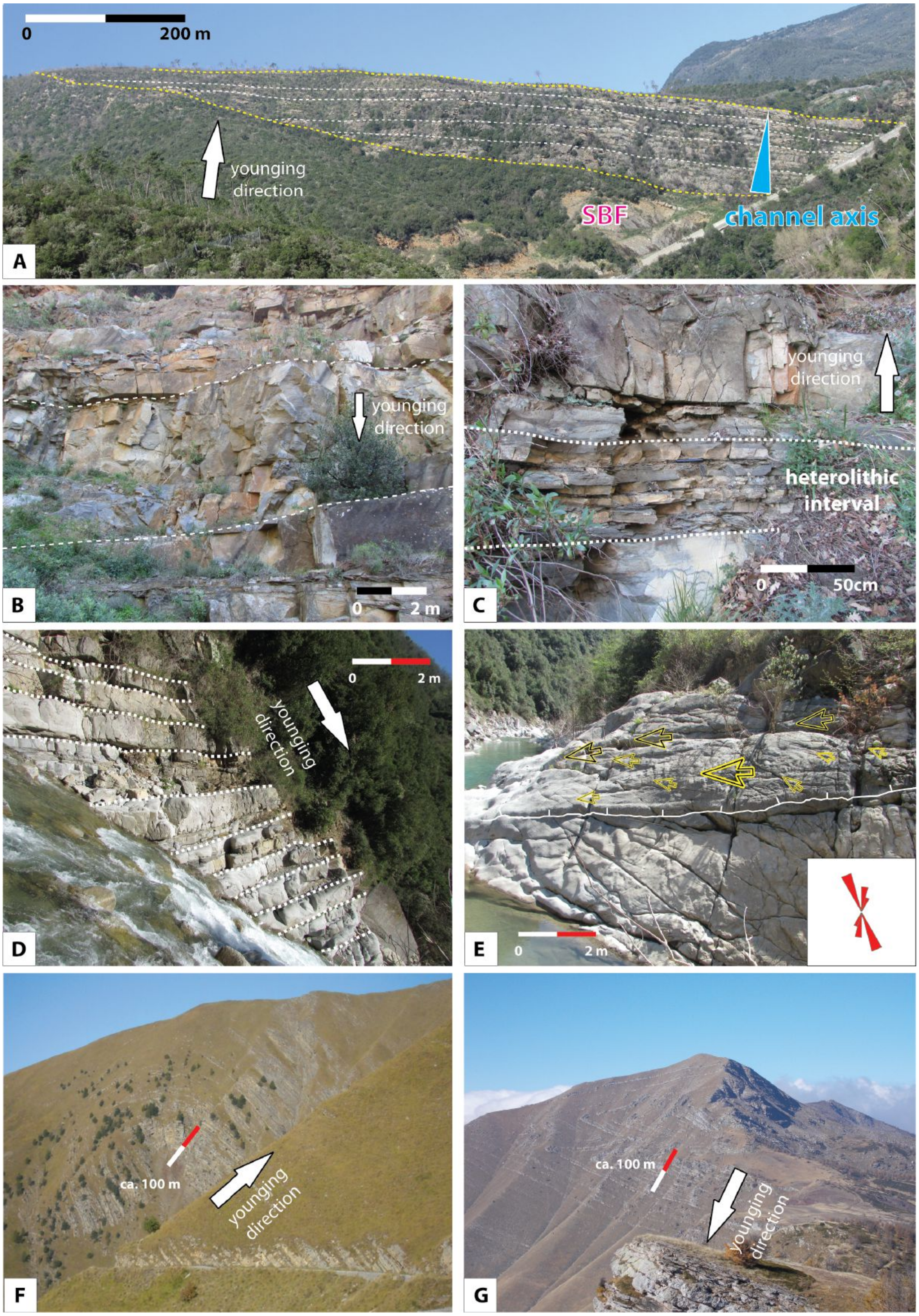

0
200 m
younging direction
SBF
channel axis
A
younging direction
0
2 m
B
younging direction
heterolithic interval
0
50cm
C
0
2 m
younging direction
D
0
2 m
E
ca. 100 m
younging direction
F
ca. 100 m
younging direction
G

Small depths of incision for individual events and limited proportions of draping heterolithic packages suggest that the individual channel elements were poorly levee-confined and probably dominated by sheet-like flow processes (Leverenz, 2000). The limited dispersal of paleocurrent orientations suggests a network defined by low-sinuosity channel elements (Hesse et al., 2001; Hubbard et al., 2014). Studies on turbidite systems in trench settings reveal a tendency of unidirectional paleocurrents in channel axes because of large-scale confinement within the trench topography (e.g. Lash, 1985; Underwood et al., 1993). The absence of features recording active slumping processes is interpreted as indicating a low gradient, suggesting the location of the axial channel in a basin-plain setting (Camacho et al., 2002).

Bed type association 1.2: Basin-floor off-axis channel association

Description:

Bed type association 1.2 constitute the largest part of section 1 (see Fig. 5.1). Comparable to Bed type association 1.1, it comprises mainly mud-poor microconglomerates and medium- to very coarse-grained "clean" sandstones. Clean bed types represent 80-90% of the overall thickness. However, in contrast to BTA 1.1, the relatively thick bed-sets made up of microconglomeratic sandstone beds are in places interrupted by heterolithic intervals consisting of alternating thin-bedded mudstones, siltstones and very fine sandstones (Fig. 5.5 C). Moreover, a decrease in average grain-size in comparison to that of bed type association 1.1 and a reduction in the proportion of basal lag facies can be observed. Among the "clean" bed types, an increase in the portions of beds exhibiting traction structures can be noted, accounting for ca. 40% of microconglomerates and sandstones. In a similar manner to bed type association 1.1, both lenticular and tabular bed geometries are found at outcrop-scale (ca. 10-15 m lateral exposure). Amalgamated bed sets typically exhibit fining-upward trends. The total amalgamation ratio of this bed type association is roughly 60%. Individual thicknesses of amalgamated intervals range from ca. 0.7 m to 6.5 m. Paleocurrent analysis reveals a generally S-N direction (vector mean = 349° N, n = 14; circular deviation = ± 46 °) with a larger variance respect to bed type association 1.1.

Interpretation:

The close spatial relationship with bed type association 1.1, the presence of lenticular bed geometries, the rather unidirectional paleocurrent pattern and the fact that bed sets are commonly outlined by fining-upward cycles suggest deposition in a low-sinuosity channelized environment as for BTA 1.1 (e.g. Campion et al., 2005; Satur et al., 2005; McHargue et al., 2011). This bed type assemblage is interpreted to represent a domain located off-axis with respect to bed type association 1.1, based on reduced overall amalgamation ratio (Romans et al., 2009; Rotzien et al., 2014), increased proportions of structured sandstones, more abundant heterolithic intervals (e.g. Camacho et al., 2002; Grecula et al., 2003; Hubbard et al., 2008; McHargue et al., 2011) and slightly finer grain-size (e.g. McHargue et al., 2011; Stanbrook et al., 2015).

Bed type association 1.3: Distributary channel / shallow scour fill association:

Description:

Bed type association 1.3 is most abundant at location 7 (See also Fig. 5.6) and it is defined by the dominant presence of highly amalgamated medium- to thick-bedded "clean" microconglomerates and sandstones. It is differentiated from BTA 1.1 and 1.2 mainly on the basis of its location with respect to the overall system extent and on the type of strata found laterally or in stratigraphic contact with it. Bed type association 1.3 has exclusively been observed in the distal domain of the preserved sediment fairway, where it is found intercalated between laterally continuous tabular (outcrop-scale; 10s of meters) strata. Notably, the facies association 1.3 passes laterally or is in direct stratigraphic contact with strata characterized by an increase in mud-enriched bed types and HEBs (bed type association 3; see below).

Sandstones exhibiting physical sedimentary structures such as wavy laminations and current-ripple laminations become more abundant towards the tops of individual bed-sets that display fining-upward trends. Locally, sandstones enriched in mud-clasts are present as well. Thickness of bed-sets ranges between ca. 2 m and 15 m; with the mean being about 5 m. Well-exposed and laterally continuous outcrops at location 7 allow observation of the lateral extent of bed type association 1.3 intervals approximately orthogonal to paleocurrent orientation. At this location, this facies association is laterally continuous for more than 300-400 meters. Bed type association 1.3 is characterized by (outcrop-scale) slightly lenticular bed-sets, expressed by generally small-scale incisions (below 25 cm) into underlying surfaces. Amalgamated interval thicknesses range from 0.95 m to 4.9 m. The mean vector of paleocurrent measurements is 15° N (circular deviation = ± 20 °; n = 4).

BTA	Descriptive characteristics, geometries, thicknesses	AR, Sand-to-mud	BT proportions	Typical Motif
1.1: Channel axis **Representative section:** **Badalucco- Quarry. GPS: 43.886135, 7.846541**	Considerably **homogeneous sand bodies** defined by the predominance of **mud-poor** massive, commonly structureless thick- to very thick-bedded microconglomerates and medium- to very coarse-grained "clean" sandstones. Subordinate presence of clean sandstones that exhibit primary sedimentary structures. **Scarcity of heterolithic intervals.** **Very rare calcareous strata and beds enriched in mud-clasts and HEBs.** Both tabular and lenticular bedset geometries (outcrop-scale). Lenticular bed-sets portray generally low (dm-scale; mean ca. 10 – 15 cm) incisional depths . Bedsets (thickness ca. 5 - 35 m) commonly organized in **fining-up sequences**. Amalgamated intervals thicknesses 0.8 m - 14.5 m; average thickness ca. 3.2 m. Paleocurrent data: **unidirectional sediment dispersal** (350° ± 20°; n=10).	**AR: ca. 75 %** **Sand-to-mud: 11 : 1** 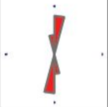	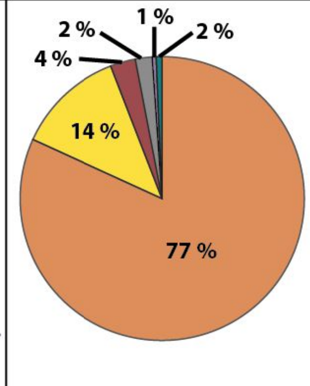	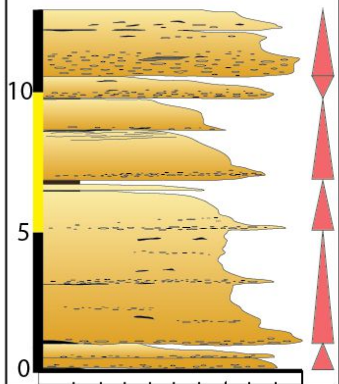
1.2: channel off-axis **Representative section:** **Monte Bignone. GPS: 43.866230 / 7.748397**	**Predominance of medium- to thick-bedded, "clean" bed types. Increase in bed types displaying primary sedimentary structures**. Decrease in mean max. grain size in comparison to BTA 1.1. **Increase in presence of heterolithic intervals**. Towards the top of the stratigraphic section, **local presence** of **mudclast-rich sandstones and HEBs**, linked to increase of calcareous mud. Either lenticular or tabular bed geometries (outcrop-scale). Bed sets internally arranged in **fining-upward cycles** (thickness 5-25 m), commonly separated by heterolithic drapes. Amalgamated intervals thicknesses 0.7 m - 6.5 m; average thickness ca. 3 m. **Comparably unidirectional paleocurrent dispersal** (360° ± 25°; n = 14).	**AR: ca. 60 %** **Sand-to-mud: 4 : 1** 	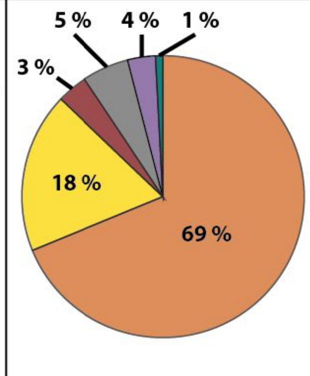	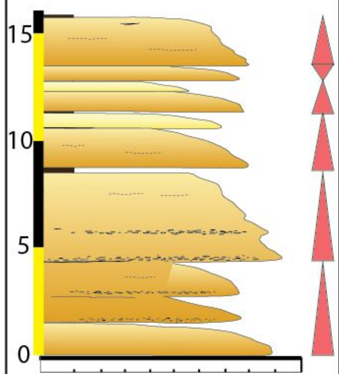
1.3: Distributary channel **Representative section:** **Farenga: GPS 44.082924, 7.734712**	**Predominance of medium- to thick-bedded "clean" bedsets.** **Exclusive distribution in the distal domain of the sediment fairway.** Interposed whithin laterally continuous tabular bed sets. Typical stratigraphic distribution in the lower and medial parts of analyzed sections. Slightly lenticular geometries (outcrop-scale), portraying small-scale incisions (< 25 cm) into underlying surfaces. **Fining-up / thinning-up** bedset patterns. Bed set thickness ca. 2 m - 15 m (mean thickness ca 5 m); Estimated width: ca. 300-400 m. **Unidirectional paleocurrent dispersal** (15° ± 10°; n = 4).	**AR: ca. 85 %** **Sand-to-mud: 9 : 1** 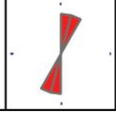	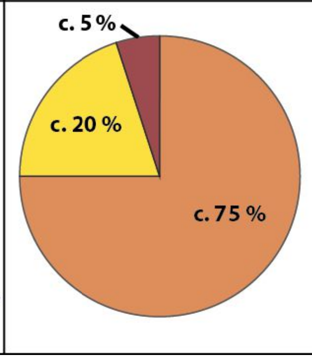	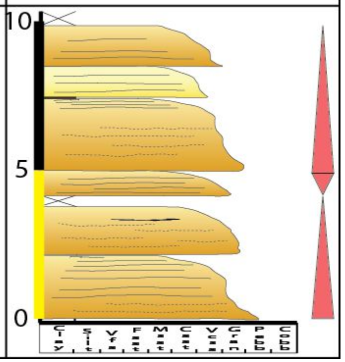

Table 5.2.1. Summary of the identified channelized bed type associations with summarizing descriptions and interpretations. For a legend of the pie-charts the reader is referred to Table 5.2.2.

Interpretation:

Slightly lenticular bed geometries, high degrees of amalgamation within individual bed sets and fining-upward cycles suggest an interpretation as channelized sand bodies. Low incisional depths (dm-scale) and the absence of associated heterolithic strata points towards bed type association 1.3 representing shallow channels of low sinuosity (e.g. Crevello et al., 2007; Rotzien et al., 2014). The absence of lateral passages into heterolithic strata furthermore suggests a lack of levee development (Posamentier & Kolla, 2003; Terlaky et al., 2016). The presence of the bed type association 1.3 in the distal domain of the system, interbedded with laterally continuous, unchannelized strata - attributed to bed type associations 3 - suggests an interpretation as distributary channels associated with intralobe environments (e.g. Brunt et al., 2013; Terlaky & Arnott, 2014). The minor thickness of individual amalgamated elements (compared to BTA 1.1 and 1.2) and the low depth-to-width ratios support this interpretation as distributive channels directly incised into a lobe environment (Saller et al., 2008; Rotzien et al., 2014) recording episodes of progradation of the system (Brunt et al., 2013). An alternative interpretation would be that of bed type association 1.3 representing sandy fills of shallow scours (Hofstra et al., 2015; Pemberton et al., 2016; Terlaky et al., 2016) that likewise would imply sediment bypass.

Bed type association 2: Composite channelized / tabular geometry association

Description:

Representative sections (Fig. 5.1; locations 3 & 4) encompass highly amalgamated, thick-bedded strata comprising both lenticular and tabular beds at the outcrop-scale (max. lateral outcrop exposure ca. 30 m; Fig. 5.5 D). Tabular bed geometries tend to be by far more abundant. Presence of different types of bed geometry is coupled with “mixed” bed type proportions comprising a variety of “clean” (mud-poor) and “dirty” (mud-enriched) bed types. Clean bed types still make up the dominant proportions. In comparison to bed type association 1, an increase in mudclast-rich beds and hybrid event beds occurs at the expense of “clean” bed types. Concerning the portions of fine-grained sediments, siliciclastic muddy and heterolithic bed types account for minor shares of overall thickness. Notably, fine-grained calcareous intervals become more abundant. Infrequent presence of microconglomeratic lags (bed type 1.2) has been observed. However, no clear grain-size trends within individual bedsets could be identified. A striking feature of bed type association 2 is the repetitive presence of irregular or locally tabular scour surfaces, typically distributed at the bases of thick bed type 5 and 6 strata (Fig. 5.5 E). Scour surfaces are elongated in the direction of the paleoflow and are ornamented by groove marks. Observed depths of incision are in the range of 25-30 cm. Scour dimensions can be in the range of 5 m by 8 m or even greater. Bed type association 2 amalgamation ratios are 65-70 % and amalgamated intervals range in thickness from a minimum of 0.75 m to a maximum of 23.5 m. Bed type association 2 crops out in two adjacent sections (lateral distance of approximately 400 m). Paleocurrent data shows a unimodal mean vector of 308º N (n = 36; see Table 5.2.2) characterized by a relatively wide range of dispersal, corresponding to a circular deviation of ± 76º.

Interpretation:

The composite presence of both lenticular and tabular beds reflects variable degrees of confinement (see Marini et al., 2015), typically found in a depositional environment typified by a loss in confinement (Brunt et al., 2013). The "mixed" bed type proportions found in this domain of the Bordighera turbidite system can be interpreted as representing sedimentation in the channel-lobe transition zone (*sensu* Mutti & Normark 1987, 1991; cf. Marini et al., 2015). The channel-lobe transition zone is commonly interpreted as marking the shift from confined to unconfined flows (cf. Gardner et al., 2003), expressed through the loss of channel confinement and associated with flow expansion and related enhanced turbulence (Terlaky & Arnott, 2014). Resultant increased erosional capability of the flows is interpreted as being documented by the presence of scours. Scour fields are common not far down-dip of channel mouths (e.g. Wynn et al., 2002; Ito, 2008). Such increased erosional capacity of the flows is also illustrated by the increased proportion of "dirty" bed types on the expense of "clean" microconglomeratic bed types in comparison to elements of bed type association 1 (cf. Fonnesu et al., 2015). The difficulty in correlating two adjacent sections ca. 400 m away from each other (on a transect orthogonal to the main sediment transport) and the presence of punctuated coarse-grained intervals with high sand-to-mud ratios suggest that this depositional interval most probably records rapid avulsions (Bryant et al., 1995; Marsset et al., 2009). As illustrated by the coarse-grained nature of the deposits and the high sandstone-to-mudstone ratio, these avulsions most probably resulted from high sediment supply rates (cf. Milli et al., 2007).

BTA	Description	AR, Sand-to-mud	BT proportions	Typical Motif
2: Composite channelized / tabular association	Predominance of **thick-bedded strata of "mixed" bed type proportions**, including a variety of "clean" (mud-poor) and "dirty" (mud-rich) bed types. **Common tabular scours**. Local presence of microconglomeratic lags. Both lenticular and tabular bedset geometries; greater abundance of tabular bedset geometries. Bed sets (thickness 4 m - 25 m) separated by muddy and heterolithic intervals. **No clear trends in fining-upward or coarsening-upward patterns**; reasonably oscillating or fluctuating scenario. Amalgamated intervals thicknesses: 0.75 m - 23.5 m; average thickness ca. 4 m. **Paleocurrent data: comparably high dispersal range** typified by a standard deviation of ±76°. Mean vector of paleocurrent orientation is 308° (n = 36).	**AR: 65 - 70 %** **Sand-to-mud: 6 : 1** 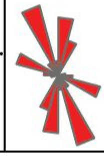	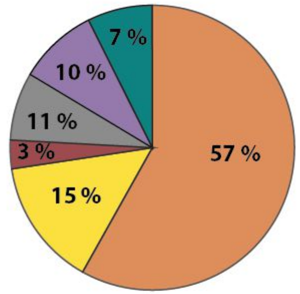	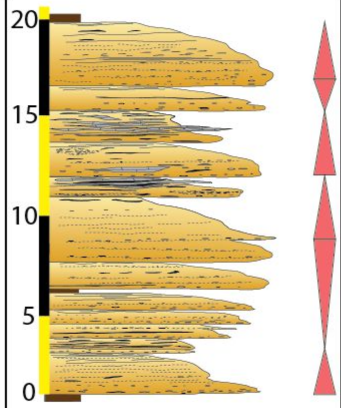

Pie-chart legend

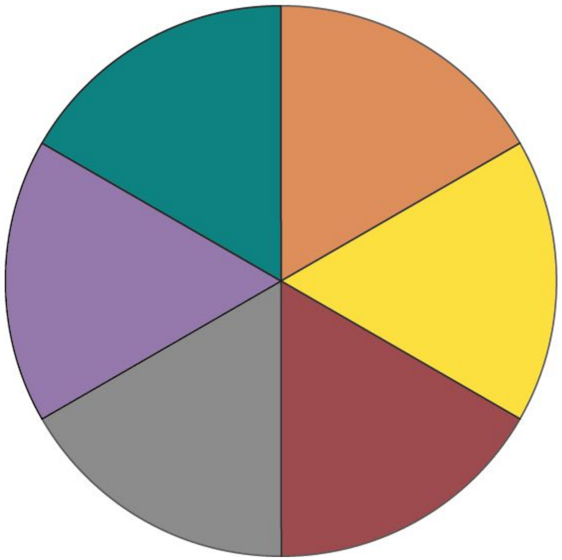

- Microconglomerates (Bed type 1)
- Sandstones (Bed type 2)
- Heterolithic intervals (Bed type 3)
- Calcareous mudstones (Bed type 4)
- Mud-clast sandstones (Bed type 5)
- Hybrid event beds (Bed type 6)

Grain size chart

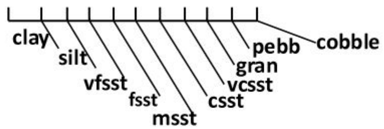

Table 5.2.2. Summary of the characteristics of the composite channelized-tabular bed type associations with summarizing descriptions and interpretations. Pie-chart legend for tables 5.1 to 5.3.

Bed type association 3: Tabular geometry associations

Bed type association 3.1: Axial / proximal lobe association

Description:

Bed type association 3.1 is mainly composed of medium to thick beds enriched in mud-clasts (bed types 5), which represent a third of the association (by thickness) and hybrid event beds (bed types 6) which account for a similar share. The remaining portion consists of "clean" sandstones, heterolithic packages and calcareous mud. Although the maximum grain size of coarse-tail graded beds can reach small to medium-sized pebbles, most beds bases include grain sizes up to granules. Some "clean" microconglomerates and "clean" sandstones are also present. Beds show good outcrop-scale lateral continuity (exposures up to 500 m wide), displaying tabular geometry (Fig. 5.5 F). At the bed-set scale, this bed type association is characterized by alternations of coarsening-upwards and fining-upwards trends within intervals denoted by high sand-to-mud ratios. Individual siliciclastic bed-sets are separated by thin intervals of calcareous muddy beds. Noteworthy, the presence of calcareous muddy beds tends to be coupled with an increasing abundance of hybrid event beds. Thicknesses of clastic bed-sets vary between ca. 10 m and 25 m. Internally, bed-sets are denoted by relatively high degrees of amalgamation (mean = 55 %). Amalgamated intervals thicknesses range from 1 m to 8 m. A detailed investigation of the proportions of "dirty" beds (bed types 5 and 6) within amalgamated packages reveals that these make up more than 70% of the amalgamated sands. Paleocurrent measurements of groove casts delineate a rather variable orientation of sediment flux with a circular deviation of $\pm 51^{o}$. Mean paleocurrent dispersal is 35^{o} N (n = 16).

Interpretation:

Tabular bedset geometries and alternations of coarsening- and fining-upward cycles suggest a distal realm where beds were deposited by poorly confined flows (e.g. Prélat et al., 2010; Mulder et al., 2010; Brunt et al., 2013). Such bedset-scale trends have been reported from a variety of lobe complexes and they are commonly interpreted to record progradation or lateral shifts of individual lobes and related compensational stacking (e.g. Mutti & Sonnino, 1981; Prélat et al., 2010; Mulder et al., 2010; Grundvåg et al., 2014). The domain characterized by this bed type association is located down-dip (according to the overall paleocurrent trend) of the interpreted channelized domain. This suggests an interpretation as frontal or terminal lobe complexes (*sensu* Morris et al., 2014; cf. Prélat et al., 2010; Mulder & Etienne, 2010). Because of the high degree of amalgamation, the succession can be attributed to the axial zone of a frontal lobe complex (Prélat et al., 2010; Pringle et al., 2010).

BTA	Description	AR, Sand-to-mud	BT proportions	Typical Motif
3.1: Axial / proximal lobe Representative section: Monte Frontè. GPS: 44.045383, 7.752036	**Predominanance** of medium- to thick-bedded strata **pronouncedly enriched in mudclasts and hybrid event beds. Reduced proportions of "clean" bed types**. Infrequent intercalations of heterolithic intervals. **Successive increase of proportions of calcareous beds** stratigraphically upwards. Prevalent coarse basal grain sizes; max. small to medium-sized pebbles. **Good lateral continuity** (outcrop-scale). Stratal geometry of beds exclusively tabular. **Large-scale coarsening-up trends** followed by a large-scale fining-up pattern. Thicknesses of high sand-to-mud bedsets ca. 10 m - 25 m. Bedsets separated by thin calcareous muddy intervals. Amalgamated intervals thicknesses 1.1 m - 8.3 m, average thickness ca. 3.2 m. **Paleocurrent data**: **high dispersal range** (mean orientation: 35°; ± 51°).	**AR: > 55 %** **Sand-to-mud: 5.5 : 1** 	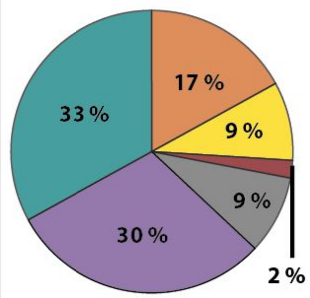	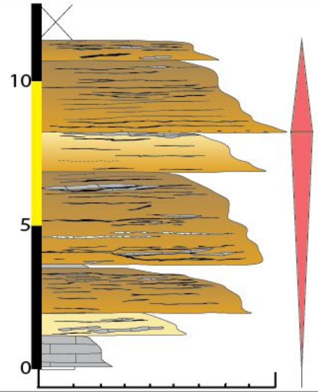
3.2: Off-axis lobe Representative section: Carmo dei Brocchi. GPS: 44.004020, 7.802283	**Balanced ratios of bed types**. Marked decrease in individual bed thicknesses in comparison to bed type association 3.1. Reduced proportions of mudclast-rich bed types. Sand-rich intervals separated by thin- to thick-bedded hetero-lithic and calcareous trata. Maximum basal grain size coarse granules. Dominant presence of sediments of tabular geometry. Sand-rich intervals commonly organized in **alternating coarsening-up and fining up cycles**. Bed set thicknesses ca. 1 m - 7 m. Reduced amalgamation ratios. Amalgamated intervals thicknesses: 0.2 m - 5.5 m; average thickness ca. 2.5 m. **Paleocurrent data**: comparably **high dispersal range** typified by a circular deviation of ±42°. The mean orientation is that of 28° (n = 7).	**AR: < 30 %** **Sand-to-mud: 1.5 : 1** 	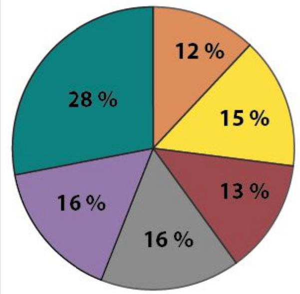	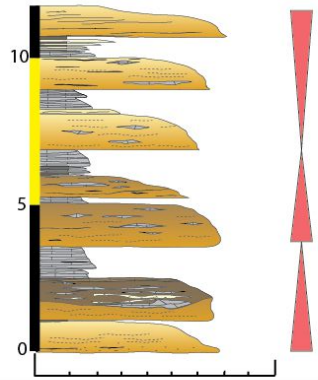
3.3: Intra-lobe / lobe fringe Representative section: Briga Alta. GPS: 44.085244, 7.755024	Predominant proportions of thin- to medium-bedded heterolithic and calcar-eous bed types. Within individual heterolithic intervals, fine-grained sand- and siltstones typicallyly display current-ripple laminations. **Local occurrence of medium-bedded hybrid event beds**. **Notable increase** in both calcareous bed types proportions. Increasing thickness of calcareous strata with further distance from high sand-to-mud intervals. Bioturbation likewise increases with further lateral distance to sandy intervals. Stratal geometries are generally tabular, with no evidence of basal erosion. **Rare to absent amalgamations**.	**AR: << 5 %** **Sand-to-mud: < 0.5 : 1** 	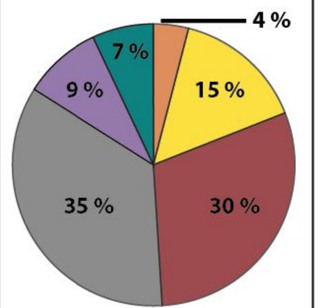	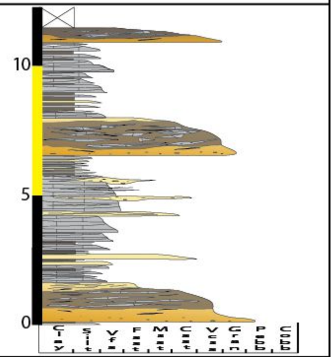

Table 5.2.3. Summary of the characteristics of the composite channelized-tabular bed type associations with summarizing descriptions and interpretations.

Bed type association 3.2: Off-axis lobe association

Description:

Bed type association 3.2 is characterized by the presence of all identified bed types (1-6) that account for roughly similar shares, with a slight tendency of HEBs being the dominant component of coarse-grained sediments and an abundance of both siliciclastic and calcareous fine-grained sediments. Sand-rich intervals are distinctly separated by packages of heterolithic strata (ranging from 0.05 m to 2.50 m; overall comprising 13% of total thickness) and by thin- to thick-bedded fine-grained calcareous beds (bed-sets ranging from 0.10 m to 4 m; representing 16% of total thickness). In comparison to bed type association 3.1, a significant decrease in sandstone-to-mudstone ratio and bed thickness can be observed. Basal grain size of both clean sandstones and argillaceous sands is up to small pebbles and it is generally finer in comparison to bed type association 3.1. Sand-rich intervals are commonly organized in coarsening-upward cycles followed by fining-upward cycles. Beds display outcrop-scale tabular geometry (up to 500 m lateral exposure; see Fig. 5.5 G). Compared to the axial lobe association (3.1), bed type association 3.2 shows reduced amalgamation ratios (mean = 29 %) and reduced thickness of amalgamated packages (ranging from 0.2 to 5.5 m). Paleocurrent data indicate a mean orientation toward 28^{o} N, with a high variability (circular deviation of $\pm$ 42^{o}; n = 7).

Interpretation:

Tabular bed geometries, together with the high dispersal of paleocurrent directions and the fact that sand-rich units are typically separated by fine-grained intervals, suggest the attribution to an unconfined lobe setting (e.g. Mutti & Normark, 1991; MacDonald et al., 2011; Etienne et al., 2012). The inconsistent stacking pattern within individual bed sets (i.e. both coarsening- and fining-upwards trends) reinforces such interpretation (Prélat & Hodgson, 2013; Terlaky et al., 2016). Based on the reduced degree of amalgamation, reduced grain size and enhanced portions of both fine-grained heterolithic and calcareous intervals, this bed type association can be attributed to the marginal or off-axis lobe realm with respect to the depositional axis of the lobe complex (cf. Prélat et al., 2010; Mulder et al., 2010; Etienne et al., 2012). The typically non-erosive character of the sandy beds is interpreted to reflect the decrease in flow capacity characteristic of distal and marginal lobe environments (e.g. Prélat & Hodgson, 2013; Rotzien et al., 2014).

Bed type association 3.3: Intralobe / lobe fringe association

Description: Bed type association 3.3 is typified by dominant proportions of thin- to very thin-bedded siliciclastic and calcareous bed types. Siliciclastic intervals are made up of alternating thin-bedded mudstones, siltstones and fine to very fine graded sandstones. Calcareous muddy beds account for almost half of the thickness. Fine-grained sandstones and siltstones frequently display current-ripple laminations. Some hybrid event beds are found, but they account for negligible bed type proportions. Microconglomerates and medium- to thick-bedded sandstones are generally absent. Moving further away from amalgamated intervals of BTA 3.1 and 3.2, a notable increase in calcareous bed thickness and proportions and in bioturbation can be observed. Individual beds do not reveal signs of basal erosion and amalgamated intervals are very rare.

Interpretation: The combination of sheet-like bed geometries at the outcrop scale (10s of meters) and the dominance of fine- to very fine-grained heterolithic intervals and muddy calcareous intercalations suggest a distal lobe environment (e.g. Prélat & Hodgson, 2013; So et al., 2013). With respect to the location within the system, bed type association 3.3 is interpreted to be lateral to the main sediment flux pathways, and can be interpreted as intralobe splay or lobe fringe (Brunt et al., 2013; Terlaky et al., 2016). The increased intensity of bioturbation away from the other bed type associations also supports this interpretation (Heard & Pickering, 2008; Bayet-Goll et al., 2014, 2016).

5.6 Discussion

5.6.1 Depositional domains

As shown by the described bed types and their proportions (summarized in Fig. 5.6), the Bordighera Sandstone can be classified as a coarse-grained, low-efficiency turbidite system (cf. Mutti et al., 1999; Mattern, 2005). It is characterized by high amalgamation ratio and high sand-to-mud ratio that persist down-system (Fig. 5.7 A & 5.8 A). Integration of the sedimentary facies analysis described above with paleocurrent measurements (Fig. 5.6 B) reveals an overall south to north, proximal to distal facies trend. Two main domains can be recognized (logs 1-4 and logs 5-10). The system comprises a relatively proximal channel-belt in the south and extensive terminal splay complexes in the north that extend for more than 30 km of down-dip distance. A striking contrast of dominant bed type proportions along a downstream transect defines a relatively short transition zone that separates the channelized from the lobate associations (Figs. 5.7 B and 5.8 B). The proximal domain is defined by the presence of channelized bed type associations characterized by highly amalgamated (up to 75 %) and thick (up to 15 m) intervals dominated by mud-poor bed types (1 and 2). High sand-to-mud ratios range from 11:1 to 4:1 (axis to off-axis). The axial channel realm (e.g. log 2, Fig. 5.6) is made up by microconglomerates (82%) and sandstones (12%). Heterolithic intervals (3%) and calcareous muddy intercalations (ca. 2%) are very rare. Mudclast-rich beds and HEBs (combined ca. 1%) are negligible. From a hydrocarbon reservoir point of view, these deposits should result in very high vertical and lateral connectivity, as migration barriers are almost absent (cf. Brunt & McCaffrey, 2007).

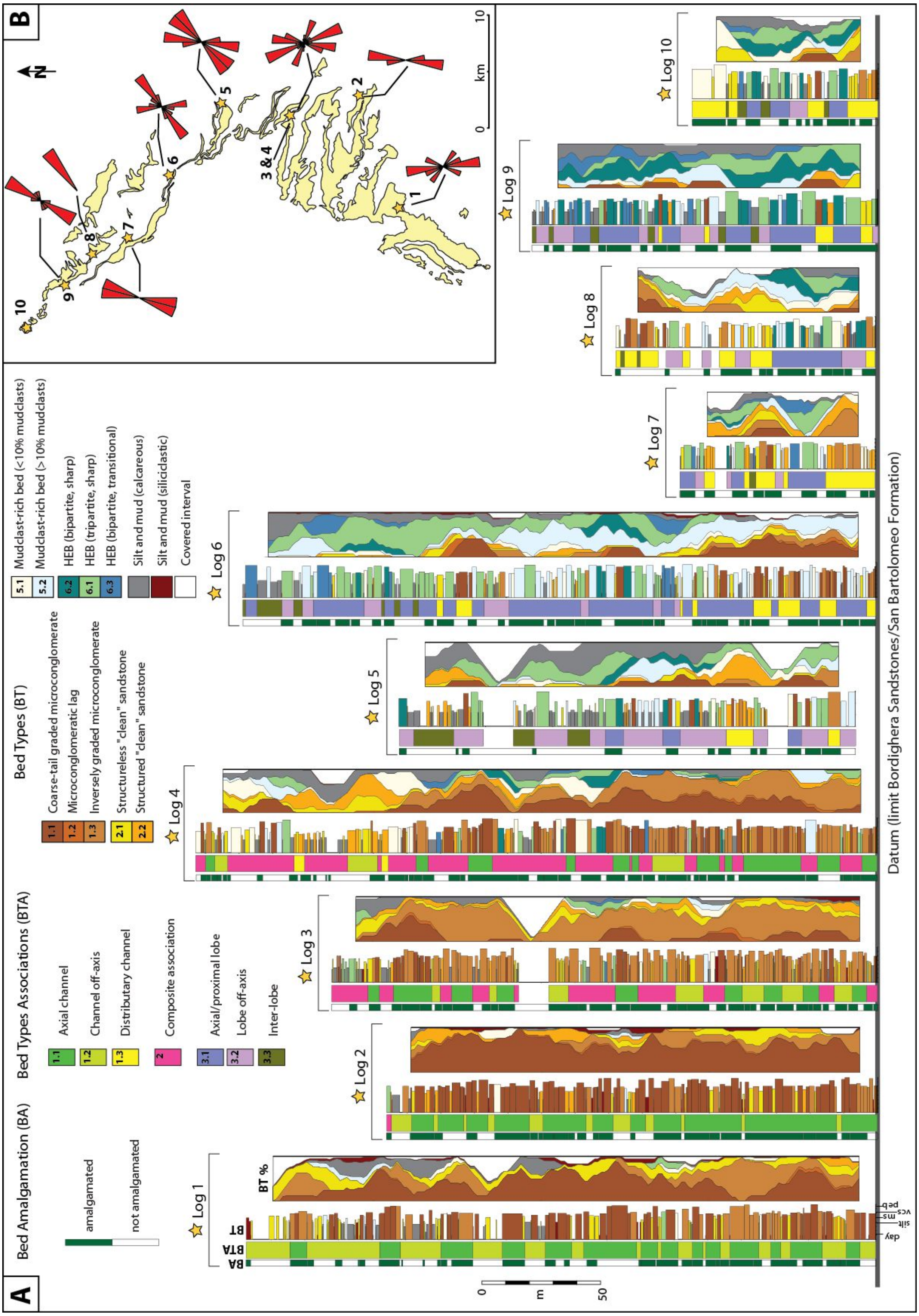

Fig. 5.6. (A) Dataset for the 10 studied sections. For each section, from left to right: i) bar indicating amalgamated intervals (green); ii) bar indicating bed type associations; iii) synthetic log showing bed

thickness, grain size and bed type (colors); iv) vertical bed type proportions (continuous running average over a window of 10 m). (B) Map of the log locations with paleocurrent measurements.

The off-axis channel realm (e.g., log 1, ca. 8 km across-current from log 2; Fig. 5.1), exhibits an increase in the proportions of clean sandstones (18%) at the expense of microconglomeratic beds (69%). Heterolithic intervals portions remain low (3%), and only a moderate increase in calcareous beds (5 %), mudclast-rich beds (4 %) and HEBs (1%) is documented. With respect to the overall S-N facies trend, the channelized domain is interpreted to represent the feeder channels that supplied depositional lobes further basin-wards (e.g. Wynn et al., 2002; Terlaky et al., 2015). As sandbody heterogeneities related to clay entrainment and levee development are negligible, the off-axis channel association similarly represents a component of the system marked by high vertical and lateral connectivity (cf. Brunt & McCaffrey, 2007).

The transitional zone between the channelized and the lobate domain is of limited basin-ward extent (c. 5-7 km; Fig. 5 B; see also Fig. 5.4, logs 3 & 4), making up only 1/10 of the preserved system (Fig. 5.6 A). The bed type association (composite channelized / tabular) is characterized by high amalgamation ratios (65 - 70%) and a mean sand-to-mud ratio of 6:1. Then two investigated sections are in close lateral vicinity (300-400 m distance orthogonal to paleoflow) and are characterized by frequent shifts regarding the stratigraphic distribution of very coarse-grained intervals (see highlighted box in Fig. 5.6 B). This is interpreted to reflect rapid avulsion due to high sediment supply. Maximum thickness of individual amalgamated intervals is the greatest in the system (up to 24 m). Notably, an increase in mud-rich beds (mud-clast rich beds: 10%; HEBs: 7%) at the expense of clean bed types (microconglomerates: 57%, sandstones: 15%) is observed. Heterolithic intervals (3%) remain relatively low, whereas calcareous muddy beds (11%) considerably increase. A more gradual transition from a proximal zone to an extensive medial domain and then to a distal submarine fan association typical of some basin plain submarine fans (e.g. Mattern, 2005) is not developed. High degrees of amalgamation and high sandstone-to-mudstone ratios are contrasted by both the emergence of sandstones rich in mud-clasts and the enhanced presence of muddy beds that would constitute flow barriers and therefore reduce reservoir volume and connectivity (cf. Brunt & McCaffrey, 2007).

The relatively short transitional domain is replaced by a lobe domain dominated by mud-clast-enriched sandstone beds and HEBs. The axial lobe bed type association (e.g. section 6; Fig. 5.4) shows high amalgamation rates (> 55%) and related high sand-to-mud ratio (5.5:1). Maximum thickness of amalgamated intervals is ca. 15 m. While mud-rich beds are dominant (mud-clast enriched beds: 30%; HEBs: 33%) and clean bed type proportions are starkly reduced (microconglomerates: 17 %; sandstone: 9%), the proportions of heterolithic intervals (2%) and calcareous intercalations (9%) do not record significant changes in abundance. On the contrary, the off-axis lobe association (e.g. section 5; Fig. 5.6 A) is characterized by a reduced degree of amalgamation (15%) and related sand-to-mud ratio (1.5:1). This is coupled with thinner bed-sets and a further decline in coarse clean bed type proportions

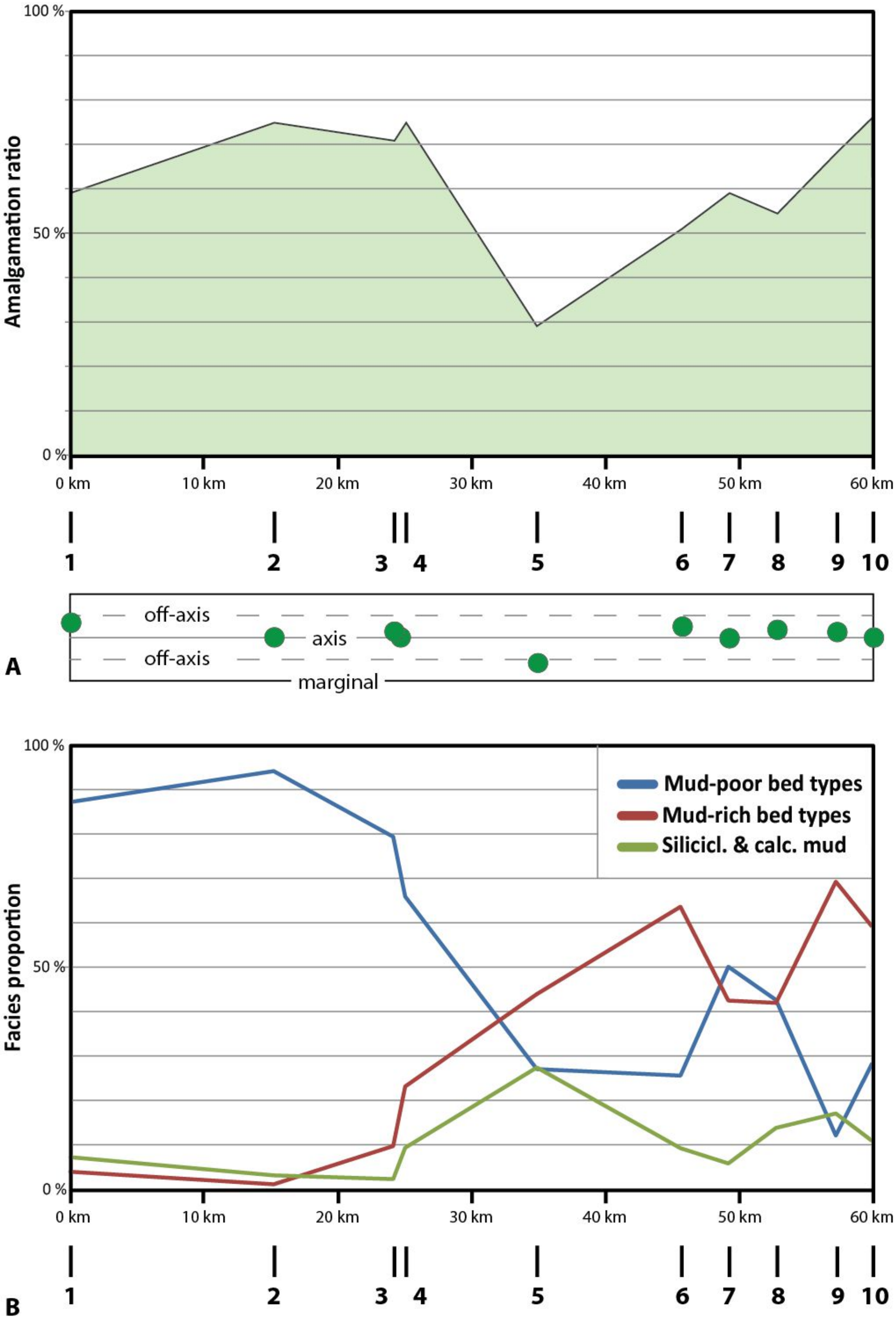

Fig. 5.7. (A) Amalgamation ratios for the ten measured sections (numbers; see Fig. 5.1) ordered from proximal to distal. Lower percentages of amalgamations are interpreted to indicate locations off-axis to marginal with respect to the axis of the sediment fairway. (B) Relative proportions of clean bed types (bed types 1 & 2), mud-rich bed types (bed types 5 & 6) and muddy strata (bed types 3 & 4) along a proximal to distal transect. Distances between sections have been calculated on the basis of their inferred depositional position after structural restoration. Numbers indicate section number; see Fig. 3.1.

(microconglomerates: 12%), which is partly compensated by sandstones increase (15%), but also, with respect to the axial lobe environment, with a smaller amount of mud-clast enriched beds and HEBs (16% and 28% of stratigraphic thickness respectively). Furthermore, fine-grained bed type proportions increase (heterolithic intervals: 13%; calcareous intercalations: 16%). Albeit defined by high degrees of amalgamation and high sand-to-mud ratios, the impact of the mud-rich sandstones within the amalgamated intervals is interpreted to result in barriers to fluid flow (cf. Brunt & McCaffrey, 2007).

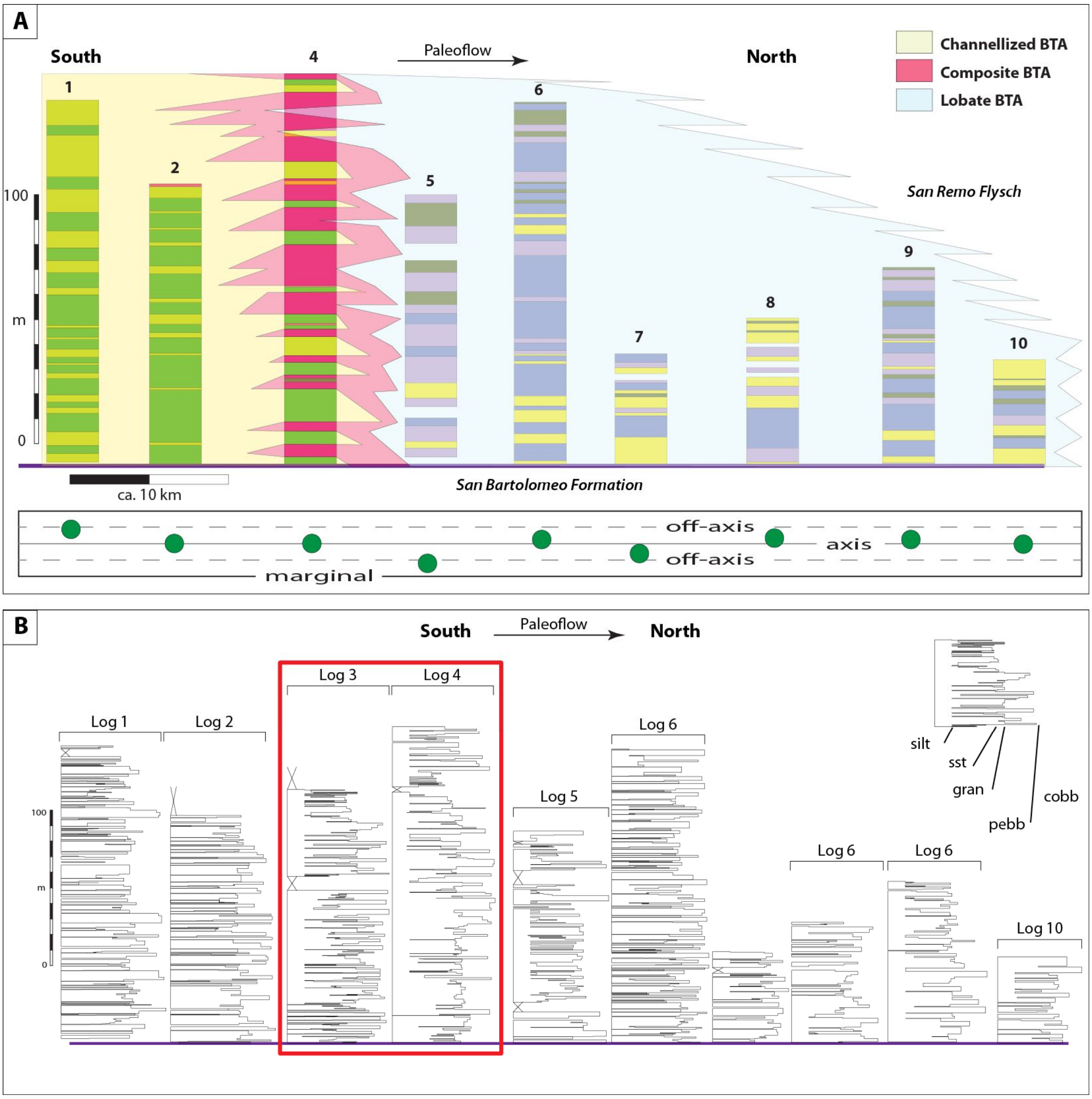

Fig. 5.8. Inferred gross geometry of the Bordighera Sandstone. (A) Inferred extension of channelized associations, composite (i.e. transitional) associations and lobe associations. (B) Vertical synthetic grain size profiles for measured logs (continuous running average over a window of 10 m). Note the presence of very coarse fractions in the distal domain. The red box highlights logs 3 and 4 (ca. 300-400 m distance orthogonal to paleoflow) where very coarse-grained intervals cannot be correlated, suggesting an environment characterized by rapid avulsions.

Finally, the marginal distal association (sections 8-10; Fig. 5.6A) records the progressive pinch-out of the siliciclastic succession. It is defined by low degrees of amalgamation (5 %), low sand-to-mud ratio and a substantial decrease in clean bed types (microconglomerates: <5 %; sandstones: ca. 10 %). The occurrence of mud-clast enriched beds (ca. 15 %) and HEBs (ca. 10 %), is coupled with abundant heterolithic and calcareous intervals (ca. 30 % each). The distributive channel association is only present in the distal domain (section 7, Fig. 5.4) and it is marked by high amalgamation rates (ca. 85 %), high sand-to-mud ratio (9:1), high proportions of clean bed types (ca. 75 % microconglomerates, ca. 20 % sandstones), minor amounts of heterolithic intervals (ca. 5 %), along with the absence of mud-rich bed types and HEBs. This facies association occurs in intervals of limited vertical thicknesses (2- 15 m; mean: ca. 5 m) and lateral extent (ca. 300-400 m estimated) and it is therewith interpreted to constitute only a limited portion of the stratigraphy in the distal domain.

3.6.2 Mud-rich sandstones

Observed bed type distributions provide the basis for idealized trends of cross-current (Fig. 5.9 A-B) and down-current stacking pattern motifs (Fig. 5.9 C). These stacking pattern motifs outline the relatively homogeneous vertical and lateral character of the channel-fill association in contrast with the more heterogeneous character (both vertically and laterally) of the unconfined domain, characterized by mudclast-rich beds and by hybrid event beds (HEBs). This onset of mud-rich sandstones occurring in the transitional domain is associated to an increase in the presence of calcareous mud intervals (see Fig. 5.7 B), which constitute the material that is commonly found incorporated in the mud-rich sandstones as mudclasts. This observation suggests that a combination of the erosive nature of the flows and the availability of cohesive calcareous substrate might have promoted HEB development.

Close resemblances between the mudclast-rich sandstone beds of the Bordighera and the matrix-rich sandstones described by Terlaky & Arnott (2014) can be noted. On the one hand, the generally coarse grain size of beds is similar. On the other hand, essentially in the case of bed type 5.2, the coarse-tail graded nature and the corresponding bi-partite internal organization of beds represent striking similarities to the type 4 matrix- rich sandstones of the Kaza Group. Furthermore, the internal texture of mudclasts, marked by angular shapes is analogous to the shape of mudclasts described by Terlaky & Arnott (2014). Commonly angular shaped clayey clasts and rafts illustrate erosion of a comparably imminent source of muddy material rather than further up-dip acquisition of muddy substrate (e.g. Terlaky & Arnott, 2014; Fonnesu et al., 2016). In terms of flow processes, both the Bordighera mudclast-rich beds and the matrix-rich strata of Terlaky & Arnott (2014) have the hyperconcentrated density flow origin of the basal clean sandstone in common.

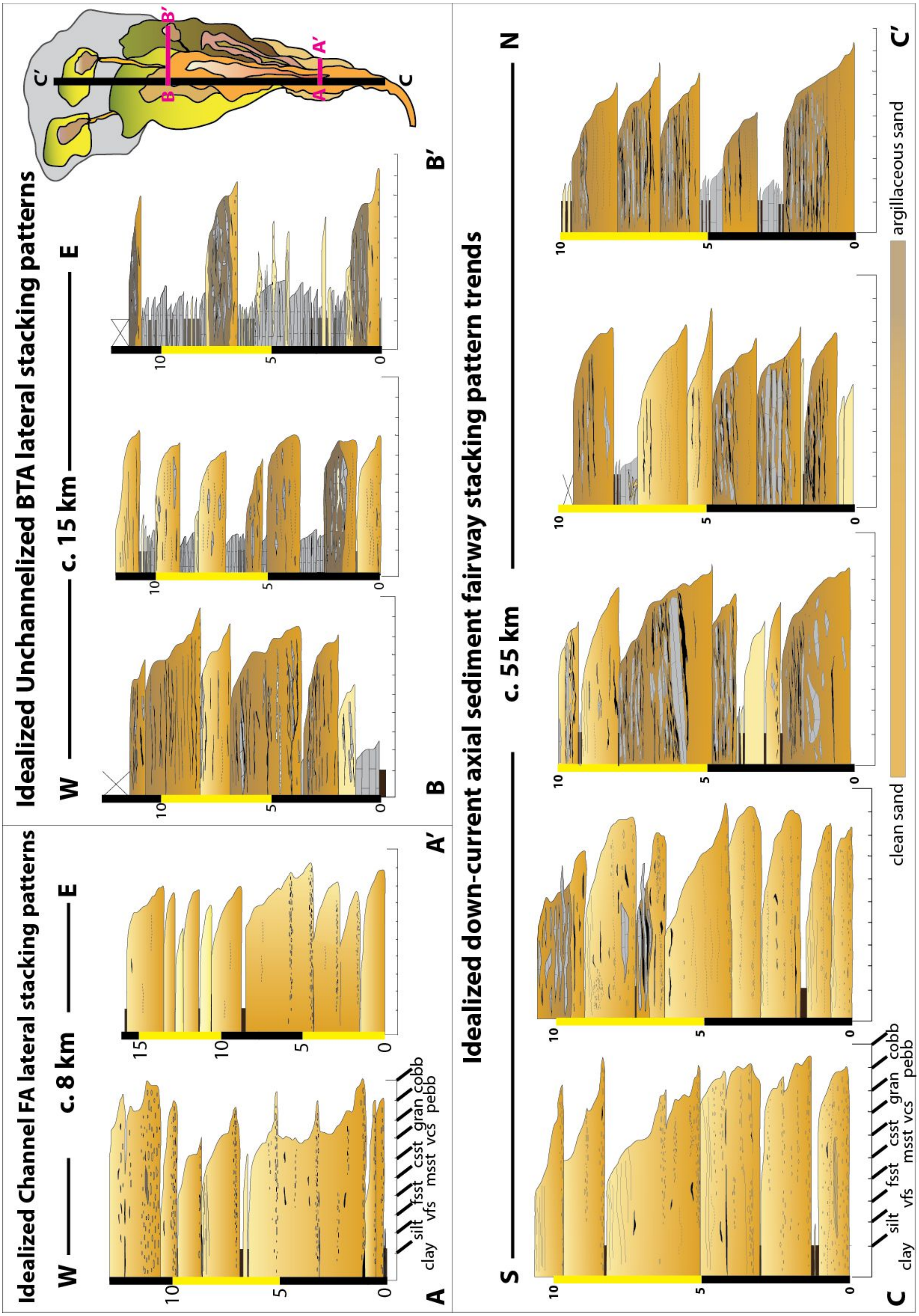

Fig. 5.9. Idealized stacking pattern motifs: (A) axial channel to off-axis channel; (B) axial lobe to off-axis lobe and (C) proximal to distal. Distances correspond to restored depositional positions of outcrops.

The hybrid event beds in the Bordighera system are characterized by a debritic division (H3 of Haughton et al., 2009) made up of an argillaceous coarse sandstone packed with calcareous mudclasts. In this respect, they are very different from the finer grained transitional flow deposits of Kane & Pontén (2012) and Southern et al. (2017). As for mudclast-rich beds, the typically angular shape of the mudclasts suggest that mud acquisition occurred within a limited basin-ward distance. This is in agreement with Fonnesu et al. (2016), who proposed the local delamination of blocks of underlying substrate as triggering progressive HEB emergence. In the Bordighera case, such tendency of local mud incorporation is both reflected by the mud-poor textural character of the bed types that define the feeder channel association and the sudden appearance of beds enriched in mudclasts in the realm defined by a loss of channel confinement. Progressive stages of mudclasts disaggregation subsequent to local substrate entrainment are reflected by increasing thicknesses of the portions of the very muddy matrix of debritic intervals that display the purported ”starry night” appearance.

Spatial distribution of HEB types (Fig. 5.10 A) shows that proportions of bed types 6.2 and 6.3 deposits tend to become greater towards the distal axial lobe domain. Analysis of the ratio of the debritic division thickness to full bed thickness of bed type 6 sub-types (Fig. 5.10 B) indicates a progressive increase in the proportion of the debritic H3 division from types 6.1 to 6.3. The combination of these two observations illustrate the occurrence of a systematic basin-ward trend of beds becoming increasingly enriched in muddy substrate. The observed spatial distribution of hybrid event beds, and in particular their abundance in the interpreted axial lobe domain, partly contrasts with published models on their occurrence in turbidite systems. The bulk of existing models place hybrid event beds in distal and lateral fan environments, particularly in fan-fringes (e.g. Haughton et al., 2009; Hodgson et al., 2009; Southern et al., 2017; Spychala et al., 2017a). More proximal occurrence of HEB development has been attributed to up-section backfilling of proximal channels (Haughton et al., 2009) as well as to rapid deceleration of sediment gravity flows in response to onlapping relationships with confining topography (Patacci et al., 2014). Conversely, the distribution of mudclast-rich sandstones and hybrid event beds in the Bordighera turbidite system appears to reveal a different scenario, namely that of their emergence in close down-dip proximity to the channel lobe transition zone. Terlaky & Arnott (2014) document a similar onset for argillaceous sandstones in the proximal basin-floor environment. The authors interpret the rapid occurrence of stacked depositional lobes as the result of avulsion at the termination of channelized structures. Resulting supercritical flows (“unconfined jet flows”) are interpreted to have entered the mud-dominated unconfined basin-floor and enhanced erosional capability promoted the incorporation of substrate and subsequent transitional flow behavior. In addition, existing models (e.g. Haughton et al., 2009; Fonnesu et al., 2015; Southern et al., 2015) assign the spatial expansion of HEB prone associations to relatively limited down-dip distances. On the contrary, in the Bordighera turbidite system the hybrid-prone interval stretches for at least 30 km down-dip. The very high-energy and coarse-grained nature of the system, coupled with the presence of cohesive calcareous substrate might be able to explain such differences, although further work is required to establish a process model for how this might occur.

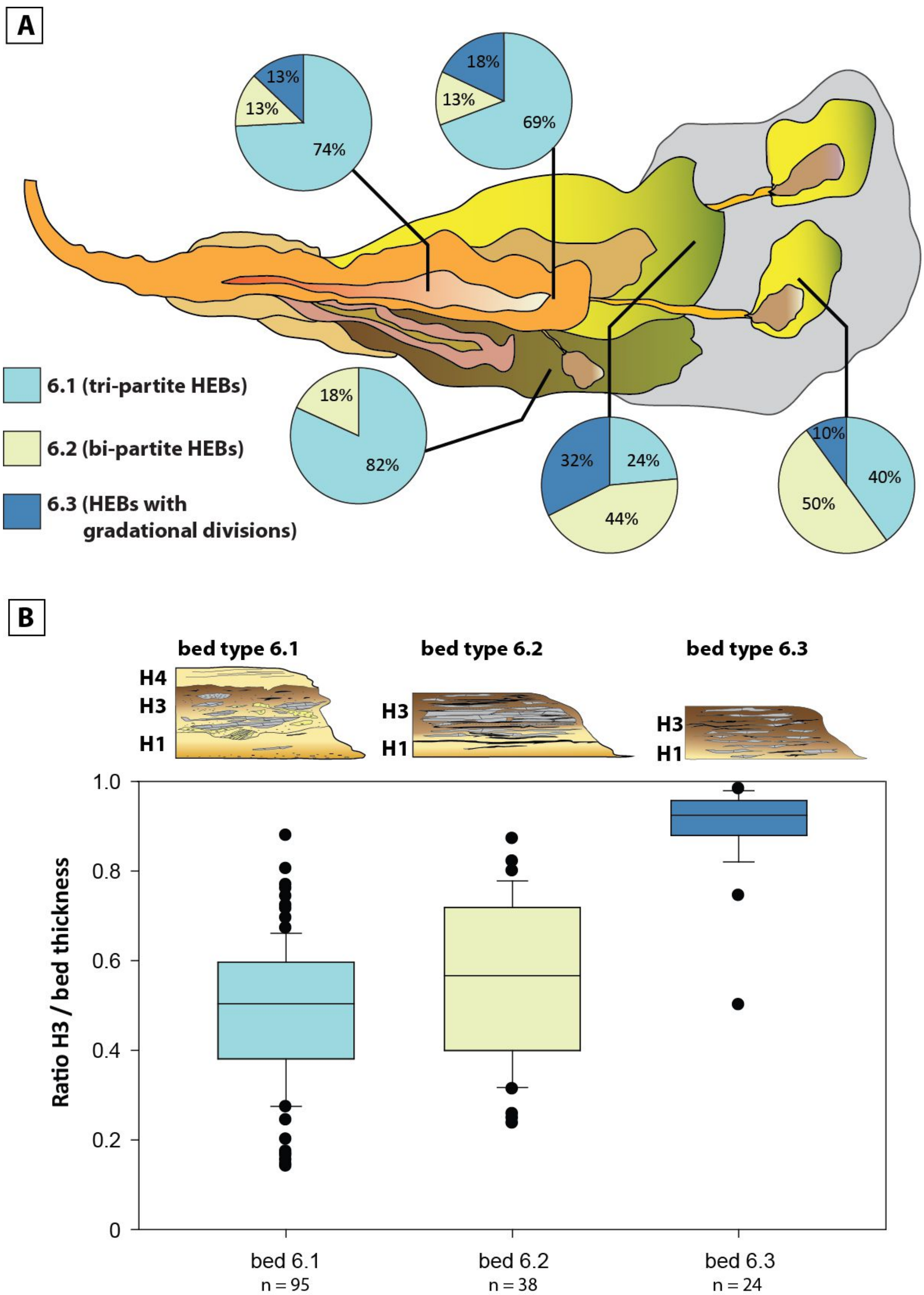

Fig. 5.10. (A) HEB types proportions in different depositional domains. (B) Box-whisker plots of the ratio of debritic interval thickness to full bed thickness of hybrid event bed types.

3.8 Conclusions

- The coarse-grained Bordighera turbidite system is characterized by high sand-to-mud ratio throughout the sediment pathway, revealing the capacity of the system in supplying coarse fractions to the very distal realms.

- The down-dip transition (of limited spatial extent) from a channelized proximal setting into an extensive sheet association is coupled with an increase in calcareous intervals and with the emergence of abundant mudclast-rich sandstones and hybrid event beds.

- The abundance of coarse-grained mudclast-rich sandstones and hybrid event beds in the high-energy axial proximal lobe environments marked by high sandstone to mudstone ratio has been reported only in a limited number of systems and it might be characteristic to the Bordighera because of the availability of cohesive calcareous mud.

- The average thickness of amalgamated intervals does not decrease significantly throughout the observed part of the system. Notwithstanding, promising high hydrocarbon reservoir quality because of the high sand-to-mud ratio is impaired by the fact that internal connectivity might be affected by bed-scale heterogeneity due to the abundance of mudclast-rich beds and hybrid event beds.

Chapter 6: Provenance analysis of the sand-rich Bordighera Sandstones and the basal complex – Implications for source area evolution during stages of early convergence

Abstract

Despite of more than 150 years of continuous research and significant advances in the understanding of subduction and obduction processes that affected the Western Alps, the paleogeographic evolution of the Alpine Tethys represents one of the yet controversially debated topics in Alpine geology. Resultant from enormous crustal shortening, oceanic units became displaced so that the reconstruction of their original positions remain uncertain. Detrital signatures of pre-collisional flysch sequences that crop out along the entire Alpine represent the exclusive evidence of the plate-tectonic setting of the areas that provided the source of the clastic detritus. The Upper Cretaceous San Remo Unit of the Western Ligurian subduction flysch complex epitomizes a trench fill that comprises a basal complex (San Bartolomeo Fm.) and two thick turbiditic sequences: a low-efficiency siliciclastic turbidite system (Bordighera Sandstones) that interfingers with a calcareous turbiditic sequence (San Remo Helminthoid Flysch) The multi-proxy sediment provenance analysis of the two terrigenous members, the basal complex and the coarse-clastic Bordighera Sandstones, is regarded as providing further insights towards a better understanding of the complex pre-collisional evolution of the Piemont-Ligurian domain and the bounding continental margins. Petrographic analysis characterizes the basal complex succession as being defined by modal averages of Q69F29L2 and a mean plagioclase/K-feldspar ratio of 0.48. By contrast, the conformably superimposing coarse Bordighera Sandstones represent texturally and compositionally immature first-cycle arkosic arenites (average modal composition: Q48F49L3; mean P/K-ratio: 0.57). The gradual provenance evolution from a stable craton or transitional continental provenance setting towards rapidly uplifted bedrock (granitoid plutons and low-grade metamorphic geobodies) can be inferred. New geochronological data (U-Pb detrital zircon ages) reveal dominant peaks in the detrital spectrum (306 Ma, 330 Ma and 357 Ma and 267 Ma) which are practically compatible with well-documented magmatic and metamorphic pulses that affected the Southern Variscides. The confrontation of detrital age clusters with available crystallization age datasets of candidate source areas reveals the strong affinity of the clastic detritus towards the Paleo-European margin. Accordingly, the importance of the lower plate (i.e. the passive margin) in providing the dominant source in inceptional convergent settings is highlighted. On the basis of this observation, the working hypothesis which explains rapid basement uplift as the result of the development of a flexural bulge due to gravitational loading of the developing accretionary prism is introduced.

6.1 Introduction

Provenance studies provide a valuable tool to determine the tectonic, paleogeographic and climatic conditions that defined the history of terrigenous sedimentary basins (e.g. Dickinson & Valloni, 1980; Suttner & Dutta, 1986; Weltje & von Eynatten, 2004). Upper Cretaceous to Paleogene turbiditic sequences mirror the onset of convergence of the Alpine cycle that led to the closure of the Piemont-Ligurian ocean in the Early Cenozoic. Recent geodynamic models emphasize on the presence of continental terranes and highlight their role in the context of the pre-collisional evolution of the Western Tethys (e.g. Froitzheim et al., 1996; 2008; Viti et al., 2009; Handy et al., 2010; 2014; Malusa et al., 2015). Provenance determinations of coarse-grained siliciclastic flysch system can provide new insights into the paleogeographic evolution that culminated in oceanic closure of the Western Tethys (e.g. Valloni & Zuffa, 1984; Fontana et al., 1994; Molli, 2008; Bracciali et al., 2014; Thum et al., 2015). In particular, the determination of the source area of the coarse-clastic Bordighera turbidite systems that forms part of the Western Ligurian Flysch Units aims to add understanding to the complex paleogeographic evolution of the Piemont-Ligurian ocean prior to Alpine collision. Western Ligurian siliciclastic turbidite successions range from Campanian-Maastrichtian to Paleocene age. Whereas pre-collisional successions of the Northern Apennines, the Internal and External Ligurides, have extensively been studied from both petrographic and geochemical perspectives (cf. Argnani et al., 2006), coarse-clastic turbiditic successions of the Western Ligurian Flysch Units remain poorly studied. Early interpretations, utterly based on petrographic studies and paleogeographic relationships of pre-collisional siliciclastic flysch successions of the Western Tethys, proposed the European margin, and in particular the Corso-Sardinian Massif as providing the provenance of the coarse clastic detritus of the Upper Cretaceous to Paleocene pre-collisional Ligurian Flysch successions (e.g Vanossi, 1965; Sestini, 1970; Zuffa & Valloni, 1984; Rowan, 1990; Fontana et al., 1994; Argnani et al., 2004; 2006). A more recent study that incorporated the geochemical "fingerprinting" approach (Bracciali et al., 2007) strengthened the interpretation of the Variscan Corsica-Sardinia Massif as representing the source area of the Internal Ligurian Units, and essentially that of the Gottero Sandstones. Notwithstanding, the strongly decoupled present-day locations of Ligurian Flysch Units cropping out in the Western Alps and their Apenninic counterparts necessitates the investigation of the linkage between the tectonic setting and the sedimentary system´s response to account for this incidence. Accordingly, sediment provenance analysis of the San Bartolomeo Formation and the Bordighera Sandstones is conducted with the main aim unraveling the geodynamic setting that controlled the development of a such uncommonly coarse-grained pre-collisional turbidite system. In order to identify whether a "passive" margin or an active margin setting promoted the marked shift towards coarse-clastic sedimentation, emphasis is put on a comprehensive source area discrimination by means of coupling petrographic analysis with U-Pb detrital zircon chronology (cf. Di Giulio et al., 2017).

6.2 Methodology

A total of 35 medium- to fine-grained rock samples were collected in the field. The sampling strategy was intended to provide the full coverage of the vertical stratigraphic expression of the Bordighera Sandstones for which 30 of the samples account. Two continuously exposed key stratigraphic sections, representative of the axial medial domain (Monte Frontè) and the most distal preserved domain (Cima di Velega), were sampled after detailed sedimentological investigation. Samples were collected from medium- to fine-grained sandstones. With respect to the previously identified retrogradational pattern of the siliciclastic turbidite system, sampling locations comprised the stratigraphic base and tops of individual sections as well as reasonable coverage of the interval in between. Both sampled sections provide a readily recognizable conformable basal contact to the San Bartolomeo Formation that served as a datum. Fresh and unweathered representative sandstone layers were identified and sampled for laboratory analysis. Stratigraphic positions of sampled strata were carefully recorded in the sedimentological logs. Regarding the divergent overall thickness of the two reference sections, reasonable quantities of samples were estimated for individual sections. The feasible stratigraphic enclosure of the Monte Frontè section (comprising a thickness of ca. 180 m) necessitated 19 rock samples out of which 21 thin-sections were produced, whereas the Cima di Velega section (ca. 62 m in total thickness) required 9 rock samples out of which 10 thin-sections were created. Additionally, the petrographic investigation of the San Bartolomeo Formation was attained. In addition to eleven thin-sections of a previous study (Compiani, 1992) that were re-investigated, four new samples of the basal complex were acquired from outcrops located in immediate vicinity to the type locality in the Valle Argentina. The sampling covered the four terrigenous lithozones. Subsequently, 31 new rock samples of the Bordighera Sandstones were prepared for thin-section analysis in the Canepa OMT laboratory, Quart (AO), whereas the author prepared four thin-sections of basal complex samples.

Subsequent compilation of the petrographic dataset was implemented by optical point-counting of 46 thin-sections under the petrographic microscope. All thin-sections were studied under both plane parallel polarized and cross polarized light. Point-counting analysis has been performed according to guidelines provided by Di Giulio & Valloni (1992), following the Gazzi-Dickinson approach (cf. Dickinson & Suczek, 1979; Dickinson, 1985). For each sample, modal analysis was performed by manually counting a minimum of 250 points per thin-section. The grain categories are illustrated in table 6.1. Since some samples were subject to intense diagenetic alteration (i.e. detrital grain dissolutions and anchimetamorphic overprint), in rare cases difficulties were encountered in distinguishing modal framework constituents. Consequently, such grains were included into the “unidentifiable grain” category and afterward excluded from the compositional analysis. Statistically rigorous confidence regions and limitations (cf. Weltje, 2002) were circumscribed and plotted into ternary diagrams with the CoDaPack software (Comas-Cufí & Thió-Henestrosa, 2011).

Apart from modal composition determination, the provenance analysis was supplemented by the integration of U-Pb detrital zircon chronology (e.g. Fedo et al., 2003; Andersen, 2005; Gehrels & Dickinson, 2009). Sandstone samples for detrital zircon age determinations were collected from fine-grained tops of turbiditic strata identical to the stratigraphic sections that were sampled for petrographic analysis. In a similar fashion, four samples for the medial Monte Frontè section and three for the more distal Cima di Velega section were collected. Bases and tops of the complete stratigraphic intervals as well as a rational number of samples covering the interval in between were sampled. Collected samples were afterwards sent to the heavy mineral separation laboratory at the University of Padova, where detrital zircon separation was established by grinding and hydrodynamic procedures. Afterwards, zircon separation by Frantz magnetic isodynamic and heavy liquid separation (separation liquid density > 2.98 g/cm³) were performed. Separated zircons were hand-picked by the author and

Qm	**monocrystalline quartz grains (> 0.0625 mm)**
Qpolycoarse	**coarse polycrystalline quartz grains**
Qpolyfine	**fine polycrystalline quartz grains**
QfragP/G	**coarse monocrystalline quartz grain in crystalline fragment**
Km	**monocrystalline (or altered) alkali feldspar grain**
KfragP/G	**alkali feldspar grain in plutonic or gneissic fragment**
Pm	**monocrystalline (or altered) plagioclase feldspar grain**
PfragP/G	**plagioclase feldspar grain in plutonic or gneissic fragment**
Lmeta	**plutonic or metamorphic lithic fragment (< 0.0625 mm)**
Lvolc	**volcanic lithic fragment (< 0.0625 mm)**
Lclast	**sedimentoclastic lithic fragment (< 0.0625 mm)**
Mica_mono	**monocrystalline mica grain**
Mica_frag	**micagrain in rock fragment**
HeayMin	**monomineralic transparent or opaque heavy minerals**
Matrix	**siliciclastic detrital matrix**
Calc_cement	**calcareous cement**
Phyllo_cement	**phyllosilicate cement**
mudchips	**siliciclastic mudclast**
calc. clasts	**calcareous clasts**
indet.	**unidentifiable grain**

Table 6.1. Grain and framework categories for petrographic analysis. Parameters are slightly modified from the ones proposed by Dickinson et al. (1983) and Di Giulio & Valloni (1992).

placed into epoxy resin mounts at the University of Pavia. The subsequent step comprised the polishing of mounted zircons to expose the zircon cores. Prior to isotopic analysis, cathodoluminescence imaging of exposed zircons was performed at the University of Genova with the aim of verifying individual analytical spots. Afterwards, detrital zircon samples were processed for age determinations using a 193 nm ArF laser-ablation microprobe coupled to a magnetic sector inductively coupled plasma-mass spectrometer (LA-IMCP) at IGG-CNR at the University of Pavia. Standard procedures applied to provide unknown age determination calibrations were conducted by means of the zircon 91500 standard which was used as the primary, and the Plešovice standard zircon as secondary reference. Isotopic data were processed using Isoplot 3.0 (Ludwig, 2003), with apparent zircon ages being based on $^{206}Pb/^{206}U$ ratios for grains younger than 1 Ga and based on $^{206}Pb/^{207}Pb$ systematics for older grains (cf. Gehrels, 2000). Probability density plots (PDPs) and kernel density estimated (KDEs) were plotted with the DensityPlotter software (Vermeesch, 2012). Confrontations of detrital zircon age spectra against crystallization ages of potential source areas and statistical analysis and were conducted utilizing the DZStats 2.2 software (Saylor & Sundell, 2016).

6.3 Description of the detrital modal assemblages and results from point-counting

Basal complex (San Bartolomeo Formation)

The average grain size of the analyzed samples of the San Bartolomeo Formation is in the range of very fine to fine sand. Sorting is predominantly well to moderate (Fig. 6.1 A), even if poorly sorted examples were noted as well. The observed grains are typically of sub-rounded to rounded shapes. Nonetheless, sporadically even small concentrations of sub-angular grains occur (Fig. 6.1 B). From a textural perspective, the very fine sandstone samples are characterized by a relatively loose to normal packing framework in which the detrital grains are arranged. This framework is denoted by an average matrix content of 19.1 %. Noteworthy, the typically silty matrix significantly varies in abundance, as it can account for 3.28% to up to 29.8% of the total rock volume. Moreover, calcareous cement represents a mean proportion of 9.03% of the total rock volume. Among the framework grains, the major modal constituents of the basal complex are represented by quartz and feldspar (See table 6.1). Detrital quartz grains represent the most dominant constituent of the clastic detritus with an average of 66.35%, quartz concentrations nonetheless span a wide range from 51.7% to 78.5%. As mirrored by a mean Qm/Qp ratio of 6.14, monocrystalline quartz, comprising roughly equal shares of straight- and undulatory extincting varieties, accounts for the clear majority of quartz components. Monocrystalline quartz grains frequently display vacuoles. The mean feldspar portion is 28.24% (min. 19.1%, max. 35.1%). Alkali feldspar varieties are significantly more copious than plagioclase (mean K/P ratio = 2.27).

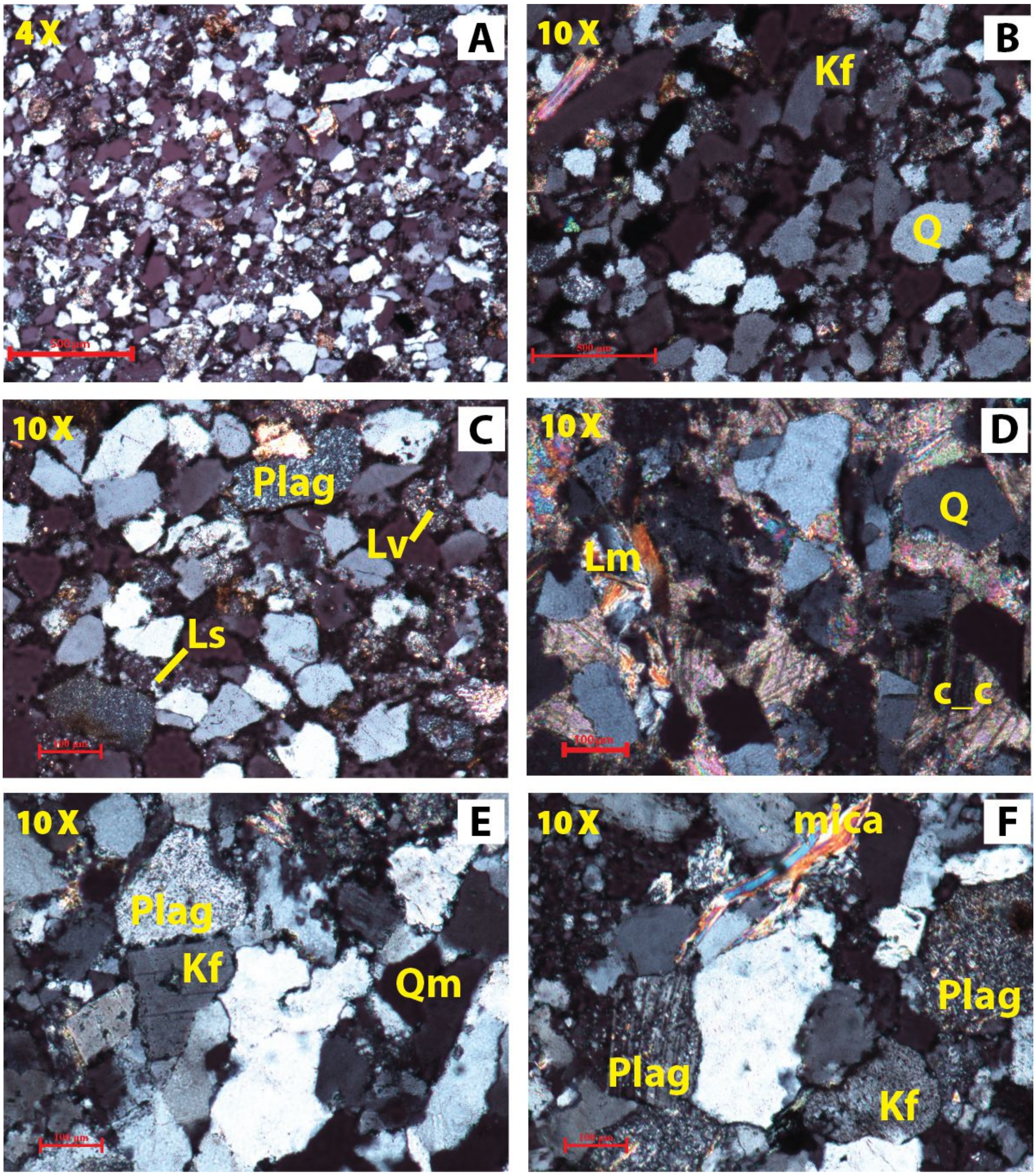

Fig. 6.1. Thin-section photomicrographs of representative detrital assemblages of the San Bartolomeo Formation (A-C) and the Bordighera Sandstones (D-F). All images acquired under crossed nichols. A) Typical appearance of relatively well-sorted, tightly packed SBF samples. Note the textural and compositional maturity of the basal complex sandstones. B) Characteristic quartz-dominated nature of fine-grained SBF thin-sections. Note the sub-rounded to occasionally rounded grain shapes. C) Uppermost SBF lithozone sample illustrating lithic fragment examples: chert fragment (Ls) and volcaniclastic fragment. D) Typical increase in average grain size and the presence of fresh feldspar grains denotive of the BGS samples. Note the abundant precipitation of sparitic calcite cementation (c_c) that essentially overgrows the feldspar is illustrated. E) Expression of alkali feldspars (Kf) in a low-grade metamorphic quartz and feldspar aggregate characteristic for the basal part of BGS. F) Divergent stages of plagioclase alteration: The plagioclase grain to the left still displays blurry twins, whereas these become unrecognizable in the grain to the left. Note the presence of mica in a foliated fragment.

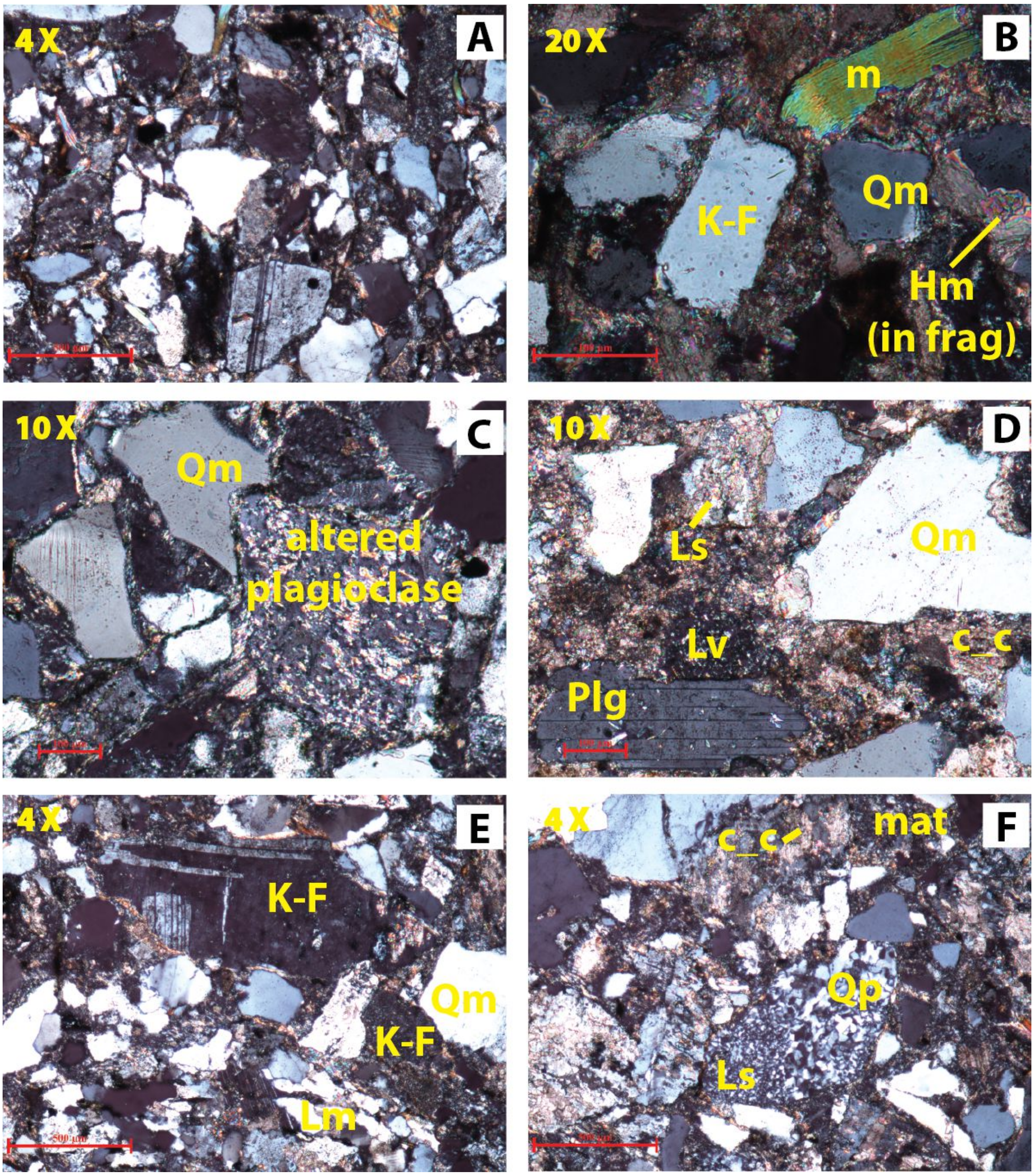

Fig. 6.2. Thin-section photomicrographs of representative detrital assemblages of the arkosic Bordighera Sandstones. All images were taken under crossed nichols. A) The poor degree of sorting, the tightly packed framework and the angularity of grains demonstrates the characteristic textural immaturity of BGS samples B) Typical constituents of the siliciclastic detritus represented by monocrystalline quartz (Qm), alkali feldspar (K-F) and mica (m). Note the heavy mineral grain ((?) staurolite) in rock fragment. C) Characteristic alteration of plagioclase (in association with monocrystalline quartz in tightly packed framework almost devoid of matrix). D) Examples of lithic fragments: arkosic fragment (Ls) and volcanic fragment (Lv) in association with Qm and plagioclase (Plg). Note also the abundant pinkish calcite cement. E) Representative arkosic composition comprising abundant quartz grains, alkalifeldspar and in granitic fragment), and metamorphic lithic grain. F) Fine- and microcrystalline polycrystalline quartz grains (Qp) in metamorphic fragment in association with silty sediment-clastic lithic fragment (Ls).

Lithic fragments merely embody a minor constituent of the detrital grains, as their average proportion accounts for 1.75% (± 1.22%). Even if individual lithic fragment types occur in variable portions, a trend of metamorphic fragments dominating over volcaniclastic and sedimentary fragments becomes evident. Accessory constituents of the total rock volume are represented by mica (mean: 2%), mudclasts (mean: 0.54%) and heavy minerals (mean: 0.44%), out of which zircons embody the most frequently observed.

Low-efficiency turbidite system (Bordighera Sandstones)

In comparison to the samples of the basal complex, thin-section analysis of both Bordighera Sandstones samples reveals a significantly lower textural maturity of the generally coarser siliciclastic detritus. The mean grain size of analyzed samples is medium sand. Nonetheless, since thin-sections supplementary to the detrital zircon analysis were acquired from fine topmost intervals of strata, a wide grain size range spanning from fine sand to very coarse sand is present in the analyzed thin-sections. The detrital assemblage is generally typified by a poor degree of sorting (Fig. 6.1 A). Framework grains are typically angular to sub-angular (Fig. 6.1. D) and loosely packed. Minor occurrences of sub-rounded grains (Fig. 6.1 E & Fig. 6.1 F) are typically limited to samples of the uppermost parts of stratigraphic sections. Both throughout the stratigraphic development, as well as along a basin-ward perspective, the major modal components of the sand-rich turbidite system are marked by rather consistent proportions. The total primary parameters´ mean composition of the two sections of the Bordighera Sandstones can be synthesized by the following recalculated QtFL values (See tables 6.3 to 6.5): Detrital quartz grains account for an average of 49.7% (± 4.81%) of the essential grain components, feldspars contribute to an average of 47.88% (± 5.49%), and lithic fragment represent an average of 2.44% (± 1.93%). Reasonably balanced ratios between quartz and feldspar grains and the scarcity of lithic fragments hence permit the classification of the clastic detritus as a "classic" arkoses (Folk, 1980). Notwithstanding, taking down-current facies relationships into account, essentially the shares of matrix, as well as calcite and phyllosilicate cement proportions demonstrate considerable lateral and stratigraphic variability.

Monte Frontè section

Among the main modal grains within the samples of the more proximal Monte Frontè section, quartz percentages make up an average of 39.29% of total rock volume (min. 27.1%; max. 48.11%). Both monocrystalline and polycrystalline quartz types have been counted. Monocrystalline quartz, distinguishable by their regularly non-undulatory fashion, accounts for the dominant portion (mean Qm: 23.18%). The average Qm/Qp-ratio of 1.82 portrays the dominance of monocrystalline quartz over polycrystalline quartz. Monocrystalline quartz grains frequently exhibit vacuoles and in exceptional cases contain inclusions (zircons and garnets). The polycrystalline quartz varieties predominantly exhibit straight domain boundaries, although sutured grain boundaries have been noted as well. Feldspar proportions account for an average of 35.21 % (min. 23.69%; max. 44.12%). Alkali feldspars (orthoclase and minor concentrations of microcline) dominate over plagioclase, as denoted by a mean K/P ratio of 1.58. The mean proportion of lithic fragments is 2.21%, with metamorphic lithic fragments representing the dominant share. Among accessory minerals, with a mean share of 2.28% of total rock volume, micas represent the most abundant constituent. Heavy minerals make up 1.18%. While calcareous clasts merely represent an accessory constituent (less than 1%), siliciclastic mudclasts contribute to an average of 2.9%. The matrix content makes up an average of 12.44%. It should however be noted that the matrix proportion varies significantly up-section. Within samples of the lower half of the Monte Frontè section the mean matrix percentage is 8.3%, whereas the matrix makes up an average of 17.6% of samples of the upper half of the stratigraphic section. Authigenic minerals are on the one hand represented by calcite cement which is typically present in the form of sparite (Fig. 6.1 D). Calcite cement accounts for an average of 4.12% of total rock volume. Notably, the presence of calcite cement is oftentimes associated to plagioclase dissolution (See Fig. 6.2 C). On the other hand, phyllosilicate cement (mean content: 1.03%) is dominantly represented by illite, as minor abundance of chlorite has been observed.

Cima di Velega section

Samples derived from the more distal Cima di Velega section are characterized by similar balanced percentages of main detrital framework components. Contributing with mean proportion of 42.44% of total rock volume, feldspar becomes notably more abundant (35.04-46.58%). Comparable to the Monte Frontè section, a similar mean K/P ratio of 1.52 signifies the dominance of alkali feldspar over plagioclase. The mean quartz proportion is that of 38.02% (30.74-40.39%). Monocrystalline quartz grains are again more copious than the polycrystalline varieties (average Qm/Qp-ratio: 1.69). In comparison to the more proximal section, lithic fragments proportions are slightly reduced, as they merely make up 1% (± 0.63%) of the main framework constituents. Lithic fragments are exclusively of metamorphic origin and no other varieties have been counted. Furthermore, in comparison to the Monte Frontè section, the mean matrix share is reduced (5.42%), whereas calcite cement (5.12%) and phyllosilicate (3.92%) proportions increase. Micas, typically muscovite and biotite, account for an average of 2.5%. Heavy minerals are very rare, as they merely make up 0.31% of the total rock volumes. Mudclasts represent an average of 2.07% of point counts, whilst calcareous clasts merely contribute to a mean of 0.05%.

	SBF_1	SBF_2	SBF_3	SBF_4	SBF_5	SBF_6	SBF_7	SBF_8	SBF_9	SBF_10	SBF_11	SBF_12
Qm	34.87%	38.73%	35.22%	33.86%	41.69%	33.43%	37.23%	42.67%	27.21%	36.21%	36.91%	47.72%
Qpcoarse	1.15%	10.58%	4.65%	0.32%	0.94%	3.28%	2.92%	0.00%	0.00%	0.29%	0.32%	0.91%
Qpfine	1.53%	1.82%	0.66%	0.00%	0.00%	0.90%	0.36%	0.33%	0.00%	0.00%	0.32%	0.91%
QfragP/G	11.12%	17.15%	21.26%	1.27%	0.94%	14.93%	12.41%	1.95%	1.97%	0.86%	1.88%	1.21%
Km	5.36%	2.55%	5.32%	10.76%	9.71%	7.76%	6.57%	5.86%	11.80%	9.77%	6.94%	6.95%
KfragP/G	4.21%	10.95%	11.63%	4.11%	2.82%	10.15%	11.68%	3.91%	2.95%	2.59%	5.68%	1.51%
Pm	3.07%	3.28%	3.65%	5.37%	4.08%	4.78%	2.55%	2.61%	3.93%	3.73%	3.15%	3.02%
PfragP/G	2.30%	6.93%	5.65%	1.58%	1.25%	8.66%	4.38%	1.30%	0.66%	0.00%	1.58%	0.91%
Lmeta	3.07%	0.00%	0.33%	0.00%	0.00%	0.90%	0.36%	0.00%	0.33%	0.57%	0.00%	0.91%
Lvolc	1.53%	1.09%	0.00%	0.00%	0.00%	0.00%	0.00%	0.00%	0.00%	0.00%	0.00%	0.00%
Lclast	1.53%	1.09%	0.00%	0.32%	0.94%	0.00%	0.00%	0.33%	0.33%	0.29%	0.32%	0.30%
Mica_mono	0.38%	1.46%	1.33%	0.32%	0.00%	2.69%	1.82%	0.00%	6.23%	0.86%	0.00%	0.30%
Mica_frag	1.53%	0.73%	3.32%	0.00%	0.31%	1.19%	0.73%	0.00%	0.33%	0.00%	0.63%	0.00%
HeayMin	1.15%	0.36%	0.00%	0.32%	0.31%	0.30%	0.00%	0.00%	0.66%	0.00%	2.21%	0.00%
Calc. clasts	1.15%	0.00%	0.00%	0.63%	0.00%	0.30%	0.00%	0.98%	0.00%	0.29%	0.00%	0.00%
Matrix	20.87%	3.28%	6.98%	24.05%	23.51%	8.36%	8.03%	25.08%	29.84%	28.45%	25.54%	25.38%
Calc_cement	1.92%	0.00%	0.00%	17.09%	12.54%	1.79%	9.49%	14.33%	11.48%	15.52%	14.20%	9.97%
Phyllos_cement	0.77%	0.00%	0.00%	0.00%	0.00%	0.60%	1.46%	0.00%	0.66%	0.00%	0.00%	0.00%
Mudchips	2.49%	0.00%	0.00%	0.00%	0.94%	0.00%	0.00%	0.65%	1.64%	0.57%	0.32%	0.00%
Total	100%	100%	100%	100%	100%	100%	100%	100%	100%	100%	100%	100%
Qt	70.72%	72.50%	69.92%	61.54%	69.80%	62.00%	67.40%	76.21%	59.33%	68.80%	69.10%	78.90%
F	21.55%	25.20%	29.70%	37.91%	28.60%	37.00%	32.10%	23.20%	39.34%	29.60%	30.40%	19.20%
L	7.73%	2.30%	0.38%	0.55%	1.50%	1.10%	0.50%	0.59%	1.33%	1.60%	0.60%	1.90%
Qm	91	106	106	107	133	112	102	131	83	126	117	158
P	14	28	28	22	17	45	19	12	14	13	15	13
K	25	37	51	47	40	60	50	30	45	43	40	28
P/Kfeld - ratio	0.56	0.76	0.55	0.47	0.43	0.75	0.38	0.40	0.31	0.30	0.38	0.46
Maturity Index	2.42	2.63	2.33	1.60	2.32	1.63	2.07	3.21	1.46	2.20	2.23	3.73

Table 6.2. Recalculated modal point-count data from samples of the San Bartolomeo Formation.

	MF_1	MF_2	MF_3	MF_4	MF_5	MF_6B	MF_7	MF_8	MF_9	MF_10	MF_11	MF_12	MF_13	MF_14.1	MF_15B
Qm	23.51%	22.59%	23.73%	27.10%	30.18%	24.36%	29.41%	24.05%	28.13%	23.58%	25.13%	19.01%	25.93%	19.68%	20.83%
Qpcoarse	4.05%	1.81%	1.98%	0.54%	3.77%	1.70%	2.14%	3.24%	1.39%	0.57%	1.85%	0.00%	1.42%	0.81%	0.00%
Qpfine	0.82%	0.30%	0.00%	0.27%	0.81%	0.57%	1.07%	0.81%	0.28%	0.00%	0.79%	0.00%	0.00%	0.27%	0.28%
QfragP/G	19.73%	20.18%	18.93%	16.26%	9.70%	10.48%	14.71%	16.49%	5.29%	5.68%	8.47%	16.53%	17.39%	7.81%	12.50%
Km	7.03%	2.71%	4.52%	5.96%	7.82%	6.23%	6.15%	6.49%	4.46%	11.36%	6.61%	7.99%	5.70%	6.74%	5.56%
KfragP/G	14.32%	16.58%	22.04%	16.27%	12.40%	13.31%	12.84%	15.68%	9.47%	5.68%	14.29%	13.22%	16.54%	14.29%	12.79%
Pm	4.86%	1.81%	3.67%	4.34%	4.85%	4.82%	5.35%	5.68%	3.06%	3.98%	5.03%	2.48%	4.27%	4.31%	5.28%
PfragP/G	10.00%	11.14%	11.58%	8.40%	7.01%	4.53%	10.96%	11.62%	6.69%	4.83%	11.38%	7.16%	13.39%	7.82%	9.72%
Lmeta	1.08%	0.60%	0.85%	1.08%	1.08%	1.42%	0.00%	0.54%	2.51%	1.42%	0.79%	1.65%	0.57%	1.89%	0.83%
Lvolc	0.00%	0.00%	0.00%	0.00%	0.00%	0.00%	0.00%	0.00%	0.00%	0.00%	0.00%	0.00%	0.00%	0.00%	0.00%
Lclast	0.00%	0.00%	0.00%	0.00%	0.00%	0.57%	0.27%	0.27%	1.11%	0.00%	0.00%	0.28%	0.57%	0.54%	1.11%
Mica_mono	2.17%	0.60%	0.85%	3.52%	1.35%	2.55%	1.34%	1.35%	0.28%	3.13%	1.59%	3.03%	0.00%	1.08%	1.94%
Mica_frag	1.62%	0.60%	0.28%	1.08%	0.81%	0.85%	0.53%	0.81%	0.28%	0.85%	0.00%	0.83%	1.99%	0.81%	1.94%
HeayMin	0.00%	2.41%	1.69%	1.63%	0.81%	0.57%	0.80%	1.35%	1.94%	0.85%	1.85%	1.65%	0.28%	1.62%	0.28%
Calc. clasts	0.27%	0.00%	0.00%	0.00%	0.54%	1.70%	1.87%	0.00%	0.28%	0.00%	0.79%	0.28%	0.00%	0.54%	0.83%
Matrix	6.22%	6.02%	6.21%	7.86%	9.97%	20.10%	4.28%	5.95%	25.63%	28.98%	10.85%	15.15%	5.41%	22.09%	17.22%
Calc_cement	0.00%	7.83%	1.41%	2.44%	8.36%	3.97%	5.61%	1.08%	4.46%	3.41%	8.20%	5.23%	2.56%	6.47%	0.83%
Phyllos_cement	1.08%	1.51%	1.13%	1.08%	0.54%	0.00%	1.60%	1.62%	0.00%	0.00%	0.00%	0.00%	3.70%	0.00%	0.00%
Mudchips	3.24%	3.31%	1.13%	2.17%	0.00%	2.27%	1.07%	2.97%	4.74%	5.68%	2.38%	5.51%	0.28%	3.23%	8.06%
Total	100%	100%	100%	100%	100%	100%	100%	100%	100%	100%	100%	100%	100%	100%	100%
Qt	56.32%	57.75%	51.13%	55.07%	57.29%	54.58%	57.10%	52.55%	56.25%	52.24%	48.75%	52.02%	52.16%	44.54%	48.79%
F	42.41%	41.47%	47.90%	43.58%	41.32%	42.50%	42.58%	46.49%	37.95%	45.27%	50.18%	45.16%	46.51%	51.68%	48.39%
L	1.27%	0.78%	0.97%	1.35%	1.39%	2.92%	0.32%	0.96%	5.80%	2.49%	1.07%	2.82%	1.33%	3.78%	2.82%
Qm	56.63	58.04	51.63	55.67	57.65	55.84	56.72	52.6	59.52	53.57	48.73	53.53	52.86	46.05	50
P	17.8	16.86	17.65	16.15	15.66	14.29	20	20.78	16.67	15.82	22.55	14.52	20.88	19.74	22.5
K	25.57	25.1	30.72	28.18	26.69	29.87	23.28	26.62	23.81	30.61	28.73	31.95	26.26	34.21	27.5
P/Kfeld - ratio	0.70	0.46	0.57	0.57	0.59	0.48	0.86	0.78	0.70	0.52	0.78	0.45	0.79	0.58	0.82
Maturity Index	1.29	1.37	1.05	1.23	1.34	1.20	1.33	1.11	1.29	1.09	0.95	1.08	1.09	0.80	0.95

Table 6.3. Recalculated modal point-count data from samples of the Monte Frontè section of the BGS.

	CdV_1	CdV_2	CdV_3	CdV_4	CdV_6	CdV_7	CdV_8	CdV_9		CdVZ_1	CdVZ_2	CdVZ_3
Qm	17.99%	26.67%	13.89%	14.61%	19.35%	21.72%	20.34%	22.99%		21.67%	22.63%	26.59%
Qpcoarse	2.29%	2.16%	1.67%	2.48%	0.36%	2.47%	1.69%	2.19%		7.88%	3.41%	0.83%
Qpfine	2.57%	1.35%	0.00%	0.00%	0.72%	0.27%	0.00%	0.00%		2.96%	0.73%	0.55%
QfragP/G	17.43%	14.56%	19.17%	22.98%	15.04%	15.93%	16.67%	14.96%		7.88%	5.84%	2.49%
Km	7.43%	8.09%	4.73%	5.28%	4.66%	6.87%	7.06%	4.01%		19.21%	15.57%	16.61%
KfragP/G	18.00%	17.52%	22.22%	20.81%	17.20%	17.59%	18.99%	20.45%		13.31%	6.57%	5.82%
Pm	6.00%	4.85%	3.61%	5.28%	5.38%	4.12%	5.37%	2.92%		8.37%	10.21%	11.36%
PfragP/G	12.86%	12.12%	13.33%	15.22%	16.13%	13.19%	14.12%	13.51%		4.43%	2.68%	3.88%
Lmeta	0.57%	0.00%	0.00%	0.31%	0.00%	0.00%	0.85%	0.00%		0.00%	0.00%	0.00%
Lvolc	0.00%	0.00%	0.00%	0.00%	0.00%	0.00%	0.00%	0.00%		0.00%	0.00%	0.00%
Lclast	0.29%	0.00%	0.00%	0.00%	0.00%	0.00%	0.00%	0.00%		0.00%	0.00%	0.00%
Mica_mono	2.00%	1.08%	3.06%	0.31%	2.87%	0.55%	0.56%	1.09%		2.96%	3.16%	0.00%
Mica_frag	1.71%	1.62%	1.94%	1.55%	1.79%	1.37%	0.85%	0.73%		0.99%	0.97%	0.00%
HeayMin	0.57%	0.81%	0.83%	0.00%	0.36%	0.27%	0.56%	0.00%		0.00%	0.00%	0.00%
Calc. clasts	0.00%	0.00%	0.28%	0.00%	0.00%	0.00%	0.00%	0.00%		0.00%	0.00%	0.28%
Matrix	1.43%	5.12%	5.00%	1.86%	1.08%	0.27%	1.13%	7.30%		5.91%	17.03%	13.30%
Calc_cement	0.00%	0.81%	4.72%	5.28%	7.89%	6.59%	3.67%	6.93%		0.00%	0.73%	16.07%
Phyllos_cement	8.57%	1.62%	3.33%	2.17%	5.38%	7.14%	3.95%	1.46%		2.46%	7.06%	0.00%
Mudchips	0.29%	1.62%	2.22%	1.86%	1.79%	1.65%	4.24%	1.46%		1.97%	3.41%	2.22%
Total	100%	100%	100%	100%	100%	100%	100%	100%		100%	100%	100%
Qt	47.16%	51.23%	44.17%	46.07%	45.00%	49.16%	45.51%	49.55%		47.13%	48.20%	44.72%
F	51.84%	48.77%	55.83%	53.57%	55.00%	50.84%	53.49%	50.45%		52.87%	51.80%	55.28%
L	1.00%	0.00%	0.00%	0.36%	0.00%	0.00%	1.00%	0.00%		0.00%	0.00%	0.00%
Qm	45.99	50.47	44.17	46.24	44.5	48.99	45.97	49.55		45.24	47.64	44.26
P	23	19.75	21.55	23.66	27.52	21.14	23.15	20.27		15.48	19.27	22.54
K	31.01	29.78	34.28	30.11	27.98	29.87	30.87	30.18		39.29	33.09	33.2
P/Kfeld - ratio	0.35	0.31	0.35	0.36	0.46	0.34	0.34	0.45		0.60	0.36	0.41
Maturity Index	0.89	1.05	0.79	0.85	0.82	0.97	0.84	0.98		0.89	0.93	0.81

Table 6.4. Recalculated modal point-count data from samples of the Cima di Velega section of the BGS.

	MFZ_1	MFZ_2	MFZ_3	MFZ_4
Qm	14.20%	11.23%	25.84%	21.93%
Qpolycoarse	7.00%	8.82%	2.43%	0.80%
Qpolyfine	1.20%	1.60%	1.52%	1.07%
QfragP/G	15.40%	13.64%	8.51%	3.21%
Km	11.20%	9.63%	13.37%	16.58%
KfragP/G	13.00%	14.71%	10.64%	6.95%
Pm	4.40%	4.81%	8.51%	13.90%
PfragP/G	11.20%	11.76%	6.69%	6.68%
Lmeta	0.60%	0.53%	0.00%	0.53%
Lvolc	0.40%	0.00%	0.00%	0.00%
Lclast	0.00%	0.00%	0.30%	0.53%
Mica_mono	0.40%	0.00%	0.91%	2.14%
Mica_frag	0.60%	0.00%	0.00%	1.07%
HeayMin	1.20%	0.00%	0.30%	0.27%
Calc. Clasts	0.00%	0.00%	0.00%	0.80%
Matrix	9.20%	7.22%	13.07%	17.65%
Calc_cement	5.00%	14.44%	4.86%	0.80%
Phyllo_cement	4.20%	1.07%	0.00%	0.00%
Mudchips	0.80%	0.53%	3.04%	5.08%
Total	100%	100%	100%	100%
Qt	48.09%	45.67%	49.22%	37.41%
F	50.64%	52.94%	50.39%	61.11%
L	1.27%	1.38%	0.39%	1.48%
Qm	47.91	45.16	48.40	37.02
P	20.42	22.22	20.00	29.39
K	31.68	32.62	31.60	0.34
P/Kfeld - ratio	0.64	0.68	0.63	0.87
Maturity Index	0.93	0.85	0.97	0.60

Table 6.5. Recalculated modal point-count data from the Monte Frontè zircon samples of the BGS.

4.4 Interpretation of the detrital modal assemblages

The dominance of monocrystalline quartz exhibiting both straight and undulatory extinctions over polycrystalline quartz varieties is interpreted to indicate dominantly granitoid to low-grade metamorphic source rocks (e.g. Palomares & Arribas, 1993; Datta, 2005; McCann & Arbues, 2012). This assumption is supported by the presence of polycrystalline quartz typically characterized by straight domain boundaries and metamorphic rock fragments that suggest that a low-grade metamorphic source rocks meaningfully contributed to the clastic detritus (Das Gupta & Pickering, 2008). Polycrystalline quartz grains that sporadically show sutured contacts are interpreted to represent features that reflect burial anchi-metamorphism (Boggs, 2009). Taking the chemically and mechanically less stable nature of feldspar grains into consideration, their abundant presence potentially rules out a recycled quartzose provenance for the coarse-clastic sediments (e.g. Dickinson et al., 1983; Najman, 2006; Garzanti et al., 2006) and thus points towards their first-cycle origin from crystalline source rocks. Moreover, the mineralogy of feldspars provides additional insights into the nature of the source rocks. The feldspar in plutonic felsic rocks and high-grade metamorphic rocks are commonly alkaline feldspars (orthoclase and microcline), whereas plagioclase is commonly associated to a magmatic arc origin (Dickinson & Suczek, 1979; Ingersoll, 1978; Boggs, 2009). Consequently, the fact that plagioclase is generally subordinate to alkali feldspar is interpreted as mirroring the foremost contribution of granitic to low-grade metamorphic source rocks (e.g. Palomares & Arribas, 1993; McCann & Arbues, 2012).

As demonstrated by the high textural and compositional maturity, the samples of the basal complex are generally defined by higher quartz proportions and therewith strikingly differ from the samples of the low-efficiency turbidite system. The better degree of sorting is interpreted to mirror the fact that these sediments were transported for further distances (Boggs, 2009). Moreover, the higher quartz content in San Bartolomeo Formation samples might indicate intense weathering of less stable grains on continental land masses that were typified by relatively low relief (Dickinson & Suczek, 1979). Extended transport along continental surfaces characterized by low paleo-relief apparently resulted in the pronounced textural and compositional maturity samples of the San Bartolomeo Formation. Notwithstanding, the high variations in both quartz content and matrix proportions illustrate the compositional and textural variability of the basal complex and might thus point towards variations in tectonic quiescence (Datta, 2005). By contrast, samples of the Bordighera Sandstones, interpreted to represent a low-efficiency turbidite system, reveal a different scenario. Generally angular to sub-angular grain morphologies and higher, still however fluctuating matrix proportions as well as the poor degree of sorting, reveal their heterogeneous, immature textural nature, whereas increased feldspar proportions on the expense of quartz percentages mirror compositional immaturity (cf. Ghazi & Mountney, 2011).

Discrimination of tectonic setting and provenance terrain lithology

In order to determine whether the diverging modal composition of the detritus of the basal complex and that of the sand-rich turbidite system were derived from identical or diverging source areas or if the observed differences result from a transformation of the tectonic setting that controlled the clastic input into the deep-marine basin, the three key framework parameters were plotted into QtFL and QmFLt ternary diagrams (cf. Dickinson et al., 1985). Furthermore, QmPK ternary diagrams (cf. Graham et al., 1976) were computed with the emphasis of investigating stratigraphic and down-current trends between continent-derived detritus rich in alkali feldspar and magmatic arc-derived provenances denotive of increased plagioclase concentrations. Maturity indexes were calculated and computed into whisker-plot diagrams with the aim of identifying possible stratigraphic and basin-ward shifts in compositional maturity. In summary, emphasis is put on considering whether the compositional variation in between the SBF samples and those of the BGS would reflect variable source terranes or if it possibly might indicate a marked change in tectonic setting.

Results

The comparison of the modal point-count data with the proposed provenance fields of Dickinson et al. (1983) illustrates that the framework compositional data of the basal complex almost entirely plots into the transitional continental field. The single exception is marked by one sample (SBF 12) that plots within the craton interior discrimination field (see Fig. 6.3 A&B). Contrastingly, the dataset derived from the Bordighera Sandstones samples largely plots into the basement uplift field, even if minor components plot in the transitional continental provenance field as well. Consequently, as outlined by the relatively steady compositional make-up that is contrasted by the evidently divergent textural maturity, the fundamentally inverse tectonic stability trend is illustrated by both the QtFL and the QmFLt plots. This would by some means hint towards a divergent tectonic setting from that of the San Bartolomeo Formation rather than towards a shift in provenance area composed of different lithologies. Basically, a distinctly, gradual change in regional tectonics, might epitomize the most feasible explanation to facilitate a such stratigraphic development (e.g. Cox & Lowe, 1995; Datta, 2005). Taking the perceptibly overlapping computed confidence regions into account (Fig. 6.4 B; cf. Weltje, 2002), the consideration of a comparably gradual change in source area tectonics is supported.

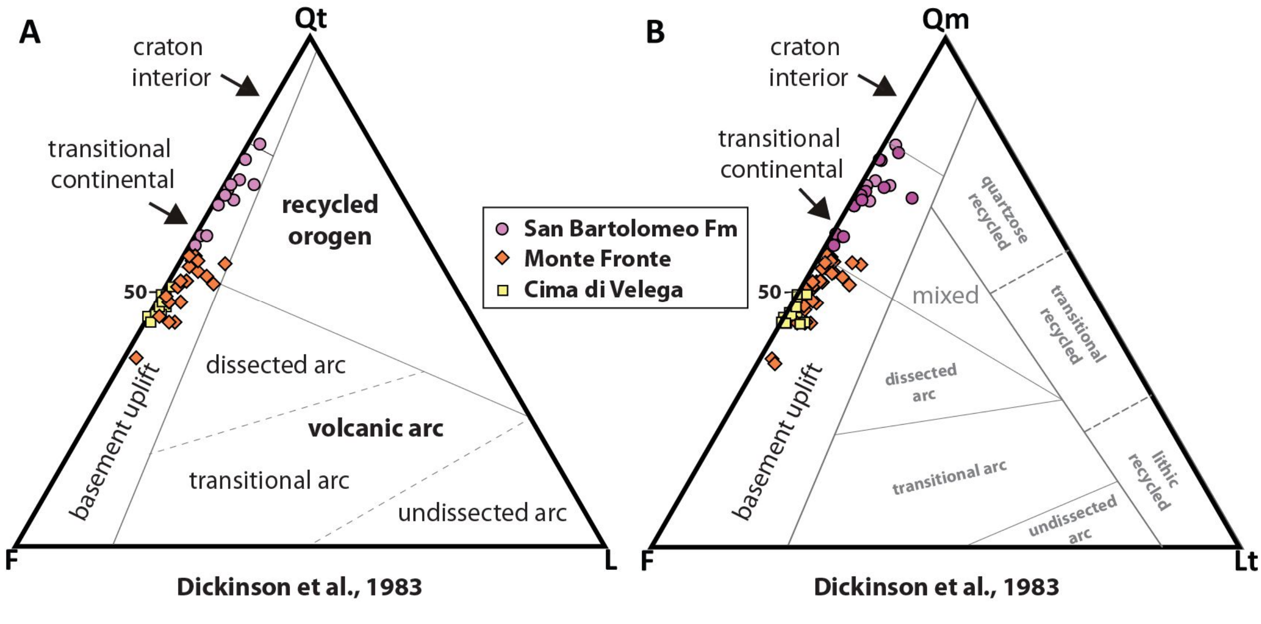

Fig. 6.3. Compositional plots allowing the provenance inference from the petrographic data of the SBF and the BGS based on schemes proposed by Dickinson et al. (1983). Framework parameters according to Table 4.1. A) QmFL ternary diagram. B) QmFLt ternary diagram.

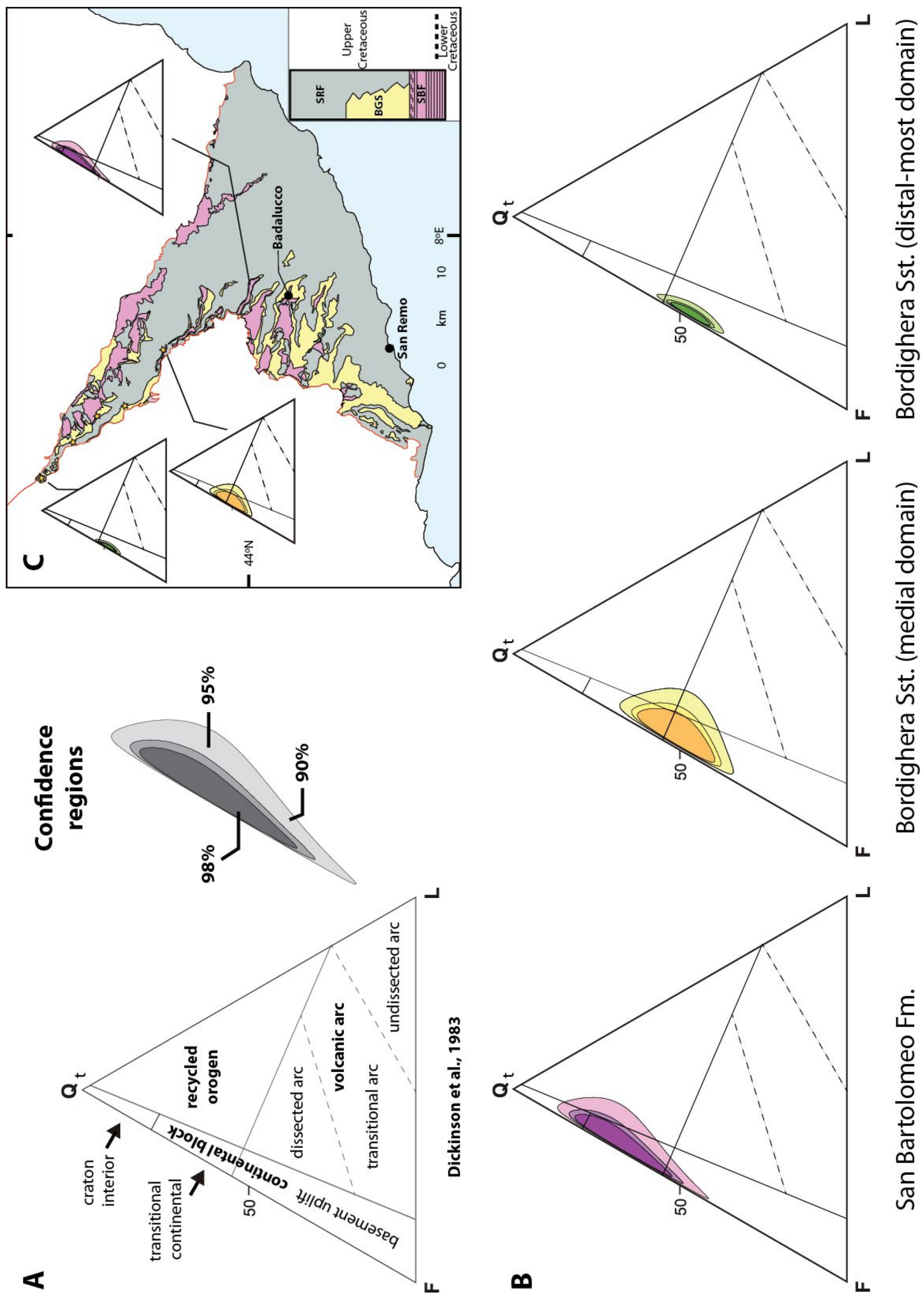

Fig. 6.4. A) Proposed provenance fields interpretation (after Dickinson et al., 1983). B) modal framework compositions (QtFL plots) with predictive confidence ellipses (cf. Weltje, 2002) and C) sampling locations.

Excluding the proportions of total lithic fragments (Lt) and differentiating feldspars into potassium plagioclase (P) and feldspar (K) proportions allows an understanding of the source rock mineralogy (Graham et al., 1976). The mean Qm proportion of the SBF samples is 66.25% ± 8.24%, while the mean plagioclase percentage is 11.33% ± 4.27% and the mean potassium feldspar content is 23.67% ± 5.37%. The mean P/K ratio of the samples is 0.48. By contrast, samples of the BGS reveal a considerable trend of increasing feldspar abundance (Fig. 6.5 A). A significant rise in plagioclase concentrations (Monte Frontè: 19.15% ± 3.64%; Cima di Velega: 21.48% ± 3.05%) accompanied by an almost equally high increase in alkali feldspar proportions is to be observed (Monte Frontè: 28.87% ± 3.32%; Cima di Velega: 31.79% ± 3.09%). The Bordighera Sandstones samples are typified by comparably retained mean P/K ratios of 0.67 (Monte Frontè section) and 0.69 (Cima di Velega section), respectively. The mean Qm concentrations reasonably decrease (Monte Frontè: mean Qm = 51.98% ± 5.55%; Cima di Velega: mean Qm = 46.64% ± 2.21%).

The compositional ratio of quartz minerals, feldspar grains and lithic fragments allows to assess the compositional maturity of sandstones (Pettijohn, 1975; Boggs, 2009). Sandstones that contain high proportions of quartz in comparison to unstable grain types such as feldspar and lithic fragments can be designated as mature rocks since quartz is typified by high resistivity to erosional processes. On the contrary, rocks defined by high concentrations of unstable feldspar grains and lithic fragments and low quartz portions can be classified as compositionally immature rocks. As proposed by Pettijohn (1975), sandstone maturity is calculated by the ratio of the total quartz grains over the sum of all feldspar grains and lithic fragments: the maturity index MI = $\frac{Q}{(F+L)}$.

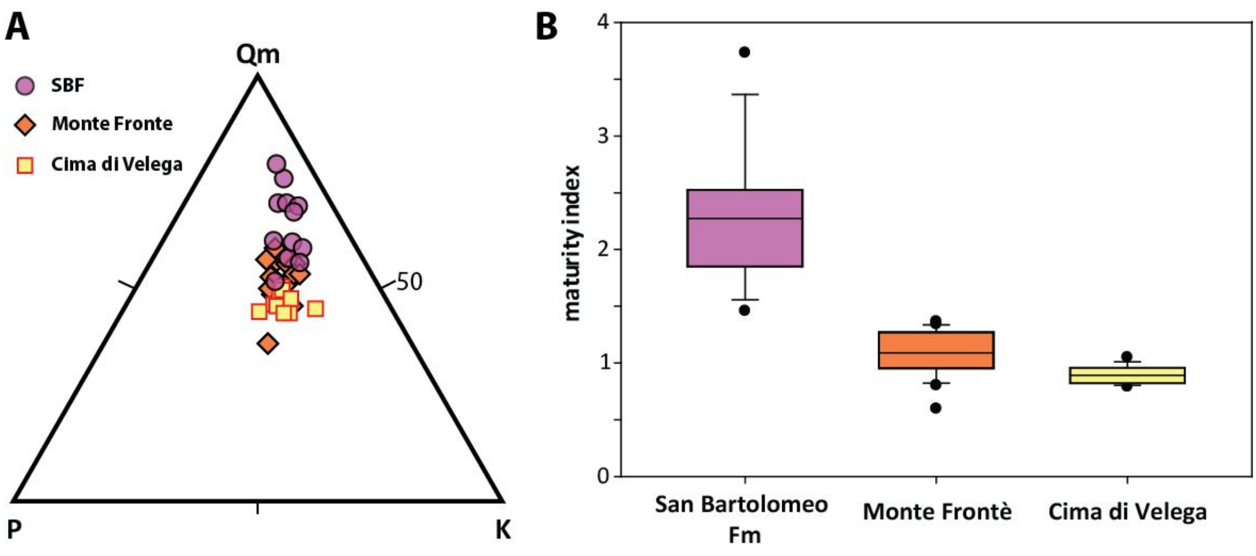

Fig. 6.5. A) QmFP ternary plot illustrating the stratigraphically persistent dominance of K-feldspar over plagioclase. B) Maturity index comparisons (whisker plots) in between the three analyzed sections.

Mineralogical maturity merely slightly varies within BGS samples. Although typified by high quartz abundances, the studied SBF samples demonstrate greater variability (Fig. 6.5B). In comparison with the petrographic data of the Bordighera Sandstones, maturity indexes are typically higher. Moreover, they are defined by a relatively short span (Monte Frontè: min. MI = 0.59, max. MI = 1.37, mean MI = 1.08; Cima di Velega: min. MI = 0.79, max MI: 1.05, mean MI = 0.89). Consequently, the essentially low maturity index of the Bordighera Sandstones samples would suggest shorter transport distances (cf. Zhang et al., 2016). The low mineralogical maturity would moreover suggest the dominance of physical weathering processes over chemical weathering, devoid of selection between stable and unstable minerals (Diekmann & Wopfner, 1996). By contrast, the mean maturity index of the basal complex corresponds to 2.32 and therewith indicates greater sandstone maturity. This advanced maturity is interpreted to reflect chemical weathering and prolonged shelfal reworking of the sand grains before they were accommodated in the final sink (Boggs, 2009; Garzanti et al., 2014).

Assessment of source area paleo-geology and geodynamic context of the provenance terrain

Previous works on the Western Ligurian Flysch Units grounded on sedimentary facies analysis assigned the San Bartolomeo Formation to a basin plain depositional environment and interpreted the Bordighera Sandstones as representing a coarse-grained trench fill (Sagri, 1980). Apparently, in the scenario in which the identical source undergoes a geodynamic evolution, the differentiation of depositional environments likewise becomes observable from the petrographic signature. This change would be expressed in terms of decreased textural maturity but comparably equal compositional maturity (Garzanti, 2016; see Fig. 6.5B). As apparently being related to the contrasting geodynamic settings, the observed tendency of conforms well with accepted models according to which of textural maturity according to which a close relationship in between sandstone modal composition and depositional environment (basin plain VS axial trench-fill) can be inferred (Boggs, 2009; Zhang et al., 2016). The quartz-rich modal framework of the samples from San Bartolomeo Formation is interpreted to result from extensive reworking by shelfal reworking processes prior to turbiditic re-sedimentation into the basin plain environment (e.g. Pettijohn, 1975; Boggs, 2009; Garzanti, 2016). Moreover, the silty to fine-sandy grain size implies a low-relief source area typified by slower erosion rates that promoted grain size reduction through weathering processes (Boggs, 2009). On the contrary, the abrupt passage towards highly immature feldspar-rich sandstones of the axial coarse-grained fan, as represented by "classic" arkoses (e.g. Folk, 1980; Basu, 1985), suggests a scenario in which sediments have almost directly been shed into the deep-marine realm. Due to rapid denudation of the source area, no significant reworking occurred that promoted unstable grains to dissolve and therewith develop progressed maturity of the clastic detritus (e.g. Shanmugam & Moiola, 1988; Mattern, 2005;

Boggs, 2009). Dominantly sub-rounded to rounded shapes of grains suggest that the detritus was subject to minor degrees of physical breakdown (Boggs, 2009) and that the sediments were likely transported over long distances (Pettijohn et al., 1987). Nonetheless, it should be noted that recent studies (Garzanti 2017) reveal that grain roundness might not necessarily reflect transport distance as roundness is depending on a complex interplay of mineralogical and physical factors. By contrast, the textural characteristics of samples from the Bordighera Sandstones that are defined by poorly sorted, angular to sub-angular grains reveal the lower degree of textural maturity (e.g. Dott, 1964; Folk, 1974). The generally lower percentage of matrix reinforces this valuation. Reduced quartz percentages with respect to elevated feldspar proportions (Fig. 6.5 A), along with the lower maturity index (Fig. 6.5 B), would furthermore suggest decreasing stability of a continental block provenance (Graham et al., 1976; Dickinson et al., 1983). The ubiquity of alkali feldspars, together with the frequent presence of vacuoles in monocrystalline quartz grains (Fig. 6.2 C&D), points towards a dominantly plutonic, plausibly granitic source rock lithology (Folk, 1974). Differentiated stages of feldspar weathering (Fig. 6.1 F) are interpreted to indicate active tectonism, rapid erosion and a relatively moderate relief (cf. Ghazi & Mountney, 2011).

As outlined by the direct comparison of the modal framework of the San Bartolomeo Formation with that of the Bordighera sandstones reveals evidence of nominal overlapping of tectonic discrimination fields. According to Mattern et al. (2005) sand-rich turbidite systems are a typical feature of active margin sedimentation. Specifically, this involves that the staging areas of sediment gravity flows are characteristically represented by narrow shelfs. This would imply that comparatively coarse sediment is practically directly shed into the final deep-marine depositional. The observed stratigraphic trend typifying the evolution from quartz-rich arkoses of the San Bartolomeo Formation to immature, quartzo-feldspathic coarse-clastic Bordighera Sandstones is interpreted to mirror a swift, nevertheless gradual changeover of the tectonic regime that controlled the two siliciclastic systems. Increasing feldspar concentrations and low proportions of metamorphic lithic fragments might indicate the rapid unroofing of the plutonic source rocks (Cox & Lowe, 1995). As additionally pointed out by the sharp transition of grain size and the general facies shift towards an immature clastic detritus, the onset of coarse sedimentation is interpreted to mark a substantial modification of the geodynamic regime. The increased sediment yield, accompanied by increased sediment caliber and the interpreted increased slope gradient hence imply rapid basement uplift (Dickinson et al., 1983). According to literature data, the Piemont-Ligurian ocean was subject to the commence of compressional tectonics that can be dated to Lower Cretaceous age (e.g. Dal Piaz et al., 2003; Froitzheim et al., 2008; Rubatto et al., 2011; Bracciali et al., 2013).

4.5 Detrital zircon chronology

Zircon morphologies

Cathodoluminescence imaging illustrates that the detrital zircons display a wide range of crystal habits (See Figs. 6.7 and 6.8). Mainly prismatic and bi-pyramidal as well as subhedral and elongated euhedral grains represent the bulk of analyzed grains. These grains typically exhibit large, typically sector-zoned cores and well-developed, relatively thin rims that show oscillatory zoning. Patchy zoning, sector zoning and complex, discontinuous zoning are typically to be observed in zircon fragments. Only in exceptional cases, cores and rims of individual zircons have been dated. The cores yield very old inherited ages, whereas the rims date later events relatable to later geological events (e.g. Fig. 6.7 A, upper left). Moreover, homogeneous varieties that do not display zonations are frequently to be found. Zircon grains are subject to various degrees of rounding. The bulk of grains are moderately rounded, except for some grains that exhibit well-rounded to almost completely rounded shapes (See Fig. 6.8 A, lower row outer right). Notwithstanding, no clear tendency relating zircon age to the degree of roundness could be ascertained. Several grains that show fractures and cracks have not been incorporated into the age determinations. The elongation ratios of prismatic zircon grains mirror the velocity of crystallization and both the composition and the temperature of the host rocks (Corfu et al., 2003 and references therein). Accordingly, zircons originated in a granitic crystallization medium tend to be more elongated than the ones of meta-sedimentary origin, whilst volcanic zircon grains are generally defined by very high length-with ratios. Weak planar zoning, oscillatory zoning and prismatic elongated shapes suggest magmatic origin of the zircons, whereas zircons displaying cores which are surrounded by oscillatory rims are regarded as representing stages of metamorphic overgrowth or recrystallization processes that overprint such inherited magmatic growth (e.g. Rubatto et al., 2001; Hoskin & Schaltegger, 2003). Although rounded zircon shapes might be caused by recrystallization processes, this morphological feature allows conclusions concerning transport distances and the nature of the transport medium (Gärtner et al., 2013). Cracks and fractures in zircons can either arise from volume expansion during crystallization or from collisions during transport (Corfu et al., 2003).

Results of detrital zircon age determinations

Out of ca. 371 single detrital grains analyzed, 237 yielded determined ages (concordance of ± 10%; see Fig. 6.9). On that premise, discordant ages were dismissed from the following comparative analysis and the provenance area interpretation. Full isotopic U-Pb analytical data tables of the analyzed detrital samples are presented in Appendix 2.1, and reference material ablation isotopic compositions utilized for calibration are presented in Appendix 2.2.

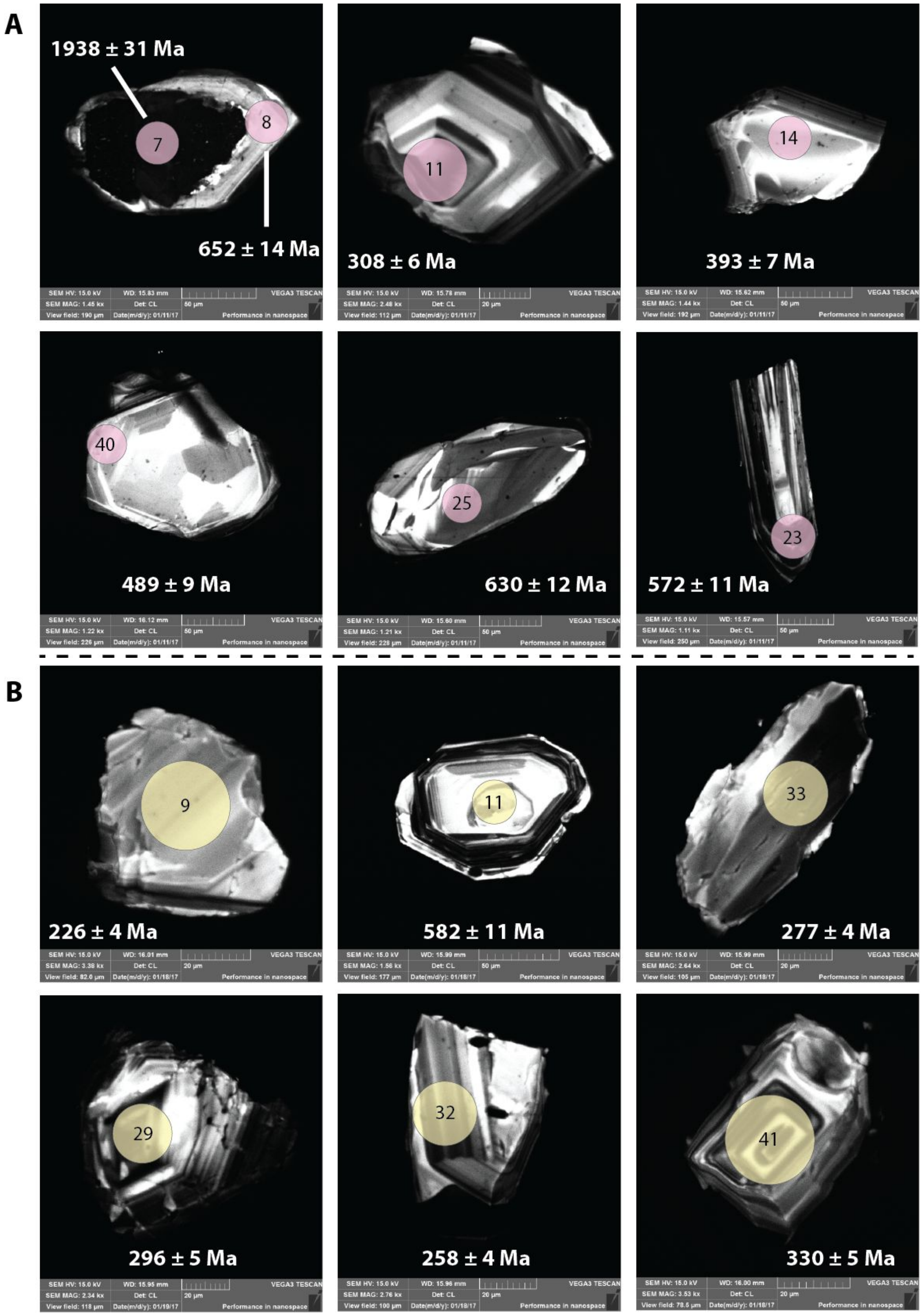

Fig. 6.7. Representative zircon cathodoluminescence images with analyzed spots and concordant ages for A) Sample MFZ_1 and B) Sample MFZ_4.

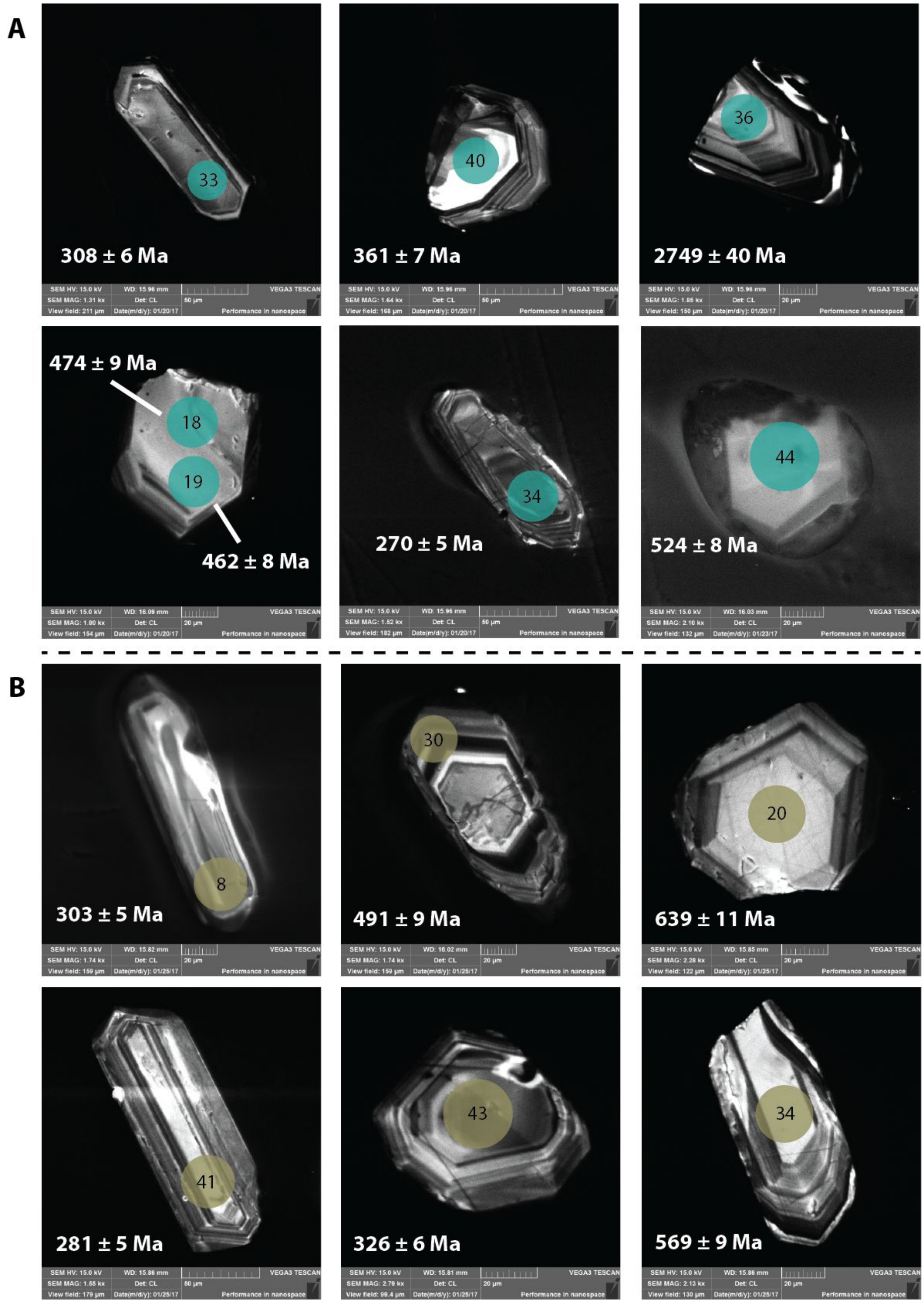

Fig. 6.8. Representative zircon cathodoluminescence images with analyzed spots and concordant ages for A) Sample CdV_1 and B) Sample CdV_3.

Detrital zircon age spectra and relative proportions of age clusters

Although ages older than 1 Ga are present, these account for accessory proportions as approximately 95 % of all detrital zircon ages are younger than 1 Ga. Paleo- and Mesoproterozoic ages account for minor peaks. Out of the group younger than 1 Ga, almost 75 % of ages comply to an interval between 200 Ma and ca. 500 Ma (See Fig. 6.9 and Table 6.3). With respect to their very broad distribution (See Fig. 6.9) and the limited sample density of detrital zircons ages (e.g. Vermeesch, 2004; Vermeesch & Garzanti, 2015; Sundell & Saylor, 2017) the population of ages older than 600 Ma spans, although accounting for 19.4% of all detrital ages, are regarded as providing inadequate direct provenance information. With a proportion of 31.6 %, the bulk of detrital zircon ages correspond to geodynamic events that can be related to the Variscan orogeny. The second largest key component of the detrital spectra is represented by ages related to the collapse of the Variscan orogen that account for 13.1% of the detrital suite. Ordovician and Silurian zircon ages make up the third main age group with 12.2 % off all detrital single grain ages. Edyacaran crystallization ages attributed to Cadomian events contribute with a total of 11%.

Distinct peaks in the cumulative probability density function distributions of all detrital ages (Fig. 6.9) on the one hand comprise a narrow Middle- to Late-Permian peak a further narrow peak at 306 Ma that corresponds to post-Variscan magmatism. On the other hand, major more broader peaks are represented by ages related to the Variscan orogeny (330 Ma and 357 Ma), ages representative of Ordovician to Silurian magmatism (447 Ma and 480 Ma) and one very broad peak reliable to events of the Cadomian orogeny (564 Ma). The oldest dated grain corresponds to a $^{206}Pb/^{207}Pb$ crystallization age of 2749 ±40 Ma, whereas the youngest grain reveals a reliable $^{206}Pb/^{238}U$ age of 235.1 ±3.7 Ma.

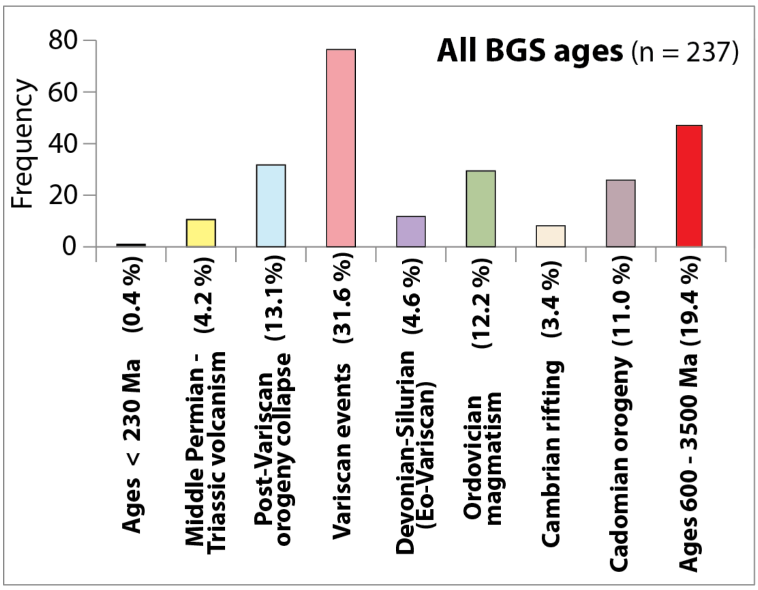

Fig. 6.9. Relative abundance of all BGS detrital ages within the defined age groups discussed below.

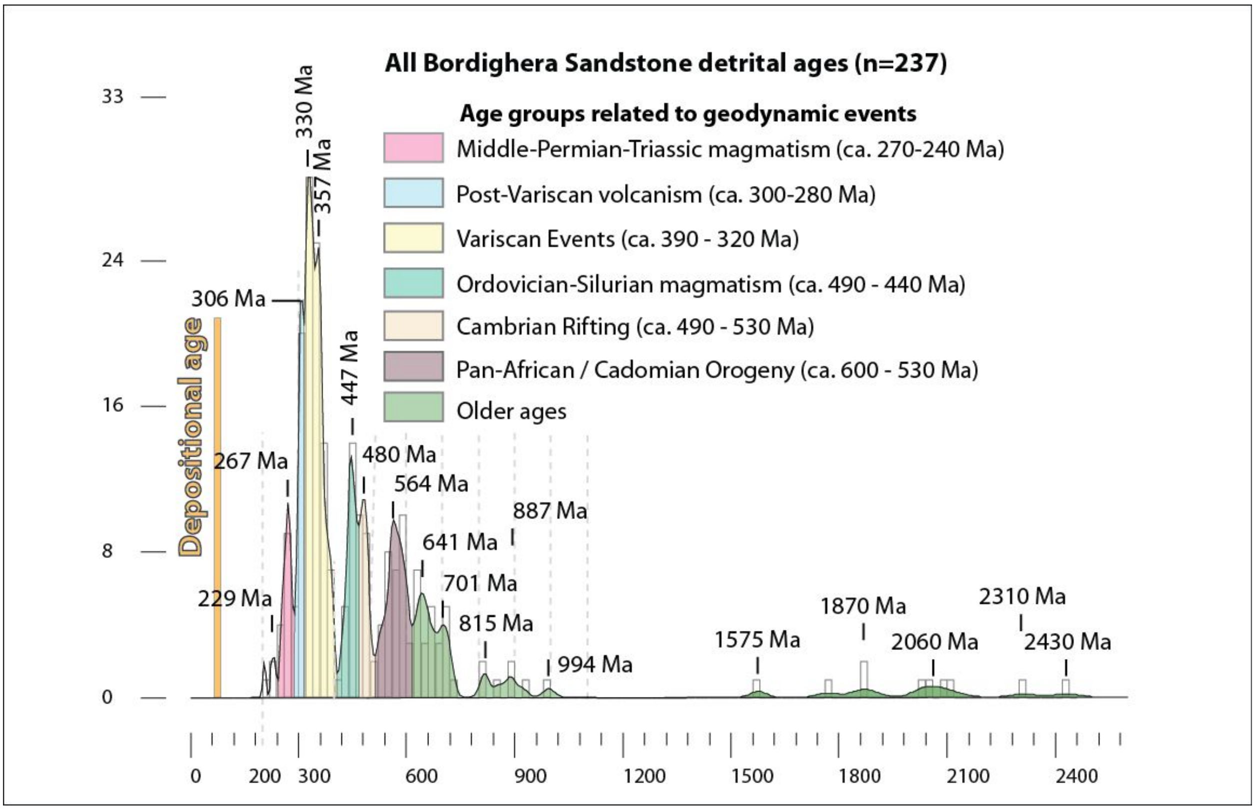

Fig. 6.10. Cumulative plot of KDE distributions of all BGS detrital zircon ages between 0 and 2500 Ma.

Definition of age groups of the detrital zircon spectra

With regards to the reasonably well-defined geodynamic framework of Central and Western Europe (e.g. von Raumer et al., 2003; Linnemann et al., 2004; Handy et al., 2010; Dallagiovanna et al., 2009; Oggiano et al., 2010, amongst many others), the determined detrital zircon age pattern reveals several similarities with age peaks of geochronologically constrained magmatic and metamorphic events of the Western Tethyan realm (Fig. 6.9 and Fig. 6.10). On that premise, the relation of clusters of detrital age populations to regional-scale geodynamic events is regarded as providing further understanding of regional paleogeography and the geodynamic setting that promoted the provenance. Although the pre-Variscan paleo-tectonic plate configuration remains poorly constrained (e.g. Stampfli et al., 2001; von Raumer et al., 2002), the defined age groups (Fig. 6.9) directly correspond to eminent regional-scale geological events from which evidence is preserved in the basement of the Alps. These age clusters embrace:

- **Ages older than 600 Ma**: This age group comprises Archean ages ranging from ca. 3000 Ma to 2.55 Ga that are interpreted to reflect the first event of craton accretion (Cawood et al., 1999). Proterozoic ages spanning an interval from ca. 2000 Ma until 1600 Ma are interpreted as representing the assembly of Laurentia and accretion along its eastern margin (Cawood et al., 1999). Ages related to the assembly of the Rodinia supercontinent, the Greenville orogeny, are dated to span an interval from ca. 1200 Ma to 1000 Ma, whereas ages ranging from ca. 600 Ma to 1 Ga can be assigned to the onset of the breakup of Rodinia. Magmatic products related to preceding rifting have been dated from ca. 850 to 750 Ma (e.g. von Raumer et al., 2014).

- **Ages related to the Pan-African / Cadomian orogenic cycles:** This age cluster comprises radiometric ages related to the Cadomian events. These widespread events, dated to have occurred from ca. 600 Ma to 450 Ma, represent a series of events of continental accretions at the margins of Gondwana which were to become involved into the preceding formation of the supercontinent Pangea. Extensive granitoid emplacement affected the pre-Variscan basement (von Raumer et al., 2013).

- **Ages related to Cambrian rifting stages**: These ages date from ca. 530-490 Ma and are associated with magmatism at the onset of the collapse of the Cadomian orogeny that gave rise to a rifting episode that marked the spreading of the Rheic ocean (Linnemann et al., 2004; Rossi et al., 2009). Stampfli et al. (2002) propose the drifting of pre-Variscan blocks away from Gondwana to form the European Hun terranes at the end of the Ordovician. These continental fragments constituted a ribbon-shaped accumulation along the North-African margin.

- **Ordovician-Silurian magmatism-related ages**: Continued collapse of the Cadomian orogeny lead to the opening of the Paleo-Tethys rift and progressive rifting of the Hun terrane in the Silurian (von Raumer et al., 2003). Consequently, Lower Paleozoic extensional tectonics gave rise to magmatism that is documented to have extensively occurred in Sardinia (Oggiano et al., 2010) as well as in the future External massifs (Argentera massif; cf. Rubatto et al., 2001; 2010). Gaggero et al. (2007) reported three distinct phases of magmatism in Sardinia that can be divided into events related to an Early Ordovician rifing stage, Middle Ordovician arc volcanism and an Upper Ordovician to Silurian stage of volcanism resultant from Continental drifting.

- **Ages representing events linked to the Variscan orogeny:** Resultant from the Permo-Carboniferous continental collision of Gondwana, Laurussia and numerous microcontinental fragments, Carboniferous magmatic events represent the most widespread zircon age signature amongst both Tethyan margins (e.g. von Raumer et al., 2003, Beltrán-Triviño et al., 2013). These events are represented by a series of granite emplacements (e.g. Calabria: Williams et al., 2012; Fornelli et al., 2016; Sardinia: Pavanetto et al., 2012; Corsica: Giacomini et al., 2008; Casini et al., 2012; Li et al., 2014; Ligurian Alps: Dallagiovanna et al., 2009; Maino et al., 2012; Internal massifs: Dora Maira: Sandrone et al., 1993; Manzotti et al., 2016; External massifs: Mont Blanc, Argentera: Ménot et al., 2004; Rubatto et al., 2001, 2011). Importantly, Variscan granitoids are more present in the Helvetic and Penninic basement than in that of the Southern Alps (Linnemann et al., 2008; cf. Beltrán-Triviño et al., 2013).

- **Ages associated to Post-Variscan magmatism**: Gravitational collapse of the thickened Variscan orogenic crust defined the Post-Variscan period (McCann et al., 2006). Alternating transpressional and transtensional tectonic regimes promoted the development of basins defined by strike-slip components in Central and Western Europe. These typical graben and half-graben structures are typically associated with syn-tectonic volcanic activity. Magmatic activity related to the initial orogen collapse is mostly documented from Calabria (Liotta et al., 2008), Sardinia (Ronca et al., 1999; Gaggero et al., 2017), and Corsica (Cabanis et al., 1990) as well as from the Southern Alps (e.g. Quick et al., 2009; Berra et al., 2014).

- **Ages attributed to Middle-Permian to Triassic magmatism:** Recent research documents a later stage of volcanism that can be restricted to have occurred in the Southern Alps (Beltrán-Triviño et al., 2013), in Calabria (Fornelli et al., 2011), Sardinia and Corsica (Traversa et al., 2003; Gaggero et al., 2007), as well as in the Liguria Alps (Dallagiovanna et al., 2009; Maino et al., 2012). These latter events are related to intense magmatic activity interpreted to reflect the onset of drifting since the Middle Triassic and might therewith epitomize the beginning of the Alpine cycle (cf. Beltrán-Triviño et al., 2013). It should furthermore be noted that these later-stage volcanic episodes can be separated from the Post-Variscan magmatic events by a period of strike-slip activity and intermittent granite emplacement (cf. McCann et al., 2006).

- **Ages younger than 230 Ma** These ages are interpreted as reflecting metasomatic and/or thermal overprinting events which resulted in Pb loss that are reported to have occurred widespread over the Western, Central and Southern Alps (e.g. Gebauer, 1993; Schaltegger & Gebauer, 1999; Rubatto, 2010; Maino et al., 2012; Zanetti et al., 2013). Given that, these ages are regarded as geologically meaningless in the context of the confrontation of detrital zircon ages against candidate source area datasets (cf. Geisler et al., 2007).

Potential source terrains

The results of modal composition analysis strongly suggest that the sediments were sourced from a rapidly exhumed continental basement block (dominantly granitoid plutons and minor contributions of low-grade metamorphic geobodies). With an overall contribution of 49.3% of all detrital ages, the dominant presence of zircon ages related to geodynamic events assignable to Variscan and post-Variscan events (Fig. 6.5 and Table 6.2), allows the assumption that specifically Variscan-age plutonic source rocks needs to be considered as representing the probable source of the siliciclastic Bordighera turbidite system. Consequently, plutonic source terranes distributed along the Southern Variscan belt margins are taking into consideration. According to available maps (e.g. von Raumer et al., 2002; Casini et al., 2015; see Fig. 6.11), the pre-Alpine continental basement assemblages of the Briançonnais presently preserved in the Ligurian Alps, the Dora-Maira Massif, the Argentera Massif, the Corsica-Sardinia Batholith as well as the Calabrian granitoid massifs are being verified as having provided the source of clastic detritus. Moreover, in the context of continental micro-fragments that constituted the reactivated hyperextended Western Tethyan margins, available geochronological data of the Sesia continental fragment of Southern Alpine heritage is incorporated into the analysis.

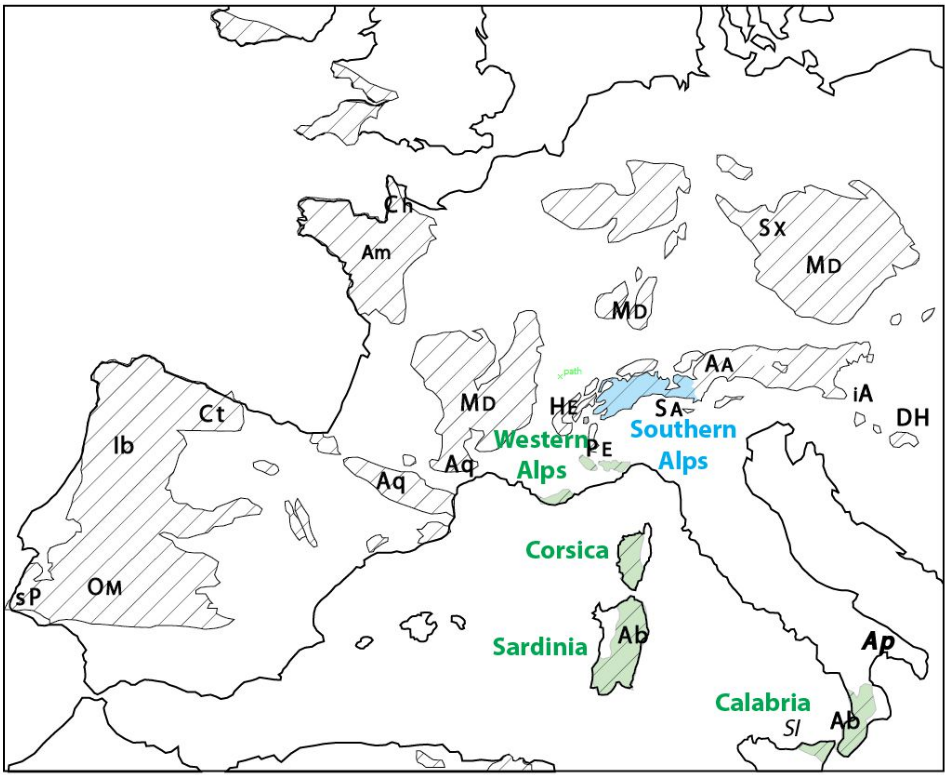

Fig. 6.11. Present day distribution of Variscan basement rocks in Western and Central Europe. Candidate source areas for the Western Tethys are highlighted in blue (Southern Alps paleogeographic domain) and green color (Paleo-European continental margin). Modified from von Raumer et al. (2002). *AA*: Austro-Alpine; *Ab*: Alboran; *Am*: Armorica; *Ap*: Apulia; *Aq*: Aquitaine; *Ch*: Channel terrane; *Ct*: Cantabria; *DH*: Dinarides-Hellenides; *He*: Helvetic; *iA*: intra-Alpine; *Ib*: Iberia; *MD*: Moldanubian; *OM*: Ossa-Morena; *Or*: Ortegal; *PE*: Penninic; *sP*: south-Portuguese; *Sx*: Saxothuringian.

Dataset compilation

Although recent studies emphasize on the qualitative correlation of U-Pb detrital ages and geochemical signatures to possible source area terrains in different Western Tethyan domains (Beltrán-Triviño et al., 2013; Li et al., 2016), none of these previous studies addressed a direct quantitative comparison of detrital and candidate provenance area crystallization age suites. An increasing number of provenance studies proves that the incorporation of statistical evaluation of detrital spectra signatures and their relation to conceivable parent rocks (e.g. Saylor et al., 2013; Pereira et al., 2016; Gärtner et al., 2017) enhances the understanding of source-to-sink relationships. This study attempts to present a combined visual, comparison and statistical evaluation of detrital spectra signatures against radiometric ages of potential source areas. Datasets were compiled according to the references listed below that provide U/Pb zircon crystallization ages for the following evaluated potential source areas, with "n" corresponding to the number of zircon ages incorporated:

Calabria (n = 266):

(1) Williams, I.S., Fiannacca, P., Cirrincione, R., Pezzino, A. (2012). Peri-Gondwanian origin and early geodynamic history of NE Sicily: a zircon tale from the basement of the Peloritani Mountains. Gondwana Research, 22, 855–865.

(2) Fornelli, A., Micheletti F., Piccarreta, G. (2016). Late‑Proterozoic to Paleozoic history of the peri‑Gondwana Calabria–Peloritani Terrane inferred from a review of zircon chronology. Springerplus, 5, 1-19.

(3) Liotta, D., Caggianelli, A., Krul, J.H., Festa, V., Prosser, G., Langone, A. (2008). Multiple injections of magmas along a Hercynian mid-crustal shear zone (Sila Massif, Calabria, Italy). Journal of Structural Geology, 30, 1202-1217.

Sardinia (n = 422)

(1) Giacomini, F., Bomparola, R.M., Ghezzo, C., Guldbransen, H. (2006). The geodynamic evolution of the Southern European Variscides: constraints from the U/Pb geochronology and gochemistry of the lower Paleozoic magmatic-sedimentary sequences of Sardinia (Italy). Contrib. Mineral. Petrol., 152, 19-42.

(2) Gaggero, L., Oggiano, G., Buzzi, L., Slejko, F., Cortesogno, L. (2007). Post-Variscan mafic dikes from the late orogenic collapse to the Tethyan rift: evidences from Sardinia. Ofioliti, 32, 15–37.

(3) Pavanetto, P., Funedda, A., Northrup, C.J., Schmitz, M., Crowley, J., Loi, A. (2012). Structure and U–Pb zircon geochronology in the Variscan foreland of SW Sardinia, Italy. Geological Journal, 47, 426-445.

(4) Gaggero, L., Gretter, N., Langone, A., Ronchi, A. (2017). U-Pb geochronology and geochemistry of late Paleozoic volcanism in Sardinia (southern Variscides). Geoscience Frontiers, 21, 1-22.

Corsica (n = 146):

(5) Giacomini, F., Dallai, L., Carminati, E., Tiepolo, M., Ghezzo, C. (2008). Exhumation of a Variscan orogenic complex: insights into the composite granulitic–amphibolitic metamorphic basement of south-east Corsica (France). J. metamorphic Geol., 26, 403–436.

(6) Casini, L., Cuccuru, S., Maino, M., Oggiano, G., Tiepolo, M. (2012). Emplacement of the Arzachena Pluton (Corsica–Sardinia Batholith) and the geodynamics of incoming Pangaea. Tectonophysics, 544-545, 31-49.

(7) Li, X.H., Faure, M., Lin, W. (2014). From crustal anatexis to mantle melting in the Variscan orogen of Corsica (France): SIMS U–Pb zircon age constraints. Tectonophysics, 634, 19–30.

Ligurian Alps (n = 189):

(8) Giacomini, F., Braga, R., Tiepolo, M., Tribuzio, R. (2007). New constraints on the origin and age of Variscan eclogitic rocks (Ligurian Alps, Italy). Contrib Mineral Petrol, 153, 29–53.
(9) Dallagiovanna, G., Gaggero, L., Maino, M., Seno, S., Tiepolo, M. (2009). U–Pb zircon ages for post-Variscan volcanism in the Ligurian Alps (northern Italy). Journal of the Geological Society, 166, 101–114.
(10) Maino, M., Dallagiovanna, G., Gaggero, L., Seno, S., Tiepolo, M. (2012). U–Pb zircon geochronological and petrographic constraints on late to postcollisional Variscan magmatism and metamorphism in the Ligurian Alps, Italy. Geological Journal, 47, 632-652.

Dora Maira (n = 111):

(11) Bussy, F. & Cadoppi, P. (1996). U-Pb zircon dating of granitoids from the Dora-Maira massif (western Italian Alps). Schweizerische mineralogische Mitteilungen, 76, 217-233.
(12) Paquette, J.L., Montel, J.M., Chopin, C. (1999). U-Th-Pb dating of the Brossasco ultra high-pressure metagranite, Dora-Maira massif, western Alps. Eur. J. Mineral., 11, 69-77.

Argentera (n = 81):

(13) Rubatto, D., Schaltegger, U., Lombardo, B. (2001). Complex Paleozoic magmatic and metamorphic evolution in the Argentera Massif (Western Alps) resolved by U-Pb dating. Schweizerische Mineralogische Mitteilungen, 81, 213-228.
(14) Rubatto, D., Ferrando, S., Compagnoni, R., Lombardo, B. (2010). Carboniferous high-pressure metamorphism of Ordovician protoliths in the Argentera Massif (Italy), Southern European Variscan belt. Lithos, 116, 65-76.
(15) Manzotti, P., Ballèvre, M., Poujol, M. (2016). Detrital zircon geochronology in the Dora-Maira and Zone Houillère: a record of sediment travel paths in the Carboniferous. Terra Nova, 28 (4), 279-288.

Sesia (n = 89):

(16) Liermann, H.-P., Isachsem, C., Altenberger, U., Oberhänsli, R. (2002). Behaviour of zircon during high-pressure, low-temperature metamorphism: Case study from the Internal Unit of the Sesia Zone (Western Italian Alps). European Journal of Mineralogy, 14, 61-71.
(17) Furrer, H., Schaltegger, U., Ovtcharova, M., Meister, P. (2008). U-Pb zircon age of volcaniclastic layers in Middle Triassic platform carbonates of the Austroalpine Silvretta nappe (Switzerland), Swiss Journal of Geosciences, 101, 595–603.
(18) Galli, A., Le Bayon, B., Schmidt, M.W., Burg, J.P., Reusser, E., Sergeev, S.A., Larionov, A. (2011). U-Pb dating of the Gruf Complex: disclosing the late Variscan granulitic lower crust of Europe stranded in the Central Alps. Contrib. Minerl. Petrol., 163, 353-378.
(19) Klötzli, U. S., Sinigoi, S., Quick, J.E., Demarchi, G., Tassinari, C.C.G., Sato, K., Günes, Z. (2014). Duration of igneous activity in the Sesia Magmatic System and implications for high-temperature metamorphism in the Ivrea–Verbano deep crust. Lithos, 206–207, 19–33.

Visual confrontation of detrital zircon ages against candidate source area crystallization ages

The obtained detrital ages, together with the above discussed chronological datasets (U-/Pb) ages of candidate source areas available from literature, have been plotted with the DZStats software to identify overlapping peaks in probability density function and similarities in cumulative age distribution functions (Fig. 6.12). The combined cumulative suite comprising cumulative detrital zircon ages from both the Monte Frontè samples as well as from the Cima di Velega section suits well into the dataset of all available ages from literature (Fig. 6.12 A, yellowish area highlighted in the CDF plot on the right-hand side). Nevertheless, the closest resemblance occurs with the dataset derived from the Calabrian Massifs. A further closely similar cumulative density function curve is represented by the available ages of the Dora-Maira. The huge distance in between the detrital spectra is regarded as reflecting the scarcity of Upper Devonian to Carboniferous ages in the Sesia sample that characterizes the continental basement of the Southern Alps (e.g. Linnemann et al., 2008, Beltrán-Triviño et al., 2013).

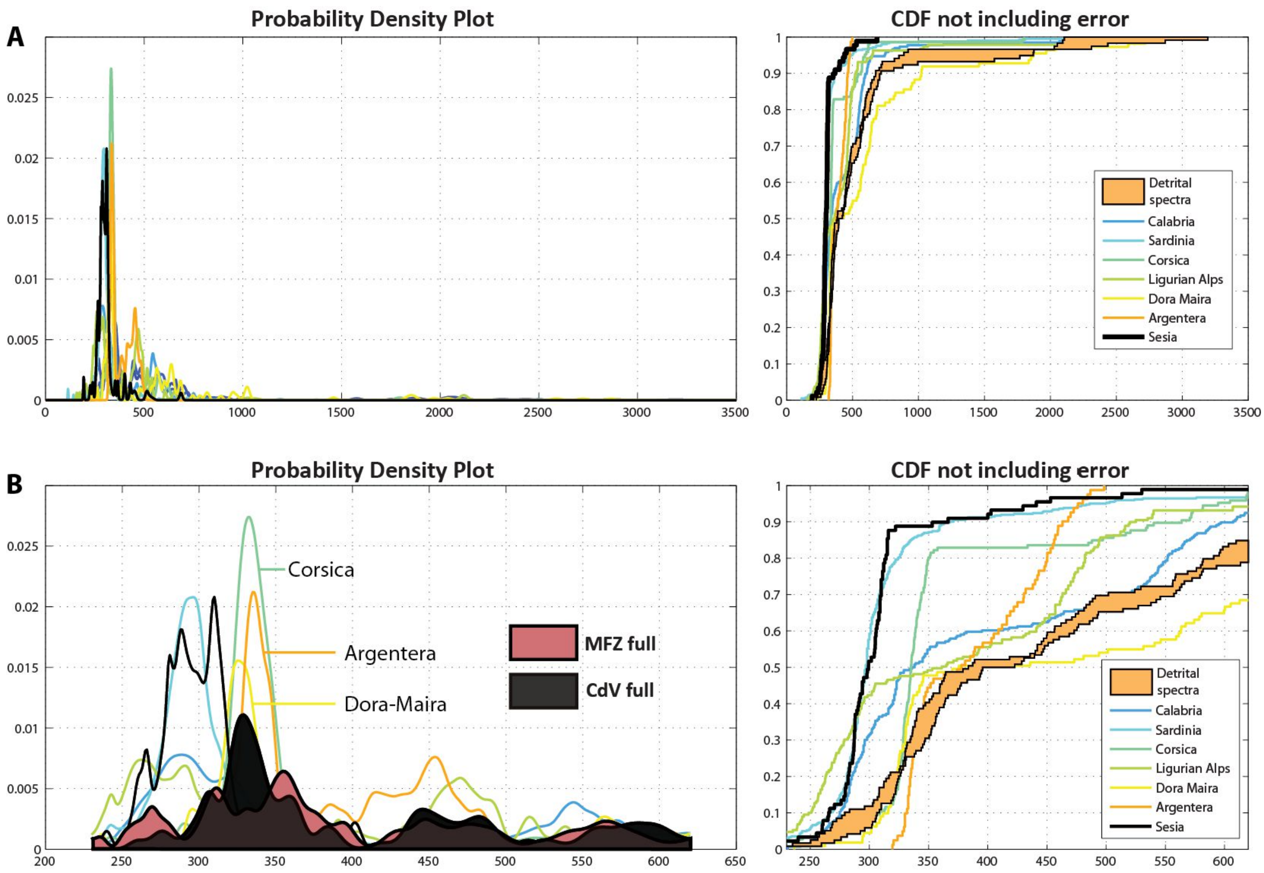

Fig. 6.12. Visual confrontation of the detrital age spectra against candidate source area crystallization ages (probability density function plots) and cumulative distribution functions for A) the period from 0 Ma to 3500 Ma and B) for the period between 230 Ma and 620 Ma. MFZ_full corresponds to combined Monte Fronte samples (MFZ_1bis & MFZ_4bis); CdV_full corresponds to combined Cima di Velega samples (CdVZ_1 and CdVZ_4).

Furthermore, the isolated examination of the time interval between 230 Ma and 620 Ma (Fig. 6.12 B) has been chosen for qualitative comparison. Confrontation of detrital ages against geochronologically better established datasets of magmatic and metamorphic episodes documented in the crystalline bed rocks cropping out along both Western Tethyan margins is regarded as providing more detailed insights into the contributions of individual candidate source terranes. Probability density plot peaks comprise a major overlapping in between the detrital suite and Corsica, Argentera Massif and the Dora-Maira Massif within the time interval ranging from ca. 300 to 370 Ma. Another recognizable peak is shared in between the detrital suite and the Ligurian Alps and the Argentera Massif in the time span between ca. 420 and 500 Ma. One specifically young, narrower peak corresponding to the time span between ca. 250 Ma and 280 Ma is only shared between the Monte Frontè detrital ages and Calabria, Sardinia, the Ligurian Alps and Sesia. Moreover, the comparative analysis of the detrital zircon age populations within the short time span ranging from ca. 250 Ma to 280 Ma reveals substantial differences since the combined Monte Frontè sample displays a significant tendency of younger detrital ages becoming more abundant.

Statistical comparison of the detrital age spectra and potential provenance datasets

Statistical tests that were applied to address the quantitative evaluation of both inter-sample similarity and resemblance towards candidate source areas included the analysis of the cross-correlation efficient (Gehrels, 2000), the likeness coefficient and the similarity coefficients of probability density function plots (Satkoski et al., 2013). Cross-correlation, likeness and similarity coefficients with a value of 1 are defined as implying an origin of the confronted age spectra from the same parent population (cf. Saylor & Sundell, 2016). For both the cross-correlation coefficient and the likeness coefficient, threshold values for "similar" distributions have been defined as ranging from 1 to 0.6, whereas the threshold limit for "similar" disseminations of the similarity coefficient have been outlined as including values in between 1 and 0.8. Furthermore, with the emphasis on providing statistically rigorous comparisons, the Kolmogorov-Smirnov test was conducted. A p-value threshold of 0.05 was adopted (cf. Saylor & Sundell, 2016) in order to apprehend whether two compared age populations were derived from the same parent population. Results of the statistical evaluation are shown in Table 6.3.

Cross-correlation coefficient values reveal the closest quantitative relationship of the detrital suite to the samples from Calabria, the Ligurian Alps and the Dora-Maira Massif. Particularly the MFZ_4 sample divulges marked similarity with the sample from the Ligurian Alps. Moreover, an appreciable resemblance in between the detrital samples MFZ_1, CdVZ_1 and CdVZ_3 can be noted, whereas the

Cross Correlation Coefficient											
	MFZ_1	MFZ_4	CdV_1	CdV_4	Calabria	Sardinia	Corsica	Lig. Alps	Dora-Maira	Argentera	Sesia
MFZ_1	1	0.26151	0.75565	0.67327	0.31304	0.08853	0.39012	0.13046	0.44139	0.51891	0.05495
MFZ_4	0.26151	1	0.41990	0.51140	0.76437	0.48205	0.12991	0.79048	0.27119	0.19886	0.41338
CdV_1	0.75565	0.41990	1	0.81149	0.54349	0.25776	0.58249	0.21173	0.77621	0.54951	0.21505
CdV_4	0.67327	0.51140	0.81149	1	0.55374	0.24313	0.56737	0.28802	0.65390	0.68929	0.18234
Calabria	0.31304	0.76437	0.54349	0.55374	1	0.71410	0.24512	0.54580	0.43186	0.16117	0.61039
Sardinia	0.08853	0.48205	0.25776	0.24313	0.71410	1	0.07463	0.41623	0.18954	0.02899	0.86746
Corsica	0.39012	0.12991	0.58249	0.56737	0.24512	0.07463	1	0.03048	0.75373	0.67002	0.02250
Lig. Alps	0.13046	0.79048	0.21173	0.28802	0.54580	0.41623	0.03048	1	0.06941	0.12225	0.33724
Dora-Maira	0.44139	0.27119	0.77621	0.65390	0.43186	0.18954	0.75373	0.06941	1	0.45649	0.14632
Argentera	0.51891	0.19886	0.54951	0.68929	0.16117	0.02899	0.67002	0.12225	0.45649	1	0.00581
Sesia	0.05495	0.41338	0.21505	0.18234	0.61039	0.86746	0.02250	0.33724	0.14632	0.00581	1
Likeness value											
	MFZ_1	MFZ_4	CdV_1	CdV_4	Calabria	Sardinia	Corsica	Lig. Alps	Dora-Maira	Argentera	Sesia
MFZ_1	1	0.54967	0.72580	0.64359	0.52416	0.28848	0.45042	0.38945	0.56331	0.49070	0.20923
MFZ_4	0.54967	1	0.59699	0.60969	0.67175	0.45004	0.35253	0.69719	0.49341	0.32138	0.39735
CdV_1	0.72580	0.59699	1	0.69723	0.60885	0.37821	0.48214	0.43178	0.65207	0.47074	0.29258
CdV_4	0.64359	0.60969	0.69723	1	0.62962	0.40282	0.52672	0.51768	0.60102	0.57806	0.30320
Calabria	0.52416	0.67175	0.60885	0.62962	1	0.61052	0.43485	0.57984	0.54742	0.30239	0.50288
Sardinia	0.28848	0.45004	0.37821	0.40282	0.61052	1	0.29297	0.47066	0.35943	0.21321	0.76111
Corsica	0.45042	0.35253	0.48214	0.52672	0.43485	0.29297	1	0.25950	0.56523	0.49513	0.21667
Lig. Alps	0.38945	0.69719	0.43178	0.51768	0.57984	0.47066	0.25950	1	0.28920	0.37477	0.43792
Dora-Maira	0.56331	0.49341	0.65207	0.60102	0.54742	0.35943	0.56523	0.28920	1	0.37071	0.26165
Argentera	0.49070	0.32138	0.47074	0.57806	0.30239	0.21321	0.49513	0.37477	0.37071	1	0.13607
Sesia	0.20923	0.39735	0.29258	0.30320	0.50288	0.76111	0.21667	0.43792	0.26165	0.13607	1
Similarity value											
	MFZ_1	MFZ_4	CdV_1	CdV_4	Calabria	Sardinia	Corsica	Lig. Alps	Dora-Maira	Argentera	Sesia
MFZ_1	1	0.77554	0.88046	0.85006	0.78188	0.60822	0.68739	0.67423	0.81048	0.72615	0.46949
MFZ_4	0.77554	1	0.82212	0.83936	0.89411	0.75394	0.62585	0.88618	0.75409	0.56233	0.66833
CdV_1	0.88046	0.82212	1	0.85790	0.84636	0.68930	0.72405	0.70613	0.84225	0.69248	0.56753
CdV_4	0.85006	0.83936	0.85790	1	0.88577	0.73231	0.79526	0.80519	0.79678	0.77475	0.61573
Calabria	0.78188	0.89411	0.84636	0.88577	1	0.83927	0.74772	0.83926	0.79210	0.55571	0.74918
Sardinia	0.60822	0.75394	0.68930	0.73231	0.83927	1	0.63843	0.79884	0.64151	0.46260	0.91907
Corsica	0.68739	0.62585	0.72405	0.79526	0.74772	0.63843	1	0.55420	0.78494	0.66511	0.48414
Lig. Alps	0.67423	0.88618	0.70613	0.80519	0.83926	0.79884	0.55420	1	0.60185	0.59526	0.72062
Dora-Maira	0.81048	0.75409	0.84225	0.79678	0.79210	0.64151	0.78494	0.60185	1	0.56573	0.51229
Argentera	0.72615	0.56233	0.69248	0.77475	0.55571	0.46260	0.66511	0.59526	0.56573	1	0.33934
Sesia	0.46949	0.66833	0.56753	0.61573	0.74918	0.91907	0.48414	0.72062	0.51229	0.33934	1
K-S test p value											
	MFZ_1	MFZ_4	CdV_1	CdV_4	Calabria	Sardinia	Corsica	Lig. Alps	Dora-Maira	Argentera	Sesia
MFZ_1	1	0.00287	0.10868	0.02304	0.00000	0.00000	0.00000	0.00000	0.00075	0.00006	0.00000
MFZ_4	0.00287	1	0.00886	0.14789	0.12589	0.00000	0.00000	0.00402	0.00992	0.00011	0.00000
CdV_1	0.10868	0.00886	1	0.18127	0.00005	0.00000	0.00000	0.00000	0.50738	0.00003	0.00000
CdV_4	0.02304	0.14789	0.18127	1	0.00013	0.00000	0.00002	0.00003	0.00741	0.02719	0.00000
Calabria	0.00000	0.12589	0.00005	0.00013	1	0.00000	0.00000	0.00023	0.00000	0.00000	0.00000
Sardinia	0.00000	0.00000	0.00000	0.00000	0.00000	1	0.00000	0.00000	0.00000	0.00000	0.25540
Corsica	0.00000	0.00000	0.00000	0.00002	0.00000	0.00000	1	0.00000	0.00000	0.00000	0.00000
Lig. Alps	0.00000	0.00402	0.00000	0.00003	0.00023	0.00000	0.00000	1	0.00000	0.00000	0.00000
Dora-Maira	0.00075	0.00992	0.50738	0.00741	0.00000	0.00000	0.00000	0.00000	1	0.00000	0.00000
Argentera	0.00006	0.00011	0.00003	0.02719	0.00000	0.00000	0.00000	0.00000	0.00000	1	0.00000
Sesia	0.00000	0.00000	0.00000	0.00000	0.00000	0.25540	0.00000	0.00000	0.00000	0.00000	1

Table 6.3. Statistical evaluation of similarity in between the detrital suite and potential source areas.

MFZ_4 sample coefficient denotes the limited similarity with the otherwise quite homogeneous samples. A similar scenario can be observed by comparing the likeness coefficient values. Samples from Calabria, the Ligurian Alps and the Dora-Maira Massif again display the closest similitude towards huge parts of the detrital spectrum. However, the MFZ_1 sample can be excluded from this hypothesis. Noteworthy, the MFZ_4 sample once more displays minor similarities with the other detrital samples. Comparison of calculated similarity coefficient values again demonstrates the resemblance with the chronological datasets from Calabria, the Ligurian Alps and the Dora-Maira Massif. Among the detrital samples, a closer relationship can be inferred, even if the lowest coefficient value can be noted in between the two Monte Frontè samples. The KS-test is interpreted to apparently demonstrate inadequate reliability, as on the one hand even internal comparisons of the detrital samples partially fail the test. Comparison to potential source areas signifies that all p-values except for Calabria and Dora-Maira fall below the threshold. On the other hand, the inexplicably high p-value of 0.5 that defines the comparison of the CdV_1 sample and the Argentera dataset might additionally reveal the vagueness of the results of the KS-test.

Stratigraphic trends in detrital zircon age distributions

The evaluation of statistical similarity detected a notable trend of variabilities within the detrital suite. A detailed analysis considering conceivable stratigraphic necessitates the division of the detrital spectra into its individual components. Relative proportions of distinct detrital populations of the two basal samples of the Bordighera Sandstones (MFZ_1 and CdVZ_1) proves their reasonable similarity (See pie-charts in Fig. 6.13). However, a distinct divergence in detrital age populations distribution can be observed in between the topmost samples (MFZ_4 and CdVZ_3). The sample from the uppermost Monte Frontè section displays a peculiar tendency of an increased relative proportion of younger age populations (See also Table 6.4). Zircon crystallization ages interpreted to be directly linked to the Variscan orogeny merely account for a very minor proportion of the overall distribution (3.9%). By contrast, detrital ages assignable to Variscan events represent the most abundant constituent in all other samples, comprising a relatively consistent share of the detrital spectra (36.3% - 42.4%). Moreover, contrasting to other samples that comprise age spectra in which detrital ages related to magmatic events in the context of the post-orogenic collapse are either not present at all or make up a maximum proportion of 1.7 %, in the MFZ_4 sample these are strongly represented as they account for 21.2 % of all zircon ages. Together with Early Permian zircon ages related to the Post-Variscan gravitational collapse of the orogen that make up 17.3% of the share, the overall contribution of 38.5% of detrital ages younger than the otherwise dominant Variscan event makes up the dominant proportion of the detrital spectra.

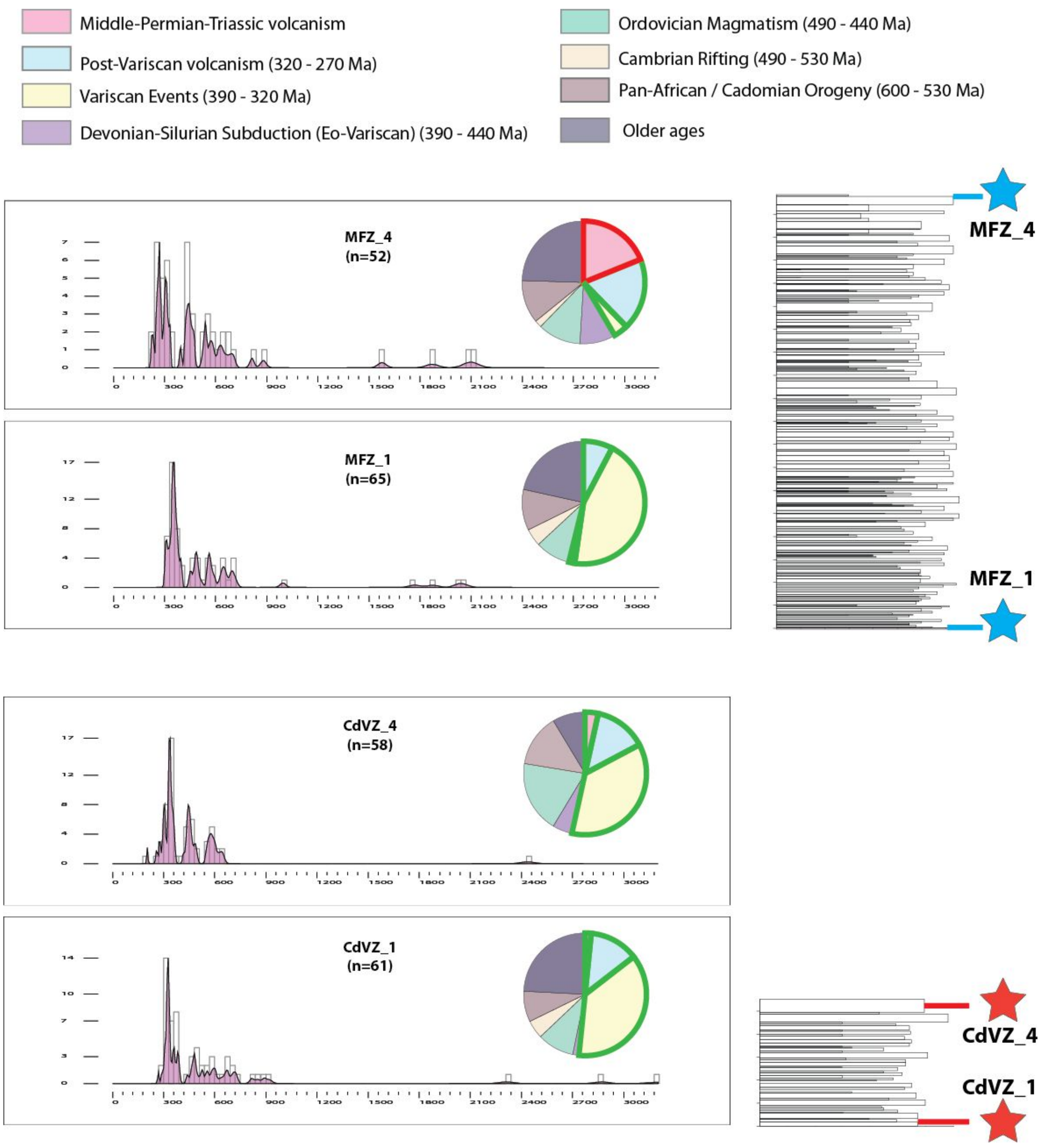

Fig. 6.13. Visual comparison of stratigraphic trends in probability density population distributions and relative abundances of age groups (pie-charts) of individual samples of the Bordighera Sandstones (PDP plots spanning from 0 to 3500 Ma). Detrital zircon ages reveal significant stratigraphic-upward variation in zircon age populations in between the lithostratigraphically equivalent BGS samples. Striking distributions of relative of age groups are highlighted in red color.

	MFZ_1	MFZ_4	CdV_1	CdV_3
ages < 230 Ma	0.0%	0.0%	0.0%	1.7%
Mid-Permian to Triassic Volcanism	0.0%	17.3%	0.0%	1.7%
Post-Variscan orogeny collapse	7.6%	21.2%	11.6%	13.8%
Variscan events	42.4%	3.9%	39.3%	36.3%
Devonia-Silurian subduction	4.5%	9.6%	1.6%	3.4%
Ordovician magmatism	9.2%	11.5%	9.8%	19.0%
Cambrian rifting stage	4.5%	1.9%	4.9%	1.7%
Cadomian events	10.6%	11.5%	8.2%	13.8%
ages > 600 Ma	21.2%	23.1%	24.6%	8.6%
	100%	100%	100%	100%

Table 6.4. Relative proportions of age groups in the Bordighera Sandstone detrital suite.

Statistical evaluation of the observed stratigraphic diversity

In order to verify the visually evident hypothesis that the detrital spectrum of the Bordighera Sandstones is characterized by statistical dissimilarity might suggest that the sedimentary system has been subject to marked changes in source contributions throughout its stratigraphic evolution, statistical test have been applied to the reduced time interval spanning from 200 to 1000 Ma. Importantly, the apparently matching cumulative distribution of detrital populations younger than 800 Ma defines the basal samples (MFZ_1 and CdVZ_1; Fig. 6.14 A). Minor mismatches are solely observable within the short time span ranging from ca. 270 to 300 Ma and within the time interval in between 800 and 950 Ma in which the MFZ_1 sample does not exhibit a detrital signature. By sharp contrast, the topmost samples are characterized by divergent age population distributions throughout the entire detrital spectra (Fig. 6.14 B). Despite for the time interval between ca. 800 and 950 Ma, the detrital populations of the MFZ_4 sample generally display younger age peaks than those derived from the CdVZ_3 sample. In direct statistical comparison, the basal samples are marked by consistently higher cross-correlation, likeness and similarity coefficients than the topmost samples (Fig. 6.14 A&B). However, taking these statistical evaluations of the cross-correlation, likeness and similarity coefficients as well as the visually apparently dissimilarity in between the basal and the topmost samples into account, the reduced KS-test p-value derived from the comparison of the MFZ_4 and the CdVZ_3 samples that would suggest a closer similarity. This observation might provide contentions concerning the reliability of the KS-test.

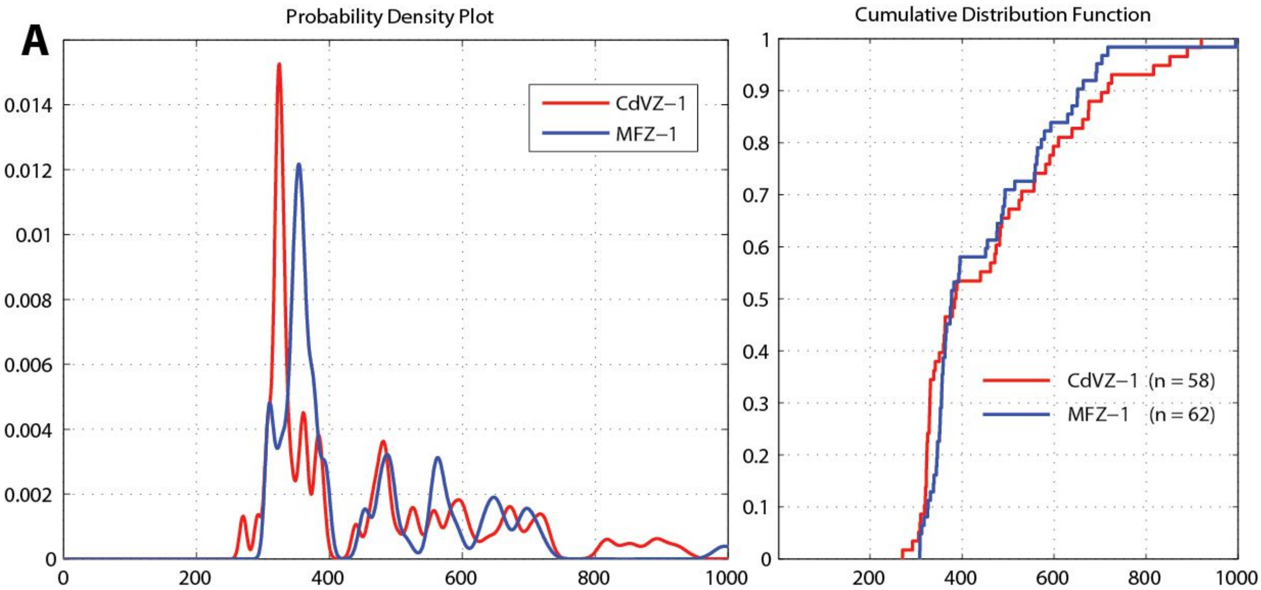

Cross correlation Coefficient	Likeness	Similarity	K-S p value
0.326	0.633	0.868	0.1

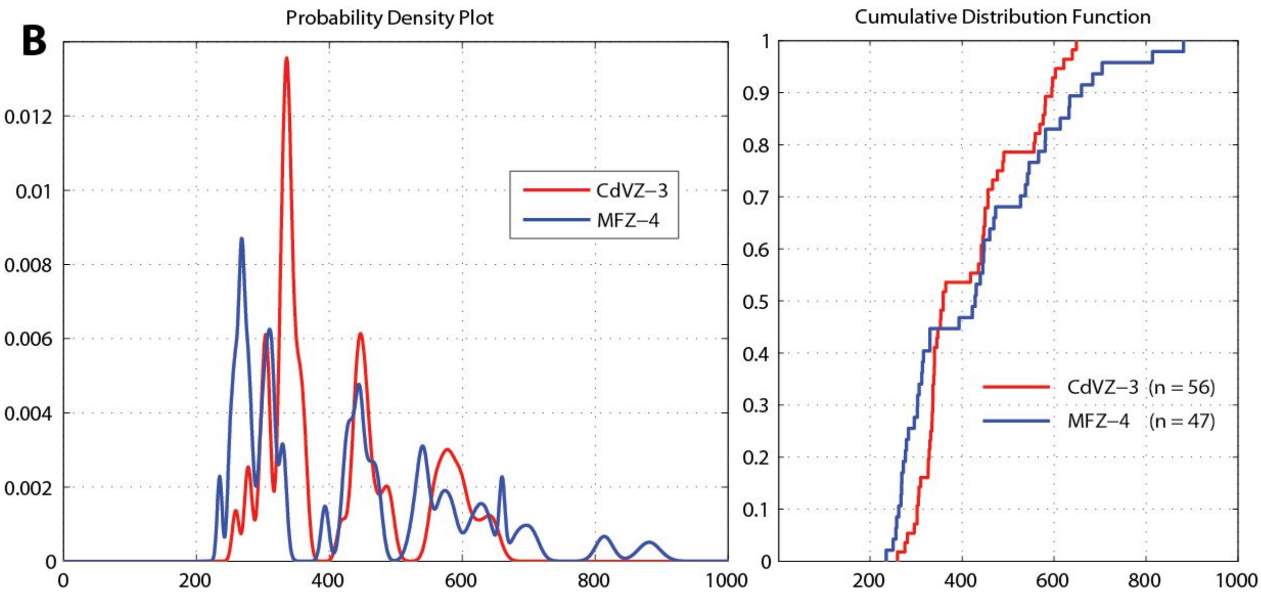

Cross correlation Coefficient	Likeness	Similarity	K-S p value
0.181	0.542	0.757	0.081

Fig. 6.14. Statistical evaluation of stratigraphic differences in detrital age spectra between A) basal detrital zircon age distributions of the BGS (MFZ_1 and CDV_1 samples) and B) the topmost (MFZ_4 and CdVZ_3 samples). Note the presence of two peaks of young detrital zircon ages (ca. 235 Ma and ca. 260 – 280 Ma) in the MFZ_4 sample. The statistically evaluated age interval ranges from 200 Ma to 1000 Ma.

Interpretation of the qualitative and quantitative comparison of the detrital spectra and potential source area crystallization ages from literature and implications for the source area

Qualitative and quantitative analysis of the detrital spectra revealed the presence of three major peaks that can practicably be attributed to magmatic and metamorphic episodes related to the Variscan orogeny (330 Ma and 357 Ma), ages representative of Ordovician to Silurian magmatism (447 Ma and 480 Ma) and a peak ascribable to events of the Cadomian orogeny (564 Ma). The confrontation of the detrital age spectra against the compiled dataset of available geochronological data of potential source areas reveals that these major peaks show marked overlapping with well-constrained stages of crystallization documented in the Southern Variscides that crop out along both the Western and Eastern margins of the Alpine Tethys. Nevertheless, basement rocks that represent the western European margin, the Adrian margin, and probable continental micro-fragments that were incorporated (e.g. Handy et al., 2010; Rubatto et al., 2011) exhibit a strongly similar crustal composition and pre-Alpine geodynamic heritage and thus record similar re-setting patterns in their zircon age distributions (e.g. Dal Piaz, 2001; von Raumer et al., 2003; Dallagiovanna et al., 2009; Chu et al., 2016).

According to the results derived from statistical comparisons, and likewise based on the absence of the Late Devonian to Carboniferous age population in the Sesia continental fragment, this supposed candidate provenance terrane can be ruled out (see Thomas et al., 2010 for discussion on deifferent European and African margin detrital zircon signatures). Importantly, with respect to the Southern Alpine inheritance (e.g. Schaltegger & Gebauer, 1999; Weber et al., 2015), the Sesia fragment hence epitomizes the active margin. The exclusion of the paleogeographic affinity of the source to the Adriatic margin hence dismisses the active margin of the Alpine Tethys. Moreover, chronological studies suggest that the Sesia fragment was subjected to a temporally complex history defined by subduction metamorphism in Late Cretaceous times (Rubatto et al., 2011). Reasoning from this fact, the detrital zircon study proves that the Northwestern margin (i.e. the Paleo European continental margin) provided the provenance of the Bordighera turbidite system. Nonetheless, even if marked by the abovementioned similar geological history, the precisely dated Post-Variscan and Early Permian magmatic events that are recorded in the basement that represents the European margin might provide further evidences to establish the likely provenance of the coarse-clastic detritus.

The documented youngest detrital age peaks of the topmost Monte Frontè sample (ca. 270 – 240 Ma) are rationally attributable to compatible Middle Permian volcanic events that are reported from Calabria, Sardinia, Corsica and the Ligurian Alps (Traversa et al., 2003; Gaggero et al., 2007, 2017; Dallagiovanna et al., 2009; Maino et al., 2012). In the context of a turbidite system characterized by an overall retrogradational pattern, the recognized presence of a such detrital signal in a strata representative of the ultimate stage of coarse-clastic sedimentation is interpreted to imply a modification in source area configuration during the latest phase of basin fill. On that basis, the key question that arises is whether this substantial shift that apparently occurred on the expense of the in all other samples dominating Variscan age associations could demonstrate a substantial modification of hinterland drainage networks that affected a heterogeneous source (e.g. Cawood et al., 2003; Link et al., 2005; Tatzel et al., 2015; Blum & Pecha, 2014). A such scenario, although reasonable, is however difficult to confirm, as, with respect to the enormous crustal shortening and related displacement of during continent-continent collision, a limited preservation potential of source-to-sink trajectories can be expected.

An alternative explanation could be that this shift in dominant proportions of the detrital zircon assemblage probably indicates the activation of a regional source area that exposed divergent lithologies. In this scenario, an additional sediment entry point of coarse-clastic detritus became increasingly important during later stages of basin fill evolution. Two divergent scenarios could be considered as promoting a such shift in of the dominant provenance terrain. On the one hand, a regional-scale longitudinal migration of remobilized local sediment sources due to the growing accretionary prism could explain increased lateral input. The study of trench-fill deposits along the modern Chile trench (Thornburg & Kulm, 1987) documents a such importance of multiple transversal entry points that supplied axial trench channels. Nonetheless, the study concerns axial trench fills that are supplied from the upper plate. With respect to the omission of the Adriatic Margin and hence the upper plate as the principal source area, this comparison appears to be of limited reliability.

On the other hand, evidence for a comparatively similar evolution to that of the Bordighera turbidite system has been documented from fossil trench systems. Based on deviating detrital zircon spectra, Malkowski et al. (2015) report a longitudinal shift of sediment entry points from the Upper Cretaceous Paleo-South American margin. This documented longitudinal alteration of sourcing areas is regarded as being induced due to longitudinally migrating basement uplift in the context of arc-continent collision. Principally oblique convergence characterized the transition from remnant ocean closure to the initial stages of foreland basin development and is interpreted as representing the major controlling on the evolution of an initially point-source fed turbidite system into a system sourced by multiple transverse sources.

Results from modal framework analysis imply that uplifted basement blocks provided the source of the texturally immature arkosic arenites. The results obtained from detrital zircon chronology allow the ascription of the source area to the lower plate. A reasonable explanation for basement uplift at the lower plate would be lithospheric flexure due to tectonic loading of the overthrust wedge that affected the continental margin of the subducted plate and facilitated the development of a flexural forebulge (e.g. Stockmal et al., 1987; DeCelles & Giles, 1996; Einsele, 2000). Stockmal et al. (1987) modeled the response of sedimentary systems to uplift and differentiated in between young crust that is defined by low flexural rigidity and old crust that is typified by high flexural rigidity. Not surprisingly, results of the simplified modeling validate that enlarged sediment yield due to greater uplift of the shelf along older margins. The modeling results deduce that the thermal state of the lithosphere moreover controls the distance between the overthrust load and the flexural bulge, as older margins are characterized by greater flexural wavelengths. The resultant differing position of the hinge line with respect to the shelf might thus explain the observed variations in sediment volume. Allen & Allen (2005) suggest that the continental lithosphere does not necessarily reveal a proportional relationship between flexural rigidity and the age of the lithosphere. Complexity might arise from the fact that continental lithosphere is likely subjected to regional differences in geothermal gradient and decoupling between the lithospheric mantle and the superimposing upper crust during bending. Moreover, the authors highlight the importance of the inherited fabric of continental lithosphere, as the inherited structural segmentation might result in stepped flexural deformation.

A such scenario of a flexural bulge migrating parallel to the frontal thrust can straightforwardly be integrated into paleogeographic and tectonic models that address the reconstruction of the evolution of the Western Alps. These models (e.g. Schmid et al. 1996; Lister et al. 2001; Rosenbaum and Lister 2005; Handy et al. 2010) demonstrate that deformation and metamorphism hugely migrated in a NW-ward directed orientation. However, it should be noted that the spatial and temporal magnitudes of deformation remain poorly constrained (Lister et al. 2001; Ford et al., 2006). Resultant from the protracted extensional evolution that characterized the onset of the Alpine cycle, the structural inheritance of the reactivated hyperextended European continental margin is inferred to have been extensively dissected by major transcurrent faults (e.g. Mohn et al., 2010; DeCarlis et al., 2014; Malusa et al., 2015). Given a such structural context, oblique convergence is hence interpreted as having induced the NW-directed, craton-ward propagation of the hinge line of the flexural bulge. The gradual provenance evolution in between from the San Bartolomeo Formation to the first-cycle Bordighera Sandstones, defined by minor compositional differences in between the essential grain proportions, is interpreted to support this assumption. Oblique convergence is inferred to have resulted in asymmetric basement uplift that affected different domains of the European margin in a stepwise fashion. Consequently, asymmetric reactivation of the dissected parts of the margin might have ensued in a stratigraphic evolution characterized by the activation of additional transversal submarine canyon systems (Malkowski et al., 2015; cf. Stow et al., 1983).

6.6 Integration of paleocurrent dispersal and facies distribution trends

With respect to the overall South-North directed facies trend determined by sedimentary facies analysis, supported by the observed paleocurrent trends that reveal a reasonably unidirectional N-NE orientation of main sediment flux, the paleogeographic position of the staging area of the coarse-grained axial basin fill can be inferred to have been located to the South-Southwest of the Bordighera turbidite system. Notwithstanding, essentially in the medial to distal domain of the system, considerable variations in paleocurrent orientation have been observed (Fig. 6.15). Although interpreted as being the consequence of a marked loss in the degree of confinement and enhanced turbulence as flows underwent transformation, as stated above, these deviations might otherwise indicate lateral sediment input. Regardless of the origin of the inconsistent paleocurrent dispersal observed at the Monte Frontè section, no direct paleocurrent observation could have been determined from the bed that bared the MFZ_4 zircons.

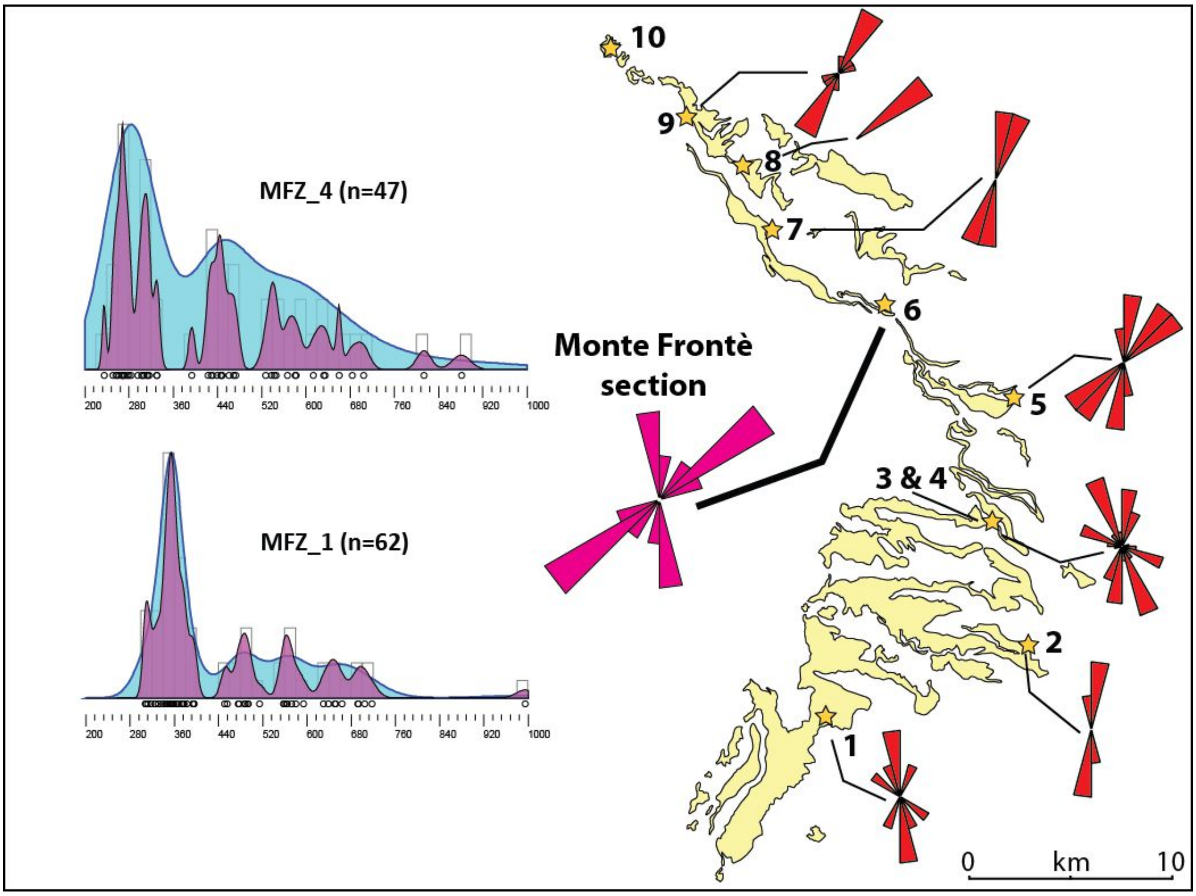

Fig. 6.15. Measured paleocurrent dispersal of the Bordighera Sandstones. Note the inconsistent paleocurrent pattern determined for the Monte Frontè section and the substantial up-section shift in detrital zircon signature (time range 200-800 Ma).

4.7 Discussion

Paleogeographic scenarios for the Upper Cretaceous Piemont-Ligurian ocean

Integrating the results from modal framework analysis, paleocurrent dispersal and the statistical evaluation of detrital zircon ages, two principal paleogeographic and geodynamic scenarios can be proposed (Fig. 6.16). Both models are divided into two distinct time-steps that represent the initial and final periods of sedimentation of the Bordighera turbidite system. As revealed by the detrital zircon signature, the exclusive staging of sediment gravity flows from the Paleo-European margin builds the framework of both models. The first scenario (Fig. 6.16 A) implies an initial stage of coarse-clastic sedimentation that was characterized by the input of texturally and compositionally immature sediments derived from basement uplift. The dominant peaks of Carboniferous zircon ages, along with the results from modal framework analysis, suggests that uplift of Variscan-age granitoid plutons and low-grade metamorphic geobodies provided the bulk of sediments. With respect to the general paleocurrent pattern and the close correspondence of detrital ages to crystallization ages of both Corsica and Sardinia, the initial style of coarse turbiditic sedimentation can be inferred as being typified by the development of point-sourced axial trench fan staged in ultimate vicinity to the Corso-Sardinian block (Fig. 6.16 A1). As revealed by the input of younger detrital zircon ages in the topmost Monte Frontè sample, the latest stages of sedimentation, in the context of a retrograding system, were typified by the increasingly important additional contribution of younger detrital material. Acknowledging the well-documented existence of post-Variscan volcanic episodes that typified the Briançonnais domain, the reworking of volcaniclastic detritus is regarded as providing the most reasonable explanation for the documented shift towards younger detrital ages. As discussed above, this later-stage activation of the Briançonnais domain can be related to the inferred oblique migration of the hinge line of the flexural bulge. Consequently, the addition of this transversal entry point defines the stratigraphic evolution of the system typified by the transition from a point-sourced axial fan into a transversal-sourced sand-rich ramp that might have induced the existence of coalescing sand-rich fans during progressed stages of ocean closure (Fig. 6.16 A2).

The second scenario (Fig. 6.16 B) accounts for intense detrital mixing that can be inferred from the statistical confrontation of the detrital signature against potential source area datasets. Taking the increased qualitative similarity towards the Calabria dataset into consideration, significant contribution from Calabria should not be ruled out. The first time-step (Fig. 4.16 B1), comparable to the previously suggested model, infers a contribution of granitoid-derived coarse-clastic sediment derived from uplifted basement of the Southern Variscides. Based on the relationship towards the detrital zircon spectra, Calabria is regarded as having contributed to the immature clastic detritus. Numerous models (e.g. Alvarez & Shimabukuro, 2009; Handy et al., 2010; Molli & Malavieille, 2011)

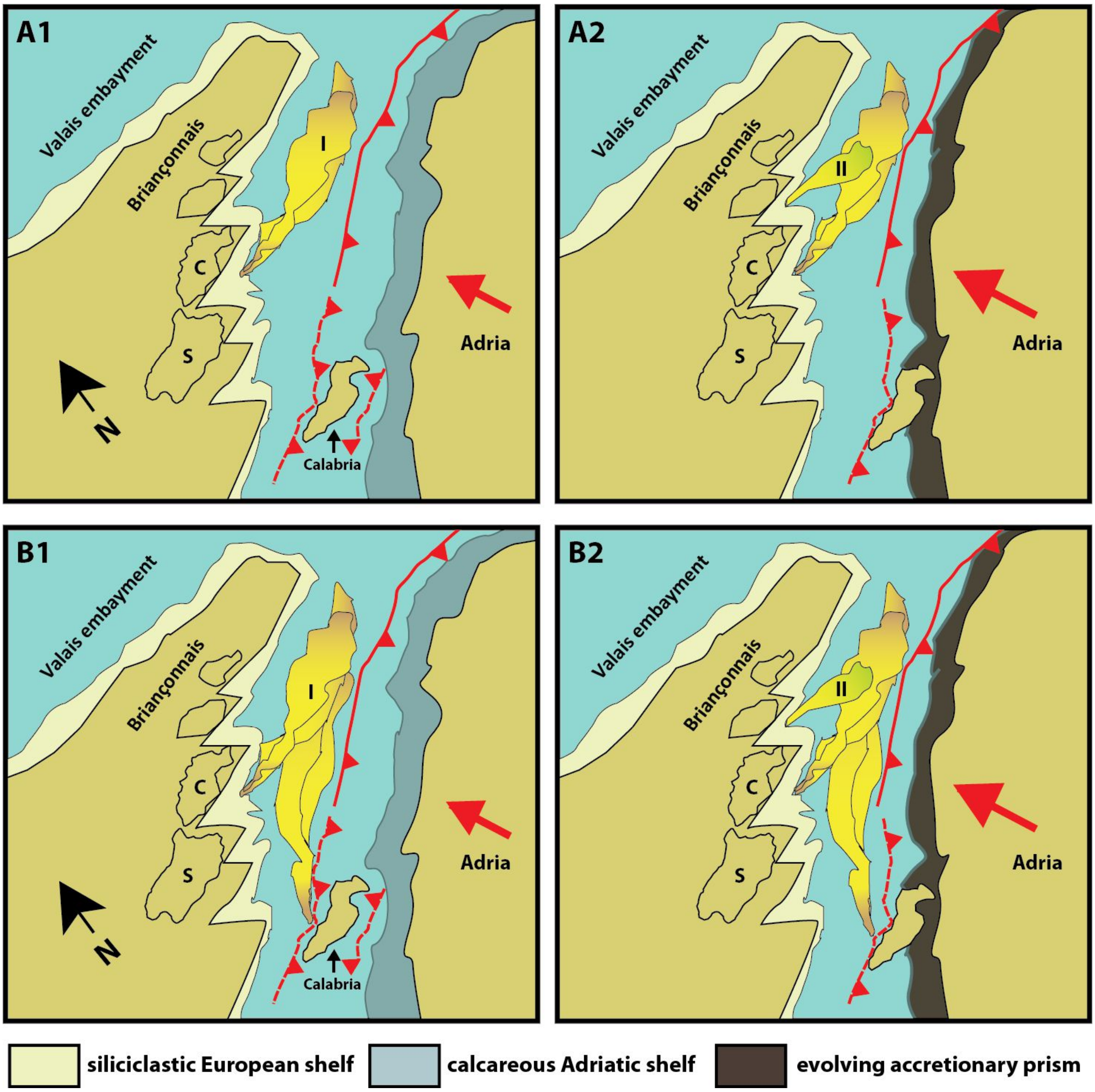

Fig. 6.16. Tentative paleogeographic reconstruction of the Piemont-Ligurian ocean in the context of progressive N-NW-ward migration of the Adriatic plate in Upper Cretaceous times. A1) Initial stage of coarse-clastic sedimentation of the Bordighera turbidite system defined by a point-source assignable to the Corso-Sardinian block. A2) Inferred activation of an additional sediment entry point that provided input of reworked younger volcaniclastic sediments. B1) Depositional scenario defined by intense mixing of coarse-clastic detritus derived from both the Corso-Sardinian block and Calabria. Note the fact that Calabria represents an active margin (See text for references). B2) Late-stage input of reworked volcaniclastic detritus due to the activation of the Briançonnais domain comparable to scenario A2.

propose an early (Upper Jurassic (?) drifting of Calabria away from Sardinia and the existence of an interoceanic subduction zone outward of the Calabrian continental micro-fragment in Upper Cretaceous times. Consequently, taking the abovementioned models into account, this scenario implies an active margin tectonic setting for Calabria that could account for the observed enhanced coarse-clastic sediment yield at the onset of Alpine convergence. In regard to the pre-collisional geodynamic model of Vignaroli et al. (2008), that, based on tomographical datasets and field relationships, proposes time-equivalent opposite dipping (i.e. Alpine and Apenninic) subduction polarities. This might also explain the divergent present-day locations of the pre-collisional flysch successions of the Western Alps and the Apennines, respectively, giving rise to the question whether the Apenninic Flysch might have been sourced from an active margin, nevertheless "European" source that was represented by the Calabria micro-fragment. The scenario illustrated for the stratigraphically later time-step (Fig. 6.16 B2) is analogous to the first model, delineating the increased proportion of transversal sediment input during the latest stage of basin fill.

With the intention of appraising the practical feasability of the proposed scenarios, the system-scale observations drawn from the sedimentological characterization of the Bordighera turbidite system (Chapter 5) need to be integrated into this evaluation. On the one hand, the average dimensions of sand-rich systems tend to be limited to a longitudinal extent of ca. 50 km (e.g. Shanmugam & Moyola, 1988; Bouma, 2000; see Mattern, 2005 for extensive review), a pattern that is apparently mirrored by the reconstructed extents of the low-efficiency Bordighera turbidite system. The low-efficiency fan concept as proposed by Mutti (1979) moreover highlights the importance of clay content in keeping the sandy grain size fraction in suspension, which might account for the fact that sand-rich systems are limited in basin-ward extent. The tendency of a scarcity in interstitial mud content could directly be deduced from the characteristic facies that define the proximal parts of the BGS which are dominantly made up of mud-poor deposits interpreted to result from hyperconcentrated to concentrated density flows. The documentation of the main architectural elements that typify low-efficiency turbidite systems (i.e. feeder channels, a transition zone in between channelized and weaker confined lobe environments and terminal lobes, respectively; cf. Mutti, 1979), and in particular the presence of large-scale incisional channels, supports this interpretation and likewise argues against a distant sediment entry point as illustrated in the second scenario. Within a such framework, the characteristics of the inferred granitoid parent rock lithologies itself that do not tend to generate large proportions of mud-sizes fractions (cf. sand generation index of Palomares & Arribas, 1993) are interpreted to document the close relationship between sand composition, grain size and gravity-flow facies and might thus represent a key control on the development of the coarse-grained low-efficiency Bordighera turbidite system that is characterized by a limited longitudinal extent of ca. 55-60 km´s. Mattern (2005) suggests a generally close vicinity of sand-rich fans to their typically spatially limited staging areas. Consequently, the first proposed scenario appears to be by far more appropriate in explaining the provenance setting and resultant facies characteristics of the Bordighera Sandstones.

Comparison to proposed provenance models for flysch successions of the Piemont-Ligurian ocean

Albeit this study highlights the importance of the integration of detrital zircon chronology into sediment provenance analysis of pre-Alpine siliciclastic deep-marine succession deposited in the Piemont-Ligurian ocean, a range of previous studies based on sandstone modal compositions and detrital heavy mineral assemblages addressed the provenance of siliciclastic successions of various stratigraphic intervals (e.g. Valloni & Zuffa, 1984; Wildi, 1985, 1987; Rowan, 1990; Fontana et al., 1994; van de Kamp & Leake, 1995; Argnani et al., 2006; Bracciali et al., 2007; Thum et al., 2015). Wildi (1985) defined a zircon-tourmaline-rutile dominated heavy mineral association as being characteristic for the Paleo-European margin and consequently claimed the European margin source for the Upper Cretaceous Flysch Units deposited in the Piemont-Ligurian ocean. In a following publication, Wildi (1987) questioned the "passive" margin configuration of the European Tethyan margin and proposed an Upper Cretaceous inversion of the European margin that provided a Corsica-derived source for siliciclastic successions intercalated into Helminthoid Flysch sequences, among which the San Remo Flysch (i.e. the Bordighera Sandstones) was positioned. Argnani et al. (2006) augmented the observations on heavy mineral assemblages of Wildi (1985) and concluded with a roughly equal Corsica-derived provenance for the coarse siliciclastic intercalation into the Western Ligurian Flysch Units and explicitly the San Remo Unit.

The majority of petrographic investigations provide datasets of Ligurian Flysch successions of the Northern Apennines. A general distinction in between Internal and External Units can be attained (e.g. Sagri & Marri, 1980; Valloni & Zuffa, 1984; Argnani et al., 2006; Bracciali et al., 2007). The Internal Units comprise deep-marine succession that superimpose ophiolitic basement and regarded as representing the part of the Piemont-Ligurian ocean in adjacency to the Corsican margin. Accordingly, the Internal Ligurian Units are attributed to a European provenance. By contrast, the External Ligurian Units, interpreted as representing the distal Adriatic margin and the transition towards the Piemont-Ligurian ocean, are generally associated to an Adriatic provenance. Among the Upper Cretaceous to Paleocene Internal Ligurian successions, Valloni & Zuffa (1984) report quartzo-feldspathic arkoses from the "Arenarie Superiori" (i.e. the Gottero Sandstones) and the Monghidoro Formation which are defined by similar primary modal parameters to the ones documented in the present study (Gottero Sandstones: mean Q51F39L10; Monghidoro Formation: mean Q59F38L3). A supplementary petrographic study by van de Kamp & Leake (1995) revealed a mean Q42F55L3 composition for the Gottero Sandstones. These documented primary modal compositions appear to be reasonably compatible to the results derived from the coarse-clastic Bordighera Sandstones (Q49F48L3). Remarkably, all the petrographical studies infer that the Corsica block provided the source interpretation for the Gottero Sandstones and the Monghidoro Formation. Notwithstanding, in comparison to the modal compositions of the Bordighera Sandstones reported in the present study, the petrographic investigations of the Gottero Sandstones by van de Kamp & Leake (1995) document opposing plagioclase proportions. The study reports elevated plagioclase/k-feldspar ratios ranging from 0.97 to 1.0 that are contrasted by a mean P/K ratio of 0.64 for samples from the Monte Frontè section and a mean P/K ratio of 0.39 for samples from the Cima di Velega section.

Reliability of the statistical confrontation of detrital zircon ages against candidate source area crystallization datasets

This study in parts highlights the difficulty of detrital zircon provenance studies in areas like the Western Tethys. On the one hand, according to the complex geodynamic history of the basement rocks that represent both margins of the Western Tethys, exclusive assignment of the clastic detritus to potential provenance based on detrital zircon chronology might bare a source of error as the candidate source terrains themselves might record biased information due to multi-stage recycling of zircon age populations. As previously stated, both margins and developed micro-continental fragments in the Piemont-Ligurian ocean were incorporated in the Alpine cycle. These basement units share a strongly similar crustal composition due to their common pre-Alpine history (e.g. Dal Piaz, 2001; von Raumer et al., 2003; Mohn et al., 2010). Incorporated available literature datasets for statistical comparisons might merely represent a fractional insight into the overall geodynamic history of the margins that bounded the Western Tethyan realm and might provide varying numbers of crystallization ages available for different potential source areas.

Besides the complications derived from the virtually analogous geological history of the opposing margins that represent the potential source areas, it could be assumed that the overall proportion of detrital ages reflects the relative presence of source rocks of corresponding age (cf. Cawood et al., 1999), the relative proportions of individual ages from available datasets needs to be carefully balanced. Major geological events are recurrently documented in available age datasets and could hence be recognized in an overrepresented manner (for instance, see the vast amount of zircon ages numerous studies yielded for Sardinia which basically cover the full age span), whereas on the contrary, other events are merely represented with few available age data. Statistical comparisons are based on evaluations of cumulative density functions. Thus, equal sizes of compared zircon age datasets seem to be required to accurately apply statistical confrontations since essentially the KS-test is sensitive to identical sample numbers (Guynn & Gehrels, 2010).

Moreover, the suitability of detrital zircon age information in supplementing traditional provenance analysis methods (i.e. point-counting) seems to be strongly dependent on a diversified chronological make-up of the potential provenance terranes. The bulk of studies that have proven the reputation of detrital zircon chronology in providing advanced provenance determinations were primarily conducted in magmatic arc settings (e.g. Cawood et al., 1999, 2012; Di Giulio et al., 2012; Malkowski et al., 2015). In contrast to this study that assesses a detrital suite typified by comparably extensive time spans between cooling ages and depositional ages, the studies from magmatic arc settings hugely evaluate almost syn-depositional detrital assemblages. Therefore, detrital mixing can almost be ruled out. Furthermore, the geodynamical context of these studies typically allows the appropriate ascription of detrital signatures to their nearby sources. Accordingly, the strong dependence of the reliability of detrital zircon ages in provenance analysis on the lag-time in between zircon crystallization and deposition can be supposed (e.g. DeGraff-Surpless et al., 2002; Fildani et al.; 2003; Sharman et al., 2015). Furthermore, concerning the preservation potential of the sediment pathways that linked sedimentary units and their associated source rocks that become incorporated into a highly deformed accretionary prism, a such distinct attribution appears to remain challenging in the context of pre-collisional provenance studies.

6.9 Conclusions

The combined provenance investigation enclosing sedimentary petrography, detrital zircon chronology and paleocurrent determinations encompassed two conformably superimposing pre-collisional turbiditic successions in the framework of incipient oceanic closure in Upper Cretaceous times. Modal framework analysis reveals a gradual provenance evolution that is typified by a progressive transition from texturally mature fine-grained quartzo-feldspathic sandstones into texturally and compositionally immature coarse-clastic arkoses. Results from modal framework analysis suggest a partially recycled origin of the samples of the basal complex, whereas the coarse sediments of the sand-rich turbidite system imply the first-cycle derivation of the clastic detritus from a rapidly exhumed provenance terrane composed of granitoid plutons and low-grade metamorphic geobodies.

New geochronological data (U-Pb detrital zircon ages) denote principal peaks in the detrital spectrum that are in unambiguous correspondence with well-documented pulses of magmatism and metamorphism that occurred along the Southern Variscides. Utilizing qualitative and statistical comparison of determined detrital zircon ages and potential source terrane zircon age populations supports the interpretation that the European margin contributed the major portion of detrital zircons to the coarse-clastic detritus. With respect to an observed overall S-N facies trend derived from paleocurrent measurements, granitoid batholiths of the Corso-Sardinian block are inferred as having provided the most important provenance.

Nevertheless, as outlined by a remarkable stratigraphic variability in detrital age populations towards the top of the succession, the system can be appraised as being characterized by rather complex source-to-sink relationships. A consistent detrital zircon spectrum that can be recognized throughout the initial stage of sand-rich turbiditic sedimentation implies a homogeneous provenance scenario during the incipient coarse-clastic phase. Nonetheless, notably divergent detrital zircon populations are recorded in sections that document the shut-down of siliciclastic input and thus suggest that the stratigraphic evolution of the system was marked by a modification in provenance arrangement. The homogeneous detrital signature distinctive for the incipient stage of the development of the sand-rich turbidite system is interpreted to indicate a point-sourced configuration of the system, whereas the divergent detrital suite that marks the latest depositional stage might suggests a shift towards at least one additional transversal entry point. Accordingly, the axial Bordighera turbidite system is interpreted to record a stratigraphic evolution from a point-sourced, canyon-fed turbidite system (Mutti & Ricci Lucchi, 1975) into a turbidite system defined by multiple entry points comparable to the submarine ramp model of Heller & Dickinson (1985) or the multiple source ramp and slope apron linear source ramp model for sand-rich systems of Reading & Richard (1994). This documented stratigraphic trend is interpreted to imply a significant shift of the overall basin configuration. The provenance evolution documented from both petrographic results and the divergent detrital zircon signatures are regarded as reflecting the gradual N-NW-directed migration of a flexural bulge due to tectonic loading on the subducted European plate. In the framework of oblique convergence, this craton-ward migration of the hinge line of the flexural bulge step-wise affected different domains of the hyperextended European margin that was likely typified by a dissected fashion. Consequently, the Briançonnais domain is inferred to have become activated during the latest stage of coarse sedimentation of the Bordighera turbidite system and provided the provenance of detritus that contained the significantly younger detrital zircons.

Chapter 7: Conclusions and recommendations for further work

This chapter integrates the insights gained from a sedimentological characterization of the Bordighera Sandstones and the implications that the provenance analysis provides. The sedimentological characterization of the system was performed by means of extensive logging of stratigraphic key sections along the down-current sediment pathway. Emphasis was put on understanding in greater detail the down-current evolution of a sand-rich turbidite system prone to abundant hybrid event bed development at both the bed-scale and the system-scale. The integration of sedimentological criteria like amalgamation ratios and sand-to-mud ratios, along with statistical bed type proportion analysis, proved to be a valuable method in discriminating depositional sub-environments and allocating heterogeneity development. The quantification of proximal to distal facies patterns revealed a sharp shift in between the dominant facies types. The proximal domain is dominated by channel-fill sandstone bodies that almost entirely comprise massive and clean sandstones. By contrast, the distal realm comprises extensive terminal splay complexes that feature high proportions of mudclast-rich sandstones and hybrid event beds. The transition zone that separates the channelized from the splay associations is of limited down-current extent and marked by the repeated presence of isolated scours.

Statistical analysis of the environmental distribution of hybrid event bed proportions denotes their origination in ultimate down-dip proximity to the transitional zone where the siliciclastic flux interfingers with calcareous Helminthoid flysch turbidites. Accordingly, the loss of confinement at the slope break and enhanced erosional capacity as the sandy flows underwent hydraulic jumps are regarded as representing the key control on hybrid event bed development. Amalgamation ratio analysis reveals the dominant presence of hybrid event beds in the high-energy axial parts of proximal splay environments (See fig. 7.1). This observation stands in sharp contrast to most models that predict hybrid event bed distribution in distal lobe environments.

The analysis of stacking pattern motifs illustrates a distinct along-current pattern of increasing ratios of the debritic subdivisions with further down-dip travel distances. The documented bed type distributions with the argillaceous sandstones rapidly making up the dominant bed types down-dip of a ‘transition zone’ is interpreted as negatively impacting on hydrocarbon reservoir quality. Recognition of the location and character of this sharp break in facies distribution is crucial in order to establish accurate reservoir models for such comparably poorly studied types of turbidite systems. The Bordighera Sandstones are hence regarded as representing a valuable analog for low-efficiency turbidite systems accumulated in mixed siliciclastic-calcareous settings. Essentially the fact that all documented hybrid event beds debritic subdivisions comprise calcareous clasts suggests that the observed facies patterns offer a good control on the loci where the incorporation of cohesive mud occurred. Mud acquisition evidently took place at the zone defined by a loss of confinement. The documentation of meso-scale scour features in this depositional sub-environment located in proximity to a basin plain environment (as suggested by the conformable contact with the basal complex) can be explained by a basin morphology defined by topographic irregularities. Within a such environment, rugged sea-floor morphology apparently resulted in the development of small- to meso-scale knickpoints that promoted hydraulic jumps to occur. Accordingly, the recognition of this location that shows a strong impact on facies distribution is crucial in order to establish accurate reservoir models for mixed siliciclastic/calcareous sand-rich turbidte systems. Reasoning from this assumption, these outcomes promote the proposal of a novel generic and depositional for such settings, as illustrated in Fig. 7.1.

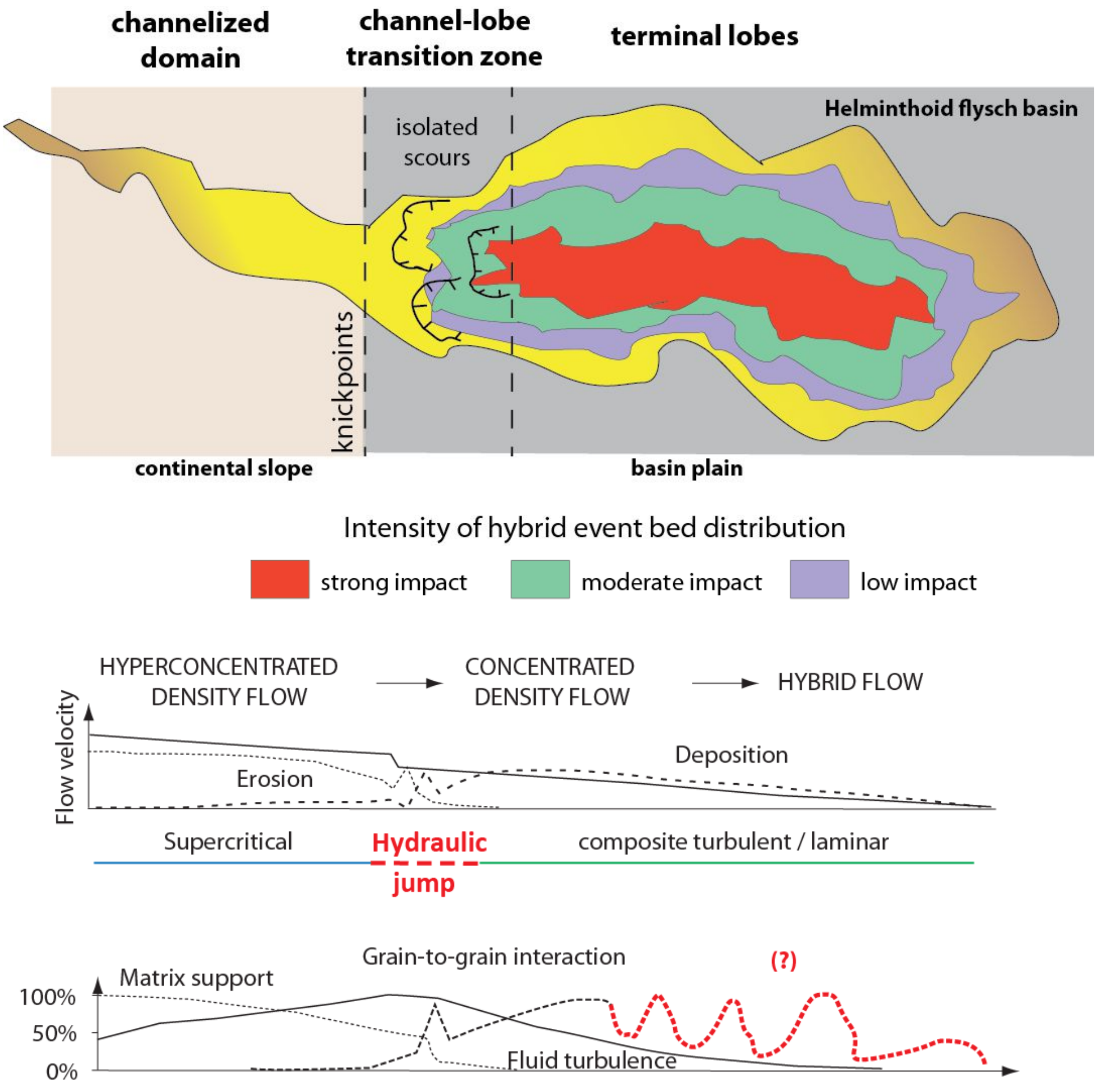

Fig. 7.1. Proposed environmental and generic model for sand-rich turbidite systems that interact with coeval fine-grained basin plain successions. The impact of erosional capacity due to enhanced turbulence at the location of the hydraulic jump at the slope break and the availability of cohesive substrate explains facilitate transitional flow behavior.

Petrographic and modal analysis of the two siliciclastic members of the San Remo Helminthoid Flysch reveals a transition from fine-grained quartzo-feldspathic sandstones that typify the basin plain succession to first-cycle coarse arkosic sandstones of the sand-rich turbidite system. Although the comparison of textural characteristics of both members documents an evidently sharp divergence in textural maturity, average modal framework compositions point towards a comparatively gradual provenance evolution that is interpreted to mirror the unroofing of a crystalline basement terrane at the early stage of Alpine convergence. In combination with new results from detrital zircon chronology that discriminate the European plate as having provided the bulk of the coarse-clastic detritus, these evidences demonstrate tectonic activity along the continental margin of the subducted plate. Consequently, a such observation contradicts the generic provenance model for subduction settings that highlight the dominant derivation of coarse detritus from the active plate. The detrital signature pattern recorded in the syn-orogenic succession of the San Remo Unit of the Western Ligurian Flysch can be explained by the gradual progression of a flexural bulge that developed in response to tectonic loading by the overthrusting Alpine accretionary wedge.

The observed pattern lithofacies distribution appears to expose a distinct relationship between the parent lithologies of the sediment source and resulting gravity flow facies. Poorly sorted, massive sandstone facies interpreted to deposited by suspension fallout from hyperconcentrated to concentrated density flows dominate the proximal domains. The lack of interaction (and mixing) with the interfingering calcareous source that characterizes the proximal environments is regarded as a providing a setting in which the assumption that these flows were defined by initial low mud contents could be verified. With regard to the clean proximal sandstones, the dominance of massive beds over beds that display primary sedimentary structures is interpreted as reflecting the mud-poor primary composition of the detritus that was provided by a crystalline source that apparently did not generate significant concentrations of mud. The overall fan dimensions, the internal facies organization and the persistent high degree of amalgamation and related high sand-to-mud ratios show a strong analogy to the low-efficiency turbidite system of Mutti (1979) and hence support this interpretation. Mutti (1979, 1985) suggests that the scarcity of clay fractions can be regarded as having prevented the flows to travel for long run-out distances.

The results attained from detrital zircon chronology furthermore allow the regional-scale appraisal of the stratigraphic evolution of the detrital inputs (Fig. 7.2). The early phase of detrital input marked by homogeneous detrital spectra that correspond to parent rock ages from the Corso-Sardinian block. However, as documented by a shift in detrital age populations that typify the final stage of coarse-clastic sedimentation, the reactivation of different segments of the hyperextended European continental margin is mirrored by the increased presence of younger detrital populations that are consistent with volcanic ages reported from the Briançonnais terrane. This detected trend implies a temporal shift from a point-sourced turbidite fan during the early phase of basin fill towards a scenario in which a transversal source became active during the final stage of coarse siliciclastic sedimentation.

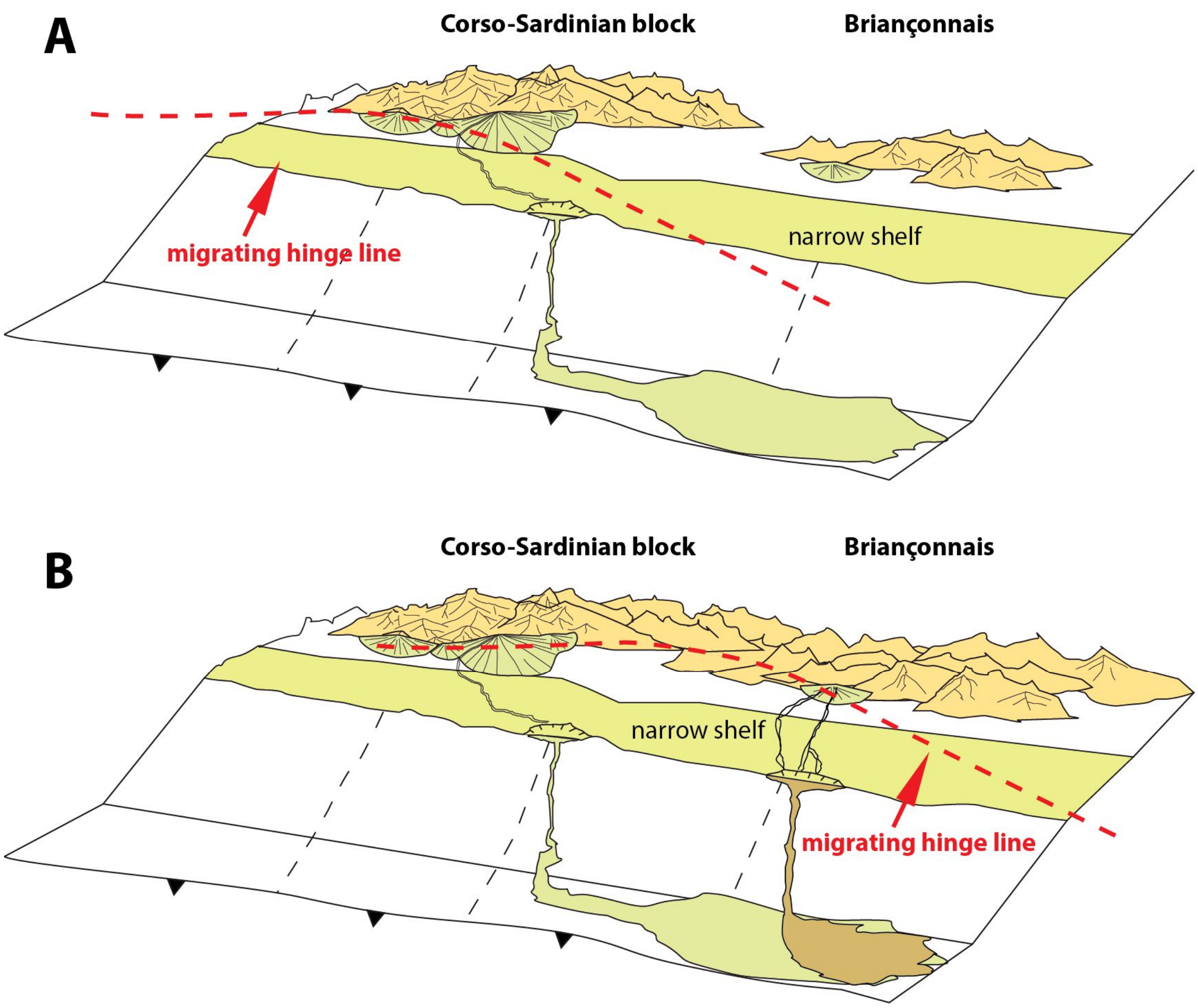

Fig. 7.2. Revised depositional model for the Bordighera Sandstones. (A) The onset of coarse-clastic sedimentation is interpreted as resulting from rapid uplift of the Corso-Sardinian block due to NW-ward migration of the hinge line of the flexural bulge that developed in response to tectonic loading on the subducted distal European plate. (B) Initiation of detrital input derived from the Briançonnais terrane during the latest stage of basin fill because of continuous progradation of the flexural bulge.

7.2 Recommendations for further work

The results of the integrated provenance and process sedimentological analysis presented in this work prompt further questions that could be addressed with the aim of advancing the general understanding of syn-orogenic deep-water successions. Essentially the peculiar presence of bed-scale heterogeneity in axial parts of the sediment fairway as documented in this work requires further understanding. As this study merely covered a fraction of the preserved system, a such investigation could on the one hand be continued in the Bordighera turbidite system. In particular the expansion of the detailed sedimentological investigation along cross-current transects could support the proposed model. The hypothesis of enhanced hybrid event bed development in response to interfingering sources of divergent lithologies could be stressed. A particular research direction could be the detailed investigation of the role of cohesivity of calcareous substrate. A potential case study would be the detailed sedimentological investigation of the Ubaye-Embrunais Nappe of the French Maritime Alps. This system, not previously investigated in great detail, represents a similar Helminthoid Flysch Unit in which a coeval siliciclastic a deep-water system and a calcareous flysch succession interacted and might hence offer a promising comparative study of the effect of basin floor cohesivity on hybrid event bed emergence. In addition, the relationship between a granitic sediment source and the responding turbidite facies types – in particular clean sands - could be investigated in other deep-water systems located in vicinity to the Corsica-Sardinian Block, such as the Annot Sandstones or the Elba Flysch.

The expansion of the provenance analysis to other Ligurian Flysch Units (Apenninic and Alpine) would provide further constraints on the complex geodynamic development of the Western Tethyan realm. To be more precise, the provenance of the Gottero Sandstones, a succession that was deposited in a similar geodynamic setting in Upper Cretaceous times, could be supplemented by detrital zircon chronology. According to their slightly stratigraphically younger position, the provenance discrimination of the Quarziti di Monte Bignone, the Upper Cretaceous to Paleocene-age siliciclastic member of the Borghetto Unit of the Western Ligurian Flysch, would offer a further comparative study case in order to evaluate the hypothesis of significant siliciclastic input staged from the Briançonnais terrane. Moreover, roughly time-equivalent sedimentary successions that represent the link between the candidate source areas and the terminal sink such as alluvial and shelfal deposits could be addressed. Likewise, the provenance investigations could be augmented by different thermochronometers such as detrital monazite and rutile as these might shed light on the metamorphic history of source terrane candidates, as the sole application detrital zircon chronology seems to meet its limitations in a framework of potential source areas that share strongly similar geological histories. Essentially geochemical "fingerprinting" with the Lu/Hf method might derive further distinctions (down to the batholith-scale) of involved crystalline basement rocks that provided the provenance.

References

Allègre, C.J. (2008). Isotope Geology. Cambridge University Press, Cambridge.

Alvarez, W. & Shimabukuro, D.H. (2009). The geological relationships between Sardinia and Calabria during Alpine and Hercynian times. Italian Journal of Geosciences (Bolletino della Societa Geologica Italiana), 128 (2), 257-268.

Amy, L.A. & Talling, P.J. (2008). Basin-plain deposits of the Marnoso-arenacea Formation, Italy. In: Nilsen, T.H., Shew, R.D., Steffens, G.S., Studlick, J.R.J. (eds.), Atlas of Deep-Water Outcrops. AAPG Studies in Geology, 56, 215-217.

Amy, L.A., Peachey, S.A., Gardiner, A.A., Talling, P.J. (2009). Prediction of hydrocarbon recovery from turbidite sandstones with linked-debrite facies: Numerical flow-simulation studies. Marine and Petroleum Geology, 26, 2032-2043.

Andersen, T., 2005. Detrital zircons as tracers of sedimentary provenance: limiting conditions from statistics and numerical simulations. Chemical geology. 40, 249-270.

Andresen, K.J. & Clausen, O.R. (2014). An integrated subsurface analysis of clastic remobilization and injection; a case study from the Oligocene succession of the eastern North Sea. Basin Research, 26 (5), 641-674.

Argnani, A. (2009). Plate Tectonics and the Boundary between Alps and Apennines. Italian Journal of Geosciences (Bolletino della Societa Geologica Italiana), 128 (2), 317-330.

Argnani, A., Fontana, D., Stefani C., Zuffa, G.G. (2004). Late Cretaceous carbonate turbidites of the Northern Apennines: shaking Adria at the onset of Alpine collision. Journal of Geoly, 112, 251–259.

Argnani, A., Fontana, D., Stefani, C. & Zuffa, G.G. (2006). Palaeogeography of the Upper Cretaceous-Eocene carbonate turbidites of the northern Apennines from provenance studies. In: G. Moratti and A. Chalouan (eds.), Tectonics of the western Mediterranean and North Africa. – Geological Society of London, Special Publications, 262, 259-275.

Baas, J.H. & Best, J.L. (2002). Turbulence modulation in clay-rich sediment-laden flows and some implications for sediment deposition. Journal of Sedimentary Research, 72, 336-340.

Baas J.H., Best J.L., Peakall J., Wang M. (2009). A phase diagram for turbulent, transitional, and laminar clay suspension flows. Journal of Sedimentary Research, v. 79, p. 162–183

Baas, J.H., Best, J.L., Peakall, J. (2011). Depositional processes, bedform development and hybrid bed formation in rapidly decelerated cohesive (mud-sand) sediment flows. Sedimentology, 58, 1953-1987.

Bagnold, R.A. (1954) Experiments on a gravity-free dispersion of large solid spheres in a Newtonian fluid under shear. Proceedings of the Royal Society of London, 225, 49-63.

Bagnold, R.A. (1962). Auto-suspension of transported sediment: turbidity currents. Royal Society of London Proceedings, Series A, 265, 315-319.

Bhatia, M.R. (1983). Plate tectonics and geochemical composition of sandstones. The Journal of Geology, 91, 611–627.

Bayet-Goll, A., Neto de Carvalho, C., Moussavi-Harami, R., Mahboubi, A., Nasiri, Y. (2014). Depositional environments and ichnology of the deep-marine succession of the Amiran Formation (Upper Maastrichtian- Paleocene), Lurestan Province, Zagros Fold-Thrust Belt, Iran. Palaeogeography, Palaeoclimatology, Palaeoecology, 401, 13-42.

Bayet-Goll, A., Monaco, P., Jalili, F., Mahmudie-Gharaie, M.-H. (2016). Depositional environments and ichnology of Upper Cretaceous deep-marine deposits in the Sistan Suture Zone, Birjand, Eastern Iran. Cretaceous Research, 60, 28-51.

Beltrán-Triviño, A., Winkler, W., von Quadt, A. (2013). Tracing Alpine sediment sources through laser ablation U–Pb dating and Hf-isotopes of detrital zircons. Sedimentology, 60, 197-224.

Beltrán-Triviño, A., Winkler, W., von Quadt, A., Gallhofer, D. (2016). Triassic magmatism on the transition from Variscan to Alpine cycles: evidence from U–Pb, Hf, and geochemistry of detrital minerals. Swiss Journal of Geosciences, DOI 10.1007/s00015-016-0234-3.

Beltrando, M., Rubatto, D., Manatschal, G. (2010). From passive margins to orogens. Geology, 38, 559-562.

Beltrando, M., Manatschal, G., Mohn, G., Dal Piaz, G.V., Brovarone, A.V., Masini, E. (2014). Recognizing remnants of magma-poor rifted margins in high-pressure orogenic belts: The Alpine case study. earth-Science Reviews, 131, 88-115.

Bernet, M., Zattin, M., Garver, J.I., Brandon, M.T., Vance, J.A. (2001). Steady-state exhumation of the European Alps. Geology, 29 (1), 35-38.

Bernoulli, D. & Winkler W. (1990). Heavy mineral assemblages from Upper Cretaceous South- and Austroalpine flysch sequences (northern Italy and southern Switzerland): source terranes and palaeotectonic implications. Eclogae Geolicae Helveticae, 83, 287-310.

Berra, F., Tiepolo, M., Caironi, V., Siletto, G.B. (2014). U–Pb zircon geochronology of volcanic deposits from the Permian basin of the Orobic Alps (Southern Alps, Lombardy): chronostratigraphic and geological implications. Geological Magazine, 152, 429-443.

Bjørlykke, K. (2010). Petroleum Geoscience: From Sedimentary Environments to Rock Physics. Springer Verlag, Berlin. 518 pages.

Blum M., & Pecha, M., 2014. Mid-Cretaceous to Paleocene North American drainage reorganization from detrital zircons. Geology, 42(2), 607-610.

Boggs, S. (2009). Petrology of Sedimentary Rocks (2nd edition). Cambridge University Press, Cambridge CB2 8RU, UK.

Bouma, A. (1962). Sedimentology of Some Flysch Deposits: a Graphic Approach to Facies Interpretation. Elsevier, New York.

Bousquet, R., Engi, M., Gosso, G., Oberhänsli, R. Berger, A. Spalla, M.I., Zucali, M., Goffé B. (2004). Explanatory notes to the map: Metamorphic structure of the Alps Transition from the western to the central Alps, Mitteilungen der Österreichischen Mineralogischen Gesellschaft, 149, 145–156.

Bowring, S.A., Schoene, B., Crowley, J.L., Ramezani, J., Condon, D.C. (2006). High-precision U–Pb zircon geochronology and the stratigraphic record: Progress and promise. In: T. Olszewski (Ed.), Geochronology: Emerging Opportunities. Paleontological Society Papers, 12, 25–45.

Bracciali, L., Marroni, M., Pandolfi, L., Rocchi, S. (2007). Geochemistry and petrography of Western Tethys Cretaceous sedimentary covers (Corsica and Northern Apennines): From source areas to configuration of margins. Special Paper of the Geological Society of America, 420, 73-93.

Bracciali, L., Pandolfi, L., Rocchi, S. (2014). A snapshot of the Late Jurassic Western Tethys seafloor composition and morphology provided by the geochemistry of pelitic sediments (Corsica, Central Alps and Northern Apennines). Basin Research, 26, 461-485.

Brown, L.F. & Fisher, W.L. (1977), Seismic stratigraphic interpretation of depositional systems: examples from Brazilian rift and pull apart basins. In: C. E. Payton (Ed.), Seismic Stratigraphy — Applications to Hydrocarbon Exploration, AAPG Memoir, 26, pp. 213–248.

Brunt R.L., Hodgson D.M., Flint S.S., Pringle, J.K., Di Celma C., Prélat A. & Grecula M. (2013). Confined to unconfined: Anatomy of a base of slope succession, Karoo Basin, South Africa. Marine and Petroleum Geology, 41, 206-221.

Bryant, M., Falk, P., Paola, C. (1995). Experimental study of avulsion frequency and rate of deposition. Geology, 23 (4), 365–368.

Bussy, F. & Cadoppi, P. (1996). U-Pb zircon dating of granitoids from the Dora-Maira massif (western Italian Alps). Schweizerische mineralogische Mitteilungen, 76, 217-233.

Butler, W.R.H., Tavarnelli, E., Grasso, M. (2006). Structural inheritance in mountain belts: An Alpine-Apennine perspective. Journal of Structural Geology, 28, 1893-1908.

Cabanis, B., Cocheme, J.J., Vellutini, P.J, Joron, J.L., Treuil, M. (1990). Post-collisional Permian volcanism in northwestern Corsica: an assessment based on mineralogy and trace-element geochemistry. Journal of Volcanology and Geothermal Research, 44 (1), 51-67.

Camacho, H., Busby Spera, C. J., Kneller, B. C. (2002). A new depositional model for the classical turbidite locality at San Clemente State Beach, California. AAPG Bulletin, 86 (9), 1543-1560.

Campion, K. M., Sprague, A.R.G., Sullivan, M. D. (2005). Architecture and lithofacies of the Capistrano formation (Miocene-Pliocene), San Clemente, California. The Pacific Section SEPM, 42 p.

Cantanzariti, R:, Ellero, A., Levi, N., Ottira, G., Pandolfi, L. (2007). Calcareous nannofossil biostratigraphy of the Antola Unit succession (Northern Apennines, Italy): new age constraints for the Late Cretaceous Helminthoid Flysch. Creatceous research, 28 (6), 841-860.

Caron, C., Homewood, P., Wildi, W. (1989). The Original Swiss Flysch: A reappraisal of the Type Deposits in the Swiss Prealps. Earth-Science Reviews (Geol. Rundschau), 26, 1–45.

Carrapa, B. (2010). Resolving tectonic problems by dating detrital minerals. Geology, 38, 191-192.

Carter, A. & Moss, S.J. (1999). Combined detrital-zircon fission-track and U-Pb dating: A new approach to understanding hinterland evolution. Geology. 27, 235-238.

Carter, A. & Bristow, C.S. (2000). Detrital zircon geochronology: enhancing the quality of sedimentary source information through improved methodology and combined U-Pb and fission track techniques. Basin Research, 12, 47-57.

Cartigny, M.J.B., Ventra, D., Postma, G., Van den Berg, J.H., (2014). Morphodynamics and sedimentary structures of bedforms under supercritical-flow conditions: New insights from flume experiments. Sedimentology, 61 (3), 712-748.

Casini, L., Cuccuru, S., Maino, M., Oggiano, G., Tiepolo, M. (2012). Emplacement of the Arzachena Pluton (Corsica–Sardinia Batholith) and the geodynamics of incoming Pangaea. Tectonophysics, 544-545, 31-49.

Casini, L., Cuccuru, S., Puccini, A., Oggiano, G., Rossi, P. (2015). Evolution of the Corsica–Sardinia Batholith and late-orogenic shearing of the Variscides. Tectonophysics, 646, 65–78.

Castellanos, A. (2005). The relationship between attractive interparticle forces and bulk behavior in dry and uncharged fine powders. Advances in Physics, 54, 263–376.

Cawood, P.A., Nemchin, A.A., Leverenz, A., Saeed, A., Ballance, P.F. (1999). U/Pb dating of detrital zircons: Implications for the provenance record of Gondwana margin terranes. Geological Society of America Bulletin, 111, 1107-1119.

Cawood, P.A., Nemchin, A.A., Freeman, M., Sircombe. E., 2003. Linking source and sedimentary basin: Detrial zircon record of sedimentary flux along modern river system and implications for provenance studies. Earth and Planetary Science Letters. 210, 259-268.

Cawood, P.A., Hawkesworth, C.J., Dhuime, B., (2012). Detrital zircon record and tectonic setting. Geology, 40(10) 875-878.

Chu, Y., Lin, W., Faure, M., Wang, Q. (2016). Detrital zircon U-Pb ages and Hf isotopic constraints on the terrigenous sediments of the Western ALps and their paleogeographic implications. Tectonics, 35, 1-20. doi:10.1002/2016TC004276.

Cibin, U., Di Giulio, A., Martelli, L. (2003). Oligocene-Early Miocene tectonic evolution of the northern Apennines (Northwestern Italy) traced through provenance of piggy-back basin fill successions. In: McCann, T., Saintot, A. (eds.), Tracing Tectonic Deformation Using the Sedimentary Record. Geological Society Special Publication, 208, 269-287.

Cobain, S.L., Peakall, J., Hodgson, D.M. (2015). Indicators of propagation direction and relative depth in clastic injectites: implications for laminar versus turbulent flow processes. Geological Society of America Bulletin, 127, 1816–1830.

Cobianchi M., Di Giulio A., Galbiati B., Mosna, S. (1991). Il ‘‘complesso di base’’ del Flysch di S. Remo nell’area di S. Bartolomeo, Liguria occidentale (nota preliminare). Atti Ticinesi Scienze della Terra, 34, 145–154.

Collinson, J.D., Mountney, N., Thompson, D.B. (2006). Sedimentary Structures. Terra Publishing, London. 292 pp.

Collombet, M., Thomas, J.C., Chauvin, A., Tricart, P., Bouillin, J.P, Gratier, J.P. (2002). Counter-clockwise rotation of the western Alps since the Oligocene: new insights from paleomagnetic data. Tectonics, 21 (4), 14-1–14-15.

Comas-Cufí M. & Thió-Henestrosa S. (2011). CoDaPack 2.0: a stand-alone, multi-platform compositional software. In: Egozcue J.J., Tolosana-Delgado R., Ortego M.I., (eds.), CoDaWork'11. 4th International Workshop on Compositional Data Analysis. Sant Feliu de Guíxols.

Compiani, P. (1992). Le Arenarie di Bordighera: studio sedimentologico-petrografico. Unpublished Master´s thesis, Università di Pavia. 123 pp.

Corfu, F. (2013). A century of U-Pb geochronology: the long quest towards concordance. Geological Society of America Bulletin, 125, 33-47.

Corfu, F., Hanchar, J.M., Hoskin, P.W.O., Kinny, P. (2003). Atlas of Zircon Textures. In: Hanchar, J.M., Hoskin, W.o. (eds.), Zircon: Reviews in Mineralogy & Geochemistry, 53, 468-500.

Covault, J.A. (2011). Submarine fans and canyon-channel systems: A review of processes, products, and models. Nature Education Knowledge, 3 (10):4.

Covault, J.A., Sylvester, Z., Hubbard, S.M., Jobe, Z.R., Sech, R.P. (2016). The Stratigraphic Record of Submarine-Channel Evolution. The Sedimentary Record, 14 (3), 4-11.

Cox, R. & Lowe, D.R. (1995). A conceptual review of regional-scale controls on the composition of clastic sediment and the co-evolution of continental blocks and their sedimentary cover. Journal of Sedimentary Research, 65, 1-12.

Crane, W.H. & Lowe, D.R. (2008). Architecture and evolution of the Paine channel complex, Cerro Toro formation (Upper Cretaceous), Silla syncline, Magallanes basin, Chile. Sedimentology, 55, 979-1009.

Crevello, P. D., H. D. Johnson, F. Tongkul, Wells, M. R. (2007). Mixed braided and leveed-channel turbidites, West Crocker fan system, northwest Borneo. *In*: T. H. Nilsen, R. D. Shew, G. S. Steffens, and J. R. J. Studlick, AAPG Deep-water Atlas.

Critelli, S., Le Pera, E. Ingersoll, R.V. (1997). The effect of source lithology, transport, deposition and sampling scale on the composition of Southern California sand. Sedimentology, 44, 653-671.

Dal Piaz, G.V. (2001). History of tectonic interpretations of the Alps. Journal of Geodynamics, 32, 99-114.

Dal Piaz, G.V., Bistacchi, A., Massironi, M. (2003). Geological outline of the Alps. Episodes, 26, 175-180.

Dallagiovanna, G., Seno, S., Vanossi, M. (1997). An example of the Alpine structural evolution of the Penninic zone in the Ligurian Alps: tectonics of the Barbassiria area. Eclogae Geologicae Helvetiae, 90, 337-344.

Dallagiovanna, G., Gaggero, L., Maino, M., Seno, S., Tiepolo, M. (2009). U–Pb zircon ages for post-Variscan volcanism in the Ligurian Alps (northern Italy). Journal of the Geological Society, 166, 101–114.

Datta, B. (2005). Provenance, tectonics and palaeoclimate of Proterozoic Chandarpur sandstones, Chattisgarh Basin: a petrographic view. Journal of Earth Sciences, 114, 227–224.

Davis, C., Haughton, P.D.W., McCaffrey, W.D., Scott, E., Hogg, N., Kitching, D. (2009) Character and distribution of hybrid sediment gravity flow deposits from the outer Forties Fan, Palaeocene Central North Sea, UKCS. Marine and Petroleum Geology, 26, 1919-1939.

Debelmas, J., Escher, A., Trümpy, R. (1983). Profiles through the Western Alps. American Geophysical Union, Geodynamic Series, 10, 83-96.

Decarlis, A., Dallagiovanna, G., Lualdi, M., Maino, M., Seno, S. (2013). Stratigraphic evolution in the Ligurian Alps between variscan heritages and the Alpine Tethys opening: a review. Earth-Science Reviews, 125, 43-68.

Decarlis, A., Maino, M., Dallagiovanna, G., Lualdi, A., Masini, E., Seno, S., Toscani, G. (2014). Salt tectonics in the SW Alps (Italy–France): From rifting to the inversion of the European continental margin in a context of oblique convergence. Tectonophysics, 636,293-314.

DeCelles, P.G. & Giles, K.A. (1996). Foreland basin systems. Basin Research, 8, 105-123.

DeGraff-Surpless, K., Graham, S.A., Wooden., J.L., McWilliams, M.O. (2002). Detrital zircon provenance analysis of the Great Valley Group, California: Evolution of an arc-forearc system. Geologic Society of America Bulletin. 114(12) 1564-1580.

Dickinson, W. R. (1970). Interpreting detrital modes of graywacke and arkose. Journal of Sedimentary Petrology, 40 (2), 695–707.

Dickinson, W. (1985). Interpreting provenance relations from detrital modes of sandstones. – In: Zuffa, G.G. (Ed.), Provenance of arenites: 165–189, NATO ASI Ser., Dordrecht (Reidel).

Dickinson, W.R. & Suczek, C. (1979). Plate tectonics and sandstone compositions. AAPG Bulletin, 63, 2164–2182.

Dickinson, W.R. & Valloni, R. (1980). Plate settings and provenance of sands in modern ocean basins. Geology 8, 82–86.

Dickinson, W.R. & Gehrels, G.E. (2009). Use of U-Pb ages of detrital zircons to infer maximum depositional ages of strata: A test against a Colorado Plateau Mesozoic database. Earth and Planetary Science Letters, 288, 115-125.

Dickinson, W. R., Beard, L. S., Brakenridge, G. R., Erjavec, J. L., Ferguson, R. C., Inman, K. F., Knepp, R. A., Lindberg, F. A., Ryberg, P. T. (1983). Provenance of North American Phanerozoic sandstones in relation to tectonic setting. Geological Society of America Bulletin, 94, 222–235.

Diekmann, B. & Wopfner, H. (1996). Petrographic and diagenetic signatures of climatic change in peri- and postglacial Karoo Sediments of SW Tanzania. Palaeogeography, Palaeoclimatology, Palaeoecology, 125, 5-25.

Di Giulio, A. (1992). The evolution of the Western Ligurian Flysch Units and the role of mud diapirism in ancient accretionary prisms (Maritime Alps, Northwestern Italy). Geologische Rundschau, 81, 655-668.

Di Giulio A. & Galbiati B. (1985). Quarzareniti nel complesso di base del Flysch di San Remo (Alpi Marittime). Rend. Soc. Geol. It, 8, 65-68.

Di Giulio, A. & Valloni, R. (1992). Analisi microscopia deele arentiti terrigene: Parametri petrologici e composizioni modali. Acta Naturalia de l´Ateneo Parmese, 28 (3/4), 55-101.

Di Giulio, A., Ronchi, A., Sanfilippo, A., Tiepolo, M., Pimentel, M., Ramos, V.A. (2012). Detrital zircon provenance from the Neuquen Basin (south-central Andes): cretaceous geodynamic evolution and sedimentary response in a retroarc-foreland basin. Geology, 40, 559–562.

Di Giulio, A., Ronchi, A., Sanfilippo, A., Balgord, E.A., Carrapa, A., Ramos, V.A. (2017). Cretaceous evolution of the Andean margin between 36°S and 40°S latitude through a multi-proxy provenance analysis of Neuquen Basin strata (Argentina). Basin Research, 29, 284-304.

Dillinger, A., Huddlestone, Holmes, C. R., Ricard, L. P., Esteban, L., Zwingmann, H. (2013). Diagenesis Impact on the Reservoir Quality of the Hutton Sandstone, Cooper Basin, South Australia. Proceedings of the Australian Geothermal Energy Conference 2013, Brisbane: 14–15.

Dott, R.H. (1964). Wacke, graywacke and matrix – What approach to immature sandstone classification? Journal of Sedimentary Research, 34 (3), 625–632.

Einsele, G. (2000). Sedimentary Basins: Evolution, Facies and Sediment Budget (2nd edition). Springer Verlag, Berlin, Heidelberg.

Elliott, T. (2000). Depositional architecture of a sand-rich, channelized turbidite system: The Upper Carboniferous Ross Sandstone Formation, Western Ireland: GCSSEPM Foundation 20th Annual Research Conference Deep-Water Reservoirs of the World, 342-373.

Espath, L. F. R., Pinto, L. C., Laizet, S., Silvestrini, J. H. (2014). Two- and three-dimensional Direct Numerical Simulation of particle-laden gravity currents. Computers and Geosciences, 63, 9–16.

Etienne, S., Mulder, T., Bez, M., G. Desaubliaux, G., Kwasniewski, A., Parize, O. Dujoncquoy, E., Salles, T. (2012). Multiple scale characterization of sand-rich distal lobe deposit variability: Examples from the Annot Sandstones Formation, Eocene–Oligocene, SE France. Sedimentary Geology, 273–274, 1-18.

Etienne, S., Mulder, T., Razin, P., Désaubliaux, G., Joussiaume, R., Tournadour, E. (2013). Proximal to distal turbiditic sheet-sand heterogeneities: Characteristics of associated internal channels. Examples from the Trois Evêchés area, Eocene-Oligocene Annot Sandstones (Grès d'Annot), SE France. Marine and Petroleum Geology, 41, 117-133.

von Eynatten, H., Pawlowsky-Glahn, V., Egozcue, J.J. (2002). Understanding perturbation on the simplex: a simple method to better visualise and interpret compositional data in ternary diagrams. Mathematical Geology, 34, 249–257.

Fedo, C.M., Sircombe, K.N., Rainbird, R.H. (2003). Detrital zircon analysis of the sedimentary record. Reviews in mineralogy and geochemistry. 53(1), 277-303.

Felix, M. (2002). Flow structure of turbidity currents. Sedimentology, 49, 397–419.

Felletti, F. (2016). Depositional architecture of a confined, sand-rich submarine system: the Bric la Croce-Castelnuovo turbidite system (Tertiary Piedmont Basin, Oligocene, NW Italy). Italian Journal of Geosciences (Bolletino della Societa Geologica Italiana), 135 (3), 365-382.

Fildani A., Cope, T.A., Graham, S.A., Wooden, J.L., 2003. Initiation of the Magallanes foreland basin: timing of the southern Patagonian Andes orogeny revised by detrital zircon provenance analysis. Geology. 31(12), 1081-1084.

Fildes, C., Stow, D., Riahi, S., Soussi, M., Patel, U., Milton, A.J. and Marsh, S. (2010). European provenance of the Numidian Flysch in northern Tunisia. Terra Nova, 22, 94–102.

Fisher, R.V. (1983). Flow transformations in sediment gravity flows. Geology, 11, 273-274.

Foeken, J.P.T., Dunai, T.J., Bertotti, G., Andriessen, P.A.M. (2003). Late Miocene to present exhumation in the Ligurian Alps (southwest Alps) with evidence for accelerated denudation during the Messinian salinity crisis. Geology, 31 (9), 797-800.

Folk, R.L. (1965). Petrology of Sedimentary Rocks, Hemphill, 170 pp.

Fonneland, H.C., Lien, T., Martinsen, O.J., Pedersen, R.B., Kosler, J. (2004) Detrital zircon ages: a key to understanding the deposition of deep marine sandstones in the Norwegian Sea- Sedimentary Geology, 164, 147-159.

Fonnesu, M., Haughton, P., Felletti, F., McCaffrey, W.D. (2015). Short length-scale variability of hybrid event beds and its applied significance. Marine and Petroleum Geology, 67, 583-603.

Fonnesu, M., Patacci, M., Haughton. P.D.W., Felletti, F., McCaffrey, W.D. (2016). Hybrid Event Beds Generated By Local Substrate Delamination On A Confined-Basin Floor. Journal of Sedimentary Research, 86 (8), 929-943.

Fontana, D., Spadafora, E., Stefani, C., Stocchi, S., Tateo, F., Villa, G., Zuffa, G.G. (1994). The Upper Cretaceous Helminthoid Flysch of the Northern Apennines: Provenance and Sedimentation. Mem. Soc. Geol. It., 48, 237-250.

Ford, M., Duchene, S., Gasquet, D., Vanderhaeghe, O. (2006). Two-phase orogenic convergence in the external and internal SW Alps. Journal of the Geological Society, London, 163, 815–826.

Fornelli, A., Langone, A., Micheletti, F., Piccareta, G. (2011). Time and duration of Variscan high-temperature metamorphic processes in the south European Variscides: constraints from U-Pb chronology and trace element chemistry of zircon. Miner. Petrol., 103, 101–122.

Fornelli A, Piccarreta G., Micheletti, F. (2014). In situ U-Pb dating combined with SEM imaging on zircon - an analytical bond for effective geological reconstruction. In: Nils Axel Morner. (Ed.): Iva Lipovic, Geochronology methods and case studies, 109 - 139, Janeza Trdine, 9 51000 Rijeka.

Fornelli A., Micheletti F., Piccarreta, G. (2016). Late-Proterozoic to Paleozoic history of the peri-Gondwana Calabria–Peloritani Terrane inferred from a review of zircon chronology. Springerplus, vol. 5, 1-19.

Frank, W. (1987). Evolution of the Austroalpine elements in the Cretaceous. In: Flügel, H.W. & FaupL, P. (Eds.): Geodynamics of the Eastern Alps. Deuticke, Vienna, 379–406.

Froitzheim, N. & Manatschal, G. (1996). Kinematics of Jurassic rifting, mantle exhumation, and passive-margin formation in the Austroalpine and Penninic nappes (eastern Switzerland). Bulletin of the Geological Society of America, 108, 1120–1133.

Froitzheim, N., Schmid, S.M., Frey, M. (1996). Mesozoic paleogeography and the timing of eclogite-facies metamorphism in the Alps: a workin hypothesis. Eclogae Geologicae Helvetiae, 89, 81-110.

Froitzheim, N., Plašienka, D., Schuster, R. (2008). Alpine tectonics of the Alps and Western Carpathians. In: McCann, T. (Ed.), The Geology of Central Europe, The Geological Society of London, 1141-1232.

Furrer, H., Schaltegger, U., Ovtcharova, M., and P. Meister, P. (2008). U-Pb zircon age of volcaniclastic layers in Middle triassic platform carbonates of the Austroalpine silvretta nappe (Switzerland). Swiss Journal of Geosciences, 101, 595–603.

Gaggero, L., Cortesogno, L. & Bertrand, J.M. (2004). The pre-Namurian basement of the Ligurian Alps: a review of the lithostratigraphy, pre-Alpine metamorphic evolution, and regional comparison. Periodico di Mineralogia, 73, 85–96.

Gaggero, L., Oggiano, G., Buzzi, L., Slejko, F., Cortesogno, L. (2007). Post-Variscan mafic dikes from the late orogenic collapse to the Tethyan rift: evidences from Sardinia. Ofioliti, 32, 15–37.

Gaggero, L., Gretter, N., Langone, A., Ronchi, A. (2017). U-Pb geochronology and geochemistry of late Palaeozoic volcanism in Sardinia (southern Variscides). Geoscince Frontiers, 21, 1-22.

Galbiati B. & Cobianchi, M. (1997). L'indipendenza tettonica dell'unita di Sanremo rispetto all'unita di Moglio-Testico. Bolletino Societa Geologica Italiana, 116, 453–472.

Galli, A., Le Bayon, B., Schmidt, M.W., Burg, J.P., Reusser, E., Sergeev, S.A., Larionov, A. (2011). U-Pb dating of the Gruf Complex: disclosing the late Variscan granulitic lower crust of Europe stranded in the Central Alps. Contributions to Mineralogy and Petrology, 163, 353-378.

Ganguly, J. & Tirone, M. (2009). Closure temperature, cooling age and and high temperature thermochronology. In: A.K. Gupta & S. Dasgupta (eds.), Physics and Chemistry of the Earth´s interior: crust, mantle and core. Indian National Science Academy, Springer Verlag.

Garcia, M. & Parker, G. (1989). Experiments on hydraulic jumps in turbidity currents near a canyon-fan transition. Science, 245, 393–396.

Gardner, M.H., Borer, J.M., Melick, J.J., Mavilla, N., Dechesne, M., Wagerle, R.N. (2003). Stratigraphic process–response model for submarine channels and related features from studies of Permian Brushy Canyon outcrops, West Texas. Marine and Petroleum Geology, 20, 757–787.

Gärtner, A., Linnemann, U., Sagawe, A., Hofmann, M., Ullrich, B., Kleber, A. (2013). Morphology of zircon crystal grains in sediments – characteristics, classifications, definitions. Geologica Saxonica, 59, 65-73.

Gärtner, A., Youbi, N., Villeneuve, M., Sagawe, A., Hofmann, M., Mahmoudi, A., Boumehdi, M.A, Linnemann, U. (2017). The zircon evidence of temporally changing sediment transport—the NW Gondwana margin during Cambrian to Devonian time (Aoucert and Smara areas, Moroccan Sahara). Int. J. Earth. Sci. (Geologische Rundschau). DOI 10.1007/s00531-017-1457-x

Garzanti, E. (2015). From static to dynamic provenance analysis—Sedimentary petrology upgraded. Sedimentary Geology, 336, 3-13.

Garzanti, E. (2016). From static to dynamic provenance analysis - Sedimentary petrology upgraded. Sedimnentary Geology, 87, 353–365.

Garzanti, E. (2017). The Maturity Myth In Sedimentology and Provenance Analysis. Journal of Sedimentary Research, 87, 353–365.

Garzanti, E. & Andò, S. (2007). Plate tectonics and heavy-mineral suites of modern sands. In: Mange, M. & Wright, D. (Eds.). Heavy minerals in use. Developments in Sedimentology, 34, 741–763. Elsevier, Amsterdam.

Garzanti, E., Andò, S., Vezzoli, G. (2006). The Continental Crust as a Source of Sand (Southern Alps Cross Section, Northern Italy). The Journal of Geology, 114 (5), 533-554.

Garzanti, E., Doglioni, C., Vezzoli, G. Andò, S. (2007). Orogenic belts and orogenic sediment provenance. The Journal of Geology, 115 (3), 315–334.

Garzanti, E., Vermeesch, P., Padoan, M., Resentini, A., Vezzoli, G., Ando, S. (2014). Provenance of Passive-Margin Sand (Southern Africa). The Journal of Geology, 122 (1), 17-42.

Gebauer, D. (1993). The Pre-Alpine evolution of the continental crust of the Central Alps – an overview. In: Von Raumer, J.F. & Neubauer, F. (eds.). "Pre-Mesozoic Geology in the Alps." Springer Verlag, 93-117.

Gehrels, G. (2000). Introduction to detrital zircons studies of Paleozoic and Triassic strata in western Nevada and northern California. In: Soreghan, M.J., and Gehrels, G.E. (eds.): Paleozoic and Triassic Paleogeography and Tectonics of Western Nevada and Northern California: Geological Society of America Special Paper, 347, 1–17.

Gehrels, G.E. (2014). Detrital Zircon U-Pb Geochronology Applied to Tectonics. Annu. Rev. Earth Planet. Sci., 42, 127–49.

Gehrels, G.E., Valencia, V.A., Joaquin, R. (2009). Enhanced precision, accuracy, and efficiency, and spatial resolution of U-Pb ages by laser ablation-multicollector-inductively coupled plasma-mass spectrometry. Geochemistry Geophysics Geosystems. 9 (3), 1-13.

Geisler T., Schaltegger U., Tomaschek F. (2007). Re-equilibration of zircon in aqueous fluids and melts. Elements, 3, 45-51.

Gerard, J., Dupont, G., Moron, J.M., Masse, P.L., Pourtoy, D., Bromley, R.G. (2000). From a refined chronostratigraphic framework to seismic interpretation: integration of quantitative palynology and micropaleontology, ichnology, sedimentology and seismic from the Lower Congo Tertiary basin (Angola). In: AAPG Annual Meeting and Exhibition. New Orleans, Louisiana Poster session.

Ghazi, S., Mountney, N.P. (2011). Petrography and provenance of the Early Permian Fluvial Warchha Sandstone, Salt Range, Pakistan. Sedimentary Geology, 233, 88-110.

Giacomini, F., Bomparola, R.M., Ghezzo, C. (2005). Petrology and geochronology of metabasites with eclogite facies relics from NE Sardinia: constraints for the Palaeozoic evolution of Southern Europe. Lithos, 82, 221-248.

Giacomini, F., Bomparola, R.M., Ghezzo, C., Guldbransen, H. (2006). The geodynamic evolution of the Southern European Variscides: constraints from the U/Pb geochronology and geochemistry of the lower Palaeozoic magmatic-sedimentary sequences of Sardinia (Italy). Contrib. Mineral. Petrol., 152, 19–42.

Giacomini, F., Braga, R., Tiepolo, M., Tribuzio, R. (2007) New constraints on the origin and age of Variscan eclogitic rocks (Ligurian Alps, Italy). Contrib Mineral Petrol, 153, 29–53.

Giacomini, F., Dallai, L., Carminati, E., Tiepolo, M., Ghezzi, C. (2008). Exhumation of a Variscan orogenic complex: insights into the composite granulitic–amphibolitic metamorphic basement of south-east Corsica (France). Journal of metamorphic Geology, 26, 403-436.

Giammarino, S., Fanucci, F., Orezzi, S., Rosti, D., & Morelli, D. (2010). Foglio 258–271 San Remo. Note illustrative della carta geologica d'Italia alla scala 1:50.000. Roma: Servizio Geologico d'Italia.

Graham, S. A., Ingersoll, R.V. etDickinson,W. R. (1976). Common provenance for lithic grains in Carboniferous sandstones from Ouachita Mountains and Black Warrior Basin. Journal of Sedimentary Petrology, 46(3), 620–632.

Grecula, M., Flint, S. S., Wickens, H. d. V., Johnson, S. D. (2003). Upward-thickening patterns and lateral continuity of Permian sand-rich turbidite channel fills, Laingsburg Karoo, South Africa. Sedimentology, 50, 831-853.

Grundvåg, S.A., Johannessen, E.P., Helland-Hansen, W., Plink-Björklund, P. (2014). Depositional architecture and evolution of progradationally stacked lobe complexes in the Eocene Central Basin of Spitsbergen. Sedimentology, 61, 535-569.

Guynn, J. & Gehrels, G. (2010). Comparison of detrital zircon age distributions using the K-S test. Tuscon, University of Arizona, 16 pages.

Haggart, J.W., Ward, P.D., 1989. New Nanaimo Group ammonites (Cretaceous, Santonian-Campanian) from British Columbia and Washington state. Journal of Paleontology. 63(2), 281-227.

Hanáček, M., Nývlt, D., Flašar, J., Stacke, V., Mida, P., Lehejček, J., Tóthová, G., Břežný, M., Procházková, B., Uxa, T., Křenovská, I. (2013). New methods to reconstruct clast transport history in different glacial sedimentary environments: Case study for Old Red sandstone clasts from polythermal Hørbyebreen and Bertilbreen valley glaciers, Central Svalbard. Czech Polar Reports, 3 (2), 107-129.

Handy, M.R., Schmid, S.M., Bousquet, R., Kissling, E., Bernoulli, D. (2010). Reconciling plate-tectonic reconstructions with the geological–geophysical record of spreading and subduction in the Alps Earth-Science Reviews, 102, 121-158.

Handy, M.R., Ustaszewski, K., Kissling, E. (2015). Reconstructing the Alps–Carpathians–Dinarides as a key to understanding switches in subduction polarity, slab gaps and surface motion. International Journal of Earth Sciences (Geol. Rundschau), 104 (1), 1-26.

Haughton, P.D.W., Barker, S.P., McCaffrey, W.D. (2003). 'Linked' debrites in sand-rich turbidite systems - origin and significance. Sedimentology, 50, 459-482.

Haughton, P.D.W., Davis, C., McCaffrey, W.D., Barker, S. (2009). Hybrid sediment gravity flow deposits - Classification, origin and significance. Marine and Petroleum Geology, 26, 1900-1918.

Heard, T.G. & Pickering, K.T. (2008). Trace fossils as diagnostic indicators of deep-marine environments, Middle Eocene Ainsa-Jaca Basin, Spanish Pyrenees. Sedimentology, 55, 809-844.

Heller, P.L. & Dickinson, W.R. (1985) Submarine ramp facies model for delta-fed, sand-rich turbidite sytems. AAPG Bulletin, 69, 960–976.

Henstra, G.A., Grundvåg, S.-A., Johannessen, E.P., Kristensen, T.B., Midtkandal, I., Nystuen, J.P., Rotevatn, A., Surlyk, F., Sæther, T., Windelstad, J. (2016). Depositional processes and stratigraphic architecture within a coarse-grained rift-margin turbidite system: the Wollaston Forland Group, east Greenland. Marine and Petroleum Geology, 76, 187–209.

Hesse, R. (1975). Turbiditic and non-turbiditic mudstone of Cretaceous flysch sections of the East Alps and other basins. Sedimentology, 22, 387-416.

Hesse, R., Klaucke, I., Khodabakhsh, S., Piper, D.J.W., Ryan, W.B.F., NAMOC Study Group (2001). Sandy submarine braid plains: Potential deep-water reservoirs. AAPG Bulletin, 85, 1499–1521.

Hodgson, D.M. (2009). Distribution and origin of hybrid beds in sand-rich submarine fans of the Tanqua depocentre, Karoo Basin, South Africa. Marine and Petroleum Geology, 26 (10): 1940-1956.

Hoskin, P.W.O., Schaltegger, U., 2003. The composition of zircon and igneous and metamorphic petrogenesis. In: J.M. Hanchar & P.W.O. Hoskin (eds.), Zircon. Reviews in Mineralogy and Geochemistry, 53, 27–62.

Hofstra, M., Hodgson, D.M., Peakall, J., Flint, S.S. (2015). Giant scour-fills in ancient channel-lobe transition zones: Formative processes and depositional architecture: Sedimentary Geology, 329, 98–114.

Horstwood, M.S.A., Košler, J., Gehrels, G., Jackson, S.E., McLean, N.M., Paton, C., Pearson, N.J., Sircombe, K., Sylvester, P., Vermeesch, P., Bowring, J.F., Condon, D.J., Schoene, B. 2016. Community-driven standards for LA-ICP-MS U-Th-Pb geochronology – uncertainty propagation, age interpretation and data reporting. Geostandards and Geoanalyitcal Research.

Hsü, K.J. (1959). Flute- and groove-casts in the Prealpine Flysch, Switzerland. American Journal of Science, 263, 97-109.

Hsü, K.J. (2004). Physics of Sedimentology. Springer, Heidelberg. 240 pp.

Hubbard, S.M., Romans, B.W., Graham, S.A. (2008). Deep-water foreland basin deposits of the Cerro Toro Formation, Magallanes basin, Chile: architectural elements of a sinuous basin axial channel belt. Sedimentology, 55, 1333-1359.

Hubbard, S.M., Covault, J.A., Fildani, A., Romans, B.W. (2014). Sediment transfer and deposition in slope channels: deciphering the record of enigmatic deep-sea processes from outcrop. GSA Bulletin 126, 857–871.

Hurst, A., Scott, A., Vigorito, M. (2011). Physical characteristics of sand injectites: Earth-Science Reviews, 106, 215–246.

Ito, M. (2008). Downfan transformation from turbidity currents to debris flows at a channel-to-lobe transitional zone; the lower Pleistocene Otadai Formation, Boso Peninsula, Japan. Journal of Sedimentary Research, 78 (10): 668-682.

Ingersoll, R. V. (1978). Petrofacies and Petrologic Evolution of the Late Cretaceous Fore-Arc Basin, Northern and Central California. The Journal of Geology, 86 (3), 335–352.

Ingersoll, R. V. & Suczek, C. A. (1979). Petrology and provenance of Neogene sand from Nicobar and Bengal fans, DSDP sites 211 and 218. Journal of Sedimentary Petrology, 49 (4), 1217–1228.

Ingersoll, R. V., Bullard, T. F., Ford, R. D., Grimm, J. P., Pickle, J. D. & Sares, S.W. (1984). The effect of grain size on detrital modes: a test of the Gazzi-Dickinson point-counting method. Journal of Sedimentary Petrology, 54 (1), 103–116.

Jackson, S., Pearson, N.J., Griffin, W.L., Belousova, E.A. (2004). The application of laser ablation-inductively coupled plasma-mass spectrometry to in-situ U-Pb zircon geochronology. Chemical Geology, 211, 47-69.

Janbu, N. E., Nemec, W., Kirman, E., Ozaksoy, V. (2007). Facies anatomy of a sand-rich channelized turbiditic system: the Eocene Kusuri Formation in the Sinop Basin, north-central Turkey. In: Nichols, G., Williams, E. and Paola, C. (Eds). Sedimentary Processes, Environments and Basins: A Tribute to Peter Friend. Special Publications of the International Association of Sedimentologists, 38, 457-517.

Jobe, Z.R., Bernhardt, A., Lowe, D.R. (2010). Facies and architectural asymmetry in a conglomerate-rich submarine channel fill, Cerro Toro Formation, Sierra Del Toro, Magallanes Basin, Chile. Journal of Sedimentary Research, 80, 1085-1108.

Johnson, S.D., Flint, S., Hinds, D. Wickens, H. (2001). Anatomy, geometry and sequency stratigraphy of basin floor to slope turbidite systems, Tanqua Karoo, South Africa. Sedimentology, 48, 987–1023.

Johnsson, M.J., Stallard, R.F., Meade, R.H. (1988), First-cycle quartz arenites in the Orinoco River basin, Venezuela and Colombia. Journal of Geology, 96, 263-277.

van de Kamp, P.C. & Leake, B.E. (1995). Petrology and geochemistry of siliciclastic rocks of mixed feldspathic and ophiolitic provenance in the Northern Apennines, Italy. Chemical Geology, 122, 1-20.

Kane, I.A. & Pontén, A.S.M. (2012). Submarine transitional flow deposits in the Paleogene Gulf of Mexico. Geology, 40, 1119-1122.

Kerckhove, C. (1969). La “zone du flysch” dans les nappes de l’Embrunais-Ubaye (Alpes Occidentales). Géologie Alpine, 45, 5-204.

Kilhams, B., Morton, A., Wilkins, A., Hurst, A. (2014). Understanding the provenance and reservoir quality of the Sele Formation sandstones of the UK Central Graben utilizing detrital garnet suites. Geological Society, London, Special Publications, 386 (1), 129-142.

Kneller, B.C. & Branney, M.J. (1995). Sustained high-density turbidity currents and the deposition of thick massive sands. Sedimentology, 42, 607-616.

Kneller, B. C., & Buckee, M. J. (2000). The structure and fluid mechanics of turbidity currents: a review of some recent studies and their geological implications. Sedimentology, 47, 62 – 94.

Klötzli, U. S., Sinigoi, S., Quick, J.E., Demarchi, G., Tassinari, C.C.G., Sato, K., Günes, Z. (2014). Duration of igneous activity in the Sesia Magmatic System and implications for high-temperature metamorphism in the Ivrea–Verbano deep crust, Lithos, 206–207, 19–33.

Kuenen, P.H. (1950). Turbidity currents of high density. In: 18th International Geological Congress, London, 1948, 44–52.

Kuenen, P.H. (1966). Experimental Turbidite Lamination in a Circular Flume. Journal of Geology, 74, 523-545.

Kuenen, Ph.H. & Migliorini, C.I. (1950). Turbidity currents as a cause of graded bedding. Journal of Geology, 58, 91–127.

Lanteaume, M., Radulescu, N., Gavos, M., & Feraud, J. (1990). Notice explicative, Carte Géol. De France (1/50.000), feuille Viève-Tende (948). Orleans: BRGM. 139 pp.

Lash, G.G. (1985). Recognition of trench fill in orogenic flysch sequences. Geology, 13, 867-870.

Leverenz, A. (2000). Trench-sedimentation versus accreted submarine fan; an approach to regional-scale facies analysis in a Mesozoic accretionary complex; "Torlesse" Terrane, northeastern North Island, New Zealand. Sedimentary Geology, 132(1-2), 125-160.

Leszczyński, S., Dziadzio, P.S., Wojciech Nemec, W. (2015). Some current sedimentological controversies in the Polish Carpathian flysch. Guide to field trip B8, 31st IAS Meeting of Sedimentology Kraków, Poland, 25–27 June.

De Leeuw, J., Eggenhuisen, J.T., Cartigny, M.J.B. (2016). Morphodynamics of submarine channel inception revealed by new experimental approach. Nature Communications, 7, 1-7.

Li, X.H., Faure, M., Lin, W. (2014). From crustal anatexis to mantle melting in the Variscan orogen of Corsica (France): SIMS U–Pb zircon age constraints. Tectonophysics, 634, 19–30.

Liati A., Froitzheim N., Fanning C.M. (2005). Jurassic ophiolites within the Valais domain of the Western and Central Alps: geochronological evidence for re-rifting of oceanic crust. Contributions to Mineralogy and Petrology, 149, 446–461.

Lien, T., Midtbø, R.E., Martinsen, O.J. (2006). Depositional facies and reservoir quality of deep-marine sandstones in the Norwegian Sea. Norwegian Journal of Geology, 86, 71–92.

Link, K., Fanning, C.M., Beranek, L.P., 2005. Reliability and longitudinal change of detrital-zircon age spectra in the Snake River system, Idaho and Wyoming: an example of reproducing the bumpy barcode. Sedimentary Geology. 182, 101- 142.

Linnemann, U., McNaughton, N., Romer, R.L., Gehmlich, M., Drost, K., Tonk, C. (2004). West African provenance for Saxo-Thuringia (Bohemian Massif): Did Armorica ever leave pre-Pangean Gondwana? – U/Pb-SHRIMP zircon evidence and the Nd-isotopic record. Int J Earth Sci (Geologische Rundschau), 93, 683–705.

Linnemann, U., Pereira, F., Jeffries, T.E., Drost, K., Gerdes, A. (2008). The Cadomian Orogeny and the opening of the Rheic Ocean: The diacrony of geotectonic processes constrained by LA-ICPMS U-Pb zircon dating (Ossa-Morena and Saxo-Thuringian Zones, Iberian and Bohemian Massifs). Tectonophysics 461, 21-43.

Liotta, D., Caggianelli, A., Kruhl, J.H., Festa, V., Prosser, G., Langone, A. (2008). Multiple injections of magmas along a Hercynian mid-crustal shear zone (Sila Massif, Calabria, Italy). Journal of Structural Geology, 30, 1202–1217.

Lister, G. S., Forster, M. A., Rawling, T. J. (2001). Episodicity during orogenesis. In: J. A. Miller, R. E. Holdsworth, I. S. Buick, M. Hand (Eds.): Continental Reactivation and Reworking. Geological Society London Special Publications, 184, 89–113.

van Loon, A.J. (2009). Soft-sediment deformation structures in siliciclastic sediments: an overview. Geologos, 15 (1), 3-55.

Lowe, D.R. (1982). Sediment gravity flows: II. Depositional models with special reference to the deposits of high-density turbidity currents. Journal of Sedimentary Petrology 52, p. 279–297.

Lowe, D.R. & Guy, M. (2000). Slurry-flow deposits in the Britannia Formation (Lower Cretaceous), North Sea: a new perspective on the turbidity current and debris flow problem. Sedimentology, 47, 31-70.

Lowe, D.R., Guy, M., Palfrey, A. (2003). Facies of slurry-flow deposits, Britannia Formation (Lower Cretaceous), North Sea: implications for flow evolution and deposit geometry: Sedimentology, 50, 45-80.

Ludwig, K.R., 2003. Isoplot/Ex version 3.0. A geochronological toolkit for Microsoft Excel. Berkeley Geochronology Center Special Publication No. 1a, 2455 Ridge Road, Berkeley CA 94709, USA.

Macauley, R. V. and Hubbard, S.M. (2013). Slope channel sedimentary processes and stratigraphic stacking, Cretaceous Tres Pasos Formation slope system, Chilean Patagonia. Marine And Petroleum Geology 41: 146-162.

Macdonald, H.A., Peakall, J., Wignall, P.B., Best, J. (2011). Sedimentation in deep-sea lobe elements: implications for the origin of thickening-upward sequences. Journal of the Geological Society of London 168, 319–331.

Maino, M. & Seno, S. (2016). The thrust zone of the Ligurian Penninic basal contact (Monte Frontè, Ligurian Alps, Italy). Journal of Maps, 12, p. 341-351.

Maino, M., Dallagiovanna, G., Dobson, K., Gaggero, L., Persano, C. Seno, S., Stuart, F.M. (2012). Testing models of orogen exhumation using zircon (U–Th)/He thermochronology: insight from the Ligurian Alps, Northern Italy. Tectonophysics, 560–561, 84–93.

Maino, M., Casini, L., Ceriani, A., Decarlis, A., Di Giulio, A., Seno, S., Setti, M., Stuart, F. (2015). Dating shallow thrusts with zircon (U-Th)/He thermochronometry —The shear heating connection, Geology, 43, 495-498.

Malgesini, G., Talling, P. J., Hogg, A. J., Armitage, D., Goater, A., Felletti, F. (2015). Quantitative analysis of submarine-flow deposit shape in the Marnoso-Arenacea Formation: what is the signature of hindered settling from dense near-bed layers? Journal of Sedimentary Research, 85 (2), 170-191.

Malkowski, M.A., Sharman, G.R., Graham, S.A., Fildani, A. (2015). Characterisation and diachronous initiation of coarse clastic deposition in the Magallanes–Austral foreland basin, Patagonian Andes. Basin Research, 29, 1-29.

Malkowski, M.A., Grove, M., Graham, S.A. (2016). Unzipping the Patagonian Andes - Long-lived influence of rifting history on foreland basin evolution. Lithosphere. 8 (1), 23-28.

Malusà, M.G., Faccenna, C., Baldwin, S.L., Fitzgerald, P.G., Rossetti, F., Balestrieri, M.L., Danisık, M., Ellero, A. Ottria, G., Piromallo, C. (2015). Contrasting styles of (U)HP rock exhumation along the Cenozoic Adria-Europe plate boundary (Western Alps, Calabria, Corsica), Geochem. Geophys. Geosyst., 16, 1786–1824.

Mansurbeg, H., Morad, S., Salem, A., Marfil, R., El-Ghali, M.A.K., Nystuen, J.P., Caja, M.A., Amorosi, A., Garcia, D., La Iglesia, A. (2008). Diagenesis and reservoir quality evolution of palaeocene deep-water, marine sandstones, the Shetland–Faroes Basin, British continental shelf Marine and Petroleum Geology, 25 (2008), 514–543.

Manzotti, P., Ballevre, B., Zucali, M., Robyr, M., Engi, M. (2014). The tectonometamorphic evolution of the Sesia-Dent Blanche nappes (internal Western Alps): review and synthesis. Swiss Journal of Geosciences, 107 (2-3), 309-336.

Manzotti, P., Ballèvre, M., Poujol, M. (2016). Detrital zircon geochronology in the Dora-Maira and Zone Houillère: a record of sediment travel paths in the Carboniferous. Terra Nova, 28 (4), 279-288.

Marchand, A.M.E., Apps, G., Li, W., Rotzien, J. R. (2015). Depositional processes and impact on reservoir quality in deepwater Paleogene reservoirs, US Gulf of Mexico: AAPG Bulletin 99 (9), 1635–1648.

Marini, M., Milli, S., Ravnås, R. (2015). A comparative study of confined vs. semi-confined turbidite lobes from the Lower Messinian Laga Basin (Central Apennines, Italy): Implications for assessment of reservoir architecture. Marine and Petroleum Geology, 62, 142-165.

Marroni, M. & Pandolfi, L. (2007). The architecture of an incipient oceanic basin: a tentative reconstruction of the Jurassic Liguria-Piemonte basin along the Northern Apennines–Alpine Corsica transect. International Journal of Earth Sciences (Geol. Rundschau), 96 (6), 1059-1078.

Marroni, M., Molli, G., Ottria, G., PAndolfi, L. (2001). Tectono-sedimentary evolution of the External Liguride units (northern Apennine, Italy): From rifting to convergence history of a fossil ocean-continent transition zone. Geodinamica Acta, 14, 307-320.

Marsset, T., Droz, L., Dennielou, B., Pichon, E. (2009). Cycles in the architecture of the quaternary Zaire turbidite system: a possible link with climate. In: Kneller, B., Martinsen, O.J., McCaffrey, W.D. (eds.), External Controls on Deep-water Depositional Systems, 92. SEPM Special Publication, 89-106.

Mattern, F. (2002). Amalgamation surfaces, bed thicknesses, and dish structures in sand-rich submarine fans: numeric differences in channelized and unchannelized deposits and their diagnostic value. Sedimentary Geology, 150, 203–228.

Mattern, F. (2005). Ancient sand-rich submarine fans: depositional systems, models, identification, and analysis. Earth-Science Reviews, 70 (3-4), 167-202.

McCann, T. & Arbues, P. (2012). Deep-marine sandstone provenance, Ainsa Basin, Southern Pyrenees, Spain. Zeitaschrift der deutschen Geowissenschaften, 22, 185-201.

McCann, T., Timmermann, M.J., Krzywiec, P., Lopez-Gomez, J., Wetzel, A., Krawczyk, C.M., Rieke, H., Lamarche, J. (2006). Post-Variscan (end Carboniferous-Early Permian) basin evolution in Western and Central Europe. Geological Society, London, Memoirs, 32, 355-388.

McHargue, T., Pyrcz, M.J., Sullivan, M.D., Clark, J., Fildani, A., Romans, B.R., Covault, J.A., Levy, M., Posamentier, H., Drinkwater, N. (2011). Architecture of turbidite channel systems on the continental slope: patterns and predictions. Marine and Petroleum Geology 28, 728-743.

Ménot, R.-P., von Raumer, J.P., Bognadoff, S., Vivier, G. (1994). Variscan basement of the Western Alps-the External Crystalline Massifs. In: J.D. Keppie (Ed.). Pre-Mesozoic Geology in France and related areas. Springer Verlag Berlin, Heidelberg. 458-466.

Miall, A. D. (1988). Architectural elements and bounding surfaces in fl uvial deposits; anatomy of the Kayenta Formation (Lower Jurassic), Southwest Colorado. Sedimentary Geology, 55 (3-4), 233-262.

Miall, A. D. (1991). Hierarchies of architectural units in terrigenous clastic rocks, and their relationship to sedimentation rate. En: The three-dimensional facies architecture of terrigenous clastic sediments and its implications for hydrocarbon discovery and recovery. In: D. Miall, Andrew & N. Tyler (eds.). Concepts in Sedimentology and Paleontology, 3, 6-12. SEPM, Tulsa, Oklahoma, United States.

Middleton, G.V. (1967). Experiments on density and turbidity currents: III. Deposition of sediment. Canadian Journal of Earth Sciences, 4, 475-505.

Middleton, G.V. (1970). Experimental studies related to problems of flysch sedimentation. In: J. Lajoie (Ed.), Flysch Sedimentology in North America, Geological Association of Canada, Special Paper, 7, 253-272.

Middleton, G.V. (1993). Sediment deposition form turbidity currents. Annual Review of Earth and Planetary Sciences, 21, 89-94.

Middleton, G.V. & Hampton, M.A. (1976). Subaqueous sediment transport and deposition by sediment gravity flows. In: Marine sediment transport and environmental management, D.J. Stanley & D.J.P. Swift (Eds.). Wiley, New York, 197-218.

Milli, M., Moscatelli, M., Stanzione, O., Falcini, F. (2007). Sedimentology and physical stratigraphy of the Messinian turbidite deposits of the Laga basin (central Apennines, Italy). Bollettino della Societa Geologica Italiana, 126, 255-281.

Mitchum, R.M. (1977). Seismic stratigraphy and global changes of sea level, part 11: glossary of terms used in seismic stratigraphy. In: C.E. Payton (Ed.). Seismic Stratigraphy — Applications to Hydrocarbon Exploration, AAPG Memoir, 26, pp. 205–212.

Mohn, G., Manatschal, G., Müntener, O., Beltrando, M., Masini, E. (2010). Unravelling the interaction between tectonic and sedimentary processes during lithospheric thinning in the Alpine Tethys margins. Int J Earth Sci (Geologische Rundschau), 99, 75-101.

Mohrig, D. & Marr, J.G. (2003). Constraining the efficiency of turbidity current generation from submarine debris flows and slides using laboratory experiments. Marine and Petroleum Geology, 20, 883-899.

Mohrig, D., Whipple, K.X., Hondzo, M., Ellis, C., Parker. G. (1998). Hydroplaning of subaqueous debris flows. Geological Society of American Bulletin, 110, 387-394.

Molli, G. (2008). Northen Apennine – Corsica orogenic system: an updated overview. Geological Society, London, Special Publications, 413-442.

Molli, G. & Malavieille, J. (2011). Orogenic processes and the Corsica/Apennines geodynamic evolution: insights from Taiwan. Int J Earth Sci (Geologische Rundschau), 100, 1207-1224.

Morris, E.A., Hodgson, D.M., Flint, S.S., Brunt, R.L., Butterworth, P.L., Verhaeghe, J. (2014). Sedimentology, Stratigraphic Architecture and Depositional Context of Submarine Frontal Lobe Complexes, Journal of Sedimentary Research 84, 763-780.

Moscardelli, L., Wood, L., Mann, P. (2006). Mass-transport complexes and associated processes in the offshore area of Trinidad and Venezuela. AAPG Bulletin, 90, 1059-1088.

Mulder, T. (2011). Gravity processes on continental slope, rise and abyssal plains. In: Hüneke, H. & Mulder, T. (Eds.), Deep-Sea Sediments. Developments in Sedimentology, 63, 25–148. Elsevier, Amsterdam.

Mulder, T. & Cochonat, P. (1996). Classification of offshore mass movements. Journal of Sedimentary Research, 66, 43–57.

Mulder, T. & Alexander, J. (2001). The physical character of subaqueous sedimentary density flows and their deposits. Sedimentology, 48 (2), 269-299.

Mulder, T. & S. Etienne, S. (2010). Lobes in deep-sea turbidite systems, state of the art. Sedimentary Geology, 229 (3), 75–80.

Mulder, T., Syvitski, J.P.M., Migeon, S., Faugères, J.-C., Savoye, B. (2003). Hyperpycnal turbidity currents: initiation, behaviour and related deposits. A review. In: Mutti, E., Steffens, G.S., Pirmez, C., Orlando, M., Roberts, D. (Eds.), Marine and Petroleum Geology, 20 (6–8), 861–882. Mulder, T., Callec, Y., Parize, O., Joseph, P., Schneider, J.-L., Robin, C., Dujoncquoy, E., Salles, T., Allard, J., Ducassou, E., Ferger, B., Gaudin, M., Linares, F., Marchés, E., Zaragosi, S. (2010). High-resolution analysis of submarine lobe deposits: seismic-scale outcrops of the Lauzanier area (SE Alps, France). Sedimentary Geology, 229, 160–191.

Mulder, T., Hüneke, H., Van Loon, A.J. (2011). Progress in Deep-Sea Sedimentology. In: Hüneke,H. & Mulder, T. (Eds.). Deep-Sea Sediments. Developments in Sedimentology, 63, 1-24. Elsevier, Amsterdam.

Mutti, E. (1979). Turbidites et cònes sous-marins profonds. In: P. Homewood (Ed.), Sedimentation détritique, pp. 353–419, Institut de Géologie, Universite de Fribourg, Fribourg.

Mutti, E. (1985). Turbidite systems and their relations to depositional sequences. In: G.G. Zuffa (Ed.), Provenance of Arenites , pp. 65–93, NATO-ASI Series, Reidel, Dordrecht.

Mutti, E. (1992). Turbidite Sandstones. San Donato Milanese, Agip-Istituto di Geologia, Universita` di Parma, Parma, 275 pp.

Mutti, E. & Ghibaudo, G. (1972). Un esempio di torbiditi di conoide esterna: le Arenarie di S. Salvatore (Formazione di Bobbio, Miocene) nell'Appennino di Piacenza. Mem. Acc. Sci. Torino, Cl. Sci. Fis. Mat. Nat., 16, 1–40.

Mutti, E. & Ricci Lucchi, F. (1972). Le torbiditi dell'Appennino settentrionale: introduzione all'analisi di facies. Mem. Soc. Geol. It., 11, 161–199.

Mutti, E. Ricci Lucchi, F. (1975). Turbidite facies and facies association. In: Examples of Turbidite Facies Associations from Selected Formation of Northern Apennines. E. Mutti, G.C. Parea, F. Ricci Lucchi, M. Sagri, G. Zanzucchi, G. Ghibaudo, S. Iaccarino (Eds.). pp. 21–36, IX Int. Cong. IAS, Field Trip Guidebook, Nice, France.

Mutti, E. & Sonnino, M. (1981). Compensation cycles: a diagnostic feature of turbidite sandstone lobes. In: Valloni, R., Colella, A., Sonnino, M., Mutti, E., Ori, G.G. (Eds.), Abstr. Int. Assoc. Sediment., 2nd Eur. Reg. Meet., Bologna, Italy, 120–123.

Mutti, E. & Normark, W.R. (1987). Comparing examples of modern and ancient turbidite systems: problems and concepts. In: Leggett, J.K., Zuffa, G.G. (Eds.), Marine Clastic Sedimentology: Concepts and Case Studies. Graham & Trotman, Oxford, pp. 1–38.

Mutti, E. & Normark, W.R. (1991). An integrated approach to the study of turbidite systems. In: Weimer, P., Link, M.H. (Eds.), Seismic Facies and Sedimentary Processes of Submarine Fans and Turbidite Systems. Springer, New York, pp. 75–106.

Mutti, E., Tinterri, R., Remacha, E., Mavilla, N., Angella, S., Fava, L. (1999). An introduction to the analysis of ancient turbidite basins from an outcrop perspective. AAPG Course Notes 39, 93 pp.

Mutti, E., Bernoulli, D., Ricci Lucchi, F. (2009). Turbidites and turbidity currents from Alpine 'flysch' to the exploration of continental margins. Sedimentology, 56, 267-318.

Muzzi Maghalaes, P. & Tinterri, R. (2010). Stratigraphy and Depositional Setting of Slurry and Contained (Reflected) Beds in the Marnoso-arenacea Formation (Langhian-Serravallian) Northern Apennines, Italy. Sedimentology, 57, 1585-1720.

Najman, Y. (2006). The detrital record of orogenesis: a review of approaches and techniques used in the Himalayan sedimentary basins. Earth-Science Reviews, 74, 1–72.

Necker, F., Härtel, C., Kleiser, L., Meiburg, E., (2002). High-resolution simulations of particle-driven gravity currents. International Journal of Multiphase Flow, 28, 279–300.

Nelson, D.R., Robinson, B.W., Myers, J.S. (2000). Complex geological histories extending for 4.0 Ga deciphered from xenocryst zircon microstructures. Earth and Planetary Science Letters, 181, 89-102.

Normark, W.R. (1970). Growth patterns of deep-sea fans. AAPG Bullettin, 54, 2170–2195.

Oggiano, G., Gaggero, L., Funedda, A., Buzzi, L., Tiepolo, M. (2010). Multiple early Paleozoic volcanic events at the northern Gondwana margin: U–Pb age evidence from the Southern Variscan branch (Sardinia, Italy). Gondwana Research, 17 (1), 44-58.

Palomares, M. & Arribas, J. (1993). Modern stream sands from compound crystalline sources: Composition and sand generation index. Geological Society of America Special Paper, 284, 313-322.

Paquette, J.L., Montel, J.M., Chopin, C. (1999). U-Th-Pb dating of the Brossasco ultra high-pressure metagranite, Dora-Maira massif, western Alps. Eur. J. Mineral., 11, 69-77.

Parker, G., Garcia, M. H., Fukushima, Y., Yu, W. (1987). Experiments on turbidity currents over erodible bed. Journal of Hydraulic Research, 25, 123–147.

Patacci, M. (2016). A high-precision Jacob's staff with improved spatial accuracy and laser sighting capability. Sedimentary Geology, 335, 66-69.

Patacci, M., Haughton, P.D.W., McCaffrey, W.D. (2014). Rheological Complexity in Sediment Gravity Flows Forced to Decelerate against a Confining Slope, Braux, SE France. Journal of Sedimentary Research, 84, 270-277.

Pavanetto, P., Funedda, A., Northrup, C.J., Schmitz, M., Crowley, J., Loi, A. (2012). Structure and U–Pb zircon geochronology in the Variscan foreland of SW Sardinia, Italy. Geological Journal, 47, 426-445.

Pemberton, E. A. L., Hubbard, S. M., Fildani, A., Romans, B., Stright, L. (2016). The stratigraphic expression of decreasing confinement along a deep-water sediment routing system; outcrop example from southern Chile. Geosphere 12(1): 114-134.

Pereira, M.F., Alabdeiro, L., Gama, C., Chichorro, M., Hofmann, M., Linnemann, U. (2016). Provenance of Holocene beach sand in the Western Iberian margin: the use of the Kolmogorov–Smirnov test for the deciphering of sediment recycling in a modern coastal system. Sedimentology, 63, 1149-1167.

Pettingill, H.S., 1997: Turbidite Giants - Lessons from the World's 40 Largest Turbidite Discoveries. *EAGE/AAPG 3rd Research Symposium, Abstracts Volume,* AO27.

Peyton, L. & Barbara Carrapa, B. (2013). An introduction to low-temperature thermochronologic techniques, methodology, and applications. In: C. Knight & J. Cuzella, (Eds.), Application of structural methods to Rocky Mountain hydrocarbon exploration and development. AAPG Studies in Geology, 65, 15–36.

Pickering, K.T. & Corregidor, J. (2005). Mass-transport complexes (MTCs) and tectonic control on basin-floor submarine fans, middle Eocene, south Spanish Pyrenees. Journal of Sedimentary Research, 75, 761-783.

Pickering, K.T., Hiscott, R.N., Hein, F.J. (1989). Deep Marine Environments: Clastic Sedimentation and Tectonics. Unwin Hyman, London, 416 pp.

Pierson, T.C. & Costa, J.E. (1987). A rheological classification of subaerial sediment-water flows. In: J.E. Costa & G.F. Wieczorek, (eds.), Debris Flows / Avalanches: Process, Recognition, and Migitation: Geological Society of America, Reviews in Engineering Geology, 7, 1-12.

Pinter, P.R., Butler, R.W.H., Hartley, A.J., Maniscalco, R., Baldassini, N., Di Stefano, A. (2017). Tracking sand-fairways through a deformed turbidite system: the Numidian (Miocene) of Central Sicily, Italy. Basin Research, 1-22, 1–22, doi: 10.1111/bre.12261.

Porten, K.W., Kane, I.A., Warchoł, M.J., Southern, S.J. (2016). A Sedimentological Process-Based Approach To Depositional Reservoir Quality of Deep-Marine Sandstones: An Example From the Springar Formation, Northwestern Vøring Basin, Norwegian Sea. Journal of Sedimentary Research, 86 (11), p. 1269 -1286.

Posamentier, H.W., Kolla, V. (2003). Seismic geomorphology and stratigraphy of depositional elements in deep-water settings. Journal of Sedimentary Research, 73 (3), 367–388.

Posamentier, H.W. & Walker, R.G. (2006). Deep-water turbidites and submarine fans. In: H.W. Posamentier & Walker, R.G. (eds.), Facies Models Revisited. SEPM (Society for Sedimentary Geology), Tulsa, Oklahoma 74135-5814, U.S.A., pp. 399-520.

Postma, G. & Cartigny, M. (2014). Supercritical and subcritical turbidity currents and their deposits — A synthesis. Geology, 42 (11), 987-990.

Postma, G., Nemec, W., Kleinspehn, K.L. (1988). Large floating clasts in turbidites: a mechanism for their emplacement. Sedimentary Geology, 58, 47–61.

Postma, G., Cartigny, M., K. Kleverlaan, K. (2009). Structureless, coarse-tail graded Bouma Ta formed by internal hydraulic jump of the turbidity current? Sedimentary Geology, 219 (1), 1–6.

Postma, G., Kleverlaan, K., Cartigny, M. (2014). Recognition of cyclic steps in sandy and gravelly turbidite sequences and consequences for the Bouma facies model. Sedimentology, 61 (7), 2268-2290.

Powichrowski, L.K. (1989). Trace fossils from the Helminthoid Flysch (Upper Cretaceous-Paleocene) of the Ligurian Alps (Italy): development of deep marine ichnoassociations in fan and basin plain environments. Eclogae Geologicae Helvetiae 82, 385-411.

Prélat, A., Hodgson, D.M., and Flint, S.S. (2009). Evolution, architecture and hierarchy of distributary deep-water deposits: A high-resolution outcrop investigation of submarine lobe deposits from the Permian Karoo Basin, South Africa, Sedimentology, 56, 2132–2154.

Prélat A. & Hodgson D.M. (2013). The full range of turbidite bed thickness patterns in submarine lobes: Controls and implications, Journal of the Geological Society, 170, pp.209-214.

Prélat, A., Covault, J.A., Hodgson, D.M., Fildani, A., Flint, S.S. (2010). Intrinsic controls on the range of volumes, morphologies, and dimensions of submarine lobes: Sedimentary Geology, 232, 66–76.

Pringle, J.K., Brunt, R.L., Hodgson, D.M., Flint, S.S. (2010). Capturing stratigraphic and sedimentological complexity from submarine channel complex outcrops to digital 3D models, Karoo Basin, South Africa. Petroleum Geoscience, 16, 307-330.

Quinn, M.Q., Hubbard, S.M., van Drecht, R., Guest, B., Matthews, W.A., Hadlari, T. (2016). Record of orogenic cyclicity in the Alberta foreland basin, Canada Cordillera. Lithosphere.

Ragusa, J., Kindler, P., Segvic, B., Ospina-Ostios, L.M. (2017). Provenance analysis of the Voirons Flysch (Gurnigel nappe, Haute-Savoie, France): stratigraphic and palaeogeographic implications. International Journal of Earth Sciences (Geol. Rundschau), DOI 10.1007/s00531-017-1474-9.

Raines, K.M., Hubbard, S.M., Kukulski, R.B., Leier, A.L., Gehrels, G.E. (2013). Sediment dispersal in an evolving foreland: Detrital zircon geochronology from Upper Jurassic and Lowermost Cretaceous stata, Alberta Basin, Canada. Geological Society of America Bulletin, 25, 741-755.

von Raumer, J.F., Stampfli, G.M., Borel, G., Bussy, F. (2002). Organization of pre-Variscan basement area at the north-Gondwanan margin. Int. J. Earth Sciences (Geol. Rundschau), 91, 35-52.

von Raumer, J.F., Stampfli, G.A., Bussy, F. (2003). Gondwana-derived microcontinents-the constituents of the Variscan and Alpine collisional orogens. Tectonophysics, 365 (1-4), 7-22.

von Raumer, J.F., Bussy, F., Stampfli, G.M. (2009). The Variscan evolution in the External massifs of the Alps and place in their Variscan framework. Comptes Rendus Geosciences, 341, 239-252.

von Raumer, J.F., Bussy, F., Schaltegger, U., Schulz, B., Stampfli, G.M. (2013). Pre-Mesozoic Alpine basements. Their place in the European Palaeozoic framework. Geological Society of America Bulletin, 125 (1-2), 89-108.

von Raumer, J.F., Stampfli, G.M., Arenas, R., Sánchez Martínez, S. (2014). Ediacaran to Cambrian oceanic rocks of the Gondwana margin and their tectonic interpretation. International Journal of Earth Sciences (Geol. Rundschau), 104, 1107–1121.

Reading, H. G. & M. Richards (1994). Turbidite systems in deep-water basin margins classified by grain size and feeder system: AAPG Bulletin, 78, 792–822.

Reimink, J.R., Davies, J.H., Waldron, J.W., Rojas, X. (2016). Dealing with discordance: a novel approach for analysing U–Pb detrital zircon datasets. Journal of the Geological Society, 173, 577-585.

Ricci Lucchi, F. & Valmori, E. (1980). Basin-wide turbidites in a Miocene, over-supplied deep-sea plain: a geometrical analysis. Sedimentology, 27, 241-270.

Richter, M. (1961). Über den Bau der Ligurischen Alpen. 3. Tektonik und Stellung der Flyschzone. Zeitschrift der Deutschen Geologischen Gesellschaft, 113, 116-149.

Romans, B.W., Hubbard, S.M., Graham, S.A. (2009). Stratigraphic evolution of an outcropping continental slope system, Tres Pasos Formation at Cerro Divisadero, Chile. Sedimentology 56, 737-764.

Ronca, S., Del Moro, A., Traversa, G. (1999). Geochronology, Sr-Nd isotope geochemistry and petrology of late-Hercynian dyke magmatism from Sarrabus (SE Sardinia). Periodo di Mineralogia, 68, 231-260.

Rosenbaum, G. & Lister, G.S. (2005). The Western Alps from the Jurassic to Oligocene: spatio-temporal constraints and evolutionary reconstructions. Earth-Science Reviews, 69 (3-4), 281-306.

Rossi, P. & Durand-Delga, M. (2001) Significance of sandstones interbedded in the Jurassic Basalts of the Balagne Ophiolithic Nappe (Corsica, France). Ofioliti, 26, 169-174.

Rotzien, J.R., Lowe, D.R., Schwalbach, J.R. (2014). Processes of Sedimentation and Stratigraphic Architecture of Deep-Water Braided Lobe Complexes: The Pliocene Repetto and Pico Formations, Ventura Basin, U.S.A. Journal of Sedimentary Research, 84 (19), 910-934.

Rowan, M.G. (1990). The Upper Cretaceous Helminthoid Flysch of the Northern Apennines and Maritime Alps: correlation and provenance. Ofioliti, 15, 305-326. Russell, H.A.J., Arnott, R.W.C. (2003). Hydraulic-jump and hyperconcentrated-flow deposits of a glacigenic subaqueous fan: oak ridges moraine, southern Ontario, Canada. Journal of Sedimentary Research 73 (6), 887–905.

Rubatto, D. & Gervers, M. (1999). Eo/Oligocene (35 Ma) high-pressure metamorphism in the Monte Rosa nappe (Western Alps): implications for paleogeography', Schweizerische Mineralogische und Petrographische Mitteilungen, 79, 353-362.

Rubatto, D., Schaltegger, U., Lombardo, B., Colombo, F., Compagnoni, R. (2001). Complex Palaeozoic magmatic and metamorphic evolution in the Argentera Massif (Western Alps) resolved with U–Pb dating. Swiss Bulletin of Mineralogy and Petrology, 81, 213–228.

Rubatto, D., D. Regis, D. Hermann, J. Boston, K. Engi, M. Beltrando, M., McAlpine, S.R.B. (2011), Yo-yo subduction recorded by accessory minerals in the Italian Western Alps, Nature Geosciences, 4, 338–342.

Sagri, M. (1980). Le Arenarie di Bordighera: una conoide sottomarina nel bacino di sedimentazione dei Flysch ad Elmintoidi di San Remo (Cretaceo Superiore, Liguria Occidentale). Bollettino della Società Geologica Italiana, 98-99, 205-226.

Sagri, M. & Marri, C. (1980). Paleobatimetria e ambienti di deposizione delle unità torbiditiche Cretaceo-Superiori dell'Appennino settentrionale. Memorie della Società Geologica Italiana, 21, 231-240.

Saller, A.H., Werner, K., Sugiaman, F., Cebastiant, A., May, R., D. Glenn, D., Barker, C. (2008). Characteristics of Pleistocene deep-water fan lobes and their application to an Upper Miocene reservoir model, offshore East Kalimantan, Indonesia. AAPG Bulletin, 92, 919-949.

Satkoski, A.M., Wilkinson, B.H., Hietpas, J.H., Samson, S.D. (2013). Likeness among detrital zircon populations – an approach to the comparison of age frequency data in time and space. Geol. Soc. Am. Bull., 125, 1783–1799.

Satur, N., Kelling, G., Cronin, B. T., Hurst, A. and Gurbuz, K. (2005). Sedimentary architecture of a canyon-style fairway feeding a deep-water clastic system, the Miocene Cingoz Formation, southern Turkey: significance for reservoir characterisation and modelling. Sedimentary Geology 173 (1-4): 91-119.

Saylor, J.E., Knowles, J.N., Horton, B.K., Nie, J.S., Mora, A. (2013). Mixing of source populations recorded in detrital zircon U-Pb age spectra of modern river sands: Journal of Geology, 121, 17–33.

Saylor, J.E. & Sundell, K.E. (2016). Quantifying comparison of large detrital geochronology data sets, Geosphere, 12 (1), 1-18.

Schaltegger, U. & Gebauer, D. (1999). Pre-Alpine geochronology of the Central, Western and Southern Alps. Schweizerische Mineralogische und Petrographische Mitteilungen, 79, 79-87.

Schaltegger, U. & Brack, P. (2007). Crustal-scale magmatic system during intracontinental stike-slip tectonics: U, Pb and Hf isotopic constraints from Permian magmatic rocks of the Southern Alps. International Journal of Earth Sciences (Geol. Rundschau), 96, 1131–51.

Schaltegger, U., Desmurs, L., Manatschal, G., Müntener, O., Meier, M., Frank, M., Bernoulli, D. (2002). The transition from rifting to sea-floor spreading within a magma-poor rifted margin: field and isotopic constraints. Terra Nova, 14, 156-162.

Schaltegger, U., Schmitt, A.K., Horstwood, M.S.A. (2015). U-Th-Pb zircon geochronology by ID-Tims, SIMS, and laser ablation ICP-MS: recipes, interpretations, and opportunities. Chemical Geology. 402, 89-110.

Schettino, A. & Turco, E. (2011). Tectonic history of the western Tethys since the Late Triassic. Geological Society of America Bulletin, 123 (1-2), 89-105.

Schmid, S.M. & Kissling, E. (2000). The arc of the western Alps in the light of geophysical data on deep crustal structure. Tectonics, 19 (1), 62-85.

Schmid, S.M., Pfiffner, O.A., Schreurs, G. (1997). Rifting and collision in the Penninic Zone of eastern Switzerland. In: O.A. Pfiffner, P. Lehner, P. Heitzman, S. Mueller, A. Steck (Eds.), Deep structure of the Swiss Alps; Results of NRP 20, Birkhäuser Verlag, Basel, pp. 160-185.

Schmid, M.S., Fügenschuh B., Kissling E., Schuster R. (2004). Tectonic map and overall architecture of the Alpine orogen. Eclogae Geologicae Helvetiae, 97, 93–117.

Schoene, B. (2014). U-Th-Pb geochronology. In: Rudnick, R., (ed.), Treatise on Geochemistry, 4.10, Elsevier, Oxford, UK, 341-378.

Scholle, P. (1971). Sedimentology of Fine-Grained Deep-Water Carbonate Turbidites, Monte Atola Flysch (Upper Cretaceous), Northern Apennines, Italy. Geological Society of America Bulletin, 82, 629-658.

Schwartz, T.M., Fosdick, J.C., Graham, S.A. (2016). Using detrital zircon U-Pb ages to calculate Late Cretaceous sedimentation rates in the Magallanes-Austral basin, Patagonia. Basin Research. 1-22.

Seno, S., Dallagiovanna, G., Vanossi, M. (2005). Pre-Piedmont and Piedmont-Ligurian nappes in the central sector of the Ligurian Alps: a possible pathway for their superposition on to the inner Briançonnais units. Bollettino della Società Geologica Italiana, 124 (2), 455-464.

Sestini, G. (1970). Sedimentation of the late geosynclinal stage. Sedimentary Geology, 4, 445–479.

Sestini, G., Bruni, P., Sagri, M. (1986). The flysch basins of the Northern Apennines: A review of facies and of Cretaceous-Neogene evolution. Memorie della Società Geologica Italiana, 31, 87-106.

Shanmugam, G. (2006). Deep-water processes and facies models: Implications for sandstone petroleum reservoirs: New York, Elsevier, 476 pp.

Shanmugam, G. & Moiola, R.J. (1988). Submarine fans: characteristics, models, classification, and reservoir potential. Earth-Science Reviews, 24, 383–428.

Sharman, G.R., Graham, S.A., Grove, M., Kimbrough, D.L., Wright, J.E. (2015). Detrital zircon provenance of the Late Cretaceous-Eocene California forearc: Influence of Laramide low-angle subduction on sediment dispersal and paleogeography.GSA Bulletin. 127(1-2), 38-60.

Sircombe, K.N. (2000). Quantitative comparison of large sets of geochronological data using multivariate analysis: a provenance study example from Australia. Geochimica et Cosmochimica Acta, 64, 1593–1616.

Sircombe, K.N. & Hazelton, M.L. (2004). Comparison of detrital zircon age distributions by kernel functional estimation. Sedimentary Geology, 171, 91–111.

Slaczka, A. & Thompson, S. III (1981). A revision of the fluxoturbidite concept based on type examples in the Polish Carpathian flysch. Ann. Soc. Geol. Pologne 51, 3-44.

Sláma, J., Košler, J., Condon, D.J., Crowley, J.L., Gerdes, A., Hanchar, J.M., Horstwood, M.S.A., Morris, G.A., Nasdala, L., Norberg, N., Schaltegger, U., Schoene, B., Tubrett, M.N., Whitehouse, M.J. (2008). Plešovice zircon – A new natural reference material for U-Pb and Hf isotopic microanalysis. Chemical Geology, 249, 1–35.

So, Y.S., Rhee, C.W., Choi, P.-Y., Kee, W.-S., Seo, J.Y., Lee, E.-J. (2013). Distal turbidite fan/lobe sucession of the Late Paleozoic Taean formation, western Korea. Geoscience Journal, 17, 9–25.

Sohn, Y.K. (1997). On traction-carpet sedimentation. Journal of Sedimentary Research, 67, 502–509.

Sohn, Y.K., Choe, M.Y., Jo, H.R. (2002). Transition from debris flow to hyperconcentrated flow in a submarine channel (the Cretaceous Cerro Toro Formation, southern Chile). Terra Nova, 14, 405-415.

Southern, S. J., Patacci, M., Felletti, F., McCaffrey, W. D. (2015). Influence of flow containment and substrate entrainment upon sandy hybrid event beds containing a co-genetic mud-clast-rich division. Sedimentary Geology 321, 105-122.

Southern, S.J., Kane, I.A., Warchoł, M.J., Porten, K.W., McCaffrey, W.D. (2017). Hybrid event beds dominated by transitional-flow facies: Character, distribution and significance in the Maastrichtian Springar Formation, north-west Vøring Basin, Norwegian Sea. Sedimentology, 64 (3), 747-776.

Spychala, Y.T., Hodgson, D.M., Prélat, A., Kane, I.A., Flint, S.S., Mountney, NP. (2017a). Frontal and Lateral Submarine Lobe Fringes: Comparing Sedimentary Facies, Architecture and Flow Processes. Journal of Sedimentary Research, 87, issue 1, 75 – 96.

Spychala, Y.T., Hodgson, D.M., Lee, D.R. (2017b). Autogenic controls on hybrid bed distribution in submarine lobe complexes. Marine and Petroleum Geology, 88, 1078-1093.

Stampfli, G.M. (1993). Le Briançonnais, terrain exotique dans les Alpes? Eclogae Geologicae Helvetiae, 86, 1-45.

Stampfli G.M. & Borel, G.D. (2002). A plate tectonic model for the Paleozoic and Mesozoic constrained by dynamic plate boundaries and restored synthetic oceanic isochrones. Earth and Planetary Science Letters, 196, 17–33.

Stampfli, G.M. & Kozur, H. (2006). Europe from the Variscan to the Alpine cycles. In: D.G. Gee & R. Stephenson (eds.), European lithosphere dynamics. Memoir of the Geological Society (London), 32, 57-82.

Stampfli, G.M., Mosar, J., Marquer, D., Marchant, R., Baudin, D., Borel, G. (1998). Subduction and obduction processes in the Swiss Alps. Tectonophysics, 296, 159-204.

Stampfli, G.M., Borel, G.D., Marchant, R., Mosar, J. (2002). Western Alps geological constraints on western Tethyan reconstructions. In: Rosenbaum, G. & Lister, G.S. (eds.). Reconstruction of the evolution of the Alpine-Himalayan Orogen. Journal of the Virtual Explorer, 7, 75-104.

Stanbrook, D., Bentley, M., Stephens, E. (2015). Controls on Architectural Styles in Turbidite Systems: The Role of Relative Confinement. Asia Petroleum Geoscience Conference & Exhibition (APGCE) conference extended abstracts.

Stevenson, C.J., Jackson, C. A.-L., Hodgson, D.M., Hubbard, S.M., Eggenhuisen, J.T. (2015). Deep-Water Sediment Bypass. Journal of Sedimentary Research, 85 (9), 1058-1081.

Stockmal, G.S., Beaumont, C., Boutilier, R. (1987). Geodynamic models of Convergent Margin Tectonics: Transition from Rifted Margin to Overthrust Belt and Consequences for Foreland basement development. AAPG Bulletin, 70 (2), 181-190.

Stow, D.A.V., Howell, D.G., Nelson, H.C. (1983). Sedimentary, tectonic, and sea-level controls on submarine fan and slope-apron turbidite systems. Geo-Marine Letters, 3, 57-64.

Stow, D.A.V., Reading, H.G., Collinson, J.D. (1996). Deep seas. In: H.G. Reading (ed.), Sedimentary Environments: Processes, facies and stratigraphy. Blackwell Science, Oxford, 395-454.

Stow, D.A.V. & Johansson, M. (2000). Deep-water massive sands: nature, origin and hydrocarbon implications. Marine and Petroleum Geology, 17 (2), 145-174.

Stow, D.A.V. & Mayall, M. (2000). Deep-water sedimentary systems: New models for the 21st century. Marine and Petroleum Geology, 17 (2), 125-135.

Sullivan, M.D., Jensen, G.N., Goulding, F.J., Jennette, D.C., Stern, D., (2000). Architectural analysis of deep-water outcrops: Implications for exploration and production of the Diana sub-basin, western Gulf of Mexico. In: P. Weimer, R.M. Slatt, A.H. Bouma and D.T. Lawrence (eds.). Gulf Coast Section, SEPM, 20th Annual Research Conference: Deep-Water Reservoirs of the World, December 3-6, 2000, Houston, pp. 1010-1032.

Sundell, K.E. & Saylor, J.E. (2017). Unmixing detrital geochronology age distributions. Geochemistry, Geophysics, Geosystems, 18, 2872-2886.

Suttner, L.J. & Basu, A. (1985). The effect of grain size on detrital modes; a test of the Gazzi-Dickinson point-counting method – Discussion. Journal of Sedimentary Petrology, 55 (4), 616–617.

Suttner, L.J. & Dutta, P.K. (1986). Alluvial sandstones composition and paleoclimate, I, framework mineralogy, Journal of Sedimentary Petrology, 56, 329 –345.

Sylvester, Z. & Lowe, D.R. (2004). Textural trends in turbidites and slurry beds from the Oligocene flysch of the East Carpathians, Romania. Sedimentology, 51 (5), 945-972.

Talling, P.J., Masson, D.G., Sumner, F.J., Malgesini G. (2012). Subaqueous sediment density flows: Depositional processes and deposit types. Sedimentology, 59, 1937–2003.

Talling, P.J., (2013). Hybrid submarine flows comprising turbidity current and cohesive debris flow: theoretical and experimental analyses, and generalized models. Geosphere, 9, 460-488.

Tatzel, M., Dunkl, I., von Eynatten, H. (2015). Provenance of Paleo-Rhine sediments from zircon thermochronology, geochemistry, P/Pb dating and heavy mineral assemblages. Basin Research, 29, 396-417.

Terlaky, V. & Arnott, R.W.C. (2014). Matrix-rich and associated matrix-poor sandstones: avulsion splays in slope and basin-floor strata. Sedimentology, 61 (5), 1175-1197.

Terlaky, V., Rochelau, J., Arnott, R.W.C. (2015). Stratal composition and stratigraphic organization of stratal elements in an ancient deep-marine basin-floor succession, Neoproterozoic Windermere Supergroup, British Columbia, Canada. Sedimentology 63, 136-175.

Terlaky, V. & Arnott, R.W.C. (2016). The Control Of Terminal-Splay Sedimentation On Depositional Patterns and Stratigraphic Evolution In Avulsion-Dominated, Unconfined, Deep-Marine Basin-Floor Systems. Journal of Sedimentary Research 86 (7): 786-799.

Thomas, M.F.H., Bodin, S., Redfern, J. (2010). Comment on `European provenance of the Numidian Flysch in northern Tunisia' by Fildes et al. (2010). Terra Nova, 22 (6), 501-503.

Thomas, W.A. (2011). Detrital-zircon geochronology and sedimentary provenance. Lithosphere, 3 (4), 304-308.

Thornburg, T.M. & Kulm, L.D. (1987). Sedimentation in the Chile Trench: Depositional morphologies, lithofacies, and stratigraphy. Geological Society of America Bulletin, 98, 33-52.

Thum, L., De Paoli, R., Stampfli, G.M., Moix, P. (2015) The Piolit, Pelat and Baiardo Upper Cretaceous flysch formations (western Alps): Geodynamic implications at the time of the Pyrenean tectonic phases. Bull. Soc. géol. France, 2015, 186 (4-5), 209-221.

Tilston, M., Arnott, R.W.C., Rennies, C.D., Long, B. (2015). The influence of grain size on the velocity and sediment concentration profiles and depositional record of turbidity currents. Geology, 43 (9), 839-842.

Tinterri, R. & Muzzi Maghalaes, P. (2011). Synsedimentary structural control on foredeep turbidites: An example from Miocene Marnoso-arenacea Formation, Northern Apennines, Italy. Marine and Petroleum Geology, 28, 629-657.

Traversa, G., Ronca, S., Del Moro, A., Pasquali, C., Buraglini, N., Barabino, G. (2003). Late to post-Hercynian dyke activity in the Sardinia-Corsica Domain: A transition from orogenic calcalkaline to anorogenic alkaline magmatism. Boll. Soc. Geol. It., Special Volume, 2, 131-152.

Tribuzio, R., Garzetti, F., Corfu, F., Tiepolo, M., Renna, M.R. (2016). U–Pb zircon geochronology of the Ligurian ophiolites (Northern Apennine, Italy): Implications for continental breakup to slow seafloor spreading. Tectonophysics, 666, 220-243.

Uchman, A. (2007). Deep-sea trace fossils from the mixed carbonate-siliciclastic flysch of the Monte Antola Formation (Late Campanian-Maastrichtian), North Apennines, Italy. Cretaceous Research, 28, 980-1004.

Underwood, M.B., Orr, R., Pickering, K., Taira, A. (1993). Provenance and dispersal patterns of sediments in the turbidite wedge of Nankai Trough. In: Hill, I.A. (Ed.), Proceedings of the Ocean Drilling Program, Scientific results, 131, College Station, Texas, Ocean Drilling Program, 15–34.

Vail, P.R., Mitchum, R.M., Thompson, S. (1977). Seismic stratigraphy and global changes of sea level, part 3: relative changes of sea level from coastal onlap. In: C.E. Payton (Ed.). Seismic Stratigraphy — Applications to Hydrocarbon Exploration, AAPG Memoir, 26, pp. 63-81.

Vanossi M., Cortesogno L., Galbiati B., Messiga B., Piccardo G., Vannucci R. (1986). Geologia delle Alpi liguri: dati, problemi, ipotesi. Memorie della Società Geoligica Italiana 28, 5–75.

Vermeesch, P. (2004). How many grains are needed for a provenance study? Earth and Planetary Science Letters, 224, 441-451.

Vermeesch, P. (2012). On the visualisation of detrital age distributions. Chem. Geol., 312–313, 190–194.

Vermeesch, P. & Garzanti, E. (2015). Making geological sense of ´Big Data´ in sedimentary provenance analysis. Chemical Geology, 409, 20-27.

Vignaroli, G.L., Faccenna, C., Jolivet, L., Piromallo, C., Rossetti, F. (2008). Subduction polarity reversal at the junction between the Western Alps and the Northern Apennines, Italy. Tectonophysics, 450, 34–50.

Vinnels, J.S., Butler, R.W.H., McCaffrey, W.D., Lickorish, H.W. (2010). Sediment Distribution and Architecture Around a Bathymetrically Complex Basin: An example from the Eastern Champsaur Basin, SE France. Journal of Sedimentary Research, 80 (3), 216-235.

Walker, R.G. (1978). Deep-water sandstone facies and ancient submarine fans: models for exploration for stratigraphic traps. AAPG Bulletin, 62, 932–966.

Weimer, P., Slatt, R.M., Pettingill, H.S. (2007). Global Overview of Deepwater Exploration and Production. In: Weimer, P. and Slatt, R. M. (Eds). Introduction to the Petroleum Geology of Deepwater Settings. AAPG Studies in Geology 57: 19-56.

Wernicke, B. (1985). Uniform-sense normal simple shear of the continental lithosphere. Canadian Journal of Earth Sciences, 22 (1), 108-125.

Weber, S., Sandmann, S., Miladinova, I., Fonseca, R.O.C., Froitzheim, N., Munker, C., Bucher, K. (2015). Dating the initiation of Piemonte-Liguria Ocean subduction: Lu–Hf garnet chronometry of eclogites from the Theodul Glacier Unit (Zermatt-Saas zone, Switzerland). Swiss Journal of Geosciences, 108 (2-3), 183-199.

Weltje, G.J. (2006). Ternary sandstone composition and provenance: an evaluation of the 'Dickinson model'. Geological Society, London, Special Publications, 264, 79-99.

Weltje, G.J. & von Eynatten, H. (2004). Quantitative provenance analysis of sediments: review and outlook. Sedimentary Geology, 171, 1–11.

Wetherill, G. (1956). Discordant Uranium-Lead ages. Transactions of the American Geophysical Union, 37, 320-326.

Wildi, W. (1985). Heavy mineral distribution and dispersal pattern in penninic and ligurian flysch basins (Alps, northern Apennines). Giornale di Geologia, 47 (1-2), 77-99.

Wildi, W. (1987). Les regions sources du materiel terrigene dans les flyschs alpins. Memoire HS Geologie Alpine: Le detritisme dans le Sud-Est de la France - Colloque Associ., 13, 379-388.

Williams, I.S., Fiannacca, P., Cirrincione, R., Pezzino, A. (2012). Peri-Gondwanian origin and early geodynamic history of NE Sicily: a zircon tale from the basement of the Peloritani Mountains. Gondwana Research, 22, 855–865.

Wynn, R.B., Kenyon, N.H., Masson, D.G., Stow, D.A.V., Weaver, P.P.E. (2002). Characterization and recognition of deep-water channel-lobe transition zones. AAPG Bulletin 86, 1441-1462.

Zanetti. A., Mazzucchelli, M., Sinigoi, S., Giovanardi, T., Peressini, G., Fanning, M. (2013). SHRIMP U–Pb Zircon Triassic Intrusion Age of the Finero Mafic Complex (Ivrea–Verbano Zone, Western Alps) and its Geodynamic Implications. Journal of Petrology, 54, 2235-2265.

Zavala, C., Arcuri, M. Di Meglio, M. Gamero Diaz, H. Contreras, C. (2011). A genetic facies tract for the analysis of sustained hyperpycnal flow deposits. In: R. M. Slatt and C. Zavala, (eds.), Sediment transfer from shelf to deep water—Revisiting the delivery system, AAPG Studies in Geology, 61, 31–51.

Zeng, J., Lowe, D.R., Prior, D.B., Wiseman Jr., W.J., Bornhold, B.D. (1991). Flow properties of turbidity currents in Bute Inlet, British Columbia. Sedimentology 38, 975–996.

Zhang, J., Dai, J. Quian, X., Ge, Y., Wang, C. (2016). Sedimentology, provenance and geochronology of the Miocene Qiuwu Formation: Implication for the uplift history of Southern Tibet. Geoscience Frontiers, 18, 1-17.

Zuffa, G.G. (1985). Optical analyses of arenites: influence of methodology on compositional results. – In: Zuffa, G.G. (ed.): Provenance of arenites. NATO ASI Series, 148, 165–189, Dordrecht (Reidel).

APPENDIX 1.1: Detailed graphic sedimentological logs for measured stratigraphic sections 1-10

Log 1: "Monte Bignone"

Log 2: "Quarry Badalucco"

Log 3: "Montalto Road"

Log 4: "Montalto River"

Log 5:"Carmo dei Brocchi"

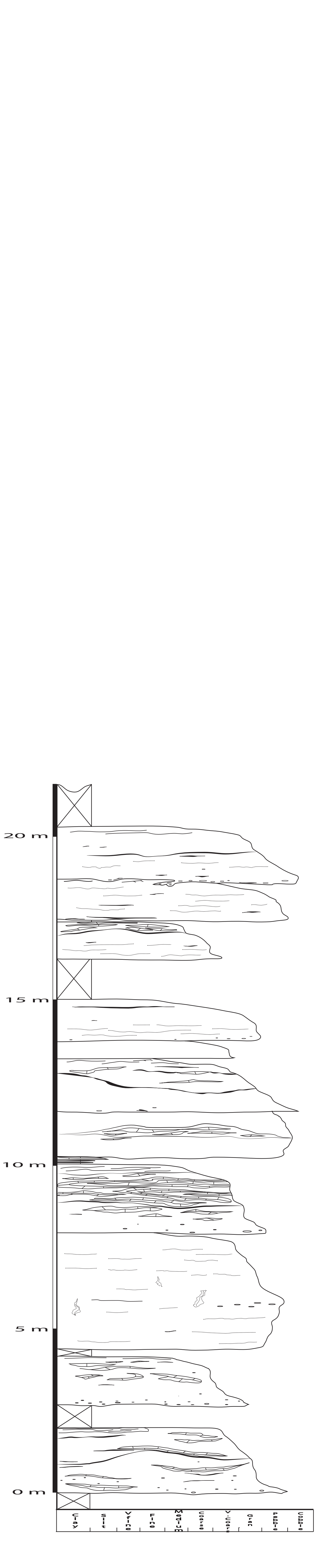

Log 6: “Monte Frontè”

Log 7: "Punto di Farenga"

Log 8a: "Margheri Binda_Center"

Log 8b: “Margheri Binda_West”

Log 9: "Cima di Bertrand"

Log 10: "Cima di Velega"

Appendix_1.2: Bed type proportions of stratigraphic thickness for measured stratigraphic sections 1 to 10

Legend to Bed Types

1.1	Coarse-tail graded microconglomerates
1.2	Microconglomeratic lag
1.3	Inversely graded microconglomerates
2.1	Structureless "clean" Sandstones
2.2	Structured "clean" sandstones
3.1	Siliciclastic beds- dominated alternations
3.3	Calcareous beds- dominated alternations
4.1	Thick-bedded calcareous beds
4.2	Thin-bedded calcareous beds
5.1	Type-A mud-enriched beds
5.2	Type-B mud-enriched beds
6.1	Tri-partite hybrid event beds
6.2	Bi-partite hybrid event beds
6.3	HEBs with undetectable HEB-subdivisions
7.1	Siliciclastic mudcaps
7.2	Calcareous mudcaps
0	covered interval

1-Monte Bignone

bed nr.	base	top	thickness	mudcap	Bed type	max. grain size	amalgamation
1	0.00	1.96	1.96	0.00	1.1	3500	0
2	1.96	2.05	0.09	0.00	7.2	4	0
3	2.05	3.03	0.98	0.00	0	0	0
4	3.03	4.48	1.45	0.00	1.1	4500	0
5	4.48	4.70	0.22	0.00	0	0	0
6	4.70	6.28	1.58	0.00	1.1	4250	1
7	6.28	8.74	2.46	0.11	1.3	12000	0
8	8.74	8.85	0.11	0.00	7.1	4	0
9	8.85	8.96	0.11	0.00	2.1	150	1
10	8.96	9.20	0.24	0.00	2.1	400	1
11	9.20	9.52	0.32	0.00	2.1	550	1
12	9.52	10.02	0.50	0.00	2.2	750	1
13	10.02	10.63	0.61	0.15	2.2	1100	0
14	10.63	11.41	0.78	0.00	2.1	1800	1
15	11.41	12.08	0.67	0.00	2.2	1200	1
16	12.08	12.67	0.59	0.00	2.1	1000	1
17	12.67	13.15	0.48	0.00	1.2	3500	1
18	13.15	14.73	1.58	0.18	1.1	7000	0
19	14.73	14.91	0.18	0.00	7.1	4	0
20	14.91	15.69	0.78	0.09	1.1	5500	0
21	15.69	15.78	0.09	0.00	7.1	4	0
22	15.78	15.89	0.11	0.02	7.1	62	0
23	15.89	17.31	1.42	0.04	1.3	7500	1
24	17.31	19.23	1.92	0.00	1.1	64000	1
25	19.23	21.07	1.84	0.02	1.1	4000	0
26	21.07	21.11	0.04	0.00	7.1	4	0
27	21.11	21.32	0.21	0.00	1.2	4000	1
28	21.32	21.57	0.25	0.00	1.2	20000	1
29	21.57	21.80	0.23	0.05	1.2	2500	0
30	21.80	21.85	0.05	0.00	7.1	4	0
31	21.85	22.43	0.58	0.07	1.1	3500	0
32	22.43	22.50	0.07	0.00	7.1	4	0
33	22.50	23.49	0.99	0.02	1.3	5000	0
34	23.49	23.51	0.02	0.00	7.1	4	0
35	23.51	25.34	1.83	0.00	1.1	4500	1
36	25.34	26.39	1.05	0.00	2.1	1900	1
37	26.39	27.86	1.47	0.00	1.1	2500	1
38	27.86	28.39	0.53	0.00	2.1	1250	1
39	28.39	29.15	0.76	0.00	1.3	6400	1
40	29.15	30.21	1.06	0.00	1.3	3500	1
41	30.21	30.85	0.64	0.00	1.3	8000	1
42	30.85	31.21	0.36	0.22	1.3	4000	0
43	31.21	31.43	0.22	0.00	7.1	4	0
44	31.43	32.54	1.11	0.05	1.3	4500	0
45	32.54	32.59	0.05	0.00	7.1	4	0
46	32.59	33.79	1.20	0.12	1.1	3000	0
47	33.79	33.91	0.12	0.00	7.1	4	0
48	33.91	34.52	0.61	0.00	5.1	2500	1

49	34.52	34.73	0.21	0.00	2.1	1800	1
50	34.73	34.86	0.13	0.00	2.2	200	1
51	34.86	36.37	1.51	0.03	1.3	5000	0
52	36.37	36.40	0.03	0.00	7.1	4	0
53	36.40	37.61	1.21	0.00	1.3	2250	1
54	37.61	39.19	1.58	0.00	1.3	55000	1
55	39.19	43.37	4.18	0.21	1.3	35000	0
56	43.37	43.58	0.21	0.00	7.1	4	0
57	43.58	45.46	1.88	0.00	1.3	3500	1
58	45.46	46.15	0.69	0.09	2.1	1850	0
59	46.15	46.24	0.09	0.00	7.1	4	0
60	46.24	47.15	0.91	0.00	1.1	2500	1
61	47.15	47.61	0.46	0.04	2.1	650	0
62	47.61	47.65	0.04	0.00	7.1	4	0
63	47.65	48.34	0.69	0.00	2.1	1800	1
64	48.34	50.58	2.24	0.12	1.1	3500	0
65	50.58	50.70	0.12	0.00	7.1	4	0
66	50.70	51.45	0.75	0.00	0	0	0
67	51.45	52.62	1.17	0.00	1.3	2750	1
68	52.62	54.51	1.89	0.04	1.1	30000	0
69	54.51	54.55	0.04	0.00	7.1	4	0
70	54.55	54.86	0.31	0.00	3.2	125	0
71	54.86	55.06	0.20	0.00	2.1	250	1
72	55.06	55.19	0.13	0.00	2.1	200	1
73	55.19	55.33	0.14	0.00	2.1	250	1
74	55.33	55.79	0.46	0.00	2.1	400	1
75	55.79	57.62	1.83	0.00	1.3	15000	0
76	57.62	58.82	1.20	0.00	0	0	0
77	58.82	59.76	0.94	0.00	5.1	3750	1
78	59.76	62.46	2.70	0.00	1.1	12000	1
79	62.46	63.82	1.36	0.00	6.1	6000	1
80	63.82	64.24	0.42	0.00	2.1	900	1
81	64.24	64.71	0.47	0.05	2.1	1300	0
82	64.71	64.76	0.05	0.00	7.1	4	0
83	64.76	64.93	0.17	0.02	3.1	62	0
84	64.93	66.34	1.41	0.00	1.1	35000	1
85	66.34	66.96	0.62	0.00	2.1	1000	1
86	66.96	68.06	1.10	0.00	1.1	5000	1
87	68.06	69.08	1.02	0.08	1.1	3000	0
88	69.08	69.16	0.08	0.00	7.1	4	0
89	69.16	69.33	0.17	0.00	2.1	250	1
90	69.33	69.91	0.58	0.05	2.1	500	0
91	69.91	70.19	0.28	0.05	3.1	250	0
92	70.19	70.79	0.60	0.00	0	0	0
93	70.79	71.18	0.39	0.04	3.1	250	0
94	71.18	73.03	1.85	0.00	1.3	5500	1
95	73.03	73.86	0.83	0.06	1.1	3750	0
96	73.86	73.92	0.06	0.00	7.1	4	0
97	73.92	78.57	4.65	0.00	1.1	45000	1
98	78.57	80.02	1.45	0.25	1.1	35000	0

99	80.02	80.27	0.25	0.00	7.1	4	0
100	80.27	82.13	1.86	0.25	1.1	3500	0
101	82.13	82.38	0.25	0.00	7.1	4	0
102	82.38	83.65	1.27	0.00	2.1	1700	1
103	83.65	83.90	0.25	0.00	2.1	900	1
104	83.90	85.31	1.41	0.15	2.1	1900	0
105	85.31	85.46	0.15	0.00	7.1	4	0
106	85.46	86.94	1.48	0.00	1.1	6000	0
107	86.94	87.54	0.60	0.00	0	0	0
108	87.54	89.39	1.85	0.00	1.1	3000	0
109	89.39	90.49	1.10	0.00	0	0	0
110	90.49	91.03	0.54	0.00	2.1	1750	1
111	91.03	92.07	1.04	0.05	1.1	2400	0
112	92.07	92.12	0.05	0.00	7.1	4	0
113	92.12	94.69	2.57	0.08	1.1	3750	0
114	94.69	94.77	0.08	0.00	7.1	4	0
115	94.77	95.35	0.58	0.05	3.1	250	0
116	95.35	97.40	2.05	0.00	1.1	3950	1
117	97.40	98.35	0.95	0.08	1.1	2250	0
118	98.35	98.43	0.08	0.00	7.2	4	0
119	98.43	98.96	0.53	0.04	3.2	64	0
120	98.96	99.10	0.14	0.00	4.2	64	0
121	99.10	99.24	0.14	0.00	4.2	64	0
122	99.24	99.37	0.13	0.00	4.2	64	0
123	99.37	99.51	0.14	0.00	4.2	64	0
124	99.51	99.66	0.15	0.00	4.2	64	0
125	99.66	99.78	0.12	0.00	2.1	300	0
126	99.78	100.08	0.30	0.00	0	0	0
127	100.08	100.34	0.26	0.00	4.2	64	0
128	100.34	100.41	0.07	0.00	4.2	64	0
129	100.41	100.74	0.33	0.05	3.2	64	0
130	100.74	102.56	1.82	0.02	1.1	2250	0
131	102.56	102.58	0.02	0.00	7.1	4	0
132	102.58	102.80	0.22	0.02	2.1	400	0
133	102.80	104.55	1.75	0.05	3.2	250	0
134	104.55	105.27	0.72	0.00	2.1	1500	1
135	105.27	111.14	5.87	0.00	1.1	3500	0
136	111.14	112.89	1.75	0.00	0	0	0
137	112.89	113.13	0.24	0.00	2.1	500	0
138	113.13	114.78	1.65	0.00	0	0	0
139	114.78	116.12	1.34	0.00	2.1	1100	0
140	116.12	116.34	0.22	0.00	4.2	100	0
141	116.34	116.64	0.30	0.00	0	0	0
142	116.64	116.82	0.18	0.00	4.2	62	0
143	116.82	118.22	1.40	0.00	0	0	0
144	118.22	119.33	1.11	0.00	1.1	3000	0
145	119.33	119.81	0.48	0.00	0	0	0
146	119.81	119.99	0.18	0.02	3.1	62	0
147	119.99	124.02	4.03	0.00	1.3	4000	1
148	124.02	124.20	0.18	0.00	2.1	700	1

149	124.20	124.37	0.17	0.00	2.1	500	1
150	124.37	126.34	1.97	0.08	1.1	5500	0
151	126.34	126.42	0.08	0.00	7.1	4	0
152	126.42	127.52	1.10	0.05	1.1	2500	0
153	127.52	127.57	0.05	0.00	7.1	4	0
154	127.57	127.70	0.13	0.00	1.2	4000	1
155	127.70	128.68	0.98	0.00	5.1	3000	1
156	128.68	129.49	0.81	0.07	1.1	3000	0
157	129.49	129.56	0.07	0.00	7.1	4	0
158	129.56	129.73	0.17	0.02	2.1	750	0
159	129.73	129.75	0.02	0.00	7.1	4	0
160	129.75	130.43	0.68	0.16	2.1	600	0
161	130.43	130.59	0.16	0.00	7.1	4	0
162	130.59	130.65	0.06	0.01	4.2	62	0
163	130.65	131.05	0.40	0.00	2.1	800	0
164	131.05	131.35	0.30	0.00	0	0	0
165	131.35	132.11	0.76	0.02	3.2	125	0
166	132.11	132.98	0.87	0.00	1.1	10000	0
167	132.98	133.22	0.24	0.00	0	0	0
168	133.22	133.80	0.58	0.00	4.1	125	0
169	133.80	134.24	0.44	0.00	4.1	10	0
170	134.24	134.32	0.08	0.00	2.1	200	0
171	134.32	134.69	0.37	0.03	2.1	300	0
172	134.69	134.72	0.03	0.00	7.1	4	0
173	134.72	135.79	1.07	0.02	1.1	2500	0
174	135.79	135.81	0.02	0.00	7.1	4	0
175	135.81	137.91	2.10	0.10	3.2	125	0
176	137.91	140.06	2.15	0.02	1.3	2500	0
177	140.06	140.08	0.02	0.00	7.1	4	0
178	140.08	140.57	0.49	0.02	3.2	62	0
179	140.57	140.68	0.11	0.00	2.1	250	0
180	140.68	140.91	0.23	0.00	2.1	650	0
181	140.91	141.48	0.57	0.00	0	0	0
182	141.48	142.86	1.38	0.00	1.3	35000	1
183	142.86	144.56	1.70	0.00	1.1	40000	1
184	144.56	146.22	1.66	0.00	1.1	30000	1
185	146.22	147.63	1.41	0.00	1.1	3750	1
186	147.63	147.89	0.26	0.03	1.2	3000	0
187	147.89	147.92	0.03	0.00	4.1	4	0
188	147.92	148.80	0.88	0.00	4.1	100	0
189	148.80	148.93	0.13	0.02	4.2	62	0
190	148.93	148.95	0.02	0.00	7.1	4	0
191	148.95	149.63	0.68	0.18	5.2	500	0
192	149.63	149.81	0.18	0.00	7.1	4	0
193	149.81	151.77	1.96	0.02	1.1	5000	0
194	151.77	151.79	0.02	0.00	7.1	4	0
195	151.79	151.93	0.14	0.03	4.2	62	0
196	151.93	151.96	0.03	0.00	7.1	4	0
197	151.96	152.17	0.21	0.00	4.2	125	0
198	152.17	152.63	0.46	0.00	5.2	1500	1

199	152.63	153.59	0.96	0.17	1.1	2250	0
200	153.59	153.76	0.17	0.00	7.1	4	0
201	153.76	154.07	0.31	0.00	2.1	650	1
202	154.07	154.18	0.11	0.02	2.1	250	0
203	154.18	154.20	0.02	0.00	7.1	4	0
204	154.20	154.77	0.57	0.05	3.1	200	0
205	154.77	155.06	0.29	0.11	2.1	500	0
206	155.06	155.17	0.11	0.00	7.1	4	0
207	155.17	155.46	0.29	0.00	4.2	100	0
208	155.46	156.32	0.86	0.00	4.1	125	0
209	156.32	157.37	1.05	0.00	4.1	125	0
210	157.37	157.81	0.44	0.00	5.2	850	0
211	157.81	158.16	0.35	0.00	0	0	0
212	158.16	158.24	0.08	0.00	2.1	125	1
213	158.24	158.44	0.20	0.00	2.1	250	1
214	158.44	159.19	0.75	0.00	4.1	150	1
215	159.19	159.40	0.21	0.00	2.1	250	1
216	159.40	159.97	0.57	0.00	2.1	500	1
217	159.97	160.29	0.32	0.00	2.1	850	1
218	160.29	161.22	0.93	0.02	1.1	3750	0
219	161.22	161.24	0.02	0.00	7.1	4	0
220	161.24	161.38	0.14	0.00	3.1	62	0
221	161.38	162.24	0.86	0.00	1.1	2500	1
222	162.24	162.75	0.51	0.00	1.1	2500	1
223	162.75	163.02	0.27	0.00	2.1	250	1
224	163.02	163.33	0.31	0.02	2.1	500	0
225	163.33	163.35	0.02	0.00	7.1	4	0
226	163.35	163.47	0.12	0.02	2.1	150	0
227	163.47	163.49	0.02	0.00	7.1	4	0
228	163.49	164.46	0.97	0.00	5.2	2250	1
229	164.46	164.72	0.26	0.02	4.2	126	0
230	164.72	164.74	0.02	0.00	7.1	4	0
231	164.74	164.94	0.20	0.01	3.2	62	0
232	164.94	166.19	1.25	0.20	2.1	1500	0
233	166.19	166.39	0.20	0.00	7.1	4	0
234	166.39	166.96	0.57	0.00	2.1	700	0
235	166.96	167.51	0.55	0.00	0	0	0
236	167.51	167.66	0.15	0.00	2.1	250	1
237	167.66	167.88	0.22	0.00	2.1	450	1
238	167.88	169.24	1.36	0.00	1.3	3250	1
239	169.24	169.34	0.10	0.10	2.1	250	0
240	169.34	169.44	0.10	0.00	7.1	4	0
241	169.44	171.86	2.42	0.00	1.3	7500	1
242	171.86	172.98	1.12	0.00	1.1	3750	1
243	172.98	174.41	1.43	0.05	1.3	3500	0
244	174.41	174.46	0.05	0.00	7.1	4	0
245	174.46	174.64	0.18	0.03	3.2	250	0
246	174.64	174.67	0.03	0.00	7.1	4	0
247	174.67	174.80	0.13	0.00	2.1	450	0
248	174.80	175.35	0.55	0.00	0	0	0

249	175.35	175.68	0.33	0.11	2.1	350	0
250	175.68	175.79	0.11	0.00	7.1	4	0
251	175.79	176.27	0.48	0.00	2.1	1200	1
252	176.27	176.49	0.22	0.00	2.1	950	0
253	176.49	177.69	1.20	0.00	0	0	0
254	177.69	178.51	0.82	0.00	2.1	1750	0
255	178.51	179.21	0.70	0.00	0	0	0
256	179.21	180.58	1.37	0.00	2.1	1750	0
257	180.58	185.58	5.00	0.00	0	0	0
258	185.58	186.03	0.45	0.15	2.1	350	0
259	186.03	186.18	0.15	0.00	7.1	4	0
260	186.18	186.66	0.48	0.00	2.1	300	1
261	186.66	187.45	0.79	0.00	2.1	950	0

2-Quarry Badalucco

bed nr.	base	top	thickness	Bed type	max. grain size	mudcap	amalgamation
1	0.00	1.02	1.02	1.3	4500	0.10	0
2	1.02	1.12	0.1	7.1	4	0.00	0
3	1.12	1.35	0.23	3.1	62	0.00	0
4	1.35	2.38	1.03	1.3	45000	0.00	1
5	2.38	3.07	0.69	1.3	3000	0.00	1
6	3.07	4.12	1.05	1.3	4050	0.00	1
7	4.12	5.07	0.95	1.3	4000	0.00	1
8	5.07	6.19	1.12	1.3	10000	0.00	1
9	6.19	8.20	2.01	1.1	7500	0.12	0
10	8.20	8.32	0.12	7.1	4	0.00	0
11	8.32	9.67	1.35	1.1	64000	0.00	1
12	9.67	10.65	0.98	1.1	35000	0.00	1
13	10.65	12.10	1.45	0.0	0	0.00	0
14	12.10	12.82	0.72	1.3	3500	0.00	1
15	12.82	14.30	1.48	1.1	25000	0.00	1
16	14.30	16.92	2.62	1.1	7000	0.00	1
17	16.92	18.28	1.36	1.1	3500	0.07	0
18	18.28	18.35	0.07	7.1	4	0.00	0
19	18.35	18.78	0.43	2.1	750	0.02	0
20	18.78	18.80	0.02	7.1	4	0.00	0
21	18.80	20.39	1.59	1.3	4050	0.00	1
22	20.39	21.21	0.82	1.1	3500	0.04	0
23	21.21	21.25	0.04	7.1	4	0.00	0
24	21.25	22.26	1.01	2.2	1500	0.05	0
25	22.26	22.31	0.05	7.1	4	0.00	0
26	22.31	23.70	1.39	1.1	5000	0.00	1
27	23.70	24.52	0.82	2.1	800	0.00	1
28	24.52	25.44	0.92	1.3	4000	0.00	1
29	25.44	26.84	1.4	1.1	4050	0.00	1
30	26.84	28.12	1.28	1.1	4050	0.00	1
31	28.12	30.43	2.31	1.1	40000	0.00	1
32	30.43	31.34	0.91	2.1	1900	0.00	1
33	31.34	32.40	1.06	1.1	4050	0.00	1
34	32.40	34.06	1.66	1.1	4100	0.00	1
35	34.06	34.68	0.62	2.1	850	0.00	1
36	34.68	35.27	0.59	2.1	850	0.00	1
37	35.27	36.93	1.66	1.3	3900	0.01	0
38	36.93	36.94	0.01	7.1	4	0.00	0
39	36.94	37.72	0.78	2.1	1950	0.00	1
40	37.72	38.36	0.64	2.1	1950	0.01	0
41	38.36	38.37	0.01	7.1	4	0.00	0
42	38.37	39.39	1.02	1.1	15000	0.04	0
43	39.39	39.43	0.04	7.1	4	0.00	0
44	39.43	39.63	0.2	3.1	64	0.02	0
45	39.63	40.07	0.44	2.1	350	0.02	0
46	40.07	40.09	0.02	7.1	4	0.00	0
47	40.09	40.52	0.43	3.1	64	0.04	0
48	40.52	40.86	0.34	1.2	15000	0.00	1

49	40.86	41.39	0.53	1.1	2050	0.00	1
50	41.39	43.51	2.12	1.1	50000	0.00	1
51	43.51	45.45	1.94	1.1	4000	0.00	1
52	45.45	46.82	1.37	1.1	7500	0.10	0
53	46.82	47.06	0.24	2.1	700	0.15	0
54	47.06	47.21	0.15	7.1	4	0.00	0
55	47.21	48.94	1.73	1.3	3200	0.00	1
56	48.94	50.06	1.12	2.1	1200	0.04	0
57	50.06	50.10	0.04	7.1	4	0.00	0
58	50.10	50.86	0.76	1.1	3700	0.03	0
59	50.86	50.89	0.03	7.1	4	0.00	0
60	50.89	52.55	1.66	1.1	30000	0.00	1
61	52.55	53.23	0.68	1.1	10000	0.00	1
62	53.23	55.41	2.18	1.1	35000	0.00	1
63	55.41	56.55	1.14	1.1	30000	0.01	0
64	56.55	56.56	0.01	7.1	4	0.00	0
65	56.56	56.87	0.31	1.2	2700	0.00	1
66	56.87	57.44	0.57	2.2	400	0.07	0
67	57.44	57.51	0.07	7.1	4	0.00	0
68	57.51	58.25	0.74	1.1	8000	0.04	0
69	58.25	58.29	0.04	7.1	4	0.00	0
70	58.29	58.41	0.12	3.1	64	0.03	0
71	58.41	60.39	1.98	1.3	3200	0.05	0
72	60.39	60.44	0.05	7.1	4	0.00	0
73	60.44	62.12	1.68	1.3	45000	0.00	1
74	62.12	64.28	2.16	1.1	20000	0.00	1
75	64.28	66.57	2.29	1.1	2250	0.02	0
76	66.57	66.59	0.02	7.1	4	0.00	0
77	66.59	66.67	0.08	3.1	62	0.03	0
78	66.67	68.06	1.39	1.1	50000	0.02	0
79	68.06	68.08	0.02	7.1	4	0.00	0
80	68.08	69.12	1.04	3.1	125	0.05	0
81	69.12	71.06	1.94	1.1	30000	0.00	1
82	71.06	72.07	1.01	1.1	2000	0.07	0
83	72.07	72.14	0.07	7.1	4	0.00	0
84	72.14	73.17	1.03	2.2	550	0.00	1
85	73.17	73.48	0.31	2.1	650	0.05	0
86	73.48	73.53	0.05	7.1	4	0.00	0
87	73.53	73.64	0.11	3.2	62	0.04	0
88	73.64	74.13	0.49	2.1	700	0.03	0
89	74.13	74.16	0.03	7.1	4	0.00	0
90	74.16	74.68	0.52	3.2	64	0.02	0
91	74.68	75.41	0.73	5.2	2050	0.00	1
92	75.41	76.60	1.19	1.3	3200	0.02	0
93	76.60	76.62	0.02	7.1	4	0.00	0
94	76.62	76.69	0.07	3.1	62	0.02	0
95	76.69	77.51	0.82	1.1	45000	0.00	1
96	77.51	78.47	0.96	1.1	2500	0.02	0
97	78.47	78.49	0.02	7.1	4	0.00	0
98	78.49	78.71	0.22	3.2	125	0.05	0

99	78.71	79.31	0.6	2.1	450	0.00	1
100	79.31	81.45	2.14	1.1	50000	0.00	1
101	81.45	82.07	0.62	2.1	750	0.00	1
102	82.07	83.04	0.97	1.1	45000	0.12	0
103	83.04	83.16	0.12	7.2	4	0.00	0
104	83.16	83.52	0.36	1.2	3200	0.00	1
105	83.52	84.26	0.74	1.1	3000	0.00	1
106	84.26	84.68	0.42	1.1	2500	0.05	0
107	84.68	84.73	0.05	7.1	4	0.00	0
108	84.73	85.21	0.48	3.1	100	0.04	0
109	85.21	86.67	1.46	1.3	3000	0.02	0
110	86.67	86.69	0.02	7.1	4	0.00	0
111	86.69	86.79	0.1	3.1	62	0.02	0
112	86.79	87.43	0.64	1.1	2800	0.00	1
113	87.43	89.46	2.03	1.1	12000	0.03	0
114	89.46	89.49	0.03	7.1	4	0.00	0
115	89.49	90.12	0.63	1.3	2500	0.04	0
116	90.12	90.16	0.04	7.1	4	0.00	0
117	90.16	90.35	0.19	1.2	3200	0.00	1
118	90.35	91.81	1.46	2.2	750	0.08	0
119	91.81	91.89	0.08	7.1	4	0.00	0
120	91.89	93.07	1.18	2.2	750	0.00	1
121	93.07	95.01	1.94	1.1	3250	0.00	1
122	95.01	96.20	1.19	1.1	2750	0.05	0
123	96.20	96.25	0.05	7.1	4	0.00	0
124	96.25	97.73	1.48	1.1	20000	0.00	1
125	97.73	99.56	1.83	1.1	15000	0.00	0
126	99.56	99.57	0.01	7.1	4	0.00	0
127	99.57	99.70	0.13	3.2	62	0.01	0
128	99.70	100.44	0.74	2.2	750	0.00	1
129	100.44	100.78	0.34	2.2	650	0.03	0
130	100.78	100.81	0.03	7.1	4	0.00	0
131	100.81	101.11	0.3	4.2	62	0.01	0
132	101.11	101.69	0.58	1.1	2500	0.00	1
133	101.69	102.03	0.34	1.2	2250	0.00	1
134	102.03	103.47	1.44	1.1	25000	0.03	0
135	103.47	103.50	0.03	7.1	4	0.00	0
136	103.50	103.68	0.18	3.1	62	0.02	0
137	103.68	107.76	4.08	1.1	4250	0.02	0
138	107.76	107.78	0.02	7.1	4	0.00	0
139	107.78	109.40	1.62	1.1	10000	0.00	1
140	109.40	111.05	1.65	1.1	3200	0.00	1
141	111.05	112.22	1.17	1.1	3000	0.00	1
142	112.22	114.15	1.93	5.1	7500	0.05	0
143	114.15	114.20	0.05	7.1	4	0.00	0
144	114.20	114.27	0.07	3.1	125	0.01	0
145	114.27	115.61	1.34	1.1	8000	0.04	0
146	115.61	115.65	0.04	7.1	4	0.00	0
147	115.65	116.00	0.35	3.1	100	0.02	0
148	116.00	118.66	2.66	1.1	30000	0.04	0

149	118.66	118.70	0.04	7.1	4	0.00	0
150	118.70	119.39	0.69	2.2	650	0.05	0
151	119.39	119.44	0.05	7.1	4	0.00	0
152	119.44	120.86	1.42	1.1	25000	0.00	1
153	120.86	122.48	1.62	1.1	15000	0.01	0
154	122.48	122.49	0.01	7.1	4	0.00	0
155	122.49	122.86	0.37	3.1	250	0.02	0
156	122.86	123.28	0.42	1.1	2500	0.00	1
157	123.28	124.21	0.93	1.1	3500	0.05	0
158	124.21	124.26	0.05	7.1	4	0.00	0
159	124.26	126.67	2.41	1.1	12000	0.07	0
160	126.67	126.74	0.07	7.1	4	0.00	0
161	126.74	127.47	0.73	2.2	800	0.01	0
162	127.47	127.48	0.01	7.1	4	0.00	0
163	127.48	128.65	1.17	1.1	5000	0.00	1
164	128.65	129.71	1.06	1.1	3000	0.02	0
165	129.71	129.73	0.02	7.1	4	0.00	0
166	129.73	130.15	0.42	1.2	3500	0.00	1
167	130.15	130.84	0.69	1.1	5000	0.00	1
168	130.84	131.77	0.93	2.2	950	0.00	1
169	131.77	131.87	0.1	2.1	300	0.10	0
170	131.87	131.97	0.1	7.1	4	0.00	0
171	131.97	133.25	1.28	1.1	3500	0.00	1
172	133.25	134.27	1.02	2.2	1200	0.00	1
173	134.27	134.90	0.63	2.2	450	0.00	1
174	134.90	137.74	2.84	1.1	4000	0.00	1
175	137.74	138.69	0.95	2.1	800	0.00	1
176	138.69	139.05	0.36	1.2	2500	0.01	0
177	139.05	139.06	0.01	7.1	4	0.00	0
178	139.06	139.63	0.57	4.1	80	0.01	0
179	139.63	139.64	0.01	7.1	4	0.00	0
180	139.64	141.36	1.72	1.3	4100	0.00	0
181	141.36	142.26	0.9	0.0	0	0.00	0
182	142.26	144.53	2.27	4.1	250	0.03	0
183	144.53	144.56	0.03	7.1	4	0.00	0
184	144.56	144.68	0.12	3.1	62	0.05	0
185	144.68	145.07	0.39	2.2	600	0.00	1
186	145.07	146.13	1.06	6.1	4250	0.00	0

3-Montalto Road-section

bed nr.	base	top	thickness	Bed type	max. grain size	mudcap	amalgamation
1	0.00	0.25	0.25	1.2	3500	0.00	1
2	0.25	0.50	0.25	2.1	1250	0.00	1
3	0.50	0.85	0.35	1.2	3750	0.00	1
4	0.85	1.70	0.85	3.2	200	0.02	0
5	1.70	1.90	0.2	2.1	400	0.00	1
6	1.90	2.50	0.6	2.2	600	0.00	1
7	2.50	2.90	0.4	6.1	750	0.00	1
8	2.90	3.15	0.25	2.1	750	0.00	1
9	3.15	3.80	0.65	1.3	10000	0.00	1
10	3.80	4.10	0.3	1.2	4000	0.10	0
11	4.10	4.20	0.1	7.2	50	0.00	0
12	4.20	5.68	1.48	1.3	15000	0.02	0
13	5.68	5.70	0.02	7.1	4	0.00	0
14	5.70	5.90	0.2	3.1	62	0.03	0
15	5.90	7.35	1.45	1.3	12500	0.00	1
16	7.35	7.70	0.35	2.2	750	0.00	1
17	7.70	8.10	0.4	2.2	550	0.00	1
18	8.10	8.22	0.12	2.2	250	0.00	1
19	8.22	8.68	0.46	2.2	750	0.04	0
20	8.68	8.72	0.04	7.1	4	0.00	0
21	8.72	9.22	0.5	3.1	100	0.04	0
22	9.22	10.97	1.75	1.3	25000	0.00	1
23	10.97	11.59	0.62	2.1	500	0.00	1
24	11.59	11.69	0.1	2.2	250	0.00	1
25	11.69	12.06	0.37	2.2	950	0.03	0
26	12.06	12.09	0.03	7.1	4	0.00	0
27	12.09	12.29	0.2	2.2	900	0.00	1
28	12.29	12.74	0.45	2.1	1750	0.03	0
29	12.74	12.77	0.03	7.1	4	0.00	0
30	12.77	12.97	0.2	3.1	125	0.02	0
31	12.97	14.36	1.39	1.1	40000	0.06	0
32	14.36	14.42	0.06	7.1	4	0.00	0
33	14.42	14.77	0.35	3.2	62	0.04	0
34	14.77	15.72	0.95	1.1	25000	0.00	1
35	15.72	16.57	0.85	1.3	25000	0.00	1
36	16.57	16.65	0.08	2.1	350	0.00	1
37	16.65	16.78	0.13	2.1	700	0.02	0
38	16.78	16.80	0.02	7.1	4	0.00	0
39	16.80	17.00	0.2	3.1	62	0.03	0
40	17.00	17.25	0.25	2.1	850	0.05	0
41	17.25	17.30	0.05	7.1	4	0.00	0
42	17.30	19.40	2.1	1.3	35000	0.00	1
43	19.40	19.53	0.13	2.1	450	0.02	0
44	19.53	19.55	0.02	7.1	4	0.00	0
45	19.55	19.80	0.25	4.2	62	0.05	0
46	19.80	19.85	0.05	7.1	4	0.00	0
47	19.85	20.93	1.08	1.3	10000	0.04	0
48	20.93	20.97	0.04	7.1	4	0.00	0

49	20.97	22.00	1.03	1.3	7500	0.00	1
50	22.00	22.20	0.2	2.2	650	0.00	1
51	22.20	22.67	0.47	1.3	3500	0.00	1
52	22.67	23.48	0.81	1.1	2250	0.00	1
53	23.48	23.73	0.25	2.2	250	0.00	1
54	23.73	24.28	0.55	2.2	1250	0.00	1
55	24.28	24.47	0.19	2.1	250	0.01	0
56	24.47	24.48	0.01	7.1	4	0.00	0
57	24.48	24.88	0.4	3.2	62	0.04	0
58	24.88	25.28	0.4	2.1	1000	0.01	0
59	25.28	25.48	0.2	3.2	62	0.02	0
60	25.48	26.68	1.2	1.3	3500	0.00	1
61	26.68	27.18	0.5	1.1	3000	0.00	1
62	27.18	27.48	0.3	2.1	1250	0.00	1
63	27.48	28.33	0.85	1.1	4500	0.00	1
64	28.33	29.43	1.1	1.3	35000	0.00	1
65	29.43	30.43	1	1.3	25000	0.00	1
66	30.43	30.65	0.22	2.1	450	0.02	0
67	30.65	30.85	0.2	1.2	4000	0.00	1
68	30.85	31.05	0.2	2.1	1750	0.02	0
69	31.05	32.15	1.1	1.3	13000	0.00	1
70	32.15	32.80	0.65	1.3	7500	0.00	1
71	32.80	33.75	0.95	1.3	6000	0.00	1
72	33.75	35.25	1.5	1.3	20000	0.02	0
73	35.25	35.35	0.1	3.2	62	0.02	0
74	35.35	35.70	0.35	2.1	1100	0.00	1
75	35.70	36.00	0.3	2.1	650	0.00	1
76	36.00	36.15	0.15	2.1	750	0.00	1
77	36.15	36.50	0.35	2.1	500	0.03	0
78	36.50	38.27	1.77	1.3	20000	0.00	1
79	38.27	39.22	0.95	1.3	6000	0.00	1
80	39.22	39.34	0.12	1.2	4000	0.00	1
81	39.34	39.89	0.55	2.2	125	0.00	0
82	39.89	40.11	0.22	4.2	62	0.00	0
83	40.11	40.46	0.35	1.2	3000	0.00	1
84	40.46	41.11	0.65	1.3	25000	0.00	1
85	41.11	41.46	0.35	1.2	7500	0.00	1
86	41.46	41.66	0.2	2.1	1250	0.00	1
87	41.66	42.56	0.9	1.3	4000	0.00	1
88	42.56	44.66	2.1	1.3	25000	0.00	0
89	44.66	44.86	0.2	3.2	62	0.00	0
90	44.86	45.03	0.17	2.2	1250	0.03	0
91	45.03	45.08	0.05	3.2	62	0.01	0
92	45.08	45.48	0.4	1.2	4000	0.00	1
93	45.48	47.33	1.85	1.1	25000	0.00	1
94	47.33	48.18	0.85	1.1	3500	0.00	0
95	48.18	48.33	0.15	3.2	62	0.00	0
96	48.33	48.41	0.08	3.2	62	0.00	0
97	48.41	49.66	1.25	5.1	15000	0.00	0
98	49.66	49.84	0.18	4.2	62	0.00	0

99	49.84	50.09	0.25	5.1	750	0.00	0
100	50.09	50.39	0.3	4.2	62	0.00	0
101	50.39	51.64	1.25	5.2	7500	0.00	1
102	51.64	54.09	2.45	1.3	5000	0.00	1
103	54.09	55.84	1.75	2.1	1500	0.00	1
104	55.84	55.99	0.15	2.2	250	0.00	1
105	55.99	56.69	0.7	1.1	4000	0.00	1
106	56.69	57.14	0.45	2.2	850	0.02	0
107	57.14	57.69	0.55	1.3	4500	0.00	1
108	57.69	58.29	0.6	1.3	15000	0.00	1
109	58.29	58.79	0.5	2.2	1250	0.04	0
110	58.79	59.44	0.65	1.3	6500	0.00	1
111	59.44	59.79	0.35	2.2	1900	0.00	0
112	59.79	59.89	0.1	4.2	62	0.01	0
113	59.89	62.39	2.5	1.3	30000	0.00	1
114	62.39	62.79	0.4	6.1	500	0.03	0
115	62.79	63.72	0.93	6.1	1250	0.14	0
116	63.72	64.77	1.05	1.3	4500	0.08	0
117	64.77	66.49	1.72	1.3	25000	0.00	1
118	66.49	67.01	0.52	2.2	700	0.00	1
119	67.01	67.37	0.36	2.2	1000	0.00	1
120	67.37	67.55	0.18	2.1	350	0.00	1
121	67.55	68.27	0.72	1.3	10000	0.00	1
122	68.27	69.75	1.48	1.3	35000	0.00	1
123	69.75	69.95	0.2	2.1	400	0.00	1
124	69.95	70.75	0.8	5.1	650	0.00	1
125	70.75	70.95	0.2	2.2	500	0.00	1
126	70.95	71.35	0.4	1.2	15000	0.00	1
127	71.35	72.50	1.15	1.3	4000	0.00	1
128	72.50	73.55	1.05	1.3	4000	0.00	1
129	73.55	73.73	0.18	2.0	250	0.00	0
130	73.73	73.88	0.15	4.2	62	0.00	0
131	73.88	74.53	0.65	1.3	7500	0.00	1
132	74.53	75.51	0.98	1.1	15000	0.00	1
133	75.51	75.68	0.17	2.1	1250	0.00	1
134	75.68	77.66	1.98	1.1	30000	0.00	1
135	77.66	77.88	0.22	2.2	250	0.04	0
136	77.88	78.68	0.8	6.1	4000	0.06	0
137	78.68	79.08	0.4	3.2	62	0.05	0
138	79.08	80.48	1.4	1.3	10000	0.00	0
139	80.48	81.13	0.65	6.3	650	0.00	1
140	81.13	81.73	0.6	6.1	850	0.00	1
141	81.73	82.48	0.75	1.3	4000	0.00	1
142	82.48	85.63	3.15	1.3	50000	0.00	0
143	85.63	86.66	1.03	4.1	125	0.20	0
144	86.66	87.31	0.65	6.1	850	0.00	1
145	87.31	87.91	0.6	6.1	1000	0.00	1
146	87.91	88.36	0.45	2.2	250	0.00	1
147	88.36	88.99	0.63	5.1	850	0.05	0
148	88.99	91.59	2.6	1.3	40000	0.00	1

149	91.59	91.74	0.15	2.1	1000	0.00	1
150	91.74	91.99	0.25	2.2	175	0.00	1
151	91.99	92.94	0.95	1.3	3000	0.00	1
152	92.94	93.06	0.12	2.2	400	0.00	1
153	93.06	93.23	0.17	2.1	1500	0.00	1
154	93.23	93.78	0.55	2.1	750	0.00	1
155	93.78	94.18	0.4	2.1	1650	0.00	1
156	94.18	94.68	0.5	2.1	950	0.00	1
157	94.68	94.85	0.17	2.1	500	0.00	1
158	94.85	95.48	0.63	2.2	1750	0.00	1
159	95.48	95.70	0.22	2.1	900	0.00	1
160	95.70	97.78	2.08	1.3	45000	0.00	0
161	97.78	106.78	9	0.0	0	0.00	0
162	106.78	106.98	0.2	2.1	450	0.00	0
163	106.98	107.06	0.08	4.2	62	0.00	0
164	107.06	107.26	0.2	2.1	400	0.00	0
165	107.26	107.56	0.3	4.2	62	0.00	0
166	107.56	108.09	0.53	2.1	900	0.08	0
167	108.09	108.16	0.07	2.1	250	0.02	0
168	108.16	108.23	0.07	4.2	62	0.00	0
169	108.23	108.88	0.65	1.3	50000	0.00	1
170	108.88	110.03	1.15	1.3	4000	0.00	1
171	110.03	110.63	0.6	1.1	2500	0.00	1
172	110.63	112.03	1.4	1.3	15000	0.00	1
173	112.03	112.70	0.67	1.3	4000	0.00	1
174	112.70	113.28	0.58	1.3	3500	0.02	0
175	113.28	113.43	0.15	3.2	62	0.03	0
176	113.43	114.83	1.4	1.3	4000	0.00	0
177	114.83	115.41	0.58	2.2	750	0.00	0
178	115.41	115.53	0.12	4.2	62	0.00	0
179	115.53	116.28	0.75	1.3	2200	0.00	1
180	116.28	118.16	1.88	1.3	40000	0.08	0
181	118.16	118.48	0.32	2.1	1000	0.05	0
182	118.48	118.96	0.48	3.2	62	0.07	0
183	118.96	119.71	0.75	1.3	4000	0.02	0
184	119.71	120.51	0.8	3.2	125	0.04	0
185	120.51	121.93	1.42	1.3	3500	0.00	1
186	121.93	124.03	2.1	1.3	4000	0.00	1
187	124.03	124.73	0.7	1.3	10000	0.00	0
188	124.73	124.88	0.15	3.2	62	0.00	0
189	124.88	125.33	0.45	1.3	12500	0.00	1
190	125.33	126.73	1.4	1.3	25000	0.00	0
191	126.73	127.45	0.72	3.2	125	0.02	0
192	127.45	129.23	1.78	1.3	40000	0.00	1
193	129.23	129.88	0.65	2.2	1950	0.00	1
194	129.88	130.08	0.2	4.2	62	0.00	0
195	130.08	130.63	0.55	1.3	2250	0.00	1
196	130.63	132.03	1.4	1.3	4000	0.00	1
197	132.03	132.31	0.28	2.1	1750	0.12	0
198	132.31	132.76	0.45	2.1	1500	0.00	0

199	132.76	133.12	0.36	4.2	62	0.01	0
200	133.12	134.67	1.55	1.1	3500	0.00	1
201	134.67	135.07	0.4	2.2	500	0.00	1
202	135.07	136.22	1.15	1.1	4000	0.00	1
203	136.22	136.54	0.32	1.2	2250	0.02	0
204	136.54	136.87	0.33	1.2	5000	0.00	1
205	136.87	138.07	1.2	1.1	12500	0.00	1
206	138.07	139.77	1.7	1.3	20000	0.00	1
207	139.77	140.92	1.15	1.3	30000	0.00	1
208	140.92	141.72	0.8	1.1	4000	0.00	1
209	141.72	141.97	0.25	2.2	350	0.02	0
210	141.97	143.17	1.2	1.1	2500	0.00	1
211	143.17	144.12	0.95	1.1	2000	0.00	1
212	144.12	144.84	0.72	2.2	500	0.00	0
213	144.84	145.36	0.52	4.1	100	0.00	0
214	145.36	145.58	0.22	2.1	1000	0.00	0
215	145.58	145.98	0.4	4.1	62	0.00	0
216	145.98	146.66	0.68	4.1	100	0.02	0
217	146.66	147.78	1.12	4.1	100	0.04	0
218	147.78	148.21	0.43	2.1	1250	0.05	0
219	148.21	149.46	1.25	1.1	2500	0.00	1
220	149.46	150.23	0.77	1.3	2250	0.00	1
221	150.23	151.58	1.35	2.1	1750	0.00	0
222	151.58	151.93	0.35	4.1	62	0.00	0
223	151.93	152.20	0.27	2.2	350	0.03	0
224	152.20	152.85	0.65	2.1	650	0.00	0
225	152.85	153.41	0.56	4.1	62	0.00	0
226	153.41	153.77	0.36	4.1	62	0.00	0
227	153.77	154.10	0.33	4.1	62	0.00	0
228	154.10	154.37	0.27	2.1	1750	0.00	0
229	154.37	154.79	0.42	4.1	62	0.00	0
230	154.79	155.11	0.32	2.1	650	0.00	0
231	155.11	155.28	0.17	4.2	62	0.00	0
232	155.28	155.63	0.35	6.1	1750	0.00	0
233	155.63	157.39	1.76	6.1	1500	0.00	0
234	157.39	157.99	0.6	4.1	100	0.00	0
235	157.99	158.44	0.45	6.1	650	0.00	0
236	158.44	158.79	0.35	4.1	62	0.00	0
237	158.79	159.34	0.55	6.1	1750	0.00	1
238	159.34	159.54	0.2	2.1	350	0.00	0
239	159.54	159.73	0.19	4.2	62	0.00	0
240	159.73	160.20	0.47	1.1	4000	0.00	0
241	160.20	160.53	0.33	4.1	125	0.00	0
242	160.53	160.83	0.3	1.2	4000	0.00	0
243	160.83	161.95	1.12	4.1	100	0.00	0
244	161.95	162.20	0.25	2.1	1500	0.00	0
245	162.20	162.40	0.2	4.2	62	0.00	0

4-Montalto River-section

bed nr.	base	top	thickness	Bed type	max. grain size	mudcap	amalgamation
1	0.00	1.05	1.05	1.3	3500	0.00	1
2	1.05	1.30	0.25	2.1	400	0.00	1
3	1.30	1.84	0.54	1.1	2250	0.00	1
4	1.84	2.32	0.48	1.1	2100	0.00	0
5	2.32	2.51	0.19	2.2	300	0.00	1
6	2.51	4.14	1.63	1.3	2200	0.00	1
7	4.14	4.46	0.32	2.2	350	0.00	1
8	4.46	5.00	0.54	6.1	2000	0.00	1
9	5.00	5.72	0.72	6.1	550	0.00	1
10	5.72	5.95	0.23	1.2	3750	0.00	1
11	5.95	7.47	1.52	1.3	3250	0.07	0
12	7.47	8.08	0.61	1.1	7500	0.00	1
13	8.08	8.77	0.69	2.2	900	0.00	1
14	8.77	9.17	0.4	2.1	850	0.00	1
15	9.17	10.12	0.95	1.3	8000	0.01	0
16	10.12	10.37	0.25	3.2	125	0.02	0
17	10.37	11.05	0.68	6.1	4500	0.03	0
18	11.05	13.45	2.4	1.3	4500	0.03	0
19	13.45	14.70	1.25	1.3	6000	0.02	0
20	14.70	16.40	1.7	1.3	7500	0.00	1
21	16.40	17.23	0.83	1.3	2100	0.00	1
22	17.23	17.70	0.47	1.2	7500	0.05	0
23	17.70	18.17	0.47	2.2	650	0.00	1
24	18.17	21.32	3.15	5.2	35000	0.00	1
25	21.32	21.55	0.23	1.2	2250	0.00	1
26	21.55	21.98	0.43	2.2	500	0.00	1
27	21.98	22.62	0.64	1.3	2000	0.00	1
28	22.62	23.83	1.21	1.1	4000	0.00	1
29	23.83	24.25	0.42	2.2	500	0.00	1
30	24.25	25.20	0.95	1.3	3800	0.00	1
31	25.20	26.28	1.08	1.3	5000	0.00	1
32	26.28	27.81	1.53	1.1	4500	0.00	1
33	27.81	28.68	0.87	1.3	2250	0.00	1
34	28.68	29.83	1.15	1.3	2100	0.00	1
35	29.83	30.76	0.93	1.1	2500	0.00	1
36	30.76	31.68	0.92	1.3	4000	0.00	1
37	31.68	34.02	2.34	1.3	3750	0.00	1
38	34.02	35.72	1.7	1.1	5000	0.00	1
39	35.72	37.52	1.8	1.3	3500	0.00	1
40	37.52	37.92	0.4	2.1	1250	0.00	1
41	37.92	38.32	0.4	1.1	3750	0.00	1
42	38.32	38.64	0.32	1.2	2500	0.00	1
43	38.64	39.51	0.87	1.3	2500	0.00	1
44	39.51	40.23	0.72	2.2	1500	0.00	1
45	40.23	40.38	0.15	1.2	2100	0.00	1
46	40.38	41.75	1.37	1.1	40000	0.00	1
47	41.75	43.15	1.4	4.1	200	0.00	0
48	43.15	44.55	1.4	1.3	4000	0.00	1

49	44.55	45.26	0.71	1.3	2500	0.02	0
50	45.26	45.41	0.15	3.2	62	0.01	0
51	45.41	45.68	0.27	6.1	1250	0.02	0
52	45.68	45.87	0.19	3.2	62	0.01	0
53	45.87	45.97	0.1	4.2	62	0.00	0
54	45.97	46.59	0.62	6.2	1750	0.00	1
55	46.59	46.87	0.28	2.2	1500	0.00	1
56	46.87	47.17	0.3	1.2	3750	0.00	1
57	47.17	48.15	0.98	1.1	4000	0.00	1
58	48.15	49.73	1.58	1.3	3750	0.00	1
59	49.73	50.27	0.54	1.1	3500	0.00	1
60	50.27	51.17	0.9	1.1	2250	0.00	0
61	51.17	51.59	0.42	4.1	120	0.00	0
62	51.59	52.44	0.85	1.1	3750	0.00	1
63	52.44	53.57	1.13	1.3	4000	0.01	0
64	53.57	53.74	0.17	3.2	125	0.01	0
65	53.74	53.83	0.09	2.1	400	0.00	1
66	53.83	55.26	1.43	1.1	30000	0.02	0
67	55.26	55.34	0.08	4.2	62	0.00	0
68	55.34	56.16	0.82	6.1	2500	0.00	1
69	56.16	56.64	0.48	5.2	2000	0.00	1
70	56.64	57.02	0.38	1.2	3000	0.00	0
71	57.02	57.21	0.19	4.2	62	0.01	0
72	57.21	59.01	1.8	1.3	3750	0.00	1
73	59.01	59.47	0.46	1.1	6000	0.00	1
74	59.47	60.22	0.75	1.3	2250	0.00	1
75	60.22	60.99	0.77	1.1	3750	0.00	1
76	60.99	62.18	1.19	1.1	3000	0.00	1
77	62.18	63.65	1.47	1.3	2250	0.20	0
78	63.65	65.00	1.35	1.3	2500	0.00	1
79	65.00	65.90	0.9	1.3	2250	0.00	0
80	65.90	66.05	0.15	4.2	62	0.00	0
81	66.05	66.88	0.83	1.3	2250	0.02	0
82	66.88	68.08	1.2	1.3	3750	0.02	0
83	68.08	69.23	1.15	6.3	30000	0.00	1
84	69.23	70.88	1.65	1.1	2000	0.35	0
85	70.88	72.93	2.05	1.1	5000	0.00	1
86	72.93	73.11	0.18	1.2	2000	0.00	1
87	73.11	73.65	0.54	5.2	1000	0.00	1
88	73.65	74.35	0.7	1.1	3000	0.00	1
89	74.35	75.07	0.72	1.1	4500	0.00	1
90	75.07	76.15	1.08	1.3	6000	0.18	0
91	76.15	77.51	1.36	1.3	40000	0.00	1
92	77.51	78.58	1.07	1.3	30000	0.00	1
93	78.58	80.76	2.18	1.1	20000	0.00	1
94	80.76	81.73	0.97	6.2	3000	0.00	1
95	81.73	83.45	1.72	6.2	4000	0.02	0
96	83.45	85.02	1.57	6.1	2100	0.00	1
97	85.02	86.22	1.2	1.3	40000	0.00	1
98	86.22	89.77	3.55	5.1	35000	0.37	0

99	89.77	92.52	2.75	1.1	55000	0.02	0
100	92.52	92.61	0.09	2.1	500	0.00	1
101	92.61	93.53	0.92	6.1	4000	0.00	1
102	93.53	94.17	0.64	6.3	1750	0.00	1
103	94.17	95.67	1.5	5.1	40000	0.00	1
104	95.67	96.31	0.64	1.1	25000	0.00	0
105	96.31	96.54	0.23	4.2	62	0.00	0
106	96.54	97.72	1.18	1.3	2500	0.00	1
107	97.72	97.89	0.17	2.1	500	0.00	1
108	97.89	98.45	0.56	2.2	750	0.00	1
109	98.45	99.30	0.85	1.3	2250	0.00	1
110	99.30	100.16	0.86	1.3	2000	0.00	1
111	100.16	100.74	0.58	1.1	4000	0.07	0
112	100.74	102.31	1.57	1.1	20000	0.00	1
113	102.31	102.79	0.48	6.1	4000	0.02	0
114	102.79	102.99	0.2	3.2	62	0.02	0
115	102.99	103.22	0.23	4.2	62	0.00	0
116	103.22	103.46	0.24	4.2	62	0.00	0
117	103.46	103.73	0.27	4.2	62	0.00	0
118	103.73	105.36	1.63	4.1	125	0.00	1
119	105.36	105.61	0.25	2.2	250	0.00	1
120	105.61	106.83	1.22	6.1	1000	0.00	1
121	106.83	108.14	1.31	5.1	40000	0.00	1
122	108.14	108.28	0.14	2.1	600	0.00	1
123	108.28	108.47	0.19	2.1	500	0.02	0
124	108.47	109.20	0.73	1.3	2500	0.00	1
125	109.20	110.56	1.36	2.2	1750	0.00	1
126	110.56	110.92	0.36	2.2	400	0.00	0
127	110.92	111.08	0.16	4.2	62	0.00	0
128	111.08	112.88	1.8	6.2	2500	0.00	1
129	112.88	114.51	1.63	1.3	45000	0.00	1
130	114.51	117.56	3.05	1.1	50000	0.00	1
131	117.56	118.10	0.54	1.1	10000	0.00	1
132	118.10	118.62	0.52	1.1	6000	0.00	1
133	118.62	118.99	0.37	5.1	1250	0.00	1
134	118.99	119.55	0.56	1.1	2500	0.00	1
135	119.55	120.53	0.98	1.1	3500	0.00	1
136	120.53	121.17	0.64	2.2	650	0.00	1
137	121.17	121.93	0.76	1.1	2500	0.00	1
138	121.93	123.71	1.78	1.3	35000	0.00	0
139	123.71	123.90	0.19	4.2	50	0.00	0
140	123.90	124.58	0.68	6.1	2500	0.02	0
141	124.58	125.07	0.49	6.1	750	0.00	1
142	125.07	125.99	0.92	2.2	750	0.00	0
143	125.99	126.10	0.11	4.2	50	0.01	0
144	126.10	128.97	2.87	1.1	3500	0.00	1
145	128.97	129.50	0.53	2.2	800	0.00	0
146	129.50	129.72	0.22	4.2	62	0.00	0
147	129.72	129.88	0.16	4.2	62	0.00	0
148	129.88	131.30	1.42	6.3	700	0.01	0

149	131.30	133.75	2.45	4.2	62	0.01	0
150	133.75	134.31	0.56	1.3	3500	0.00	1
151	134.31	136.95	2.64	1.3	25000	0.00	1
152	136.95	137.14	0.19	2.2	350	0.00	0
153	137.14	137.28	0.14	4.2	50	0.01	0
154	137.28	138.08	0.8	1.1	12000	0.00	1
155	138.08	139.23	1.15	5.1	4000	0.00	1
156	139.23	139.93	0.7	5.1	3000	0.00	1
157	139.93	140.33	0.4	2.1	750	0.00	1
158	140.33	141.21	0.88	1.1	2500	0.00	1
159	141.21	141.36	0.15	2.1	1250	0.02	0
160	141.36	141.76	0.4	3.2	125	0.02	0
161	141.76	142.62	0.86	5.1	2250	0.00	1
162	142.62	145.49	2.87	5.1	4000	0.00	1
163	145.49	147.27	1.78	2.2	1500	0.00	1
164	147.27	147.55	0.28	2.1	350	0.02	0
165	147.55	147.73	0.18	4.2	50	0.00	0
166	147.73	148.21	0.48	2.2	350	0.00	0
167	148.21	148.62	0.41	4.1	62	0.05	0
168	148.62	150.28	1.66	2.2	800	0.00	1
169	150.28	150.66	0.38	1.2	25000	0.00	1
170	150.66	151.38	0.72	2.1	1750	0.00	1
171	151.38	153.21	1.83	2.1	1900	0.02	0
172	153.21	153.63	0.42	4.1	62	0.10	0
173	153.63	154.27	0.64	2.1	1500	0.00	1
174	154.27	155.35	1.08	2.2	1750	0.01	0
175	155.35	157.60	2.25	2.2	1250	0.15	0
176	157.60	158.06	0.46	4.2	62	0.01	0
177	158.06	158.66	0.6	3.2	62	0.02	0
178	158.66	159.03	0.37	2.1	200	0.06	0
179	159.03	159.88	0.85	4.2	62	0.02	0
180	159.88	160.55	0.67	4.1	62	0.02	0
181	160.55	163.95	3.4	0.0	0	0.00	0
182	163.95	164.65	0.7	3.2	125	0.02	0
183	164.65	165.18	0.53	2.1	1000	0.01	0
184	165.18	165.32	0.14	4.2	62	0.01	0
185	165.32	165.70	0.38	3.2	125	0.01	0
186	165.70	165.98	0.28	2.2	600	0.00	0
187	165.98	166.35	0.37	4.1	62	0.00	0
188	166.35	166.89	0.54	5.1	800	0.07	0
189	166.89	167.04	0.15	3.1	62	0.02	0
190	167.04	167.80	0.76	2.2	500	0.00	0
191	167.80	168.14	0.34	3.2	62	0.01	0
192	168.14	168.42	0.28	4.2	62	0.02	0
193	168.42	168.82	0.4	4.1	62	0.00	0
194	168.82	168.91	0.09	2.1	125	0.00	1
195	168.91	169.66	0.75	2.2	500	0.00	0
196	169.66	170.49	0.83	4.1	62	0.00	0
197	170.49	171.06	0.57	2.2	400	0.00	1
198	171.06	171.68	0.62	2.2	350	0.00	1

199	171.68	172.25	0.57	2.2	350	0.00	1
200	172.25	173.03	0.78	2.1	750	0.00	1
201	173.03	173.57	0.54	2.2	350	0.02	0
202	173.57	174.69	1.12	3.2	125	0.05	0
203	174.69	176.96	2.27	6.1	35000	0.07	0
204	176.96	177.16	0.2	3.2	62	0.02	0
205	177.16	178.86	1.7	5.2	15000	0.00	1
206	178.86	180.44	1.58	1.1	12500	0.00	1
207	180.44	180.82	0.38	5.2	700	0.00	1
208	180.82	181.42	0.6	3.2	62	0.01	0
209	181.42	182.35	0.93	5.2	2250	0.00	1
210	182.35	183.87	1.52	1.1	20000	0.01	0
211	183.87	184.01	0.14	4.2	62	0.00	0
212	184.01	184.26	0.25	2.1	250	0.00	0
213	184.26	184.49	0.23	4.2	62	0.00	2
214	184.49	185.15	0.66	4.2	62	0.00	0
215	185.15	185.32	0.17	2.1	350	0.00	1
216	185.32	186.90	1.58	5.1	3250	0.12	0
217	186.90	188.25	1.35	2.1	1500	0.00	0
218	188.25	188.93	0.68	4.2	62	0.02	0
219	188.93	189.45	0.52	2.2	250	0.00	0
220	189.45	192.35	2.9	5.1	3000	0.00	0
221	192.35	193.35	1	0	0	0.00	0
222	193.35	194.28	0.93	2.1	950	0.02	1
223	194.28	194.51	0.23	2.1	250	0.00	1
224	194.51	194.63	0.12	2.1	200	0.00	1
225	194.63	195.23	0.6	5.2	500	0.00	1
226	195.23	195.42	0.19	4.2	62	0.00	0
227	195.42	196.27	0.85	1.1	3000	0.00	1
228	196.27	196.61	0.34	2.1	250	0.00	0
229	196.61	197.24	0.63	3.2	62	0.02	0
230	197.24	197.67	0.43	2.1	500	0.00	1
231	197.67	198.26	0.59	2.1	1000	0.00	1
232	198.26	199.67	1.41	1.3	15000	0.00	1
233	199.67	200.01	0.34	2.1	400	0.00	0
234	200.01	200.30	0.29	4.2	62	0.01	0
235	200.30	200.53	0.23	2.2	1000	0.00	1
236	200.53	201.41	0.88	1.1	12500	0.00	1
237	201.41	201.98	0.57	5.1	1000	0.00	1
238	201.98	202.90	0.92	5.1	1000	0.01	0

5-Carmo dei Brocchi

bed nr.	base	top	thickness	Bed type	max. grain size	mudcap	amalgamation
1	0.00	1.97	1.97	5.2	25000	0.00	0
2	1.97	2.67	0.7	0.0	0	0.00	0
3	2.67	4.15	1.48	5.2	1750	0.00	0
4	4.15	4.35	0.2	0.0	0	0.00	0
5	4.35	7.87	3.52	1.3	25000	0.00	1
6	7.87	9.90	2.03	6.1	4000	0.02	0
7	9.90	9.97	0.07	3.2	62	0.01	0
8	9.97	11.37	1.4	6.1	4000	0.00	1
9	11.37	12.92	1.55	5.2	5500	0.00	1
10	12.92	13.45	0.53	2.1	1500	0.00	1
11	13.45	14.72	1.27	1.1	3750	0.00	0
12	14.72	15.92	1.2	0.0	0	0.00	0
13	15.92	17.14	1.22	6.1	1250	0.02	0
14	17.14	18.38	1.24	1.1	15000	0.00	1
15	18.38	19.99	1.61	5.1	15000	0.00	0
16	19.99	26.14	6.15	0.0	0	0.00	0
17	26.14	26.71	0.57	2.2	150	0.00	1
18	26.71	26.81	0.1	2.1	100	0.00	1
19	26.81	26.89	0.08	2.1	200	0.01	0
20	26.89	27.16	0.27	2.2	250	0.00	1
21	27.16	27.65	0.49	5.1	250	0.00	1
22	27.65	28.11	0.46	2.2	200	0.11	0
23	28.11	28.91	0.8	6.1	1000	0.08	0
24	28.91	30.01	1.1	6.1	5000	0.00	1
25	30.01	30.87	0.86	2.2	200	0.01	0
26	30.87	30.96	0.09	3.2	62	0.01	0
27	30.96	31.95	0.99	2.2	250	0.01	0
28	31.95	32.17	0.22	3.2	125	0.02	0
29	32.17	32.47	0.3	2.2	1500	0.00	1
30	32.47	33.47	1	2.2	1750	0.02	0
31	33.47	34.57	1.1	1.3	3000	0.03	0
32	34.57	35.42	0.85	2.2	950	0.03	0
33	35.42	36.12	0.7	5.1	2500	0.06	0
34	36.12	36.72	0.6	1.1	4000	0.01	0
35	36.72	38.22	1.5	2.2	650	0.00	1
36	38.22	38.91	0.69	5.1	2000	0.00	1
37	38.91	39.94	1.03	6.1	2000	0.00	1
38	39.94	40.61	0.67	2.2	250	0.25	0
39	40.61	41.33	0.72	6.1	1000	0.04	0
40	41.33	41.48	0.15	4.2	62	0.00	0
41	41.48	42.76	1.28	5.1	4000	0.00	1
42	42.76	43.52	0.76	6.1	1500	0.00	0
43	43.52	43.92	0.4	4.1	62	0.00	0
44	43.92	44.92	1	4.1	100	0.00	0
45	44.92	45.47	0.55	4.1	62	0.00	0
46	45.47	46.15	0.68	2.2	1950	0.04	0
47	46.15	46.27	0.12	4.2	62	0.00	0
48	46.27	46.49	0.22	4.2	62	0.00	0

49	46.49	47.75	1.26	6.2	3500	0.07	0
50	47.75	49.30	1.55	1.1	2500	0.02	0
51	49.30	51.10	1.8	3.2	100	0.02	0
52	51.10	51.40	0.3	4.2	62	0.02	0
53	51.40	52.00	0.6	3.2	62	0.02	0
54	52.00	53.38	1.38	2.1	1750	0.00	1
55	53.38	54.53	1.15	5.2	3500	0.00	1
56	54.53	55.65	1.12	1.1	3750	0.05	0
57	55.65	57.12	1.47	6.2	2500	0.00	0
58	57.12	57.47	0.35	4.1	62	0.00	0
59	57.47	57.77	0.3	4.2	62	0.00	0
60	57.77	58.02	0.25	4.2	62	0.00	0
61	58.02	58.22	0.2	4.2	62	0.00	0
62	58.22	59.70	1.48	5.2	4000	0.00	0
63	59.70	59.90	0.2	4.2	62	0.00	0
64	59.90	60.60	0.7	5.2	1750	0.02	0
65	60.60	60.95	0.35	3.2	62	0.03	0
66	60.95	61.52	0.57	4.1	62	0.00	0
67	61.52	62.73	1.21	5.2	1850	0.02	0
68	62.73	62.85	0.12	2.2	125	0.01	0
69	62.85	63.27	0.42	4.1	62	0.01	0
70	63.27	63.55	0.28	4.2	62	0.01	0
71	63.55	64.70	1.15	5.2	2250	0.02	0
72	64.70	65.35	0.65	3.2	62	0.02	0
73	65.35	66.47	1.12	1.1	4000	0.08	0
74	66.47	66.94	0.47	5.1	950	0.01	0
75	66.94	67.59	0.65	3.2	125	0.02	0
76	67.59	68.04	0.45	2.2	1000	0.00	0
77	68.04	68.30	0.26	4.1	62	0.00	0
78	68.30	68.65	0.35	2.2	750	0.00	0
79	68.65	68.92	0.27	4.2	62	0.00	0
80	68.92	69.12	0.2	4.2	50	0.00	0
81	69.12	71.17	2.05	6.2	4000	0.00	1
82	71.17	74.32	3.15	6.1	3000	0.09	0
83	74.32	74.90	0.58	3.2	62	0.03	0
84	74.90	76.35	1.45	6.1	4000	0.02	0
85	76.35	77.25	0.9	3.2	62	0.01	0
86	77.25	77.41	0.16	2.1	1000	0.01	0
87	77.41	77.61	0.2	3.2	62	0.01	0
88	77.61	77.83	0.22	4.2	62	0.01	0
89	77.83	77.93	0.1	3.2	62	0.01	0
90	77.93	78.23	0.3	3.2	62	0.02	0
91	78.23	78.90	0.67	4.1	100	0.00	0
92	78.90	79.05	0.15	2.2	500	0.00	0
93	79.05	80.45	1.4	4.1	125	0.00	0
94	80.45	81.22	0.77	3.2	62	0.02	0
95	81.22	82.62	1.4	6.1	3000	0.00	0
96	82.62	82.80	0.18	4.2	62	0.00	0
97	82.80	83.60	0.8	3.2	62	0.02	0
98	83.60	84.60	1	3.2	125	0.01	0

99	84.60	85.50	0.9	3.2	62	0.02	0
100	85.50	86.04	0.54	5.2	2000	0.00	0
101	86.04	86.84	0.8	0.0	0	0.00	0
102	86.84	87.40	0.56	2.1	250	0.00	0
103	87.40	88.70	1.3	0.0	0	0.00	0
104	88.70	89.34	0.64	6.1	1500	0.01	0
105	89.34	89.49	0.15	3.2	62	0.01	0
106	89.49	89.80	0.31	4.1	62	0.01	0
107	89.80	90.15	0.35	3.2	62	0.01	0
108	90.15	90.59	0.44	4.1	100	0.00	0
109	90.59	91.01	0.42	4.1	100	0.01	0
110	91.01	91.12	0.11	3.2	62	0.02	0
111	91.12	94.69	3.57	6.1	30000	0.08	0
112	94.69	95.17	0.48	5.1	350	0.00	1
113	95.17	95.51	0.34	5.1	250	0.00	1
114	95.51	95.79	0.28	5.1	175	0.02	0
115	95.79	96.23	0.44	3.2	62	0.03	0
116	96.23	96.79	0.56	4.1	125	0.01	0
117	96.79	97.43	0.64	4.1	100	0.03	0
118	97.43	97.97	0.54	3.2	62	0.02	0
119	97.97	98.62	0.65	6.1	650	0.01	0
120	98.62	99.52	0.9	0.0	0	0.00	0
121	99.52	100.37	0.85	4.1	100	0.01	0
122	100.37	100.91	0.54	2.2	450	0.00	0
123	100.91	101.59	0.68	5.2	2000	0.00	0
124	101.59	110.59	9	0.0	0	0.00	0
125	110.59	110.79	0.2	4.2	62	0.01	0
126	110.79	110.93	0.14	4.2	62	0.00	0
127	110.93	111.48	0.55	6.1	2000	0.00	1
128	111.48	112.12	0.64	6.1	2100	0.03	0
129	112.12	112.32	0.2	4.2	62	0.01	0
130	112.32	114.36	2.04	6.1	25000	0.02	0
131	114.36	114.50	0.14	3.2	62	0.02	0
132	114.50	115.17	0.67	2.2	300	0.00	1
133	115.17	116.55	1.38	1.1	17000	0.00	0
134	116.55	118.15	1.6	4.1	150	0.00	0
135	118.15	118.47	0.32	2.1	125	0.00	0
136	118.47	118.87	0.4	3.2	62	0.02	0
137	118.87	119.02	0.15	4.2	62	0.00	0
138	119.02	119.17	0.15	3.2	62	0.01	0
139	119.17	119.42	0.25	4.2	62	0.02	0
140	119.42	120.12	0.7	3.2	100	0.02	0
141	120.12	120.47	0.35	6.1	550	0.06	0
142	120.47	121.32	0.85	2.2	500	0.00	0
143	121.32	121.52	0.2	4.2	62	0.05	0
144	121.52	122.50	0.98	2.2	1750	0.00	0
145	122.50	122.80	0.3	4.2	62	0.01	0
146	122.80	123.20	0.4	4.1	62	0.02	0
147	123.20	123.40	0.2	4.2	62	0.02	0
148	123.40	123.80	0.4	4.1	62	0.01	0

149	123.80	124.28	0.48	2.2	500	0.00	0
150	124.28	125.58	1.3	0.0	0	0.00	0
151	125.58	125.78	0.2	2.1	400	0.00	0
152	125.78	126.08	0.3	4.2	62	0.00	0
153	126.08	126.18	0.1	2.1	250	0.00	1
154	126.18	126.30	0.12	2.1	350	0.00	0
155	126.30	126.53	0.23	4.2	62	0.00	0
156	126.53	127.48	0.95	2.2	1750	0.00	0
157	127.48	129.48	2	0.0	0	0.00	0
158	129.48	130.68	1.2	3.2	100	0.04	0
159	130.68	131.33	0.65	4.1	100	0.00	0
160	131.33	131.93	0.6	4.1	62	0.00	0
161	131.93	132.63	0.7	4.1	62	0.00	0
162	132.63	133.23	0.6	3.2	62	0.04	0
163	133.23	133.45	0.22	2.2	400	0.00	1
164	133.45	135.80	2.35	6.2	4000	0.00	0

6-Monte Fronte

bed nr.	base	top	thickness	Bed type	max. grain size	mudcap	amalgamation
1	0.00	0.28	0.28	1.2	18000	0.00	1
2	0.28	0.68	0.4	1.2	7500	0.00	1
3	0.68	1.25	0.57	1.3	3000	0.00	1
4	1.25	1.73	0.48	1.3	2000	0.00	1
5	1.73	2.27	0.54	1.1	2000	0.00	1
6	2.27	2.95	0.68	5.1	4000	0.00	1
7	2.95	3.75	0.8	5.2	12500	0.00	1
8	3.75	4.55	0.8	2.1	1000	0.00	0
9	4.55	4.95	0.4	0.0	0	0.00	0
10	4.95	5.67	0.72	5.2	2000	0.05	1
11	5.67	5.72	0.05	7.2	62	0.00	0
12	5.72	5.92	0.2	1.2	2500	0.00	1
13	5.92	6.59	0.67	5.1	750	0.00	1
14	6.59	7.33	0.74	5.2	7500	0.00	1
15	7.33	8.53	1.2	5.2	4000	0.08	0
16	8.53	8.61	0.08	7.1	4	0.00	0
17	8.61	9.26	0.65	1.1	12500	0.00	1
18	9.26	9.71	0.45	1.2	20000	0.00	1
19	9.71	10.16	0.45	4.1	100	0.00	0
20	10.16	10.41	0.25	2.0	62	0.00	0
21	10.41	11.57	1.16	5.2	3000	0.00	1
22	11.57	12.05	0.48	1.1	3500	0.00	1
23	12.05	12.70	0.65	1.1	4000	0.00	1
24	12.70	13.40	0.7	1.3	6500	0.00	1
25	13.40	13.76	0.36	1.2	3500	0.00	1
26	13.76	14.74	0.98	1.1	5000	0.00	1
27	14.74	15.84	1.1	1.3	10000	0.00	1
28	15.84	16.66	0.82	1.1	2500	0.00	0
29	16.66	17.16	0.5	0.0	0	0.00	0
30	17.16	17.88	0.72	5.2	3500	0.00	1
31	17.88	18.84	0.96	5.1	14000	0.00	1
32	18.84	19.50	0.66	5.2	30000	0.00	1
33	19.50	19.75	0.25	0.0	0	0.00	0
34	19.75	21.59	1.84	5.2	3750	0.02	0
35	21.59	21.61	0.02	7.1	4	0.00	0
36	21.61	22.54	0.93	5.2	6500	0.00	1
37	22.54	22.97	0.43	1.1	4000	0.00	1
38	22.97	23.79	0.82	1.1	3500	0.00	1
39	23.79	24.35	0.56	1.1	3750	0.00	1
40	24.35	25.75	1.4	1.3	3750	0.00	0
41	25.75	25.95	0.2	0.0	0	0.00	0
42	25.95	26.63	0.68	2.2	1200	0.12	0
43	26.63	26.75	0.12	7.1	4	0.00	0
44	26.75	27.38	0.63	2.1	1000	0.05	0
45	27.38	27.43	0.05	7.1	4	0.00	0
46	27.43	28.55	1.12	1.1	15000	0.00	1
47	28.55	28.95	0.4	1.2	3750	0.00	0
48	28.95	29.50	0.55	0.0	0	0.00	0

49	29.50	30.42	0.92	5.2	12500	0.00	0
50	30.42	31.02	0.6	0.0	0	0.00	0
51	31.02	31.40	0.38	2.1	300	0.05	0
52	31.40	31.45	0.05	7.1	4	0.00	0
53	31.45	31.68	0.23	2.1	250	0.03	0
54	31.68	31.71	0.03	7.1	4	0.00	0
55	31.71	32.04	0.33	5.1	250	0.01	0
56	32.04	32.05	0.01	7.1	4	0.00	0
57	32.05	33.01	0.96	1.1	15000	0.00	1
58	33.01	33.41	0.4	2.1	750	0.00	1
59	33.41	34.16	0.75	1.1	2000	0.00	1
60	34.16	35.88	1.72	1.1	18000	0.00	1
61	35.88	36.32	0.44	1.1	2250	0.00	0
62	36.32	36.92	0.6	0.0	0	0.00	0
63	36.92	37.58	0.66	5.1	1500	0.00	1
64	37.58	38.29	0.71	5.2	3250	0.00	0
65	38.29	38.34	0.05	7.1	4	0.00	0
66	38.34	39.86	1.52	5.2	7500	0.60	0
67	39.86	40.46	0.6	7.2	100	0.00	0
68	40.46	40.98	0.52	4.1	62	0.00	0
69	40.98	42.26	1.28	5.2	2500	0.18	0
70	42.26	42.44	0.18	7.1	4	0.00	0
71	42.44	43.34	0.9	2.1	1500	0.14	0
72	43.34	43.48	0.14	7.1	4	0.00	0
73	43.48	44.26	0.78	5.2	1250	0.00	1
74	44.26	46.32	2.06	1.1	5000	0.06	0
75	46.32	46.38	0.06	7.1	4	0.00	0
76	46.38	46.54	0.16	2.1	300	0.02	0
77	46.54	46.56	0.02	7.1	4	0.00	0
78	46.56	46.88	0.32	2.1	1000	0.06	0
79	46.88	46.94	0.06	7.1	4	0.00	0
80	46.94	47.98	1.04	1.3	25000	0.01	0
81	47.98	47.99	0.01	7.1	4	0.00	0
82	47.99	49.90	1.91	5.2	35000	0.02	0
83	49.90	49.92	0.02	7.1	4	0.00	0
84	49.92	50.16	0.24	2.1	500	0.00	1
85	50.16	51.27	1.11	5.1	4000	0.09	0
86	51.27	51.36	0.09	7.1	4	0.00	0
87	51.36	53.13	1.77	6.1	15000	0.00	1
88	53.13	53.45	0.32	2.1	1500	0.00	1
89	53.45	53.87	0.42	1.1	2500	0.00	1
90	53.87	54.09	0.22	2.1	750	0.00	0
91	54.09	54.39	0.3	0.0	0	0.00	0
92	54.39	54.51	0.12	2.1	250	0.10	0
93	54.51	54.61	0.1	7.1	4	0.00	0
94	54.61	57.41	2.8	5.2	35000	0.10	0
95	57.41	57.51	0.1	7.1	4	0.00	0
96	57.51	57.77	0.26	2.1	550	0.00	0
97	57.77	58.17	0.4	0.0	0	0.00	0
98	58.17	58.74	0.57	5.2	2250	0.20	0

99	58.74	58.94	0.2	7.1	4	0.00	0
100	58.94	59.36	0.42	2.1	800	0.20	0
101	59.36	59.56	0.2	7.2	62	0.00	0
102	59.56	59.76	0.2	2.1	500	0.20	0
103	59.76	59.96	0.2	7.2	62	0.00	0
104	59.96	60.84	0.88	6.3	17500	0.08	0
105	60.84	60.92	0.08	7.1	4	0.00	0
106	60.92	61.12	0.2	4.2	62	0.00	0
107	61.12	62.75	1.63	6.3	10000	0.05	0
108	62.75	62.80	0.05	7.1	4	0.00	0
109	62.80	63.52	0.72	6.3	25000	0.00	1
110	63.52	63.68	0.16	5.2	2500	0.01	0
111	63.68	63.69	0.01	7.1	4	0.00	0
112	63.69	63.90	0.21	2.2	350	0.03	0
113	63.90	63.93	0.03	7.1	4	0.00	0
114	63.93	64.80	0.87	6.1	1000	0.00	1
115	64.80	65.45	0.65	6.1	1250	0.00	1
116	65.45	65.82	0.37	6.1	2750	0.00	0
117	65.82	66.17	0.35	4.1	62	0.05	0
118	66.17	68.24	2.07	5.2	25000	0.00	1
119	68.24	69.32	1.08	6.1	1500	0.05	0
120	69.32	69.37	0.05	7.1	4	0.00	0
121	69.37	71.59	2.22	6.1	20000	0.00	1
122	71.59	72.81	1.22	5.2	3500	0.00	1
123	72.81	75.08	2.27	6.2	20000	0.00	1
124	75.08	77.21	2.13	1.1	15000	0.00	1
125	77.21	77.68	0.47	2.1	1950	0.15	0
126	77.68	77.83	0.15	7.1	4	0.00	0
127	77.83	80.32	2.49	5.2	30000	0.09	0
128	80.32	80.41	0.09	7.1	4	0.00	0
129	80.41	81.48	1.07	6.1	3750	0.15	0
130	81.48	81.63	0.15	7.1	4	0.00	0
131	81.63	83.11	1.48	6.2	20000	0.00	1
132	83.11	85.45	2.34	5.2	25000	0.00	1
133	85.45	86.50	1.05	1.3	5000	0.05	0
134	86.50	86.55	0.05	7.1	4	0.00	0
135	86.55	87.76	1.21	6.1	1750	0.01	0
136	87.76	87.77	0.01	7.1	4	0.00	0
137	87.77	88.85	1.08	6.1	10000	0.00	1
138	88.85	89.33	0.48	2.2	175	0.00	1
139	89.33	89.53	0.2	2.2	300	0.25	0
140	89.53	89.78	0.25	7.2	62	0.00	0
141	89.78	90.61	0.83	6.1	4000	0.00	1
142	90.61	92.19	1.58	5.2	25000	0.00	1
143	92.19	93.17	0.98	5.1	3000	0.00	1
144	93.17	94.79	1.62	5.2	10000	0.00	1
145	94.79	95.21	0.42	2.2	650	0.00	0
146	95.21	95.61	0.4	0.0	0	0.00	0
147	95.61	95.93	0.32	2.1	300	0.00	1
148	95.93	96.37	0.44	2.2	250	0.00	1

149	96.37	96.97	0.6	5.1	2750	0.00	1
150	96.97	97.89	0.92	5.2	3750	0.00	0
151	97.89	98.95	1.06	4.1	100	0.01	0
152	98.95	99.72	0.77	5.2	650	0.00	1
153	99.72	101.27	1.55	5.2	4000	0.15	0
154	101.27	101.42	0.15	7.2	62	0.00	0
155	101.42	104.49	3.07	6.1	30000	0.07	0
156	104.49	104.56	0.07	7.1	4	0.00	0
157	104.56	105.97	1.41	5.2	10000	0.03	0
158	105.97	107.52	1.55	5.2	10000	0.00	1
159	107.52	108.47	0.95	5.1	2000	0.00	1
160	108.47	109.17	0.7	5.2	2000	0.00	0
161	109.17	110.42	1.25	0.0	0	0.00	0
162	110.42	111.87	1.45	1.3	3000	0.02	0
163	111.87	111.89	0.02	7.1	4	0.00	0
164	111.89	112.33	0.44	2.1	1500	0.03	0
165	112.33	112.36	0.03	7.1	4	0.00	0
166	112.36	113.06	0.7	3.2	100	0.04	0
167	113.06	113.35	0.29	2.2	550	0.05	0
168	113.35	113.40	0.05	7.1	4	0.00	0
169	113.40	113.97	0.57	3.2	62	0.05	0
170	113.97	115.45	1.48	6.1	4000	0.42	0
171	115.45	115.87	0.42	7.2	62	0.00	0
172	115.87	116.19	0.32	2.2	1900	0.02	0
173	116.19	116.21	0.02	7.1	4	0.00	0
174	116.21	116.64	0.43	2.2	300	0.07	0
175	116.64	116.71	0.07	7.1	4	0.00	0
176	116.71	118.76	2.05	6.1	3500	0.02	0
177	118.76	118.78	0.02	7.1	4	0.00	0
178	118.78	118.88	0.1	3.2	62	0.01	0
179	118.88	120.12	1.24	5.2	15000	0.02	0
180	120.12	120.14	0.02	7.1	4	0.00	0
181	120.14	121.10	0.96	1.1	2500	0.00	1
182	121.10	121.48	0.38	5.2	850	0.02	0
183	121.48	121.50	0.02	7.1	4	0.00	0
184	121.50	121.58	0.08	3.2	62	0.01	0
185	121.58	124.01	2.43	1.1	3000	0.12	0
186	124.01	124.13	0.12	7.1	4	0.00	0
187	124.13	124.88	0.75	1.1	2000	0.17	0
188	124.88	125.05	0.17	7.1	4	0.00	0
189	125.05	125.26	0.21	4.2	62	0.00	0
190	125.26	125.46	0.2	4.2	62	0.00	0
191	125.46	125.66	0.2	4.2	62	0.03	0
192	125.66	128.00	2.34	6.1	3500	0.00	1
193	128.00	128.81	0.81	5.2	400	0.02	0
194	128.81	128.83	0.02	7.1	4	0.00	0
195	128.83	130.61	1.78	2.1	1250	0.17	0
196	130.61	130.78	0.17	7.1	4	0.00	0
197	130.78	131.13	0.35	5.1	750	0.02	0
198	131.13	131.15	0.02	7.1	4	0.00	0

199	131.15	131.61	0.46	3.2	62	0.04	0
200	131.61	132.95	1.34	6.1	2250	0.00	1
201	132.95	134.21	1.26	6.1	2100	0.07	0
202	134.21	134.28	0.07	7.1	4	0.00	0
203	134.28	136.00	1.72	6.1	3500	0.04	0
204	136.00	136.04	0.04	7.1	4	0.00	0
205	136.04	136.21	0.17	4.2	62	0.06	0
206	136.21	137.03	0.82	6.1	1750	0.09	0
207	137.03	137.12	0.09	7.2	62	0.00	0
208	137.12	137.79	0.67	4.1	100	0.00	0
209	137.79	141.57	3.78	6.1	7500	0.05	0
210	141.57	141.62	0.05	7.1	4	0.00	0
211	141.62	141.92	0.3	4.2	62	0.08	0
212	141.92	142.17	0.25	3.2	62	0.03	0
213	142.17	142.65	0.48	5.2	350	0.01	0
214	142.65	142.66	0.01	7.1	4	0.00	0
215	142.66	142.72	0.06	3.1	62	0.01	0
216	142.72	142.95	0.23	4.2	62	0.01	0
217	142.95	143.15	0.2	4.2	62	0.01	0
218	143.15	143.25	0.1	4.2	62	0.02	0
219	143.25	144.07	0.82	6.1	2250	0.00	1
220	144.07	144.93	0.86	6.3	3500	0.00	1
221	144.93	146.24	1.31	6.2	15000	0.12	0
222	146.24	146.36	0.12	7.1	4	0.00	0
223	146.36	146.67	0.31	4.2	100	0.00	0
224	146.67	146.87	0.2	4.2	62	0.00	0
225	146.87	147.07	0.2	4.2	62	0.00	0
226	147.07	147.17	0.1	4.2	62	0.03	0
227	147.17	149.33	2.16	6.1	20000	0.02	0
228	149.33	149.35	0.02	7.1	4	0.00	0
229	149.35	149.75	0.4	2.2	450	0.00	0
230	149.75	149.93	0.18	4.2	62	0.05	0
231	149.93	151.21	1.28	6.1	12500	0.20	0
232	151.21	151.41	0.2	7.2	62	0.00	0
233	151.41	152.42	1.01	5.1	5000	0.15	0
234	152.42	152.57	0.15	7.2	4	0.00	0
235	152.57	153.33	0.76	6.1	2000	0.00	1
236	153.33	154.80	1.47	6.2	2500	0.00	1
237	154.80	155.78	0.98	6.1	1750	0.16	0
238	155.78	155.94	0.16	7.2	4	0.00	0
239	155.94	156.31	0.37	3.2	62	0.02	0
240	156.31	158.22	1.91	6.1	2500	0.00	1
241	158.22	160.46	2.24	6.1	15000	0.08	0
242	160.46	160.54	0.08	7.1	4	0.00	0
243	160.54	161.05	0.51	5.1	1750	0.04	0
244	161.05	161.09	0.04	7.1	4	0.00	0
245	161.09	161.77	0.68	2.1	1000	0.03	0
246	161.77	161.80	0.03	7.1	4	0.00	0
247	161.80	162.04	0.24	3.2	62	0.02	0
248	162.04	162.85	0.81	6.3	2500	0.00	1

249	162.85	166.24	3.39	6.3	25000	0.03	1
250	166.24	166.27	0.03	7.1	4	0.00	0
251	166.27	167.49	1.22	5.2	3250	0.12	0
252	167.49	167.61	0.12	7.1	4	0.00	0
253	167.61	168.29	0.68	6.1	1000	0.00	1
254	168.29	170.70	2.41	5.2	20000	0.05	0
255	170.70	170.75	0.05	7.1	4	0.00	0
256	170.75	171.13	0.38	4.1	62	0.00	0
257	171.13	171.67	0.54	5.2	2500	0.00	0
258	171.67	173.35	1.68	4.1	200	0.08	0
259	173.35	173.62	0.27	5.1	3750	0.00	1
260	173.62	176.81	3.19	6.1	4000	0.15	0
261	176.81	176.96	0.15	7.1	4	0.00	0
262	176.96	178.16	1.2	4.1	200	0.00	0
263	178.16	179.26	1.1	4.1	125	0.00	0
264	179.26	180.26	1	4.1	125	0.00	0
265	180.26	181.31	1.05	5.2	15000	0.00	0
266	181.31	183.96	2.65	4.1	200	0.02	0
267	183.96	184.21	0.25	3.2	62	0.03	0
268	184.21	187.65	3.44	6.3	25000	0.18	0
269	187.65	187.83	0.18	7.1	4	0.00	0
270	187.83	188.44	0.61	4.1	62	0.00	0

7-Cima di Farenga

bed nr.	base	top	thickness	Bed type	max. grain size	mudcap	amalgamation
1	0.00	0.96	0.96	2.2	450	0.00	1
2	0.96	1.58	0.62	2.2	300	0.00	1
3	1.58	1.93	0.35	0.0	0	0.00	0
4	1.93	2.21	0.28	2.2	450	0.00	0
5	2.21	2.33	0.12	2.1	550	0.00	1
6	2.33	3.05	0.72	5.1	1100	0.00	1
7	3.05	3.27	0.22	2.2	650	0.00	1
8	3.27	4.34	1.07	5.1	1000	0.10	0
9	4.34	6.50	2.16	1.3	2750	0.05	0
10	6.50	8.10	1.6	1.3	2500	0.00	0
11	8.10	8.50	0.4	0.0	0	0.00	0
12	8.50	9.32	0.82	2.2	1950	0.00	1
13	9.32	11.77	2.45	1.3	3500	0.07	0
14	11.77	12.84	1.07	2.2	1250	0.00	1
15	12.84	14.21	1.37	2.2	1950	0.00	0
16	14.21	14.66	0.45	0.0	0	0.00	0
17	14.66	15.21	0.55	4.1	100	0.00	0
18	15.21	16.18	0.97	5.2	1000	0.00	0
19	16.18	16.98	0.8	0.0	0	0.00	0
20	16.98	18.20	1.22	6.1	2750	0.00	1
21	18.20	21.45	3.25	6.1	4250	0.00	0
22	21.45	22.45	1	0.0	0	0.00	0
23	22.45	25.18	2.73	6.3	3000	0.00	0
24	25.18	25.78	0.6	0.0	0	0.00	0
25	25.78	26.94	1.16	2.2	800	0.00	0
26	26.94	27.24	0.3	0.0	0	0.00	0
27	27.24	27.69	0.45	5.2	650	0.00	1
28	27.69	28.01	0.32	2.2	350	0.00	1
29	28.01	29.43	1.42	5.2	3000	0.00	1
30	29.43	30.30	0.87	2.1	1750	0.00	1
31	30.30	32.08	1.78	1.1	2100	0.00	0
32	32.08	32.35	0.27	4.2	62	0.00	0
33	32.35	34.32	1.97	1.3	6500	0.00	1
34	34.32	35.40	1.08	2.1	1000	0.00	0
35	35.40	35.72	0.32	4.2	62	0.02	0
36	35.72	36.24	0.52	6.3	750	0.00	0
37	36.24	37.19	0.95	4.1	126	0.01	0
38	37.19	37.43	0.24	2.1	850	0.00	1
39	37.43	38.31	0.88	2.2	1800	0.00	1
40	38.31	38.94	0.63	2.2	700	0.00	1
41	38.94	41.56	2.62	6.1	5000	0.00	0
42	41.56	41.96	0.4	0.0	0	0.00	0
43	41.96	42.60	0.64	5.2	800	0.00	1
44	42.60	42.77	0.17	4.2	62	0.00	0
45	42.77	42.92	0.15	1.2	2500	0.00	0
46	42.92	43.37	0.45	4.1	62	0.00	0
47	43.37	44.09	0.72	6.2	1500	0.00	0
48	44.09	47.69	3.6	0.0	0	0.00	0

49	47.69	48.31	0.62	2.2	950	0.00	1
50	48.31	48.97	0.66	2.2	1100	0.00	1
51	48.97	50.00	1.03	2.2	1500	0.00	1
52	50.00	50.74	0.74	2.2	600	0.00	0
53	50.74	51.02	0.28	4.2	62	0.00	0
54	51.02	52.19	1.17	6.1	4000	0.00	0
55	52.19	52.39	0.2	4.2	62	0.00	0
56	52.39	52.83	0.44	5.1	700	0.00	0
57	52.83	53.03	0.2	4.2	62	0.00	0
58	53.03	53.43	0.4	0.0	0	0.00	0
59	53.43	54.61	1.18	6.3	1100	0.00	1
60	54.61	56.83	2.22	6.1	1800	0.00	1
61	56.83	57.67	0.84	2.1	950	0.00	0
62	57.67	57.97	0.3	4.2	62	0.00	0

8-Margheri Binda

bed nr.	base	top	thickness	Bed type	max. grain size	mudcap	amalgamation
1	0.00	0.30	0.3	2.2	900	0.00	1
2	0.30	0.75	0.45	2.2	650	0.00	1
3	0.75	2.68	1.93	1.3	15000	0.00	1
4	2.68	4.03	1.35	6.2	5000	0.04	0
5	4.03	5.67	1.64	6.2	3750	0.00	0
6	5.67	5.78	0.11	4.2	62	0.00	0
7	5.78	5.88	0.1	4.2	125	0.00	0
8	5.88	6.42	0.54	4.1	100	0.00	0
9	6.42	7.09	0.67	3.2	62	0.03	0
10	7.09	7.56	0.47	6.3	4000	0.00	1
11	7.56	8.45	0.89	1.1	2100	0.00	1
12	8.45	9.29	0.84	2.2	750	0.00	0
13	9.29	9.60	0.31	4.1	62	0.00	0
14	9.60	10.04	0.44	5.2	1100	0.00	1
15	10.04	12.91	2.87	5.1	3750	0.12	0
16	12.91	15.57	2.66	6.1	15000	0.00	1
17	15.57	16.17	0.6	6.2	900	0.03	0
18	16.17	16.56	0.39	3.2	62	0.02	0
19	16.56	18.24	1.68	4.1	100	0.00	0
20	18.24	19.33	1.09	6.1	1000	0.00	1
21	19.33	19.88	0.55	5.2	500	0.00	1
22	19.88	20.75	0.87	2.2	500	0.04	0
23	20.75	21.22	0.47	6.2	750	0.00	1
24	21.22	22.09	0.87	6.2	1000	0.00	1
25	22.09	22.62	0.53	5.2	700	0.00	1
26	22.62	24.27	1.65	5.1	7500	0.00	1
27	24.27	26.53	2.26	6.2	3000	0.00	1
28	26.53	27.63	1.1	5.2	2100	0.00	1
29	27.63	28.49	0.86	5.2	2000	0.00	1
30	28.49	29.43	0.94	5.2	4000	0.18	0
31	29.43	30.27	0.84	6.2	1000	0.00	0
32	30.27	30.51	0.24	4.2	62	0.00	0
33	30.51	30.64	0.13	0.0	0	0.00	0
34	30.64	31.22	0.58	2.1	500	0.00	1
35	31.22	32.64	1.42	2.1	950	0.00	0
36	32.64	32.79	0.15	0.0	0	0.00	0
37	32.79	33.43	0.64	2.2	1000	0.00	1
38	33.43	33.75	0.32	2.1	750	0.00	1
39	33.75	34.77	1.02	5.1	1750	0.00	0
40	34.77	35.92	1.15	0.0	0	0.00	0
41	35.92	36.90	0.98	2.1	750	0.00	0
42	36.90	37.05	0.15	0.0	0	0.00	0
43	37.05	37.86	0.81	2.1	600	0.00	1
44	37.86	39.10	1.24	5.2	2000	0.00	1
45	39.10	39.99	0.89	2.2	1000	0.00	1
46	39.99	41.84	1.85	5.2	1150	0.00	1
47	41.84	42.84	1	2.2	1250	0.00	1
48	42.84	43.76	0.92	5.1	1750	0.00	1

49	43.76	45.63	1.87	1.3	3000	0.04	0
50	45.63	46.41	0.78	2.2	500	0.00	0
51	46.41	48.91	2.5	0.0	0	0.00	0
52	48.91	49.75	0.84	4.1	62	0.00	0
53	49.75	50.67	0.92	5.2	1000	1.00	1
54	50.67	51.56	0.89	5.2	3000	0.00	0
55	51.56	55.06	3.5	0.0	0	0.00	0
56	55.06	56.40	1.34	2.2	1750	0.00	0
57	56.40	56.70	0.3	0.0	0	0.00	0
58	56.70	57.32	0.62	5.1	600	0.00	0
59	57.32	58.52	1.2	0.0	0	0.00	0
60	58.52	61.25	2.73	6.1	4000	0.00	0
61	61.25	61.55	0.3	0.0	0	0.00	0
62	61.55	61.83	0.28	2.1	350	0.07	0
63	61.83	62.19	0.36	5.1	500	0.00	1
64	62.19	63.16	0.97	1.1	2100	0.00	0
65	63.16	64.36	1.2	0.0	0	0.00	0
66	64.36	64.60	0.24	2.2	300	0.00	1
67	64.60	64.80	0.2	2.2	250	0.00	1
68	64.80	65.52	0.72	2.1	550	0.00	0
69	65.52	65.92	0.4	0.0	0	0.00	0
70	65.92	67.92	2	1.3	4000	0.00	0
71	67.92	69.90	1.98	1.1	2000	0.02	0
72	69.90	70.75	0.85	3.2	62	0.04	0
73	70.75	72.89	2.14	1.3	7500	0.12	0
74	72.89	74.23	1.34	1.1	10000	0.05	0
75	74.23	74.41	0.18	4.2	62	0.00	0
76	74.41	74.47	0.06	4.2	62	0.00	0
77	74.47	74.70	0.23	4.2	62	0.00	0
78	74.70	75.80	1.1	0.0	0	0.00	0
79	75.80	75.97	0.17	2.1	250	0.00	1
80	75.97	76.12	0.15	2.1	200	0.00	1
81	76.12	76.17	0.05	2.1	150	0.00	1
82	76.17	77.21	1.04	5.1	950	0.00	0

9-Cima Bertrand

bed nr.	base	top	thickness	Bed type	max. grain size	mudcap	amalgamation
1	0.00	1.74	1.74	6.1	3500	0.00	1
2	1.74	3.18	1.44	2.1	1900	0.00	1
3	3.18	3.39	0.21	2.1	500	0.00	1
4	3.39	4.95	1.56	2.1	1750	0.00	1
5	4.95	9.36	4.41	6.1	5000	0.00	1
6	9.36	10.17	0.81	5.2	1000	0.00	1
7	10.17	13.05	2.88	6.2	10000	0.00	1
8	13.05	14.92	1.87	2.2	1000	0.00	0
9	14.92	14.99	0.07	4.2	62	0.01	0
10	14.99	16.37	1.38	6.2	3000	0.00	1
11	16.37	17.74	1.37	1.1	2500	0.15	0
12	17.74	18.30	0.56	1.1	2500	0.00	0
13	18.30	18.41	0.11	4.2	62	0.00	0
14	18.41	22.33	3.92	6.1	35000	0.04	0
15	22.33	22.73	0.4	3.2	125	0.02	0
16	22.73	23.87	1.14	5.2	2100	0.00	1
17	23.87	27.06	3.19	6.2	20000	0.00	1
18	27.06	28.47	1.41	6.3	2500	0.00	1
19	28.47	29.58	1.11	5.2	12000	0.00	1
20	29.58	32.01	2.43	6.2	2500	0.04	0
21	32.01	32.41	0.4	3.2	62	0.01	0
22	32.41	35.31	2.9	6.1	5000	0.00	0
23	35.31	37.61	2.3	4.1	250	0.00	0
24	37.61	38.59	0.98	6.3	2000	0.00	1
25	38.59	40.47	1.88	6.2	2250	0.00	1
26	40.47	41.54	1.07	6.2	3000	0.00	1
27	41.54	45.16	3.62	6.1	40000	0.04	0
28	45.16	47.36	2.2	3.2	62	0.02	0
29	47.36	50.14	2.78	5.3	6500	0.00	1
30	50.14	50.58	0.44	1.1	5000	0.00	1
31	50.58	51.63	1.05	1.1	3000	0.00	1
32	51.63	52.69	1.06	5.2	2200	0.00	1
33	52.69	53.96	1.27	6.1	3000	0.00	0
34	53.96	54.81	0.85	4.1	125	0.03	0
35	54.81	56.53	1.72	6.3	3500	0.00	0
36	56.53	57.08	0.55	4.1	62	0.00	0
37	57.08	57.67	0.59	4.1	62	0.00	0
38	57.67	58.22	0.55	5.2	850	0.00	0
39	58.22	58.62	0.4	0.0	0	0.00	0
40	58.62	60.24	1.62	5.2	1750	0.00	1
41	60.24	61.21	0.97	6.2	2500	0.00	1
42	61.21	62.31	1.1	2.2	1250	0.04	0
43	62.31	62.47	0.16	4.2	62	0.02	0
44	62.47	64.05	1.58	6.2	2250	0.00	1
45	64.05	65.15	1.1	1.1	15000	0.07	0
46	65.15	66.33	1.18	6.2	2500	0.00	1
47	66.33	66.99	0.66	4.1	175	0.00	0
48	66.99	68.31	1.32	4.1	62	0.00	0

49	68.31	69.27	0.96	6.1	1500	0.00	1
50	69.27	70.30	1.03	5.3	1900	0.00	0
51	70.30	71.13	0.83	3.2	125	0.01	0
52	71.13	72.68	1.55	6.2	2250	0.00	1
53	72.68	73.10	0.42	2.2	700	0.00	1
54	73.10	73.89	0.79	6.3	1350	0.00	1
55	73.89	74.66	0.77	6.3	950	0.00	1
56	74.66	75.70	1.04	6.3	4000	0.00	1
57	75.70	76.62	0.92	6.2	1750	0.00	1
58	76.62	77.58	0.96	5.1	1750	0.00	1
59	77.58	78.58	1	6.2	1400	0.00	1
60	78.58	80.54	1.96	6.2	3500	0.00	1
61	80.54	80.78	0.24	4.2	62	0.01	0
62	80.78	81.51	0.73	1.1	2250	0.05	0
63	81.51	82.93	1.42	6.2	2100	0.00	0
64	82.93	84.65	1.72	4.1	200	0.00	0
65	84.65	85.51	0.86	3.2	62	0.01	0
66	85.51	86.94	1.43	6.3	2100	0.00	1
67	86.94	88.03	1.09	5.2	1000	0.00	1
68	88.03	89.31	1.28	6.2	3900	0.00	1
69	89.31	90.53	1.22	6.3	2100	0.00	1
70	90.53	90.93	0.4	3.2	125	0.01	0
71	90.93	91.75	0.82	6.3	1250	0.00	0
72	91.75	91.95	0.2	4.2	62	0.01	0
73	91.95	92.22	0.27	4.2	125	0.00	0
74	92.22	93.26	1.04	4.1	62	0.01	0
75	93.26	95.09	1.83	6.2	2500	0.00	1
76	95.09	96.05	0.96	5.2	1800	0.00	1
77	96.05	96.57	0.52	2.2	150	0.00	0
78	96.57	96.90	0.33	4.2	100	0.01	0
79	96.90	97.76	0.86	4.1	0	0.01	0
80	97.76	97.88	0.12	2.2	250	0.00	1
81	97.88	98.47	0.59	6.3	1250	0.00	1
82	98.47	99.21	0.74	6.3	2250	0.00	0
83	99.21	99.65	0.44	4.1	62	0.00	0
84	99.65	99.85	0.2	2.2	300	0.00	0
85	99.85	100.70	0.85	4.1	62	0.00	0
86	100.70	101.67	0.97	5.2	2250	0.00	0
87	101.67	101.97	0.3	4.2	62	0.00	0
88	101.97	102.32	0.35	4.1	100	0.00	0
89	102.32	102.39	0.07	2.1	125	0.00	0
90	102.39	102.81	0.42	4.1	62	0.00	0

10-Cima di Velega

bed nr.	base	top	thickness	Bed type	max. grain size	mudcap	amalgamation
1	0.00	1.83	1.83	1.3	2750	0.10	0
2	1.83	2.89	1.06	2.2	950	0.00	1
3	2.89	3.10	0.21	2.1	240	0.00	1
4	3.10	3.28	0.18	2.1	240	0.00	1
5	3.28	5.64	2.36	1.3	2750	0.05	0
6	5.64	5.84	0.2	0.0	0	0.00	0
7	5.84	5.92	0.08	4.2	65	0.00	0
8	5.92	6.98	1.06	2.1	1000	0.07	0
9	6.98	7.89	0.91	2.1	500	0.00	1
10	7.89	8.58	0.69	2.1	450	0.00	0
11	8.58	8.98	0.4	0.0	0	0.00	0
12	8.98	11.46	2.48	6.2	4000	0.00	1
13	11.46	12.13	0.67	5.2	650	0.00	1
14	12.13	14.45	2.32	6.1	2500	0.00	0
15	14.45	14.99	0.54	4.1	100	0.00	0
16	14.99	15.79	0.8	0.0	0	0.00	0
17	15.79	16.86	1.07	5.2	1400	0.00	1
18	16.86	18.60	1.74	1.1	2050	0.00	0
19	18.60	19.70	1.1	0.0	0	0.00	0
20	19.70	20.07	0.37	2.1	350	0.00	1
21	20.07	20.94	0.87	2.2	800	0.02	0
22	20.94	21.88	0.94	3.2	62	0.01	0
23	21.88	22.13	0.25	4.2	62	0.00	0
24	22.13	23.25	1.12	6.2	1250	0.00	1
25	23.25	23.73	0.48	5.1	500	0.00	0
26	23.73	24.08	0.35	0.0	0	0.00	0
27	24.08	25.51	1.43	5.1	1000	0.15	0
28	25.51	25.75	0.24	3.2	62	0.01	0
29	25.75	26.20	0.45	0.0	0	0.00	0
30	26.20	27.64	1.44	6.2	1500	0.00	1
31	27.64	28.89	1.25	6.1	1500	0.00	0
32	28.89	29.57	0.68	4.1	75	0.00	0
33	29.57	31.99	2.42	6.1	4500	0.07	0
34	31.99	32.17	0.18	3.2	62	0.01	0
35	32.17	32.27	0.1	4.2	62	0.00	0
36	32.27	32.65	0.38	4.1	62	0.00	0
37	32.65	32.80	0.15	3.2	62	0.03	0
38	32.80	33.96	1.16	5.1	500	0.00	0
39	33.96	34.39	0.43	4.1	100	0.01	0
40	34.39	34.73	0.34	3.2	62	0.02	0
41	34.73	36.08	1.35	6.2	1800	0.00	1
42	36.08	37.50	1.42	6.2	2000	0.00	1
43	37.50	39.04	1.54	6.1	1400	0.02	0
44	39.04	39.39	0.35	3.2	62	0.02	0
45	39.39	40.02	0.63	4.1	62	0.00	0
46	40.02	41.24	1.22	6.3	1900	0.00	0
47	41.24	41.78	0.54	4.1	62	0.00	1
48	41.78	43.60	1.82	2.1	1800	0.00	1

49	43.60	44.52	0.92	2.1	900	0.01	0
50	44.52	45.17	0.65	3.2	62	0.04	0
51	45.17	48.75	3.58	5.1	12500	0.00	1
52	48.75	49.41	0.66	2.1	400	0.00	1
53	49.41	55.26	5.85	5.1	3800	0.00	0

APPENDIX 2.1: Recalculated tables of unknown U-Pb detrital zircon ages of samples

19th March 2017, IGG-CNR U.O.S. of Pavia						Data for Wetherill plot[3]					Ages[3]							Concordant ages	
Identifier	Zrc#	Spot location	Zoning	$^{207}Pb/^{206}Pb$	1σ abs	$^{207}Pb/^{235}U$	1σ abs	$^{206}Pb/^{238}U$	1σ abs	Rho	$^{207}Pb/^{206}Pb$	1σ abs	$^{207}Pb/^{235}U$	1σ abs	$^{206}Pb/^{238}U$	1σ abs	% U-Pb disc[4]		2σ abs
Sample MFZ_1bis																			
Ma03a007	1.2	Core	dark - homog.	0.11876	0.00189	3.64443	0.07434	0.22226	0.00428	0.9	1938	31	1559	32	~~1294~~	~~25~~	17.0		
Ma03a008	1.2	Rim	oscillatory	0.06927	0.00122	0.90098	0.01956	0.09422	0.00184	0.9	907	16	652	14	~~580~~	~~11~~	11.0		
Ma03a009	1.3	Core	sect. - br	0.06091	0.00123	0.41374	0.00972	0.04914	0.00093	0.8	636	13	352	8	~~309~~	~~6~~	12.0		
Ma03a010	1.5	Core	oscillatory z.	0.05350	0.00103	0.38269	0.00895	0.05173	0.00102	0.8	350	7	329	8	325	6	1.2	326	12
Ma03a011	1.6	Core	oscillatory z.	0.05271	0.00137	0.35677	0.01004	0.04898	0.00092	0.7	316	8	310	9	308	6	0.5	308	11
Ma03a012	1.9	Core	oscillatory z.	0.05295	0.00117	0.35884	0.00924	0.04899	0.00099	0.8	327	7	311	8	308	6	1.0	309	12
Ma03a013	1.10	Core	oscillatory	0.05807	0.00144	0.66694	0.01869	0.08304	0.00170	0.7	532	13	519	15	514	11	0.9	516	20
Ma03a014	1.12	Core	bright hom.	0.05376	0.00112	0.46697	0.01121	0.06284	0.00119	0.8	361	7	389	9	393	7	-1.0	392	14
Ma03a015	1.14	Core	oscillatory z.	0.13586	0.00218	6.33496	0.12751	0.33740	0.00628	0.9	2175	35	2023	41	1874	35	7.4		
Ma03a016	1.15	Core	oscillatory z.	0.05319	0.00113	0.43007	0.01059	0.05846	0.00113	0.8	337	7	363	9	366	7	-0.8	365	13
Ma03a017	1.17	Core	oscillatory z.	0.05673	0.00107	0.61423	0.01400	0.07829	0.00151	0.8	481	9	486	11	486	9	0.1	486	17
Ma03a018	1.18	Core	bright hom.	0.05442	0.00111	0.47492	0.01140	0.06311	0.00121	0.8	388	8	395	9	395	8	0.0	395	14
Ma03a019	2.18	Core top	bright hom.	0.06343	0.00129	1.01178	0.02389	0.11544	0.00217	0.8	723	15	710	17	704	13	0.8	708	23
Ma03a020	2.18	Core low	bright hom.	0.06343	0.00135	1.03115	0.02511	0.11766	0.00223	0.8	723	15	720	18	717	14	0.3	718	24
Ma03a021	2.17	Rim	oscillatory	0.05210	0.00092	0.39826	0.00864	0.05531	0.00104	0.9	290	5	340	7	347	7	-2.0		
Ma03a022	2.16	Core	bright hom.	0.06299	0.00237	0.45070	0.01763	0.05181	0.00105	0.5	708	27	378	15	~~326~~	~~7~~	13.8		
Ma03a023	2.15	Rim	oscillatory	0.05950	0.00110	0.76266	0.01697	0.09285	0.00175	0.8	585	11	576	13	572	11	0.6	574	19
Ma03a024	2.14	Core	bright hom.	0.07335	0.00121	0.34523	0.00707	0.03410	0.00063	0.9	1024	17	301	6	~~216~~	~~4~~	28.2		
Ma03a025	2.13	Core	bright hom.	0.06062	0.00116	0.85868	0.01938	0.10264	0.00190	0.8	626	12	629	14	630	12	-0.1	630	21
Ma03a026	2.12	Rim	oscillatory	0.05888	0.00105	0.73345	0.01580	0.09028	0.00166	0.9	563	10	559	12	557	10	0.2	558	18
Ma03a027	2.11	Rim 1	oscillatory	0.05598	0.00099	0.56000	0.01218	0.07247	0.00135	0.9	452	8	452	10	451	8	0.1	451	15
Ma03a028	2.11	Rim 2	oscillatory	0.05928	0.00107	0.62519	0.01331	0.07653	0.00137	0.8	577	10	493	11	475	9	3.6		
Ma03a029	2.10	Core	bright hom.	0.05890	0.00158	0.76366	0.02246	0.09400	0.00179	0.6	563	15	576	17	579	11	-0.5	578	21
Ma03a030	2.9	Core	bright hom.	0.05399	0.00101	0.42139	0.00940	0.05664	0.00105	0.8	371	7	357	8	355	7	0.5	356	13
Ma03a037	2.8	Rim	homogen.	0.06347	0.00198	0.48787	0.01641	0.05584	0.00110	0.6	724	23	403	14	~~350~~	~~7~~	13.2		
Ma03a038	2.5	Rim	oscillatory	0.05606	0.00105	0.40036	0.00905	0.05189	0.00096	0.8	455	9	342	8	326	6	4.6		
Ma03a039	2.4	Rim	oscillatory	0.05316	0.00114	0.41158	0.00999	0.05627	0.00100	0.7	336	7	350	8	353	6	-0.8	352	12
Ma03a040	2.3	Rim	oscillatory	0.06119	0.00125	0.66275	0.01564	0.07878	0.00144	0.8	646	13	516	12	489	9	5.3		
Ma03a041	2.2	Core	homogen.	0.11853	0.00207	5.14219	0.10783	0.31565	0.00564	0.9	1934	34	1843	39	1768	32	4.1		
Ma03a042	2.1	Core	oscillatory	0.07495	0.00207	0.98946	0.02971	0.09598	0.00184	0.6	1067	29	698	21	~~591~~	~~11~~	15.4		
Ma03a043	3.1	Rim	homogen.	0.06567	0.00128	0.95863	0.02176	0.10611	0.00191	0.8	796	16	683	15	650	12	4.8		
Ma03a044	3.2	Core	oscillatory	0.06295	0.00116	0.98016	0.02176	0.11325	0.00206	0.8	707	13	694	15	692	13	0.3	693	22
Ma03a045	3.3	Core	homog / oscill	0.05762	0.00127	0.62906	0.01596	0.07940	0.00146	0.7	515	11	496	13	493	9	0.6	493	17
Ma03a046	3.5	Rim	oscillatory	0.05689	0.00150	0.42273	0.01236	0.05404	0.00103	0.7	487	13	358	10	339	6	5.2		
Ma03a047	3.6	Rim	oscillatory	0.05328	0.00124	0.39425	0.01047	0.05381	0.00101	0.7	341	8	337	9	338	6	-0.1	338	12
Ma03a048	3.7	Rim	oscillatory	0.05899	0.00118	0.44613	0.01048	0.05497	0.00100	0.8	567	11	375	9	345	6	7.9		
Ma03a049	3.9	Rim	oscillatory	0.06748	0.00116	0.44156	0.00947	0.04758	0.00087	0.8	853	15	371	8	~~300~~	~~5~~	19.3		
Ma03a050	3.11	Rim	oscillatory	0.05652	0.00102	0.46899	0.01034	0.06031	0.00109	0.8	473	9	390	9	378	7	3.3		
Ma03a051	3.12	Rim	oscillatory	0.05688	0.00118	0.44412	0.01086	0.05676	0.00106	0.8	487	10	373	9	356	7	4.6		
Ma03a052	3.14	Rim 1	oscillatory	0.05637	0.00106	0.44367	0.01010	0.05720	0.00104	0.8	467	9	373	8	359	7	3.8		
Ma03a053	3.14	Rim 2	oscillatory	0.05379	0.00123	0.42984	0.01108	0.05804	0.00105	0.7	362	8	363	9	364	7	-0.2	364	13
Ma03a054	3.15	Rim	oscillatory	0.06177	0.00113	0.92193	0.02044	0.10839	0.00197	0.8	666	12	663	15	663	12	0.0	663	21
Ma03a055	3.16	Rim	oscillatory	0.06202	0.00159	0.53367	0.01534	0.06251	0.00118	0.7	675	17	434	12	~~391~~	~~7~~	10.0		
Ma03a056	4.15	Core	bright hom.	0.05822	0.00134	0.45647	0.01192	0.05691	0.00105	0.7	538	12	382	10	357	7	6.5		
Ma07b007	4.14	Core		0.07602	0.00288	1.21505	0.04458	0.11591	0.00198	0.5	1096	41	808	30	~~707~~	~~12~~	12.4		
Ma07b008	4.13	Rim	oscillatory	0.06098	0.00216	0.89421	0.03093	0.10634	0.00184	0.5	639	23	649	22	651	11	-0.4	651	21

Ma07b009	4.12	Rim	oscillatory	0.05411	0.00175	0.42755	0.01342	0.05729	0.00095	0.5	376	12	361	11	359	6	0.6	359	12
Ma07b010	4.11	Core	homog. Bright	0.05360	0.00170	0.38930	0.01190	0.05268	0.00086	0.5	354	11	334	10	331	5	0.9	331	11
Ma07b011	4.10	Core	homog. Bright	0.05771	0.00200	0.45989	0.01571	0.05790	0.00104	0.5	519	18	384	13	363	7	5.6		
Ma07b012	4.9	Rim	oscillatory	0.05930	0.00174	0.74708	0.02118	0.09136	0.00149	0.6	578	17	567	16	564	9	0.5	564	17
Ma07b013	4.8	Core	homog. Bright	0.05934	0.00179	0.74585	0.02199	0.09113	0.00158	0.6	580	17	566	17	562	10	0.6	563	18
Ma07b014	4.8	Rim	oscillatory	0.06135	0.00191	0.46817	0.01390	0.05532	0.00089	0.5	652	20	390	12	~~347~~	~~6~~	11.0		
Ma07b015	4.7	Rim	oscillatory	0.05427	0.00165	0.41287	0.01201	0.05517	0.00087	0.5	382	12	351	10	346	5	1.4	346	11
Ma07b016	4.6	Core	homog. Bright	0.06458	0.00266	1.01036	0.04067	0.11347	0.00196	0.4	761	31	709	29	693	12	2.3	694	22
Ma07b017	4.5	Core	homog. Bright	0.05678	0.00173	0.62266	0.01841	0.07955	0.00132	0.6	483	15	492	15	493	8	-0.4	493	16
Ma07b018	4.4	Core	homog. Bright	0.05297	0.00173	0.42473	0.01335	0.05814	0.00096	0.5	328	11	359	11	364	6	-1.4	364	12
Ma07b019	4.3	Rim	planar comple	0.05968	0.00199	0.46735	0.01509	0.05678	0.00095	0.5	592	20	389	13	356	6	8.6		
Ma07b020	4.2	Core	homog. Bright	0.05597	0.00194	0.56259	0.01922	0.07318	0.00131	0.5	451	16	453	15	455	8	-0.5	455	16
Ma07b021	4.1	Core	homog. Bright	0.05939	0.00179	0.78861	0.02321	0.09639	0.00165	0.6	581	18	590	17	593	10	-0.5	593	19
Ma07b022	5.1	Core	homog. Bright	0.06337	0.00202	0.42780	0.01323	0.04897	0.00083	0.6	721	23	362	11	~~308~~	~~5~~	14.8		
Ma07b028	5.3	Core	homog. Bright	0.05617	0.00185	0.39090	0.01257	0.05051	0.00087	0.5	459	15	335	11	318	5	5.2		
Ma07b029	5.4	Core	homog. Bright	0.06126	0.00193	0.53431	0.01632	0.06327	0.00106	0.5	648	20	435	13	395	7	9.0		
Ma07b030	5.5	Core	homog. Bright	0.07900	0.00285	0.66433	0.02343	0.06115	0.00111	0.5	1172	42	517	18	~~383~~	~~7~~	26.0		
Ma07b031	5.6	Core	homog. Bright	0.05422	0.00184	0.41930	0.01384	0.05611	0.00097	0.5	380	13	356	12	352	6	1.0	352	12
Ma07b032	5.9	Core	homog. Bright	0.05164	0.00156	0.42506	0.01239	0.05971	0.00099	0.6	270	8	360	10	374	6	-3.9		
Ma07b033	5.9	Rim	oscill. & secto	0.05246	0.00155	0.40610	0.01173	0.05615	0.00095	0.6	306	9	346	10	352	6	-1.8		
Ma07b034	5.10	Core	homog. Bright	0.05770	0.00188	0.39327	0.01264	0.04963	0.00088	0.6	518	17	337	11	312	6	7.3		
Ma07b035	5.10	Rim	oscillatory	0.05634	0.00163	0.42535	0.01199	0.05476	0.00092	0.6	466	14	360	10	344	6	4.5		
Ma07b036	5.11	Core	homog. Bright	0.06834	0.00213	1.57077	0.04693	0.16684	0.00275	0.6	879	27	959	29	995	16	-3.7		
Ma07b037	5.12	Core	homog. Bright	0.11320	0.00331	5.84879	0.16637	0.37487	0.00637	0.6	1851	54	1954	56	2052	35	-5.0		
Ma07b038	5.13	Core	homog. Bright	0.06294	0.00227	0.48076	0.01707	0.05560	0.00101	0.5	706	26	399	14	~~349~~	~~6~~	12.5		
Ma07b039	5.13	Rim	oscillatory	0.05464	0.00175	0.45082	0.01380	0.05985	0.00097	0.5	398	13	378	12	375	6	0.8	375	12
Ma07b040	5.14	Core	homog. Dark	0.11627	0.00331	5.92534	0.16160	0.36989	0.00600	0.6	1900	54	1965	54	2029	33	-3.3		
Ma07b041	5.14	Rim	oscillatory	0.05929	0.00185	0.73989	0.02246	0.09062	0.00154	0.6	578	18	562	17	559	9	0.6	560	18
Ma07b042	5.15	Core	homog. Bright	0.05682	0.00184	0.60104	0.01890	0.07674	0.00129	0.5	485	16	478	15	477	8	0.3	477	15
Ma07b043	6.17	Core	homog. Bright	0.06078	0.00230	0.87134	0.03214	0.10419	0.00183	0.5	631	24	636	23	639	11	-0.4	639	21
Ma07b044	6.15	Core	homog. Dark	0.05160	0.00178	0.34810	0.01173	0.04894	0.00083	0.5	268	9	303	10	308	5	-1.6	308	10
Ma07b045	6.13	Rim	oscillatory	0.05368	0.00168	0.41323	0.01251	0.05587	0.00094	0.6	358	11	351	11	350	6	0.2	351	11
Ma07b046	6.10	Rim	oscillatory	0.05536	0.00163	0.45878	0.01298	0.06014	0.00098	0.6	427	13	383	11	376	6	1.8	377	12

19th March 2017, IGG-CNR U.O.S. of Pavia						Data for Wetherill plot[3]					Ages[3]							Concordant ages	
Identifier	Zrc#	Spot location	Zoning	$^{207}Pb/^{206}Pb$	1s abs	$^{207}Pb/^{235}U$	1s abs	$^{206}Pb/^{238}U$	1s abs	Rho	$^{207}Pb/^{206}Pb$	1s abs	$^{207}Pb/^{235}U$	1s abs	$^{206}Pb/^{238}U$	1s abs	% U-Pb disc[4]		2s abs
Sample MFZ4_bis																			
Ap04a008	1.2	Core	oscillatory	0.05316	0.00128	0.36311	0.00739	0.04961	0.00093	0.9	336	8	315	6	312	6	0.8	314	11
Ap04a009	1.3	Core	bright homog.	0.05578	0.00140	0.27317	0.00592	0.03563	0.00067	0.9	444	11	245	5	226	4	8.0		
Ap04a010	1.4	Core	bright homog.	0.06948	0.00177	1.03291	0.02322	0.10781	0.00214	0.9	913	23	720	16	660	13	8.4		
Ap04a011	1.5	Core	oscillatory	0.05927	0.00152	0.77062	0.01706	0.09444	0.00177	0.8	577	15	580	13	582	11	-0.3	581	19
Ap04a012	1.6	Rim	oscillatory	0.05243	0.00132	0.32384	0.00696	0.04491	0.00083	0.9	304	8	285	6	283	5	0.6	284	10
Ap04a013	1.8	Core	dark homog.	0.05190	0.00138	0.34405	0.00810	0.04809	0.00094	0.8	281	7	300	7	303	6	-0.8	302	11
Ap04a014	1.9	Rim	oscillatory	0.08429	0.00199	0.68763	0.01358	0.05931	0.00110	0.9	~~1299~~	~~31~~	~~531~~	~~10~~	~~371~~	~~7~~	30.1		
Ap04a015	1.10	Rim	oscillatory	0.05390	0.00149	0.39027	0.00957	0.05258	0.00101	0.8	367	10	335	8	330	6	1.3	331	12
Ap04a016	1.11	Core	bright homog.	0.06041	0.00149	0.78247	0.01644	0.09426	0.00175	0.9	618	15	587	12	581	11	1.1	586	19
Ap04a017	1.13	Core	oscillatory	0.06895	0.00198	0.50475	0.01281	0.05319	0.00100	0.7	~~897~~	~~26~~	~~415~~	~~11~~	~~334~~	~~6~~	19.5		
Ap04a018	2.13	Core	bright homog.	0.06222	0.00152	0.95734	0.01978	0.11191	0.00207	0.9	682	17	682	14	684	13	-0.3	682	20
Ap04a019	2.12	Rim	oscillatory	0.05749	0.00144	0.59681	0.01283	0.07542	0.00142	0.9	510	13	475	10	469	9	1.4	473	16
Ap04a020	2.10	Rim	oscillatory	0.05211	0.00146	0.29111	0.00732	0.04058	0.00079	0.8	290	8	259	7	256	5	1.2	257	10
Ap04a026	6.10	Core	oscillatory	0.06850	0.00186	0.97614	0.02351	0.10338	0.00204	0.8	884	24	692	17	634	13	8.3		
Ap04a027	7.10	Rim	oscillatory	0.13032	0.00310	6.87918	0.13785	0.38380	0.00716	0.9	2102	50	2096	42	2094	39	0.1	2097	24
Ap04a028	8.8	Core	bright homog.	0.09611	0.00233	0.59201	0.01243	0.04470	0.00087	0.9	~~1550~~	~~37~~	~~472~~	~~10~~	~~282~~	~~6~~	40.3		
Ap04a029	8.6	Core	dark homog.	0.05564	0.00149	0.52835	0.01223	0.06908	0.00129	0.8	438	12	431	10	431	8	0.0	431	15
Ap04a030	8.7	Core	bright homog.	0.11370	0.00323	5.26450	0.13242	0.33673	0.00658	0.8	1859	53	1863	47	1871	37	-0.4	1862	42
Ap04a031	8.4	Rim	oscillatory	0.06835	0.00179	1.37697	0.03126	0.14647	0.00275	0.8	879	23	879	20	881	17	-0.2	879	27
Ap04a032	4.4	Core	oscillatory	0.06214	0.00162	0.72759	0.01621	0.08520	0.00157	0.8	679	18	555	12	527	10	5.1		
~~Ap04a033~~	~~7.3~~	~~Rim~~	~~bright homog.~~	~~0.06224~~	~~0.00251~~	~~0.49775~~	~~0.01880~~	~~0.05803~~	~~0.00121~~	~~0.6~~	~~682~~	~~28~~	~~410~~	~~15~~	~~364~~	~~8~~	~~11.3~~		
Ap04a034	2.2	Rim	oscillatory	0.05242	0.00129	0.29833	0.00615	0.04152	0.00075	0.9	304	7	265	5	262	5	1.1	263	9
Ap04a035	2.3	Core	oscillatory	0.13951	0.00599	7.43270	0.29764	0.38621	0.00918	0.6	2221	95	2165	87	2105	50	2.8		
Ap04a036	6.2	Core	bright homog.	0.05250	0.00129	0.31128	0.00673	0.04312	0.00085	0.9	307	8	275	6	272	5	1.1	274	10
Ap04a037	6.2	Rim	oscillatory	0.06304	0.00155	0.62402	0.01319	0.07196	0.00136	0.9	710	17	492	10	448	8	9.0		
Ap04a038	14.1	Core	dark homog.	0.06095	0.00192	0.86469	0.02506	0.10305	0.00210	0.7	637	20	633	18	632	13	0.1	632	24
~~Ap04a039~~	~~7.4~~	~~Core~~	~~dark homog.~~	~~0.06326~~	~~0.00179~~	~~0.42400~~	~~0.01063~~	~~0.04871~~	~~0.00092~~	~~0.8~~	~~717~~	~~20~~	~~359~~	~~9~~	~~307~~	~~6~~	~~14.6~~		
Ap04a040	7.2	Rim	oscillatory	0.05236	0.00129	0.31909	0.00688	0.04424	0.00085	0.9	301	7	281	6	279	5	0.8	280	10
Ap04a041	13.1	Core	dark homog.	0.05674	0.00146	0.39287	0.00883	0.05031	0.00095	0.8	481	12	336	8	316	6	6.0		
~~Ap04a042~~	~~4.5~~	~~Core~~	~~bright homog.~~	~~0.06044~~	~~0.00159~~	~~0.34103~~	~~0.00780~~	~~0.04098~~	~~0.00077~~	~~0.8~~	~~619~~	~~16~~	~~298~~	~~7~~	~~259~~	~~5~~	~~13.1~~		
~~Ap04a043~~	~~12.9~~	~~Core~~	~~bright homog.~~	~~0.06400~~	~~0.00179~~	~~0.62227~~	~~0.01554~~	~~0.07061~~	~~0.00135~~	~~0.8~~	~~742~~	~~21~~	~~491~~	~~12~~	~~440~~	~~8~~	~~10.5~~		
Ap04a044	3.1	Core	bright homog.	0.06348	0.00173	0.62729	0.01513	0.07176	0.00137	0.8	724	20	494	12	447	9	9.6		
Ap04a045	2.1	Rim	oscillatory	0.05253	0.00134	0.35250	0.00780	0.04874	0.00091	0.8	309	8	307	7	307	6	-0.1	307	11
Ap04a046	14.2	Core	dark homog.	0.06396	0.00155	0.87970	0.01841	0.09983	0.00188	0.9	740	18	641	13	613	12	4.3		
Ap04b007	11.6	Rim	oscillatory	0.06416	0.00101	0.77546	0.01303	0.08776	0.00137	0.9	747	12	583	10	542	8	7.0		
Ap04b008	2.13	Rim	oscillatory	0.05677	0.00110	0.56071	0.01081	0.07155	0.00105	0.8	483	9	452	9	445	7	1.4	447	12
Ap04b009	2.10	Core	dark homog.	0.05627	0.00120	0.57333	0.01256	0.07400	0.00119	0.7	463	10	460	10	460	7	0.0	460	14
~~Ap04b010~~	~~3.9~~	~~Core~~	~~oscillatory~~	~~0.10946~~	~~0.00201~~	~~1.87409~~	~~0.03544~~	~~0.12427~~	~~0.00201~~	~~0.9~~	~~1790~~	~~33~~	~~1072~~	~~20~~	~~755~~	~~12~~	~~29.6~~		
Ap04b011	3.10	Core	bright homog.	0.05910	0.00091	0.74954	0.01162	0.09177	0.00134	0.9	571	9	568	9	566	8	0.3	569	13
Ap04b012	3.11	Core	bright homog.	0.06598	0.00133	1.22850	0.02469	0.13454	0.00210	0.8	806	16	814	16	814	13	0.0	814	22
~~Ap04b013~~	~~4.10~~	~~Core~~	~~bright homog.~~	~~0.34333~~	~~0.00586~~	~~2.46578~~	~~0.04100~~	~~0.05227~~	~~0.00082~~	~~0.9~~	~~3678~~	~~63~~	~~1262~~	~~21~~	~~328~~	~~5~~	~~74.0~~		
~~Ap04b014~~	~~5.8~~	~~Core~~	~~oscillatory~~	~~0.06799~~	~~0.00136~~	~~0.60041~~	~~0.01190~~	~~0.06450~~	~~0.00094~~	~~0.7~~	~~868~~	~~17~~	~~477~~	~~9~~	~~403~~	~~6~~	~~15.6~~		
~~Ap04b015~~	~~5.6~~	~~Rim~~	~~complex z.~~	~~0.47103~~	~~0.01164~~	~~4.98984~~	~~0.10955~~	~~0.07652~~	~~0.00150~~	~~0.9~~	~~4153~~	~~103~~	~~1818~~	~~40~~	~~475~~	~~9~~	~~73.8~~		
~~Ap04b016~~	~~5.4~~	~~Rim~~	~~oscillatory~~	~~0.07956~~	~~0.00180~~	~~1.16919~~	~~0.02664~~	~~0.10752~~	~~0.00166~~	~~0.7~~	~~1186~~	~~27~~	~~786~~	~~18~~	~~658~~	~~10~~	~~16.3~~		
Ap04b017	6.7	~~Core~~	~~bright homog.~~	0.05864	0.00143	0.71449	0.01743	0.08835	0.00143	0.7	554	14	547	13	546	9	0.3	546	17
~~Ap04b018~~	~~6.8~~	~~Core~~	~~dark homog.~~	~~0.07551~~	~~0.00139~~	~~1.12165~~	~~0.02311~~	~~0.10788~~	~~0.00182~~	~~0.8~~	~~1082~~	~~20~~	~~764~~	~~16~~	~~660~~	~~11~~	~~13.5~~		
~~Ap04b019~~	~~6.9~~	~~Core~~	~~oscillatory~~	~~0.16256~~	~~0.00260~~	~~1.79969~~	~~0.03277~~	~~0.08028~~	~~0.00139~~	~~0.9~~	~~2482~~	~~40~~	~~1045~~	~~19~~	~~498~~	~~9~~	~~52.4~~		
Ap04b020	7.7	Rim	oscillatory	0.06272	0.00108	0.60943	0.01184	0.07055	0.00118	0.9	699	12	483	9	439	7	9.1		
Ap04b021	2.8	Core	dark homog.	0.05490	0.00097	0.52315	0.00948	0.06875	0.00108	0.9	408	7	427	8	429	7	-0.3	428	12

Ap04b022	5.2	Core	bright homog.	0.05203	0.00085	0.34624	0.00575	0.04823	0.00072	0.9	287	5	302	5	304	5	-0.6	303	9
Ap04b023	12.5	Core	oscillatory	0.05720	0.00111	0.69498	0.01351	0.08700	0.00134	0.8	499	10	536	10	538	8	-0.4	537	15
Ap04b024	11.5	Core	bright homog.	0.05430	0.00087	0.47081	0.00761	0.06296	0.00091	0.9	384	6	392	6	394	6	-0.5	392	10
~~Ap04b025~~	~~11.2~~	~~Core~~	~~dark homog.~~	~~0.09260~~	~~0.00316~~	~~0.69593~~	~~0.02396~~	~~0.05465~~	~~0.00101~~	~~0.5~~	~~1480~~	~~51~~	~~536~~	~~18~~	~~343~~	~~6~~	~~36.0~~		
Ap04b026	12.3	Rim	oscillatory	0.05097	0.00074	0.30009	0.00474	0.04259	0.00066	1.0	239	3	266	4	269	4	-0.9		
Ap04b027	12.2	Core	oscillatory	0.05120	0.00096	0.30400	0.00569	0.04249	0.00064	0.8	250	5	270	5	268	4	0.5	269	8
Ap04b028	12.1	Rim	oscillatory	0.09852	0.00138	3.75707	0.05430	0.27698	0.00414	0.9	1596	22	1584	23	1576	24	0.5	1588	18
Ap04b029	11.1	Rim	oscillatory	0.05117	0.00172	0.33161	0.01100	0.04695	0.00079	0.5	248	8	291	10	296	5	-1.7	296	10
Ap04b030	9.1	Core	dark homog.	0.05154	0.00089	0.26362	0.00476	0.03715	0.00059	0.9	265	5	238	4	235	4	1.0	236	7
~~Ap04b031~~	~~6.1~~	~~Core~~	~~oscillatory~~	~~1.50604~~	~~1.53538~~	~~-24.42811~~	~~-16.93700~~	~~-0.11782~~	~~-0.11974~~	~~1.5~~	~~5807~~	~~5920~~	~~#VALUE!~~	~~#VALUE!~~	~~-808~~	~~-821~~	~~#VALUE!~~		
Ap04b032	8.3	Rim	oscillatory	0.06051	0.00110	0.33439	0.00631	0.04079	0.00064	0.8	622	11	293	6	258	4	12.0		
Ap04b033	3.3	Core	dark homog.	0.05216	0.00108	0.31349	0.00665	0.04385	0.00070	0.8	292	6	277	6	277	4	0.1	277	9
Ap04b034	7.5	Core	bright homog.	0.05183	0.00086	0.28242	0.00477	0.03957	0.00060	0.9	278	5	253	4	250	4	1.0	251	7
Ap04b035	7.4_B	Core	dark homog.	0.05211	0.00126	0.30509	0.00735	0.04231	0.00068	0.7	290	7	270	7	267	4	1.2	267	8
~~Ap04b036~~	~~6.4~~	~~Core~~	~~bright homog.~~	~~0.06813~~	~~0.00156~~	~~0.43279~~	~~0.01052~~	~~0.04621~~	~~0.00079~~	~~0.7~~	~~873~~	~~20~~	~~365~~	~~9~~	~~291~~	~~5~~	~~20.3~~		
~~Ap04b037~~	~~5.3~~	~~Core~~	~~dark homog.~~	~~0.06029~~	~~0.00135~~	~~0.36291~~	~~0.00824~~	~~0.04457~~	~~0.00073~~	~~0.7~~	~~614~~	~~14~~	~~314~~	~~7~~	~~281~~	~~5~~	~~10.6~~		
Ap04b038	10.5	Core	oscillatory	0.05510	0.00126	0.51161	0.01213	0.06777	0.00114	0.7	416	10	420	10	423	7	-0.8	422	13
Ap04b039	9.2	Core	bright homog.	0.05249	0.00105	0.35987	0.00724	0.04989	0.00075	0.7	307	6	312	6	314	5	-0.6	314	9
Ap04b040	7.1	Core	complex z.	0.06270	0.00181	0.99862	0.02857	0.11550	0.00196	0.6	698	20	703	20	705	12	-0.2	704	22
Ap04b041	8.2	Core	oscillatory	0.05344	0.00072	0.38634	0.00563	0.05258	0.00080	1.0	348	5	332	5	330	5	0.4	336	6
Ap04b042	4.3	Core	dark homog.	0.05651	0.00074	0.59272	0.00853	0.07614	0.00118	0.9	472	6	473	7	473	7	-0.1	472	10
~~Ap04b043~~	~~3.5~~	~~Core~~	~~oscillatory~~	~~7.60871~~	~~14.75232~~	~~-21.23492~~	~~-8.86204~~	~~-0.02030~~	~~-0.03916~~	~~4.6~~	~~7970~~	~~15453~~	~~#VALUE!~~	~~#VALUE!~~	~~-132~~	~~-255~~	~~#VALUE!~~		

07th April 2017, IGG-CNR U.O.S. of Pavia						Data for Wetherill plot[3]					Ages[3]							Concordant ages	
Identifier	Zrc#	Spot location	Zoning	$^{207}Pb/^{206}Pb$	1s abs	$^{207}Pb/^{235}U$	1s abs	$^{206}Pb/^{238}U$	1s abs	Rho	$^{207}Pb/^{206}Pb$	1s abs	$^{207}Pb/^{235}U$	1s abs	$^{206}Pb/^{238}U$	1s abs	% U-Pb disc[4]		2s abs
Sample CdVZ_1																			
Ap04c007	5.1	Core	dark homog.	0.05474	0.00082	0.39641	0.00629	0.05253	0.00092	1.1	402	6	339	5	330	6	2.7		
Ap04c008	5.2	Core	dark homog.	0.06621	0.00123	1.28928	0.02406	0.14127	0.00247	0.9	813	15	841	16	852	15	-1.3		
Ap04c009	5.3	Rim	oscillatory	0.05625	0.00092	0.35978	0.00616	0.04640	0.00082	1.0	462	8	312	5	292	5	6.3		
Ap04c011	5.4	Core	bright homog.	0.06932	0.00127	1.03436	0.01911	0.10823	0.00191	1.0	908	17	721	13	662	12	8.1		
Ap04c012	5.6	Core	oscillatory	0.06535	0.00121	0.93863	0.01846	0.10422	0.00192	0.9	786	15	672	13	639	12	4.9		
Ap04c013	5.7	Core	dark homog.	0.05978	0.00084	0.74279	0.01094	0.09010	0.00156	1.2	596	8	564	8	556	10	1.4		
Ap04c014	5.8	Core	oscillatory	0.06028	0.00102	0.71099	0.01253	0.08558	0.00152	1.0	614	10	545	10	529	9	2.9		
Ap04c015	5.9	Core	complex zon.	0.05346	0.00078	0.37586	0.00590	0.05099	0.00091	1.0	348	5	324	5	321	6	1.0		
~~Ap04c016~~	~~6.9~~	~~Core~~	~~complex zon.~~	~~0.11741~~	~~0.00159~~	~~3.34814~~	~~0.05096~~	~~0.20685~~	~~0.00374~~	~~1.2~~	~~1917~~	~~26~~	~~1492~~	~~23~~	~~1212~~	~~22~~	~~18.8~~		
Ap04c017	6.8	Rim	oscillatory	0.05383	0.00080	0.46150	0.00740	0.06217	0.00111	1.1	364	5	385	6	389	7	-0.9		
Ap04c018	6.4	Core	bright homog.	0.05799	0.00131	0.60987	0.01451	0.07632	0.00147	0.8	529	12	483	11	474	9	1.9		
Ap04c019	6.7	Rim	oscillatory	0.05618	0.00090	0.57552	0.00954	0.07428	0.00131	1.0	459	7	462	8	462	8	-0.1	460	7
Ap04c020	6.6	Rim	oscillatory	0.06243	0.00119	0.85326	0.01691	0.09921	0.00180	0.9	689	13	626	12	610	11	2.7		
Ap04c021	6.5	Rim	oscillatory	0.06050	0.00113	0.80068	0.01533	0.09598	0.00171	0.9	622	12	597	11	591	11	1.1	600	17
Ap04c022	6.3	Core	dark homog.	0.05674	0.00092	0.42174	0.00726	0.05391	0.00097	1.0	481	8	357	6	338	6	5.3		
~~Ap04c030~~	~~6.1B~~	~~Core~~	~~bright homog.~~	~~0.06356~~	~~0.00153~~	~~0.46490~~	~~0.01144~~	~~0.05305~~	~~0.00099~~	~~0.8~~	~~727~~	~~17~~	~~388~~	~~10~~	~~333~~	~~6~~	~~14.0~~		
Ap04c031	6.1B	Rim	oscillatory	0.05359	0.00091	0.37580	0.00678	0.05086	0.00092	1.0	354	6	324	6	320	6	1.3		
Ap04c032	6.2	Core	dark homog.	0.05306	0.00082	0.42456	0.00704	0.05803	0.00104	1.1	331	5	359	6	364	7	-1.2		
Ap04c033	7.8	Core	bright homog.	0.05122	0.00076	0.34599	0.00554	0.04901	0.00088	1.1	251	4	302	5	308	6	-2.2		
Ap04c034	7.7	Core	complex zon.	0.05427	0.00102	0.32058	0.00660	0.04284	0.00083	0.9	382	7	282	6	270	5	4.2		
Ap04c035	8.9	Core	bright homog.	0.05621	0.00090	0.60332	0.01018	0.07780	0.00138	1.1	461	7	479	8	483	9	-0.8		
Ap04c036	8.8	Rim	oscillatory	0.19075	0.00274	16.86322	0.26246	0.64110	0.01155	1.2	2749	40	2927	46	3193	58	-9.1		
Ap04c037	8.7	Core	bright homog.	0.06294	0.00122	0.70257	0.01436	0.08095	0.00149	0.9	706	14	540	11	502	9	7.1		
Ap04c038	8.6	Core	bright homog.	0.06676	0.00101	1.01729	0.01649	0.11052	0.00197	1.1	830	13	713	12	676	12	5.2		
Ap04c039	8.5	Rim	oscillatory	0.07466	0.00165	1.58135	0.03617	0.15347	0.00287	0.8	1059	23	963	22	920	17	4.4		
Ap04c040	9.5	Core	bright homog.	0.05438	0.00092	0.43196	0.00772	0.05763	0.00105	1.0	387	7	365	7	361	7	0.9		
Ap04c041	9.4	Rim	oscillatory	0.05299	0.00092	0.38439	0.00697	0.05263	0.00094	1.0	328	6	330	6	331	6	-0.1	329	9
Ap04c042	10.6	Core	oscillatory	0.05688	0.00107	0.59440	0.01154	0.07582	0.00137	0.9	487	9	474	9	471	9	0.5	474	15
Ap04c043	10.4	Rim	oscillatory	0.05669	0.00099	0.43675	0.00789	0.05591	0.00100	1.0	479	8	368	7	351	6	4.7		
Ap04c044	11.5	Core	bright homog.	0.14793	0.00221	8.77791	0.13641	0.43133	0.00764	1.0	2322	35	2315	36	2312	41	0.2	2317	7
Ap04c045	11.9	Core	complex zon.	0.05353	0.00077	0.42312	0.00653	0.05736	0.00102	1.0	351	5	358	6	360	6	-0.4	355	5
Ap04c046	11.10	Core	oscillatory	0.05351	0.00125	0.37926	0.00902	0.05144	0.00094	0.8	350	8	326	8	323	6	1.0	324	11
Ap05a007	21.12	Rim	oscillatory	0.06792	0.00124	0.88388	0.01728	0.09445	0.00131	0.7	866	16	643	13	582	8	9.5		
Ap05a008	21.11	Rim	oscillatory	0.05666	0.00129	0.61161	0.01438	0.07832	0.00110	0.6	478	11	485	11	486	7	-0.3	486	13
~~Ap05a009~~	~~21.11~~	~~Rim~~	~~oscillatory~~	~~0.06506~~	~~0.00125~~	~~0.65666~~	~~0.01357~~	~~0.07323~~	~~0.00104~~	~~0.7~~	~~776~~	~~15~~	~~513~~	~~11~~	~~456~~	~~6~~	~~11.1~~		
Ap05a010	21.10	Core	oscillatory	0.05294	0.00113	0.37386	0.00845	0.05123	0.00073	0.6	326	7	323	7	322	5	0.1	322	9
Ap05a011	21.8	Core	oscillatory	0.05241	0.00110	0.37755	0.00861	0.05226	0.00078	0.7	303	6	325	7	328	5	-1.0	328	10
Ap05a012	21.8	Rim	oscillatory	0.05374	0.00115	0.36500	0.00838	0.04926	0.00073	0.6	360	8	316	7	310	5	1.9	311	9
Ap05a013	21.7	Rim	oscillatory	0.06301	0.00162	1.02248	0.02738	0.11775	0.00175	0.6	709	18	715	19	718	11	-0.3	717	20
Ap05a014	21.6	Core	complex zon.	0.06253	0.00117	0.99269	0.02007	0.11519	0.00163	0.7	692	13	700	14	703	10	-0.4	702	18
~~Ap05a015~~	~~21.4~~	~~Core~~	~~oscillatory~~	~~0.15623~~	~~0.00270~~	~~7.13826~~	~~0.14083~~	~~0.33142~~	~~0.00495~~	~~0.8~~	~~2415~~	~~42~~	~~2129~~	~~42~~	~~1845~~	~~28~~	~~13.3~~		
Ap05a016	20.2	Core	bright homog.	0.05853	0.00155	0.72994	0.02038	0.09047	0.00144	0.6	550	15	557	16	558	9	-0.3	558	17
Ap05a017	20.3	Core	complex zon.	0.06603	0.00208	1.00390	0.03217	0.11029	0.00173	0.5	807	25	706	23	674	11	4.4		
Ap05a018	20.5	Rim	oscillatory	0.05587	0.00138	0.40318	0.01054	0.05232	0.00082	0.6	447	11	344	9	329	5	4.4		
Ap05a019	20.8	Core	oscillatory	0.05377	0.00108	0.38907	0.00851	0.05248	0.00077	0.7	361	7	334	7	330	5	1.2	330	9
Ap05a020	20.7	Core	oscillatory	0.05755	0.00114	0.40995	0.00887	0.05167	0.00076	0.7	513	10	349	8	325	5	6.9		
~~Ap05a021~~	~~20.9~~	~~Core~~	~~dark homog.~~	~~0.06134~~	~~0.00144~~	~~0.42796~~	~~0.01067~~	~~0.05060~~	~~0.00077~~	~~0.6~~	~~651~~	~~15~~	~~362~~	~~9~~	~~318~~	~~5~~	~~12.0~~		
Ap05a023	17.8	Core	bright homog.	0.05385	0.00116	0.38056	0.00899	0.05125	0.00079	0.7	365	8	327	8	322	5	1.6	323	10
~~Ap05a024~~	~~18.5~~	~~Core~~	~~oscillatory~~	~~0.06563~~	~~0.00130~~	~~0.73516~~	~~0.01560~~	~~0.08127~~	~~0.00116~~	~~0.7~~	~~795~~	~~16~~	~~560~~	~~12~~	~~504~~	~~7~~	~~10.0~~		
Ap05a025	19.11	Core	bright homog.	0.06141	0.00144	0.52412	0.01311	0.06190	0.00096	0.6	654	15	428	11	387	6	9.5		

Ap05a026	19.9	Rim	oscillatory	0.05302	0.00119	0.36993	0.00865	0.05061	0.00071	0.6	330	7	320	7	318	4	0.4	318	9
Ap05a027	19.9	Core	dark homog.	0.05614	0.00110	0.39739	0.00837	0.05135	0.00072	0.7	458	9	340	7	323	5	5.0		
~~Ap05a028~~	~~19.7~~	~~Core~~	~~bright homog.~~	~~0.12652~~	~~0.00224~~	~~5.02247~~	~~0.09886~~	~~0.28792~~	~~0.00416~~	~~0.7~~	~~2050~~	~~36~~	~~1823~~	~~36~~	~~1631~~	~~24~~	~~10.5~~		
Ap05a029	19.8	Core	complex zon.	0.07638	0.00145	1.55907	0.03274	0.14804	0.00221	0.7	1105	21	954	20	890	13	6.7		
Ap05a036	20.10	Rim	oscillatory	0.05242	0.00151	0.38114	0.01128	0.05273	0.00079	0.5	304	9	328	10	331	5	-1.0	331	10
Ap05a037	17.9	Core	oscillatory	0.05600	0.00126	0.54548	0.01309	0.07063	0.00105	0.6	452	10	442	11	440	7	0.5	440	13
Ap05a038	16.9	Core	oscillatory	0.05997	0.00118	0.80451	0.01702	0.09729	0.00138	0.7	602	12	599	13	599	8	0.1	599	16
~~Ap05a039~~	~~13.9~~	~~Core~~	~~oscillatory~~	~~0.06205~~	~~0.00147~~	~~0.46137~~	~~0.01159~~	~~0.05391~~	~~0.00081~~	~~0.6~~	~~676~~	~~16~~	~~385~~	~~10~~	~~338~~	~~5~~	~~12.1~~		
Ap05a040	13.8	Core	oscillatory	0.05557	0.00134	0.39481	0.00979	0.05153	0.00072	0.6	435	10	338	8	324	5	4.1		
Ap05a041	13.6	Core	oscillatory	0.05478	0.00133	0.45727	0.01133	0.06055	0.00084	0.6	403	10	382	9	379	5	0.9	379	10
Ap05a042	13.7	Core	complex zon.	0.06388	0.00114	1.04843	0.02085	0.11902	0.00173	0.7	738	13	728	14	725	11	0.4	726	19
~~Ap05a043~~	~~13.5~~	~~Rim~~	~~oscillatory~~	~~0.12332~~	~~0.00214~~	~~4.73700~~	~~0.09214~~	~~0.27855~~	~~0.00402~~	~~0.7~~	~~2005~~	~~35~~	~~1774~~	~~35~~	~~1584~~	~~23~~	~~10.7~~		
Ap05a044	13.4	Core	complex zon.	0.05864	0.00119	0.68493	0.01506	0.08471	0.00124	0.7	554	11	530	12	524	8	1.1	525	14
~~Ap05a045~~	~~13.3~~	~~Core~~	~~bright homog.~~	~~0.06131~~	~~0.00144~~	~~0.42890~~	~~0.01071~~	~~0.05072~~	~~0.00076~~	~~0.6~~	~~650~~	~~15~~	~~362~~	~~9~~	~~319~~	~~5~~	~~12.0~~		
Ap05a046	13.2	Rim	oscillatory	0.06008	0.00149	0.50815	0.01320	0.06132	0.00092	0.6	606	15	417	11	384	6	8.0		
~~Ap05a047~~	~~14.3~~	~~Rim~~	~~oscillatory~~	~~0.06095~~	~~0.00120~~	~~0.41293~~	~~0.00889~~	~~0.04913~~	~~0.00072~~	~~0.7~~	~~637~~	~~13~~	~~351~~	~~8~~	~~309~~	~~5~~	~~11.9~~		
Ap05a048	14.2	Core	dark homog.	0.05573	0.00114	0.37326	0.00826	0.04856	0.00071	0.7	442	9	322	7	306	4	5.1		
Ap05a049	14.4	~~Core~~	~~complex zon.~~	0.06093	0.00118	1.13495	0.02435	0.13505	0.00199	0.7	637	12	770	17	817	12	-6.0		
Ap05a050	14.1	Rim	oscillatory	0.05711	0.00104	0.61041	0.01219	0.07753	0.00111	0.7	496	9	484	10	481	7	0.5	482	13
Ap05a051	15.2	~~Rim~~	~~oscillatory~~	0.20176	0.00348	15.61243	0.29719	0.56115	0.00786	0.7	2840	49	2853	54	2871	40	-0.6	2850	35
~~Ap05a052~~	~~16.4~~	~~Core~~	~~complex zon.~~	~~0.06788~~	~~0.00142~~	~~0.44024~~	~~0.01005~~	~~0.04705~~	~~0.00072~~	~~0.7~~	~~865~~	~~18~~	~~370~~	~~8~~	~~296~~	~~5~~	~~20.0~~		
Ap05a053	17.4	~~Core~~	~~complex zon.~~	0.05444	0.00187	0.43431	0.01516	0.05789	0.00090	0.4	389	13	366	13	363	6	0.9	363	11
Ap05a054	17.5	~~Rim~~	~~oscillatory~~	0.05439	0.00121	0.40796	0.00982	0.05440	0.00082	0.6	387	9	347	8	341	5	1.7	342	10

05th April2017, IGG-CNR U.O.S. of Pavia						Data for Wetherill plot[3]							Ages[3]						Concordant ages	
Identifier	Zrc#	Spot location	Zoning	$^{207}Pb/^{206}Pb$	1s abs	$^{207}Pb/^{235}U$	1s abs	$^{206}Pb/^{238}U$	1s abs	Rho	$^{207}Pb/^{206}Pb$	1s abs	$^{207}Pb/^{235}U$	1s abs	$^{206}Pb/^{238}U$	1s abs	% U-Pb disc[4]		2s abs
Sample CdVZ_4																			
Ap05b007	14.1	Core	complex zon.	0.05255	0.00097	0.37873	0.00854	0.05227	0.00086	0.7	309	6	326	7	328	5	-0.7	328	10
Ap05b008	8.15	Rim	oscillatory	0.05511	0.00086	0.53936	0.01082	0.07095	0.00113	0.8	417	7	438	9	442	7	-0.9	440	13
Ap05b009	8.14	Core	oscillatory	0.05170	0.00097	0.34691	0.00787	0.04868	0.00080	0.7	272	5	302	7	306	5	-1.3	306	10
~~Ap05b010~~	~~8.11~~	~~Rim~~	~~oscillatory~~	~~0.06767~~	~~0.00121~~	~~0.21694~~	~~0.00468~~	~~0.02324~~	~~0.00037~~	~~0.7~~	~~858~~	~~15~~	~~199~~	~~4~~	~~148~~	~~2~~	~~25.7~~		
Ap05b011	8.12	Rim	oscillatory	0.05341	0.00083	0.54053	0.01086	0.07340	0.00118	0.8	346	5	439	9	457	7	-4.1		
Ap05b012	8.13	Core	complex zon.	0.05487	0.00115	0.33101	0.00814	0.04373	0.00072	0.7	407	9	290	7	276	5	5.0		
Ap05b013	6.3	Core	complex zon.	0.05354	0.00084	0.39378	0.00803	0.05335	0.00087	0.8	352	6	337	7	335	5	0.6	336	11
Ap05b014	6.2	Rim	oscillatory	0.05345	0.00100	0.34630	0.00788	0.04699	0.00077	0.7	348	7	302	7	296	5	2.0	297	10
Ap05b015	13.1	Core	bright homog.	0.05526	0.00087	0.53279	0.01092	0.06994	0.00114	0.8	423	7	434	9	436	7	-0.5	435	13
Ap05b016	13.2	Core	oscillatory	0.05408	0.00092	0.70192	0.01512	0.09413	0.00156	0.8	374	6	540	12	580	10	-7.4		
Ap05b017	16.13	Rim	oscillatory	0.05306	0.00107	0.36042	0.00872	0.04927	0.00084	0.7	331	7	313	8	310	5	0.8	310	10
Ap05b018	16.13	Core	complex zon.	0.05357	0.00118	0.39565	0.01006	0.05357	0.00090	0.7	353	8	338	9	336	6	0.6	337	11
Ap05b019	15.15	Core	dark homog.	0.05341	0.00080	0.39854	0.00792	0.05412	0.00088	0.8	346	5	341	7	340	6	0.2	340	11
~~Ap05b020~~	~~15.16~~	~~Core~~	~~dark homog.~~	~~0.10188~~	~~0.00151~~	~~0.69013~~	~~0.01389~~	~~0.04915~~	~~0.00083~~	~~0.8~~	~~1659~~	~~25~~	~~533~~	~~11~~	~~309~~	~~5~~	~~42.0~~		
Ap05b021	15.15	Core	oscillatory	0.05312	0.00175	0.38137	0.01324	0.05200	0.00090	0.5	334	11	328	11	327	6	0.4	327	11
Ap05b022	15.14	Core	bright homog.	0.16796	0.00271	10.63650	0.21864	0.45899	0.00754	0.8	2537	41	2492	51	2435	40	2.3		
Ap05b023	14.11	Core	oscillatory	0.05977	0.00100	0.83374	0.01766	0.10116	0.00166	0.8	595	10	616	13	621	10	-0.9	618	18
Ap05b027	12.13	Core	oscillatory	0.05503	0.00090	0.50874	0.01068	0.06705	0.00110	0.8	413	7	418	9	418	7	-0.2	418	13
Ap05b028	12.14	Rim	oscillatory	0.05950	0.00088	0.79529	0.01580	0.09694	0.00159	0.8	585	9	594	12	596	10	-0.4	595	17
Ap05b029	12.12	Core	bright homog.	0.05444	0.00096	0.43668	0.00962	0.05817	0.00096	0.8	389	7	368	8	364	6	0.9	365	12
Ap05b030	12.11	Core	oscillatory	0.05260	0.00083	0.38092	0.00778	0.05252	0.00086	0.8	312	5	328	7	330	5	-0.7	329	10
Ap05b032	11.14	Core	bright homog.	0.05355	0.00104	0.40646	0.00946	0.05505	0.00091	0.7	352	7	346	8	345	6	0.3	346	11
Ap05b033	11.15	Rim	oscillatory	0.05301	0.00092	0.57545	0.01282	0.07872	0.00136	0.8	329	6	462	10	488	8	-5.8		
Ap05b034	11.13	Core	bright homog.	0.05998	0.00096	0.76293	0.01571	0.09222	0.00151	0.8	603	10	576	12	569	9	1.2	572	17
Ap05b035	11.12	Rim	oscillatory	0.05014	0.00081	0.39620	0.00825	0.05731	0.00094	0.8	201	3	339	7	359	6	-6.0		
~~Ap05b038~~	~~15.13~~	~~Rim~~	~~oscillatory~~	~~0.13252~~	~~0.00251~~	~~1.82596~~	~~0.04093~~	~~0.09989~~	~~0.00164~~	~~0.7~~	~~2132~~	~~40~~	~~1055~~	~~24~~	~~614~~	~~10~~	~~41.8~~		
Ap05b039	15.12	Rim	oscillatory	0.05836	0.00133	0.43512	0.01140	0.05409	0.00094	0.7	543	12	367	10	340	6	7.4		
Ap05b040	15.12	Core	complex zon.	0.05566	0.00094	0.69494	0.01467	0.09054	0.00146	0.8	439	7	536	11	559	9	-4.3		
Ap05b041	15.8	Core	oscillatory	0.05421	0.00102	0.42040	0.00951	0.05623	0.00092	0.7	380	7	356	8	353	6	1.0	353	11
Ap05b042	15.7	Core	complex zon.	0.04981	0.00082	0.36575	0.00767	0.05325	0.00088	0.8	186	3	316	7	334	6	-5.7		
Ap05b043	15.3	Core	oscillatory	0.05106	0.00088	0.37939	0.00822	0.05389	0.00089	0.8	244	4	327	7	338	6	-3.6		
Ap05b044	15.2	Core	bright homog.	0.05997	0.00110	0.81135	0.01825	0.09811	0.00164	0.7	602	11	603	14	603	10	0.0	603	18
~~Ap05c007~~	~~7.1~~	~~Core~~	~~dark homog.~~	~~0.06359~~	~~0.00174~~	~~0.46864~~	~~0.01435~~	~~0.05346~~	~~0.00097~~	~~0.6~~	~~728~~	~~20~~	~~390~~	~~12~~	~~336~~	~~6~~	~~14.0~~		
Ap05c008	14.2	Rim	oscillatory	0.05255	0.00118	0.34829	0.00934	0.04808	0.00087	0.7	309	7	303	8	303	5	0.2	303	11
Ap05c010	14.4	Core	oscillatory	0.05399	0.00153	0.41972	0.01315	0.05641	0.00100	0.6	371	11	356	11	354	6	0.6	354	12
Ap05c011	14.5	Rim	oscillatory	0.06143	0.00146	0.79903	0.02194	0.09435	0.00166	0.6	654	16	596	16	581	10	2.5		
~~Ap05c012~~	~~14.6~~	~~Core~~	~~oscillatory~~	~~0.06975~~	~~0.00153~~	~~0.58204~~	~~0.01532~~	~~0.06052~~	~~0.00109~~	~~0.7~~	~~921~~	~~20~~	~~466~~	~~12~~	~~379~~	~~7~~	~~18.7~~		
~~Ap05c014~~	~~14.7~~	~~Core~~	~~oscillatory~~	~~0.08189~~	~~0.00184~~	~~0.63584~~	~~0.01714~~	~~0.05635~~	~~0.00104~~	~~0.7~~	~~1243~~	~~28~~	~~500~~	~~13~~	~~353~~	~~7~~	~~29.3~~		
~~Ap05c015~~	7.3	Core	oscillatory	~~0.06035~~	~~0.00173~~	~~0.43583~~	~~0.01380~~	~~0.05239~~	~~0.00094~~	~~0.6~~	~~616~~	~~18~~	~~367~~	~~12~~	~~329~~	~~6~~	~~10.4~~		
~~Ap05c016~~	7.2	Rim	oscillatory	~~0.07001~~	~~0.00182~~	~~0.79837~~	~~0.02362~~	~~0.08272~~	~~0.00151~~	~~0.6~~	~~929~~	~~24~~	~~596~~	~~18~~	~~512~~	~~9~~	~~14.0~~		
Ap05c017	12.5	Core	dark homog.	0.05496	0.00120	0.54183	0.01422	0.07152	0.00128	0.7	411	9	440	12	445	8	-1.3	444	15
Ap05c018	12.8	Rim	complex zon.	0.05482	0.00126	0.41836	0.01133	0.05534	0.00099	0.7	405	9	355	10	347	6	2.2	348	12
Ap05c019	11.7	Rim	oscillatory	0.05609	0.00127	0.55505	0.01472	0.07182	0.00125	0.7	456	10	448	12	447	8	0.3	447	15
Ap05c020	11.6	Core	bright homog.	0.06000	0.00133	0.86307	0.02290	0.10428	0.00187	0.7	604	13	632	17	639	11	-1.2	637	21
Ap05c021	11.5	Rim	oscillatory	0.06163	0.00130	0.89854	0.02312	0.10577	0.00189	0.7	661	14	651	17	648	12	0.4	649	21
Ap05c027	10.15	Core	oscillatory	0.05354	0.00116	0.39506	0.01030	0.05353	0.00096	0.7	352	8	338	9	336	6	0.6	336	12
Ap05c028	10.13	Core	dark homog.	0.05829	0.00141	0.61691	0.01761	0.07672	0.00142	0.6	541	13	488	14	477	9	2.3	478	17
~~Ap05c029~~	~~10.16~~	~~Core~~	~~oscillatory~~	~~0.05978~~	~~0.00132~~	~~0.29575~~	~~0.00791~~	~~0.03589~~	~~0.00065~~	~~0.7~~	~~596~~	~~13~~	~~263~~	~~7~~	~~227~~	~~4~~	~~13.6~~		
Ap05c030	10.12	Rim	oscillatory	0.05717	0.00138	0.62329	0.01738	0.07913	0.00141	0.6	498	12	492	14	491	9	0.2	491	17
Ap05c031	10.10	Rim	oscillatory	0.05536	0.00123	0.55189	0.01473	0.07232	0.00130	0.7	427	10	446	12	450	8	-0.9	449	15
Ap05c032	11.5	Core	oscillatory	0.05271	0.00115	0.35206	0.00927	0.04845	0.00087	0.7	316	7	306	8	305	5	0.4	305	11

Ap05c033	11.6	Rim	oscillatory	0.05886	0.00138	0.43519	0.01201	0.05363	0.00097	0.7	562	13	367	10	337	6	8.2		
Ap05c034	11.7	Core	bright homog.	0.05689	0.00142	0.56662	0.01658	0.07225	0.00137	0.6	487	12	456	13	450	9	1.3	451	16
~~Ap05c035~~	~~11.8~~	~~Core~~	~~oscillatory~~	~~0.07381~~	~~0.00189~~	~~0.53047~~	~~0.01536~~	~~0.05218~~	~~0.00093~~	~~0.6~~	~~1036~~	~~27~~	~~432~~	~~13~~	~~328~~	~~6~~	~~24.1~~		
Ap05c037	14.10	Core	complex zon.	0.05380	0.00129	0.40158	0.01133	0.05415	0.00099	0.7	363	9	343	10	340	6	0.8	340	12
Ap05c038	9.10 B	Rim	oscillatory	0.06004	0.00153	0.80096	0.02339	0.09676	0.00175	0.6	605	15	597	17	595	11	0.3	596	20
Ap05c039	9.8	Rim	oscillatory	0.05823	0.00135	0.72185	0.01952	0.09013	0.00159	0.7	538	12	552	15	556	10	-0.8	555	18
Ap05c040	9.7	Core	oscillatory	0.05861	0.00128	0.75526	0.01983	0.09348	0.00167	0.7	553	12	571	15	576	10	-0.8	575	19
Ap05c041	9.9	Rim	oscillatory	0.05234	0.00131	0.32175	0.00924	0.04458	0.00080	0.6	300	7	283	8	281	5	0.7	281	10
~~Ap05c042~~	~~9.1~~	~~Core~~	~~complex zon.~~	~~0.20002~~	~~0.00432~~	~~14.43106~~	~~0.38217~~	~~0.52321~~	~~0.00980~~	~~0.7~~	~~2826~~	~~61~~	~~2778~~	~~74~~	~~2713~~	~~51~~	~~2.4~~		
Ap05c043	9.11	Core	oscillatory	0.05350	0.00157	0.38180	0.01235	0.05190	0.00094	0.6	350	10	328	11	326	6	0.7	326	11
Ap05c044	9.11 B	Core	bright homog.	0.05585	0.00162	0.36940	0.01191	0.04796	0.00090	0.6	446	13	319	10	302	6	5.4		
~~Ap05c045~~	~~9.13~~	~~Rim~~	~~oscillatory~~	~~0.05999~~	~~0.00142~~	~~0.81671~~	~~0.02268~~	~~0.09880~~	~~0.00179~~	~~0.7~~	~~603~~	~~14~~	~~606~~	~~17~~	~~607~~	~~11~~	~~-0.2~~	~~607~~	~~20~~
Ap05c046	9.13 B	Rim	complex zon.	0.05560	0.00141	0.54388	0.01604	0.07096	0.00133	0.6	436	11	441	13	442	8	-0.2	442	16
Ap06a007	16.3	Rim	oscillatory	0.05340	0.00094	0.38877	0.00673	0.05283	0.00101	1.0	346	6	333	6	332	6	0.5	337	6
Ap06a008	16.1	Core	oscillatory	0.06779	0.00156	0.30232	0.00698	0.03236	0.00066	0.9	862	20	268	6	205	4	23.5		
~~Ap06a009~~	~~16.2~~	~~Rim~~	~~oscillatory~~	~~0.11584~~	~~0.00181~~	~~4.77246~~	~~0.06930~~	~~0.29940~~	~~0.00553~~	~~1.3~~	~~1893~~	~~30~~	~~1780~~	~~26~~	~~1688~~	~~31~~	~~5.2~~		
~~Ap06a010~~	~~16.6~~	~~Core~~	~~complex zon.~~	~~0.05996~~	~~0.00096~~	~~0.76638~~	~~0.01215~~	~~0.09287~~	~~0.00179~~	~~1.0~~	~~602~~	~~10~~	~~578~~	~~9~~	~~572~~	~~11~~	~~0.9~~	~~586~~	~~6~~
Ap06a011	16.7	Rim	oscillatory	0.05657	0.00091	0.58440	0.00915	0.07496	0.00142	1.0	475	8	467	7	466	9	0.3	470	5
Ap06a012	16.8	Core	complex zon.	0.05627	0.00110	0.31837	0.00625	0.04106	0.00082	1.0	463	9	281	6	259	5	7.6		
Ap06a014	16.9	Core	bright homog.	0.05592	0.00085	0.56517	0.00838	0.07334	0.00138	1.0	449	7	455	7	456	9	-0.3	453	5
~~Ap06a015~~	~~16.10~~	~~Core~~	~~oscillatory~~	~~0.06318~~	~~0.00100~~	~~1.05072~~	~~0.01610~~	~~0.12069~~	~~0.00228~~	~~1.0~~	~~714~~	~~11~~	~~729~~	~~11~~	~~735~~	~~14~~	~~-0.7~~	~~722~~	~~6~~
Ap06a016	16.12	Rim	oscillatory	0.05339	0.00087	0.42162	0.00666	0.05730	0.00109	1.0	345	6	357	6	359	7	-0.6	353	4

APPENDIX 2.2: Standard tables (LA-ICP-MS)

IGG-CNR U.O.S. of Pavia		$^{207}Pb/^{206}Pb$			$^{207}Pb/^{235}U$			$^{206}Pb/^{238}U$			Ages[3]					
Identifier	Comments	Ratio	1σ %	1σ % (Prop	Ratio	1σ %	1σ % (Prop	Ratio	1σ %	1σ % (Prop	$^{207}Pb/^{206}Pb$	1σ abs	$^{207}Pb/^{235}U$	1σ abs	$^{206}Pb/^{238}U$	1σ abs
Sample MFZ1_bis																
Ma03a002		0.06059	0.07%	0.10%	0.82364	1.43%	1.75%	0.09859	0.17%	0.20%	625	11	610	13	606	12
Ma03a003		0.06005	0.07%	0.10%	0.79656	1.38%	1.69%	0.09615	0.16%	0.19%	605	10	595	13	592	12
Ma03a004		0.05975	0.07%	0.10%	0.8086	1.41%	1.72%	0.09806	0.17%	0.19%	595	10	602	13	603	12
Ma03a031		0.05917	0.08%	0.11%	0.80276	1.43%	1.74%	0.09846	0.15%	0.18%	573	10	598	13	605	11
Ma03a032		0.06133	0.08%	0.11%	0.81834	1.46%	1.77%	0.09686	0.15%	0.18%	651	12	607	13	596	11
Ma03a058		0.06009	0.09%	0.11%	0.80858	1.60%	1.88%	0.09761	0.15%	0.18%	607	11	602	14	600	11
Ma07b004		0.06019	0.08%	0.18%	0.80984	1.40%	2.32%	0.09759	0.15%	0.16%	610	18	602	17	600	10
Ma07b023		0.05944	0.08%	0.18%	0.80736	1.38%	2.31%	0.0985	0.15%	0.16%	583	17	601	17	606	10
Ma07b024		0.06062	0.08%	0.18%	0.8083	1.38%	2.31%	0.0967	0.15%	0.16%	626	19	601	17	595	10
Ma07b047		0.06263	0.08%	0.18%	0.83905	1.42%	2.39%	0.09725	0.15%	0.16%	696	20	619	18	598	10
Ma07b048		0.05833	0.08%	0.17%	0.78696	1.33%	2.24%	0.09794	0.15%	0.16%	542	16	589	17	602	10
Sample MFZ4_bis																
Ap04a003		0.06032	0.08%	0.15%	0.81071	1.23%	1.76%	0.09754	0.13%	0.18%	615	16	603	13	600	11
Ap04a004		0.06057	0.08%	0.15%	0.80099	1.19%	1.72%	0.09599	0.13%	0.18%	624	16	597	13	591	11
Ap04a005		0.05939	0.08%	0.15%	0.81639	1.22%	1.76%	0.09978	0.13%	0.19%	581	15	606	13	613	12
Ap04a021		0.06231	0.08%	0.16%	0.82715	1.22%	1.77%	0.0965	0.12%	0.18%	685	17	612	13	594	11
Ap04a022		0.05813	0.08%	0.15%	0.79105	1.20%	1.71%	0.09892	0.13%	0.19%	535	13	592	13	608	11
Ap04a047		0.05968	0.09%	0.15%	0.79956	1.31%	1.81%	0.09722	0.13%	0.18%	592	15	597	13	598	11
Ap04a050		0.06055	0.09%	0.16%	0.81804	1.35%	1.86%	0.09796	0.13%	0.19%	623	16	607	14	602	11
Ap04b002		0.06065	0.08%	0.10%	0.81606	1.26%	1.37%	0.09761	0.13%	0.15%	627	10	606	10	600	9
Ap04b004		0.05955	0.08%	0.10%	0.80332	1.29%	1.39%	0.09789	0.13%	0.15%	587	10	599	10	602	9
Ap04b046		0.06002	0.08%	0.09%	0.81453	1.22%	1.33%	0.09848	0.13%	0.15%	604	9	605	10	605	9
Ap04b048		0.0607	0.08%	0.09%	0.80817	1.18%	1.30%	0.09657	0.13%	0.15%	629	9	601	10	594	9
Ap04b050		0.0599	0.08%	0.09%	0.81397	1.24%	1.35%	0.09856	0.13%	0.16%	600	9	605	10	606	10
Sample CdVZ_1																
Ap04c001		0.05968	0.08%	0.09%	0.80993	1.26%	1.32%	0.09848	0.13%	0.17%	592	9	602	10	605	11
Ap04c002		0.06002	0.08%	0.09%	0.8108	1.28%	1.34%	0.09803	0.13%	0.17%	604	10	603	10	603	11
Ap04c003		0.06096	0.08%	0.10%	0.80693	1.28%	1.34%	0.09605	0.13%	0.17%	638	10	601	10	591	10
Ap04c024		0.06026	0.08%	0.10%	0.81537	1.34%	1.40%	0.09813	0.14%	0.18%	613	10	605	10	603	11
Ap04c025		0.05994	0.08%	0.10%	0.80335	1.32%	1.38%	0.09719	0.14%	0.17%	601	10	599	10	598	11
Ap04c048		0.06001	0.08%	0.10%	0.81205	1.31%	1.37%	0.0982	0.14%	0.18%	604	10	604	10	604	11

Ap04c049	0.05953	0.08%	0.10%	0.81155	1.33%	1.39%	0.09894	0.14%	0.18%	587	10	603	10	608	11
Ap04c050	0.06085	0.08%	0.10%	0.80501	1.30%	1.36%	0.09601	0.13%	0.17%	634	10	600	10	591	11
Ap05a001	0.05942	0.07%	0.11%	0.80293	1.21%	1.63%	0.09803	0.13%	0.14%	583	11	598	12	603	9
Ap05a002	0.06101	0.08%	0.12%	0.81689	1.24%	1.66%	0.09715	0.13%	0.14%	640	12	606	12	598	8
Ap05a033	0.05999	0.08%	0.11%	0.80747	1.30%	1.70%	0.09762	0.14%	0.14%	603	12	601	13	600	9
Ap05a059	0.06106	0.08%	0.11%	0.82384	1.27%	1.69%	0.09785	0.14%	0.14%	641	12	610	13	602	9
Ap05a060	0.0593	0.07%	0.11%	0.79622	1.23%	1.64%	0.09737	0.14%	0.14%	578	11	595	12	599	9
Sample CdVZ_4															
Ap05b001	0.05972	0.07%	0.10%	0.80424	1.20%	1.70%	0.0977	0.13%	0.16%	593	10	599	13	601	10
Ap05b002	0.06127	0.08%	0.10%	0.82615	1.24%	1.75%	0.09782	0.13%	0.16%	649	11	611	13	602	10
Ap05b003	0.05945	0.08%	0.10%	0.8078	1.22%	1.73%	0.09857	0.14%	0.16%	584	10	601	13	606	10
Ap05b024	0.06041	0.08%	0.10%	0.80959	1.21%	1.72%	0.09719	0.13%	0.16%	618	10	602	13	598	10
Ap05b025	0.05987	0.07%	0.10%	0.79307	1.19%	1.69%	0.09607	0.13%	0.16%	599	10	593	13	591	10
Ap05b048	0.06074	0.08%	0.10%	0.82613	1.26%	1.77%	0.09864	0.14%	0.16%	630	11	611	13	606	10
Ap05b049	0.05954	0.08%	0.10%	0.80312	1.23%	1.73%	0.09782	0.14%	0.16%	587	10	599	13	602	10
Ap05c002	0.06157	0.08%	0.14%	0.82386	1.27%	2.18%	0.09707	0.14%	0.17%	659	15	610	16	597	11
Ap05c003	0.06125	0.08%	0.14%	0.83254	1.29%	2.21%	0.09861	0.14%	0.18%	648	14	615	16	606	11
Ap05c004	0.05809	0.08%	0.13%	0.78165	1.24%	2.09%	0.09761	0.14%	0.18%	533	12	586	16	600	11
Ap05c022	0.05892	0.08%	0.13%	0.79675	1.27%	2.13%	0.0981	0.14%	0.18%	564	13	595	16	603	11
Ap05c023	0.06034	0.08%	0.14%	0.81681	1.32%	2.20%	0.0982	0.14%	0.18%	616	14	606	16	604	11
Ap05c024	0.05984	0.08%	0.14%	0.78788	1.28%	2.13%	0.09551	0.13%	0.17%	598	14	590	16	588	11
Ap05c048	0.06041	0.08%	0.14%	0.82402	1.33%	2.22%	0.09896	0.14%	0.18%	618	14	610	16	608	11
Ap05c049	0.0607	0.08%	0.14%	0.80658	1.30%	2.17%	0.0964	0.13%	0.17%	629	14	601	16	593	11
Ap05c050	0.06007	0.08%	0.14%	0.81307	1.33%	2.20%	0.09818	0.14%	0.18%	606	14	604	16	604	11
Ap06a001	0.0604	0.07%	0.09%	0.80379	1.15%	1.24%	0.09657	0.13%	0.19%	618	10	599	9	594	11
Ap06a002	0.05956	0.07%	0.09%	0.81653	1.19%	1.28%	0.09949	0.13%	0.19%	588	9	606	9	611	12
Ap06a004	0.06041	0.08%	0.10%	0.81033	1.18%	1.27%	0.09734	0.13%	0.19%	618	10	603	9	599	11
Ap06a017	0.0608	0.08%	0.10%	0.80808	1.23%	1.31%	0.09645	0.12%	0.18%	632	11	601	10	594	11
Ap06a018	0.05944	0.08%	0.10%	0.80921	1.25%	1.33%	0.09878	0.13%	0.19%	583	10	602	10	607	11